VOLUME 75 JANUARY 7, 1971 NUMBER 1

JPCHAx

THE JOURNAL OF PHYSICAL CHEMISTRY

PUBLISHED BIWEEKLY BY THE AMERICAN CHEMICAL SOCIETY

RADIATION CHEMISTRY

ADVANCES IN CHEMISTRY SERIES NOS. 81 AND 82

Seventy-seven papers and 34 abstracts from the International Conference on Radiation Chemistry at Argonne National Laboratories, chaired by Edwin J. Hart. Includes review and research papers from 12 countries besides U.S., Canada, and England, including 8 from U.S.S.R. and two other East European countries.

Volume I groups papers on radiation in aqueous media, radiation of biological systems, dosimetry, and one plenary lecture.

Volume II has papers on radiation of gases, of solids, and of organic liquids, plus three plenary lectures.

No. 81 Radiation Chemistry—I — 616 pages with index
No. 82 Radiation Chemistry—II — 558 pages with index
Each $16.00
Cloth (1968) Ordered together $30.00

Set of L.C. cards free with library orders.

Other books in the ADVANCES IN CHEMISTRY SERIES in physical and colloid chemistry include:

No. 68 Mössbauer Effect and its Application in Chemistry. Ten papers that will familiarize chemists with Mössbauer spectroscopy as an analytical tool, for studying chemical bonding, crystal structure, electron density, magnetism, and other properties. 178 pages
Cloth (1967) $8.00

No. 67 Equilibrium Concepts in Natural Water Systems. Sixteen papers represent the collaboration of aquatic chemists, analytical chemists, geologists, oceanographers, limnologists, and sanitary engineers, working with simplified models to produce fruitful generalizations and valuable insights into the factors that control the chemistry of natural systems. 344 pages
Cloth (1967) $11.00

No. 64 Regenerative EMF Cells. Seventeen papers survey current progress and research on regenerative systems for converting and storing electrical energy. Principal emphasis is on thermally regenerative systems, but chemical and photochemical systems are considered. 309 pages
Cloth (1967) $11.00

No. 63 Ordered Fluids and Liquid Crystals. Twenty-two studies on characterization, properties, and occurance of these phenomena in many substances such as tristearin, p-azoxyanisole, mono-and di-hydric alcohols, phospholipids and polypeptides. 332 pages
Cloth (1967) $11.50

No. 58 Ion-Molecule Reactions in the Gas Phase. Eighteen papers survey spectrometric and other methods for producing and studying ion-molecule reactions, such as pulsed sources for studing thermal ions, reactions in flames and electrical discharges. 336 pages
Cloth (1966) $10.50

No. 54 Advanced Propellant Chemistry. Primarily directed to the search for new oxidizers; 26 papers survey oxygen-containing oxidizers, fuels and binders, fluorine systems including oxygen difluoride and difluoramines and liquid systems. 290 pages
Cloth (1966) $10.50

No. 47 Fuel Cell Systems. Developments in theory, performance, construction, and new systems for the energy converter that is proving itself in military and space uses. 360 pages
Cloth (1965) $10.50

No. 43 Contact Angle, Wettability, and Adhesion. Twenty-six papers on theoretical and practical approaches to wettability and adhesion; with summary of the surface chemical studies of W. A. Zisman, the 1963 Kendall Award winner. 389 pages
Cloth (1964) $10.50

No. 40 Mass Spectral Correlations. By Fred W. McLafferty. Over 4000 spectral listed by mass/charge ratios of fragment ions with the most probable original structures for each. 117 pages
Paper (1963) $6.00

No. 33 Solid Surfaces and the Gas-Solid Interface. Thirty-seven papers from the Kendall Award Symposium honoring Stephen Brunauer. Theory and techniques for studying surface phenomena.
Cloth (1961) $12.00

No. 31 Critical Solution Temperatures. By Alfred W. Francis. CST answers the question, "Do two liquids mix?" and is widely used for screening solvents. Over 6000 systems are included, 70% with a hydrocarbon as one component; nearly 1100 non-hydrocarbon solvents are listed. 246 pages
Cloth (1961) $8.00

No. 29 Physical Properties of Chemical Compounds—III. By Robert R. Dreisbach. Supplements earlier volumes with properties of 434 aliphatic compounds and 22 miscellaneous compounds and elements. Index to volumes I, II, and III. 489 pages
Cloth (1961) $10.00

No. 25 Physical Functions of Hydrocolloids. Papers on natural gums, gelatin pectins and related polysaccharides, and theoretical and functional aspects of hydrocolloids, emulsions, foams, and dispersions. Strong food industry emphasis. 103 pages
Paper (1960) $5.00

No. 22 Physical Properties of Chemical Compounds—II. By Robert R. Dreisbach. Properties of 476 alkanes, haloalkanes, alkenes, haloalkenes, diolefins, and alkynes. 491 pages
Cloth (1959) $10.00

No. 18 Thermodynamic Properties of the Elements. By D. R. Stull and G. C. Sinke. Tabulated values of heat capacity, heat content, entropy, and free energy function of solid, liquid, and gas states of first 92 elements in range of 298° to 3000°K. Some auxiliary data frequently included.
Cloth (1956) $8.00

No. 15 Physical Properties of Chemical Compounds. By Robert R. Dreisbach. Tables of parameters for calculating physical properties of 511 organic cyclic compounds. 536 pages
Cloth (1955) $10.00

All books postpaid in U.S. and Canada; plus 30 cents in PUAS and elsewhere.

Order from: SPECIAL ISSUES SALES,
AMERICAN CHEMICAL SOCIETY
1155 SIXTEENTH ST., N.W.
WASHINGTON, D.C. 20036

THE JOURNAL OF PHYSICAL CHEMISTRY

Volume 75

JANUARY—APRIL 1971

PAGES 1—1332

THE JOURNAL OF

PHYSICAL CHEMISTRY

AMERICAN CHEMICAL SOCIETY, PUBLICATIONS DIVISION,
1155 Sixteenth St., N.W., Washington, D. C. 20036
RICHARD L. KENYON, *Director*
JOSEPH H. KUNEY, *Director of Business Operations and Director of Publications Research*
DAVID E. GUSHEE, *Publication Manager, Journals*

 Published biweekly by the American Chemical Society at 20th and Northampton Sts., Easton, Pa. 18042. Second-class postage paid at Easton, Pa.

All manuscripts should be sent to *The Journal of Physical Chemistry*, Department of Chemistry, University of Minnesota, Minneapolis, Minn. 55455.

Additions and Corrections are published once yearly in the final issue. See Volume 74, Number 26 for the proper form.

Extensive or unusual alterations in an article after it has been set in type are made at the author's expense, and it is understood that by requesting such alterations the author agrees to defray the cost thereof.

The American Chemical Society and the Editor of *The Journal of Physical Chemistry* assume no responsibility for the statements and opinions advanced by contributors.

Correspondence regarding accepted copy, proofs, and reprints should be directed to Editorial Production Office, American Chemical Society, 20th and Northampton Sts., Easton, Pa. 18042. Manager: CHARLES R. BERTSCH. Assistant Editor: EDWARD A. BORGER. Editorial Assistant: EVELYN J. UHLER.

Advertising Office: Century Communications Corporation, 142 East Avenue, Norwalk, Conn. 06851.

Business and Subscription Information

Remittances and orders for subscriptions and for single copies, notices of changes of address and new professional connections, and claims for missing numbers should be sent to the Subscription Service Department, American Chemical Society, 1155 Sixteenth St., N.W., Washington, D. C. 20036. Allow 4 weeks for changes of address. Please include an old address label with the notification.

Claims for missing numbers will not be allowed (1) if received more than sixty days from date of issue, (2) if loss was due to failure of notice of change of address to be received before the date specified in the preceding paragraph, or (3) if the reason for the claim is "missing from files."

Subscription rates (1971): members of the American Chemical Society, $20.00 for 1 year; to nonmembers, $40.00 for 1 year. Those interested in becoming members should write to the Admissions Department, American Chemical Society, 1155 Sixteenth St., N.W., Washington, D. C. 20036. Postage to Canada and countries in the Pan-American Union, $4.00; all other countries, $5.00. Single copies for current year: $2.00. Rates for back issues from Volume 56 to date are available from the Special Issues Sales Department, 1155 Sixteenth St., N.W., Washington, D. C. 20036.

This publication and the other ACS periodical publications are now available on microfilm. For information write to: MICROFILM, Special Issues Sales Department, 1155 Sixteenth St., N.W., Washington, D. C. 20036.

Notice to Authors last printed in the issue of December 24, 1970

The Range of Research in Physical And So Is the List of Books

REACTIONS UNDER PLASMA CONDITIONS
Volume I

Edited by MUNDIYATH VENUGOPALAN, *Western Illinois University*

This is the first part of an important new two-volume survey of the fundamental physical theories and properties of matter in the plasma state. Volume I emphasizes plasma physics and plasma diagnostics, making it particularly valuable to physicists. The volumes deal with the types of reactions that can be achieved in a plasma medium—with special emphasis on the reaction-kinetical process—and the practical methods that can be applied for their investigation in both natural and laboratory physics. 1971 In press

PHYSICAL CHEMISTRY OF ADHESION

By D. H. KAELBLE, *North American Rockwell Corporation*

This book treats the fields of thermodynamics, surface chemistry, polymer physics, rheology, and specialized topics in the mechanics of fracture. The book is intended to introduce, develop, and interconnect these outwardly unrelated subjects in relation to adhesion and cohesion, and to familiarize the chemist and physicist with the basic concepts and theories in these fields. The author has included historical discussions to acquaint the reader with classical viewpoints, and introduces new theoretical propositions and derivations.

1971 528 pages In press

MOLECULAR PHOTOELECTRON SPECTROSCOPY
A Handbook of the He584 Spectra

By D. W. TURNER, *University of Oxford, England;* C. BAKER, *B. P. Chemicals, Surrey, England;* A. D. BAKER, *Swansea University, England;* and C. R. BRUNDLE, *Bell Telephone Laboratories, New Jersey*

A convenient reference book for researchers, this is essentially an account of the work done by a pioneering group of workers in the field of photoelectron spectroscopy. In the basic format of a handbook, it presents over 300 D.E. spectra using the Helium Resonance Line. It gives a general account of the underlying physical nature of the processes involved and of the experimental techniques developed by the authors in the course of their work. This volume is the first extensive compilation of the photoelectron spectra of gaseous molecules ranging from atoms and diatomic molecules through complex organic and inorganic systems.

1970 386 pages $19.50

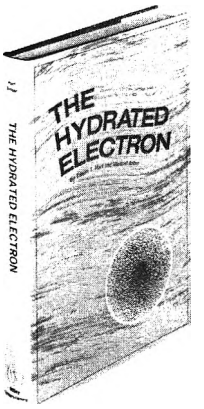

THE HYDRATED ELECTRON

By EDWIN J. HART, *Argonne National Laboratory;* and MICHAEL ANBAR, *Stanford Research Institute*

"Discovered by radiation chemists within the last decade, the hydrated electron ranks with the hydrogen and hydroxide ions as fundamental species of aqueous solutions. . . ."
—*from the Preface*

Devoted to the present and potential importance of the hydrated electron, this monograph concentrates on its physical and chemical characteristics. It also reviews the peripheral topics of radiation chemistry, solvated electrons, and pulse radiolysis. With comprehensive coverage of this new field, the book will be an indispensable aid to researchers working in this or related fields. 1970 267 pages $12.95

SURFACE AND COLLOID SCIENCE
Volume 3

Edited by EGON MATIJEVIC, *Clarkson College of Technology*

"On the whole, these volumes comprise a good beginning for the fulfillment of the editors' aim of providing a comprehensive treatise on surface and colloid science. It is hoped that future volumes will continue to maintain the standards set here. . . ."—from a review of Volumes 1 and 2 in *Science*

Volume 3, the most recent volume in this series, continues the high standards and comprehensive coverage of its predecessors. Since the field of surface and colloid science covers a wide range of topics, the articles include many interdisciplinary aspects of physics, chemistry, biology, and engineering. 1971 320 pages $16.95

CHEMICAL AND MECHANICAL BEHAVIOR OF INORGANIC MATERIALS

Edited by ALAN W. SEARCY, *University of California, Berkeley;* DAVID RAGONE, *Carnegie-Mellon University;* and UMBERTO COLOMBO, *Montecatini Edison Company, Novara, Italy*

Of value to all workers in the fields of materials science, this is a comprehensive review of the present status of many specialty fields in this research area. The articles cover such topics as the evaporation of inorganic materials, thermodynamics and kinetics, dislocations and fracture, and the kinetics of densification. The papers comprising the book come from the two-week advanced course on ceramic science presented at the first International Conference on Materials Science, sponsored by Academia Nazionale del Lincei, at Tremezzo, Italy, in 1968. 1970 715 pages $27.50

THE JOURNAL OF

PHYSICAL CHEMISTRY

Volume 75, Number 1 January 7, 1971

NOTES

COMMUNICATIONS TO THE EDITOR

AUTHOR INDEX

THE JOURNAL OF
PHYSICAL CHEMISTRY

VOLUME 75, NUMBER 1 JANUARY 7, 1971

Shock Tube Experiments on the Pyrolysis of Deuterium-Substituted Ethylenes

by Gordon B. Skinner,* Ronald C. Sweet, and Steven K. Davis

Department of Chemistry, Wright State University, Dayton, Ohio 45431 *(Received February 25, 1970)*

Publication costs assisted by the Petroleum Research Fund

Dilute mixtures of C_2H_4, $C_2H_4 + C_2D_4$, *trans*-1,2-$C_2H_2D_2$, and $C_2H_2 + D_2$ in argon were pyrolyzed in a single-pulse shock tube. Empirically, in ethylene pyrolysis the order with respect to argon was 0 ± 0.2, and that with respect to ethylene 1.2 ± 0.2. Pyrolysis data are summarized in terms of first-order (in ethylene) rate constants as follows: $8.9 \times 10^8 e^{-46,400/RT}$ sec^{-1} for 0.1% C_2H_4, $1.05 \times 10^9 e^{-48,800/RT}$ sec^{-1} for 0.05% C_2H_4 + 0.05% C_2D_4 and 0.1% $C_2H_2D_2$, and $1.8 \times 10^9 e^{-48,800/RT}$ sec^{-1} for 0.25% C_2H_4 + 0.25% C_2D_4 and 0.5% $C_2H_2D_2$, at 3 atm total reaction pressure, and 1100–1500°K. The isotopic distribution of ethylene after reaction indicated that isotope exchange is nearly first order in ethylene, the rate constant for the step producing C_2H_3D and C_2HD_3 from C_2H_4 and C_2D_4 being $3.4 \times 10^7 e^{-32,000/RT}$ sec^{-1}. Rates of subsequent steps are governed by the statistics of the reactions. Isotope distributions of acetylene and hydrogen (the chief decomposition products of ethylene) and of ethylene produced by hydrogenation of acetylene indicate that both ethylene decomposition and acetylene hydrogenation occur by free-radical rather than molecular mechanisms. Isotope exchange reactions were considerably faster than either ethylene decomposition or acetylene hydrogenation.

Introduction

During the past 10 years several experimental studies[1-5] of ethylene pyrolysis have been made using the shock tube technique. The temperature range covered has been 1150–2250°K. In all cases the ethylene was diluted with an inert gas, the partial pressure of ethylene ranging from 0.02 to 1 atm during the reaction. There is general agreement that under these conditions ethylene decomposes primarily to acetylene and hydrogen, and that the rate of the reaction shows approximately first-order dependence on the ethylene concentration. Gay, Kern, Kistiakowsky, and Niki[4] included some experiments with deuterium-substituted ethylene, while Bauer[6] has reported on the reaction between ethylene and deuterium.

However, all these experimental results have been insufficient to establish what the mechanism of ethylene pyrolysis is. Benson and Haugen[7] made a kinetic analysis of the reaction, concluding that a free-radical chain should predominate in the lower part of the temperature range, while elimination of molecular hydrogen should predominate at higher temperatures. They made an effort to correlate all available data, both kinetic and thermodynamic, in their analysis, but did not predict the temperature dependence of the pyrolysis reaction very well.

It seemed highly desirable to carry out further pyrolysis experiments using deuterium-substituted ethylenes. The product distributions from these experiments can provide direct evidence as to the type of reaction occurring (free radical or molecular) and also provide addi-

(1) G. B. Skinner and E. M. Sokoloski, *J. Phys. Chem.*, **64**, 1028 (1960).

(2) T. Asaba, K. Yoneda, and T. Hikita, *Kogyo Kagaku Zasshi*, **65**, 1811 (1962).

(3) G. I. Kozlov and V. G. Knorre, *Kinet. Katal.*, **4**, 189 (1963).

(4) I. D Gay, R. D. Kern, G. B. Kistiakowsky, and H. Niki, *J. Chem. Phys.*, **45**, 2371 (1966).

(5) J. B Homer and G. B. Kistiakowsky, *ibid.*, **47**, 5290 (1967).

(6) S. H Bauer, *Symp. (Int.) Combust. Proc.*, **11**, 105 (1967).

(7) S. W. Benson and G. R. Haugen, *J. Phys. Chem.*, **71**, 1735 (1967).

tional data of a kind not previously available for testing proposed reaction mechanisms.

Study of the hydrogenation of acetylene is another approach to the understanding of this reaction system. Skinner and Sokoloski[1] carried out some hydrogenation experiments, and Benson and Haugen[7] included them in their kinetic analysis. Kuratani and Bauer[8] studied the reaction of C_2H_2 with D_2 in terms of the exchange reaction, but reported only a cursory look, with essentially negative results, into the formation of ethylenes. Accordingly, it seemed useful to study the isotope distribution of ethylenes produced by this reaction.

Experimental Section

A single-pulse shock tube of the general nature of that described by Lifshitz, Bauer, and Resler[9] was used. The reaction section was 1.8 m long and 3.9 cm in diameter, with an expansion tank of 110-l. capacity attached by a short length of 3.9-cm pipe at a point 15 cm downstream from the diaphragm. The driver section was also 3.9 cm in diameter and of variable length, but a typical length was about 1.8 m.

For measuring the incident shock speed, SLM Model 603 pressure transducers spaced 75 cm apart near the downstream end of the reaction section were used. A third transducer could be mounted midway between these two to permit measurements of shock attenuation. Transducer outputs were amplified by identical circuits and used to start and stop a microsecond timer and also to start an oscilloscope. This recorded the pressure, by means of another SLM transducer mounted 5 cm from the downstream end of the reaction section. Directly opposite the transducer was a valve through which samples could be drawn for analysis.

The temperature (T_5) and pressure (P_5) behind the reflected shock wave as it began to move away from the end plate of the tube were calculated from the shock speed, corrected for the attenuation observed in calibration experiments. The pressure record showed that the pressure immediately behind the reflected shock wave was within 2% of that calculated from the speed of the incident wave (allowing for attenuation). For the first millisecond after passage of the reflected wave the pressure rose slowly to about 10% above its initial value, and subsequently fell slowly back to near its initial value. The pressure drop is probably due to some loss of gas into the expansion tank. Typical dwell times were 5 msec, followed by a rapid expansion at a typical initial rate of 3×10^5°K per second. The cooling part of the process would contribute approximately 2% of the total reaction for an activation energy of 50 kcal, and 12% for 20 kcal, in our temperature range.

To allow for these pressure changes, it was assumed that T_5 and P_5 were actually realized just behind the reflected shock wave, and that subsequent pressure changes caused changes in temperature given by the adiabatic equation

$$\frac{T}{T_5} = \left(\frac{P}{P_5}\right)^{(\gamma-1)/\gamma}$$

where γ is the specific heat ratio C_p/C_v. This is reasonable since pressure drift behind the reflected shock is essentially shockless and therefore involves negligible entropy changes. A graph of T *vs.* time was plotted for each run, and the arithmetic average temperature was taken as the temperature of the run. (In kinetic calculations the actual time–temperature history of each sample was used. This average temperature is simply a nominal one for identification and plotting graphs.)

Consideration has been given to heat losses from the samples to the shock tube walls. To do this it is first necessary to define the sample that was taken for analysis. This was 150 cc in volume and would occupy 21 cm of shock tube length. Since the total gas sample would (with no interfacial mixing) occupy a total length of 100 cm after the expansion of the driver gas into the tank, the sample taken for analysis is about one-fifth of the total. Since the gas sampling valve was small, it took 2 or 3 sec to withdraw the sample, so that the gas flow in the shock tube during the process would be laminar (Reynolds number ~300), and along the tube axis some gas could have been drawn from as far as 40 cm from the end. A considerable amount of radial mixing probably occurred during and after the expansion of the sample, but to the extent that this was incomplete we tended to sample the central part of the sample rather than the boundary layer. In view of the above discussion, we consider that our analytical samples are representative of the 30% of the total sample nearest the end wall of the shock tube, and have based our further analysis on this assumption.

This part of the gas sample is traversed by the incident shock wave (in a typical experiment) in 0.7 msec, and by the reflected shock wave in 0.2 msec. It is compressed to 10-cm length by the latter wave, and at the end of the 5-msec heating period the expansion wave traverses the sample in about 0.1 msec. It is clear that the whole 10-cm long sample experiences essentially the same interval of heating behind the reflected shock (during which reaction occurs) and that times and temperatures derived from pressure measurements made 5 cm from the end plate are good average ones over the small range that exists. Boundary-layer cooling behind the incident wave occurs over a period of 0.9 msec for the part of the gas sample first heated (and of course zero time for the part last heated), for an average of 0.5 msec. Behind the reflected shock, the hot gas may

(8) K. Kuratani and S. H. Bauer, *J. Amer. Chem. Soc.*, **87**, 150 (1965).

(9) A. Lifshitz, S. H. Bauer, and E. L. Resler, Jr., *J. Chem. Phys.*, **38**, 2056 (1963).

lose heat to the shock tube walls for 5 msec, a considerably longer period.

In a discussion of shock tube experiments under conditions very similar to ours, Tschuikow-Roux and Marte[10] pointed out that the incident shock boundary layer will be turbulent in most of the range of interest and indicated a method of obtaining temperatures in the boundary layer. If it is assumed that the gas in the boundary layer is brought to rest by the combination of a reflected shock weaker than that in the free stream, and an isentropic compression to equalize the pressure across the tube, an approximate temperature profile of the boundary layer behind the reflected shock may be obtained. In the rather narrow operating range we used (initial gas pressures 80–130 Torr, final pressure 3 atm in all but one series of experiments, final temperature 1100–1500°K, for a reaction with an activation energy of 50 kcal with low conversion), this boundary-layer cooling reduces the extent of reaction to about 88% of that with no cooling. Reaction is almost entirely suppressed in the 0.8 mm of original sample adjacent to the walls, and significantly affected out to about 2 mm from the walls. For higher conversions the effect is less, and at high enough temperatures conversions will approach 100%.

Heat transfer from the stagnant gas during the 5-msec dwell time is due primarily to conduction[11] and the temperature effects may be calculated using Goldsworthy's approach.[12] If it is assumed that the gas is all at the same initial temperature, and the wall temperature does not change, his relationship may be written

$$T_s(t) = T_w + (T_\infty - T_w)\,\mathrm{erf}\frac{\rho_\infty Y_s(t=0)}{2(k_1 pt/C_p R)^{1/2}}$$

where t = time, starting with $t = 0$ at the instant the wall and gas first come in contact at the high temperature condition; $T_s(t)$ = temperature at time t of an element of gas that was originally at a distance Y_s from the wall; T_w = wall temperature; T_∞ = initial gas temperature; erf = error function; ρ_∞ = initial gas density; $Y_s(t = 0)$ = distance of an element of gas from the wall at time zero; k_1 = coefficient in the equation k(thermal conductivity) = $k_1 T$(absolute temperature);[13] p = pressure of the gas; C_p = specific heat of the gas at constant pressure; R = gas constant.

This equation makes no allowance for temperature changes due to chemical reaction. If these are small (as in our experiments), they may be included as correction terms in Goldsworthy's equation.[14] The equation was derived for a flat plate and has been used for this purpose by Dove and Moulton[15] but will be valid for a tube as long as the boundary layer is thin compared to the tube radius. In our configuration the end plate of the tube has an area 10% that of the curved surface involved. The correct overall surface-to-volume ratio can be maintained by using a tube radius of 1.75 cm instead of 1.95, and leaving out any reference to the end plate.

By numerical integration over small annular volume elements and time increments, we have calculated the chemical conversion expected with wall cooling behind the reflected shock *only*, and found that under the typical conditions given above, and a dwell time of 5 msec, the calculated conversion is 0.86 of that for no cooling. When the effects of both incident and reflected boundary-layer cooling are combined, the calculated conversion is 0.80 of that for no cooling. The effects of the two parts of the wall cooling process are not additive, since once a temperature gradient is established near the wall, further development of the gradient proceeds more slowly. For an activation energy of 20 kcal and otherwise similar conditions, the calculated fraction is 0.84.

The method of calculation was checked experimentally by comparison of observed and calculated conversions of ethylene with acetylene at high temperatures, where conversions are high and relatively insensitive to changes in rate constant (see Table I). The kinetic data for the calculations were obtained by extrapolation of lower temperature data. In these experiments the dwell time was about 1.5 msec. The fact that 90–94% of the ethylene was converted into acetylene indicates that the bulk of the sample was experiencing close to ideal shock conditions. Since the calculations account for the residual ethylene reason-

Table I: Test of the Calculations for Wall Cooling

Mol % C_2H_4 originally present	Run temp, °K	Fraction ethylene remaining		
			Calculated	
		Observed	No wall cooling	With wall cooling
0.25	1986	0.062	0.000	0.057
1.00	1884	0.092	0.026	0.108
1.00	2052	0.057	0.000	0.031

(10) E. Tschuikow-Roux and J. E. Marte, *J. Chem. Phys.*, **42**, 2049 (1965).

(11) K. Scheller, *Dissertation Abstr.*, **30**, 2668-B (1969).

(12) F. A. Goldsworthy, *J. Fluid Mech.*, **5**, 164 (1959).

(13) In fact, the thermal conductivity of argon in the range of interest depends on the temperature to the 0.7 to 0.8 power, but the first-power assumption simplified the mathematics without introducing a serious error.

(14) This method of calculating heat losses was brought to our attention by Professor Assa Lifshitz, who has recently completed several detailed calculations, and a series of experiments which verifies them. We have used Professor Lifshitz' nomenclature. This work has been published recently: A. Lifshitz, A. Bar-Nun, P. C. T. de Boer, and E. L. Resler, Jr., *J. Chem. Phys.*, **53**, 3050 (1970).

(15) J. E. Dove and D. McL. Moulton, *Proc. Roy. Soc., Ser. A*, **283**, 216 (1965).

ably well, they were used in obtaining kinetic data from all of our experimental results.

Gas mixtures were made up beforehand by pressure, and the concentration of each gas was known within 1–2% of its value. All of the mixtures were analyzed by gas chromatograph and mass spectrometer before use. Argon, helium (driver gas), and acetylene from Air Reduction Co., reasearch grade ethylene and CP grade deuterium from Matheson Co., and ethylene-d_4 and *trans*-ethylene-d_2 from Merck, Sharp and Dohme of Canada were used without further purification. Somewhat to our surprise, even a sample of acetylene withdrawn from the cylinder without any trap to collect solvent showed only a few ppm impurities on the mass spectrometer.

The shock tube was evacuated to below 5 μ pressure before each run and had a leak rate below 1 μ/min. Since the tube was filled with argon just before final evacuation, this evacuation took about 3 min, and about 1 min was required to introduce the sample and driver gases, we consider that the maximum air contamination is 5 μ, or 1 μ of oxygen, the active ingredient. A special series of experiments was carried out to see what effect, if any, this would have on the pyrolysis reactions.

Small amounts of argon were usually mixed with the helium driver gas in the shock tube, to minimize shock interaction at the sample-driver interface.

Gas samples were analyzed before and after reaction for ethylene, ethane, acetylene, and methane with a gas chromatograph fitted with a flame ionization detector. Hydrogen and helium could be determined on another column fitted with a thermocouple detector. Small amounts of helium from the driver gas (typically 1–5%) were found in the samples. Hydrogen and helium were also determined by mass spectrometer (Consolidated Model 21-104) using 18-V ionizing potential to minimize the contributions to the hydrogen peaks due to dissociation of the hydrocarbons. Samples of ethylene and acetylene separated on the gas chromatograph were collected and analyzed for isotopic distribution on the mass spectrometer. Of the three ethylene-d_2 species, a partial separation of 1,1- from 1,2-ethylene-d_2 could be made, but the mass spectrometer could not distinguish between *cis*- and *trans*-ethylene-d_2. For most of the runs only the total ethylene-d_2 concentration could be found.

Results

Ten gas mixtures were used in this study. Besides the argon diluent, the various samples contained the following mol % of reactants.

6	0.1% C_2H_4
7	0.25% C_2H_4 + 0.25% C_2D_4
8	0.05% C_2H_4 + 0.05% C_2D_4
9	0.5% *trans*-1,2-$C_2H_2D_2$
10	0.1% *trans*-1,2-$C_2H_2D_2$
11	5% C_2H_2 + 10% D_2
12	0.25% C_2H_4
13	1.0% C_2H_4
14	0.25% C_2H_4 + 0.0052% O_2
15	0.25% C_2H_4 + 0.025% O_2

Four types of data for mixtures 6–10 were obtained: total amount of ethylene pyrolyzed, and isotopic distributions of ethylene, acetylene, and hydrogen. For mixtures 12–15, only the total amount of pyrolysis was measured. These data are listed below, followed by the results for mixture 11.

Pyrolysis of Ethylene. Since previous experience showed that ethylene pyrolysis under these conditions is nearly first order in ethylene concentration, equations for first-order rate constants were calculated. The procedure was to assume "reasonable" values of A and B in an Arrhenius-type equation

$$\log k = A + B/T$$

calculate the conversion of ethylene to be expected in each run and compare this with the observed conversion. The calculations took into account the actual time–temperature history of the runs obtained from the pressure records, corrected for the heat absorbed by the pyrolysis reaction and for cooling by the walls of the shock tube. Successive approximations to A and B were made until the average of the observed/calculated ratios was unity and independent of temperature for the set of runs under consideration. Reflected shock pressures for mixtures 6–10 were 3.0 ± 0.1 atm.

We used the equation obtained in our earlier paper[1] for mixture 1 (0.5% C_2H_4 in argon) as a first approximation for the present mixture 6, and came close to a good fit to the data. We also found that the data of mixtures 7 and 9, and 8 and 10, gave identical equations. The coefficients are listed in Table II. The standard deviation of log (observed conversion/calculated conversion) was 0.07 to 0.08 in each calculation, corresponding to a standard deviation of 20% in the rate constant, k. In order to simplify the comparison of the 7, 9 and 8, 10 data, empirical curves were calculated using the average of the activation energies calculated for the two sets of data (48.8 kcal), thereby allowing all of the differences to show up in the constant term. This increased the standard deviation of log (observed conversion/calculated conversion) by only about 5%. Since the difference between the A values for the two sets of data is 0.24, or about 3 standard deviations, it may be significant. If it is attributed to the difference in ethylene concentration in the two sets of data, the implication is that the empirical reac-

Table II: Constants in the Empirical Rate Equations for Ethylene Pyrolysis

Mixture	A	$-B$	E, kcal/mol
6	8.95	10,150	46.4
7, 9	9.12	10,490	48.0
8, 10	9.14	10,830	49.6
7, 9[a]	9.26	10,670	48.8
8, 10[a]	9.02	10,670	48.8
12[b]	9.50	11,280	51.7
13	9.48	11,280	51.7
12	8.95	10,150	46.4
14	9.13	10,150	46.4
15	9.38	10,150	46.4

[a] Modified by using the average value of B (and E) for all four mixtures. [b] 12 atm.

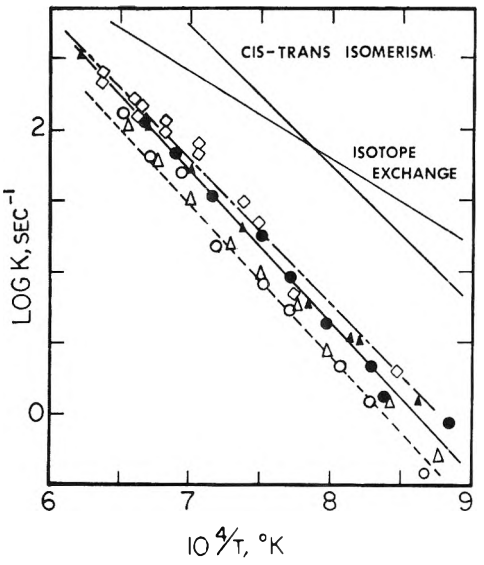

Figure 1. Rate constants for ethylene pyrolysis, cis–trans isomerization, and the isotope exchange reaction between C_2H_4 and C_2D_4: ◇, — — —, mixture 6; ●, mixture 7; ○, mixture 8; ▲, mixture 9; △, mixture 10; —— mixtures 7 and 9; - - - - - mixtures 8 and 10.

tion order with respect to ethylene is 1.34 rather than 1, as assumed. On the other hand, mixtures 6 and 12 give identical A and E values, indicating an ethylene order of 1.0. An average of these results would be an empirical ethylene order of 1.2 ± 0.2.

Figure 1 shows the distribution of the experimental points. The lines are from the first, fourth, and fifth sets of constants in Table II. The points deviate from the lines by log (observed conversion/calculated conversion), which is essentially the same as log (experimental rate constant/calculated rate constant) since most of the conversions were low. We cannot quote real experimental rate constants at definite temperatures since the experiments were not isothermal. The other curves in Figure 1 are explained below.

The argon order in ethylene pyrolysis was determined by conducting a series of pyrolysis experiments in the temperature range 1200–1800°K with mixture 12 at 13.0 ± 0.8 atm, and mixture 13 at 3.0 ± 0.2 atm, so that the ethylene partial pressure remained nearly the same in both sets of experiments. (The quoted pressures are averages for each series, and the uncertainties are standard deviations of the average pressure in each run from the series average. We had intended to have an average of 12 atm pressure for mixture 12, but the 8% deviation is unimportant since the experiments reported above show that the ethylene order is close to 1.) The data were fitted by Arrhenius equations with the same B values, and A values differing by only 0.02. Therefore the argon order is 0.05 ± 0.2, or essentially zero. These runs were made with 0.7-msec dwell time, compared with 5 msec for the others, which may account for the somewhat lower conversions at low temperatures and the higher observed activation energies.

Three sets of eight experiments each were carried out with mixtures 12, 14, and 15 to test the effect of oxygen on ethylene pyrolysis. Total reflected shock pressures were 3.0 ± 0.1 atm, dwell times approximately 5 msec, and the temperature range 1100–1500° K. Constants in the empirical rate equations for the conversion of ethylene into acetylene are given in Table II, the standard deviation in log A being 0.11. The most significant result for this study is that addition of 0.0053% O_2 to the ethylene mixture produced a 50% increase in rate of pyrolysis to acetylene. Since the maximum accidental oxygen impurity level is 1 μ, or 0.001% in a 100 Torr sample used in typical experiments, it may be concluded that the experimental results are, at most, 10% high because of the presence of oxygen as an impurity.

We are not in a position to state the manner in which the oxygen accelerated the reaction. It was not by simply raising the temperature by combustion of part of the ethylene, since the small amount of oxygen would not produce enough heat for this. Within experimental error, the fractional increase was uniform over the temperature and conversion (0.25–58%) ranges studied. The most probable explanation, consistent with our discussion below, is that the oxygen reacts directly with the ethylene to start free-radical chains, and may participate also in chain propagation. We plan to study the ethylene–oxygen reaction further in the near future.

Since we made every effort to exclude oxygen from our samples and probably had less than 0.001% oxygen in most of them, we have made no correction for oxygen in our calculations.

Isotope Distribution of Ethylene. For each of mixtures 7–10 we obtained relative amounts of the five deuterated compositions (zero to four deuteriums per molecule), seven to nine experiments at different temperatures

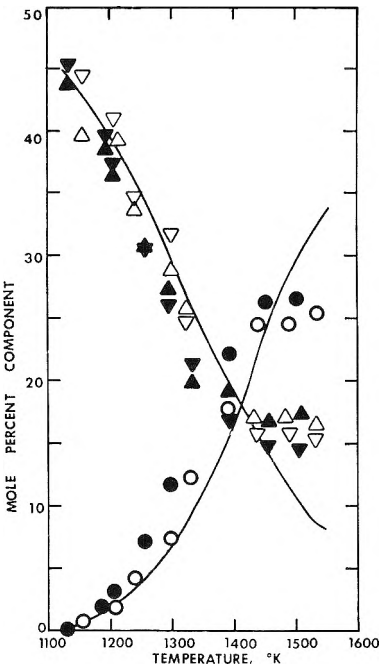

Figure 2. Isotope distribution of ethylenes following pyrolysis of mixtures 7 and 8: ▼, mixture 7, C_2H_4; ●, mixture 7, $C_2H_2D_2$; ▲, mixture 7, C_2D_4; ▽, mixture 8, C_2H_4; ○, mixture 8, $C_2H_2D_2$; △, mixture 8, C_2D_4. Curves are calculated from equations discussed in the text.

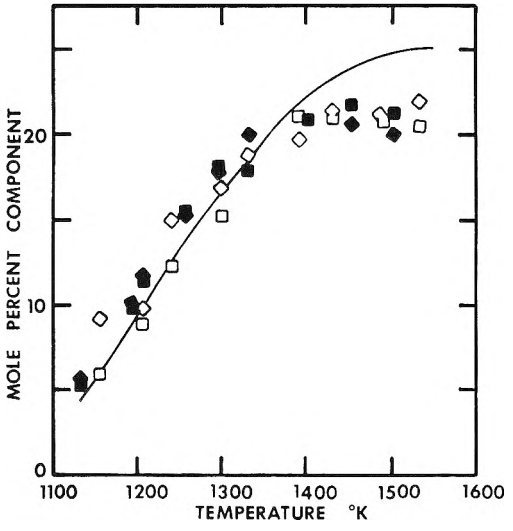

Figure 3. Isotope distribution of ethylenes following pyrolysis of mixtures 7 and 8, continued: ◆, mixture 7, C_2H_3D; ■, mixture 7, C_2HD_3; ◇, mixture 8, C_2H_3D; □, mixture 8, C_2HD_3. Curves are calculated from equations discussed in the text.

being carried out for each mixture. There were 170 data points in all, but it turned out that these could be empirically correlated rather simply.

First, the exchange reaction appeared to be close to first order in ethylene concentration, since the fractional conversions for mixtures 7 and 8, and 9 and 10, were very similar, as shown in Figures 2, 3, and 4. Second, it was found that the kinetics could be expressed by two equations

$$C_2H_4 + C_2D_4 \longrightarrow C_2H_3D + C_2HD_3$$

$$C_2H_3D + C_2HD_3 \longrightarrow 2C_2H_2D_2$$

in which the relative rates of the four forward and reverse reactions are given only by the statistics. As explained in the Appendix, the relative rate constants of first-order symmetrical reactions such as

$$\text{rate} = k[C_2H_4]^{1/2}[C_2D_4]^{1/2}$$

will be 4:1:3:2 for the forward and reverse rate constants of the first and second reactions, respectively, where all the $C_2H_2D_2$ species are taken together. The forward rate constant for the first reaction was found to be

$$\log k = 7.53 - 7000/T$$

corresponding to an activation energy of 32 kcal.

The experimental data are shown in Figures 2, 3, and 4 along with the conversions calculated from the above considerations. Deviations at the higher temperatures may be attributed to the effect of the acetylene-forming reactions on isotope exchange. To show the relative rates of isotope exchange and pyrolysis, the rate constant for the first step in isotope exchange has been plotted in Figure 1 along with the pyrolysis data. It is clear that at the lower temperatures studied isotope exchange is by far the more extensive, while at higher temperatures the two processes occur at comparable rates.

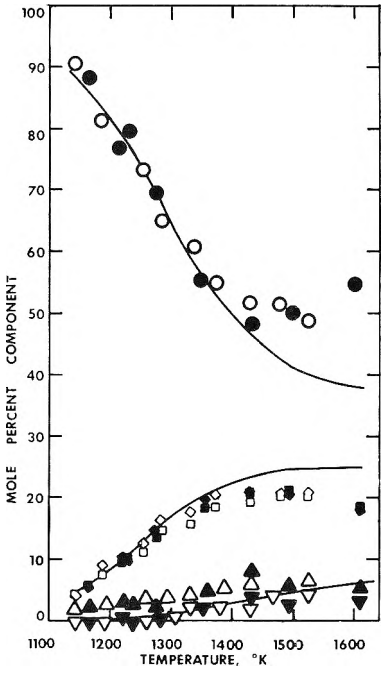

Figure 4. Isotope distribution of ethylenes following pyrolysis of mixtures 9 and 10: ▼, mixture 9, C_2H_4; ◆, mixture 9, C_2H_3D; ●, mixture 9, $C_2H_2D_2$; ■, mixture 9, C_2HD_3; ▲, mixture 9, C_2D_4; ▽, mixture 10, C_2H_4; ◇, mixture 10, C_2H_3D; ○, mixture 10, $C_2H_2D_2$; □, mixture 10, C_2HD_3; △, mixture 10, C_2D_4. Curves are calculated from equations discussed in the text.

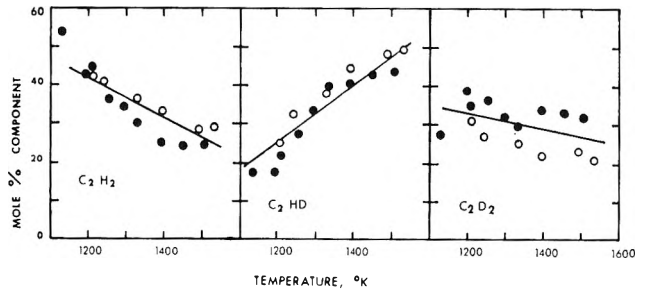

Figure 5. Isotope distribution of acetylenes following pyrolysis of mixtures 7 and 8: ●, mixture 7; ○, mixture 8.

Isotope Distribution of Acetylene. The relative amounts of the three forms of acetylene were determined for each shock tube experiment. For the four deuterium-containing ethylene mixtures the acetylene analyses were less precise than the ethylene analysis, primarily because we had less acetylene than ethylene to work with. These data are shown in Figures 5 and 6. Evidently the $C_2H_2/C_2HD/C_2D_2$ ratio approaches 1:2:1 at higher temperatures, but departs from this at lower temperatures.

Isotope Distribution of Hydrogen. Hydrogen analyses were made on the samples as taken from the shock tube, since we were not able to separate the hydrogen quantitatively from the rest of the sample, as we had done with ethylene and acetylene. This resulted in their concentrations being quite low, and the background peak for H_2 introduced a serious uncertainty in its analysis, so the only quantity we can report with confidence is the HD/D_2 ratio. This turned out to be independent of temperature (and therefore of amount of reaction) and of concentration. For mixtures 7 and 8 the HD/D_2 ratio was 2.5 ± 0.2, while for mixtures 9 and 10 it was 2.8 ± 0.4, the listed uncertainties being standard deviations from the mean values.

Reaction of Deuterium with Acetylene. For mixture 11, containing 5% C_2H_2 and 10% D_2, we measured the degree of conversion to the other hydrocarbons, and the isotopic distribution of the acetylene, ethylene, and hydrogen. Results are summarized in Table III and Figure 7.

The data on total hydrocarbon conversion show that, as expected, the chief product was ethylene, but that a small amount of methane was also formed. In all experiments the amount of ethylene produced was far below the equilibrium amount, so that little reverse decomposition of the ethylene would be expected. Also, the amount of acetylene converted into ethylene was about 10% of that converted into C_2HD. There are too few rate data to derive a rate law for ethylene formation, but the temperature dependence of the ethylene formation rate indicates an activation energy of approximately 20 kcal.

Table III: Data on the Reaction between Deuterium and Acetylene

Average temperature, °K	Time, msec	Fraction C_2H_2 converted into C_2H_4	Fraction C_2H_2 converted into CH_4
1069	5.6	0.005	0.000
1129	5.4	0.012	0.002
1158	5.3	0.021	0.004
1167	5.3	0.019	0.004
1241	5.1	0.029	0.008
1286	5.0	0.025	0.007

	Relative amounts of acetylenes		
	C_2H_2	C_2HD	C_2D_2
1069	0.973	0.026	0.001
1129	0.885	0.109	0.006
1158	0.825	0.162	0.013
1167	0.801	0.182	0.017
1241	0.654	0.298	0.048
1286	0.562	0.356	0.082

	Relative amounts of hydrogens			
	H_2	HD	D_2	[HD]/[C_2HD]
1069	0.001	0.013	0.986	1.00
1129	0.002	0.053	0.945	0.97
1158	0.006	0.089	0.905	1.10
1167	0.007	0.094	0.899	1.03
1241	0.029	0.163	0.812	1.09
1286	0.027	0.215	0.758	1.21

	Relative amounts of ethylenes				
	C_2H_4	C_2H_3D	$C_2H_2D_2$	C_2HD_3	C_2D_4
1069	0.230	0.664	0.019	0.008	0.001
1129	0.290	0.515	0.147	0.048	0.000
1158	0.202	0.527	0.225	0.043	0.003
1167	0.209	0.497	0.238	0.057	0.003
1241	0.195	0.398	0.301	0.094	0.012
1286	0.161	0.345	0.336	0.138	0.020

Discussion

On the whole, the various studies of ethylene pyrolysis rates referred to earlier[1-5] and our present data are in reasonably good agreement although, as is common in this type of study, the calculated activation energies cover a considerable range, *ca.* 40–74 kcal. This reflects to some extent different experimental conditions. Since our present data agree closely with earlier data[1] obtained with a different shock tube, we have some confidence that the activation energy for the pyrolysis of dilute (<1%) ethylene mixtures in argon at 1150–1600°K lies in the range of 45–55 kcal.

Most experimenters have reported that the pyrolysis reaction is first order in ethylene concentration. The present data indicate an ethylene order of 1.2 ± 0.2. In view of the probable complexity of the reaction, one would not expect it to have an integral reaction order over a wide range of temperatures and concentrations, and the concentration range of these studies is lower than that of most earlier work. Our value therefore does not seem to be in fundamental disagreement with earlier work, but is simply another piece of information

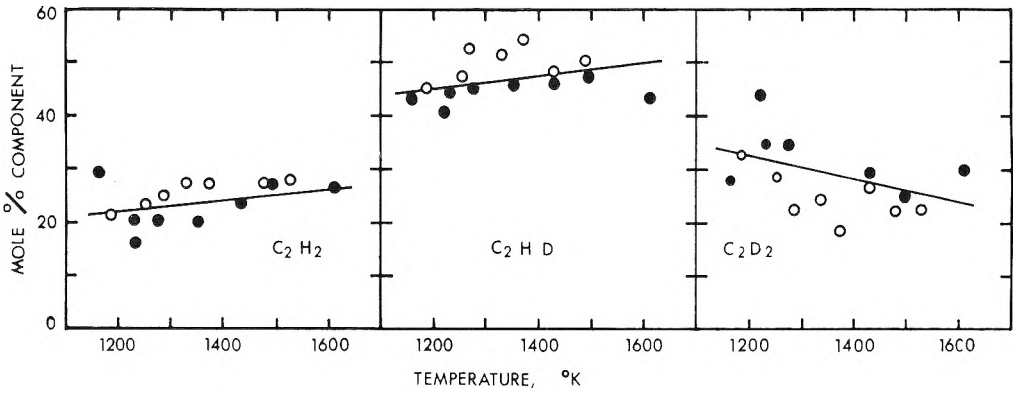

Figure 6. Isotope distribution of acetylenes following pyrolysis of mixtures 9 and 10: ●, mixture 9; ○, mixture 10.

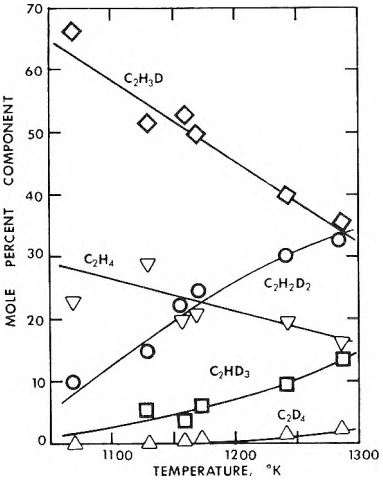

Figure 7. Isotope distribution of ethylenes following pyrolysis of mixture 11: ▽, C_2H_4; ◇, C_2H_3D; ○, $C_2H_2D_2$; □, C_2HD_3; △, C_2D_4. Curves are empirical.

to be considered in making a kinetic analysis of the reaction.

Previous measurements of the order of the reaction with respect to inert gas have been made by Gay and coworkers,[4] who reported that the order with respect to neon in the pressure range 0.3–2 atm, and at 1700–2300°K, is 0.5. Bauer[6] reported on argon order of 0.6 at 0.5–3 atm and 1120–1560°K. Our data are not incompatible with theirs, since raising the pressure to 3 atm and above could be moving the reaction from the fall-off region to the high-pressure limit. For a process such as

$$A + M \rightleftarrows A^* + M$$

$$A^* \longrightarrow A^{\ddagger}$$

$$A^{\ddagger} \longrightarrow \text{products}$$

(where A is a reactant molecule, A* an energized molecule, $A^{\ddagger}$ an activated complex, and M an inert gas molecule) the order with respect to M is $^1/_2$ when the apparent first-order rate constant with respect to A is half that of the high-pressure limit. One can, therefore, estimate the high-pressure rate equation from their data. This would apply whether the decomposing species is ethylene itself or an intermediate (such as C_2H_3) in a chain reaction.

The data on isotope exchange may be somewhat apart from the main point of learning how ethylene dissociates, but they again point out the large amount of reaction that goes on unnoticed when many compounds are heated. In the lower part of our temperature range, ten molecules of ethylene exchange hydrogens for each one that decomposes to acetylene. The exchange reactions forced us to work at low conversions in order to observe, as far as possible, the decomposition of our starting materials.

We were not able to study the trans–cis isomerization of ethylene-d_2, and this could have had an important effect on the interpretation of our results. This reaction was studied in the 700–850°K range by Douglas, Rabinovitch, and Looney,[16] while Lifshitz, Bauer, and Resler[9] and Jeffers and Shaub[17] studied the isomerization of 2-butene and 1,2-$C_2H_2F_2$ in shock tubes in the 1000–1300°K range. If it is assumed that the shock tube experiments lie within the high-pressure unimolecular region, these data indicate a rate constant of about $10^{13}e^{-62,000/RT}$ sec^{-1} for the cis–trans isomerization of ethylene. This reaction has been taken to be intramolecular, in contrast to the exchange reactions which must involve more than one molecule. In our temperature range, the rate constant for cis–trans isomerization is about the same as for isotope exchange, as indicated in Figure 1. From the experimental activation energies, or a glance at Figure 1, it would seem likely that at lower temperatures the exchange reactions would occur more rapidly than the cis–trans isomerization, yet Douglas and coworkers found just the opposite. This apparent discrepancy can be explained in terms of a free-radical mechanism.

(16) J. E. Douglas, B. S. Rabinovitch, and F. S. Looney, *J. Chem. Phys.*, **23**, 315 (1955).

(17) P. M. Jeffers and W. Shaub, *J. Amer. Chem. Soc.*, **91**, 7706 (1969).

While several of our experiments were less clear-cut than we would have liked, due to the scrambling reactions which tended to produce mixtures of ethylenes, and therefore forced us to try to get data at low conversion where the analyses were not very accurate, the data we have support the free-radical as opposed to the molecular mechanism of ethylene pyrolysis in our temperature and composition range. One indication is the large amount of HD produced from pyrolysis of the C_2H_4–C_2D_4 mixtures, whereas a molecular mechanism should have produced mainly H_2 and D_2 with little HD at lower temperatures where isotope scrambling was minimal. The data of Bauer and Ossa[18] indicate that, especially at the lower temperatures, this HD would not form from H_2 and D_2 produced earlier from ethylene. The acetylene distribution from these mixtures was not indicative of the mechanism, since both mechanisms would tend to give C_2H_2 and C_2D_2 as the chief products.

The acetylene and hydrogen distributions from *trans*-ethylene-d_2 also support the free-radical mechanism, which would predict that C_2HD and HD would make up about 50% of the acetylenes and hydrogens, whereas the molecular mechanism would lead to nearly all C_2HD and HD at lower temperatures if our estimate of the amount of trans–cis isomerization is not much too low. Similarly, if addition of deuterium to acetylene occurred by a molecular mechanism, one would expect to obtain primarily $C_2H_2D_2$, while actually C_2H_3D was present in larger quantities. In each case where a clear distinction can be made, a free-radical mechanism is indicated.

Our data on the acetylene–deuterium exchange reaction agree fairly well with those of Kuratani and Bauer,[8] but we have more data which are at variance with some of their conclusions. In our experiments the rates of appearance of C_2HD and HD were nearly the same, especially at our lower temperatures, as indicated in Table III. The rate constant for their appearance, using Kuratani and Bauer's relationship for the appearance of C_2HD

$$R_\alpha = k_\alpha[C_2H_2]^{0.24}[D_2]^{1.0}$$

was approximately twice as high as their empirical equation gave, which was

$$k_\alpha = 8 \times 10^7 e^{-33,800/RT}\ (\text{mol/l.})^{-0.24}\ \text{sec}^{-1}$$

This is reasonably close, since our data were below their experimental temperature range, and an extrapolation of their curve had to be made for comparison.

However, Kuratani and Bauer measured different rates of C_2HD and HD formation, and from this concluded that the rate of C_2D_2 should be one-half that of C_2HD and that C_2D_2 is produced in the same process as C_2HD. Our data show that the amount of C_2D_2 produced is much less than one-half the C_2HD, and it seems more reasonable to suppose that it is formed by a subsequent reaction of C_2HD with another D_2 molecule.

Since our product distributions indicate the likelihood of free-radical mechanisms, we have tried to interpret our data in terms of the mechanism suggested by Gay and coworkers[4] and worked out in detail by Benson and Haugen.[7,19] In ref 7 the following reactions were used.

$$2C_2H_4 \xrightarrow{iP} C_2H_3 + C_2H_5$$

$$C_2H_3 + M \xrightarrow{1} C_2H_2 + H + M$$

$$H + C_2H_4 \xrightarrow{2} C_2H_3 + H_2$$

$$C_2H_5 + M \underset{}{\overset{8}{\rightleftharpoons}} C_2H_4 + H + M$$

$$C_2H_3 + H \xrightarrow{tHV} (\text{termination})$$

$$2C_2H_3 \xrightarrow{tV} (\text{termination})$$

Reaction 8 was assumed to come to equilibrium while the other reverse reactions were assumed to be negligible. At lower temperatures termination occurs primarily by reaction tV, and if steady-state radical concentrations are taken, the rate of acetylene formation is

$$R_{C_2H_2} = k_1\left(\frac{k_{iP}}{k_{tV}}\right)^{1/2}(C_2H_4)(M) \qquad (1)$$

At higher temperatures and lower ethylene concentrations, termination by reaction tHV becomes important, and the rate of acetylene formation is

$$R_{C_2H_2} = \left(\frac{k_{iP}}{k_{tV}}\right)^{1/2}\frac{k_2(C_2H_4)^2}{(\alpha\omega + \omega^2)^{1/2}} \qquad (2)$$

where $\alpha = k_{tHV}/k_{tV}$ and

$$\omega = \frac{(C_2H_3)_{ss}}{(H)_{ss}} = \frac{k_2(C_2H_4)}{k_1(M)} \qquad (3)$$

If reaction tHV becomes dominant, then the rate simplifies to

$$R_{C_2H_2} = (k_1k_2)^{1/2}\left(\frac{k_{iP}}{K_{tHV}}\right)^{1/2}(C_2H_4)^{3/2}(M)^{1/2} \qquad (4)$$

The recombination of H atoms with argon as third body is a relatively slow process[20] and would not be significant.

Benson and Haugen expressed their rate constants in the form

$$k = 10^{\log A} \times 10^{-E/2.3RT}$$

and we have listed their values of log A and E in Table IV. From these data one obtains an activation energy

(18) S. H. Bauer and E. Ossa, *J. Chem. Phys.*, **45**, 434 (1966).

(19) S. W. Benson and G. R. Haugen, *J. Phys. Chem.*, **71**, 4404 (1967).

(20) W. G. Bourne, D. R. White, and G. R. Smookler, *Symp. (Int.) Combust. Proc. 12th*, 557 (1969).

Table IV: Rate Constants of Reactions in Ethylene Pyrolysis

Reaction	Benson and Haugen log A	Benson and Haugen E	This research log A	This research E
iP	11.7	64.7	12.3	55
1 (2nd order)	11.9	31.5		
1 (1st order)			11.2	38
2	10.8	6.0	11.2	14
8 (1st order)	14.3	41.2	13.8	37
−8	10.4	0	9.9	−3
tV	10.0	0	9.9	−3
tHV	9.6	0	10.3	0

for acetylene formation of 64 kcal at low temperatures (eq 1) and 51 kcal at high temperatures (eq 4).

Some modifications are necessary in Benson and Haugen's calculations to make them compatible with our data. First, since we found an argon order of zero, we would conclude that reaction 1 has reached its high-pressure limit in 3 atm of argon, and if so, reaction 8 would be expected to have done so too. Therefore, we have taken these reactions to be first order and have converted the rate constant for reaction 1 by putting argon concentrations corresponding to 3 atm pressure.

Second, their rate constants do not bring the radical concentrations up to steady-state values in a short enough time to reproduce our experimental results at 0.5% ethylene and below at 3 atm, the discrepancy being greatest at the lower temperatures, naturally. The difficulty can be corrected by increasing the value of k_{iP} somewhat, by lowering its assumed activation energy and by making smaller changes in some of the other rate constants. Since ΔH for reaction iP at 1350°K is about 52.5 kcal, according to Bauer,[6] we have taken the activation energy to be 55 kcal.

Third, Benson and Haugen did not consider isotope exchange reactions in any detail, although they mention the possibility of them occurring *via* cyclobutane. It would seem that this mechanism would favor the process

$$C_2H_4 + C_2D_4 \longrightarrow 2CH_2{=}CD_2$$

whereas we found single atom transfer to be the first process to occur. Accordingly, we have considered that reaction 8, which would bring about single atom transfer, is the most likely vehicle for isotope exchange. The initial rate of isotope exchange in an equimolar mixture of C_2H_4 and C_2D_4 will be about one-third the rate of reaction 8 (or of reaction −8, since this reaction rapidly reaches equilibrium) since only half the additions of H or D to C_2H_4 or C_2D_4 will lead to C_2H_4D or C_2HD_4, and only two-thirds of the decompositions of the mixed radicals will lead to mixed ethylenes.

The ratio of the rate of mixing to the rate of pyrolysis is therefore $k_{-8}/3k_2$, and with Benson and Haugen's data the difference in activation energy is 6 kcal, the value of E_2, since E_{-8} is taken as zero. However, this value of E_2 may be considerably low, since Baldwin[21] has reported that the activation energy for the reaction

$$H + C_2H_6 \longrightarrow C_2H_5 + H_2$$

is 9.4 kcal, while Bauer[6] indicates that the C_2H_3–H bond energy is 4.4 kcal greater than that of C_2H_5–H. Accordingly, we have estimated E_2 to be 14 kcal, a value which leads to a larger ratio of the rate of mixing to the rate of pyrolysis.

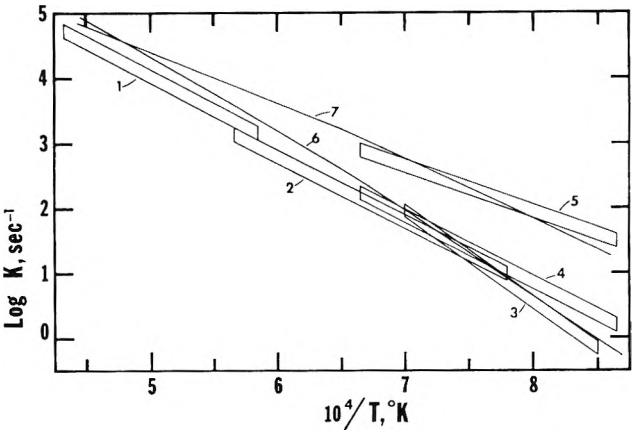

Figure 8. Comparison of observed and calculated rate constants for the pyrolysis and isotope exchange reactions of ethylene. Curve 1, pyrolysis, ref 4; curve 2, pyrolysis, ref 1, 0.5% C_2H_4 in 5 atm of argon; curve 3, pyrolysis, ref 1, 6% C_2H_4 in 5 atm of argon; curve 4, pyrolysis, this research, 0.1% C_2H_4 in 3 atm of argon; curve 5, first step in C_2H_4–C_2D_4 exchange, this research; curve 6, pyrolysis, calculated; curve 7, first step in C_2H_4–C_2D_4 exchange, calculated.

The rate constants we used are listed in Table IV. A comparison of our calculated results with our present ethylene pyrolysis and isotope exchange results and those of several earlier papers is shown in Figure 8. The calculated activation energies for pyrolysis (59 kcal) and exchange (42 kcal) in the 1200–1500°K range are higher than our experimental ones (49 kcal and 32 kcal), but the absolute values are in reasonable agreement. The curves are consistent with the observations of Gay and coworkers that isotope mixing becomes less important than pyrolysis at high temperatures, while the fall-off in rate at low temperatures due to failure to reach steady-state radical concentrations could explain the lack of isotope mixing observed by Douglas, Rabinovitch, and Looney[16] at lower temperatures.

Since considerable isotope mixing occurred in all the experiments, it is not possible to draw quantitative conclusions about isotope effects from the acetylene and hydrogen analyses. However, the data are qualitatively understandable in terms of the small isotope effects expected at high temperatures.[22] It seems

(21) R. R. Baldwin, D. Jackson, R. W. Walker, and S. J. Webster, *Symp. (Int.) Combust. Proc. 10*, 423 (1965).

(22) (a) E. Tschuikow-Roux and D. D. Macdonald, *J. Chem. Phys.*, **49**, 5342 (1968); (b) D. D. Macdonald and E. Tschuikow-Roux, *ibid.*, **49**, 5345 (1968).

reasonable that the C_2H_4–C_2D_4 mixtures should produce mainly C_2H_2 and C_2D_2 at lower temperatures, with more C_2H_2 than C_2D_2, as Figure 5 indicates. Similarly, one would expect D to be lost more slowly than H from $C_2H_2D_2$, leading to less than 25% C_2H_2 and more than 25% C_2D_2, as shown in Figure 6. At higher temperatures, both processes lead to near-equilibrium acetylene distributions, due to isotope mixing. Since hydrogen is set free more easily than deuterium, one would expect that the H_2/HD ratio would be greater than 0.5, while the HD/D_2 ratio would be greater than 2:1. Gay and coworkers[4] observed the first effect, while we observed the second. It would seem reasonable for our HD/D_2 ratio to approach 2 at greater conversions, by analogy with the acetylene data, although we did not observe this. Perhaps there was a change that was hidden by the experimental error.

The activation energy for acetylene hydrogenation of 20 kcal seems high, in view of our activation energies for pyrolysis of 45 to 50 kcal, and the 44-kcal heat of reaction.[6] Experimentally, our result is confirmed by our earlier results[1] from which Gay and coworkers[4] calculated a value of 17 kcal, and by Bauer,[6] who reported 27 kcal. This apparent discrepancy is due to the complexity of ethylene pyrolysis, which produces butadiene and many other products besides acetylene and hydrogen at low temperatures and high pressures. For such a complex reaction, forward and reverse rate constants are related by the equilibrium constant only when reactant concentrations that are at equilibrium are used, and for all of our hydrogenation data the equilibrium ethylene concentrations were greater than those in our pyrolysis data. In our earlier work[1] we showed that when equilibrium concentrations were used the ratio of the rate constants did give the equilibrium constant.

In their free-radical mechanism for the hydrogenation and isotope exchange of ethylene, Benson and Haugen assumed the following reactions (which we have modified to fit our experimental conditions by replacing H_2 by D_2)

$$C_2H_2 + D_2 \xrightarrow{iH} C_2H_2D + D$$

$$C_2H_2D + D_2 \xrightarrow{-2} C_2H_2D_2 + D$$

$$C_2H_2D \underset{-1}{\overset{1}{\rightleftharpoons}} C_2HD + H \text{ or } C_2H_2 + D$$

$$H \text{ or } D + C_2H_3 \xrightarrow{tHV} \text{termination}$$

These reactions reproduce fairly well the rates of hydrogenation reported in ref 1 and in this paper, although their calculated activation energy is somewhat greater than 20 kcal. Reactions −1 and −2 lead to hydrogenation, while 1 and −1 lead to hydrogen–deuterium exchange of acetylene. Since reaction 2 is exothermic by about 1 kcal,[6] we would take E_{-2} = 15 kcal, and since reactions 1 and −2 are competitive, the difference in their activation energies (38–15 kcal) should be equal to the difference in the activation energies for mixing, which Bauer and Kuratani give as 34 kcal, and for hydrogenation, which we estimate as 20 kcal. The 9-kcal discrepancy is larger than one would like, but perhaps not unexpected in view of the uncertainties of some of the activation energies leading to it.

Since loss of H would be faster than loss of D in reaction 1, at the steady state the H concentration would exceed that of D, and reaction −1 would produce more C_2H_3 than C_2H_2D, at least near the beginning of the reaction, before significant C_2H_2–D_2 interchange had occurred. Reaction 2 would then produce more C_2H_3D than $C_2H_2D_2$, which we observed. The formation of a significant amount of C_2H_4 might be due to reaction of some of the C_2H_3 with C_2H_2 rather than D_2

$$C_2H_3 + C_2H_2 \longrightarrow C_2H_4 + C_2H$$

The C_2H could react further with acetylene to produce vinyl acetylene or diacetylene, which are known pyrolysis products of acetylene,[23,24] or with D_2 to produce C_2HD_2. The above reaction, which is endothermic by about 9 kcal,[6] could well proceed at a rate comparable to that of reaction −2.

It seems premature to make quantitative calculations beyond those of Benson and Haugen on the basis of the six experiments of Table III and Figure 7. The above discussion shows the possibility of understanding the production of mainly C_2H_3D and C_2H_4 at low temperatures in terms of free-radical processes. At high temperatures, all of the concentrations are approaching equilibrium values, as they should.

Acknowledgment. Acknowledgment is made to the donors of the Petroleum Research Fund, administered by the American Chemical Society, for partial support of this research.

Appendix. Kinetics of Ethylene Isotope Exchange Reactions

Suppose that the exchange reactions occur by two basic processes

$$C_2H_4 + C_2D_4 \longrightarrow C_2H_3D + C_2HD_3 \qquad (A1)$$

$$C_2H_3D + C_2HD_3 \longrightarrow 2C_2H_2D_2 \qquad (A2)$$

Since there are three kinds of $C_2H_2D_2$, there are actually six subreactions (to produce cis + cis, trans + trans, gem + gem, cis + trans, trans + gem, and gem + cis). Symmetry numbers are 4 for C_2H_4 and C_2D_4, 1 for C_2H_3D and C_2HD_3, and 2 for each of the $C_2H_2D_2$'s. If energy effects are insignificant, the equilibrium constants will be K_1 = 16; K_2 = 0.25 for each of the reactions of type 2.

If the exchange occurred by elementary bimolecular

(23) G. B. Skinner and E. M. Sokoloski, *J. Phys. Chem.*, **64**, 1952 (1960).

(24) I. D. Gay, G. B. Kistiakowsky, J. V. Michael, and H. Niki, *J. Chem. Phys.*, **43**, 1720 (1965).

reactions as indicated, then the ratio of the forward to reverse rate constants for reaction 1 would be 16. This result could also be derived from the statistical factor, since for the forward reaction any H of C_2H_4 could react with any D of C_2D_4, to give 16 possibilities for the forward reaction, whereas only the reaction of the D of C_2H_3D with the H of C_2HD_3 would lead to the reverse reaction. At equilibrium, if the mixture contained equal amounts of H and D, the concentrations of C_2H_3D and C_2HD_3 would be four times those of C_2H_4 and C_2D_4.

Considering the eq 2 reactions, at equilibrium the concentration of each of the three $C_2H_2D_2$'s would be half that of C_2H_3D and C_2HD_3, so that the total concentration of $C_2H_2D_2$ would be $^3/_2$ that of C_2H_3D. Therefore the relative equilibrium concentrations of all five compositions are as follows.

C_2H_4	1
C_2H_3D	4
$C_2H_2D_2$	6
C_2HD_3	4
C_2D_4	1

The rate constant for each of the reverse reaction 2's would be four times that of the corresponding forward reaction. Since we did not separate the three types of $C_2H_2D_2$, we prefer to write a pseudo rate constant for the reverse reaction, which would be multiplied by the square of the total concentration of $C_2H_2D_2$'s to give the rate of reaction. This would be $^1/_9$ of the real reverse rate constant or $^4/_9$ of the rate constant for the corresponding forward reaction. Since all of the six subreaction 2's have the same equilibrium constant, this same ratio would apply to rate constants for the total reaction of all $C_2H_2D_2$'s to form C_2H_3D and C_2HD_3, and the total reaction of C_2H_3D and C_2HD_3 to produce all forms of $C_2H_2D_2$.

The statistical factor for the total forward reaction 2 is 9, since any H of C_2H_3D could react with any D of C_2HD_3. This relationship combined with the others mentioned above leads to the ratio $k_{1F}:k_{1R}:k_{2F}:k_{2R} = 16:1:9:4$, where $k_{1F}[C_2H_4][C_2D_4]$ is the rate of reaction of C_2H_4 and C_2D_4 to produce C_2H_3D and C_2HD_3, $k_{1R}\cdot[C_2H_3D][C_2HD_3]$ is the rate of reaction of C_2H_3D and C_2HD_3 to produce C_2H_4 and C_2D_4, $k_{2F}[C_2H_3D][C_2HD_3]$ is the total rate of reaction of C_2H_3D and C_2HD_3 to produce all forms of $C_2H_2D_2$, $k_{2R}[C_2H_2D_2][C_2H_2D_2]$ is half the rate of reaction of $C_2H_2D_2$ (all forms) to form C_2H_3D and C_2HD_3, and the value of $[C_2H_2D_2]$ is the total concentration of all forms of $C_2H_2D_2$.

The above calculations were made in terms of bimolecular reactions and second-order kinetics since they seem clearest in those terms, but experimentally the exchange reactions are first order in ethylene concentration. Since we have no reason so far to believe otherwise, we have taken the rate laws to be symmetrical (for example, the rate of the first forward reaction would be $k'_{1F}[C_2H_4]^{0.5}[C_2D_4]^{0.5}$). In these terms, all the rate constant ratios would be converted by taking square roots, so that we have $k'_{1F}:k'_{1R}:k'_{2F}:k'_{2R} = 4:1:3:2$.

Ion-Molecule Reactions in Dimethylsilane, Trimethylsilane, and Tetramethylsilane[1]

by P. Potzinger and F. W. Lampe*

Whitmore Laboratory, Department of Chemistry, The Pennsylvania State University, University Park, Pennsylvania 16802 *(Received July 22, 1970)*

Publication costs assisted by the Research Division, United States Atomic Energy Commission

Ion–molecule reactions initiated by electron impact in pure dimethylsilane, trimethylsilane, and tetramethylsilane are identified, and specific reaction rates are measured. The predominant reaction in dimethylsilane and trimethylsilane is H^- transfer to CH_3SiH^+, $CH_3SiH_2^+$, and $(CH_3)_2Si^+$ from the former molecule, and to $(CH_3)_2Si^+$ and $(CH_3)_2SiH^+$ from the latter. Hydride transfer is not observed in tetramethylsilane, the major reaction being inferred to be a collisional dissociation of $(CH_3)_4Si^+$ to $(CH_3)_3Si^+$, C_2H_6, and $(CH_3)_3Si$.

This paper reports a continuation of our studies of the ion–molecule reactions of methylsilanes. In two previous papers we have shown that the predominant reacting ions in monosilane[2] and methylsilane[3] are the SiH_2^+ and CH_3SiH^+ ions, respectively, and that in both cases the fastest reaction was hydride ion transfer from the reactant molecule to the attacking ion. On the other hand, the ions SiH_3^+ and $CH_3SiH_2^+$ were found to be quite unreactive toward their parent gases.

Experimental Section

All experiments were conducted in a Bendix 14-101 time-of-flight mass spectrometer and in a Nuclide Associates 12-90-G magnetic sector mass spectrometer. Both instruments have been described previously,[2,4] as have the pertinent techniques for data collection and treatment.[2-5] The rate constants refer to thermal-energy ions at 70°.

Dimethylsilane, trimethylchlorosilane, and tetramethylsilane were purchased from the Peninsular Chemical Co. Before use the dimethylsilane was subjected to vacuum-line degassing and trap-to-trap distillation at −97 and −130°, while the tetramethylsilane was simply degassed. Trimethylsilane was prepared by the lithium aluminum hydride reduction of trimethylchlorosilane and was distilled on the vacuum line before use. In all cases no significant impurities could be detected by mass spectrometry.

Results and Discussion

Dimethylsilane. Our studies of ion–molecule reactions in SiH_4[2] and CH_3SiH_3[3] lead us to expect that the principal reactant ions in $(CH_3)_2SiH_2$ will be the bivalent ions $(CH_3)_2Si^+$, CH_3SiH^+, and SiH_2^+. It can be seen in Figure 1, which depicts the relative intensities of primary ions in the mass spectra of pertinent alkylsilanes, that $(CH_3)_2Si^+$ (*m/e* 58) and CH_3SiH^+ (*m/e* 44) are major primary ions of comparable intensity, whereas SiH_2^+ is present only at very small intensity. That our expectations concerning reactant ions are borne out can be seen in Figure 2 in that the fractional ion intensities, $(I_i/\sum I_i)$ of $(CH_3)_2Si^+$ and CH_3SiH^+ show the required decrease with increasing ion-source pressure. No decrease in the fractional ion intensity of SiH_2^+ was observed. While our failure to observe a decrease in the fractional intensity of SiH_2^+ may be related to its low abundance, we may safely conclude that SiH_2^+ is not a significant reactant in this system. In contrast to studies in SiH_4[2] and CH_3SiH_3[3], the trivalent siliconium ion, $CH_3SiH_2^+$, appears to be a reactant ion in collisions with the parent molecule, as judged by the decrease with increasing source pressure in the fractional intensity of *m/e* 45. The fractional intensities of *m/e* 43 and 31 are independent of source pressure, indicating that CH_3Si^+ and SiH_3^+ neither react nor are formed in collision reactions. The increase in the fractional intensity of *m/e* 59 with increasing source pressure shows that $(CH_3)_2SiH^+$ is the major product ion, accounting for ~70% of the total reaction of the three reactant species. The masses and relative intensities of all the product ions in $(CH_3)_2SiH_2$ are shown in Figure 3. The fractional intensity increases and decreases in this system agree within 2%.

Energetic considerations do not rule out the participation of any of the three reactant ions in the hydride transfer process that forms $(CH_3)_2SiH^+$. Thus (1), *viz.*

$$(CH_3)_2Si^+ + (CH_3)_2SiH_2 \longrightarrow (CH_3)_2SiH^+ + (CH_3)_2SiH \quad (1)$$

is energetically feasible if $D[(CH_3)_2SiH\text{–}H] \leq 95$ kcal/mol, where D refers to the dissociation energy of

(1) United States Atomic Energy Commission Document NYO-3570-16.

(2) G. G. Hess and F. W. Lampe, *J. Chem. Phys.*, **44**, 2257 (1966).

(3) P. Potzinger and F. W. Lampe, *J. Phys. Chem.*, **74**, 587 (1970).

(4) P. Potzinger and F. W. Lampe, *ibid.*, **73**, 3912 (1969).

(5) D. P. Beggs and F. W. Lampe, *ibid.*, **73**, 3307 (1969).

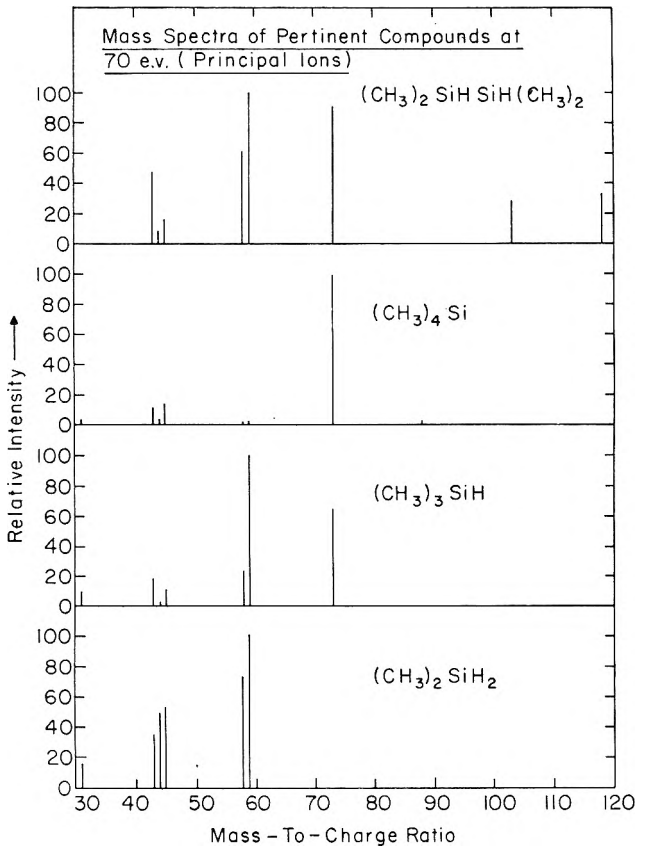

Figure 1. Principal ions in the mass spectra (70 eV) of dimethylsilane, trimethylsilane, tetramethylsilane, and tetramethyldisilane.

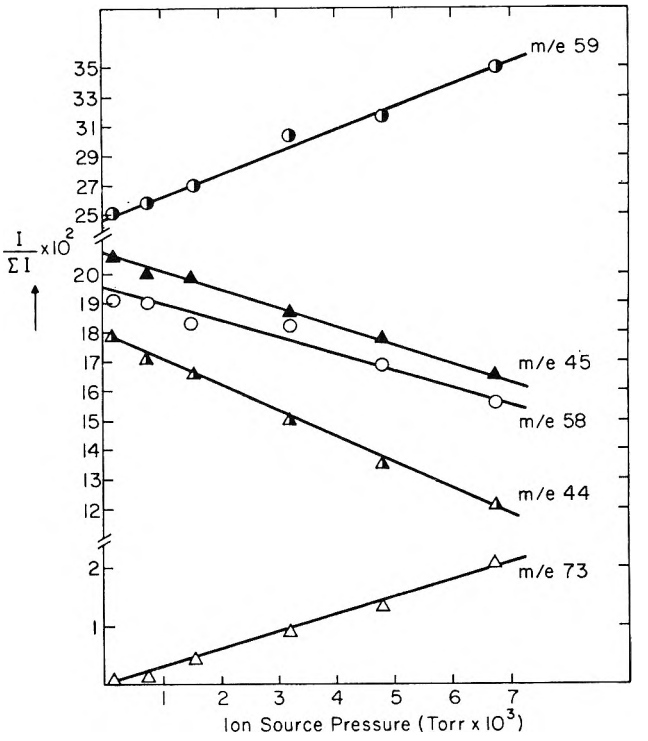

Figure 2. Fractional ion intensities in dimethylsilane as a function of ion-source pressure: △, *m/e* 73; ◑, *m/e* 59; ○, *m/e* 58; △, *m/e* 45; ▲, *m/e* 44.

the indicated bond. Inasmuch as $D[SiH_3-H]$ has been reported as 96 kcal/mol[4] and $D[(CH_3)_3Si-H]$ as 79 kcal/mol,[6] the energetic requirements that (1) be thermoneutral or exothermic would appear to be fulfilled. Reaction 2, namely

$$CH_3SiH^+ + (CH_3)_2SiH_2 \longrightarrow (CH_3)_2SiH^+ + CH_3SiH_2 \quad (2)$$

requires, for energetic feasibility, only that $D[CH_3SiH_2-H] \leq 108$ kcal/mol, and this is undoubtedly true. Finally for reaction 3, *viz.*

$$CH_3SiH_2^+ + (CH_3)_2SiH_2 \longrightarrow (CH_3)_2SiH^+ + CH_3SiH_3 \quad (3)$$

$\Delta H = -17$ kcal/mol.

Comparison of the total increase in fractional intensity of $(CH_3)_2SiH^+$ (*m/e* 59) with the fractional decreases of the reactant ions shows that (1) and (3) cannot account for all of the $(CH_3)_2SiH^+$ formed and that, therefore, (2) must take place. Reactions 2 and 3 alone could just account for the formation of $(CH_3)_2SiH^+$. Hydride transfer from SiH_4[2,5] and CH_3SiH_3[3] and, indeed, from most molecules[7] seems to be such a general occurrence (when energetically allowed) that we believe it most probable that all three reactants produce $(CH_3)_2SiH^+$. The appearance potentials of the reactant ions lie sufficiently close to each other that differentiation by a study of ionization–efficiency curves is not practical.

As was observed in the case of CH_3SiH_3, the primary ion SiH_3^+ does not abstract hydride ion from the parent molecule even though the reaction is energetically feasible. It would appear on energetic grounds that CH_3Si^+ could also participate in a hydride abstraction reaction with $(CH_3)_2SiH_2$, but it does not.

Product ions that are heavier than the parent molecule appear in three distinct groups (*cf.* Figure 3), namely *m/e* 69–75, *m/e* 84–89, and *m/e* 99–105. In addition, a secondary ion at a very low but real intensity is observed at *m/e* 116. Stoichiometric requirements, applied to the three possible reactants, make it clear that this product can come only from reaction 4, *viz.*

$$(CH_3)_2Si^+ + (CH_3)_2SiH_2 \longrightarrow (CH_3)_2Si_2(CH_3)_2^+ + H_2 \quad (4)$$

If we make the assumption, as would seem to be reasonable on the basis of our studies with monosilane,[2,5] that the reactant ion forms with the parent molecule a strong collision complex which is vibrationally excited,

(6) P. Potzinger and F. W. Lampe, *J. Phys. Chem.* **74**, 719 (1970).

(7) J. H. Futrell and T. O. Tiernan, "Fundamental Processes in Radiation Chemistry," P. Ausloos, Ed., Interscience, New York, N. Y., 1968, pp 171–280.

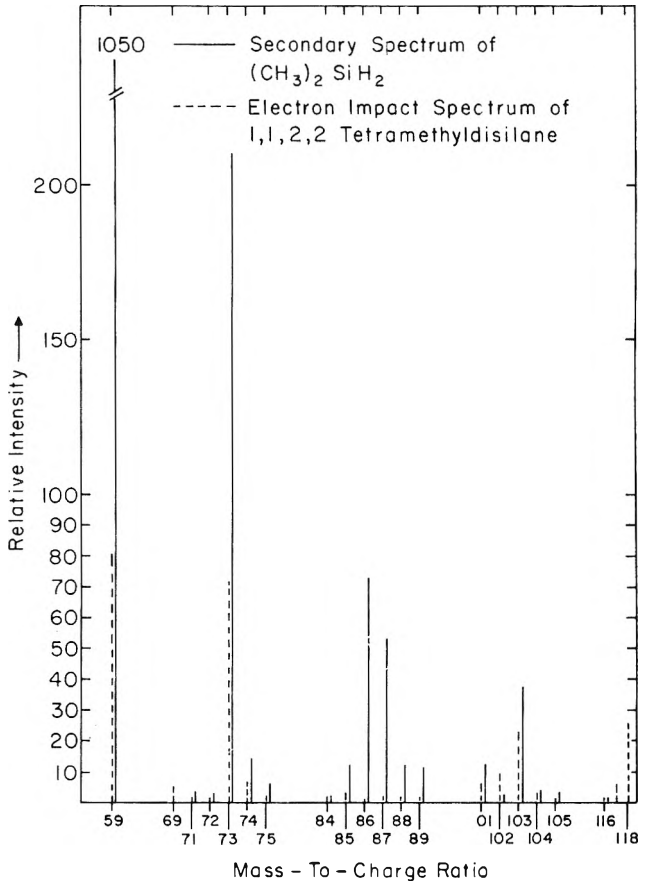

Figure 3. Comparison of the secondary ion mass spectrum of dimethylsilane (solid lines) with the primary mass spectrum of tetramethyldisilane (broken lines).

then we can view the reaction in terms of the unimolecular decomposition of the complex. This collision complex has a very narrow energy distribution as compared with the energy distribution of the same ion formed by electron impact. However, it has been reported in some cases that the intensity distributions of the fragment ions from two such complexes (with different energy distributions) are similar.[2,7-10] Adopting this approach, namely that the strong collision complex of (4) is an excited tetramethyldisilane ion formed by insertion of $(CH_3)_2Si^+$ into an Si–H bond of $(CH_3)_2SiH_2$, we may compare the secondary ion mass spectrum of $(CH_3)_2SiH_2$ with the primary electron impact mass spectrum of $(CH_3)_2SiH–SiH(CH_3)_2$.

This comparison is shown in Figure 3 in which the peaks at *m/e* 116 have been normalized to unity. Due to the high energy content (and narrow energy distribution) in the complex formed by (4) no parent ion is expected[2] nor is one observed. Considerably more $(CH_3)_2SiH^+$ (*m/e* 59) is produced by (4) than by electron impact dissociation of $(CH_3)_2SiHSiH(CH_3)_2$. This is certainly not unexpected since we know $(CH_3)_2SiH^+$ is produced by other reactant ions and, in addition, the relatively simple hydride transfer may proceed *via* a reaction not involving a strong collision complex. A similar observation regarding hydride ion transfer was made in the study of the ionic reactions of SiH_4.[2]

The agreement of the primary mass spectrum of $(CH_3)_2SiHSiH(CH_3)_2$ with the secondary mass spectrum of $(CH_3)_2SiH_2$ is surprisingly good in the 101–105 mass group, and it is tempting to conclude that the preponderant part of this group of ions arises from reactions of $(CH_3)_2Si^+$. What differences do exist could be the result of contributions from the other two reacting ions. However, we really cannot be sure the entire group arises solely from reactions of $(CH_3)_2Si^+$ and at any rate these products comprise only ~5% of the total reaction of this ion.

The pattern of intensities of the secondary ions in the 84–89 mass range is in complete disagreement with the primary ion spectrum of $(CH_3)_2SiHSiH(CH_3)_2$, suggesting $(CH_3)_2Si^+$ is not a significant precursor to this group of products.

There is at least a qualitative similarity of the primary and secondary mass spectra in the 69–75 mass range.

m/e 69–75. With regard to this mass range, the largest discrepancy in the comparison is that the *m/e* 73 (the most intense high-mass product ion) is much larger in the secondary spectrum than in the primary. If we assign the most stable structure to the *m/e* 73 product ion, namely $(CH_3)_3Si^+$, then reactions 5–7 are all strongly exothermic and, therefore, quite feasible energetically.

$$(CH_3)_2Si^+ + (CH_3)_2SiH_2 \longrightarrow (CH_3)_3Si^+ + CH_3SiH_2 \quad (5)$$

$$(CH_3)SiH^+ + (CH_3)_2SiH_2 \longrightarrow (CH_3)_3Si^+ + SiH_3 \quad (6)$$

$$(CH_3)SiH_2^+ + (CH_3)_2SiH_2 \longrightarrow (CH_3)_3Si^+ + SiH_4 \quad (7)$$

The comparison of the pattern of peaks in the secondary and primary spectra (Figure 3) suggests that (5) is a significant contributor to *m/e* 73. This reaction could be easily envisioned as an exchange (in either direction) of methyl groups and hydrogen atoms between the two silicon atoms of the complex. A similar exchange (in one direction) in an analogous complex involving insertion of CH_3SiH^+ in an SiH bond of $(CH_3)_2SiH_2$ can be easily pictured as the manner in which reaction 6 contributes to *m/e* 73. No such analogous insertion complex can easily be pictured for reaction 7, but we cannot for this reason rule it out. Isotopic considerations do rule out the possibility that *m/e* 73 contains a significant contribution from the ion $CH_3Si_2H_2^+$.

(8) F. H. Field, J. L. Franklin, and F. W. Lampe, *J. Amer. Chem. Soc.*, **79**, 2419 (1957).

(9) See ref 8, p 2665.

(10) R. Fuchs, *Z. Naturforsch.*, *A*, **16**, 1026 (1961).

Table I: Isotope Corrected Secondary Spectrum of $(CH_3)_2SiH_2$ and Some Rate Constants

m/e	Intensity	Depletion of reactant ions	
59	100.0	$CH_3SiH^+ + (CH_3)_2SiH_2 \xrightarrow{k_{44}}$ products	$k_{44} = 1.3 \times 10^{-9}$ cm³ molecule⁻¹ sec⁻¹
69	0.2		
71	0.4	$CH_3SiH_2^+ + (CH_3)_2SiH_2 \xrightarrow{k_{45}}$ products	$k_{45} = 7.5 \times 10^{-10}$ cm³ molecule⁻¹ sec⁻¹
72	0.3		
73	20.0	$(CH_3)_2Si^+ + (CH_3)_2SiH_2 \xrightarrow{k_{58}}$ products	$k_{58} = 7.0 \times 10^{-10}$ cm³ molecule⁻¹ sec⁻¹
74	0.5		
84	0.2		
85	1.2		
86	7.3		
87	4.6	Rate Constants for Some Specific Reactions	
88	0.2	$CH_3SiH^+ + (CH_3)_2SiH_2 \rightarrow Si_2(CH_3)_2 + CH_4 + H_2$	
89	0.9		
99	0.25		$k_{86} = 1.6 \times 10^{-10}$ cm³ molecule⁻¹ sec⁻¹
100	0.2	$(CH_3)_2Si^+ + (CH_3)_2SiH_2 \rightarrow Si_2(CH_3)_3H_2^+ + CH_3$	
101	1.3		
102	0.16		$k_{103} = 2.4 \times 10^{-11}$ cm³ molecule⁻¹ sec⁻¹
103	3.8	$(CH_3)_2Si^+ + (CH_3)_2SiH_2 \rightarrow Si_2(CH_3)_4 + H_2$	
116	0.1		
			$k_{116} = 6.3 \times 10^{-12}$ cm³ molecule⁻¹ sec⁻¹

m/e 84–89. As mentioned before, the lack of any sort of agreement between the secondary and primary spectra in the 84–89 mass range strongly suggests that $(CH_3)_2Si^+$ is not a significant precursor for any product ions in this group. From our previous studies of ionic decompositions in SiH_4,[4] Si_2H_6,[4] and $(CH_3)_nSiH_{4-n}$ (n = 1–4)[6] and of ion–molecule reactions in CH_3SiH_3,[3] it is possible to derive a value of 255 ± 5 kcal/mol for the heat of formation of $(CH_3)_2Si_2^+$. This is the stoichiometric formula of *m/e* 86, the largest ion in this group, and we believe the most likely structure in view of the much greater strength of CH bonds as opposed to SiH bonds.[4] This estimate of $\Delta H_f^\circ[(CH_3)_2Si_2^+]$ results in a large endothermicity for the thermochemically most favorable reactions to form it of $(CH_3)_2Si^+$ and $CH_3SiH_2^+$. Such an exclusion leaves only reaction 8, as a feasible explanation of *m/e* 86.

$$CH_3SiH^+ + (CH_3)_2SiH_2 \longrightarrow (CH_3)_2Si_2^+ + CH_4 + H_2 \quad (8)$$

The second largest peak in this group (*m/e* 87) can be formed in thermochemically favorable reactions of both CH_3SiH^+ and $CH_3SiH_2^+$.

m/e 99–105. The most intense product ion in this group, *m/e* 103, can be formed in energetically feasible reactions by all three reactant ions. However, in view of the agreement of the primary and secondary spectra in this mass range, we suggest that $(CH_3)_2Si^+$ is the major precursor to this entire group, and that the specific reaction forming *m/e* 103 is (9), *viz.*

$$(CH_3)_2Si^+ + (CH_3)_2SiH_2 \longrightarrow (CH_3)_3Si_2H_2^+ + CH_3 \quad (9)$$

We may conclude this section by saying that all secondary ions which are formed *via* a complex mechanism have to have at least two precursors, namely $(CH_3)_2Si^+$ and CH_3SiH^+. Reactions of the siliconium ion, $CH_3SiH_2^+$, are very often endothermic in this system and can often be ruled out. Moreover, energetic considerations show that only secondary ions with an odd mass number can be formed from this reactant.

In Table I we present the secondary mass spectrum of $(CH_3)_2SiH_2$ corrected for isotopic contributions to the various ionic products. Specific reaction rates for the depletion of the reactants, $(CH_3)_2Si^+$, CH_3SiH^+, and $CH_3SiH_2^+$ are given, and in addition, rate constants for the production of $(CH_3)_4Si_2^+$, $(CH_3)_3Si_2H_2^+$, and $(CH_3)_2Si_2^+$ (*m/e* 116, 103, and 86, respectively) are also given. It is only in the cases of these three specific products that we feel reasonably certain that only one reactant ion is the precursor.

Trimethylsilane. As shown in Figure 4, in which fractional ion intensities, $I_i/\sum_i I_i$, are plotted as a function of ion-source pressure, $(CH_3)_2SiH^+$ (*m/e* 59) and $(CH_3)_2Si^+$ (*m/e* 58) are reactant ions while $(CH_3)_3Si^+$ (*m/e* 73) is a product ion. No other reactant ions were found in this system nor are there any other products of lesser mass than *m/e* 73. Although heavier product ions up to *m/e* 147 were observed and their intensity dependence on pressure was studied, the hydride transfer reaction to form $(CH_3)_3Si^+$ is the overwhelmingly predominant reaction (~96%) of the two reactant ions. This is shown in Figure 5 in which the secondary mass spectrum (log relative intensity) of $(CH_3)_3SiH$ is shown. Thus we may conclude that the hydride transfer reactions 10 and 11, *viz.*

Table II: Rate Constants for the Ionic Reactions in $(CH_3)_3SiH$

Product *m/e*	Process assigned	$k \times 10^{10}$, cm³ molecule⁻¹ sec⁻¹
73	$(CH_3)_2Si^+ + (CH_3)_3SiH \rightarrow (CH_3)_3Si^+ + (CH_3)_2SiH$	12
	$(CH_3)_2SiH^+ + (CH_3)_3SiH \rightarrow (CH_3)_3Si^+ + (CH_3)_2SiH_2$	6
86	$(CH_3)_2Si^+ + (CH_3)_3SiH \rightarrow Si_2(CH_3)_2^+ + C_2H_6 + CH_4$	0.03
87	$(CH_3)_2Si^+ + (CH_3)_3SiH \rightarrow HSi_2(CH_3)_2^+ + C_2H_6 + CH_3$	0.03
	or $(CH_3)_2SiH^+ + (CH_3)_3SiH \rightarrow HSi_2(CH_3)_2^+ + C_2H_6 + CH_4$	0.007
99	$(CH_3)_2Si^+ + (CH_3)_3SiH \rightarrow CH_3SiCHSiCH_3^+ + C_2H_6 + H_2 + H$	0.03
	or $(CH_3)_2SiH^+ + (CH_3)_3SiH \rightarrow CH_3SiCHSiCH_3^+ + C_2H_6 + 2H_2$	0.007
100	$(CH_3)_2Si^+ + (CH_3)_3SiH \rightarrow CH_3SiCH_2SiCH_3^+ + C_2H_6 + H_2$	0.02
	or $(CH_3)_2SiH^+ + (CH_3)_3SiH \rightarrow CH_3SiCH_2SiCH_3^+ + C_2H_6 + H$	0.004
101	$(CH_3)_2Si^+ + (CH_3)_3SiH \rightarrow (CH_3)_3Si_2^+ + C_2H_6 + H$	0.2
	or $(CH_3)_2SiH^+ + (CH_3)_3SiH \rightarrow (CH_3)_3Si_2^+ + C_2H_6 + H_2$	0.04
103	$(CH_3)_2SiH^+ + (CH_3)_3SiH \rightarrow (CH_3)_3Si_2H_2^+ + C_2H_6$	0.02
115	$(CH_3)_2Si^+ + (CH_3)_3SiH \rightarrow (CH_3)_2SiCH_2SiCH_3^+ + H_2 + CH_3$	0.02
	or $(CH_3)_2SiH^+ + (CH_3)_3SiH \rightarrow (CH_3)_2SiCH_2SiCH_3^+ + H_2 + CH_4$	0.004
117	$(CH_3)_2Si^+ + (CH_3)_3SiH \rightarrow Si_2(CH_3)_4H^+ + CH_3$	0.3
	$(CH_3)_2SiH^+ + (CH_3)_3SiH \rightarrow Si_2(CH_3)_4H^+ + CH_4$	0.07
147	$(CH_3)_3Si^+ + (CH_3)_3SiH \rightarrow Si_2(CH_3)_6H^+$	0.03
	$(CH_3)_3SiH^+ + (CH_3)_3SiH \rightarrow Si_2(CH_3)_6H^+ + H$	0.7

$$(CH_3)_2Si^+ + (CH_3)_3SiH \longrightarrow (CH_3)_3Si^+ + (CH_3)_2SiH \quad (10)$$

$$(CH_3)_2SiH^+ + (CH_3)_3SiH \longrightarrow (CH_3)_3Si^+ + (CH_3)_2SiH_2 \quad (11)$$

are almost the sole fates of the reactant ions. In view of this dominance of (10) and (11) we may with little error, equate the disappearance rates of *m/e* 58 and 59 with the rates of hydride ion transfer from $(CH_3)_3SiH$ to the respective ions. The specific reaction rates found in this way (Table II) are of the same order of magnitude as found for the hydride transfer reaction in other silane systems.[2,3,5]

Secondary ions of higher mass than the reactant molecule exhibit intensities that are two to three orders of magnitude smaller than the $(CH_3)_3Si^+$ produced by hydride ion transfer. In most cases we are not able at this time to rule out either reactant ion as a precursor to the various secondary ions nor to estimate the relative contributions, so in Table II we have calculated the rate constants for each reaction as if that reaction alone produced the ion in question. In the case of the product ion at *m/e* 86, energetic considerations do enable us to conclude that the reaction is (12), *viz.*

$$(CH_3)_2Si^+ + (CH_3)_3SiH \longrightarrow (CH_3)_2Si_2^+ + CH_4 + C_2H_6 \quad (12)$$

As shown in Figure 5, an ion exhibiting secondary behavior is observed at *m/e* 147. In pure $(CH_3)_3SiH$ this ion could only arise by undetected reactions of $(CH_3)_3Si^+$ or $(CH_3)_3SiH^+$ ions with $(CH_3)_3SiH$. However, this ion is the largest peak in the spectrum of $(CH_3)_3SiOSi(CH_3)_3$, and it is possible that this impurity could

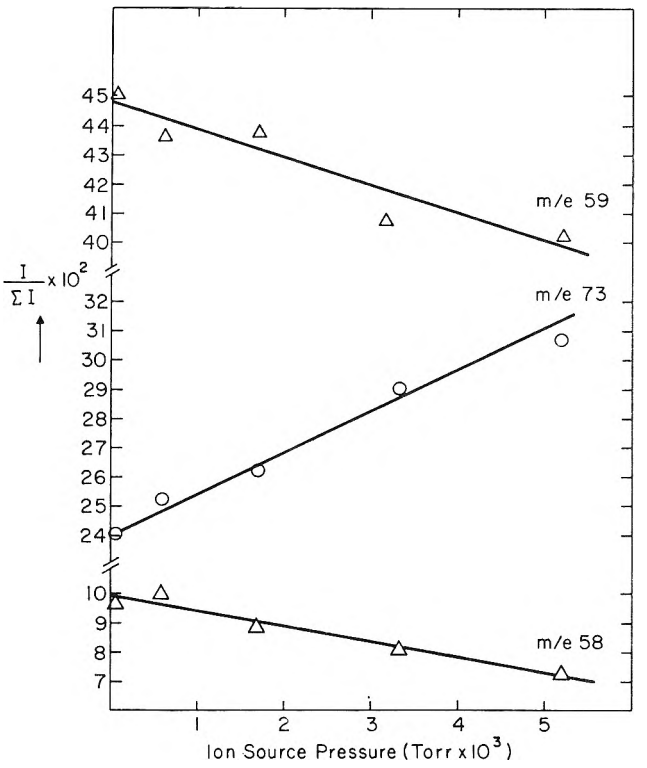

Figure 4. Fractional ion intensities in trimethylsilane as a function of ion-source pressure.

be produced by a reaction of $(CH_3)_3SiH$ with H_2O on the surfaces of the ion source that is second order in pressure. For this reason and the fact that no decline in the fractional intensities of either possible reactant ion could be observed in this system, we are quite uncertain as to the nature of the product ion having *m/e* 147.

Tetramethylsilane. Although expected, the most striking feature of the study of ionic reactions in

Table III: Rate Constants for the Ionic Reactions in $(CH_3)_4Si$

Product m/e	Process assigned	$k \times 10^{10}$, cm³ molecule⁻¹ sec⁻¹
73	$(CH_3)_4Si^+ + (CH_3)_4Si \rightarrow Si(CH_3)_3^+ + Si(CH_3)_3 + C_2H_6$	16
101	$CH_3SiH_2^+ + (CH_3)_4Si \rightarrow Si(CH_3)_3^+ + H_2 + C_2H_6$	0.25
103	$CH_3SiH_2^+ + (CH_3)_4Si \rightarrow Si(CH_3)_3H_2^+ + C_2H_6$	0.03
115	$(CH_3)_4Si^+ + (CH_3)_4Si \rightarrow CH_3SiCH_2Si(CH_3)_2^+ + CH_4 + C_2H_6 + CH_3$	1.2
116	$(CH_3)_4Si^+ + (CH_3)_4Si \rightarrow (CH_3)_4Si_2^+ + 2C_2H_6$	0.13
117	$(CH_3)_4Si^+ + (CH_3)_4Si \rightarrow HSi_2(CH_3)_4^+ + C_2H_5 + C_2H_6$	0.38
131	$(CH_3)_4Si^+ + (CH_3)_4Si \rightarrow Si_2(CH_3)_5^+ + C_2H_6 + CH_3$	2.0
141	$(CH_3)_4Si^+ + (CH_3)_4Si \rightarrow Si_2C_6H_{13}^+ + C_2H_6 + 2H_2 + H$	0.2
145	$(CH_3)_4Si^+ + (CH_3)_4Si \rightarrow (CH_3)_2SiCH_2Si(CH_3)_3^+ + CH_4 + CH_3$	0.25
161	$(CH_3)_4Si^+ + (CH_3)_4Si \rightarrow (CH_3)_3SiCH_2Si(CH_3)_3H^+ + CH_3$	0.16

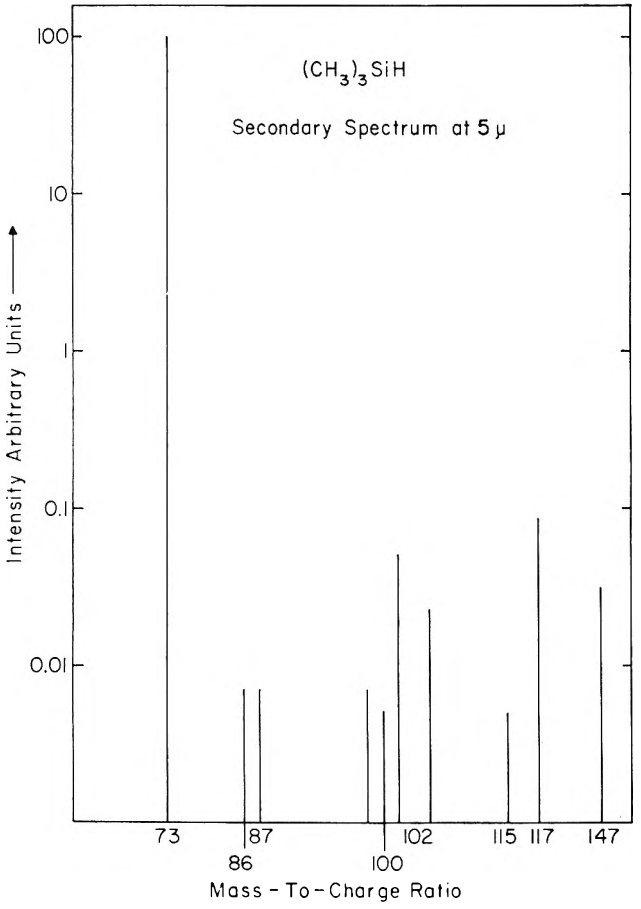

Figure 5. Secondary ion mass spectrum of trimethylsilane at an ion-source pressure of 5×10^{-3} Torr.

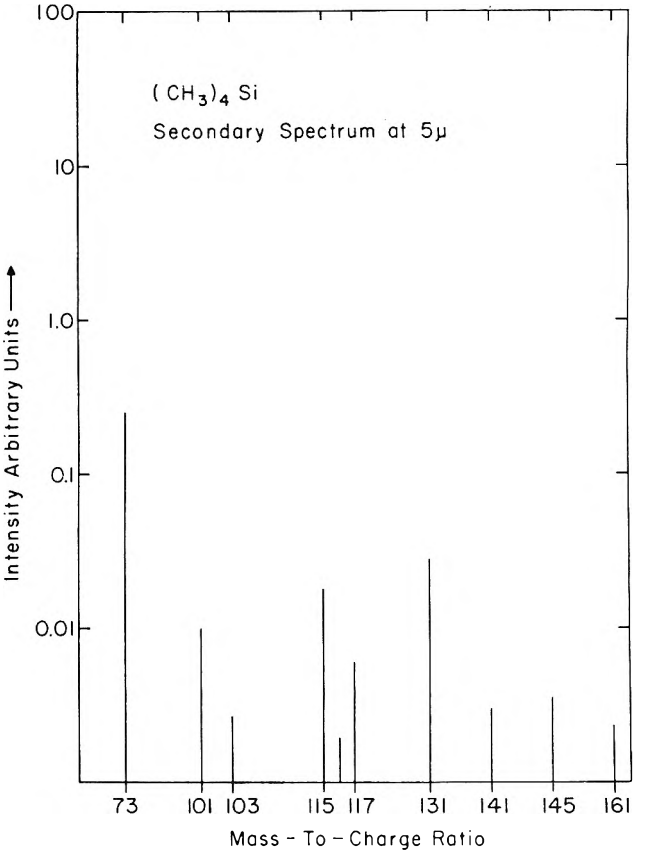

Figure 6. Secondary ion mass spectrum of tetramethylsilane at an ion-source pressure of 5×10^{-3} Torr.

$(CH_3)_4Si$ is the complete absence of a hydride transfer reaction from the parent molecule to any ion. The occurrence of even a small amount of such reaction would have been detectable in this case since m/e 87 $[(CH_3)_3SiCH_2^+]$ is absent in the primary mass spectrum. The reason for the absence of hydride transfer is most likely energetic, because to transfer a hydride ion to any reactant ion of significant intensity (Figure 1) requires the breaking of a CH bond and the formation of a relatively weaker SiH bond.

Studies of the fractional intensities of the primary ions show that the only reactant ion whose fractional intensity decreases is the parent, namely $(CH_3)_4Si^+$. The fractional decrease of this ion with increasing source pressure is four times as large as the sum of the fractional increases of the product ions having m/e values larger than the parent, namely larger than m/e 88. This means that there must be a collisional reaction of $(CH_3)_4Si^+$ that forms a primary ion. One feasible possible reaction, from an energetic point of view,[6] would appear to be (13), *viz.*

$$(CH_3)_4Si^+ + (CH_3)_4Si \longrightarrow$$
$$(CH_3)_3Si^+ + (CH_3)_3Si + C_2H_6 \quad (13)$$

The $(CH_3)_3Si^+$ (m/e 73) is the most abundant ion in the primary mass spectrum of $(CH_3)_4Si$, and the amount of increase of m/e 73 *via* (13) is so small, for the pressure range studied (10^{-3} to 10^{-2} Torr), that within our precision we were unable to detect an increase in m/e 73. This is immediately apparent by reference to Figure 1, which indicates that even if *all* of m/e 88 were converted into m/e 73 the increase in m/e 73 would be only 2%; the maximum fraction of m/e 88 reacting to form m/e 73 (Table III) is 0.05 and hence the maximum increase in m/e 73 that could occur in this work is 0.1%. We should also mention that the overall intensity of secondary ions is so small that a number of product ions may have precursors whose fractional intensities did not exhibit a detectable decrease as the source pressure was increased. The reactions assigned and the rate constants determined are presented in Table III. In constructing Table III we have taken the product ion in question to be formed by a reaction of $(CH_3)_4Si^+$ unless such reaction is energetically unfeasible. Two such cases arise, namely, formation of m/e 101 and 103. The only primary ion that could be the precursor to these products, on energetic grounds, is $CH_3SiH_2^+$. As in Tables I and II, the neutral products are taken to be those which make the reaction most favorable thermochemically.

The polarization of the SiH bond is generally accepted[11] to be $Si^{\delta+}$–$H^{\delta-}$, which should result in these compounds being very susceptible to H^- transfer to an attacking positive ion. In view of this it is interesting to consider the percentage of ion molecule reactions in silicon compounds that are H^- transfer reactions. As shown in Table IV, H^- transfer to attacking silicon ions is the dominant reaction in all compounds that contain SiH bonds, but is of no consequence in the absence of SiH bonds. Moreover, there is an increasing tendency towards H^- transfer as the hydrogen is replaced by methyl groups. This tendency is paralleled by a decrease in the ionization potential of the $(CH_3)_nSiH_{3-n}$ radical, which in turn most probably leads to an increased polarization of the $Si^{\delta+}$–$H^{\delta-}$ bond.

Table IV: Hydride Ion Transfer in $(CH_3)_nSiH_{4-n}$ Compounds

n	Reacting ions	$I_z[(CH_3)_nSiH_{3-n}]$	H^- transfer percentage
0	SiH_2^+	8.1[a,b]	42
1	CH_3SiH^+	...	37
2	$(CH_3)_2Si^+$ $CH_3SiH_2^+$ CH_3SiH^+	...	70
3	$(CH_3)_2Si^+$ $(CH_3)_2SiH^+$	7.0[a]	96
4	$(CH_3)_4Si^+$ $CH_3SiH_2^+$	...	0

[a] Reference 6. [b] W. C. Steele, L. D. Nichols, and F. G. A. Stone, *J. Amer. Chem. Soc.*, 84, 4441 (1962).

Acknowledgment. This work was supported by the United States Atomic Energy Commission under Contract No. AT(30-1)-3570. We also wish to thank the National Science Foundation for providing financial assistance in the original purchase of the mass spectrometers.

(11) E. A. V. Ebsworth, "Volatile Silicon Compounds," Pergamon Press, London, 1963.

The Influence of Temperature on the γ Radiolysis of Isopropyl Alcohol Vapor. Effect of Molecular Structure on the Nonchain and Chain Decompositions of Alcohol Vapors[1]

by H. J. van der Linde and G. R. Freeman*

Department of Chemistry, University of Alberta, Edmonton, Alberta, Canada *(Received August 7, 1970)*

Publication costs assisted by the University of Alberta

Isopropyl alcohol vapor at a density of 0.78 g/l. was irradiated to a dose of 3.2×10^{19} eV/g at temperatures from 125 to 400°. The yields of all the measured products except pinacol were independent of temperature between 125 and 205°. The G values were H_2, 7.2; CH_4, 4.8; CO, 0.52; C_2H_4, 0.21; C_2H_6, 0.16; CH_3CHO, 2.9; C_2H_5OH, 0.66; C_3H_6, 2.5; $(CH_3)_2CO$, 4.0; diisopropyl ether, 0.36; and pinacol, 1.0–1.5. The results are compared with those from the radiolyses of methanol and ethanol vapors. As the alcohol molecule size increases the amounts of C–O and C–C bond cleavage increase at the expense of C–H and O–H cleavage. The total ionization yield and the net amount of alcohol decomposition do not vary greatly from one alcohol to the next: G(ionization) = 4.1 ± 0.2 and $G(-\text{alcohol})$ = 14 ± 1 for each of the alcohols in the "nonchain" decomposition region of temperatures. At temperatures above about 250° chain reactions became important in isopropyl alcohol vapor. There were four modes of radiation induced chain decomposition. The stoichiometric representation of the modes, with their G values at 380° and activation energies (kcal/mol) were $C_3H_7OH \rightarrow H_2 + (CH_3)_2CO$, 600 (32 ± 4); $C_3H_7OH \rightarrow CH_4 + CH_3CHO$, 43 (18 ± 2); $C_3H_7OH \rightarrow H_2O + C_3H_6$, ~1200 (40 ± 10); $2C_3H_7OH \rightarrow H_2O + (C_3H_7)_2O$, 300 (41 ± 2). The activation energies were similar to those of the corresponding modes in the radiation-induced pyrolysis of ethanol under similar conditions. However, the rates of all the modes except demethanation were an order of magnitude greater in isopropyl alcohol than in ethanol. Demethanation occurred at similar rates in the two alcohols.

Introduction

The radiolysis of ethanol vapor is relatively insensitive to temperature at temperatures below 300°,[2,3] but above 300° both free-radical[3] and cationic[4] chain reactions occur.

The radiation-induced cationic chain reaction forms ether and water. It also occurs in isopropyl alcohol vapor,[5] but it begins at a lower temperature in isopropyl alcohol (~250°) than in ethanol.

The present article reports the normal radiolysis and several modes of radiation-sensitized chain decomposition of isopropyl alcohol vapor. Effects of molecular structure upon the different modes of alcohol reaction are discussed.

Experimental Section

Materials, Sample Preparation, and Handling. The methods of purification of materials and the experimental techniques used were the same as those reported earlier,[5] unless otherwise mentioned. The irradiation dose rate in isopropyl alcohol was 3.5×10^{19} eV/(g hr).

Product Analysis. The gaseous products were separated from the irradiated sample by low-temperature distillation under vacuum. The gases were collected and measured in a McLeod–Toepler apparatus, then injected into a gas chromatograph that had a thermal conductivity detector.

The liquid products were measured by injecting 1 μl of the irradiated sample into a gas chromatograph that had a flame ionization detector.

The different products were analyzed with the following gc columns and conditions: (a) hydrogen, methane, and carbon monoxide; 9 ft × 1/4 in. copper tubing packed with molecular sieve 5A, 100°, helium carrier gas at 75 ml/min; (b) methane, ethane, ethylene, and propylene; 6 ft × 1/4 in. copper tubing packed with Porapak Q (150–200 mesh), programmed from 80 to 120°, helium carrier gas at 75 ml/min; (c) acetone and diisopropyl ether; 12 ft × 3/16 in. glass tubing packed with 10% Carbowax 1540 on Chromosorb WAW, 75°, helium at 60 ml/min; (d) acetaldehyde and ethanol; 3 ft × 3/16 in. glass tubing packed with Porapak QS (150–200 mesh), 130°, helium at 75 ml/min; (e) pinacol; 6 ft × 3/16 in. glass tubing packed with 1% FFAP on glass beads (60–80 mesh), 110°, helium at 30 ml/min.

Results

Samples of isopropyl alcohol at a density of 0.78 g/l.

(1) The authors are grateful to the National Research Council of Canada for financial assistance.

(2) K. M. Bansal and G. R. Freeman, *J. Amer. Chem. Soc.*, 90, 7183 (1968).

(3) K. M. Bansal and G. R. Freeman, *ibid.*, 90, 7190 (1968).

(4) K. M. Bansal and G. R. Freeman, *ibid.*, 92, 4173 (1970).

(5) H. J. van der Linde and G. R. Freeman, *ibid.*, 92, 4417 (1970).

(500 Torr at 350°) were irradiated to a dose of 3.2×10^{19} eV/g at temperatures from 125 to 400°. The yields of all the measured products except pinacol were independent of temperature between 125 and 205°, but increased at higher temperatures. The temperature at which the yield began to increase varied from about 250 to about 340°, depending on the product. However, the G value of pinacol went through a maximum at about 200°; it was 1.0 at 124°, 1.5 at 205°, 0.7 at 271°, 0.2 at 301°, and 0.0 at 332° and higher temperatures.

The large yields of products at the high temperatures were formed by chain reactions, so it is convenient to divide the temperature range into "nonchain" and "chain" regions and to present the results of each region separately.

"Blank" samples were prepared and heated in the same way as the normal samples, but were not irradiated. The amounts of products formed in the blanks were negligible at temperatures below 300°, but at high temperatures were sometimes several per cent of the amounts formed in the irradiated samples. The reported G values have had the blank yields subtracted from them.

Nonchain Region. The 100-eV yields of the measured products at temperatures from 125 to 205° are listed in Table I. The major products in decreasing order of their yields are hydrogen, methane, acetone, acetaldehyde, water, propylene, and pinacol.

Table I: Nonchain Product Yields, 125 to 205°[a]

Product	G	Chain threshold temp, °C
H_2	7.2	~250
CH_4	4.8	~250
CO	0.52	~310
C_2H_4	0.21	~340
C_2H_6	0.16	~340
CH_3CHO	2.9	~250
C_2H_5OH	0.66	~250
C_3H_6	2.5	~250
$(CH_3)_2CO$	4.0	~250
$(i\text{-}C_3H_7)_2O$	0.36	~250
$[(CH_3)_2COH]_2$	1.0-1.5	
H_2O	~2.8[b]	
$-C_3H_7OH$	14[c]	

[a] Isopropyl alcohol density 0.78 g/l. (350 Torr at 165°); dose = 3.2×10^{19} eV/g. [b] Sum of C_3H_6 and $(i\text{-}C_3H_7)_2O$ yields. [c] $G(-C_3H_7OH) = 0.33\ \Sigma\ G$(carbon atoms in products).

The approximate upper temperature limit of the nonchain region, which is also the threshold temperature of the chain region, is listed for each product in Table I.

Chain Region. The G values of the products of the chain reactions were estimated by subtracting the nonchain G values of Table I from the yields measured at higher temperatures. Subtraction of the nonchain yields was necessary to obtain a reasonable Arrhenius plot of the chain yields at temperatures just above the chain threshold temperature. At higher temperatures the correction was negligible. This procedure was satisfactory, though not exact.

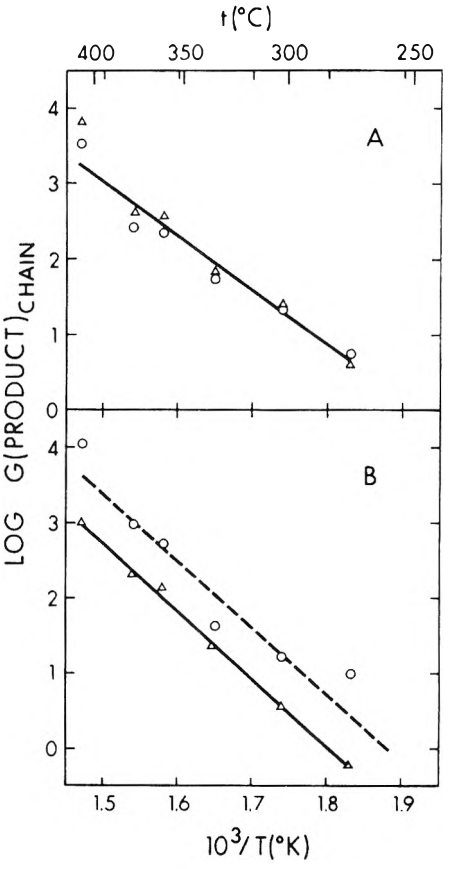

Figure 1. Arrhenius plots of the major radiation-induced chain product yields in isopropyl alcohol vapor. Vapor density = 0.78 g/l. A: ○, hydrogen; △, acetone. B: ○, propylene; △, diisopropyl ether. G_{chain} at temperature t is the measured value at t minus the nonchain value listed in Table I.

The main products formed by chain mechanisms were hydrogen, acetone, propylene, and diisopropyl ether. Arrhenius plots of the chain yields of these compounds are shown in Figure 1. Water, the conjugate product of propylene and diisopropyl ether, was also detected but was not measured quantitatively.

The results for propylene were less precise than those for the other products because of the lack of reproducibility of the propylene blanks. Isopropyl alcohol was evidently catalytically dehydrated to propylene on the vessel wall, sometimes at a rate that was similar to that of the radiation-induced reaction.

Minor chain mechanisms formed methane, acetaldehyde, ethanol, ethylene, ethane, and carbon monoxide. Arrhenius plots of the chain yields of these compounds are shown in Figure 2.

The activation energies of formation of the various

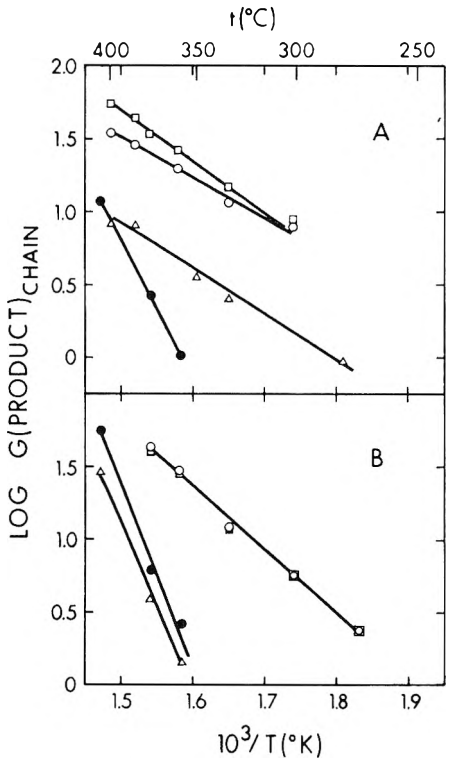

Figure 2. Arrhenius plots of the minor radiation-induced chain product yields in isopropyl alcohol vapor. Vapor density = 0.78 g/l. A: ○, acetaldehyde; ●, carbon monoxide; △, ethanol; □, ($CH_3CHO + C_2H_5OH + CO$). B: ○, methane; ●, ethylene; △, ethane; □, ($CH_4 - CO$). G_{chain} at temperature t is the measured value at t minus the nonchain value listed in Table I.

Table II: Activation Energies of Formation and G Values of Chain Products from Isopropyl Alcohol at 380°[a]

Product	E_a, kcal/mol	G_{chain}
H_2	32 ± 4	600
$(CH_3)_2CO$	32 ± 4	600
C_3H_6	40 ± 10	~1200
$(i\text{-}C_3H_7)_2O$	41 ± 2	300
CH_4	20 ± 2	46
CH_3CHO	13 ± 2	27
C_2H_5OH	15 ± 2	6
C_2H_4	58 ± 3	10
C_2H_6	54 ± 3	6
CO	45 ± 3	3

[a] Isopropyl alcohol density = 0.78 g/l. (530 Torr); dose = 3.2×10^{19} eV/g.

products are listed in Table II. To give an idea of the relative extents of the different reactions, G values estimated for 380° are also given in the table.

Discussion

Nonchain Region ($t < 250°$). Alcohol molecules can decompose in several different ways, by cleavage of a C–H, O–H, C–O, or C–C bond. A measure of the total amount of C–H and O–H cleavage is given by the value of $G(H_2)$. Similarly, the amounts of C–O and C–C cleavage are indicated by the G values of the resulting products. It is interesting to compare the extents of the different modes of decomposition of methanol,[6] ethanol,[2] and isopropyl alcohol during γ radiolysis in the vapor phase. As one proceeds through the alcohols in order of increasing molecular size, the amounts of C–O and C–C cleavage increase at the expense of C–H and O–H cleavage (Table III).

Table III: Radiolytic Decomposition of Methanol, Ethanol, and Isopropyl Alcohol Vapors

	CH_3OH[a]	C_2H_5OH[b]	$i\text{-}C_3H_7OH$[c]
$G(H_2)$[d]	10.4	9.9	7.2
G(C–O cleavage)	0.3	1.8	2.9
G(C–C cleavage)		3.3	5.3
G(CO)	0.8	0.7	0.5
G(ion pairs)[e]	4.1 ± 0.2	4.1 ± 0.2	4.1 ± 0.2
G(−alcohol)	13	15	14

[a] Reference 6, t = 21°. [b] Reference 2, t = 150°. [c] Present work, t = 125–205°. [d] $G(H_2)$ is a measure of the total of C–H and O–H cleavage. [e] References 10 and 11.

The large increase in G(C–O cleavage) on going from methanol to ethanol is related to the fact that methanol cannot be dehydrated to form an olefin, whereas ethanol can. Dehydration to form an olefin is much less endothermic than simple C–O bond cleavage.[7]

$$CH_3OH \longrightarrow CH_3 + OH \quad -92 \text{ kcal/mol} \quad (1)$$

$$C_2H_5OH \longrightarrow C_2H_4 + H_2O \quad -11 \text{ kcal/mol} \quad (2)$$

The further increase on going from ethanol to isopropyl alcohol correlates with the fact that secondary alcohols are more readily dehydrated than are primary alcohols by acid catalysis.[8,9] The net reactions 2 and 3 are nearly equally endothermic.[7]

$$i\text{-}C_3H_7OH \longrightarrow C_3H_6 + H_2O \quad -12 \text{ kcal/mol} \quad (3)$$

In methanol there is no C–C bond to cleave, but in both ethanol and isopropyl alcohol G(C–C cleavage)/G(C–O cleavage) = 1.8 (Table III). The ratio (no. of C–C bonds)/(no. of C–O bonds) for isopropyl alcohol is double for ethanol, so the constancy of the cleavage ratio is somewhat surprising.

Carbon monoxide must result from the decomposition of highly excited species, because all four appendages of the ⩾C–O– group in the alcohol must be removed. The

(6) J. H. Baxendale and R. D. Sedgwick, *Trans. Faraday Soc.*, 57, 2157 (1961).

(7) S. W. Benson, *J. Chem. Educ.*, 42, 502 (1965).

(8) C. R. Noller, "Chemistry of Organic Compounds," 3rd ed, W. B. Saunders Co., London, 1965, p 148ff.

(9) J. L. Beauchamp, *J. Amer. Chem. Soc.*, 91, 5925 (1969).

Table IV: Modes of Decomposition during Radiation-Induced Pyrolysis of Alcohols at 380°

	Mode	C_2H_5OH[a] G_{chain}	C_2H_5OH[a] E_a, kcal/mol	i-C_3H_7OH[b] G_{chain}	i-C_3H_7OH[b] E_a, kcal/mol
(7)	alcohol → H_2 + carbonyl	100	30 ± 2	600	32 ± 4
(8)	→ CH_4 + aldehyde	64	20 ± 2	43	18 ± 2
(9)	→ H_2O + olefin	45	27 ± 2	~1200	40 ± 10
(10)	→ H_2O + ether	21	43 ± 4	300	41 ± 2
		Σ = 230		Σ = 2140	

[a] Values taken from Figures 8 and 9 of ref 3 and Figure 2 of ref 4. Ethanol pressure = 580 Torr. Dose rate = 4×10^{19} eV/(g hr). [b] Present work. Isopropyl alcohol pressure = 530 Torr. Dose rate = 3.5×10^{19} eV/(g hr).

decrease in carbon monoxide yield as one proceeds from methanol to isopropyl alcohol (Table III) reflects the increasing number of possible modes of decomposition of the alcohol molecules, and other related properties.

The total ionization yield and the net amount of alcohol decomposition do not vary greatly from one alcohol to the next: G(ionization) = 4.1 ± 0.2[10,11] and G(−alcohol) = 14 ± 1 for each of the three compounds listed in Table III.

Chain Region (t > 250°). Pinacol was formed by reaction 4. The pinacol yield declined at temperatures

$$2(CH_3)_2\dot{C}OH \longrightarrow [(CH_3)_2COH]_2 \quad (4)$$

above about 250°, in the same region where the chain mechanisms began to operate. The decline in the pinacol yield is attributed to the decomposition of the alcohol radical.

$$(CH_3)_2\dot{C}OH \longrightarrow (CH_3)_2CO + H \quad (5)$$

Reaction 5 is also one of the chain propagation reactions for acetone formation, the other one being

$$R + (CH_3)_2CHOH \longrightarrow RH + (CH_3)_2\dot{C}OH \quad (6)$$

where R is any free radical in the system.

Four main modes of chain decomposition occur during the radiation-induced pyrolysis of isopropyl alcohol. The modes are analogous to those that were found in the radiation-induced pyrolysis of ethanol,[3,4] and it is instructive to compare the two systems.

The four modes are represented by the following stoichiometric equations.

$$\text{alcohol} \longrightarrow H_2 + \text{carbonyl} \quad (7)$$

$$\longrightarrow CH_4 + \text{aldehyde} \quad (8)$$

$$\longrightarrow H_2O + \text{olefin} \quad (9)$$

$$\longrightarrow H_2O + \text{ether} \quad (10)$$

The rates of dehydrogenation (7) and dehydration (9 and 10) are roughly an order of magnitude greater in isopropyl alcohol than in ethanol, while the rates of demethanation (8) are similar in the two systems under the same conditions (Table IV).

In ethanol at 380° and 530 Torr the relative rates of the different modes are dehydrogenation (7) > demethanation (8) > dehydration to olefin (9) > dehydration to ether (10), whereas in isopropyl alcohol under similar conditions the relative rates are dehydration to olefin (9) > dehydrogenation (7) > dehydration to ether (10) > demethanation (8).

The activation energy of the dehydrogenation chain reaction in isopropyl alcohol vapor is 32 ± 4 kcal/mol, obtained from an Arrhenius plot of the hydrogen and acetone yields. The acetone yield was corrected slightly for the amount produced by the secondary reaction 11.

$$CH_3CHO + i\text{-}C_3H_7OH \longrightarrow C_2H_5OH + (CH_3)_2CO \quad (11)$$

By analogy with the thermal reaction 12 that occurs

$$CH_2O + C_2H_5OH \longrightarrow CH_3OH + CH_3CHO \quad (12)$$

readily in the vapor phase at temperatures above 250°,[4] it is suggested that the ethanol in the present system is produced by (11).

The rate of the demethanation chain reaction 8 in isopropyl alcohol is not represented simply by the rate of formation of methane or of acetaldehyde, because the latter two are not equal (see Table II or Figure 2). The aldehyde undergoes secondary reactions including (11) and decomposition to methane and carbon monoxide

$$CH_3CHO \longrightarrow CH_4 + CO \quad (13)$$

The yield of (8) can be estimated from either eq i or ii.

$$G_8 = G(CH_3CHO) + G(C_2H_5OH) + G(CO) \quad \text{(i)}$$

$$G_8 = G(CH_4) - G(CO) \quad \text{(ii)}$$

An Arrhenius plot of the right-hand side of eq i gave an activation energy E_8 = 16 kcal/mol (Figure 2A), and that of the right-hand side of eq ii gave E_8 = 19 kcal/mol (Figure 2B). It is concluded that E_8 = 18 ± 2 kcal/mol.

The activation energies of the dehydration reactions

(10) P. Adler and H. K. Bothe, *Z. Naturforsch. A*, **20**, 1700 (1965).

(11) R. M. Leblanc and J. A. Herman, *J. Chim. Phys.*, **63**, 1055 (1966).

9 and 10 are obtained from Arrhenius plots of the olefin and ether yields, respectively. In isopropyl alcohol we obtained $E_9 = 40 \pm 10$ kcal/mol and $E_{10} = 41 \pm 2$ kcal/mol.

The activation energies of the four decomposition modes in the radiation-induced pyrolysis of isopropyl alcohol are similar to those of the corresponding modes in ethanol (Table IV).

The Radiolysis of Carbon Tetrachloride. Radical Yields and the Formation of Tetrachloroethylene as an Initial Product[1]

by Ned E. Bibler

Savannah River Laboratory, E. I. du Pont de Nemours and Company, Aiken, South Carolina 29801
(Received August 11, 1970)

Publication costs assisted by the U. S. Atomic Energy Commission

The radiolysis of liquid, air-free carbon tetrachloride containing a variety of solutes at 25° was investigated in detail. With Br_2 and HI as radical scavengers, the measured initial 100-eV yield of CCl_3 radicals was equal to 7.0 ± 0.2. The organic products resulting from spur reactions in these solutions were C_2Cl_4 and C_2Cl_6 (G = 0.08 and 0.47 molecule/100 eV, respectively). The total yield of scavengeable chlorine was 8.3 atoms/100 eV. With these two scavengers, evidence for the existence of intermediates other than Cl and CCl_3 was obtained. When I_2 was the scavenger, ICl was the most abundant product. The other major product, CCl_3I, was very susceptible to radical attack, and eventually all the initial iodine atoms appeared as ICl. In solutions containing ICl as a scavenger, $G(-ICl)$, $G(I_2)$, and $G(CCl_3I)$ were all equal to zero. With each of the above scavengers, tetrachloroethylene was an initial product; in the absence of scavengers, tetrachloroethylene presumably is removed by reaction with Cl or Cl_2. To explain C_2Cl_4 formation in the presence of ICl, an ICl_2 intermediate is proposed. Other scavengers suitable for Cl atoms included NH_3, C_2H_4, CH_3Cl, CH_2Cl_2, and $CHCl_3$; CCl_3Br was not an efficient scavenger as suggested by the absence of C_2Cl_4 as a product. In solutions containing NH_3, a precipitate containing Cl^- ions was formed by the radiolysis. Also, in the presence of the chloromethanes, CH_2Cl_2 and $CHCl_3$, the radical yield in carbon tetrachloride was lowered considerably, apparently by an energy- or charge-transfer mechanism.

Introduction

Various authors have estimated[2-7] widely differing 100-eV yields of radicals in the ^{60}Co γ radiolysis of liquid air-free carbon tetrachloride with a variety of scavengers (Table I). These differences may be partly attributed to differences in the reactivity of the scavengers toward electronically excited or ionic precursors of the radicals and also the reactivity of the scavengers toward the radicals themselves.[8] However, there is no apparent reason for the differences obtained when the halogens Br_2 or I_2 are used as the scavengers. Both halogens have been shown to scavenge CCl_3 radicals in the radiolysis of chloroform;[9] both have ionization potentials lower than that for carbon tetrachloride;[10] and both can undergo exothermic reactions with CCl_3 radicals or Cl atoms. Accordingly, we have investigated the radiolysis of liquid carbon tetrachloride in detail using a variety of scavengers including Br_2, I_2, ICl, and HI. In the presence of these and other solutes (including NH_3, CH_2Cl_2, and C_2H_4) capable of reacting with Cl atoms, tetrachloroethylene was an initial product of the radiolysis. This compound is not produced in the radiolysis of pure carbon tetrachloride[2,3] or of carbon tetrachloride containing oxygen.[4]

(1) The information contained in this article was developed during the course of work under Contract AT(07-2)-1 with the U. S. Atomic Energy Commission. This work was sponsored by Division of Peaceful Nuclear Explosives.

(2) J. W. Schulte, *J. Amer. Chem. Soc.*, **79**, 4643 (1957).

(3) F. P. Abramson, B. M. Buckhold, and R. F. Firestone, *ibid.*, **84**, 2285 (1962).

(4) T. H. Chen, K. Y. Wong, and F. J. Johnston, *J. Phys. Chem.*, **64**, 1023 (1960).

(5) S. Ciborowski, N. Colebourne, E. Collinson, and F. S. Dainton, *Trans. Faraday Soc.*, **57**, 1123 (1961).

(6) E. Collinson, F. S. Dainton, and H. Gillis, *J. Phys. Chem.*, **65**, 695 (1961).

(7) A. Chapiro, *ibid.*, **63**, 801 (1959).

(8) R. A. Holroyd in "Fundamental Processes in Radiation Chemistry," P. Ansloos, Ed., Interscience, New York, N. Y., 1968, p 457.

(9) H. R. Werner and R. F. Firestone, *J. Phys. Chem.*, **69**, 840 (1965).

(10) K. Watanabe, *J. Chem. Phys.*, **26**, 542 (1957).

Table I: Values Estimated for $G(CCl_3)$ in the Radiolysis of Carbon Tetrachloride at ~23° with Various Scavengers

Scavenger	$G(CCl_3)$	Ref
Cl_2	<3.5	2
Br_2	>9.0	3
I_2	>12.0	3
$CHCl_3$	3–3.5	4
DPPH[a]	2.9	5
Ferrocene	>2.3	6
MMA[b]	19	7

[a] DPPH = Diphenylpicrylhydrazyl. [b] MMA = Methyl methacrylate.

Experimental Section

Carbon tetrachloride (Matheson Co.) was further purified by triple distillation in an inert atmosphere through a 1 m × 2 cm o.d. column filled with glass helices. In the final distillate no impurity was detected by gas chromatography (sensitivity ~10^{-4} mol %). Iodine (research grade) was resublimed before use and research grade bromine was used without further purification. Hydrogen iodide was prepared by dehydrating a solution of hydriodic acid (Baker 47% aqueous HI solution) with P_2O_5 on a vacuum line.[11] Crystals of pure iodine monochloride were sublimed directly from research grade ICl at 25°. These crystals were freshly sublimed each time that solutions were prepared for radiolysis. All other solutes (NH_3, C_2H_4, CH_3Cl, CH_2Cl_2, $CHCl_3$, C_2H_3, and CCl_3Br) were research grade materials and were further purified either by trap-to-trap distillation of the vapor or by distillation of the liquid.

Samples were prepared for irradiation by passing the carbon tetrachloride solution through a 5-Å molecular sieve attached to a buret[12] connected directly to a vacuum line. Aliquots (3 ml) of this solution were then passed from the buret to the vacuum line and degassed by several freeze–pump–thaw cycles. The entire aliquot was then distilled into the irradiation vessel (15-mm o.d. tube) and further degassed and sealed from the line while the sample was frozen with liquid nitrogen.

When the solutes to be dissolved in the carbon tetrachloride were solids or liquids at room temperature, they were added to the solution before it was passed through the sieve. The only suitable drying agent for solutions containing ICl was "Drierite" (Registered trademark of W. A. Hammond Drierite Co.) because other drying agents reacted with ICl to produce I_2 and presumably Cl^-. When the solutes to be dissolved were gases at room temperature, measured amounts were added to samples of carbon tetrachloride after it was distilled into the irradiation cells. In these cells the void space above the liquid was approximately 10–20% of the volume of the liquid, and all the gas was assumed to be dissolved in the sample.

The samples were irradiated at 25 ± 1° with a ^{60}Co Gammacell 220 (Atomic Energy of Canada Ltd.). The dose rate in carbon tetrachloride, determined by multiplying the appropriate electron density ratio by the dose rate in the Fricke dosimeter, was 1.77×10^{16} eV/(g) (sec).

Free halogens in the samples after irradiation were analyzed with a Beckman DU spectrophotometer. Molar absorptivities for Cl_2, BrCl, Br_2, I_2, and ICl were determined and were in good agreement with published values.[13] Chlorine was also determined by breaking open the irradiation cell containing the sample while the cell was immersed in an 0.1 *M* solution of KI. The liberated I_2 was titrated with 0.01 *N* $Na_2S_2O_3$ to a starch end point.

Organic products were determined with an F & M Model 400 gas chromatograph with a flame ionization detection system. For $CHCl_3$ and CCl_3Br a 12-ft long, $^1/_4$-in. column (20% Silicone 200) was operated isothermally at 90°. For CCl_2Br_2, C_2Cl_4, and C_2Cl_6 a 50-ft long, $^1/_8$-in. column (2% SE-30) was used isothermally at 100°. The columns were calibrated each time samples were analyzed. All the solutes used to prepare standard solutions of radiolytic products except CCl_2Br_2 were research grade and were further purified. Dichlorodibromomethane was prepared by photolyzing a mixture of $CHCl_2Br$ and Br_2. The final product was purified using an F & M Model 776 preparative gas chromatograph.

In the irradiated solutions of carbon tetrachloride containing iodine in addition to ICl, a product suspected to be CCl_3I was formed. Pure CCl_3I could not be synthesized because of its limited thermal stability, but its presence in the irradiated solutions was proven as follows. The production of an organic iodide was indicated because: (1) radioactivity was retained by carbon tetrachloride after irradiation in the presence of $^{131}I_2$ and washing with an aqueous sulfite solution to remove unreacted I_2, and (2) after standing ~16 hr these extracted solutions became pink. The organic iodide was shown to be CCl_3I because its retention time on the gas chromatograph was slightly less than that for $C_2H_2Cl_4$, which boils only four degrees higher than CCl_3I. Also, the height of the peak assigned to CCl_3I at any dose, *d*, was directly proportional to the quantity $2[I_2]_0 - 2[I_2]_d - [ICl]_d$ where $[I_2]_0$ is the initial concentration of iodine and $[I_2]_d$ and $[ICl]_d$ are the concentrations of these species at the dose *d*.

Results and Discussion

Carbon Tetrachloride Containing the Halogens Br_2, I_2, or ICl. In air-free carbon tetrachloride with Br_2

(11) I. Mani and R. J. Hanrahan, *J. Phys. Chem.*, **70**, 2233 (1966).

(12) R. J. Hanrahan, *J. Chem. Educ.*, **41**, 623 (1964).

(13) R. E. Buckles and J. F. Mills, *J. Amer. Chem. Soc.*, **75**, 552 (1953); A. I. Popov and J. J. Mannion, *ibid.*, **74**, 222 (1952); R. M. Keefer and T. L. Allen, *J. Chem. Phys.*, **25**, 1059 (1956); P. A. D. de Maine, *ibid.*, **26**, 1192 (1957); *Can. J. Chem.*, **35**, 573 (1957).

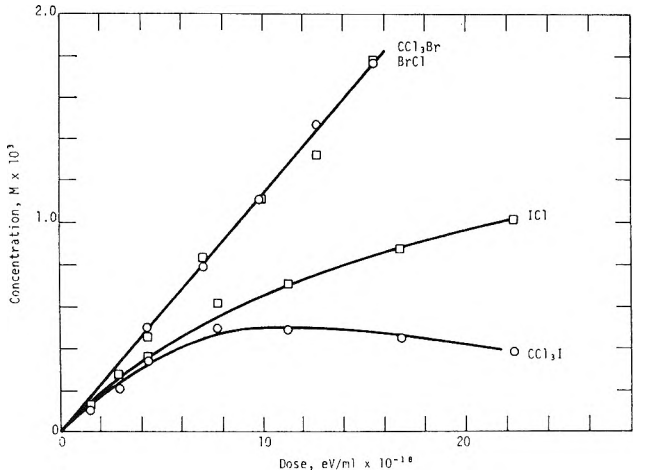

Figure 1. Dose dependence of the major radiolysis products of CCl_4 containing Br_2 or I_2: ○, CCl_3X; □, XCl.

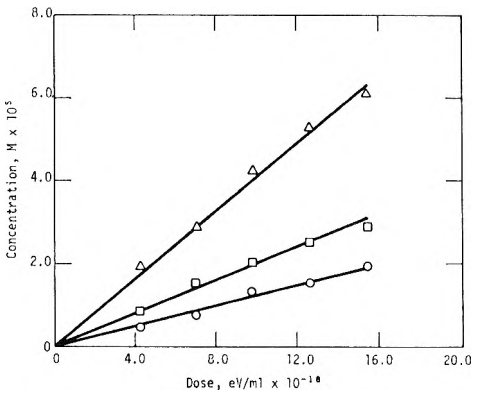

Figure 2. Dose dependence of the minor radiolysis products of CCl_4 containing 0.027 M Br_2: △, $C_2Cl_6/2$; □, CCl_2Br_2; ○, C_2Cl_4.

as scavenger, the radiolysis products and their 100-eV yields were: CCl_3Br, 7.1; BrCl, 7; C_2Cl_6, 0.48; C_2Cl_4, 0.07; and CCl_2Br_2, 0.12. The dose dependence of the concentrations of the major products is shown in Figure 1 and that of the minor products in Figure 2. Also shown in Figure 1 is the dose dependence of the major products in the radiolysis of carbon tetrachloride containing I_2. Clearly, in this system the 100-e Vyields of CCl_3I and ICl are dose dependent, with $G(CCl_3I)$ becoming negative at large doses. At very large doses ($>10^{20}$ eV/ml), the only iodine-containing product in these solutions was ICl. This is similar to results from the radiolysis of air-saturated solutions of I_2 in carbon tetrachloride where ICl is the only iodine-containing product at all doses.[14] In the degassed CCl_4–I_2 system, as in the system containing Br_2, the concentrations of the minor products, C_2Cl_6 and C_2Cl_4, were linear with dose. Their 100-eV yields were 0.45 and 0.073, respectively, in a 2×10^{-3} M solution of I_2. In the radiolysis of carbon tetrachloride containing 10^{-2} M ICl, the only products were C_2Cl_6 ($G = 0.54$) and C_2Cl_4 ($G = 0.12$). The compounds CCl_3I and I_2 were not detected and $G(-\text{ICl})$ was equal to zero.

The major radiolytic products in solutions containing Br_2 or I_2 indicate that CCl_3 radicals and Cl atoms are the most significant neutral intermediates formed by ionic or neutral dissociation processes and charge neutralization reactions. When Br_2 was present, both $G(CCl_3Br)$ and $G(BrCl)$ were approximately equal to the 100-eV yield for the disappearance of Br_2, suggesting the following mechanism as seen in eq 1–3.

$$Cl + Br_2 \longrightarrow BrCl + Br \quad (1)$$

$$CCl_3 + Br_2 \longrightarrow CCl_3Br + Br \quad (2)$$

$$2Br \longrightarrow Br_2 \quad (3)$$

Reactions similar to eq 1–3 can be written for the mechanism in the system with I_2 as a scavenger.

Reactions consistent with the slow decrease of CCl_3I at large doses are shown in eq 4 and 5.

$$Cl + CCl_3I \longrightarrow ICl + CCl_3 \quad (4)$$

$$CCl_3 + ICl \longrightarrow CCl_4 + I \quad (5)$$

As the dose increases, the concentration of I_2 decreases, and an increasing fraction of the Cl atoms reacts with CCl_3I as in reaction 4. Also, as the concentration of ICl increases, more of the CCl_3 radicals react with ICl as in reaction 5 and are converted back to CCl_4. Reaction 4 is proposed instead of an alternative reaction in which Cl_2 and CCl_2I are products because the energy of the C–I bond is about 30 kcal/mol lower than that for a C–Cl bond,[15] while the bond strength of Cl_2 is only approximately 7 kcal/mol greater than that for ICl.[15] The exclusive occurrence of reaction 5 over an alternative reaction in which CCl_3I and Cl are products is established by the absence of CCl_3I in the radiolysis of carbon tetrachloride containing ICl as a scavenger. Based on standard heats of formation,[16] the alternative reaction is slightly endothermic (neglecting solvation energies), while reaction 5 is exothermic.

The concentration of ICl at large doses in the carbon tetrachloride–iodine system increases, regardless of the identity of the products formed by the attack of Cl atoms on ICl. If Cl_2 results from the Cl atom attack, it will react spontaneously with the I_2 to form ICl.[17] If ICl results from the Cl atom attack, the resulting Cl atom will eventually appear as ICl either by recombination with an I atom or by forming Cl_2 that would subsequently react with I_2. These reactions explain the fact that $G(-\text{ICl})$ is equal to zero in the solutions containing ICl as a scavenger and also account for the failure to observe the formation of I_2 in these solutions.

Of the three radical scavengers (Br_2, I_2, and ICl), only in solutions with Br_2 can the initial 100-eV yield

(14) N. E. Bibler, *J. Chem. Educ.*, **45**, 722 (1968).

(15) T. L. Cottrell, "The Strengths of Chemical Bonds," 2nd ed, Butterworth's Scientific Publications, London, 1958, p 173.

(16) S. W. Benson, *J. Chem. Educ.*, **42**, 502 (1965).

(17) A. E. Gillam and R. A. Morton, *Proc. Roy. Soc.*, 604 (1929).

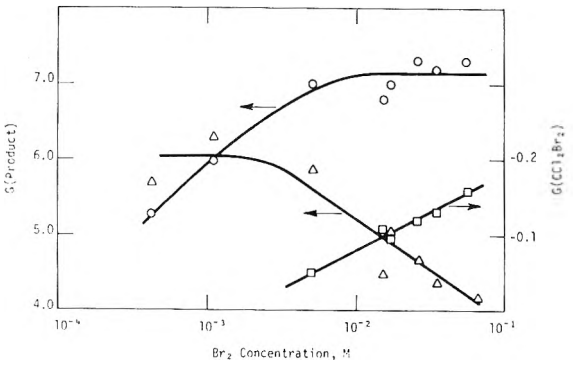

Figure 3. Dependence of the 100-eV yields of CCl_3Br, C_2Cl_6, and CCl_2Br_2 on the concentration of Br_2: ○, $G(CCl_3Br)$; △, $G(C_2Cl_6) \times 10$; □, $G(CCl_2Br_2)$.

of radicals be determined. When I_2 is the scavenger, the yields of the products of the scavenging reactions are dose dependent; when ICl is the scavenger, the products of the scavenger reactions cannot be measured. In the system containing Br_2, the initial 100-eV yield of CCl_3 radicals can be measured accurately because CCl_3Br is formed. The yield of Cl atoms cannot be measured as accurately since they form BrCl; small concentrations of this compound cannot be accurately measured in 50–100 times excess Br_2 because of the overlapping absorption spectra of the two compounds. However, in most of the experiments G(BrCl) is usually within 15% of $G(CCl_3Br)$. Values for $G(CCl_3Br)$ were dependent upon the initial concentration of Br_2 as shown in Figure 3. In solutions with >0.005 M Br_2, $G(CCl_3Br)$ is constant at 7.1 ± 0.2 molecules/100 eV. This is equal to the 100-eV yield of CCl_3 radicals and agrees well with 7.0 radicals/100 eV calculated for this quantity from the data of Schulte.[2,18] In his experiments Cl_2 containing ^{36}Cl was used as a scavenger. The radiation-induced formation of CCl_4 containing ^{36}Cl was then measured.

The formation of C_2Cl_6 in the presence of Br_2, I_2, or ICl is evidence for the occurrence of spur reactions. Whether CCl_3 radicals are the precursors is not certain. As shown in Figure 3, Br_2 can compete for these precursors, suggesting that they may be CCl_3 radicals. However, the data in Figure 3 are not conclusive because the expected increase in $G(CCl_3Br)$ as Br_2 competes with the spur reactions is within the limits of the experimental uncertainty in determining $G(CCl_3Br)$.

The formation of CCl_2Br_2 in the system containing Br_2 indicates that intermediates other than CCl_3 radicals or Cl atoms are being scavenged. These intermediates may be CCl_2 radicals, and the CCl_2Br_2 molecules result from successive bromination. If I_2 or ICl is the scavenger, the expected product is CCl_2I_2 or CCl_4. CCl_2I_2 may not be detected because of its low thermal stability rather than its lack of formation. As shown in Figure 3, the value for $G(CCl_2Br_2)$ increases as the concentration of Br_2 increases. This indicates that the scavenging process is incomplete and that the initial 100-eV yield of these intermediates is >0.16. Evidence implying the existence of CCl_2 radicals has also been obtained in the radiolysis of liquid chloroform.[9] When chloroform containing 0.045 M Br_2 was irradiated, CCl_2Br_2 was formed with a 100-eV yield of 0.4. Precursors of CCl_2 may be ions or excited CCl_4 molecules.

Previous to this study tetrachloroethylene has not been reported as a product in the radiolysis of liquid carbon tetrachloride. Recently, Marcotte and Hanrahan[19] have reported that this product is formed in the gamma radiolysis of mixtures of CCl_4 and CF_4 vapor at 920 mm and 85°. In the radiolysis of liquid carbon tetrachloride, C_2Cl_4 is not a product in solutions containing Cl_2,[2] O_2,[3] or in pure CCl_4.[2,3] These results have been confirmed in this laboratory. However, C_2Cl_4 is an initial product when Br_2 is present as a scavenger (Figure 2). C_2Cl_4 is also an initial product in solutions containing I_2 or ICl. In each of the solutions where C_2Cl_4 is not formed, Cl_2 is a major product.[2,3] Also in these solutions, the Cl atoms probably have much longer lifetimes than in the presence of Br_2 or I_2. Both Cl_2 and Cl atoms may easily react with and saturate any C_2Cl_4 that is formed. If a scavenger in carbon tetrachloride converts Cl atoms (or Cl_2) to a less reactive species, the C_2Cl_4 may be protected. This is possible when Br_2 or I_2 is present.

In the solutions with ICl, Cl probably reacts with ICl to abstract an I atom. Because this abstraction of I does not remove Cl atoms as an abundant intermediate, this reaction is not compatible with the appearance of C_2Cl_4 as a product. It is proposed that Cl atoms add to ICl to form ICl_2. This intermediate would then react with an I atom to produce two molecules of ICl. Possible support for the transient existence of ICl_2 is that in the pulse radiolysis of carbon tetrachloride evidence has been obtained for the formation of Cl atom–solute complexes when electron donating solutes are present.[20]

Carbon Tetrachloride Containing Hydrogen Iodide. Hydrogen iodide was investigated as a solute to provide additional confirmation of initial radical yields obtained in the CCl_4–Br_2 system. When solutions of carbon tetrachloride containing 0.01 M HI were irradiated, the products and their 100-eV yields were: $CHCl_3$, 7.4; I_2, 8.9; C_2Cl_6, 0.52; C_2Cl_4, 0.12; and C_2HCl_5, 0.07. Each of these 100-eV yields is independent of dose up to 1.36×10^{19} eV/ml, the largest dose used. Gas chromatographic analysis of these irradiated solutions indicated that CCl_3I was not a product. From the absorption

(18) In his original calculations a factor of 2 was omitted and the 100-eV yield of CCl_3 radicals reported as 3.5.

(19) R. E. Marcotte and R. J. Hanrahan, Abstracts of the Southeastern Regional Meeting of the American Chemical Society, Dec 4–7, 1968, Tallahassee, Fla., p 46.

(20) R. E. Bühler and M. Ebert, *Nature*, **214**, 1220 (1967); R. Cooper and J. K. Thomas, *Advan. Chem. Ser.*, **82**, 351 (1968).

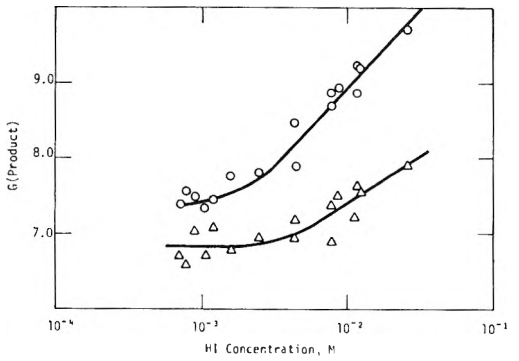

Figure 4. Dependence of the 100-eV yields of I_2 and $CHCl_3$ on the concentration of HI: ○, $G(I_2)$; △, $G(CHCl_3)$.

spectrum of solutions irradiated to the largest dose, the 100-eV yield of ICl was estimated to be less than 7% of $G(I_2)$ or ~0.5 molecule/100 eV.

For formation of the major products the following mechanism is proposed.

$$CCl_3 + HI \longrightarrow CHCl_3 + I \quad (6)$$

$$Cl + HI \longrightarrow HCl + I \quad (7)$$

$$2I \longrightarrow I_2 \quad (8)$$

Although the yield of HCl was not measured, its formation can be inferred because $G(I_2)$ is greater than $G(ICl)$. From this mechanism, it follows that $G(CHCl_3)$ should equal $G(I_2)$. However, as shown in Figure 4, $G(I_2)$ is always greater than $G(CHCl_3)$ at all concentrations of the scavenger. Part of this difference can be attributed to the spur reactions forming C_2Cl_4 and C_2Cl_6. For each molecule of C_2Cl_6 or C_2Cl_4 formed, either two or four Cl atoms remain to react either as Cl_2 molecules or as Cl atoms with HI to increase the yield of I_2. Consequently, $G(I_2)$ should equal $G(CHCl_3) + G(C_2Cl_6) + 2G(C_2Cl_4)$ and thus be 0.8 unit larger than $G(CHCl_3)$. As shown in Figure 4, this is the case at HI concentrations lower than ~0.002 M. The increases in $G(CHCl_3)$ and $G(I_2)$ at higher concentrations of HI probably result from energy or charge transfer mechanisms. Similar effects have been observed in the radiolysis of hydrocarbons containing HI. The yields of alkyl iodides[21] and also iodine[22] increase with increasing scavenger concentration. As shown in Figure 4, $G(CHCl_3)$ and $G(I_2)$ become constant below approximately 1.5 mM HI. These data indicate that the initial 100-eV yield of CCl_3 radicals is 6.8 ± 0.2 radicals/100 eV. This is within the experimental error of values determined with Br_2. From mass balance considerations, the lower limit of the initial yield of Cl atoms is 6.8 since it is not certain whether Cl or Cl_2 results from the spur reactions.

Values for $G(C_2Cl_6)$ and $G(C_2Cl_4)$ are close to those observed when the halogens were used as scavengers. In the solutions with HI, the small yield of C_2HCl_5 may result from the scavenging of C_2Cl_5 radicals. These radicals may result from the dissociation of excited C_2Cl_6 molecules formed by recombination of CCl_3 radicals or from the addition of a small portion (<1%) of the Cl atoms to C_2Cl_4. In carbon tetrachloride containing Br_2 or I_2, C_2Cl_5Br, and C_2Cl_5I were not detected. These products were either not formed or were not detected because of the poorer sensitivity for their analysis than for that of C_2HCl_5.

No evidence for any CCl_2 species was obtained when HI was the scavenger. The products CH_2Cl_2 and $CHCl_2I$ were not detected at concentrations of HI sufficiently large (0.06 M) to ensure scavenging of at least a portion of the precursors of the CCl_2Br_2 in the other system (see Figure 3). This suggests that the CCl_2-Br_2 does not result from successive bromination of CCl_2 because the expected product in the presence of HI is CH_2Cl_2. If the precursors of CCl_2Br_2 are CCl_2^+ ions, these might preferentially abstract I atoms from HI leading eventually to CCl_2I_2, which cannot be analyzed.

Carbon Tetrachloride Containing Other Solutes. Solutions of carbon tetrachloride containing other solutes were irradiated primarily to determine the effect of these solutes on the formation of C_2Cl_4. The results are summarized in Table II. Tetrachloroethylene was a product in all the solutions except those containing CCl_3Br. All the solutes are presumably capable of reacting with Cl atoms to produce free radicals that do not react with C_2Cl_4. However, it has been shown[23]

Table II: Products in the Radiolysis of Carbon Tetrachloride Containing Various Solutes (~0.02 M) at 25°

Solute	Products[a]
NH_3	C_2Cl_4 0.10); C_2Cl_6 (2.8); Cl^-[b]
C_2H_4	C_2Cl_4 (0.10); C_2Cl_6 (4.3); $CCl_3CH_2CH_2Cl$; CCl_3CHCH_2
$CHCl_3$	C_2Cl_4 (0.09); C_2Cl_6 (2.7)
CH_2Cl_2	C_2Cl_4 (0.10); $CHCl_3$ (2.0); $C_2H_2Cl_4$ (0.4); C_2HCl_5 (1.7); C_2Cl_6 (2.6)
CH_3Cl	C_2Cl_4 (0.13); CH_2Cl_2 (5.5); $CHCl_3$ (0.1); C_2Cl_6 (2.8)[c]
CCl_3Br	C_2Cl_6 (0.75);[d] Cl_2 (0.47);[e] BrCl (0.24);[e] Br_2 (0.04)[e]

[a] 100-eV yields are given in parentheses, where determined. [b] This species was in the form of an insoluble salt in the irradiated solution. [c] Other products were present but not identified. [d] This yield was nonlinear with dose (see Figure 5). [e] Determined at doses >2.7 × 10^{19} eV/ml.

(21) C. E. McCauley and R. H. Schuler, *J. Amer. Chem. Soc.*, 79, 4008 (1957); R. W. Fessenden and R. H. Schuler, *ibid.*, 79, 273 (1957).

(22) For a summary of these results see R. A. Holroyd in "Aspects of Hydrocarbon Radiolysis," T. Gaumann and J. Hoigne, Ed., Academic Press, London, 1968, p 5.

(23) A. Horowitz and L. A. Rajbenbach, *J. Amer. Chem. Soc.*, 91, 4626 (1969).

that organic radicals produced by the radiolysis of various hydrocarbons can react with C_2Cl_4 added initially to the solutions. In the present study, the radicals do not react with C_2Cl_4. Similar results were found[24] when C_2Cl_4 appeared as a product of the radiolytically induced chain reactions in cyclohexane containing mM concentrations of C_2Cl_6. In this study[24] C_2Cl_4 resulted from the dissociation of C_2Cl_5 radicals formed by the abstraction of Cl atoms from C_2Cl_6 by c-C_6H_{11}. A similar mode of formation of C_2Cl_4 in the radiolysis of carbon tetrachloride is possible if C_2Cl_5 radicals result from the dissociation of a portion of the excited C_2Cl_6 molecules formed by the recombination of CCl_3 radicals. However, this possibility is eliminated by the observation that in those systems where $G(C_2Cl_6)$ has increased (Table II) over its value in presence of the halogens, $G(C_2Cl_4)$ has not increased significantly.

In the irradiated solutions containing NH_3, a precipitate that contained Cl^- ions was formed. Davis and Hanrahan,[25] by irradiating carbon tetrachloride that contained 0.2 M NH_3, have demonstrated that this solid is predominantly NH_4Cl. In their study, they determined that the 100-eV yields for NH_4Cl and C_2Cl_6 were 25 and 2.1, respectively, but they apparently failed to detect C_2Cl_4. Their value for $G(C_2Cl_6)$ is lower than that determined in the present study, but this may be caused by more CCl_3 radicals being scavenged by NH_3 in their experiments since higher scavenger concentrations were used. Assuming the absence of a chain mechanism, an estimate of the yield of the scavengeable organic radicals in their experiments can be calculated by summing the yields of the carbon atoms in all the products and subtracting from this sum the yield of C_2Cl_6 molecules formed by spur reactions. This latter yield is 0.5 molecule/100-eV, and the calculated organic radical yield is 9 radicals/100-eV. This value is somewhat higher than that determined in this study using Br_2 or HI. Part of the larger yield may result from the interaction of the NH_3 at such high concentrations with the ionic processes in the carbon tetrachloride. This effect has been observed in chloroform[26] where the presence of NH_3 at concentrations greater than 0.03 M increases the yield of radicals.

In the presence of ethylene, C_2Cl_4 was a product, and evidence was obtained for both the addition of Cl atoms to C_2H_4 and the loss of H atoms from C_2H_4 leading to the formation of $CCl_3CH_2CH_2Cl$ or CCl_3CHCH_2.

When the chloromethanes were used to react with the Cl atoms, CCl_3, $CHCl_2$, and CH_2Cl radicals were formed from $CHCl_3$, CH_2Cl, and CH_3Cl, respectively (Table II). In the presence of any of these three solutes, Cl_2 was not a product. This agrees with other results[4] on the radiolysis of carbon tetrachloride that indicate that $CHCl_3$ inhibits the formation of Cl_2. In the present study, most of the experiments with chloromethanes were with CH_2Cl_2 and the results of these are summarized in Table III. The following mechanism is consistent with the results.

$$Cl + CH_2Cl_2 \longrightarrow HCl + CHCl_2 \quad (9)$$

$$CHCl_2 + CCl_4 \longrightarrow CHCl_3 + CCl_3 \quad (10)$$

$$2CHCl_2 \longrightarrow C_2H_2Cl_4 \quad (11)$$

$$CHCl_2 + CCl_3 \longrightarrow C_2HCl_5 \quad (12)$$

$$2CCl_3 \longrightarrow C_2Cl_6 \quad (13)$$

Table III: Products in the Radiolysis of Carbon Tetrachloride Containing CH_2Cl_2

CH_2Cl_2, M	100-eV yield				
	$CHCl_3$	C_2Cl_4	$C_2H_2Cl_4$	C_2HCl_5	C_2Cl_6
0.001	1.9	0.09	0.15	1.2	2.6
0.007	2.0	0.10	0.41	1.6	2.6
0.057	2.0	0.11	0.40	1.7	2.6
0.12	2.0	0.10	0.38	1.8	2.5

All of the Cl atoms are reacting with CH_2Cl_2 because an increase in scavenger concentration did not increase the yield of $CHCl_2$ radicals. Reaction 10 is reasonable because it is exothermic based on gas phase heats of formation. From the low yield of $CHCl_3$ when CH_3Cl was the solute, the $CHCl_3$ in the system containing CH_2Cl_2 is not a result of CCl_3 radicals attacking CH_2Cl_2. This reaction is probably close to 4 kcal endothermic based on heats of formation.[27] From the above mechanism, the sum $2G(C_2H_2Cl_4) + G(C_2HCl_5) + G(CHCl_3)$ should equal $2G(C_2Cl_6) + G(C_2HCl_5) - G(CHCl_3)$. The average values of these quantities using the data in Table III are 4.5 and 4.8, respectively. These are equal within experimental error, lending support to the proposed mechanism. This number can be equated to the yield of Cl atoms in this system and is close to the value for $G(HCl)$ (5.1 molecules/100 eV) determined by Johnston and coworkers[4] in the radiolysis of carbon tetrachloride containing 0.016 M $CHCl_3$. These values are considerably lower than the 100-eV yield of Cl atoms determined with Br_2 or HI scavengers. These data suggest that both CH_2Cl_2 and $CHCl_3$ are in some manner inhibiting the formation of radicals in irradiated carbon tetrachloride. This process is fairly efficient because the inhibition is complete at 7×10^{-3} M CH_2Cl_2. Presumably these solutes interact with the intermediates in the radiolysis of carbon tetrachloride by an energy- or charge-transfer mechanism.

(24) A. Horowitz and L. A. Rajbenbach, *J. Phys. Chem.*, **74**, 678 (1970).

(25) D. D. Davis and R. J. Hanrahan, *J. Amer. Chem. Soc.*, **87**, 3088 (1965).

(26) J. N. Baxter and N. E. Bibler, *J. Chem. Phys.*, **53**, 3444 (1970).

(27) S. Furuyama, D. M. Golden, and S. W. Benson, *J. Amer. Chem. Soc.*, **91**, 7564 (1969).

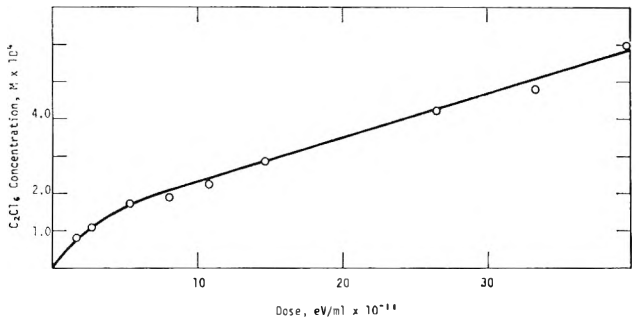

Figure 5. Dose dependence of C_2Cl_6 in the radiolysis of CCl_4 containing CCl_3Br (~0.02 M).

Failure to detect C_2Cl_4 as a product when CCl_3Br is a solute is consistent with the appearance of Cl_2 as the most abundant free halogen. As mentioned earlier, in all other systems reported when Cl_2 is a product, C_2Cl_4 is not. This suggests that CCl_3Br does not scavenge Cl atoms efficiently and these atoms either recombine or react with C_2Cl_4. The nonlinearity (at low doses) of the dose dependence of the yield of C_2Cl_6 (Figure 5) is similar to that observed for Cl_2 in the radiolysis of pure carbon tetrachloride at temperatures of 60° and above.[3,28] Also, from the slope of the linear portion of Figure 5, $G(C_2Cl_6)$ is 0.75, a value equal to $G(Cl_2)$ and $G(C_2Cl_6)$ determined in pure carbon tetrachloride.[2,3] This system is similar to pure carbon tetrachloride[3] except that a fraction (21%) of the free halogen is bromine. It is suggested that the nonlinearity of Figure 5 at low doses results from the dose necessary for the free halogen concentration to become large enough to scavenge CCl_3 radicals and cause a decrease in the rate of production of C_2Cl_6.

Conclusions

The initial 100-eV yield of CCl_3 radicals in the radiolysis of carbon tetrachloride measured by Br_2 or HI is 7.0 ± 0.2. In the experiments with HI, $7.0 < G(Cl) < 8.3$. In addition to a spur yield of C_2Cl_6, C_2Cl_4 is also an initial radiolytic product (G = 0.07 – 0.10 molecule/100 eV). In pure CCl_4 or in solutions containing solutes that do not remove Cl atoms or Cl_2, these intermediates react with C_2Cl_4 and remove it as a product. When CH_2Cl_2 or $CHCl_3$ are solutes, the values of $G(CCl_3)$ and $G(Cl)$ are lowered considerably by an interaction that does not involve the scavenging of Cl atoms.

(28) Experiments in this laboratory have established that the yield of C_2Cl_6 is also nonlinear with dose in the radiolysis of pure carbon tetrachloride at 25°. Preliminary results indicate that the extent of nonlinearity is dependent on the void space above the sample. As the void space increases, the dose necessary to reach the linear portion of the curve increases.

On the Contribution of H Atoms to G_{H_2} in the Radiation Chemistry of Aqueous Solutions

by E. Peled, U. Mirski, and G. Czapski*

Department of Physical Chemistry, The Hebrew University, Jerusalem, Israel *(Received July 30, 1970)*

Publication costs borne completely by the Journal of Physical Chemistry

G_{H_2} was determined in neutral and in 1 M NaOH air-saturated solutions as a function of $[N_3^-]$. It was found that N_3^- reduces G_{H_2} from 0.43 at 10^{-3} M N_3^- to 0.157 at 5 M N_3^- in neutral solutions and from 0.37 at 0.5 M N_3^- to 0.21 at 4 M N_3^- in alkaline solutions. Through pulse radiolysis studies it was found that the value of the rate constant $k_{e_{aq}+N_3^-}$ was $\leq 1.5 \times 10^6$ M^{-1} sec^{-1} and that N_3^- had no effect on $G_{e_{aq}}$. In competition experiments between N_3^- and isopropyl alcohol, $k_{H+N_3^-} = 2.7 \times 10^9$ M^{-1} sec^{-1} was obtained. From the decrease of G_{H_2} by efficient electron scavengers it was concluded that the reaction $H + e_{aq} \rightarrow H_2 + OH^-$ in spurs makes a major contribution to G_{H_2}. This conclusion together with other experimental results makes necessary the assumption that in addition to a distribution in the number of radicals in various spurs there is a distribution of concentrations of radicals in each kind of spur. The "condensed spurs" (spurs with higher initial concentration of radicals) have an important contribution to G_{H_2}.

It is generally accepted that in the γ radiolysis of aqueous solutions, molecular hydrogen (G_{H_2}) is produced as a result of the recombination of radicals in spurs. Recently, Schwarz[1] has reviewed and compared the results of the computer calculations made by the application of the spur diffusion model and most of the available experimental results. By assuming a primary source of molecular hydrogen yield ($G_{H_2}^0 = 0.15$) and hydrogen atoms yield ($G_H^0 = 0.6$), he showed that no real disagreement exists between the model and the experimental results. The precursors of the remainder of the molecular hydrogen yield were assumed to be e_{aq} and H. These precursors mainly react in the spurs by reactions 1 and 2.

$$e_{aq} + e_{aq} \longrightarrow H_2 + 2OH^- \quad (1)$$

$$H + e_{aq} \longrightarrow H_2 + OH^- \quad (2)$$

A small fraction of H_2 (except in very concentrated acid solutions) is produced in the reaction

$$H + H \longrightarrow H_2 \quad (3)$$

Other precursors of the molecular hydrogen, such as H_3O,[2] H^-,[3] excited water molecules,[4] and dry electrons,[5] were suggested.

The effect of electron scavengers on G_{H_2} provides good evidence that e_{aq} is one of the main precursors of the molecular hydrogen, probably through reactions 1 and 2.[6,7] The H atoms yield(G_H) arises at least partially in spurs through reaction 4.

$$e_{aq} + H^+ \longrightarrow H \quad (4)$$

This was shown by the effect of H^+ scavengers on G_H.[8,9]

The relative contribution of reactions 1 and 2 to the yield of H_2 has never been measured, but calculations using the diffusion model show that the contribution of reaction 2 is important.[1] It was recently suggested[7] that reaction 2 may be even more important in "condensed spurs" where the initial concentrations of radicals are higher than the average.

In this investigation we have tried to determine the importance of reaction 2 in the formation of the molecular hydrogen. This has been done by measuring G_{H_2} as a function of azide concentration. Azide was chosen as it reacts very fast with H atoms but rather slowly with e_{aq}.

Experimental Section

Materials. Triple-distilled water was used for all solutions. NaOH and isopropyl alcohol were of analytical grade. NaN_3 (BDH) was used without further purification.

Dosimetry and Irradiation Source. The irradiations were carried out in a Cs^{137} γ source. A Fricke do-

* On sabbatical leave at Radiation Research Laboratories, Mellon Institute, Carnegie-Mellon University, Pittsburgh, Pa. 15213.

(1) H. A. Schwarz, *J. Phys. Chem.*, **73**, 1928 (1969).

(2) T. J. Sworski, *Advan. Chem. Ser.*, **No. 50** (1965).

(3) M. Faragi and J. Desalos, *Int. J. Radiat. Phys. Chem.*, **1**, 335 (1969).

(4) M. Anbar, S. Guttmann, and G. Stein, *J. Chem. Phys.*, **34**, 703 (1961).

(5) W. H. Hamill, *J. Phys. Chem.*, **73**, 1341 (1969).

(6) E. Hayon, *Nature (London)*, **194**, 737 (1962).

(7) E. Peled and G. Czapski, *J. Phys. Chem.*, **74**, 2903 (1970).

(8) A. Appleby, "The Chemistry of Ionization and Excitation," G. R. A. Johnson and G. Scholes, Ed., Taylor and Francis, London, 1967.

(9) (a) G. Czapski and E. Peled, unpublished results. (b) $(k_{e_{aq}+S})_{p.\mu}$ means that $k_{e_{aq}+S}$ is at the proper ionic strength (μ).

simeter was used to determine the dose rates taking $G(Fe^{3+}) = 15.5$. The absorbed dose in concentrated solutions was corrected according to the increase in electron density of the solutions. The dose rates were either 200 or 80 rads/min approximately. Total doses used were 1.1×10^{18} to 3.8×10^{18} eV/cm^3.

$G(H_2)$ Determination. All solutions were irradiated in 10-cm^3 syringes and the gas products were determined by gas chromatography. Details of this technique have been described elsewhere.[10]

Results

The Effect of N_3^- on G_{H_2}. The molecular hydrogen yield was measured in irradiated aerated azide solutions. The presence of oxygen (air) prevents the reactions $e_{aq} + e_{aq} \rightarrow H_2$ and $e_{aq} + H_2O \rightarrow H$ in the bulk of the solution while this low O_2 concentration hardly affects G_{H_2}. G_{H_2} values were calculated from the slopes of linear yield *vs.* dose plots, each from 5 to 11 points.

A. Basic Solutions. G_{H_2} values were measured in solutions containing 1 *M* NaOH and various azide concentrations. The results are summarized in Table I.

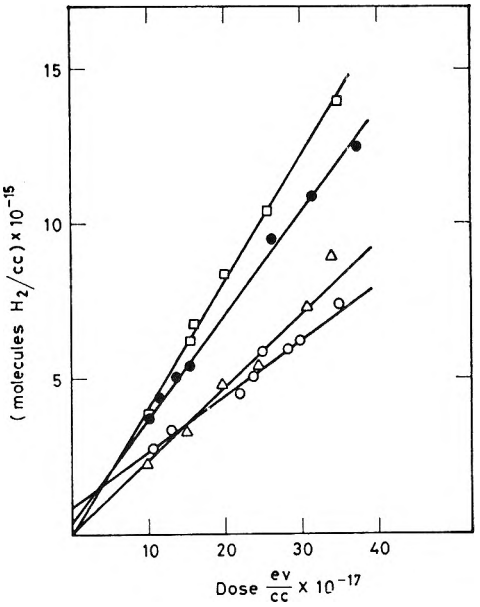

Figure 1. The molecular hydrogen yield as a function of dose: □, 10^{-2} *M* NaN_3; ●, 0.5 *M* NaN_3; ○, 4 *M* NaN_3; △, 4 *M* NaN_3 +1 *M* NaOH.

Table I: The Dependence of G_{H_2} on Azide Concentration in 1 *M* NaOH Aerated Solutions

[NaN_3], *M*	G_{H_2}	G_{H_2}[a]
0.5	0.39	0.37
1	0.366	0.33
2	0.31	0.27
4	0.245	0.21

[a] G_{H_2} values are corrected for the increase of the electron density in the solutions.

B. Neutral Solutions. In neutral solutions the molecular hydrogen yields were found to be linear with dose (for all azide concentrations), but at concentrations above 0.5 *M* NaN_3, positive intercepts were observed in yield *vs.* dose plots. These intercepts increased with the increase in azide concentrations as can be seen in Figure 1.

It was reported[11] that in the photochemistry of solutions of high azide concentrations ($[N_3^-] > 1$ *M*) H_2 is formed (in N_3^- solutions of lower concentration no H_2 was found). A possible source of the hydrogen is the reaction with N_3^- of an intermediate formed during the irradiation. We tried to scavenge this unknown intermediate using several scavengers (S = 0.1 *M* ethanol, 10^{-4} *M* Br^-, or 0.05 *M* I^-) but without any success. As we could not avoid the positive intercepts in the concentrated solutions, we calculated G_{H_2} values from the yield *vs.* dose plots (Figure 1). The results are summarized in Table II.

Determination of $k_{H+N_3^-}$. The value of $k_{H+N_3^-}$ was determined using the competition method. $G(H_2)$ values in irradiated argon-saturated azide solutions containing isopropyl alcohol were measured. In addition, these solutions contained 5×10^{-4} *M* NO_3^- to prevent the reactions $e_{aq} + e_{aq} \rightarrow H_2$ and $e_{aq} + H_2O \rightarrow H$ in the bulk. The experimental results are given in Table III. The competition reactions are

Table II: The Dependence of G_{H_2} on Azide Concentration in Aerated Neutral Solutions

[NaN_3], *M*	G_{H_2}	G_{H_2}[a]
10^{-3}	0.43	
10^{-2}	0.42	
0.1	0.38	
0.2	0.38	
0.5	0.35	
1	0.31	0.30
2	0.27	0.25
4	0.19	0.17
5	0.18	0.157

[a] G_{H_2} values are corrected for the increase of the electron density in the solutions.

$$CH_3CHOHCH_3 + H \longrightarrow H_2 + CH_3COHCH_3 \quad (5)$$

$$N_3^- + H \longrightarrow \text{products } (\neq H_2) \quad (6)$$

Thus $G(H_2)$ should obey the equation

$$G(H_2) = G_{H_2} + G_H \frac{1}{1 + \frac{k_6[N_3^-]}{k_5[ROH]}} \quad (7)$$

(10) G. Czapski and E. Peled, *Israel J. Chem.*, 6, 421 (1968).

(11) E. Burak, Ph.D. Thesis, The Hebrew University, Jerusalem, Israel.

or

$$\frac{1}{G(H_2) - G_{H_2}} = \frac{1}{G_H} + \frac{1}{G_H} \times \frac{k_6[N_3^-]}{k_5[ROH]} \quad (8)$$

Figure 2 shows a plot of $1/(G(H_2) - G_{H_2})$ as a function of $[N_3^-]/[ROH]$. From the slope of this plot and assuming $k_5 = 5 \times 10^7\ M^{-1}\ sec^{-1}$,[12] we obtained $k_6 = 2.7 \times 10^9\ M^{-1}\ sec^{-1}$. The intercept yields $G_H \approx 0.75$.

Table III: The Dependence of $G(H_2)$ on the Ratio $[N_3^-]/[Isopropyl\ Alcohol]$ in Irradiated Argon-Saturated Solutions of 10^{-3} M Azide and Isopropyl Alcohol. All Solutions Contained 5×10^{-4} M NO_3^-; Total Dose ~30,000 Rads

[ROH], M	$[N_3^-]/[ROH]$	$G(H_2)$
0.5	2×10^{-3}	1.18
0.2	5×10^{-3}	1.05
0.125	8×10^{-3}	0.98
0.08	1.25×10^{-2}	0.92
0.0625	1.6×10^{-2}	0.86
0.05	2×10^{-2}	0.82

Determination of $k_{e_{aq}+N_3^-}$ and the Effect of N_3^- on $G_{e_{aq}^-}$. We measured $k_{e_{aq}+N_3^-}$ using the pulse radiolysis technique and following the decay of e_{aq} in an argon-saturated 1 M N_3^- solution. We found that e_{aq} reacts very slowly with N_3^-: $k_{e_{aq}+N_3} \leq 1.5 \times 10^6\ M^{-1}\ sec^{-1}$ and that 1 M N_3^- did not change the initial absorbance of e_{aq}^-. This would indicate that N_3^- reacts neither with e_{aq} nor with its precursors.

Discussion

The results show quite clearly that the addition of N_3^- causes a decrease in G_{H_2} (in the presence of 5 M N_3^- G_{H_2} is decreased to about one-third of its original value). This effect shows that N_3^- interferes with the formation of the molecular hydrogen. It is generally accepted that most of G_{H_2} is formed in the spurs, through reactions 1–3. However, quite recently Hamill[5] suggested that dry electrons are the precursors of H_2. Recently some possible supporting evidence for the existence of e_{dry} was found.[13,14] It was shown that the apparent ratios of the rate constant of $H^+ + e_{aq}$ to those of e_{aq} with H_2O_2, acetone, Cd^{2+}, and NO_3^- decrease as all these concentrations increase. This behavior could be interpreted as if the precursor of e_{aq}, and therefore also of H_2 and H, is e_{dry}. Such interpretation assumes that e_{dry} reacts with all the above-mentioned scavengers of e_{aq} except with H^+. The effect of N_3^- on G_{H_2} could be due either to the reaction of N_3^- with the dry electrons or to some processes competing with the formation of H_2 in the spurs.

The role and existence of dry electrons in aqueous irradiated solutions are not yet well established. Hunt,[13] *et al.*, showed that e_{aq}^- is formed within less than 10^{-11} sec. So, if e_{dry} is the precursor of e_{aq} and of other species, as suggested by Hamill, then these species must be formed in less than 10^{-11} sec.

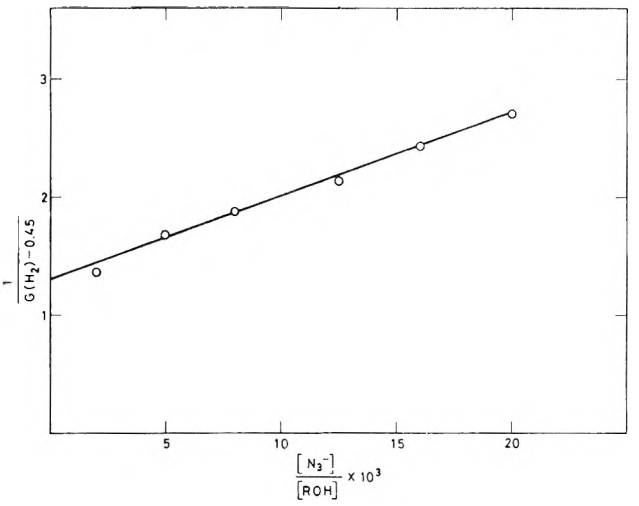

Figure 2. $1/(G(H_2) - 0.45)$ as a function of $[N_3^-]/[$isopropyl alcohol$]$. The results were taken from Table III.

We can rule out, however, the possibility that N_3^- affects G_{H_2} due to scavenging of the dry electrons. We found that 1 M N_3^- has no effect on the initial yield of e_{aq}. Furthermore, at the end of a 100-nsec pulse, the absorption due to e_{aq} is unaltered by the addition of 1 M N_3^- in air-free solutions. Should the dry electrons not be the precursors of e_{aq} but form H_2 directly, the reaction of e_{dry} with azide cannot be ruled out. However, such properties of e_{dry} appear quite arbitrary and improbable. (Such an assumption would lead us to conclude that less than 30% of G_{H_2} would be formed in spur reactions, contrary to earlier determinations.) Thus we come to the conclusion that the effect of N_3^- on G_{H_2} must be due to the reaction of this ion with species in the spurs. Therefore, we will consider the reactions of N_3^- with e_{aq}, OH, H^+, and H atoms and the possible effects of these reactions on G_{H_2}.

The slow reaction rate of e_{aq} with azide excludes any effect of N_3^- on reactions involving e_{aq} in the spurs. (Even in 5 M N_3^-, $\tau_{1/2}$ of the reaction $e_{aq} + N_3^-$ is ~10^{-7} sec, longer by more than one order of magnitude than the spur's lifetime.)

The OH radical reacts with N_3^- to yield the N_3 radical,[12] with $k_{OH+N_3^-} = 6.5 \times 10^9\ M^{-1}\ sec^{-1}$.[12] This reaction may affect G_{H_2} only indirectly according to the properties of the N_3 radical.

When N_3^- scavenges OH in the spurs, the spurs originally containing only e_{aq}, H, OH, and H^+ are changed into spurs containing N_3 instead of the OH or at least part of the OH's. In this case, instead of or in

(12) M. Anbar and P. Neta, *Int. J. Appl. Radiat. Isotop.*, 18, 493 (1967).

(13) R. K. Wolf, M. J. Bronskill, and J. W. Hunt, submitted for publication.

(14) G. Czapski and E. Peled, unpublished results.

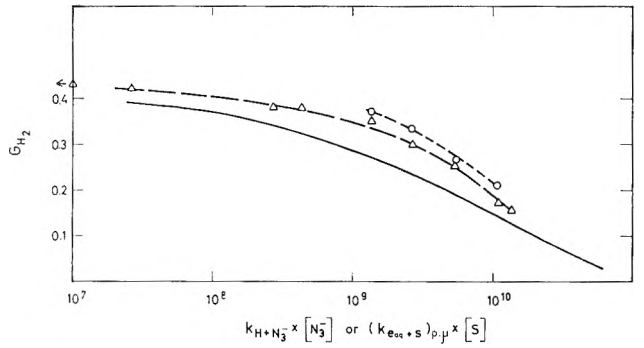

Figure 3. G_{H_2} as a function of $(k_{e_{aq}+S})_{p.\mu} \times [S]$ and as a function of $k_{H+N_3^-} \times [N_3^-]$ (where S is hydrated electron scavengers): ○, NaN_3 + 1 M NaOH; △, NaN_3, neutral solutions; solid line, e_{aq} scavengers.[7] [$(k_{e_{aq}+S})_{p.\mu}$ is the rate constant of the reaction of e_{aq} + S which was measured in the proper ionic strength.]

addition to the reactions H + OH, e_{aq} + OH, and OH + OH, one has to consider the reactions H + N_3, e_{aq} + N_3, OH + N_3, and N_3 + N_3.

If N_3 radicals react with e_{aq} or H atoms faster than the OH radicals, then the azide may decrease G_{H_2}, but in the case where N_3 radicals react with e_{aq} or H atoms slower than OH radicals, N_3^- may increase G_{H_2}. It is indeed difficult to gauge such an effect without computer calculations on the diffusion model, but is seems improbable that replacing OH with N_3 in the reactions with H and e_{aq} could bring about a decrease of G_{H_2} down to one-third of its value as found in the absence of azide.

Another reason for the azide's effect on G_{H_2} might be its reaction with H^+ in the spurs. As HN_3 is a rather weak acid (pK = 4.7) and the initial $[H^+]$ in the spur is high, azide may scavenge H^+ ions and consequently decrease the amount of reaction 4 in the spur. Such an effect does not explain our results as OH^- (a much more effective H^+ scavenger) reduced G_{H_2} in 1 M NaOH only by about 10–15%.[15,16]

Figure 3 shows that N_3^- is less efficient in decreasing G_{H_2} in 1 M NaOH than in neutral solutions. This lower efficiency may be due to lower yields of H atoms formed through reaction 4 in alkaline solutions, as OH^- scavenges most of the H^+ ions. This effect has been confirmed experimentally.[8,9]

Figure 3 shows that the plots of G_{H_2} as a function of $(k_{e_{aq}+S})_{p.\mu} \times [S]$[9b] (S being an e_{aq} scavenger) and as a function of $k_{H+N_3^-} \times [N_3^-]$ produce two curves, having the same shape. The azide curve lies above the e_{aq} scavenger curve. Several reasons may be responsible for the difference in these two curves.

1. This difference may indicate that in the spurs the H atoms have a narrower initial distribution than e_{aq}, and thus the molecular yield will be more sensitive toward e_{aq} scavengers than toward H atom scavengers. This behavior might indicate that reaction 1 contributes more to G_{H_2} than does reaction 3.

2. In the spurs, a fraction of the azide ions may react with H^+ to yield HN_3 and, as $k_{H+HN_3} \ll k_{H+N_3^-}$ ($k_{H+HN_3} = 1.7 \times 10^8\ M^{-1}\ sec^{-1}$ [12]), a lower efficiency in reducing G_{H_2} may be observed. This phenomenon is of a lesser importance in high azide concentrations, where $[N_3^-] \gg [H^+]$.

We conclude from the above discussion that the effect of N_3^- is due to its reaction with H atoms in the spurs ($k_{H+N_3^-} = 2.7 \times 10^9\ M^{-1}\ sec^{-1}$). This work confirms Schwarz' calculations[1] and also our previous suggestion[7] that the reaction e_{aq} + H is of importance in the formation of molecular hydrogen. We suggested earlier[7] that in order to get a good agreement between many experimental results and the diffusion model it is necessary to assume a distribution of radical concentrations in the various spurs in addition to the distribution of the number of radicals in the spurs. "Normal spurs" are the ones with initial concentrations of radicals about that assumed in previous calculations[1] and "condensed spurs" are spurs with much higher initial radical concentration than "normal spurs." Our hypothesis that the main part of the molecular hydrogen is formed in the reaction e_{aq} + H in "condensed" spurs,[7] as supported by this work, removes some previous difficulties in interpretation of several experimental results which seemed in direct contradiction to the diffusion model.

Table IV: The Effect of e_{aq} Scavengers on G_{H_2} and on the Isotopic Effect in H_2 Formation ($\alpha(H_2)$)

[Scavenger], M	G_{H_2}	$\alpha(H_2)^c$	Ref for $\alpha(H_2)$
1×10^{-3} NaBr	0.4[a]	2.15 ± 0.15	*d*
1.0 $CoSO_4$ + 10^{-3} NaBr	0.33[b]	1.9 ± 0.15	*d*
1.0 $NiSO_4$ + 10^{-3} NaBr	0.29[a]	1.8 ± 0.15	*d*
1.0 $CdSO_4$ + 10^{-3} NaBr	0.24[a]	1.65 ± 0.15	*d*
0.5 $CuSO_4$ + 10^{-3} NaBr	0.24[a]	1.6 ± 0.15	*e*
1.0 $NaNO_3$ + 10^{-3} NaBr	0.09[a]	1.5 ± 0.2	*d*

[a] These G values have been calculated assuming G_{H_2} = 0.4 in 10^{-3} M NaBr; see footnote *f*. [b] Reference 7. [c] For 1:1 H–D aqueous solutions (for other H/D ratios slightly different results were obtained). [d] S. Alfasi, M. Anbar, and D. Meyerstein, unpublished results. [e] C. Lifshitz, *Can. J. Chem.*, **41**, 2175 (1963). [f] D. Meyerstein, Ph.D. Thesis, The Hebrew University, Jerusalem, Israel, 1965.

We have previously discussed[7] the following points.

A. The "condensed" spurs may be the source of G_H^0 and $G_{H_2}^0$, as proposed by Schwarz.[1]

B. The "condensed" spur model may explain the break of the line in plots of G_{H_2} against the cube root of the concentration of e_{aq}^- scavengers, as shown by

(15) M. J. Bronskill, R. K. Wolf, and J. W. Hunt, *J. Phys. Chem.*, **73**, 1175 (1969).

(16) E. Hayon, *Trans. Faraday Soc.*, **61**, 734 (1964).

Hayon,[17] Mahlman,[18] and Peled, *et al.*;[7] *i.e.*, it explains the real difficulty of scavenging the last remnant of G_{H_2}.

C. Theis otopic effect in the formation of H_2 ($\alpha(H_2)$) in the "condensed" spurs should be about 1.6, equal to that of the reaction $e_{aq} + H$.[19] This value is in reasonable agreement with the value Schwarz[1] used for $G_{H_2}^0$ ($\alpha(H_2^0) = 1.8$) in order to obtain a proper value for the isotopic effect in the overall formation of the molecular hydrogen.

The "condensed" spur model might also explain the effect of the e_{aq}^- scavengers on the isotopic effect in H_2 formation. It was found that e_{aq} scavengers decrease G_{H_2} and, simultaneously, reduce the isotopic effect in H_2 formation, as shown in Table IV. The increase of the concentration of e_{aq} scavengers prevents mainly the formation of H_2 in "normal" spurs; thus the rest of the H_2 is formed in the "condensed" spurs. Therefore the rest of the molecular hydrogen should have an isotopic effect similar to that of the reaction $e_{aq} + H$ ($\alpha = 1.6$)[19] which occurs in the "condensed" spurs.

The effect of LET on the isotopic effect in H_2 formation is in good agreement with the "condensed" spurs model. It has been found that the isotopic effect in H_2 formation decreases from 2.2[19] for γ radiation to 1.86 and 1.93 for higher LET radiations, of $^{10}B(n,\alpha)Li$ and $^{6}Li(n,\alpha)T$, respectively.[20] It could be expected that the fraction of the reaction $e_{aq} + H$ (with an isotopic effect of 1.6) would increase with the increase of the LET.

Acknowledgment. I wish to thank Dr. K. M. Bansal for helpful comments on this manuscript.

(17) E. Hayon, *Nature (London)*, **194**, 737 (1962).
(18) H. A. Mahlman, *J. Chem. Phys.*, **32**, 601 (1960).
(19) M. Anbar and D. Meyerstein, *Trans. Faraday Soc.*, **62**, 2121 (1966).
(20) M. Anbar and D. Meyerstein, *ibid.*, **61**, 263 (1965).

Paramagnetic Species Produced by Ultraviolet Irradiation of Lithium, Potassium, Sodium, Magnesium, and Cadmium in 3-Methylpentane at 77°K[1]

by F. W. Frobon and J. E. Willard*

Department of Chemistry, University of Wisconsin, Madison, Wisconsin 53706 *(Received June 24, 1970)*

Publication costs assisted by the U. S. Atomic Energy Commission and the University of Wisconsin

An esr singlet with characteristics expected for the signal of trapped electrons is observed when Li, K, Na, Mg, or Cd in a 3-methylpentane matrix deposited from the vapor at 77°K is irradiated at wavelengths in the region of 250 nm. This is flanked by lines from another species which grow to the photostationary state and decay from it with a half-life of less than 0.2 sec, in parallel with the singlet. The flanking lines may be due to a cationic species with which the electron recombines. A photosensitized decomposition of the matrix to produce relatively stable free radicals also occurs in the case of sodium. For all the metals the photoionization threshold is lower than the gas phase ionization potential and (with the possible exception of Mg) higher than the photoelectric work function. The short trapping lifetime of the electron and the narrowness of the esr singlet indicate that the available electron trapping sites in the matrix deposited from the vapor are weaker than those in a matrix formed by cooling liquid 3-methylpentane to 77°K.

Introduction

Electrons produced in hydrocarbon glasses at low temperatures by ionizing radiation or by photoionization of organic amines can be trapped in the matrix in substantial yields observable[2] by esr and optical spectrometry. The efficiency of electron scavengers in reducing trapping yields suggests that the electrons often travel hundreds of molecular diameters before being trapped, while decay kinetics and photobleaching quantum yields of the trapped electrons indicate that each eventually reacts with a *predestined* radical or

(1) This work has been supported in part by the U. S. Atomic Energy Commission under Contract AT(11-1)-1715 and by the W. F. Vilas Trust of the University of Wisconsin.

positive ion rather than at random. The average distance of a randomly trapped electron from a positive charge at the concentrations typically achieved ($\geqq 1.6 \times 10^{-4}$ mf)[3] is only *ca.* 9 molecular diameters and the coulomb attraction is of the order of 0.2 eV. The nature of the trapping sites and the mechanism of trapping is still a matter of debate.[2]

To investigate further the variables which govern electron trapping in hydrocarbons we have photoionized Li, K, Na, Mg, and Cd in matrices made by deposition from the vapor phase of mixtures of the metals with 3-methylpentane (3MP). Unlike the spontaneous production of trapped electrons when alkali metals are deposited on solid alcohols or ice,[4] there is no reaction of the metals with hydrocarbons without irradiation. Information has been sought on whether the lifetimes of the trapped electrons produced by photoionization of the metals depend on the nature of the metal ionized, the photon energy in excess of the ionization threshold, or the method of deposition of the matrix. The ionization thresholds have been compared with the gas-phase ionization potentials and photoelectric work functions of the metals and the trapping lifetimes have been compared[5] with those of electrons produced by γ irradiation or photoionization of amines in hydrocarbon glasses rapidly frozen to the glassy state from the liquid.

Experimental Section

Sample Preparation and Measurement. Li, K, Na, Mg, and Cd dispersed in 3MP matrices were prepared by deposition on a Suprasil tube at 77°K from a flowing gaseous mixture (Figure 1). The rate of deposition and the ratio of 3MP to metal were qualitatively controlled by the temperatures of the 3MP and the metal. In typical experiments the 3MP was at −78° (vapor pressure 0.2 Torr) and the metal temperature was adjusted to give a vapor pressure of 10^{-4} to 5×10^{-3} Torr (450–750°).[6] About 40 min was required to form a deposit a few tenths of 1 mm thick. During this time the appearance changed from whitish to light blue to dark blue or violet, except in the case of Cd which was gray. The deposits were opaque or translucent in contrast to the transparent 3MP glass formed by rapid cooling of liquid 3MP to 77°K. If the relative rates of evaporation of the 3MP and metal were proportional to their equilibrium vapor pressures, the ratio of 3MP to metal in the deposits was in the range of 100:1 to 500:1; the actual values were not determined. The "electron" yields observed on irradiation of the deposits were not critically dependent on the depth of color, thickness, or metal concentration in the deposits over a wide range, suggesting that in all cases tested all of the light beam was absorbed or scattered. The distance from the evaporating metal to the cold finger was about 20 cm. Use of substantially greater distances resulted in loss of the metallic vapor to the outer walls before the cold finger was reached. When a desired deposit had been formed, the cold finger was sealed off from the reservoir and oven at the point indicated in Figure 1, the stopcock to the pumps was closed, and the dewar was removed from the vacuum line. the cold finger was then positioned with the 3MP–metal deposit in the sensitive region of a Varian V-4531 esr cavity. The esr spectrum was determined before, during, and after irradiation with a focused beam from a quartz-jacketed 100-W AH4 medium-pressure mercury lamp which delivered about 10^{15} photons sec^{-1}

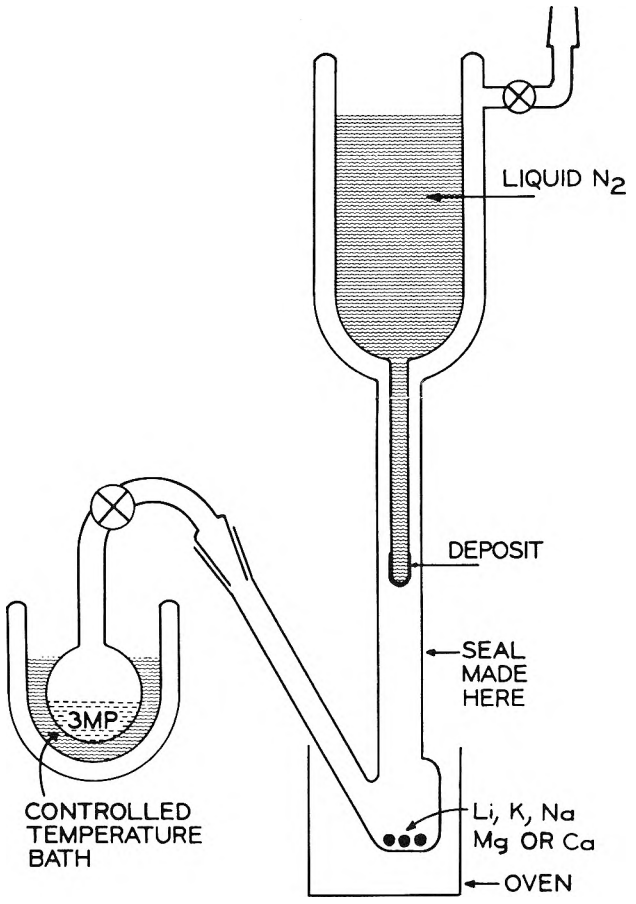

Figure 1. Equipment used for preparing deposits of metals in hydrocarbons for esr and optical analysis. The inner and outer tubes in the region of the deposit were made of Suprasil; the remainder of the equipment was Pyrex.

(2) For reviews of the field and references see: (a) J. E. Willard, "Radiation Chemistry of Organic Solids," a chapter in "Fundamentals of Radiation Chemistry," P. Ausloos, Ed., Wiley, New York, N. Y., 1969; (b) W. H. Hamill, "Ionic Processes in Irradiated Organic Solids," a chapter in "Radical Ions," E. T. Kaiser and L. Kevan, Ed., Wiley, New York, N. Y., 1968; (c) A. Ekstrom, *Radiat. Res. Rev.*, in press.

(3) A. Ekstrom, R. Suenram, and J. E. Willard, *J. Phys. Chem.*, **74**, 1888 (1970).

(4) J. E. Bennett, B. Mile, and A. Thomas, *J. Chem. Soc., A*, 1393, 1399 (1967); 1502 (1969).

(5) (a) J. Lin, K. Tsuji, and F. Williams, *J. Amer. Chem. Soc.*, **90**, 2766 (1968); *J. Chem. Phys.*, **46**, 4982 (1967); (b) K. Tsuji and F. Williams, *Int. J. Radiat. Phys. Chem.*, **1**, 383 (1969).

(6) Landholt-Börnstein, Physikalisch-Chemische Tabellen, Vol. II 2a, Springer-Verlag, West Berlin and Heidelberg, 1960.

at wavelengths below 300 nm to the portion of the sample in the sensitive region of the cavity. Esr measurements were made with an X-band Varian V-4500 spectrometer with 100-kc field modulation using powers of 35 μW or below.

Estimates of the threshold wavelengths for production of esr signals during irradiation of the 3MP–metal deposits were made with the aid of the filters listed in Table I.

Table I: Filters Used for Photoionization Experiments

Corning filter	Cutoff wavelength, nm	Wavelength, nm: 240	280	320	360	400	440
		% transmittance					
Vycor	210	50	82	88	92	92	92
7-54	230	15	78	90	85	14	...
7-51	295	...	...	11	82	22	...
7-39	305	...	...	7	57	3	...
4-70	320	...	...	...	50	78	85
4-72	340	...	...	...	14	50	67
0-52	340	...	...	...	50	86	90
0-51	360	...	...	...	1	64	82
3-72	420	...	...	...	...	...	15
3-71	460	...	...	...	...	...	...

Materials. 3-Methylpentane (Phillips Pure grade) was further purified by passage through 3 ft of freshly activated silica gel, degassed by freeze–thaw cycles, and stored under vacuum over a sodium mirror. For use it was distilled into the bulb of Figure 1 and further degassed by pumping while in the liquid state at Dry Ice temperature, to ensure removal of CO_2.

Sodium (Baker 99.9%), potassium (Baker 99.9%), and lithium (Eimer and Amend 99.9%) metals were stored under purified 3MP after mechanical cleaning of the surface. For each experiment, pieces with fresh surfaces were cut and prepared by heating under vacuum to 150°. Freshly cut Mg (Fisher Scientific Co.) and Cd (Merck) were prepared by heating under vacuum at 150°.

Results

Optical Spectrum of Na in 3MP Glass. The optical spectrum of a typical 3MP–Na matrix determined on a Cary recording spectrophotometer with the analyzing beam passing through the center of the semiopaque deposit on a cold finger of the type of Figure 1 is shown in Figure 2. The absorption bands in the 500–600-nm region are similar in position to those which have been observed for Na in an Ar matrix at 4°K between 535 and 600 nm[7] and in an Xe matrix between 540 and 580 nm.[8] The optical density in the 320–450-nm region and that underlying the structural features at higher wavelengths presumably result from scattering by the matrix. 3MP deposited in a similar fashion without metal had a nearly constant OD of several tenths of a unit from 600 to 300 nm, which increased at lower wavelengths with the increased scattering in this region, as in Figure 2. The rise in OD below 300 nm in Figure 2 must also include absorption by the metal, to account for the photochemical effects observed by esr reported below. The sample of Figure 2 was deposited with the 3MP reservoir at −78° (vapor pressure 0.2 Torr) and the Na oven at 260° (vapor pressure 3×10^{-3} Torr).

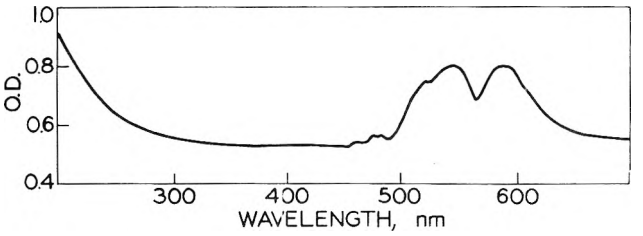

Figure 2. Optical spectrum of Na deposited in a 3MP matrix by the technique of Figure 1.

Products of Uv Irradiation. None of the 3MP–metal deposits showed an esr signal before irradiation. This indicates that the spectra of the alkali metal atoms, which have been observed in rare gas matrices at 4°K,[9,10] are obscured by line broadening or that the metals are not monatomically dispersed. The metals were not present in continuous films or large clusters, since the cavity could be readily tuned at low powers, which was not possible when agglomeration was allowed to occur by melting and refreezing the sample.

Irradiation of the dispersed metals in the 3MP matrices at 77°K with the AH4 lamp produced esr signals indicative of two products which were observed only in the steady state during irradiation and two relatively stable trapped free radicals. The spectra consist of (1) a Gaussian singlet 0.1–0.3 G wide (ΔH_{ms}), at $g = 2.0001 \pm 0.0002$ (Figure 3), which exhibits power saturation starting at about 35 μW; (2) several lines about 1 G wide with splitting of *ca.* 3 G, which flank the singlet and are 0.1–0.005 as intense (Figure 4) and which do not exhibit saturation below about 350 μW; (3) in the case of Na, some ten lines about 3 G wide with splitting of *ca.* 24 G, representing two or more trapped radicals (Figure 5). The singlet of Figure 3 and the flanking lines of Figure 4 achieve a steady state after illumination in a time shorter than the 0.2-sec response time of the recorder used and decay equally rapidly when the irradiation is stopped. For a given sample the signal intensity is proportional to the radiation intensity (as varied by neutral density filters).

The maximum steady-state spin yields of the singlet were estimated to be, approximately: Na, 2×10^{14}; K,

(7) W. Weyhmann and F. M. Pipkin, *Phys. Rev. A*, **137**, 490 (1965).

(8) R. B. Merrithew, G. V. Marusak, and C. E. Blount, *J. Mol. Spectrosc.*, **29**, 54 (1969).

(9) C. K. Jen, V. A. Bowers, E. L. Cochran, and S. N. Foner, *Phys. Rev.*, **126**, 1749 (1962).

(10) P. H. Kasai, *Phys. Rev. Lett.*, **21**, 67 (1968).

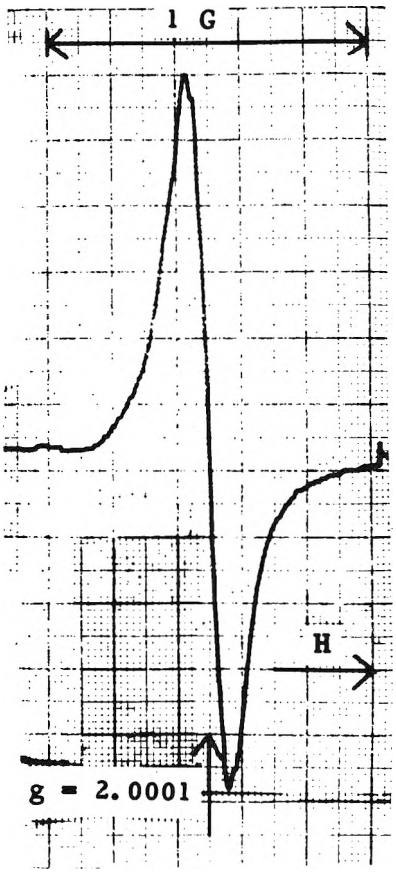

Figure 3. Esr singlet observed in the photostationary state during irradiation of Na in 3MP at 77°K with AH4 lamp with Vycor filter. Microwave power 0.03 mW; modulation amplitude 10; signal level 25.

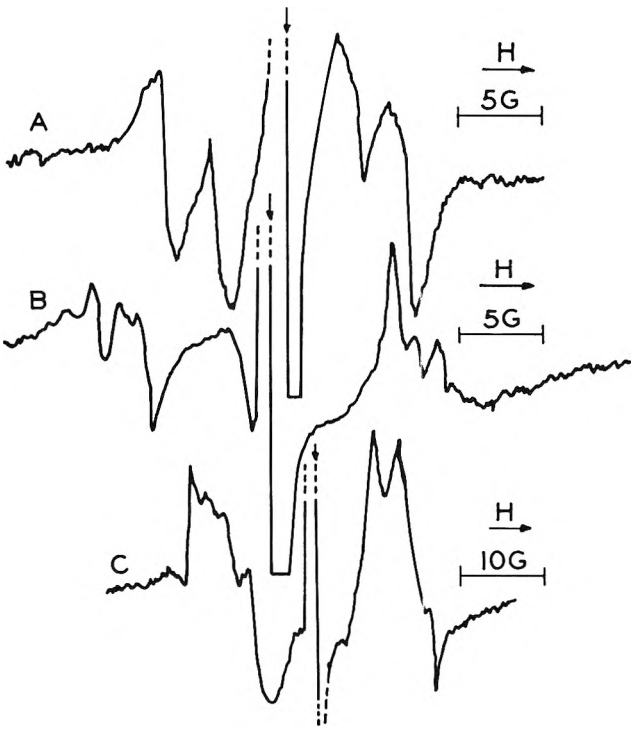

Figure 4. Photostationary esr spectra at 77°K of (A) Na in 3MP, modulation amplitude 100, signal level 200; (B) K in 3MP, modulation amplitude 100, signal level 250; (C) Mg in 3MP, modulation amplitude 400, signal level 160. Microwave power 0.1 mW in all cases. Vycor filter used for Na and K.

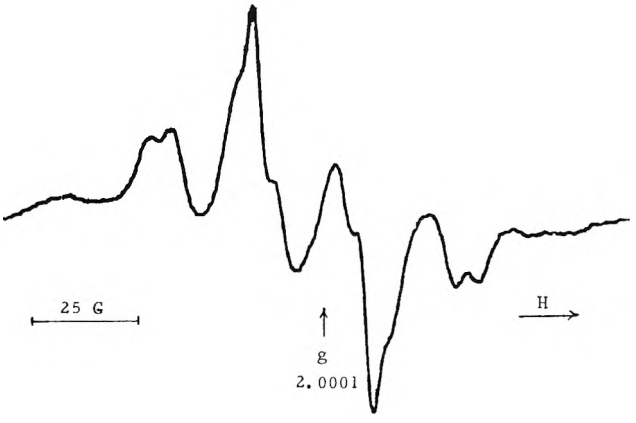

Figure 5. Esr spectrum of trapped radicals in a 3MP–Na matrix at 77°K following AH4 irradiation. Microwave power 15 mW; modulation amplitude 320; signal level 40.

2×10^{13}; Li, 5×10^{11}; Mg, 5×10^{12}; Cd, 2×10^{11}, by comparison with a standard-pitch sample, on the assumption that the number of spins observed is proportional to $(\Delta H_{ms})^2$ times the signal height of the first derivative. Variations of severalfold sometimes occurred between samples prepared in the same manner. The shapes of the flanking lines often undergo some change during the first 0.5 hr of continuous irradiation but very little thereafter.

The free-radical spectrum of Figure 5 grew linearly with time of irradiation. On standing at 77°K following irradiation, the spectrum changed, suggesting a relatively rapid decay ($t_{1/2}$ *ca.* 20 min) of one radical, leaving what appeared to be the 3MP radical, which decayed only slightly over several hours.

Experiments to Estimate Photoionization Thresholds. Figure 6 shows the relative intensities of the esr singlet for each metal as a function of irradiation with the different filters listed in Table I. The relative intensity of the radiation from the unfiltered AH4 lamp as a function of wavelength is indicated by the solid line. All of the intensity points plotted above the base line of Figure 6 are significantly above the noise level. In normalizing to the value of 100 for Li in the absence of any filter, the relative values for Mg, K, and Na have been reduced by large factors. All points for each metal were determined on a single sample.

Comparison of γ-Irradiated and Uv-Irradiated Matrices. The esr singlet of Figure 3 is most probably attributable to trapped electrons, yet it decays much more rapidly than trapped electrons produced by γ irradiation of a 3MP matrix frozen from the liquid state. To determine whether the difference is the result of the difference in mode of production of electrons or in

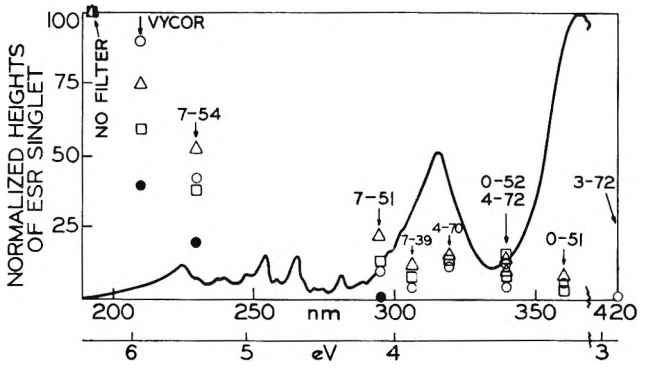

Figure 6. Effect of filters on photostationary state height of the esr singlet during irradiation of metals in 3MP at 77°K using a AH4 lamp: ●, Li; △, Na; □, Mg; ○, K. All points for a given metal are taken on the same sample. Signals for all metals with no filter normalized to 100. Solid line shows variation in relative intensity of AH4 lamp with wavelength: J. G. Calvert and J. N. Pilts, Jr., "Photochemistry," Wiley, New York, N. Y., 1966. Filter transmittances are given in Table I.

the mode of production of the matrix we have endeavored to observe trapped electrons produced by γ irradiation of a 3MP sample deposited from the vapor. Such tests could not be made with the cold finger of Figure 1 because the esr signal from the large mass of γ-irradiated Suprasil obscured the signal from the hydrocarbon sample. Attempts to transfer the deposit to a small esr tube under liquid nitrogen after removing the outer tube of the cold finger under liquid nitrogen were unsuccessful because the density of the scraped-off matrix fragments is close to that of liquid N_2. One experiment was completed in which the usual cold finger on which the matrix was deposited was replaced by a smaller (4-mm o.d.) tube. The tube with the deposit was broken off under liquid nitrogen, γ irradiated under liquid nitrogen, and transferred to a Varian esr dewar containing liquid nitrogen. It gave a 3MP radical signal 10% as great as that from a glassy 3MP sample of arbitrary size, prepared by cooling liquid 3MP to 77°K, which received the same γ dose. However, the vapor-deposited sample showed no singlet as compared to a 100 mm high singlet in the glass. Both samples were processed in near darkness to avoid photobleaching of the electron signal.

Discussion

Species Responsible for Esr Singlet. The esr singlet produced by uv irradiation of 3MP–metal matrices has a combination of g value, line width, esr saturation characteristics, and lifetime which strongly indicates that it is a weakly trapped electron. No other species which might be produced would be expected to have these properties. The line width (0.1–0.3 G), which is less than that of trapped electrons in glassy hydrocarbons and still less than that in polar compounds, indicates relatively little interaction with molecules of the matrix and is qualitatively consistent with the lifetime of <0.1 sec, as compared to the lifetimes in glassy 3MP of 5–40 min[6b] (dependent on the rate of cooling from the liquid to the glassy state).

An estimate of the rate of photon absorption by the alkali metal is *ca.* 10^{15} sec^{-1}. Coupling this with the estimated steady-state concentration of electrons of 2×10^{14} observed in the 3MP–Na matrix and assuming that decay is by first-order geminate recombination give for the steady state $d[e_{tr}^-]/dt = 10^{15} - k(2 \times 10^{14}) = 0$, with $k = 5$ and $t_{1/2} = 0.14$ sec. Since the chart speed used in observing growth and decay was 0.33 cm sec^{-1}, the minimum $t_{1/2}$ for which a deviation from a vertical rise to the steady state would have been detected is about 0.2 sec. Allowing for the substantial error possible in the estimates of the rate of photon absorption and the concentration of electrons at the steady state, it appears that the half-life must lie within the range of about 0.02–0.2 sec. Electrons undergoing geminate combination without trapping may be expected to return to the parent positive ion within less than 10^{-11} sec.[11]

It is noteworthy that within the limits of resolution of these experiments, electrons produced with energies varying as much as 3 eV show no difference in lifetime. This, coupled with knowledge of the much longer lifetimes of electrons produced by photoionization of TMPD in 3MP glass or by γ irradiation of 3MP glass, indicates strongly that the 3MP matrix deposited from the vapor does not contain as "deep" traps as 3MP glass made from the liquid. The preliminary experiments reported in the Results section on γ irradiation of such matrices are consistent with this conclusion.

Species Responsible for the Flanking Lines. The several esr lines with widths of *ca.* 1 G and splittings of *ca.* 3 G which flank the central singlet have striking similarities for Na, K, and Mg (Figure 4) but also marked differences. Their growth and decay in parallel with the growth and decay of the singlet suggest that they are genetically related to it. The relatively small line width of the singlet and the lower microwave power at which it saturates indicate that the added lines are due to a separate species and are not the result of hyperfine coupling of the trapped electron. The most plausible conclusion seems to be that the lines are caused by cationic species formed by photoionization, which disappear by recombination with the electron. Na_2^+, K_2^+, and Mg_2^+ are to be considered. However, the similarities in the spectra from different metals would not be expected for species with as great differences in nuclear magnetic moment. Thus, the assignment of the lines remains in doubt.

Trapped Free-Radical Production. The dominating feature of Figure 5 is a six-line spectrum with *ca.* 24-G splittings, assignable to the *sec*-3MP radical.[12] Super-

(11) A. H. Samuel and J. L. Magee, *J. Chem. Phys.*, 21, 1080 (1953).

imposed on this is a second spectrum which appears to have four lines, also with splittings of approximately 24 G.[13] The number of lines and splittings as well as the rapid decay relative to the 3MP radical suggests the methyl radical, although C–C bond rupture is unexpected in such a system.

The metal-photosensitized formation of radicals may be presumed to occur as a result of the transfer of energy from the neutralization process ($M^+ + e^- \rightarrow M^*$) to matrix molecules.

Energy Threshold for Electron Production. The relative yields of the electron singlet as a function of metal irradiated and of wavelength (Figure 6) depend on the wavelength dependence of (a) the extinction coefficient of the metal, (b) the intensity of the AH4 lamp, and (c) the photoionization quantum yields. Despite this combination of variables which affect the absolute yields, the relative yields of Figure 6 are adequate to show that the photoionization thresholds of all of the metals in the 3MP matrix are lower than the gas-phase ionization potentials and higher (with the possible exception of Mg) than the photoelectric work function for removal of electrons from the solid (Table II).

It may be reasoned that the energy for ionization of isolated metal atoms in 3MP must equal the gas-phase ionization potential minus the electronic polarization energies of the separated electron and cation in the medium plus the repulsive energy for the electron in the medium. If the metal atoms in the experiments of Figure 6 are monatomic or in aggregates of only a few atoms, the polarization energies must exceed the repulsive energy, to be consistent with the data of Table II. It seems possible, however, that many or all of the metal atoms exist as larger agglomerates.

Table II: Approximate Photoionization Thresholds in 3MP–Metal Matrices Compared to Gas-Phase Ionization Potentials and Photoelectric Work Functions[a,b]

	Threshold	Ionization potentials[c]				Work function
		M_1	M_2	M_3	M_4	
Li	5.1	5.4	5.15	...	...	2.3–2.4
Na	3.4	5.14	4.9	3.9	4.2	2.27
K	2.8	4.34	4.0	3.4	3.6	2.24
Mg	3.1	7.65	...	...	...	3.6–3.8
Cd	5.9	8.99	...	...	...	4

[a] In units of eV. [b] P. J. Foster, R. E. Leckenby, and E. J. Robbins, *Proc. Phys. Soc., London (At. Mol. Phys.)*, **2**, 478 (1969). [c] For the species with one to four metal atoms.

(12) D. J. Henderson and J. E. Willard, *J. Amer. Chem. Soc.*, **91**, 3014 (1969).

(13) Work of L. Glasgow in our laboratory shows that photolysis of carefully purified 3MP glass at 77°K with 185- or 254-nm radiation produces 3MP radicals and a species which gives some added structure to the esr signal. This is presumed to result from absorption of radiation by difficultly removed oxygen complexes. Similar spectra have been observed when deposits of pure 3MP were irradiated on the cold finger used in the present work, but their intensity for identical irradiations was less than one-tenth that observed for the 3MP–Na matrices.

Production of H, OH, and H_2O_2 in the Flash Photolysis of Ice[1]

by J. A. Ghormley and C. J. Hochanadel*

Chemistry Division, Oak Ridge National Laboratory, Oak Ridge, Tennessee 37830 *(Received August 24, 1970)*

Publication costs assisted by the Oak Ridge National Laboratory

No absorption by trapped electrons was observed in the flash photolysis of ice at −10° by light above 1600 Å although electrons had previously been observed on flashing water at 24°. Absorption in the ultraviolet, produced during the flash, was very similar to that observed in the flash photolysis of water and is attributed to H and OH radicals.

We had previously observed[2] the formation of hydrated electrons (also H, OH, and H_2O_2) in the flash photolysis of pure water at 24° with photons having energy ≥6.5 eV (1920 Å). The overall reaction

$$2H_2O_{aq} \longrightarrow e_{aq}^- + OH_{aq} + H_3O_{aq}^+ \qquad (1)$$

is endothermic by about 5.8 eV, and for the hydration energy to be available in time requires that the electron be stabilized in preexisting traps (configuration of suitably oriented water dipoles). It was of interest, therefore, to examine the possible formation of trapped electrons by the flash photolysis of pure ice.

(1) Research sponsored by the U. S. Atomic Energy Commission under contract with the Union Carbide Corp.

(2) J. W. Boyle, J. A. Ghormley, C. J. Hochanadel, and J. F. Riley, *Radiat. Res.*, 31, 582 (1967); *J. Phys. Chem.*, 73, 2886 (1969).

An extensive study of the pulse radiolysis of pure ice at various temperatures was made recently by Taub and Eiben.[3] In ice irradiated at temperatures below −56° they observed optical absorption bands with peaks near 6700, 2800, and 2300 Å which they attributed to solvated electrons, OH radicals, and HO_2 radicals, respectively. At −14° only the 6700- and 2300-Å peaks were observed. Shubin, *et al.*,[4] and Nilsson, *et al.*,[5] also studied the trapped electron produced by the pulse radiolysis of ice. They all found a broad absorption band with a maximum (~6800 Å at −10°) in the same spectral range as in liquid water (~7200 Å at 25°), indicating about the same trapping energy in both phases. The band is narrower in ice than in water, and the extinction coefficient at the maximum may be about double that in water.[5]

Taub and Eiben[3] and also Nilsson, *et al.*,[5] found the yield of trapped electrons to be temperature dependent, decreasing rapidly from −5 to −40° and then slowly at lower temperatures. G values at −5, −40, −130, and −196° were approximately 0.3, 0.07, 0.003, and 0.0006, compared with ~3 for liquid water at room temperature.

In the γ radiolysis of ice at −196°, Ghormley and Stewart[6] observed a large peak at 2800 Å with a small shoulder at 2300 Å. On warming, the two bands annealed out simultaneously in two temperature ranges. Taub and Eiben[3] observed that neither the buildups at −196° nor the annealings of the two bands after pulse radiolysis at −56° were simultaneous.

Experimental Section

Beautifully clear cylindrical samples of ice were prepared by slowly lowering (1 cm/hr) sealed ampoules of degassed water into a bath thermostated at −1.5°. The samples were then annealed at this temperature at least overnight before using. The water was purified by several distillations as before[2] and degassed by purging with helium, followed by several freeze–pump–thaw cycles. After removing the ice from the tube, about 1–2 cm was removed from each end, and the ends were flattened with a smooth aluminum plate giving an optically clear sample about 23 cm long × 2.2 cm in diameter. The sample was suspended between two 25 cm long flash lamps inside a magnesium oxide coated reflector. The temperature of the sample was held at −10 ± 2° by a stream of cold nitrogen blowing through the reflector.[7] The flash was usually a 24-kV discharge (288 J) in Xe at 15 Torr, with a duration of ~3 μsec. The measuring equipment was described previously.[8,9] The absorption spectra produced by the flash were taken spectrophotometrically point by point. Measurements were made using the mercury lines emitted by a Hanovia 200-W Hg–Xe lamp (901B-1), or the Xe continuum from a Hanovia 300-W Xe lamp (914C-1). For some measurements the analytical lamp was pulsed by discharging a capacitor through the glowing lamp, thereby increasing the light output by a factor of ~50 for the xenon lamp or for the Hg–Xe lamp at wavelengths off the Hg lines.

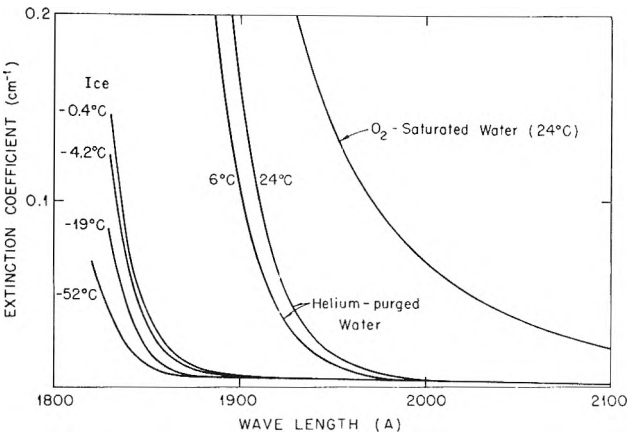

Figure 1. Absorption spectrum of ice at several temperatures compared with the spectrum of liquid water. The absorption spectrum of oxygen-saturated water (1.24×10^{-3} M) is shown also.

It is known that the absorption spectra of liquid water[10] and ice[11,12] are shifted to shorter wavelengths relative to water vapor.[13] The peaks occur at 1500 and 1670 Å in the liquid and vapor, respectively. The long-wavelength cutoff of ice relative to liquid water was of interest to us and had not been measured accurately before. We measured the absorption spectrum of pure ice at several temperatures using a Model 15 Cary spectrophotometer purged with nitrogen. The ice samples (10 cm long × 2.2 cm in diameter) were cooled below the desired temperature and then, with thermocouple attached, were placed in an insulating block and the spectra run while the samples warmed slowly. The spectra are shown in Figure 1, along with the absorption spectra of helium-purged and oxygen-saturated water. The water spectra were measured in 10-

(3) I. A. Taub and K. Eiben, *J. Chem. Phys.*, **49**, 2499 (1968).

(4) V. N. Shubin, V. A. Zhigunov, V. I. Zolotarevsky, and P. I. Dolin, *Nature (London)*, **212**, 1002 (1966).

(5) G. Nilsson, H. C. Christensen, J. Fenger, P. Pagsberg, and S. O. Nielsen, *Advan. Chem. Ser.*, **No. 81**, 71 (1968).

(6) J. A. Ghormley and A. C. Stewart, *J. Amer. Chem. Soc.*, **78**, 2934 (1956).

(7) Our first samples of ice were prepared by slowly lowering an ampoule of water into a bath at −5°. We then tried to make measurements while the sample was melting. However, on warming to 0° the samples developed a crazing throughout which greatly reduced the light transmission.

(8) C. J. Hochanadel, J. A. Ghormley, and J. W. Boyle, *J. Chem. Phys.*, **48**, 2416 (1968).

(9) C. J. Hochanadel, J. A. Ghormley, J. W. Boyle, and J. F. Riley, *Rev. Sci. Instrum.*, **39**, 1144 (1968).

(10) L. R. Painter, R. D. Birkhoff, and E. T. Arakawa, *J. Chem. Phys.*, **51**, 243 (1969).

(11) K. Dressler and O. Schnepp, *ibid.*, **33**, 270 (1960).

(12) R. Onaka and T. Takahashi, *J. Phys. Soc. Jap.*, **24**, 548 (1968).

(13) K. Watanabe and M. Zelikoff, *J. Opt. Soc. Amer.*, **43**, 753 (1953).

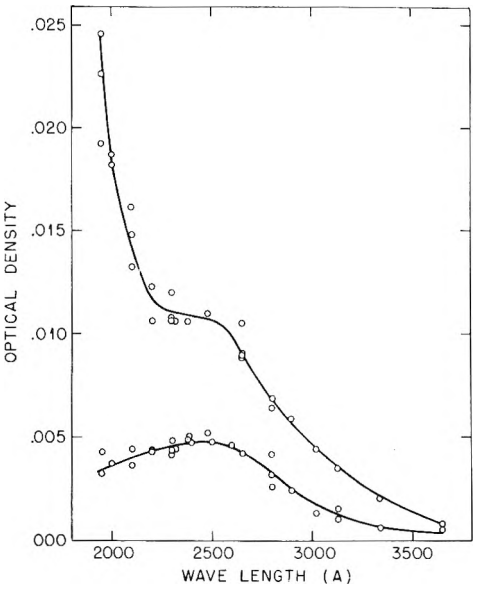

Figure 2. Absorption spectrum produced by the flash photolysis of pure crystalline ice at −10°. The upper curve was measured ~40 μsec after the start of the flash and the lower curve ~8 msec afterward. Values for two different samples are plotted together, normalized to the same o.d. at 2650 Å to compensate for a 20% difference in measured o.d. Two other samples, measured in the range 2300–3550 Å, gave the same spectrum. Samples were 23 cm long × ~2.2 cm in diameter. The flash was 288 J at 24 kV.

cm cells with Suprasil windows. The blank (mostly reflection from the cell windows) was taken to be half the reading for the empty (N_2-filled) cell. All spectra were run against N_2 in the reference beam. The absorption by ice was assumed to be the same as that by liquid water at 2100 Å. The observed shift of the spectrum of liquid water to shorter wavelengths as the water is cooled is in agreement with measurements of Weeks, *et al.*[14] On changing from liquid to ice the spectrum shifts ~70 Å.

The flash lamps[9] were constructed of pure fused silica (Suprasil) which transmits ~95% of the light above 1600 Å. The ice sample, because of the shift in spectrum, absorbs much less of the flash energy than does liquid water.

Results and Discussion

Within the limits of our sensitivity, we could detect no absorption (<0.1%) at 5780 or 7000 Å by trapped electrons. This was true for the first flash received by the sample or for a sample that had been flashed many times. Because of scattered photolytic light, measurements could not be made at high sensitivity until about 15 μsec after the start of the flash. However, the lifetime of trapped electrons at this temperature is sufficiently long[3] that they could have been observed. The quantum yield of e_{aq}^- in liquid water at 24° was ~5% of the OH yield.[2] In ice we observed ~2% absorption by OH at 2650 Å (Figure 2). Assuming the same ratio of quantum yields in ice as in water (0.05) and the same ratio of extinction coefficients as in water (18,500/370) the initial absorption by trapped electrons would have been ~5% and easily observable. Apparently, traps do not exist in ice which can provide the necessary hydration energy for the solid-state equivalent of reaction 1.

Absorption was observed in the ultraviolet; the spectra measured 40 μsec and 8 msec after the start of the flash are shown in Figure 2. We observed little or no difference in the amount of absorption produced or in the decay characteristics for the 4th or the 40th flash on the same sample. The spectrum measured shortly after the flash is very similar to the spectrum we observed in the flash photolysis of pure water, attributed to H and OH radicals.[2] In water the OH absorption peaks at ~2300 Å, and the H absorption starts at ~2250 Å and increases toward shorter wavelengths.[15] The initial products in ice are expected to be H and OH, and the spectrum we observed is consistent with this. Maximum absorption was reached within 15 μsec after the beginning of the flash, and, although the absorption was too weak to allow accurate kinetic analysis of the decay, there were at least two different components. One had a half-life of about 1 msec and the other about 5 sec. The spectrum of the long-lived component, shown in Figure 2, is similar to the OH spectrum in water.

Both H and H_2 are relatively mobile in ice at −10°. In fact, Flournoy, *et al.*,[16] showed by esr measurements that H atoms are stable at −269°, but begin to diffuse at −253° and react with other H atoms and with OH. The simplest explanation of our results is that the H atoms disappear by reacting rapidly with H and with some of the OH, leaving the remaining OH to react slowly with OH and with H_2.

There is some doubt about assigning the spectrum of the long-lived component with a peak at 2450 Å to OH because it also resembles the spectrum of HO_2 in liquid water. Secondary reaction of OH with H_2O_2 would produce a small amount of HO_2, but computer calculations of the kinetics in liquid water[2] indicate that the concentration would always be very small and could not account for our spectrum observed at 8 msec (Figure 2). In a typical flash photolysis experiment with liquid water,[2] the concentrations of OH, H_2O_2, and HO_2 (or O_2^-) produced were 4.3×10^{-6}, 9×10^{-7}, and 2×10^{-9} *M*. The mole ratio of final H_2O_2 to initial OH is about 0.2 in ice or in liquid water indicating that 40% of the OH radicals combine to form H_2O_2 in either phase. In the faster (msec) reaction in ice, half of the OH radicals disappear; we postulate that these OH

(14) J. L. Weeks, G. M. A. C. Meaburn, and S. Gordon, *Radiat. Res.*, **19**, 559 (1963).

(15) The spectrum of H atoms in water was first identified by S. O. Nielsen, P. Pagsberg, J. Rabani, H. Christensen, and G. Nilsson, *Chem. Commun.*, **23**, 1523 (1968); *J. Phys. Chem.*, **73**, 1029 (1969).

(16) J. M. Flournoy, L. H. Baum, and S. Siegel, *J. Chem. Phys.*, **36**, 2229 (1962), and earlier papers.

react with H, producing no H_2O_2. It follows from the H_2O_2 observed after melting (Figure 3) that in the slower reaction, about 80% of the remaining OH radicals react with each other to form H_2O_2 and no more than about 20% react with H_2.

From the initial absorption at 2650 Å, assuming e = 370 as in liquid water, the concentration of OH produced in ice was about 1.0×10^{-6} M, about one-fourth the amount produced in liquid water by a similar flash. The reduced amount of OH in ice is attributed to less photolytic light absorption, although the quantum yield in ice may be lower due to more geminate recombination.

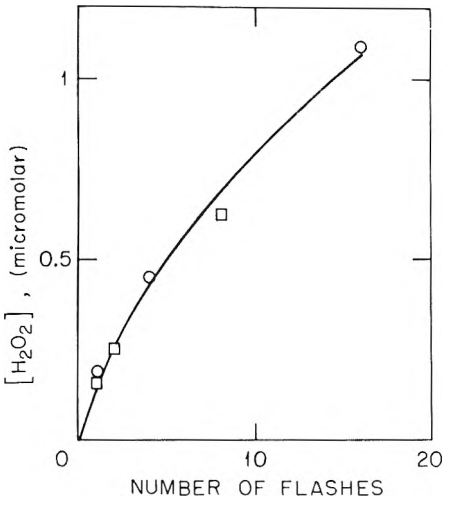

Figure 3. Formation of H_2O_2 in the flash photolysis of ice at −10°: ○, sample 1; □, sample 2.

The long decay time (~5 sec) is reasonable for reaction of OH with OH in ice at −10°. In liquid water the reaction is diffusion limited ($k = 4 \times 10^9$ M^{-1} sec^{-1}). It may be assumed that the reaction in ice is also diffusion limited and that the rate of diffusion depends on hydrogen bonding of the OH. To a first approximation it may also be assumed that hydrogen bonding of OH is about the same as that of H_2O. The diffusion coefficient of water is about 4×10^{-5} cm^2 sec^{-1} in the liquid at room temperature and only 2×10^{-11} cm^2 sec^{-1} in ice[17] at −10°. The rate constant for OH + OH in ice at 10° is therefore estimated to be $\sim 2 \times 10^3$ M^{-1} sec and the lifetime for 10^{-6} M OH is 3 min, which, within the uncertainty of the estimate, is consistent with the ~5 sec observed decay of the long-lived component. Our measurements at times as short as 15 μsec show no change in absorption any faster than the msec decay indicating that the faster reaction we observed is H + H and H + OH. We assume then that our much slower reaction is mainly OH + OH.

Taub and Eiben, in pulse radiolysis of ice at −14°, found only the 2300-Å band. They attributed over half of this absorption to OH and the remainder to HO_2 (ref 3, Figures 11 and 14d). They proposed that some of the OH reacted with H on a time scale too fast to measure, and the remainder disappeared by OH + OH with a half-life of ~1 msec. They attributed the much slower decay to $HO_2 + HO_2$. Since they expected OH in ice to be hydrogen bonded (called $OH_t\cdot$ by them) and to diffuse about the same as H_2O in ice (as we assume also) it was necessary for them to postulate conversion of $OH_t\cdot$ to $OH_m\cdot$, a form having mobility nearly equivalent to OH in liquid water, in order to allow the OH + OH reaction to occur with $t_{1/2} \sim 1$ msec.

We propose that the OH radicals which absorb at lower temperatures with a peak at 2800 Å are trapped interstitially with little or no hydrogen bonding and diffuse to react with each other at much lower temperatures than substitutionally trapped OH. When ice irradiated at −196° is warmed,[6] the absorption at 2800 Å, which we attribute to interstitial OH radicals, disappears completely at about −150°. On the other hand, in ice irradiated at higher temperatures, we propose that the OH radicals become trapped in substitutional positions, and this hydrogen-bonded OH is expected to have an absorption spectrum similar to that of OH in liquid water. This is consistent with the absorption spectrum observed in ice at −10° subjected to flash photolysis and ice at −14° subjected to pulse radiolysis.[3] The absorption spectrum of interstitial OH in ice is expected to be more like that of OH in the vapor phase which shows strong absorption at 3064 Å.

It seems to be generally assumed that when ice is exposed to ionizing radiation, water molecules dissociate, but only the hydrogen atom leaves the site of the original water molecule and OH remains behind, hydrogen bonded to water molecules. The deposition of just enough energy from a fast electron to dissociate a water molecule is unlikely and in most cases sufficient energy is involved to break all the hydrogen bonds of a water molecule and to eject both of the fragments, H and OH, into interstitial positions in the ice. For example, ignoring hydration energy and hydrogen-bonding energy, 5.1 eV is required to dissociate a water molecule to H and OH. If this is accomplished through recombination of an electron with H_2O^+, the energy available exceeds the energy necessary to break the bond by 7.5 eV. On the other hand, under the conditions of the flash photolysis described here only enough energy goes into a water molecule to break an HOH bond, and it seems logical that the OH radical remains in its original site, while the H atom diffuses away.

Box, *et al.*,[18] examined the esr absorption of OH radi-

(17) P. Delibaltas, O. Dengal, D. Helmreich, N. Riehl, and H. Simon, *Phys. Kondens. Mater.*, 5, 166 (1966).

(18) H. C. Box, K. T. Lilga, E. E. Budzinski, and R. Dere, *J. Chem. Phys.*, 50, 5422 (1969).

cals (produced by X-rays) in single crystals of ice at 4.2°K and suggested that the three absorptions they observed are consistent with what is expected for OH in substitutional positions. It seems reasonable to suggest that interstitial OH radicals at 4.2°K might also be trapped in certain preferred orientations.

Vibrational Spectra of *trans*- and *cis*-Crotononitrile[1]

by J. R. Durig,* C. K. Tong, C. W. Hawley, and J. Bragin

Department of Chemistry, University of South Carolina, Columbia, South Carolina 29208 *(Received August 21, 1970)*

Publication costs borne completely by The Journal of Physical Chemistry

The infrared spectra of *trans*- and *cis*-crotononitrile, $CH_3CHCHCN$, in the liquid and gaseous states have been recorded from 4000 to 100 cm^{-1}. The infrared spectra of the solids have also been investigated from 33 to 500 cm^{-1}. The Raman spectra of the liquids have been recorded and quantitative depolarization values have been measured. A complete vibrational assignment based on band contours, positions, and depolarization is given for both the cis and trans isomers and the spectra are interpreted in detail. The interesting methyl torsional modes were observed in the spectra of the solids at 178 and 219 cm^{-1} for the trans and cis isomers, respectively. The calculated barriers are 1.76 and 3.08 kcal/mol for the *trans*- and *cis*-crotononitrile molecules. The lattice frequencies of the trans isomer show marked temperature dependence, particularly in the Raman spectrum. It is concluded that this isomer may exist in two distinct crystalline forms.

Introduction

Although many investigators have reported carbon–nitrogen stretching frequencies for a number of nitriles, few complete vibrational assignments have been given for this important class of compounds. Crotononitrile is no exception. Only four reports have dealt with the vibrational spectra of the two isomers (cis and trans) of this molecule.[2-4] Two Raman studies were done on crotononitrile during the 1930's, when Hemptinne and Wouters[2a] observed 14 of the 48 Raman active fundamentals of the two molecules and Reitz and Sabathy[2b] obtained 24 additional frequencies but were unable to complete the vibrational assignment. Tramer and Wierzchowski[3] attempted to assign the planar fundamentals of both isomers by calculating the frequencies of these modes and comparing the calculated values with those reported by Reitz and Sabathy; however, the assignment of the former authors is inconsistent with any reasonable assignment of the out-of-plane vibrations. Wyss and Günthard[4] obtained the infrared spectrum of the liquid trans isomer to a low frequency limit of 650 cm^{-1} and proposed a complete assignment for the vibrations of this isomer. Unfortunately the Raman spectrum of the trans isomer reported by Reitz and Sabathy contains a strong band due to cis impurity and this led Wyss and Günthard to a misassignment of the fundamentals in the former molecule. Thus, the assignments for both isomers are incomplete and subject to doubt. In addition, no frequencies have been recorded for the gaseous molecules and these data are important for the calculation of statistical thermodynamic quantities;[5] neither is there a valid assignment for the interesting methyl torsional frequency in either molecule.

Experimental Section

The sample of crotononitrile containing both isomers was obtained from Columbia Organic Co. and was separated by fractional distillation with a Teflon spinning band. The trans crotononitrile was further purified on an Aerograph Model A90-P3 gas chromatograph using a 20-ft TECP column under a flow rate of He of 90 ml/min, a column temperature of 130°, detector temperature 165°, and injector temperature of 150°. The cis isomer was better than 99% pure under the same conditions.

The Raman spectra of the two isomers were taken with a Cary Model 81 Raman spectrometer which used a filter solution composed of ethyl violet and *O*-nitro-

(1) Taken in part from the thesis of C. W. Hawley.

(2) (a) M. Hemptinne and J. Wouters, *Ann. Bruxelles*, **53**, 215 (1933); (b) A. W. Reitz and R. Sabathy, *Sitzber. Akad. Wiss. Wien Math-Naturwiss. Kl, Abt. 2B*, **146**, 577 (1938).

(3) A. Tramer and K. L. Wierzchowski, *Bull. Acad. Pol. Sci. Cl. Troisieme*, **5**, 335 (1957).

(4) H. R. Wyss and Hs. H. Günthard, *Helv. Chim. Acta*, **44**, 625 (1961).

(5) W. G. Fateley, I. Matsubara, and R. E. Witkowski, *Spectrochim. Acta*, **20**, 1461 (1964).

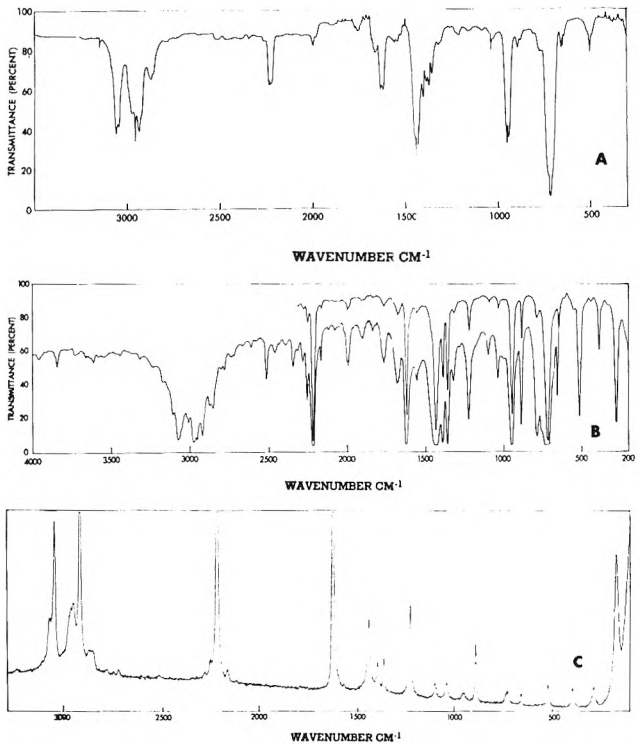

Figure 1. A, Infrared spectrum of gaseous *cis*-crotononitrile. B, Infrared spectrum of liquid *cis*-crotononitrile. C, Raman spectrum of liquid *cis*-crotononitrile.

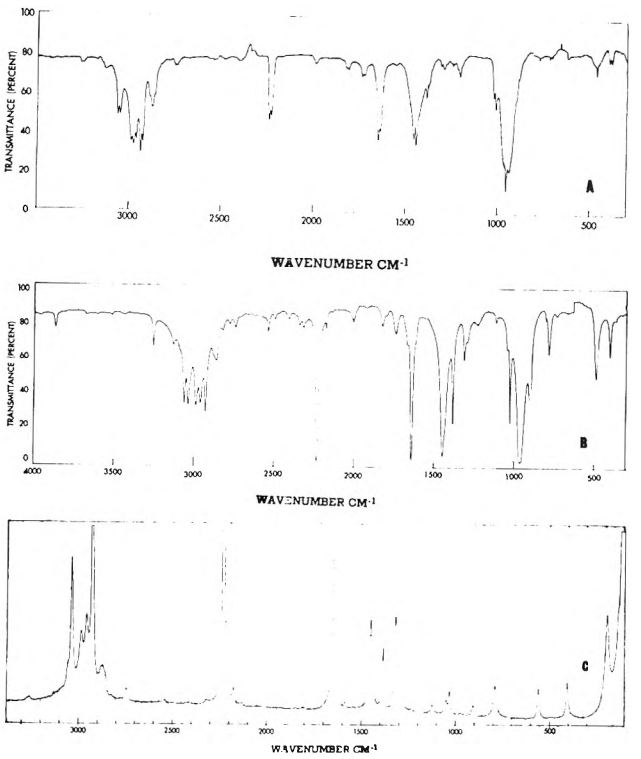

Figure 2. A, Infrared spectrum of gaseous *trans*-crotononitrile. B, Infrared spectrum of liquid *trans*-crotononitrile. C, Raman spectrum of liquid *trans*-crotononitrile.

toluene to isolate the 4358-Å mercury excitation line. Depolarization values were measured by the standard Polaroid technique. Some spectra were also taken with He–Ne laser excitation of 6328-Å wavelength. The instrument was calibrated with emission lines from a neon lamp over the spectral range from 0 to 4000 cm^{-1}. Typical Raman spectra are shown in Figures 1 and 2 and the frequencies are listed in Tables I and II. The frequencies for all sharp lines should be good to ± 2 cm^{-1}.

The mid-infrared spectra in the region 4000 to 200 cm^{-1} were recorded with a Perkin-Elmer Model 621. The instrument, which is equipped with an extended source, was continuously purged with dry air to remove atmospheric water vapor and was calibrated with standard gases.[6] The infrared spectra of the liquids were recorded as films between CsI plates and the spectra of the vapors were recorded by using 20-cm cells equipped with CsBr windows. The frequencies are listed in Tables I and II and are expected to be accurate to ± 2 cm^{-1}. Typical spectra are shown in Figures 1 and 2.

The far-infrared spectra in the region from 500 to 33 cm^{-1} were taken with a Beckman IR-11 double-beam grating spectrometer which was purged with dry air and calibrated with water vapor.[7,8] For the spectra of the solids the samples were condensed onto a silicon support plate which was cooled with liquid nitrogen. The samples were repeatedly annealed until no further changes were noted. The far-infrared spectra are shown in Figures 3 and 4 and the observed frequencies are listed in Table III.

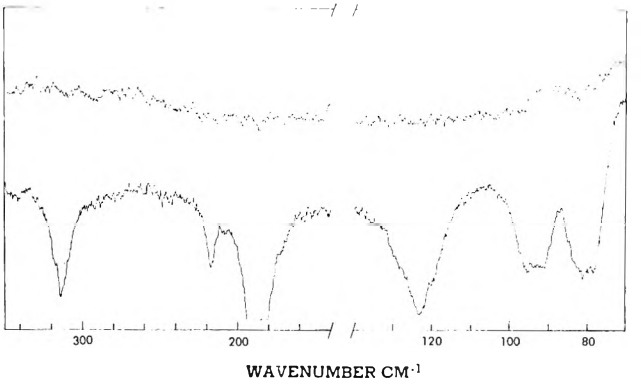

Figure 3. Far-infrared spectrum of *cis*-crotononitrile.

Results

Both isomers of crotononitrile have a plane of symmetry[9,10] and belong to the C_s point group. Twenty-four normal modes are expected for each isomer of

(6) IUPAC, "Tables of Wave Numbers for Calibration of Infrared Spectrometers," Butterworths, Washington, D. C., 1961.

(7) H. M. Randall, D. M. Dennison, H. Ginsberg, and L. R. Weber, *Phys. Rev.*, **52**, 160 (1939).

(8) R. T. Hall and J. M. Dowling, *J. Chem. Phys.*, **47**, 2454 (1967).

(9) N. Suzuki and K. Kozima, *Mol. Spectrosc. J.*, **33**, 407 (1970).

(10) R. A. Beaudet, *J. Chem. Phys.*, **38**, 2548 (1963).

Table I: Infrared and Raman Frequencies of *cis*-Crotononitrile

Infrared					Raman			
Gas			Liquid		Liquid			
ν, cm^{-1}	Rel int	Band type	ν, cm^{-1}	Rel int	$\Delta\nu$, cm^{-1}	Rel int	Depol ratio	Assignment
			3845	vw				$\nu_5 + \nu_6 = 3854$
			3235	vw				$\nu_1 + \nu_{16} = 3240$
			3170	w				$\nu_5 + \nu_{20} = 3171$
			3110	w				$\nu_6 + \nu_{13} = 3111$
3077 R								
3070 ctr	ms	A	3070	m	3078	6	0.86	ν_1 (a′) HCCH unsymmetrical stretch
3062 P								
			3052	w, sh	3054	20	0.30	ν_2 (a′) HCCH symmetrical stretch
			3010	w				$\nu_6 + \nu_8 = 3033$
2987 R								
2972 ctr	m	A	2967	s	2969	7	0.86	ν_3 (a′) CH_3 antisymmetric stretch
2970 P								
2952 Q	ms	C	2947	s	2956	7	0.86	ν_{17} (a″) CH_3 antisymmetric stretch
2931 R								
2922 ctr	ms	A	2917	s	2926	36	0.15	ν_4 (a′) CH_3 symmetric stretch
2914 P								
2870 R								
2861 ctr	w	B	2870	mw	2868	1		$2\nu_7 = 2866$
2852 P								
			2852	mw	2852	1		$\nu_6 + \nu_{11} = 2860$
			2800	w				$\nu_7 + \nu_9 = 2793$
			2780	w	2781	<1		$2\nu_8 = 2796$
			2735	vw	2748	<1		$\nu_5 + \nu_{22} = 2740$
			2719	vw	2722	<1		$2\nu_9 = 2720$
			2610	vw				$\nu_5 + \nu_{15} = 2613$
			2513	mw				$\nu_6 + \nu_{13} = 2527$
			2458	vw				$2\nu_{11} = 2450$
			2388	vw				$\nu_5 + \nu_{16} = 2389$
			2344	mw				$\nu_6 + \nu_{21} = 2357$
			2281	mw	2285	<1		$\nu_6 + \nu_{14} = 2290$
			2252	mw	2255	1		$\nu_9 + \nu_{13} = 2252$
2236 R								
2230 ctr	m	A	2219	vs	2223	100	0.30	ν_5 (a′) C≡N stretch
2223 P								
			2168	mw	2170	1		$\nu_{11} + \nu_{20} = 2177$
1997 R								
1990 ctr	w	A	1992	m				$\nu_9 + \nu_{14} = 2015$
1980 P								
			1900	w				$2\nu_{20} = 1904$
			1845	w				$\nu_{13} + \nu_{20} = 1844$
1780 R								
1773 ctr	w		1765	mw				$2\nu_{13} = 1784$
1763 P								
1690 R								
1683 ctr	w	A	1679	w				$\nu_{20} + \nu_{21} = 1674$
1673 P								
1637 R								
1631 ctr	m	A	1635	vs	1629	58	0.25	ν_6 (a′) C=C stretch
1621 P								
1560 ctr	w	A or B	1555	w				$\nu_{13} + \nu_{14} = 1547$
1457 R								
1450 Q	s	A(?) & C	1433	vs, brd	1445	7	0.60	ν_7, ν_{18} (a′, a″) CH_3 antisymmetric deformation
1447 Q								
1440 P								
1406 R								
1399 ctr	m	A	1398	s	1397	3	0.86	ν_8 (a′) HCCH unsymmetrical deformation
1390 P								
1380 R								
1376 ctr	m	A	1360	s	1365	5	0.30	ν_9 (a′) CH_3 symmetric deformation
1365 P								

Table I (*Continued*)

Infrared					Raman			
Gas			Liquid		Liquid			
ν, cm^{-1}	Rel int	Band type	ν, cm^{-1}	Rel int	$\Delta\nu$, cm^{-1}	Rel int	Depol ratio	Assignment
1320 ctr 1240 R	vw	A or B	1321	w	1329	<1	?	ν_{10} (a′) HCCH symmetrical deformation
1232 ctr 1223 P	vw	A or B	1225	m	1231	12	0.30	ν_{11} (a′) C—CH_3 stretch
			1102	w	1104	2	0.30	ν_{12} (a′) CH_3 rocking
1044 R 1034 Q 1026 P	w	C	1042	mw	1045	2	0.86	ν_{19} (a″) CH_3 rocking
965 R 954 Q 946 Q 942 P	s	C	952	vs	959	1	0.86	ν_{20} (a″) HCCH unsymmetrical bending
900 R 892 ctr 884 P	w	B	892	s	895	5	0.13	ν_{13} (a′) C—CN stretch
790 R 782 ctr 773 P	w	A	785	m				$\nu_{22} + \nu_{23} = 797$
731 R 726 Q 723 Q 710 P	vs	C	722	vs	734	2	0.86	ν_{21} (a″) HCCH symmetrical bending
664 R 658 ctr 650 P	w	A	655	m	663	1	0.30	ν_{14} (a′) C≡C—CN bending
525 R 517 Q 510 Q 500 P	m	C	517	s	523	2	0.86	ν_{22} (a″) C≡C—CH_3 bending
			394	m	398	3	0.65	ν_{15} (a′) C≡C—CH_3 bending
290 R 278 Q 268 P	s	C	280	m	287	2	0.86	ν_{23} (a″) C—C≡N bending
162 R 154 ctr 148 P	s	B	170	s	169	16	0.86	ν_{16} (a′) C—C≡N bending

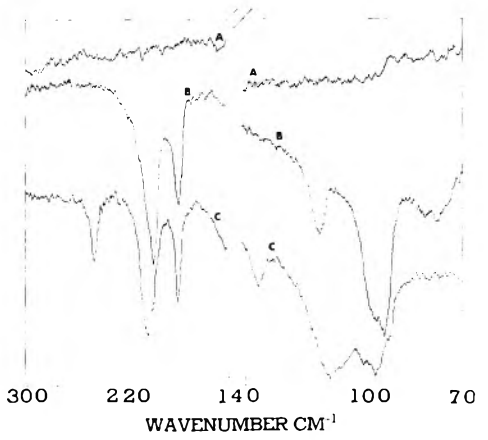

Figure 4. Far-infrared spectrum of *trans*-crotononitrile.

which 16 are planar (a′) vibrations and 8 are out-of-plane motions (a″). Since all fundamentals are both infrared and Raman active, 16 of the 24 Raman lines expected for each isomer may show less than the maximum depolarization ratio (0.86). The planar fundamentals of both isomers will give rise to bands showing A, B, or hybrid contours, whereas the out-of-plane vibrations will give rise to C type bands. The microwave spectra of the cis[10] and trans[9] isomers have been assigned and the rotational constants derived in these studies have been used in a computer program which calculates the vibrational band contours.[11] The results are summarized in Table IV. The trans isomer is a near prolate symmetric rotor ($\kappa = -0.994$)[9] and subbands spaced by 2.39 cm^{-1} are expected to appear on the B and C type bands of this molecule.

Vibrational Assignment for cis-Crotononitrile. Carbon-Hydrogen Stretching Modes. Two of these modes

(11) Ivan Haller, R. C. 1152, IBM Watson Research Center, Yorktown Heights, N. Y., 1965.

Table II: Infrared and Raman Frequencies of *trans*-Crotononitrile

Infrared					Raman			
Gas			Liquid		Liquid			
ν, cm^{-1}	Rel int	Band type	ν, cm^{-1}	Rel int	$\Delta\nu$, cm^{-1}	Rel int	Depol ratio	Assignment
			3860	w				$\nu_3 + \nu_{13} = 3873$
3276 R								
3271 ctr	w	A or B	3250	m	3252	<1	0.32	$2\nu_6 = 3268$
3265 P								
3158 R								
3146 Q	w	A or B	3125	w				$\nu_{16} + \nu_{17} = 3140$
3141 P								
3070 R								
3060 ctr	m	A or B	3055	m	3053	1	0.40	ν_1 (a′) HCCH unsymmetrical stretch
3053 P								
			3030	m	3036	16	0.40	ν_2 (a′) HCCH symmetrical stretch
2994 R								
2987 ctr	ms	A or B	2980	m	2985	2	0.86	ν_3 (a′) antisymmetric stretch
2979 P								
2965 Q	ms	C	2956	m	2956	2	0.86	ν_{17} (a″) CH_3 antisymmetric stretch
2942 R								
2932 ctr	s	A or B	2927	m	2927	44	0.26	ν_4 (a′) CH_3 symmetric stretch
2926 P								
2899 R								$2\nu_{18} = 2870$
2880 P, R	m, brd	A or B	2867	m, brd	2874	2, brd	0.25	$\nu_1 - \nu_{16} = 2871$
2868 P		A or B						
			2810	vw				$\nu_8 + \nu_7 = 2822$
			2772	vw				$\nu_{17} - \nu_{16} = 2772$
2758 R								
2752 ctr	w	A or B	2740	vw	2743	1	0.42	$2\nu_8 = 2748$
2747 P								
			2536	w	2539	<1	?	$\nu_6 + \nu_{13} = 2527$
			2490	w				$\nu_7 + \nu_{19} = 2493$
			2400	w				$\nu_5 + \nu_{16} = 2412$
			2335	w	2332	<1	?	$\nu_{12} + \nu_9 = 2328$
			2314	w				$\nu_8 + \nu_{20} = 2324$
2237 R								
2232 ctr	m	A or B	2228	s	2231	100	0.40	ν_5 (a′) C≡N stretch
2226 P								
			2173	w	2174	1	0.28	$\nu_{10} + \nu_{13} = 2183$
1995 ctr	vw, brd	A or B	1998	w, brd				$\nu_{14} + \nu_{18} = 1990$
			1918	w, brd				$\nu_{12} + \nu_{13} = 1913$
1834 R								
1826 ctr	w	A or B	1818	w				$\nu_6 + \nu_{16} = 1818$
1820 P								
			1790	vw, sh				$\nu_{12} + \nu_{21} = 1800$
1747 R								
1740 ctr	w	A or B	1738	w				$\nu_{20} + \nu_{21} = 1730$
1735 P								
			1660	w, sh	1667	1	0.86	$\nu_{13} + \nu_{21} = 1673$
1648 R								
1640 ctr	s	A or B	1634	vs	1641	45	0.40	ν_6 (a′) C=C stretch
1635 P								
1578 R								
1573 ctr	vw	A or B	1573	vw, brd	1586	<1	0.86	$\nu_{14} + \nu_{12} = 1585$
1567 P								
1463 R								
1453 ctr	s	A or B			1448	7	0.60	ν_7 (a′) CH_3 antisymmetric deformation
1449 Q	s	C	1435	vs				ν_{18} (a″) CH_3 antisymmetric deformation
1390 R								
1381 Q	w	A	1374	s	1383	4	0.62	ν_9 (a′) CH_3 symmetric deformation
1376 P								
1316 R								
1309 ctr	w	A or B	1308	m	1316	9	0.35	ν_9 (a′) HCCH symmetrical deformation
1302 P								
1302 R								

Table II (*Continued*)

Infrared					Raman			
Gas			Liquid		Liquid			
ν, cm^{-1}	Rel int	Band type	ν, cm^{-1}	Rel int	$\Delta\nu$, cm^{-1}	Rel int	Depol ratio	Assignment
1289 Q	w	A	1290	m, sh	1299	3, sh	0.40	ν_{10} (a′) HCCH unsymmetrical deformation
1283 P								
1240 R								
1232 ctr	vvw	A or B	1225	w, brd	1231	<1		ν_{11} *cis*-crotononitrile
1223 P								
1115 ctr	w	A or B	1111	w	1121	1	0.86	ν_{11} (a′) CH_2 rocking
1044 Q	w	C	1040	w, sh	1045	1	0.86	ν_{19} (a″) CH_3 rocking
1029 R								
1023 ctr	w	A or B	1020	s	1030	2	0.62	ν_{12} (a′) C—CH_3 stretch
1017 P								
957 Q	vs	C	950	vs	967	<1	dp	ν_{20} (a″) HCCH unsymmetrical bending
906 R								
898 ctr	vw, sh	A or B	893	s	902	1	0.62	ν_{13} (a′) C—CN stretch
890 P								
800 R								
788 Q								
784 Q	vw	C	780	m	787	2	0.86	ν_{21} (a″) HCCH symmetrical bending
775 P								
731 R								
726 Q								
722 Q	vw	C	722	w				ν_{21} *cis*-crotononitrile
710 P					555	2	0.20	ν_{14} (a′) C=C—CN bending
470 R								
461 Q	w	C	482	m	484	<1	0.86	ν_{22} (a″) C=C—CH_3 bending
452 P								
404 R								
398 ctr	w	A or B	400	m	402	2	0.50	ν_{15} (a′) C=C—CH_3 bending
392 P								
173	vs	?	184	vs	188	6	0.86	ν_{16} (a′) C—C≡N bending

Table III: Far Infrared Frequencies of Solids *cis*- and *trans*-Crotononitrile

trans				trans				cis		
Phase I				Phase II						
Ir		Raman		Ir		Raman		Ir		
ν, cm^{-1}	Rel int	$\Delta\nu$, cm^{-1}	Rel int	ν, cm^{-1}	Rel int	$\Delta\nu$, cm^{-1}	Rel int	ν, cm^{-1}	Rel int	Assignment
		247	w	246	w	234	w	315	m	C—C≡N out-of-plane bend
200	s	198	m	205	s	197	m	186	s	C—C≡N in-plane bend
178	m			181	m			219	w	CH_3 torsion
		134	w	135	w			129	m	Lattice mode
116	w			112	s	118	w	92	m	Lattice mode
97	s	101	s	98	s	105	m	86	m	Lattice mode
95	s	96	s			90	s			Lattice mode
79	w					70	s			Lattice mode

are motions of the olefinic protons which are known to occur above 3000 cm^{-1}.[12] The strong Raman line at 3078 cm^{-1} which has an infrared counterpart of type A contour at 3070 cm^{-1} is assigned to the out-of-phase or unsymmetrical mode (ν_1). The in-phase or symmetrical motion (ν_2) should give rise to a strong polarized Raman line with a weak infrared counterpart. The strong, polarized Raman line at 3054 cm^{-1} is assigned to this vibration.

The methyl protons give rise to three C–H stretching modes, two of which are degenerate under the local C_{3v} symmetry of the methyl group and are not expected to be greatly split by the molecular symmetry plane. The prominent Q branch of the C-type band at 2952 cm^{-1} is assigned to the out-of-plane antisymmetric methyl C–H stretch (ν_{17}). Two barely resolved Raman lines appear in this region of the spectrum. The lower

(12) L. J. Bellamy, "The Infrared Spectra of Complex Molecules," Wiley, New York, N. Y., 1962.

Table IV: P-R Separations of *cis*- and *trans*-Crotononitrile

	cis	trans
	Rotational constants, cm^{-1}	
I_A	42.6448[a]	13.281[b]
I_B	143.427	220.009
I_C	183.183	230.222
	P-R Separations	
Type A	13.5	13.6
Type B	16.8	16.8
Type C	21.2	26.2

[a] Reference 10. [b] Reference 9.

frequency, 2956 cm^{-1}, is assigned to ν_{17} and the upper frequency to the in-plane methyl C–H antisymmetric stretch (ν_3). The very intense, strongly polarized Raman line at 2926 cm^{-1} may be confidently assigned to the symmetric methyl C–H stretch (ν_4).

Carbon–Hydrogen Deformation Modes. Nine modes of this type are expected and of these five are internal motions of the methyl group. The CH_3 deformation mode, which is degenerate under the local symmetry of the methyl group, is expected near 1460 cm^{-1}.[12] Under C_s symmetry this mode correlates to an a′ and an a″ component which should not be appreciably split. A slightly polarized Raman line is observed at 1445 cm^{-1} and the counterpart of this band in the infrared spectrum of the gaseous molecule is complex showing two Q branches at 1450 and 1447 cm^{-1}. Therefore, both components of the CH_3 antisymmetric deformation (ν_7 and ν_{18}) are assigned a frequency of 1445 cm^{-1}. The symmetric deformation of the methyl is expected to fall in the frequency range 1385–1370 cm^{-1} [12] and should give rise to a polarized Raman line. The Raman line at 1365 cm^{-1} and its infrared counterpart observed at 1376 cm^{-1} in the spectrum of gaseous *cis*-crotononitrile are assigned to this mode (ν_9).

The methyl rocking vibrations of hydrocarbons are mass sensitive and difficult to characterize because they tend to interact with skeletal stretching motions.[13] The b_2 (planar) and b_1 (out-of-plane) CH_3 rocking modes in *cis*-2-butene have been assigned at 1134 and 1037 cm^{-1} in the Raman spectrum of that molecule,[14] and bands at 1107 and 1060 cm^{-1} have been assigned to a′ and a″ rocking vibrations, respectively, in the spectrum of gaseous 2-methyl-2-butene.[15] The polarized Raman line at 1104 cm^{-1} is assigned to the planar methyl rocking mode (ν_{12}). A depolarized Raman line appearing at 1045 cm^{-1} which has an infrared counterpart showing type C contour is assigned to the out-of-plane methyl rocking mode (ν_{19}).

Four carbon–hydrogen deformations are motions of the olefinic protons. Of the two planar vibrations only the unsymmetrical or rocking motion is well characterized[13,16,17] and the frequency of this mode should fall in the range 1429–1397 cm^{-1}.[13] The depolarized Raman line at 1397 cm^{-1} is assigned to this mode (ν_8). The symmetrical motion, ν_{10}, should appear above 1200 cm^{-1}. Only two features were observed in this region of the spectrum of *cis*-crotononitrile. For reasons which will be given below the strong Raman line at 1331 cm^{-1} is assigned to the C–CH_3 stretching motion and the very weak feature at 1321 cm^{-1} in the infrared spectrum of the liquid has been assigned to ν_{10}. In maleonitrile (*cis*-dicyanoethylene) the in-plane olefinic proton deformations have been assigned at 1200 (a_1) and 1371 (b_2) cm^{-1} [18] and the corresponding modes in *cis*-2-butene have been assigned at 1267 (a_1) and 1390 (b_2) cm^{-1}.[14,19]

The two out-of-plane olefinic proton motions have not yet been assigned. These vibrations have been thoroughly discussed in a paper by Potts and Nyquist.[20] The vibration of both olefinic protons moving out of the skeletal plane simultaneously absorbs strongly in the infrared in the frequency range 675–730 cm^{-1}. The very strong type C band at 724 cm^{-1} is assigned to this mode (ν_{21}). The other out-of-plane motion of the olefinic hydrogen atoms should have a higher frequency and only the depolarized Raman line at 959 cm^{-1} and strong C-type infrared band at 950 cm^{-1} can be assigned to this mode (ν_{20}). Potts and Nyquist[20] state that this mode should produce little or no dipole change but they also note that this prediction depends on the similarity of the attached groups.

Skeletal Stretching Modes. There are four skeketal stretching vibrations in each of the crotononitrile isomers. The cyanide and olefinic bond stretching frequencies are well characterized[12,13,17] and the very strong, polarized lines at 2223 and 1629 cm^{-1} in the Raman spectrum of the cis isomer are assigned to these modes (ν_5 and ν_6). The other two skeletal stretches involve displacement of the carbon–carbon single bonds. In acrylonitrile[21] this motion gives rise to a polarized Raman line at 871 cm^{-1}. The only band in the frequency range 800–1100 cm^{-1} which can be assigned to a planar fundamental is the B-type band centered at 892 cm^{-1}.

(13) N. B. Colthup, L. H. Daly, and S. E. Wiberley, "Introduction to Infrared and Raman Spectroscopy," Academic Press, New York, N. Y., 1964.

(14) C. M. Richards and J. R. Nielsen, *J. Opt. Soc. Amer.*, **40**, 442 (1950).

(15) D. W. Scott, G. Waddington, J. C. Smith, and H. M. Huffman, *J. Amer. Chem. Soc.*, **71**, 2768 (1949).

(16) L. J. Bellamy, "Advances in Group Frequencies," Barnes and Noble, New York, N. Y., 1968.

(17) C. N. R. Rao, "Chemical Applications of Infrared Spectroscopy," Academic Press, New York, N. Y., 1968.

(18) F. A. Miller, O. Sala, P. Devlin, J. Overend, E. Lippert, W. Luder, H. Moser, and J. Varchmin, *Spectrochim. Acta*, **20**, 1283 (1964).

(19) J. W. Kilpatrick and K. S. Pitzer, *J. Res. Nat. Bur. Stand.*, **38**, 191 (1947).

(20) W. J. Potts and R. A. Nyquist, *Spectrochim. Acta*, **13**, 679 (1959).

(21) F. Halverson, R. F. Stamm, and J. J. Whalen, *J. Chem. Phys.*, **16**, 808 (1948).

The Raman counterpart of this band at 895 cm^{-1} is strongly polarized and these features are assigned to the carbon–cyanide stretch (ν_{13}). The strong, polarized Raman line at 1231 cm^{-1} is assigned to the C–CH_3 stretching mode by analogy with the assignments for 2-cyano-,[22] 2-chloro-,[23] 2-bromo-,[24] 2-iodopropene,[25] and the perdeutero derivatives of these compounds. It should be noted that the Raman lines at 895 and 1231 cm^{-1} are the only strong features in the Raman spectrum of *cis*-crotononitrile in the range 200–1400 cm^{-1}.

Skeletal Deformation Modes. Of the six low-frequency modes in *cis*-crotononitrile five involve bending of the heavy atom skeleton and the sixth is the methyl torsion. Studies of a number of organic cyanides[2,18,21,26] show that this group gives rise to two characteristic low-frequency vibrations: an in-plane deformation near 200 cm^{-1} and an out-of-plane deformation near 300 cm^{-1}. The low-frequency vibration is particularly important because it always gives rise to a strong Raman line. The in-plane bending of the cyanide group as a whole occurs in the region around 600 cm^{-1}. A strong Raman line was observed at 169 cm^{-1} in liquid *cis*-crotononitrile and the counterpart of this line in the infrared spectrum of the gaseous molecule exhibits type B contour. These features are confidently assigned to the planar deformation of the cyanide group (ν_{16}). A strong C-type band was observed in the infrared spectrum of the gaseous molecule at 278 cm^{-1} and a depolarized Raman counterpart was observed at 287 cm^{-1} in the spectrum of the liquid. These features can only be assigned to the out-of-plane cyanide deformation (ν_{23}). Of the spectral features not yet assigned only the polarized Raman line at 663 cm^{-1} is in the frequency range of the cyanide bending and can be assigned to a planar fundamental. This line is assigned to the planar cyanide bending vibration (ν_{14}). The depolarized Raman line at 523 cm^{-1} has an infrared counterpart of type-C contour and for this reason it is assigned to the out-of-plane methyl bend (ν_{22}). The polarized Raman line at 398 cm^{-1} must be the in-plane methyl bending (ν_{15}).

Methyl Torsion. Beaudet[10] has obtained a barrier to methyl torsion in *cis*-crotononitrile of 1.40 kcal/mol by analysis of the tunneling splittings in the ground-state rotational spectrum of that molecule. The microwave value of the barrier leads to a torsional frequency of 143 cm^{-1}. Unfortunately this region of the far-infrared spectrum of the gaseous molecule is obscured by the strong absorption due to ν_{16}. Recent investigation[27–30] of low-temperature solid-state far-infrared spectra of molecules containing methyl rotors have shown the utility of this technique in obtaining torsional frequencies and barriers to internal rotation in the solid. The torsional mode usually appears as a sharp band in the infrared spectrum and can be easily distinguished from the skeletal modes since the corresponding band in the Raman spectrum of the solid is usually very weak or unobserved. Such an experiment has been performed on both crotononitrile isomers.

For the cis isomer the bands fall into two groups: 186, 219, and 315 cm^{-1} which must be due to internal vibration, and 129, 92, and 86 cm^{-1} which can only arise from lattice vibrations. In the far-infrared spectrum of liquid *cis*-crotononitrile a strong band was observed at 170 cm^{-1} and medium bands were observed at 280 and 394 cm^{-1}. Previous experience[27–30] has shown that deformation modes never shift down on solidification and usually show a positive shift of 5–10 cm^{-1}. The large π cloud of the cyanide group should make modes involving movement of this moiety particularly sensitive to molecular environment and we would expect both ν_{16} and ν_{23} to exhibit appreciable, positive frequency shifts on solidification. Thus, the bands observed at 186 and 315 cm^{-1} in the infrared spectrum of solid *cis*-crotononitrile are assigned to the planar (ν_{16}) and out-of-plane (ν_{23}) cyanide deformations, respectively. In the region of the internal fundamentals only the 210-cm^{-1} band is unaccounted for and this feature is assigned to the methyl torsion in the crystal. It should be emphasized that without deuterium data such an assignment must be considered tentative; however, vapor phase chromatograms showed the material to be better than 99.5% pure and repeated purification by vpc did not change the relative intensity of any of the bands. The absence of a corresponding peak in the Raman spectrum of the solid at low temperatures is further support for the assignment. The barrier to methyl torsion in solid *cis*-crotononitrile is 3108 kcal/mol; this value was calculated assuming that the microwave geometry of the gaseous molecule was applicable to the molecule in the crystal.

No references were found to crystal structural data for either crotononitrile isomer and for this reason no further work was done on the lattice frequency assignments.

Vibrational Assignment for trans-Crotononitrile. Carbon–Hydrogen Stretching Modes. The olefinic proton stretching modes may be assigned by analogy with the cis isomer. The unsymmetrical or out-of-phase mode (ν_1) is weak in the Raman and strong in the in-

(22) K. Kizer, private communication.

(23) H. Hunziker and Hs. H. Günthard, *Spectrochim. Acta*, 21, 51 (1965).

(24) R. Meyer and Hs. H. Günthard, *Spectrochim. Acta, Part A*, 23, 2341 (1967).

(25) R. Meyer, H. Hunziker, and Hs. H. Gunthard, *ibid.*, 25, 295 (1968).

(26) J. R. Durig and D. W. Wertz, *ibid.*, 24, 21 (1968).

(27) J. R. Durig, S. M. Craven, and J. Bragin, *J. Chem. Phys.*, 51, 5663 (1969).

(28) J. R. Durig, S. M. Craven, and J. Bragin, *ibid.*, 52, 2046 (1970).

(29) J. R. Durig, C. M. Player, Jr., and J. Bragin, *ibid.*, 52, 4224 (1970).

(30) J. R. Durig, S. M. Craven, and J. Bragin, *ibid.*, 53, 38 (1970).

frared and this mode must give rise to the weak feature in the Raman spectrum at 3053 cm^{-1}. The reverse is true of the symmetrical or in-phase mode (ν_2) and this vibration must give rise to the strong Raman line at 3036 cm^{-1}. As was found for the cis isomer, the antisymmetric methyl C–H stretch is not greatly split by the molecular symmetry plane. The strong Q branch of the C-type band observed in the infrared spectrum of the gas at 2965 cm^{-1} is assigned to the out-of-plane component (ν_{17}) and the A-type band at 2987 cm^{-1} is assigned to the in-plane component (ν_3). The very strong line at 2927 cm^{-1} in the Raman spectrum of *trans*-crotononitrile must be due to ν_4, the totally symmetric methyl C–H stretch.

Carbon–Hydrogen Deformation Modes. Significant differences in the vibrational spectra of the two crotononitrile isomers are expected for some of these modes. The different arrangement of the functional groups in the two isomers will considerably change the intensities and contours of the vibrational bands. The descriptions of the vibrations will also be different because of the effect of functional group arrangement on mode mixing. Finally, the near-prolate nature of the trans isomer and the large value of the A rotational constant will produce sub-band structure on the perpendicular (B and C) bands.

The HCH deformations of the methyl group are relatively independent of the nature of the rest of the molecule and the frequencies of these modes should be very nearly the same in the two crotononitrile isomers. As in the cis isomer, the antisymmetric methyl deformation is not greatly split by the molecular symmetry plane. The strong infrared absorption at 1435 cm^{-1} in the liquid must be due to the out-of-plane component (ν_{18}) and the strong polarized Raman line at 1448 cm^{-1} can be confidently assigned to the in-plane component (ν_7). The strong polarized Raman line at 1383 cm^{-1} and the A-type infrared band at 1381 cm^{-1} can only be assigned to the symmetric methyl deformation motion (ν_8). Surprisingly, the methyl rocking modes are little affected by the different functional group arrangement in the two isomers. The Q branch of the weak C-type band at 1044 cm^{-1} is assigned to ν_{19}, the out-of-plane CH_3 rocking mode. A weak A- or B-type band was observed at 1115 cm^{-1} in the infrared spectrum of the gaseous trans isomer and this absorption has been assigned to the in-plane methyl rock (ν_{11}). It is unlikely that either feature is due to an overtone since the Raman counterparts of both bands appear with appreciable intensity. Raman bands at 1146 and 1039 cm^{-1} have been assigned to the a_g (planar) and b_g (out-of-plane) methyl rocking vibrations in the spectrum of *trans*-2-butene.[14]

Only two spectral features in the region 1100–1600 cm^{-1} have not yet been assigned. The A- or B-type band at 1311 cm^{-1} and the polarized Raman counterpart at 1316 are assigned to the symmetrical (to the geometrical center of the molecule) deformation of the olefinic protons (ν_9). The A-type band at 1288 cm^{-1} and its Raman counterpart at 1299 cm^{-1} are assigned to the unsymmetrical HCCH deformation (ν_{10}). The analogous vibrations in fumaronitrile (*trans*-dicyanoethylene) have been assigned at 1297 and 1260 cm^{-1}, respectively.[18] Vibrational analysis of *trans*-2-butene[19] has supported assigning 1309 and 1304 cm^{-1} to the symmetrical and unsymmetrical olefinic deformations, respectively, in that molecule.

The unsymmetrical (to the geometric center of the molecule) out-of-plane olefinic hydrogen atom deformation has been shown to be well characterized by Potts and Nyquist[20] and to absorb strongly in the infrared near 965 cm^{-1}. Thus, the very strong C-type band at 957 cm^{-1} is assigned to ν_6. The symmetrical out-of-plane deformation of the olefinic protons (ν_{21}) is not expected to produce a significant dipole change since the dipole moment in *trans*-crotononitrile lies very nearly along the A molecular axis.[9] This mode is assigned to the very weak C-type band observed at 788 cm^{-1}. In fumaronitrile the analogous modes have been assigned at 945 (a_u) and 845 (b_g) cm^{-1}. In *trans*-2-butene these assignments are 964 (a_u) and 746 (b_g).[14,19]

Skeletal Stretching Modes. The cyanide and olefinic bond stretching frequencies (ν_5 and ν_6) were observed at 2228 and 1640 cm^{-1}, respectively, in the infrared spectrum of gaseous *trans*-crotononitrile. Two polarized Raman lines at 1030 and 902 cm^{-1} have not yet been assigned. These are the only features in the vibrational spectrum above 600 cm^{-1} which are as yet unassigned and they are accordingly attributed to the C–CH_3 (ν_{12}) and C–CN (ν_{13}) skeletal stretching motions, respectively. It should be pointed out that coupling between these normal modes is a strong possibility. In fumaronitrile both C–CN stretches are assigned at 1000 cm^{-1} [18] and in *trans*-2-butene the in-phase and out-of-phase C–CH_3 stretches have been assigned at 870 and 1065 cm^{-1}, respectively.[14,19]

Skeletal Deformation Modes. Of the six low-frequency modes in *trans*-crotononitrile no more than three can give rise to polarized Raman lines. These three modes are: the cyanide group deformation (ν_{16}), which should be the lowest Raman line observed since the methyl torsion is expected to be vanishingly weak in the Raman effect, and the in-plane cyanide and methyl group bendings, ν_{14} and ν_{15}, respectively. The planar cyanide deformation in *cis*-crotononitrile gives rise to a completely depolarized Raman line at 169 cm^{-1} and by analogy the strong line at 188 cm^{-1} in the Raman spectrum of liquid *trans*-crotononitrile is assigned to this mode. There are only three strong lines below 600 cm^{-1} in the Raman spectrum of the trans isomer. One of these has already been assigned to ν_{16}; therefore, 555 and 402 cm^{-1}, which are both polarized, must be assigned to the planar skeletal deformations ν_{14} and

ν_{15}, respectively. The weak C-type band observed at 461 cm^{-1} in the infrared spectrum of the gaseous trans isomer must be ν_{22}, the out-of-plane methyl bending. Two modes, the out-of-plane cyanide deformation (ν_{23}) and the methyl torsion (ν_{24}), were unobserved in the Raman and infrared spectra of the fluid phases of *trans*-crotononitrile. These modes have been assigned from the infrared and Raman spectra of the solid trans isomer.

The Far-Infrared and Low-Frequency Raman Spectra of Solid Trans Crotononitrile. Two types of spectra were obtained for solid *trans*-crotononitrile in the far-infrared. On annealing the sample to −100° and recooling to −196°, curve B of Figure 4 (phase I) was obtained. When the same sample was annealed to −50° and recooled to −196°, curve C of Figure 4 (phase II) was recorded. A sample in phase II at −196° could be transformed to phase I by annealing at −100°. Finally, phase I was produced by slowly cooling a sample from −50 through −100° to −196°. Thus, phase II is the stable phase from −100 to −196° but phase I is easily supercooled. In order to obtain additional confirmation of this interpretation of the solid-state far-infrared data the low-frequency Raman spectrum of the trans isomer was obtained in both phase I (Figure 5) and phase II (Figure 6). Table III summarizes the frequencies recorded for the solid crotononitriles. For the trans isomer in both phases the infrared and Raman bands may be grouped into two classes: those observed above 178 cm^{-1} and those appearing below 135 cm^{-1}. The bands in the latter group must be due entirely to lattice motions since no internal fundamentals of *trans*-crotononitrile are expected to be so low in frequency. These vibrations will not be discussed further. The high-frequency bands are entirely due to intramolecular fundamentals since no lattice modes are expected to occur so high in frequency. In *trans*-crotononitrile only the cyanide group deformations (ν_{16} and ν_{23}) and the methyl torsion (ν_{24}) are expected below 300 cm^{-1}. Because the internal rotation of the methyl group in *trans*-crotononitrile should produce little or no polarizability change this mode is not expected to appear in the Raman spectrum of the solid. Thus, the infrared band observed at 178 and 181 cm^{-1} in phases I and II, respectively, but unobserved in the Raman spectrum of the solid trans isomer is assigned to ν_{24}. The strong infrared bands observed at 200 and 205 cm^{-1} in phases I and II and the Raman bands at 198 and 197 cm^{-1} in these two phases are assigned to ν_{16}. This fundamental appears strongly in both the infrared and the Raman spectra of liquid *trans*-crotononitrile. Finally, the very weak lines at 247 and 234 cm^{-1} in the Raman spectra of phases I and II and the weak infrared band observed at 246 cm^{-1} in the spectrum of phase II are assigned to the out-of-plane cyanide deformation, ν_{23}. These assignments must be considered as tentative in the absence of data

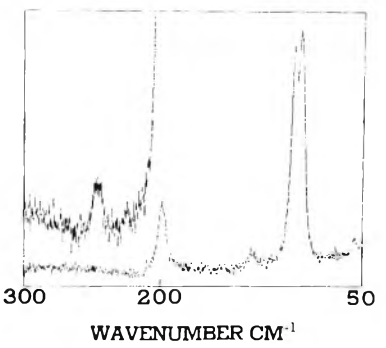

Figure 5. Low-frequency Raman spectrum of *trans*-crotononitrile in phase I.

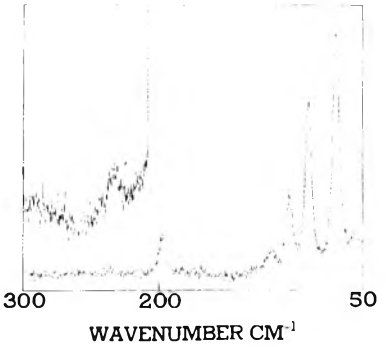

Figure 6. Low-frequency Raman spectrum of *trans*-crotononitrile in phase II.

for the deuterated molecule; however, the observed intensities and frequency shifts on condensation are as expected. For example, in the trans isomer, ν_{16} shifts 16 cm^{-1} on solidification and the corresponding shift in the cis compound is 16 cm^{-1}. Unfortunately, no direct observation of the torsional frequency in either the gaseous, liquid, or solid state has been reported for *trans*-crotononitrile. Suzuki and Kozima[9] have assigned the microwave spectrum of this molecule and they report a value of the torsional barrier in the gas phase of 1.94 ± 0.1 kcal/mol. This is equivalent to a torsional frequency of 187 cm^{-1} if one assumes, as Suzuki and Kozima did, that the methyl group moment of inertia in *trans*-crotononitrile is the same as in propylene.[31] The uncertainty in the methyl group geometry is likely to be significant[32] and could account for a 4 or 5 cm^{-1} error in the torsional frequency derived from the microwave torsional barrier. Thus, within the limits of experimental error, the torsional frequency of 181 cm^{-1} found for phase II *trans*-crotononitrile is the same as the value derived from the microwave spectrum of the gaseous molecule.

Fine Structure. Sub-band structure was observed on several C-type bands in the infrared spectrum of *trans*-crotononitrile and Figure 7 shows an expanded scale

(31) E. Hirota, *J. Chem. Phys.*, **45**, 1984 (1966).

(32) H. Dreizler and H. D. Rudolph, *Z. Naturforsch. A*, **17**, 712 (1962).

Table V: Summary of the Fundamental Vibrations[a] of *trans*- and *cis*-Crotononitrile

Fundamental				
trans	cis	Approximate description	trans	cis
		a′ Species		
1	1	HCCH unsymmetrical stretch	3060	3070
2	2	HCCH symmetrical stretch	3036[b]	3052[b]
3	3	CH_3 antisymmetric stretch	2987	2972
4	4	CH_3 symmetric stretch	2932	2922
5	5	C≡N stretch	2232	2230
6	6	C=C stretch	1640	1631
7	7	CH_3 antisymmetric deformation	1453	1450
8	9	CH_3 symmetric deformation	1381	1376
9	10	HCCH symmetrical deformation	1311	1320
10	8	HCCH unsymmetrical deformation	1288	1399
11	12	CH_3 rocking	1115	1104[b]
12	11	C—CH_3 stretch	1023	1232
13	13	C—CN stretch	896	892
14	14	C=C—CN bend	555	658
15	15	C=C—CH_3 bend	398	398[b]
16	16	C—C≡N bend	173	154
		a″ Species		
17	17	CH_3 antisymmetric stretch	2965	2952
18	18	CH_3 antisymmetric deformation	1449	1447
19	19	CH_3 rock	1044	1034
20	20	HCCH unsymmetrical bend	957	954
21	21	HCCH symmetrical bend	788	726
22	22	C=C—CH_3 bend	461	517
23	23	C—C≡N bend	246[c]	278
24	24	CH_3 torsion	181[c]	219[c]

[a] All frequencies observed in the infrared spectrum of the gas unless noted. [b] Raman spectrum of liquid. [c] Far-infrared spectrum of solid.

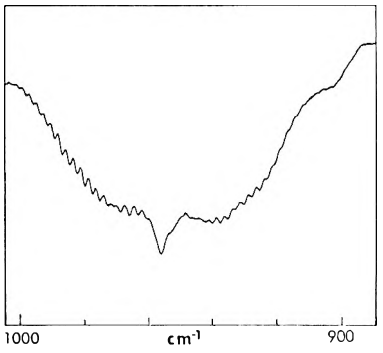

Figure 7. Expanded scale recording of the substructure on ν_{20}.

recording of the substructure on ν_{20}. A least-squares straight line with slope 2.4 ± 0.1 cm^{-1} and intercept 957.6 cm^{-1} resulted from fitting the positions of the 26 "Q" branches observed for ν_{20}. A trial fit to a second-order equation showed that the second-order coefficient was poorly determined but it was not significant for the frequency precision and low K values under consideration. The sub-band spacings were also calculated from the rigid rotor expressions[11] and the microwave rotational constants of Table IV. The average calculated spacing was 2.4 cm^{-1}.

Thermodynamic Quantities and Isomerization Equilibrium. Wyss and Günthard[4] have calculated thermodynamic quantities for *trans*-crotononitrile but they have mistakenly assigned a Raman line at 286 cm^{-1},

Table VI: Thermodynamic Functions for *cis*- and *trans*-Crotononitrile

T, °K	S	$(F - H_0)/T$	$(H - H_0)/T$	C_p
		trans-Crotononitrile		
298.16	93.625	79.740	13.885	20.726
300	93.753	79.826	13.927	20.806
400	100.321	84.141	16.180	25.026
500	106.320	87.987	18.333	28.780
600	111.859	91.513	20.347	32.004
700	117.005	94.792	22.213	34.763
800	121.803	97.874	23.929	37.132
900	126.299	100.784	25.514	39.172
1000	130.522	103.546	26.975	40.933
		cis-Crotononitrile		
298.16	94.339	80.572	13.767	20.062
300	94.463	80.657	13.806	20.140
400	100.833	84.922	15.912	24.319
500	106.681	88.696	17.985	28.144
600	112.111	92.154	19.956	31.461
700	117.183	95.368	21.815	34.299
800	121.926	98.393	23.532	36.743
900	126.378	101.255	25.122	38.845
1000	130.566	103.979	26.586	40.659

which is due to cis impurity, to the methyl torsional mode of the trans isomer. These data have, therefore, been recalculated and are presented in Table VI along with the corresponding quantities for the cis isomer.

Butler and McAlpine[33] have studied the thermal isomerization of crotononitrile and have reported the thermodynamic functions and equilibrium ratios for the reaction. The assignment of Table V and the microwave rotational constants and torsional barriers have been used to calculate these data using statistical mechanical formula. For the equilibrium cis → trans over the temperature range 300–500°, the experimental values for ΔH and ΔS are 0.17 ± 0.12 kcal/mol and −0.39 ± 0.19 cal/mol °K. The corresponding statistical values are 0.259 kcal/mol and −0.211 cal/mol °K. The experimental cis/trans ratio in the same temperature range is 1.39 and the statistical value is 1.38.

Butler and McAlpine point out that *cis*-crotononitrile is more stable than *trans*-crotononitrile and that in this respect crotononitrile is similar to difluoro[34] and dichloroethylene.[35,36] However, for the dihaloethylenes the stability of the cis isomer results from a large positive value of ΔH, whereas for crotononitrile the stability of the cis isomer is due to the negative value of ΔS which arises from the low torsional barrier in this molecule. This in turn may be attributed to the interaction between the in-plane methyl C–H bond, which eclipses the C=C bond, and the cyanide group as has been suggested by several authors.[10,33] A similar situation exists in the 2-butenes and has been suggested as the determining factor of the equilibrium ratio of the isomers in those compounds.[37,38]

Conclusions

All the vibrational fundamentals of *cis*- and *trans*-crotononitrile have been observed and a tentative description of the normal modes of vibration has been proposed for both isomers. The frequencies of the methyl torsional vibrations have been directly observed for the first time in the crystals and the barriers to methyl group rotation in the solid have been calculated. Sub-band structure has been resolved in the spectrum of the trans isomer and the observed spacing is in excellent agreement with the value calculated from previously known rotational constants and the expressions for the rigid-rotor energy levels. Statistical thermodynamic data have been calculated for both isomers and the statistical equilibrium ratio for the isomerization is in excellent agreement with the value found by experiment.

Acknowledgment. The authors gratefully acknowledge the financial support given this work by the National Science Foundation by Grant GP-20723.

(33) J. N. Butler and R. D. McAlpine, *Can. J. Chem.*, **41**, 2487 (1963).

(34) N. C. Craig and E. A. Entemann, *J. Amer. Chem. Soc.*, **83**, 3047 (1961).

(35) R. E. Wood and D. P. Stevenson, *ibid.*, **56**, 1320 (1934).

(36) A. R. Olson and W. Maroney, *ibid.*, **56**, 1320 (1934).

(37) S. Kondo, Y. Sakurai, E. Hirota, and Y. Morino, *J. Mol. Spectrosc.*, **34**, 231 (1970).

(38) R. B. Scott, W. J. Ferguson, and F. G. Brickwedde, *J. Res. Nat. Bur. Stand.*, **33**, 1 (1944).

Spectroscopic Studies of Ionic Solvation. VIII. Alkali Metal Salts in Acetone Solutions

by Ming Keong Wong, William J. McKinney, and Alexander I. Popov*[1]

Department of Chemistry, Michigan State University, East Lansing, Michigan 48823 *(Received August 13, 1970)*

Publication costs assisted by the National Science Foundation

Infrared and proton nmr studies were carried out on solutions of lithium and sodium salts as well as on potassium thiocyanate in acetone and in acetone–nitromethane solutions. Cation–acetone vibrational bands were identified at 425 ± 3 cm^{-1} for Li^+, 195 ± 4 cm^{-1} for Na^+, and 148 ± 5 cm^{-1} for K^+. The dependence of these frequencies on isotopic substitution of the solvent (d_6-acetone) and of the solute (^6Li) indicate that the observed vibrations clearly involve both the cation and the solvent. The observed frequencies showed anion dependence in the case of LiCl and LiBr which indicates that the respective halide ions participate in the observed vibration. Both the infrared and the nmr measurements indicate that the solvation number of the lithium ion is 4 in acetone solutions and in acetone–nitromethane solutions as long as the acetone/Li^+ mole ratio is ≥ 4. Below this value the anions penetrate into the solvation shell of the cation.

Introduction

During the past few years it became evident that both the far-infrared and the nuclear magnetic resonance techniques can be very useful in the elucidation of the structure of electrolyte solutions.[2-5] In the far-infrared measurements of alkali metal, ammonium, or tetraalkylammonium salts, a band was observed which could not be assigned to the solvent or the solute and whose frequency was dependent on the mass of the cation. In polar solvents such as dimethyl sulfoxide[4a-c] and 1-methyl-2-pyrrolidone[4d-e] or in solvents with strong donor ability, such as pyridine,[4f] the frequency of the band, with very few exceptions, was independent of the nature or the mass of the anion. In nonpolar solvents, such as benzene[2] and tetrahydrofuran,[3] the band frequencies were anion dependent. It has been postulated that in the first case the bands were due to the vibration of the cation in the solvent cage, while in the latter, the bands were probably due to the vibration of an unsolvated ion pair or to cation vibrating in a cage which contains the anion of the salt.

This work was undertaken to study the solvation of the alkali metal ions in acetone solutions. In general, acetone is a solvent with intermediate solvating power. It has a dielectric constant of 20.76 at 25°[6] and has medium donor strength.[7] Preliminary investigation indicated that many of the common lithium salts and some of the sodium salts were reasonably soluble in acetone and that the solvent has reasonable transparency in the far-infrared region.

Experimental Section

Reagents. Reagent grade acetone was refluxed over anhydrous calcium sulfate and then fractionally distilled through a 100-cm helices-packed column. The water content of the purified product, as determined by the Karl Fisher titration, was <0.01%.

Nitromethane was purified by percolation through a 20-cm column of Dowex 50W-X8 cation-exchange resin. The eluent was dried over $CaSO_4$ and then fractionally distilled.

The ^6Li compounds were prepared by previously described methods.[4e] Lithium thiocyanate was purified by recrystallization from anhydrous ether and drying.[8] Lithium tetraphenylborate was prepared by the method of Bhattacharyya, *et al.*[9]

All other alkali metal salts were of analytical reagent grade and were used without further purification except for drying.

Spectral Measurements. Infrared spectra in the 4000–600-cm^{-1} region were obtained on a Perkin-Elmer Model 225 spectrometer, while spectra in the 600–80-cm^{-1} region were obtained with a Perkin-Elmer Model 301 spectrometer. Standard demountable cells with KBr windows were used from 4000 to 600 cm^{-1} and poly-

(1) To whom correspondence should be addressed.

(2) J. C. Evans and G. Y. S. Lo, *J. Phys. Chem.*, **69**, 3223 (1965).

(3) (a) W. F. Edgell, A. T. Watts, J. Lyford, and W. Risen, *J. Amer. Chem. Soc.*, **88**, 1815 (1966); (b) W. F. Edgell, J. Lyford, R. Wright, W. Risen, and A. Watts, *ibid.*, **92**, 2240 (1970).

(4) (a) B. W. Maxey and A. I. Popov, *ibid.*, **89**, 2230 (1967); (b) *ibid.*, **90**, 4470 (1968); (c) *ibid.*, **91**, 20 (1969); (d) J. L. Wuepper and A. I. Popov, *ibid.*, **91**, 4352 (1969); (e) *ibid.*, **92**, 1493 (1970); (f) W. J. McKinney and A. I. Popov, *J. Phys. Chem.*, **74**, 535 (1970).

(5) M. J. French and J. L. Wood, *J. Chem. Phys.*, **49**, 2358 (1968).

(6) National Bureau of Standards Circular 514, U. S. Government Printing Office, Washington, D.C., 1951.

(7) V. Gutmann, "Principles of Coordination Chemistry in Nonaqueous Solutions," Springer-Verlag, Vienna, 1968, p 19.

(8) D. A. Lee, *Inorg. Chem.*, **3**, 289 (1964).

(9) D. N. Bhattacharyya, C. L. Lee, J. Smid, and M. Szwarc, *J. Phys. Chem.*, **69**, 608 (1965).

ethylene cells with 0.1- or 0.2-mm path lengths, purchased from Barnes Engineering Co., were used below 600 cm^{-1}.

Raman spectra were obtained using a Spectra-Physics 700 Raman Spectrometer, with a 6328-Å He–Ne laser.

Nuclear magnetic resonance measurements were performed on a Varian A-56/60D spectrometer. Tetramethylsilane was used as an internal standard for all measurements.

Results and Discussion

Far-Ir and Raman Spectra. The frequencies of the far-infrared bands of lithium, sodium, and potassium salts are shown in Table I. In the latter case only the thiocyanate was found to be sufficiently soluble (~0.7 *M*) to yield observable spectra. For lithium and sodium salts the concentration ranged between 0.1 and 3 *M*. The intensities of the observed bands were proportional to the concentrations. Solubilities of most of the more common ammonium, rubidium, and cesium salts in acetone were too low to allow infrared spectral measurements.

Table I: Absorption Bands of Alkali Metal Salts in Acetone

Salt	ν_{max}, cm^{-1}	Acetone-d_3	ν_{max}, cm^{-1}
$LiClO_4$	425 ± 3	LiBr	372 ± 4
LiSCN	425	LiI	389
$LiBPh_4$	424	$LiNO_3$	389
$LiNO_3$	420	$LiClO_4$	388
LiCl	409	$LiBPh_4$	390
LiBr	412	$NaClO_4$	191 ± 5
LiI	423	$NaBPh_4$	190
NaSCN	196 ± 4	NaSCN	192
$NaClO_4$	195	NaI	186
$NaBPh_4$	196		
NaI	192		
KSCN	148 ± 5		
$^6LiClO_4$	435 ± 4		
$^6LiNO_3$	434		
^6LiCl	412		
^6LiBr	420		
^6LiI	436		

It is seen from the data that for lithium salts with polyatomic anions as well as for the iodide, the band frequencies are independent of the anion. There is, however, a decrease in the frequency of the observed band for the bromide and the chloride. It seems reasonable to assume that in these cases some ion pair formation may take place especially since the two halide ions may form ion pairs more easily than the bulkier polyatomic anions.

Solutions of four sodium salts all give bands whose frequencies are the same within experimental error. The only potassium salt measured gave a band at ~150 cm^{-1}. In general, the bands of the three cations occur at about the same frequencies as in dimethyl sulfoxide solutions.[4c] The intensities of the bands were linearly proportional to the salt concentrations.

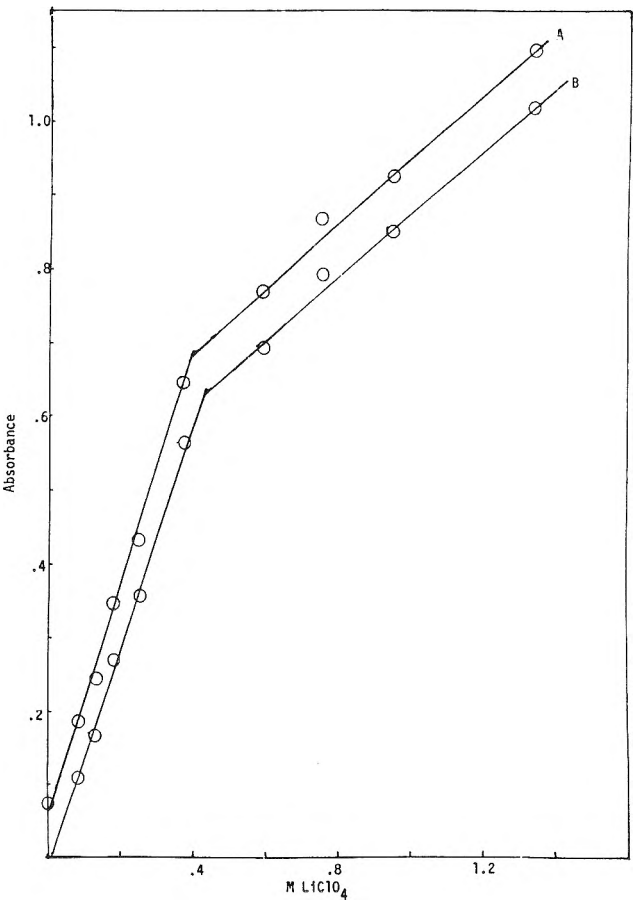

Figure 1. Absorbance of 425-cm^{-1} band *vs.* concentration of $LiClO_4$: concentration of acetone = 1.5 *M*; solvent: nitromethane; A, without subtraction of base line; B, with the base line subtracted.

The intensity of the 425-cm^{-1} band was also measured as a function of lithium perchlorate concentration in nitromethane solutions which were 1.5 *M* in acetone. A typical Beer's law plot was obtained for solutions which were $\leq$0.4 *M* $LiClO_4$ (Figure 1). At higher concentrations, while the plot was still linear, the slope was considerably different. At the same time, while the frequency of the band is not changed appreciably, the band begins to broaden. The broadening may indicate that a new absorption band is formed whose frequency does not differ appreciably from that of the original band. The data, therefore, indicate that below 4:1 mole ratio of acetone/Li^-, a new absorbing species is formed. The change in absorbance and the band broadening may be due to a change in the solvation number of the Li^+ ion or to a replacement of either one or more acetone molecules in the solvation shell by the ClO_4^- ion (see below).

Raman spectra in the 3000–150-cm^{-1} spectral region were obtained of the lithium nitrate, bromide, and per-

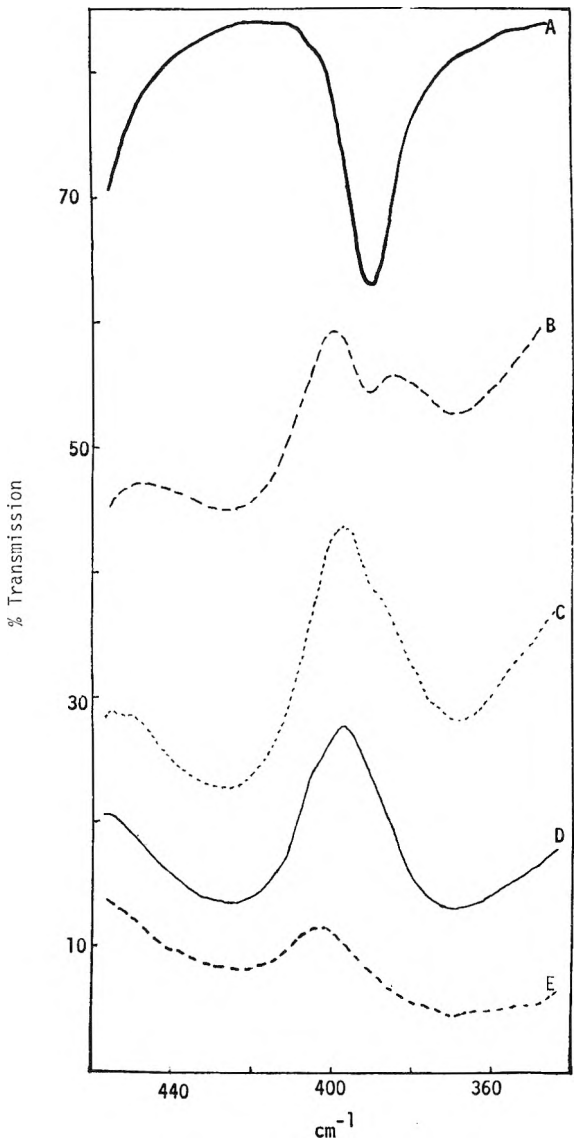

Figure 2. Spectra of solutions of acetone + $LiClO_4$ in nitromethane. The 425- and 390-cm^{-1} bands: A, blank = 1.5 *M* acetone; B, acetone/$LiClO_4$ ratio = 8:1; C, acetone/$LiClO_4$ ratio = 4:1; D, acetone/$LiClO_4$ ratio = 2:1; E, acetone/$LiClO_4$ ratio ≈ 1:1.

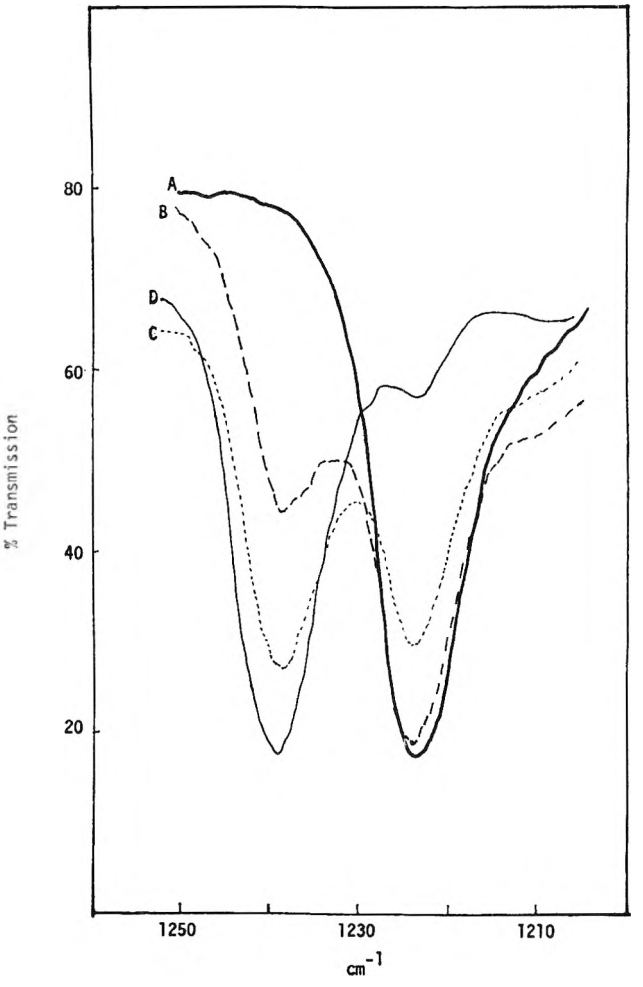

Figure 3. Spectra of solutions of acetone + $LiClO_4$ in nitromethane. The 1224-cm^{-1} acetone band: A, blank = 1.5 *M* acetone; B, acetone/$LiClO_4$ ratio = 10:1; C, acetone/$LiClO_4$ ratio = 4:1; D, acetone/$LiClO_4$ ratio = 1.7:1.

chlorate and of sodium perchlorate solutions in acetone and in acetone–nitromethane mixtures in the 0.6–3.0 *M* concentration range. The 425-cm^{-1} Li^+–acetone and 195-cm^{-1} Na^+–acetone bands were not observed. It seems that the bands are Raman-inactive and, therefore, the cation–solvent bonding is essentially electrostatic as postulated by Edgell, *et al.*[3b]

Studies of Acetone Vibrations. There are a number of reports in the literature discussing the influence of metal salts on the vibrational spectrum of acetone, some of which are cited below.[10–15] These studies were carried out in the 3000–400-cm^{-1} range and all measurements were made in pure acetone as solvent.

In this study we wished to observe the behavior of the acetone vibrations as a function of acetone–Li^+ mole ratio. It was necessary, therefore, to use an inert solvent as diluent. The difficulties of selecting inert solvents have been discussed in a previous publication.[4d] In the present case it was found possible to use nitromethane as the diluent. While it cannot be stated that nitromethane is devoid of all solvating ability, the relative inertness is well known[7] and it is quite unlikely that it can compete with acetone in the solvation of lithium ions.

A series of nitromethane solutions were prepared

(10) A. D. E. Pullin and J. McC. Pollock, *Trans. Faraday Soc.*, **54**, 11 (1958).

(11) (a) H. Yamada, *Bull. Chem. Soc. Jap.*, **33**, 666 (1960); (b) *ibid.*, **33**, 780 (1960).

(12) (a) S. Minc, Z. Kecki, and T. Gulik-Krzywicki, *Spectrochim. Acta*, **19**, 353 (1963); (b) T. Gulik-Krzywicki and Z. Kecki, *Rocz. Chem.*, **39**, 1281 (1965).

(13) I. S. Perelygin, *Opt. Spektrosk.*, **16**, 40 (1964).

(14) A. Z. Gadzhiev and I. S. Pominov, *Zh. Neorgan. Khim.*, **10**, 1490 (1965).

(15) W. L. Driessen and W. L. Groeneveld, *Recl. Trav. Chim. Pays-Bas*, **88**, 977 (1969).

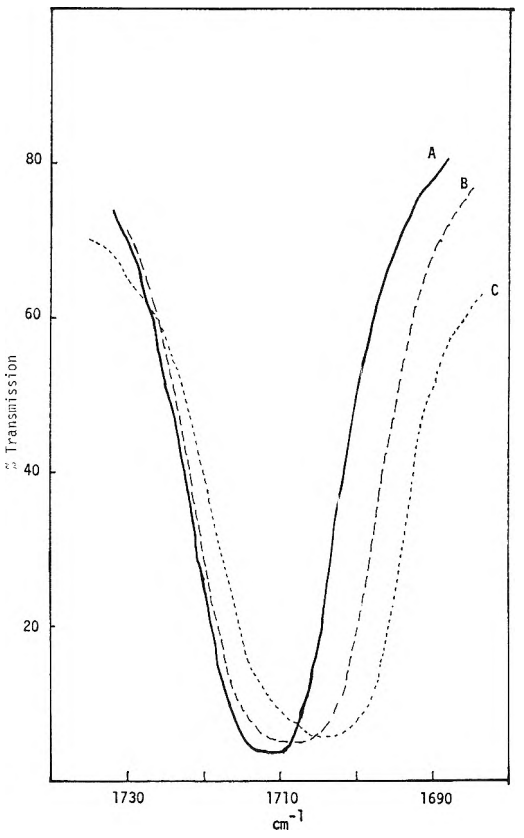

Figure 4. Spectra of solutions of acetone + $LiClO_4$ in nitromethane. The 1712-cm^{-1} acetone band: A, blank = 1.5 *M* acetone; B, acetone/$LiClO_4$ ratio = 10:1; C, acetone/$LiClO_4$ ratio = 4:1.

1.50 *M* in acetone and containing varying amounts of lithium perchlorate. The changes in the frequencies of four strong acetone vibrational bands at 390, 528, 1224, and 1712 cm^{-1} were followed as a function of acetone–$LiClO_4$ mole ratio.

The 390- (C–C–C deformation), 528- (C–C–O bending) and 1224-cm^{-1} (C–C asymmetric stretch) bands were split, with new bands appearing at 369, 539 and 1239 cm^{-1}. These new bands can be attributed to vibrations of the complexed acetone. The relative intensities of the various bands as a function of acetone–$LiClO_4$ mole ratios are shown in Figures 2 and 3. No split was observed for the 1712-cm^{-1} C=O stretch, but the band was shifted to lower wave number with decreasing acetone–$LiClO_4$ mole ratio, as shown in Figure 4.

Similar shifting and splitting of the acetone fundamental frequencies were observed with LiI, indicating that Li^+ is the species that interacts with acetone.

The intensity of the 390-cm^{-1} acetone band decreases gradually with decreasing acetone/$LiClO_4$ mole ratio, and a new band at 369 ± 3 cm^{-1} appears. This new band, in contrast to the 1239- and 539-cm^{-1} acetone bands, was observed to be dependent on the nature of the cation. When $^6LiClO_4$ was substituted for $^7LiClO_4$, the 390-cm^{-1} acetone band was shifted gradually (no apparent splitting was observed) to lower frequency as the acetone–Li^+ mole ratio was decreased. The band appeared to reach a limiting value of 380 ± 3 cm^{-1} at acetone/$^6LiClO_4$ mole ratio of 4:1.

Effects of Anion. The anion dependence of some of the solvation bands, notably for the lithium halides, seems to indicate that at least in the system studied, the halides may form a part of the solvation sphere. Recent electrical conductance studies,[16] indicate that lithium chloride forms unsolvated contact ion pairs, while with lithium iodide the ion pair was said to be formed from fully solvated ions. Lithium bromide represents an intermediate case. The observed frequencies of the solvation bands for those halides are consistent with the above explanation. The frequency of the LiI solvation band is identical with that of $LiClO_4$, LiSCN, and $LiBPh_4$ indicating that the vibration must be that of the cations in the solvent cage. The band shifts to progressively lower frequencies as the iodide ion is replaced first by the bromide and then by the chloride ions. Thus, if our model is correct, the bromide and the chloride ions can successfully compete with acetone molecules for the position in the solvent cage even when the concentration of acetone is relatively high as compared with that of Cl^- or Br^-.

The fact that the Cl^- and Br^- ions have a strong affinity for the cation is further demonstrated by the following studies. The position and the intensity of the solvation band in 0.5 *M* $LiClO_4$ solutions was measured as a function of the concentration of added salts, Bu_4NClO_4, Bu_4NI, and Bu_4NBr. The band remained practically unchanged upon the addition of 0.4 *M* Bu_4NClO_4 or 0.4 *M* Bu_4NI. However, with the addition of Bu_4NBr, the band shifted progressively from 424 to 412, and the 369-cm^{-1} band also shifted to 358 cm^{-1}. The data are given in Table II. Similar results were obtained with lithium iodide as the solute. Acetone solutions of the various tetrabutylammonium salt did not show any new bands in the measured spectral region. It seems from the above data that the 369-cm^{-1} band is also associated with the cation–solvent vibration.

Table II: The Shifting of the 424- and 369-cm^{-1} Bands

Concn $LiClO_4$, *M*	Concn Bu_4NBr, *M*	Frequency	
0.54	0.00	424 ± 3 cm^{-1}	369 ± 4 cm^{-1}
0.53	0.12	420	368
0.53	0.23	418	368
0.53	0.37	415	364
0.52	0.55	413	362
0.53	0.87	412	358
0.00	0.30	..	..

(16) L. G. Savedoff, *J. Amer. Chem. Soc.*, **88**, 664 (1966).

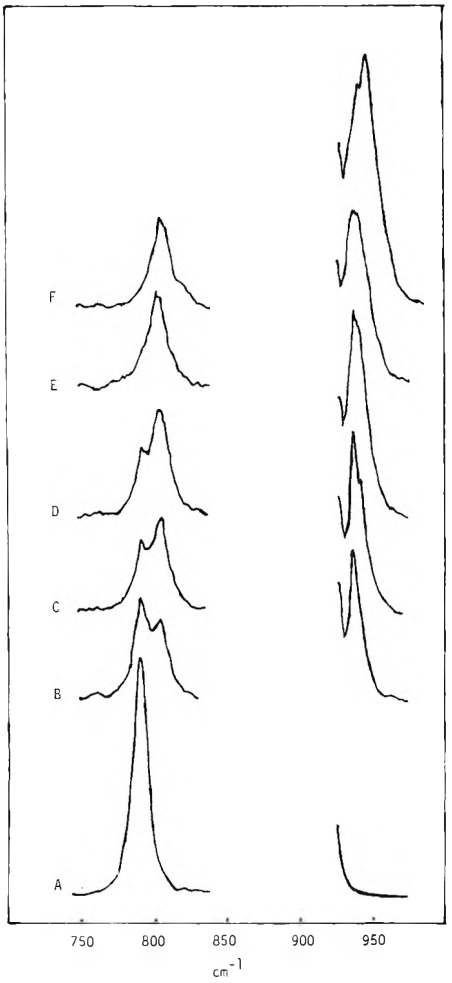

Figure 5. The 789-cm^{-1} acetone and the 935-cm^{-1} ClO_4^- Raman bands: A, 3.5 *M* acetone in nitromethane; B, acetone/$LiClO_4$ ratio = 6:1; C, acetone/$LiClO_4$ ratio = 4:1; D, acetone/$LiClO_4$ ratio = 3:1; E, acetone/$LiClO_4$ ratio = 2:1; F, acetone/$LiClO_4$ ratio = ~1:1; band intensity semiquantitative.

Symmetrical polyatomic anions, such as ClO_4^-, have little tendency to form contact ion pairs in the presence of sufficient amounts of a solvating solvent. The Raman band of ClO_4^- at 935 cm^{-1} remains unchanged when the acetone/$LiClO_4$ mole ratio is ≥ 4. Below this value, however, the band progressively broadens and shifts to higher frequency. These data offer additional evidence that the solvation number of Li^+ is four and where the system does not contain enough acetone to maintain the solvation shell, the deficiency is made up by the perchlorate ion which then forms a contact ion pair with the cation. The results are shown in Figure 5. It is seen from the figure that parallel with the change in the perchlorate band, there is a change in the appearance of the 789-cm^{-1} Raman band of acetone. As the concentration of lithium is increased, a new band appears at 803 cm^{-1} representing the acetone molecule bound to the lithium ion.

Nmr Mole Ratio Studies. In order to further establish the stoichiometry of the solvated species, mole ratio studies on the acetone–Li^+ system were carried out using proton nmr spectra.[17] Again nitromethane was used as the inert solvent, and the position of the methyl proton resonance of acetone was followed as a function of the acetone–Li^+ ratio. Four studies were performed. In the first study, the acetone concentration was kept constant at 1.5 *M* and the concentration of $LiClO_4$ was varied. The results, shown in Figure 6, show that there is a definite break at acetone to salt

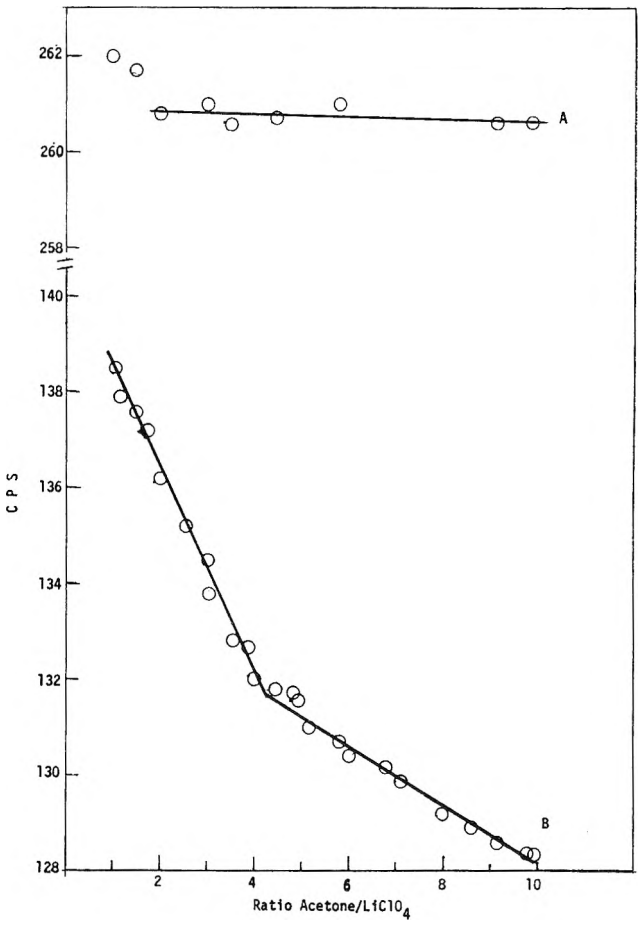

Figure 6. Chemical shifts of the methyl protons of acetone and nitromethane *vs.* acetone/$LiClO_4$ mole ratio: concentration of acetone = 1.5 *M*; concentration of $LiClO_4$ varied; solvent: nitromethane; A, nitromethane; B, acetone.

ratio of 4.3. The position of the methyl proton resonance of nitromethane remains practically unchanged down to about 1:1 mole ratio. In the second study, the $LiClO_4$ concentration was kept constant at 0.5 *M* and the concentration of acetone was varied. Again a break at acetone/$LiClO_4$ mole ratio of 4.4:1 was observed. Two other studies were carried out using LiI instead of $LiClO_4$. Similar breaks at acetone/LiI

(17) E. Schaschel and M. C. Day, *J. Amer. Chem. Soc.*, 90, 503 (1968).

mole ratio of 4.4:1 and 4.5:1 were obtained. The results indicate that Li^+ is solvated by four molecules of acetone.

Acknowledgment. The authors gratefully acknowledge the support of this work by a grant from the National Science Foundation.

Application of the Polanyi Adsorption Potential Theory to Adsorption from Solution on Activated Carbon. II. Adsorption of Partially Miscible Organic Liquids from Water Solution[1,2]

by David A. Wohleber and Milton Manes*[3]

Chemistry Department, Kent State University, Kent, Ohio 44240 *(Received June 25, 1970)*

Publication costs assisted by Pittsburgh Activated Carbon Division, Calgon, Corporation

A method is presented for estimating the adsorption isotherm of a partially miscible organic liquid, from water solution onto an activated carbon, from its solubility, molar volume, and refractive index, together with a "characteristic curve" for the carbon that may in turn be determined from either gas-phase or liquid-phase adsorption data. The method, which is based on the Polanyi adsorption potential theory, and which is applicable over a wide range of capacities, is illustrated by estimated gas-phase and experimental liquid-phase data on 1,2-dichloroethane, diethyl ether, ethyl acetate, methylene chloride, and propionitrile.

Introduction

The Polanyi adsorption potential theory has been applied by Hansen and Fackler[4] to the adsorption of liquid mixtures on carbon black, and by Manes and Hofer[5] to the adsorption of solids from various solvents on activated carbon. The expected relation between gas- and liquid-phase adsorption was found by Manes and Hofer at low loadings; however, solute adsorption at high loadings did not fit their gas-phase correlation curve, presumably because of packing effects. A better fit should be expected if the adsorbate is a liquid, *i.e.*, in the adsorption of relatively strongly adsorbed solvent. A good example is the adsorption of partially miscible organic liquids from water.

The principal experimental problem was in the determination of solute concentrations at low loadings on the adsorbent (down to 0.1 wt %), where the bulk phase concentrations of most organic liquids become undetectably low. This problem was met by limiting the investigation to solutes of low molecular weight and significant solubility and by the use of a gas chromatograph with a flame ionization detector to analyze concentrations down to the parts-per-million range.

The investigation consisted of the determination of the solubilities in water solution and the adsorption isotherms at 25° from water solution of 1,2-dichloroethane, diethyl ether, ethyl acetate, methylene chloride, and propionitrile on the same activated carbon that was used by Manes and Hofer. A gas-phase correlation curve [*i.e.*, a plot of the volume adsorbed *vs.* the adsorption potential per unit volume, (ϵ/V)] was calculated for each solute, using the hydrocarbon correlation curve reported for this carbon by Manes and Hofer.

Theoretical. The underlying theory, which is given in more detail by Manes and Hofer, may be summarized as follows.

For gas-phase adsorption on a given carbon, a plot of the adsorbate volume against the adsorption potential per unit volume ($\alpha = \epsilon/V$) is approximately the same in a series of similar compounds (*e.g.*, the hydrocarbon series). Compounds of different refractive index give the same plot (correlation curve) except for the scale of the abscissa. The gas-phase characteristic curve for the vapor of a liquid of given refractive index

(1) Based on a thesis submitted by David A. Wohleber to Kent State University in partial fulfillment of the requirements for the Ph.D. degree.

(2) Reference 5 may now be considered as the first article in the series.

(3) To whom inquiries should be directed.

(4) R. S. Hansen and W. V. Fackler, *J. Phys. Chem.*, **57**, 634 (1953).

(5) M. Manes and L. J. E. Hofer, *ibid.*, **73**, 584 (1969).

may be made to coincide with the hydrocarbon correlation curve by the operation

$$\gamma_s \equiv \frac{\alpha_s}{\alpha_h} = \frac{p_s}{p_h} \quad (1)$$

where α_s and α_h are the respective adsorption potentials per unit volume of the solute and of the hydrocarbon line at the same adsorbate volume; p_i is defined as

$$p_i = \frac{n_i^2 - 1}{n_i^2 + 2} \quad (2)$$

where n_i is the refractive index of component i, and where s and h refer to solute and heptane; it is proportional to the polarizability per unit volume.

Equation 1 is a good approximation for most organic vapors, but it breaks down badly for water, for which ϵ/V is considerably lower (as we shall see, by a factor of about 3) than one would calculate from its refractive index. (It is this anomalously low adsorption potential per unit volume that accounts for the strong adsorption of organic solutes from water.) We cannot, therefore, use eq 1 to estimate the gas-phase correlation curve for water.

In the liquid-phase adsorption of a solute from a relatively weakly adsorbed solvent, a plot of the adsorbate volume against ϵ_{sl}/V (where ϵ_{sl} is RT ln c_s/c and c_s and c are the saturation and equilibrium concentrations) should be the same as the hydrocarbon correlation line, except that the scale factor γ_{sl} is now given by

$$\gamma_{sl} = \gamma_s - \gamma_l = \frac{p_s - p_l}{p_h} \quad (3)$$

As noted earlier, the last equality in eq 3 does not apply to the adsorption from water. However, given the estimated correlation curve for the adsorption of the organic vapor and the experimental correlation curve for the adsorption of the organic liquid from water, one might expect to estimate γ_l as the difference between γ_s for the solute and γ_{sl} for adsorption from water. Given an empirical correlation curve for water, we should now be able to predict the adsorption from water of a wide range of organic liquids. This has been borne out by the data.

An essential feature of the adsorption potential theory is that the definitions of adsorbate volume in gas-phase and in liquid-phase adsorption are quite similar, namely the volumes between the solid–adsorbate interface and either the adsorbate–gas or the adsorbate–solution interface. Just as the calculation of the adsorbate volume in gas-phase adsorption is somewhat complicated at elevated pressures[6] but quite straightforward at low pressures, the similar calculation in adsorption from the aqueous phase becomes quite simple if one can assume that the adsorbate has the properties of the bulk liquid and if the equilibrium solution is relatively dilute; both assumptions are reasonable for the present case. If carbon is added to V_0 ml of solution at concentration c_0 (in g/ml) of organic solute, and if V ml of neat liquid is adsorbed (*i.e.*, the adsorption volume is V ml) then, assuming volume additivity, the aqueous phase at equilibrium, at concentration c, occupies $(V_0 - V)$ ml. If we equate the total masses of the organic component before and after adsorption we get

$$c_0V_0 = c(V_0 - V) + \rho V \quad (4)$$

or

$$V = \frac{V_0(c_0 - c)}{\rho - c} \quad (5)$$

where ρ is the density of the adsorbed liquid. For dilute solution and even up to saturation for liquids of low solubility we can neglect c in the denominator.

Experimental Section

Isotherms for the adsorption of 1,2-dichloroethane, diethyl ether, ethyl acetate, methylene chloride, and propionitrile from water onto activated carbon were determined at 25°. The solutes had a minimum purity of 99.5%, as determined by gas chromatography. As noted earlier, the adsorbent was the same as was used by Manes and Hofer, and came from a single batch of Pittsburgh Activated Carbon grade CAL activated carbon. Except for drying at 110° for 16 hr before weighing, the carbon was used as received. The surface area (BET) was 1140 m^2/g.

The solute, solvent, and carbon were shaken in 125-ml screw-capped erlenmeyer flasks, in a bath thermostated at 25°, until equilibration was achieved. Check experiments showed that 16 hr shaking sufficed for equilibration. After equilibration, the flasks were allowed to stand in the thermostated bath until the carbon had settled out, and a portion of the supernatant was removed and analyzed. The concentration of the solute was determined by gas chromatography (gc) using an internal standard technique. Poropak Q®, a cross-linked polystyrene, was used as the stationary phase. A 6 ft × 1/4 in. o.d. column of this material operated at 180° and 40 cc/min carrier gas flow rate resolved the organic solute from water for sample sizes less than 25 μl. By using dual flame ionization detectors, concentrations of organic solutes as low as 10 ppm could be accurately determined in this size sample. Lower concentrations could be determined by first extracting a portion of the supernatant with toluene[7] and chromatographing the toluene extract. Concentrations in the range of 0.05–0.1 ppm were determined with a sample size of 100 μl.

(6) R. J. Grant, M. Manes, and S. B. Smith, *A.I.Ch.E. J.*, 8 [3], 403 (1962).

(7) More volatile impurities (notably benzene) were removed from the toluene by distillation at a reflux ratio of 60:1 or greater.

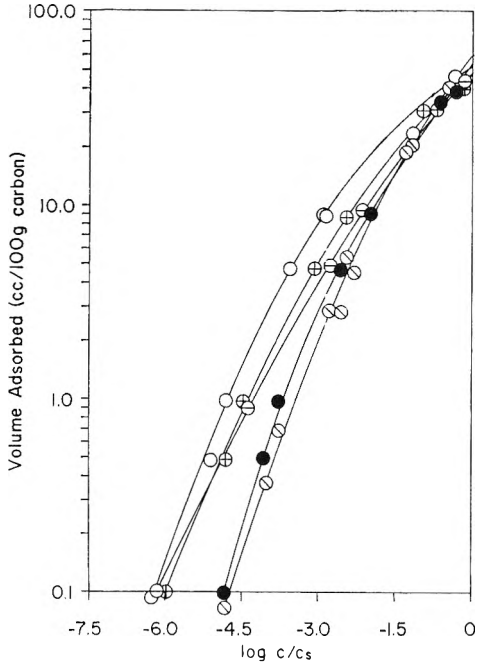

Figure 1. Adsorption isotherms for 1,2-dichloroethane (⊖), diethyl ether (⊕), ethyl acetate (○), methylene chloride (●), and propionitrile (⊘); plotted as volume adsorbed *vs.* log relative concentration. Temperature is 25°.

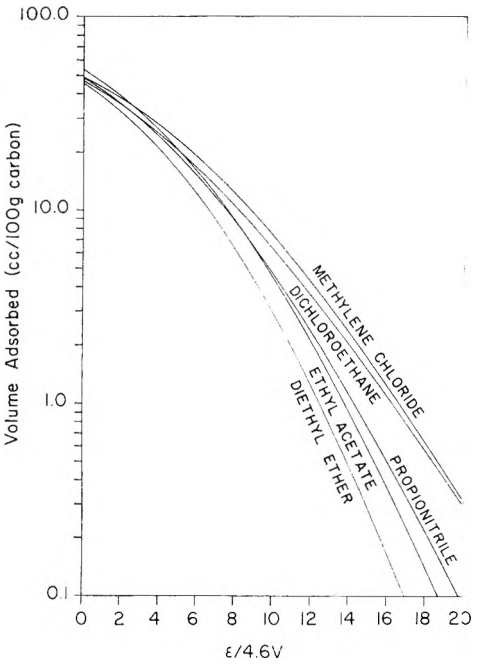

Figure 2. Volume of 1,2-dichloroethane, diethyl ether ethyl acetate, methylene chloride, and propionitrile plotted as a function of adsorption potential.

The solubilities of the solutes at 25° were determined by equilibrating water with excess solute and determining the concentration of the solute in the aqueous phase by gc.

The molar volume of each adsorbate in the adsorbed phase was assumed to be equal to the molar volume of bulk liquid at 25°.

Data and Results

Figure 1 gives the 25° adsorption isotherms of 1,2-dichloroethane, diethyl ether, ethyl acetate, methylene chloride, and propionitrile, from water, onto CAL carbon. The solubilities of the organic solutes (in g/100 g of water) at 25° are: 1,2-dichloroethane, 0.99; diethyl ether, 2.50; ethyl acetate, 8.88; methylene chloride, 1.60; and propionitrile, 10.50. Correlation curves for the liquid-phase adsorption of the five solutes were calculated by taking points at equal intervals from the corresponding isotherms. Figure 2 shows these curves, plotted as cc solute adsorbed per 100 g of carbon *vs.* $\epsilon/4.6V$, following the notation of earlier publications.

For each solute the value of γ_{sl} was determined as noted earlier, *i.e.*, by plotting the volume adsorbed *vs.* ϵ/V and comparing the resulting curve with the hydrocarbon correlation curve. Equation 3 was then used to determine γ_l for water, p_s being determined from eq 2. According to theory, the same value of γ_l should be found for each of the five systems, and the data in Table I show that this is the case. The gas-phase correlation curve for water, calculated from the average value of γ_l for the five systems, is shown in Figure 3. Also shown is the correlation curve calculated from the vapor-phase adsorption isotherm of water on the same carbon. The agreement between the two curves is a measure of the accuracy of the results reported here. The expected parallel between gas- and liquid-phase adsorption is better shown by partially miscible liquids than by solids.

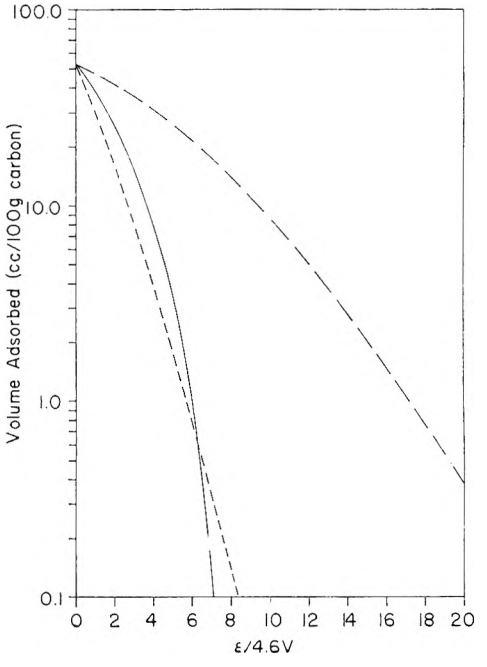

Figure 3. Correlation curves for water: ——, calculated from adsorption isotherm; - - - -, calculated from $\gamma_l = 0.28$; — — —, calculated from refractive index.

Table I: γ Values for Solutes and Water

Compd	γ_s	γ_{sl}	γ_l
1,2-Dichloroethane	1.12	0.80	0.32
Diethyl ether	0.91	0.62	0.29
Ethyl acetate	0.96	0.69	0.27
Methylene chloride	1.08	0.83	0.25
Propionitrile	0.95	0.70	0.25
		Av	0.28

Discussion

The reported results appear to be the first application of the Polanyi adsorption potential theory to the adsorption of partially miscible liquids. For all five systems the upper limit of adsorption was in excellent agreement with that found in gas-phase adsorption and is significantly greater than found for adsorption of solids on the same adsorbent. This is what one would expect if one assumes with Polanyi that adsorption from the gas phase is enhanced liquefaction.

In addition to confirming the Polanyi adsorption potential theory of liquid-phase adsorption, and thereby providing a method for estimating adsorption isotherms of partially miscible liquids from water solution, the reported results provide an improved method for the determination of the characteristic (or correlation) curve for an activated carbon. The reported data may be considered, for example, as five individual determinations of the characteristic curve over the entire loading range and at a single temperature. This may be compared with the determinations of the characteristic curve from gas-phase adsorption, which can be done with a single gas only with considerable experimental difficulty and/or a long extrapolation of vapor pressures. For these reasons, for example, the gas-phase correlation curves reported by Grant, Manes, and Smith[6] and by Grant and Manes[8] are all composite curves comprising segments determined for different hydrocarbon gases. Although there was overlapping of points in their reported characteristic curves, the data at low loadings were measured only for methane. The results reported here, therefore, represent an improved method both in range and in experimental convenience for determining the characteristic curve for a carbon. Gas-phase and liquid-phase data thereby become largely interchangeable.

Finally, while it is possible that polar organic compounds in the vapor phase might show some specific interactions with inorganic impurities or oxygenated complexes on the carbon surface, one would expect such effects to be swamped out in water solution. Water may therefore turn out to be a surprisingly convenient solvent for adsorption on activated carbon in spite of its own rather anomalous adsorption.

Conclusions

1. The characteristic curves (and therefore the adsorption isotherms) of some partially miscible organic solutes from water solution have been correlated over a wide range of capacities from the corresponding gas-phase characteristic curves, which in turn have been estimated from refractive indices.

2. An estimated characteristic curve for water is arrived at from eq 3 and is in excellent agreement with the characteristic curve calculated from the water adsorption isotherm for the same carbon.

Acknowledgments. This work was supported in part by a grant from the Pittsburgh Activated Carbon Division, Calgon Corp. In addition, D. A. Wohleber received support from an N.D.E.A. Title IV Fellowship and from the Goodyear Tire and Rubber Fellowship Fund.

(8) R. J. Grant and M. Manes, *Ind. Eng. Chem. Fundam.*, 3(3), 221 (1964); 5(4), 490 (1966).

On the Theory of the Stabilization of Dispersions by Adsorbed Macromolecules. I. Statistics of the Change of Some Configurational Properties of Adsorbed Macromolecules on the Approach of an Impenetrable Interface

by F. Th. Hesselink

van't Hoff Laboratorium der Rijksuniversiteit, Sterrenbos 19, Utrecht, The Netherlands *(Received May 28, 1970)*

Publication costs borne completely by The Journal of Physical Chemistry

Density distributions for the segments of adsorbed macromolecules as function of the distance from the interface are derived for three loop size distributions. The density distribution for a copolymer attached by anchor groups goes through a maximum, whereas the distribution curve for an adsorbed homopolymer only shows an exponentional decrease. It is shown that during the diffusion-controlled approach of two colloidal particles with macromolecules adsorbed on their surfaces no time is available for a rearrangement of the loop size distribution; each loop, however, has time to accommodate its configuration to the volume restricted by the second particle. The rise in configurational free energy, Δf, due to the restricting second interface is calculated for a tail, a loop, and a bridge (a chain connecting two particles). On the approach of the second interface, Δf rises continuously for a tail and a loop, but for a bridge it goes through a minimum. Density distributions for a tail and a loop between two parallel interfaces are derived. The effect of the second interface is to compress the density curve and to raise its maximum.

Introduction

Several properties of a macromolecule that is attached to an interface change when a second impenetrable interface approaches. This approaching impenetrable interface can be a model for, *e.g.*, a second colloidal particle approaching a given one in a suspension stabilized by adsorbed macromolecules or a second crystallite in a polymer melt or a micro phase boundary in a block copolymer system. Statistical evaluation of the effects of this approach is thus useful for a quantitative theory of the stabilization of dispersions by adsorbed macromolecules,[1-3] for a quantitative description of the crystallization of polymers from the melt,[4,5] and for the formation of lamellar and spherical domains in block copolymers.[6-8]

In this paper we are mainly concerned with the stabilization of dispersions by adsorbed macromolecules, but application of our results to the other fields mentioned above is possible. A description of the state of an adsorbed macromolecule in the absence of a second interface has been given by Silberberg,[9] Hoeve, *et al.*,[10] Motomura and Matuura,[11] Rubin,[12] Roe,[13] and several others (see reviews by Stromberg[14] and by Patat, *et al.*[15]). These treatments handle the case of a homogeneous adsorbed macromolecule, homogeneous in the sense that all segments have *a priori* an equal chance to become adsorbed (no anchor segments). They predict an adsorption in loops and an exponentially decreasing density distribution for the segments of all loops together. In a previous paper[16] we have derived expressions for the density distribution (the fraction of the segments located at a distance between x and $x + dx$ from the interface) of the segments of a polymeric chain terminally adsorbed at one end (tail) and at both ends (loop).

In this paper we will derive density distributions for adsorbed macromolecules with several loop size distributions; then we will formulate the influence of a second interface parallel to the adsorbing one on the configurational free energy for a loop, a tail, and a bridge

(1) E. L. Mackor, *J. Colloid Sci.*, **6**, 492 (1951); E. L. Mackor and J. H. van der Waals, *ibid.*, **7**, 535 (1952).

(2) E. J. Clayfield and E. C. Lumb, *ibid.*, **22**, 269, 285 (1966); *Macromolecules*, **1**, 133 (1968).

(3) D. J. Meier, *J. Phys. Chem.*, **71**, 1861 (1967).

(4) H. G. Zachmann and P. Spelucci, *Kolloid Z. Z. Polym.*, **213**, 39 (1966).

(5) J. M. Peterson and P. H. Lindenmeyer, *Makromol. Chem.*, **118**, 343 (1968).

(6) P. Grosius, Y. Gallot, and A. Skoulios, *ibid.*, **127**, 94 (1969).

(7) D. J. Meier, *J. Polym. Sci., Part C*, **26**, 81 (1969).

(8) T. Inoue, T. Soen, T. Hashimoto, and H. Kawai, *J. Polymer Sci., Part A-2*, **7**, 1283 (1969); *Macromolecules*, **3**, 87 (1970).

(9) A. Silberberg, (a) *J. Phys. Chem.*, **66**, 1872, 1884 (1962); (b) *J. Chem. Phys.*, **46**, 1105 (1967); (c) *ibid.*, **48**, 2835 (1968).

(10) (a) C. A. J. Hoeve, E. A. DiMarzio, and P. Peyser, *ibid.*, **42**, 2558 (1965); (b) C. A. J. Hoeve, *ibid.*, **43**, 3007 (1965).

(11) K. Motomura and R. Matuura, (a) *Mem. Fac. Sci. Kyushu Univ.*, **6**, 97 (1968); (b) *J. Chem. Phys.*, **50**, 1281 (1969).

(12) R. J. Rubin, *ibid.*, **43**, 2392 (1965).

(13) R. J. Roe, *ibid.*, (a) **43**, 1591 (1965); (b) **44**, 4264 (1966).

(14) R. R. Stromberg in "Treatise on Adhesion and Adhesives," Vol. I, R. L. Patrick, Ed., Marcel Dekker, New York, N. Y., 1967.

(15) F. Patat, E. Killmann, and C. Schliebener, *Fortschr. Hochpolym. Forsch.*, **3**, 332 (1964).

(16) F. Th. Hesselink, *J. Phys. Chem.*, **73**, 3488 (1969).

(a chain with a terminal segment on both interfaces) and finally we will derive density distributions for a loop and a tail adjusted for the presence of a second interface.

The consequences of these results for the stabilizing action of adsorbed macromolecules will be investigated in the next paper.[17] Unless explicitly stated we assume the second interface not to adsorb segments of a macromolecule attached to the first interface, *e.g.*, because no adsorption places are free.

Density Distribution of Segments of Adsorbed Macromolecules

The configurational behavior of multipoint adsorbed macromolecules depends strongly on the size distribution of the loops. A large number of possible size distributions can be imagined; we will apply three of them to find the density distribution for those specific combinations of the loops. The resulting distributions are compared in Figure 1 for an equal mean number of segments in a loop. With an equal number of loops per unit surface area the particles are then covered by an equal amount of polymeric material.

The density distribution $\rho_2(i,x)$ of the segments of a single loop of size i on a six choice cubic lattice with independent extensions in the x, y, z direction, in the direction x normal to the adsorbing interface (subscript 2 refers to a single loop) has been given before[16,18]

$$\rho_2(i,x) = 12x(il^2)^{-1} \exp\{-6x^2/il^2\} \qquad (1)$$

where l is the length of a segment and $\int_0^\infty \rho_2(i,x)\mathrm{d}x = 1$. To derive eq 1 we have taken into account all possible configurations for a chain that starts at interface A and finds its end anywhere on A without having an intermediate segment touching A. When every loop of an adsorbed macromolecule has the same number of segments the normalized density distribution ρ_e for this combination of loops will have the same form as eq 1 (see Figure 1).

Homopolymer. For the case of an adsorbed homopolymer, Hoeve, *et al.*,[10] have found a loop size distribution of the form (see Appendix)

$$n_i = Ai^{-3/2}e^{i\lambda} \qquad (2)$$

where n_i is the number of loops of i segments, A a normalizing constant, and λ the free energy of adsorption per segment in units kT (in case of adsorption $\lambda < 0$). Motomura and Matuura[11] have found a complicated analytic relation between the mean loop size $\bar{i}$ and the energy gain per adsorbed segment. In case of multipoint adsorption their results are in qualitative agreement with those of Hoeve, *et al.*[10] (compare Figure 1 of ref 11b with Figure 4 of ref 10a). The last authors have found approximately for small values of λ $\bar{i} \approx a(-\lambda)^{-1/2}$ with $a \approx 0.7$[19,20] (numerical constant). This result can be used to express A in the parameters $\bar{i}$ and n, where n is the total number of segments in the

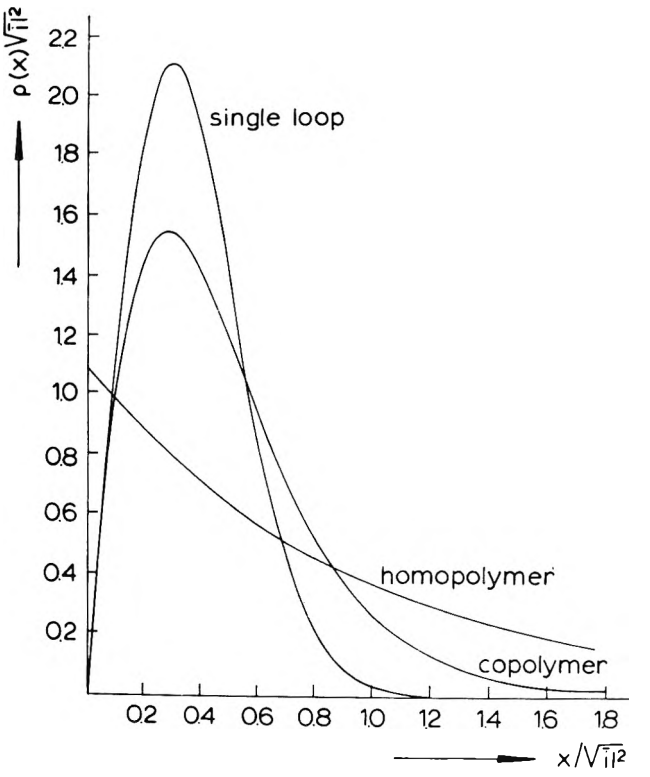

Figure 1. Normalized density distributions for the segments of a single loop (eq 1), for the segments of an adsorbed homopolymer with a mean loop size $\bar{i} = 10$ or $\lambda = -0.005$ (eq 5), and for the segments of a copolymer attached to the interface by anchor segments randomly distributed along the chain (eq 7).

loops, with $n = \Sigma i n_i$. This gives after integration over i

$$n_i = na\pi^{-1/2}(\bar{i})^{-1}i^{-3/2} \exp(-ia^2/\bar{i}^2) \qquad (3)$$

The normalized density distribution ρ for any adsorbed macromolecule (end effects neglected) is given by

$$\rho = n^{-1} \sum i n_i \rho_2(i,x) \qquad (4)$$

Substitution of eq 1 and 3 in 4 gives[21,22] for the density distribution ρ_h of an adsorbed homopolymer

$$\rho_h = 2a\sqrt{6}(\bar{i}l)^{-1} \exp(-2ax\sqrt{6}/\bar{i}l) \qquad (5)$$

an exponential decrease of ρ_h with x as already found before.[9c,10-13] A numerical example is shown in Figure 1.

Copolymer. Macromolecules used to stabilize dis-

(17) F. Th. Hesselink, A. Vrij, and J. Th. G. Overbeek, in preparation.

(18) E. A. DiMarzio, *Polym. Prepr. Amer. Chem. Soc., Div. Polym. Chem.*, **9**, 256 (1968).

(19) More accurately we can calculate[10,20] for $\lambda \to 0$, $a = 0.679$, for $\lambda = 10^{-3}$, $a = 0.690$, and for $\lambda = -10^{-2}$, $a = 0.714$.

(20) C. Truesdell, *Ann. Math.*, **46**, 44 (1945).

(21) Replacing the sum over i by an integration, $0 < i < \infty$.

(22) Using $\int_0^\infty i^{-3/2} \exp(-pi - q/i)\mathrm{d}i = (\pi/q)^{1/2} \exp\{-2(pq)^{1/2}\}$.

persions are often attached to the particles by some anchor segments. The loop size distribution is then determined by the distribution of the sequence lengths of the soluble component (m) in the copolymers. For a copolymer with anchor segments randomly distributed along the chain the probability N_i that an m sequence picked at random consists of i units is given by[23]

$$N_i = p(1 - p)^{i-1}$$

where p is the probability that an anchor segment is added to an m sequence. When only a few anchor segments are distributed along the chain the probability of anchor–anchor links will vanish, the factor $(1 - p)$ goes to unity and $p = (\bar{i})^{-1}$ so that we find, replacing $i - 1$ by i, for n_i, the m sequence size distribution

$$n_i = N_i n/\bar{i} = n(\bar{i})^{-2}e^{-i/\bar{i}} \qquad (6)$$

a "most probable size distribution."[24] When we assume every anchor segment to be adsorbed the m sequence size distribution acts as loop size distribution, and we find for the density distribution, ρ_c, of the segments of this copolymer after substituting[21] eq 6 and 1 in 4

$$\rho_c = 12x(\bar{i}l)^{-2} \int_0^\infty \exp(-i/\bar{i} - 6x^2/il^2)\mathrm{d}i \qquad (7)$$

Evaluation of this integral leads to a tabulated Hankel function of the order one for a pure imaginary argument.[25,26] In Figure 1 the result is compared with the other density distributions ρ_e and ρ_h. It is also interesting to compare the mean-square distance of the segments from the interface, $\langle x^2 \rangle$, for the three density distributions. From eq 1 we find $\langle x^2 \rangle_e = \bar{i}l^2/6$, from eq 5 we find $\langle x^2 \rangle_h = \bar{i}^2l^2/12a^2$, and from eq 7 we find $\langle x^2 \rangle_c = \bar{i}l^2/3$. Thus $\langle x^2 \rangle$ is the smallest for the case of equal loops. Further, for a homopolymer the thickness of the adsorbed layer ($\approx \sqrt{\langle x^2 \rangle}$) is proportional with $\bar{i}$ whereas in the other cases it is proportional with $(\bar{i})^{1/2}$.

Figure 1 shows that the maximum of the density curve for a loop size distribution compared with the case of equal loops is shifted slightly toward the adsorbing interface. The density curves for a loop size distribution are much less steep than those for the case of equal loops. This is of direct importance for the stabilizing effect of adsorbed macromolecules, for it will result in a more gradual repulsion between colloidal particles covered by these macromolecules. Interesting in Figure 1 is also the low density area near the adsorbing interface for a single loop and for an anchor attached copolymer. This effect is not found for an adsorbed homopolymer. The reason for this is that the interface repels statistically the macromolecule but for its adsorbing segments. In case of a homopolymer any segment can be adsorbed whereas in the other cases only the anchor segments can. Using a Monte Carlo technique DiMarzio and McCrackin[27] have found density curves, some showing a maximum as those for ρ_e and ρ_c, others showing only a decrease as for ρ_h. Density curves showing a maximum were also found before by Roe[13] for a combination of tails and by us[16] for a single tail. In the next paper[17] we will investigate the consequences for the stabilizing action of the different density distributions.

Time Scale of the Approach of the Second Interface

The crucial moment for the stability of a colloidal dispersion is the encounter of two particles. When the approach of the second particle (interface) takes more time than the time necessary for an adsorbed macromolecule to reach its equilibrium configuration, a process known to take minutes or more,[14,15,28] the loop size distribution of an adsorbed homopolymer will be continuously rearranged; long loops are more hindered than short loops and thus they will be converted into shorter loops and if possible more segments will be adsorbed (see Appendix).

The time, t_{ap}, it takes for two spherical colloidal particles of radius a in Brownian motion to pervade each others polymeric protection layers of thickness δ from a separation 2δ to δ, however, is very much shorter than the time necessary for a loop size rearrangement. This time can be found according to Frens[29] by a combination of Einstein's mean-square displacement relation with a mutual diffusion coefficient $D_{12} = 2D$ and Stokes' law for the friction coefficient of a sphere.[30,31] Then

$$t_{ap} = 3\pi\eta a\delta^2/2kT$$

where η and T are viscosity and absolute temperature of the system and k the Boltzmann constant. For a particle radius of 500 Å and a polymeric layer of 60 Å we have at room temperature in cgs units $t_{ap} \sim 2 \times 10^{-4}\eta$. Even in very viscous media the encounter time is only a fraction of a second. It is clear therefore that during the encounter of two colloidal particles not

(23) T. Alfrey, Jr., J. J. Bohrer, and H. Mark, "Copolymerization," "High Polymers VII," Interscience, New York, N. Y., 1952.

(24) P. J. Flory, "Principles of Polymer Chemistry," Cornell University Press, Ithaca, N. Y., 1953.

(25) I. S. Gradshtein and I. M. Ryznik, "Tables of Integrals, Series, and Products," Academic Press, New York, N. Y., 1965, pp 307, 952.

(26) E. Jahnke and F. Emde, "Tables of Functions," Dover, N. Y., 1945, p 237.

(27) E. A. DiMarzio and F. L. McCrackin, *J. Chem. Phys.*, **43**, 539 (1965).

(28) J. J. Kipling, "Adsorption from Solutions of Non-Electrolytes," Academic Press, New York, N. Y., 1965.

(29) G. Frens, "The Reversibility of Irreversible Colloids," Thesis, Utrecht, 1968.

(30) We neglect secondary effects such as acceleration because of van der Waals attraction forces, a retardation due to incipient repulsive action of the adsorbed polymeric layers, and extra viscous forces caused by these layers and by the difficulty for solvent molecules to escape from the area between the particles.[31]

(31) (a) B. V. Deryagin and V. M. Muller, *Dokl. Akad. Nauk SSSR*, **176**, 869 (1967); (b) G. J. Roebersen, private communication.

sufficient time is available for a rearrangement of the loop size distribution. Therefore we will assume this loop size distribution to be constant.

Each individual loop, however, has to accommodate its configuration to the volume restriction imposed by the second particle. This configuration is only correctly described by the statistics of a random flight in a limited region when the terminal relaxation time, τ_1, for the adsorbed loop is shorter than the time of approach of the two particles. From oscillatory flow measurements Thurston, *et al.*,[32] have calculated values for τ_1 for polystyrene chains in a chlorinated aromatic solvent (Aroclor 1248, with $\eta = 2.23$ P) for solutions of finite concentration for which there is significant interaction between the polymer molecules. They found for polystyrene of $M_w = 2000$ $\tau_1 = 5 \times 10^{-7}$ sec, for $M_w = 10^4$ $\tau_1 = 2 \times 10^{-5}$ sec, and for $M_w = 5 \times 10^4$ $\tau_1 = 2 \times 10^{-4}$ sec. Comparing these values for τ_1 and t_{ap} we conclude that during a Brownian encounter of two particles a loop with $M_w \lesssim 5 \times 10^4$ (480 monomers)[33] has sufficient time for continuously finding its time-averaged configuration in the region restricted by the two interfaces without making additional contacts with the adsorbing interface for, as we argued above, this process of extra adsorption takes too much time. (This is of course an approximation for occasionally a single segment might find an adsorption place in a time shorter than t_{ap}.) Thus in calculating the interaction between two particles covered by adsorbed macromolecules we have to derive first for the individual loops and tails the change of configurational properties such as the total number of configurations and the density distributions of the segments.

The Configurational Free Energy for a Tail, a Loop, and a Bridge in a Slab

The number of configurations for a tail and a loop—and any adsorbed macromolecule forms a combination of tails and loops—diminishes on the approach of a second impenetrable interface. To derive expressions for this loss in configurational entropy we will first consider as before[16] the case of a tail and a loop on a one-dimensional lattice in which steps are possible in the positive and negative ξ directions.

The number of configurations for a tail of i segments, $Z_A(i,\xi)$ that begins at interface A ($\xi = 0$), ends at ξ, while the other segments are restricted to $\xi > 0$ is given by[10,16,34]

$$Z_A(i,\xi) = (2/\pi)^{1/2} 2^i \xi i^{-3/2} e^{-\xi^2/2i} \qquad (8)$$

for both ξ, i even or uneven and $i \gg \xi$. The total number of configurations for this tail, $Z_A(i)$, is found by integration of eq 8 over every allowed value of ξ to be[16]

$$Z_A(i) = (2\pi i)^{-1/2} 2^i \qquad (9)$$

A loop of i segments can be formed from a tail of

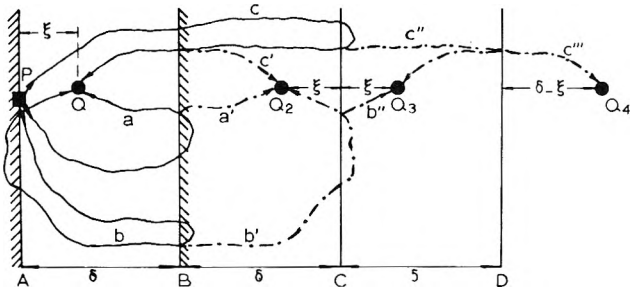

Figure 2. The effect of a second impenetrable interface on the number of configurations for a terminally adsorbed chain (TAIL), b′ is the image of b with respect to B, b″ the image of b′ with respect to C, etc.

$i - 1$ segments that ends at $\xi = 1$ by linking this tail with an ith segment to the interface. This ith segment has only one possible orientation, and consequently the number of configurations for a loop (subscript 2) of i segments, $Z_{2A}(i)$, is equal to that of a tail of $(i - 1)$ segments that ends at $\xi = 1$ or

$$Z_{2A}(i) = Z_A(i - 1, \xi = 1) \qquad (10)$$

Substitution of eq 8 in 10 gives

$$Z_{2A}(i) = (2\pi)^{-1/2} 2^i i^{-3/2} \qquad (11)$$

This result can also be derived considering a loop as a combination of two connected tails.[16]

When a second interface B is placed parallel to A at a distance $\xi = \delta$ (see Figure 2) the number of configurations for a tail of i segments $Z_A(i,\xi,\delta)$ that begins at $\xi = 0$, ends at ξ without further touching the interfaces is found by subtracting from $Z_A(i,\xi)$ the number of chains $Z_B^*(i,\xi)$ that touch only interface B. At first sight $Z_B^*(i,\xi)$ seems to be equal (see Figure 2) to the number of chains that would go from P to Q_2 in the absence of interface B, $Z_A(i,2\delta - \xi)$ for when a chain such as a in Figure 2 touches the interface B it has as much chance to end at Q_2 as at Q. Zachmann and Spelucci[4] used an equivalent of this idea. It overestimates, however, the effect of the second interface. The collection $Z_A(i,2\delta - \xi)$ contains too many chains, *e.g.*, chain b′ (Figure 2), for b (the original of b′) touches A and has therefore already been removed. In the absence of B chains like b′ have as much chance to end at Q_2 as at Q_3. Therefore we can correct the overestimate by adding the number of chains that end at Q_3 without touching A, $Z_A(i,2\delta + \xi)$. In this collection $Z_A(i,2\delta + \xi)$, however, there are chains like c″ that were correctly removed. This extra addition must be corrected for by subtracting the number of chains that

(32) G. B. Thurston and J. L. Schrag, *J. Polymer Sci., Part A-2*, 6, 1331 (1968); G. B. Thurston and J. D. Morrison, *Polymer*, 10, 421 (1969).

(33) For such long loops the thickness of the adsorbed layer $\delta >$ 60 Å and thus $t_{ap} > 2 \times 10^{-4}\eta$ and therefore we still expect $t_{ap} \gg \tau_1$.

(34) S. Chandrasekhar, *Rev. Mod. Phys.*, 15, 1 (1943).

end at Q_4, $Z_A(i,4\delta - \xi)$ for chains like c'' have as much chance to end at Q_3 as at Q_4, etc. Thus

$$Z_A(i,\xi,\delta) = Z_A(i,\xi) - Z_A(i,2\delta - \xi) + Z_A(i,2\delta + \xi) - Z_A(i,4\delta - \xi) + \ldots \quad (12)$$

Substitution of eq 8 in 12 gives[35] thus for a tail

$$Z_A(i,\xi,\delta) = (2/\pi)^{1/2} 2^i i^{-3/2} \sum_{v=-\infty}^{\infty} (\xi + 2v\delta) \times \exp\{-(\xi + 2v\delta)^2/2i\} \quad (13)$$

where v goes through all integral numbers including zero. The total number of configurations for a tail, $Z_A(i,\delta)$, that starts at $\xi = 0$ without further touching the interfaces is found by appropriate integration of eq 13

$$Z_A(i,\delta) = (2\pi i)^{-1/2} 2^i \sum_{v=-\infty}^{\infty} [\exp\{-2v^2\delta^2/i\} - \exp\{-(2v+1)^2\delta^2/2i\}] \quad (14)$$

The number of configurations for a loop of i segments that does not touch either A or B except for its ends on A, $Z_{2A}(i,\delta)$, is now found using eq 13 with $\xi = 1$ and $i \rightarrow i - 1$ (see eq 10) to be

$$Z_{2A}(i,\delta) = (2\pi)^{-1/2} i^{-3/2} 2^i \sum_{v=-\infty}^{\infty} (1 + 2v\delta) \times \exp\{-2v\delta(v\delta + 1)/i\} \quad (15)$$

Now we can derive an expression for the relative loss of configurations because of the second interface for a tail (subscript 1), $R_1(i,\delta)$ and for a loop, $R_2(i,\delta)$, both of i segments. By definition

$$R_1(i,\delta) = Z_A(i,\delta)/Z_A(i)$$
$$R_2(i,\delta) = Z_{2A}(i,\delta)/Z_{2A}(i) \quad (16)$$

For a six-choice cubic lattice we find assuming the extensions in x, y, z directions to be independent and replacing ξ and δ by x/l and d/l, l being the length of a segment by a slight generalization of eq 9, 11, 14, 15

$$R_1(i,d) = \sum_{v=-\infty}^{\infty} [\exp\{-6v^2d^2/il^2\} - \exp\{-3d^2(2v+1)^2/2il^2\}] \quad (17)$$

and[36]

$$R_2(i,d) = \sum_{v=-\infty}^{\infty} (1 + 2vd/l) \exp\{-6vd(vd + l)/il^2\} \quad (18)$$

Both $R_1(i,d)$ and $R_2(i,d) \rightarrow 1$ when $d \rightarrow \infty$. Equation 17 has been found before by Meier,[3] who solved the diffusion equation for a random walk in a slab, $0 < x < d$, using the method of "sources and sinks."[37] The points $Q_{2,3,4}$ in Figure 2 show a likeness with these sources and sinks. This approach, however, is not very appropriate for a loop.

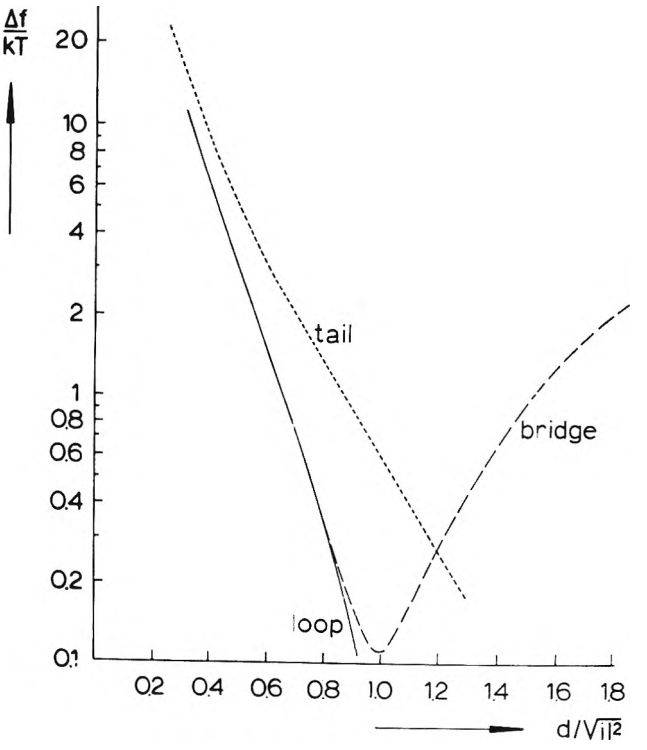

Figure 3. The free energy of a tail (eq 17), a loop (eq 18), and a bridge (eq 21) in a slab as a function of the distance between the interfaces. The tail is compared with a tail at $d = \infty$; the loop and the bridge with a loop at $d = \infty$.

The rise in free energy Δf for a tail and a loop because of the configurational restriction due to an approaching second interface is given by

$$\Delta f_j = -kT \ln R_j(i,d) \qquad (j = 1, 2) \quad (19)$$

This rise in free energy for a tail and a loop because of an approaching interface is shown[38] in Figure 3. It is of direct importance for the stabilization of dispersions by adsorbed macromolecules[2,3] and for the formation of lamellar structures in block copolymers,[6] for a rise in free energy means a repulsion between the interfaces. These consequences will be treated later.[17] Clayfield and Lumb[2] have simulated tails on a cubic lattice, and they have calculated the fraction of the tails with

(35) W. Feller, "Introduction to Probability Theory and Its Applications," Vol. I, New York, N. Y., 1957, p 336, gives eq 13 except for the factor 2^i to describe the probability of ruin after i trials for a gambler with initial capital ξ playing against an adversary with initial capital $d - \xi$. Statistically this problem is equivalent with our configurational problem.

(36) Considering a loop as a combination of two tails we can derive

$$R_2(i,d) = \sum_{v=-\infty}^{\infty} (1 - 12v^2d^2/il^2) \exp(-6v^2d^2/il^2)$$

This result is also found from eq 18 by series expansion and retaining the first terms of $\exp(\pm 6vd/il)$; numerical evaluation shows the practical equality of this result with eq 18.

(37) H. S. Carslaw and J. C. Jaeger, "Conduction of Heat in Solids," Clarendon Press, Oxford, 1959.

(38) Calculated with the Electrologica X8 computer of the Electronisch Rekencentrum, Utrecht.

no segment extended away from the interface beyond certain values of x. Direct comparison of their results with eq 17 is difficult due to a different plotting procedure but their curves for Δf *vs.* d show a great resemblance with the curve for a tail shown in Figure 3.

Bridge. Closely related to the problem of the configurational behavior of a loop and a tail on the approach of a second interface is the problem of the number of configurations for a "*bridge*," a polymeric chain that starts at interface A, ends at B without further touching the interfaces. Macromolecular bridges are supposed to play a crucial role in the flocculation of dispersions by macromolecules.[39,40]

The number of configurations for a bridge $Z_b(i,d)$ is found in a similar way as used for a loop by considering a bridge of i segments as a combination of a tail of $(i - 1)$ segments in a slab, $0 < \xi < \delta$, that ends at $\xi = \delta - 1$ and a "tail" of one segment that goes from $\xi = \delta - 1$ to $\xi = \delta$ or analogous to eq 10

$$Z_b(i,\delta) = Z_A(i - 1, \xi = \delta - 1,\delta) \qquad (20)$$

A polymeric chain with an anchor segment at both its ends can form a bridge as well as a loop, and therefore we will formulate the number of configurations for a bridge, divided by those for an unrestricted loop, $S(i,d)$, with $S(i,d) = Z_b(i,d)/Z_{2A}(i)$. Using eq 11, 13, and 20 we find for a six-choice cubic lattice

$$S(i,d) = \sum_{v=-\infty}^{\infty} \{(2v + 1)d/l - 1\} \times \exp\{-3[((2v + 1)^2d^2/l^2) - 2(2v + 1)d/l]/2i\} \qquad (21)$$

The free energy for a bridge compared to that for a loop, Δf_b is calculated[38] from $\Delta f_b = -kT \ln S(i,d)$ and shown in Figure 3. The curve has a minimum at $d = (il^2)^{1/2}$.[41] A bridge of two terminal anchor segments functions thus as a spring. At an extension more than the critical value of $d = (il^2)^{1/2}$, the particles are drawn together whereas at an extension less than $(il^2)^{1/2}$ the bridge pushes the particles away from each other just as effectively as a loop. This explains the loose structure of La Mer's[39] flocculates.

Density Distributions for a Tail and a Loop in a Slab

When two particles both covered by polymeric material approach each other, the layers of the adsorbed macromolecules will interpenetrate. To calculate the free-energy effects of this approach we first need a description of this interpenetration. Therefore we will derive the density distribution for a tail and a loop in a slab of thickness d.

Tail. For a one-dimensional lattice the probability to find the kth segment of a tail of i segments in a slab of thickness δ at distance ξ, $P_1(i,k,\delta,\xi)$ is given by[16]

$$P_1(i,k,\delta,\xi) = Z_A(k,\xi,\delta)Z_{A\xi}(i - k,\delta)/Z_A(i,\delta) \qquad (22)$$

where $Z_A(k,\xi,\delta)$ is the number of configurations for a tail of k segments that ends at ξ in a slab, $Z_{A\xi}(i - k,\delta)$ is the number of configurations for an unadsorbed chain of $(i - k)$ segments that starts at ξ in a slab. Thus the numerator gives the number of configurations for a tail of i segments with its kth segment at ξ in a slab. Kuhn[42] has derived an equation for $Z_{A\xi}(i - k,\delta)$ which can be written[43] as

$$Z_{A\xi}(i - k,\delta) = (2\pi)^{-1/2}(i - k)^{-1/2}2^{i-k} \times \int_0^{\delta}\left[\sum_{v=-\infty}^{\infty} \exp\{-(\xi - \beta + 2v\delta)^2/2(i - k)\} - \exp\{-(\xi + \beta + 2v\delta)^2/2(i - k)\}\right] d\beta \qquad (23)$$

This result can also be derived combining the argument on the influence of a second interface on a random chain given in the previous section with the argument given before[16] to find $Z_{A\xi}(i - k, \delta \to \infty)$. The normalized average number of segments $\rho_1(\xi,\delta)$ for a tail of i segments in a slab is given by

$$\rho_1(\xi,\delta) = i^{-1}\sum_{k=1}^{i} P_1(i,k,\xi,\delta) \qquad (24)$$

Substituting eq 13, 14, and 23 in 22 we find for a six-choice cubic lattice with eq 24, with $\beta = b/l$ and the assumptions made before introducing this lattice

$$\rho_1(x,d) = \frac{3(il^2)^{-1}}{R_1(i,d)} \sum_{v=-\infty}^{\infty}\left[v\int_0^d \{\exp[-q(vd - d + x - b/2)^2] - 2\exp[-q(vd - b/2)^2] + \exp[-q(vd + d - x - b/2)^2]\}db + \int_x^d \{\exp[-q(vd + b/2)^2] - \exp[-q(vd + x - b/2)^2]\}db\right] \qquad (25)$$

where $R_1(i,d)$ is given by eq 17, $q = 6/il^2$ and $\int_0^d \rho_1(x,d)\,dx = 1$. For $d \to \infty$, eq 25 becomes identical with the result obtained before[16] for a tail in the absence of a second interface.

Loop. For a one-dimensional lattice the probability to find the kth segment of a loop of size i in a slab of thickness δ at distance ξ, $P_2(i,k,\xi,\delta)$ is given by[16]

$$P_2(i,k,\xi,\delta) = Z_A(k,\xi,\delta)Z_A(i - k,\xi,\delta)/Z_{2A}(i,\delta) \qquad (26)$$

Here the numerator gives the number of configurations for a loop of i segments with its kth segment at ξ, the denominator accounts for the normalization. The nor-

(39) V. K. La Mer, *Discussions Faraday Soc.*, **42**, 248 (1966); V. K. La Mer and T. W. Healy, *Rev. Pure Appl. Chem.*, **13**, 112 (1963); T. W. Healy and V. K. La Mer, *J. Colloid Sci.*, **19**, 323 (1964).

(40) W. E. Walles, *J. Colloid Interface Sci.*, **27**, 797 (1968).

(41) A free chain has its rms end-to-end distance just at this value $(il^2)^{1/2}$, but this is not relevant here because the root mean square end-to-end distance in the x direction for a free chain is equal to $(1/3il^2)^{1/2}$.

(42) H. Kuhn, *Helv. Chim. Acta*, **31**, 1677 (1948); eq 10.

(43) Using ref 37, p 274, eq 10-2, 4, 5.

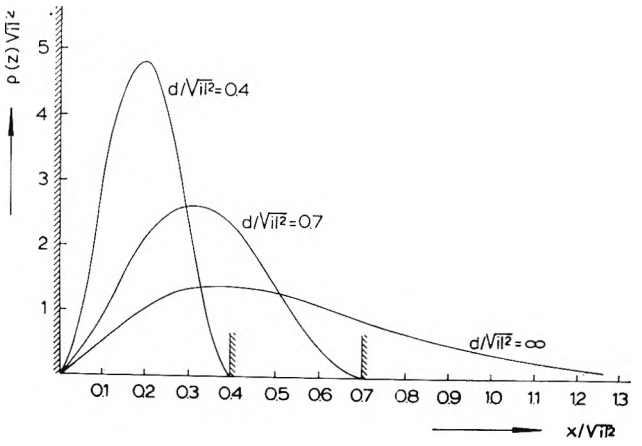

Figure 4. Normalized density distribution of the segments of a tail (eq 25) with a second impenetrable interface at $d/\sqrt{il^2} = 0.4, 0.7, \infty$.

malized density distribution $\rho_2(x,d)$ for a loop in a slab is found analogous to eq 24.

After substitution of eq 13 and 15 in 26 we find for a six-choice cubic lattice

$$\rho_2(x,d) = 12d(il^2)^{-1}R_2^{-1}(i,d) \times \sum_{v=-\infty}^{\infty}\left[(v + 1)(v + x/d)\exp\left\{-\frac{6d^2}{il^2} \times (v + x/d)^2\right\} - v^2\exp\left\{-\frac{6d^2v^2}{il^2}\right\}\right] \quad (27)$$

with $\int_0^d \rho_2(x,d)dx = 1$; for $d \to \infty$ eq 27 becomes identical with eq 1. As could be expected, the second interface compresses the density distribution for a loop and a tail toward the adsorbing interface. Figure 4 shows the density distribution for a tail calculated[38] from eq 25 for several values of the thickness of the slab; similar results are obtained for a loop.

In the next paper[17] we will use eq 25 and 27 to calculate the extra free energy of mixing of polymeric segments when two colloidal particles covered by adsorbed macromolecules approach each other.

Acknowledgment. The author wishes to thank Professor J. Th. G. Overbeek and Professor A. Vrij for stimulating discussions and for critical reading of the manuscript.

Appendix

When the approach of the second interface is slow enough the loop size distribution of the adsorbed macromolecules will continuously be rearranged as an adjustment to the continuous decrease of the partition function for each loop. In the absence of a second interface, Hoeve, *et al.*,[10] have found the loop size distribution given by eq 2 by first formulating the partition function q for a macromolecule adsorbed in trains on the surface connected by loops dangling in solution

$$q = \sum(m!)^2\Pi_i(\omega_i^{n_i}/n_i!)\Pi_j(\nu_j^{m_j}/m_j!) \quad (A\text{-}1)$$

where m is the total number of loops and trains, ω_i and ν_j the partition functions, respectively, for a loop of size i and a train of size j, n_i and m_j the number of loops of size i, respectively, of trains of size j. With a free chain as reference the partition function for a loop, ω_i, in the presence of a second interface is given by eq 15, or

$$\omega_i = ci^{-3/2}R_2(i,d) \quad (A\text{-}2)$$

where c is a flexibility parameter (*e.g.*, for a one-dimensional lattice $c = (2\pi)^{-1/2}$, see eq 15). With eq A-2 substituted in eq A-1 we can find the maximum term in A-1 as described by Hoeve, *et al.*,[10] and we get

$$n_i = Ai^{-3/2}e^{i\lambda}R_2(i,d) \quad (A\text{-}3)$$

For d goes to infinity $R_2(i,d)$ becomes unity and we have eq 2. When $d/\sqrt{i}$ decreases $R_2(i,d)$ decreases very fast (see Figure 3). Thus long loops will disappear by conversion in smaller loops as already expected above. A quantitative analysis of these effects will be omitted because in most cases of interest there is no time available for this process of rearrangement of the loop size distribution.

Variational Bounds on the Intrinsic Viscosity[1]

by Stephen Prager

Department of Chemistry, University of Minnesota, Minneapolis, Minnesota 55455 *(Received June 5, 1970)*

Publication costs assisted by the National Science Foundation

The principle of minimum energy dissipation is applied to obtain lower bounds on the intrinsic viscosity of a polymer molecule consisting of N spherical beads. The forces which the beads exert on one another need not be restricted to Hooke's law interactions—the main result, inequality 29, holds for any internal potential energy function. Brownian motion and hydrodynamic interaction effects are taken into account, and the preaveraging of the diffusion tensor used by most authors working in this area is avoided. For an isolated bead ($N = 1$) the present treatment gives the correct value of the intrinsic viscosity as obtained by Einstein, whereas previous theories, which are designed for use at high molecular weights only, give $[\eta] = 0$ in this limit. Explicit results are obtained for dumbells ($N = 2$) and for looped chains; the effect of preaveraging on calculated values of $[\eta]$ is discussed for the case of a Gaussian loop in the limit of large N.

Introduction

Two types of approaches have been developed for the treatment of intrinsic viscosity in polymer solutions: the porous sphere model of Debye[2] and the hydrodynamic interaction theory of Kirkwood and Riseman.[3] In the former, the actual random coil is replaced by a uniform porous sphere, which permits an exact solution of the hydrodynamic problem; the latter approach uses a much more realistic model, the Gaussian chain, but introduces approximations in the hydrodynamic equations, whose effect is difficult to assess.

An improved theory of intrinsic viscosity should seek to (1) treat hydrodynamic interactions between different parts of the polymer chain at the level of rigor achieved by Debye, and (2) take proper account of the forces between both adjacent and nonadjacent chain segments. In a recent paper[4] we developed a variational treatment of the friction coefficient in polymer solutions, a treatment which we feel meets both criteria. In the present article we extend our method to obtain rigorous lower bounds on the intrinsic viscosity.

The assumptions under which we claim rigor are fairly broad. (1) We represent the polymer molecule as a set of spherical beads connected by bonds. The bonds need not be Hookean springs, and the chain which they form may have branches and loops; van der Waals type interactions between unconnected beads are included (in particular no two beads may approach to within less than one diameter of one another), as are restrictions on bond angles. Only the beads offer hydrodynamic resistance—the bonds in between have no dimension. Each bead may rotate freely about its center, but such a rotation is in no way coupled to any change in bond angles. (2) The solvent is represented as a continuum fluid, whose motion is governed by the creeping flow Navier–Stokes equations. Inertia effects in the motions of the beads are also neglected. (3) Brownian motion of the beads is assumed to be governed by a many-particle diffusion equation for the configurational distribution function of the polymer molecule. Following Kirkwood,[5] we introduce hydrodynamic interaction between beads by replacing the usual scalar diffusion coefficient with a diffusion tensor; however, our tensor differs from that used by Kirkwood.[5] Our variational inequalities are restricted to steady, small shear rates. Oscillating shears and non-Newtonian behavior lie outside the scope of this paper.

Energy Dissipation

Consider an isolated polymer molecule of N beads suspended between two parallel plates normal to the z axis, the force per unit area acting on the upper and lower plate being, respectively, γ and $-\gamma$ in the x direction. Let the beads be momentarily located at positions $\mathbf{r}_1, \ldots, \mathbf{r}_N$, and let the forces acting on them be $\mathbf{f}_1, \ldots, \mathbf{f}_N$. The rate of energy dissipation resulting from this system of forces should have the bilinear form

$$E = \frac{1}{kT} \sum_{i,j} \mathsf{D}_{ij} : \mathbf{f}_i \mathbf{f}_j + 2 \sum_i \mathsf{A}_i : \mathbf{f}_i \gamma + \mathsf{B} : \gamma\gamma \quad (1)$$

where the tensors D_{ij}, A_i, and B will, in general, be functions of $\mathbf{r}_1, \ldots, \mathbf{r}_N$.

An alternative expression for E may be obtained in terms of the stress distribution in the solvent. If $\mathfrak{d}(\mathbf{r})$ represents the viscous stress at some point $\mathbf{r}$, and η_0 is the viscosity of this solvent, then

$$E = \frac{1}{2\eta_0} \int_{\Omega'} \mathfrak{d}(\mathbf{r}) : \mathfrak{d}(\mathbf{r}) d^3\mathbf{r} \quad (2)$$

the integral extending over the multiply connected

(1) Work supported by a grant from the National Science Foundation.

(2) P. Debye, *Phys. Rev.*, **71**, 486 (1947).

(3) J. G. Kirkwood and J. Riseman, *J. Chem. Phys.*, **16**, 565 (1948).

(4) J. Rotne and S. Prager, *ibid.*, **50**, 483 (1969).

(5) J. G. Kirkwood, *Rec. Trav. Chim.*, **68**, 649 (1949).

region Ω' consisting of all points located between the plates but not in the interior of a bead.

The key to our variational method is the principle of minimum energy dissipation, which states[6] that if, in place of the true viscous stress distribution $\mathfrak{d}^*(\mathbf{r})$, we use a trial function $\mathfrak{d}^*(\mathbf{r})$ satisfying the conditions

$$\mathrm{tr}\ \mathfrak{d}^* = 0 \tag{3a}$$

$$\mathfrak{d}^* = (\mathfrak{d}^*)^{\mathrm{T}} \tag{3b}$$

$$\frac{\partial}{\partial \mathbf{r}} \cdot \mathfrak{d}^* = -\frac{\partial p^*}{\partial \mathbf{r}} \tag{3c}$$

at all points $\mathbf{r}$ in Ω' as well as the further requirements

$$\int_{S_i} (\mathfrak{d}^* + p^* \mathbf{I}) \cdot \hat{\mathbf{v}} \mathrm{d}^2\mathbf{r} = \mathbf{f}_i \tag{4a}$$

$$\int_{S_i} [(\mathfrak{d}^* + p^* \mathbf{I}) \cdot \hat{\mathbf{v}}] \times \hat{\mathbf{v}} \mathrm{d}^2\mathbf{r} = 0 \tag{4b}$$

$$\frac{1}{\mathcal{A}} \int_{S_+ \text{ or } S_-} (\mathfrak{d}^*(\mathbf{r}) + p^* \mathbf{I}) \cdot \hat{\mathbf{z}} \mathrm{d}^2\mathbf{r} = -\gamma \hat{\mathbf{x}} \tag{5}$$

the resulting estimate E^* of the energy dissipation rate will be too large. In these equations $p^*(\mathbf{r})$ is a scalar function representing the trial pressure distribution, the superscript T designates the transpose of a tensor, and $\mathbf{I}$ is the unit tensor; S_i, S_+, and S_- are, respectively, the surfaces of sphere i, the upper plate, and the lower plate, $\hat{\mathbf{v}}(\mathbf{r})$ is the unit inward pointing normal to the surface of Ω' at $\mathbf{r}$, and $\hat{\mathbf{z}}$ is the unit vector in the positive z direction; $\mathcal{A}$ is the plate area. Condition 3a is nothing but the definition of a viscous stress as the nonhydrostatic part of a total stress tensor. The remaining conditions ensure that an admissible trial stress will at least not give rise to unbalanced forces or torques on any sphere or element of fluid. Minimization of E^* subject to these conditions leads to an optimal $\mathfrak{d}(\mathbf{r})$ equal to η_0 times the symmetrized gradient of a divergence-free velocity field which is compatible with rigid-body translation and rotation of the spheres and the motion of the plates in the $+$ and $-x$ directions.

Complete minimization is thus equivalent to solving the Navier–Stokes equations subject to appropriate boundary conditions in Ω'. In view of the complex geometry of Ω', this is clearly not possible, but it is not at all hard to construct trial functions $\mathfrak{d}^*$ which will give upper bounds on E. These bounds can then in turn be converted into lower bounds on the intrinsic viscosity, as we shall show.

Trial Stress Distributions

As in ref 4, we shall construct $\mathfrak{d}^*$ by superposition of contributions from individual spheres

$$\mathfrak{d}^*(\mathbf{r}) = \gamma_0 \boldsymbol{\Gamma} + \sum_i \mathfrak{d}_i(\boldsymbol{\varrho}_i) \tag{6}$$

where γ_0 is a scalar constant, $\boldsymbol{\varrho}_i \equiv \mathbf{r} - \mathbf{r}_i$, and

$$\boldsymbol{\Gamma} \equiv \hat{\mathbf{x}}\hat{\mathbf{z}} + \hat{\mathbf{z}}\hat{\mathbf{x}}$$

is the symmetrized dyadic product of the unit vectors in the x and z directions (we may think of the $\gamma_0\boldsymbol{\Gamma}$ term as the contribution made by the parallel plates).

For $\mathfrak{d}_i$ we shall use, following Guth and Simha,[7] the viscous stress distribution around an isolated sphere of radius a, subject to a force $\mathbf{f}_i$, and suspended in a large body of solvent which is being acted upon by a shearing stress $\beta\gamma_0\boldsymbol{\Gamma}$

$$\mathfrak{d}_i(\boldsymbol{\varrho}_i) = \mathfrak{d}_i^{(S)}(\boldsymbol{\varrho}_i) + \beta \mathfrak{d}_i^{(E)}(\boldsymbol{\varrho}_i) \tag{7}$$

where

$$\mathfrak{d}_i^{(S,E)} = \eta_0 \left[\left(\frac{\partial \mathbf{u}_i^{(S,E)}}{\partial \boldsymbol{\varrho}_i} \right) + \left(\frac{\partial \mathbf{u}_i^{(S,E)}}{\partial \boldsymbol{\varrho}_i} \right)^{\mathrm{T}} \right]$$

and

$$\mathbf{u}_i^{(S)} = \frac{1}{8\pi\eta_0} \mathbf{f}_i \cdot \left[\frac{\boldsymbol{\varrho}_i\boldsymbol{\varrho}_i - \boldsymbol{\varrho}^2\mathbf{I}}{\boldsymbol{\varrho}^3} + \frac{a^2}{3} \cdot \frac{\boldsymbol{\varrho}_i^2\mathbf{I} - 3\boldsymbol{\varrho}_i\boldsymbol{\varrho}_i}{\boldsymbol{\varrho}_i^5} \right] \tag{8}$$

$$\mathbf{u}_i^{(E)} = \frac{\gamma_0 a^3}{4\eta_0} \left[\frac{5}{\rho_i^5} \left(\frac{a^2}{\rho_i^2} - 1 \right) \boldsymbol{\Gamma} : \boldsymbol{\varrho}_i\boldsymbol{\varrho}_i\boldsymbol{\varrho}_i - \frac{a^2}{\rho_i^5} \boldsymbol{\Gamma} \cdot \boldsymbol{\varrho}_i \right]$$

are the familiar Stokes and Einstein velocity perturbations. That this choice for $\mathfrak{d}^*$ satisfies conditions 3 and 4 is easily verified; condition 5 can always be fulfilled by an appropriate choice of γ_0. The dimensionless parameter β may be adjusted to minimize E^*.

The energy dissipation rate corresponding to (6) is

$$E^* = \frac{1}{2\eta_0} \left[\gamma_0^2 \boldsymbol{\Gamma} : \boldsymbol{\Gamma} \left(V - \frac{4\pi a^3}{3} N \right) + 2\gamma_0 \boldsymbol{\Gamma} : \sum_i \int_{\Omega'} \mathfrak{d}_i(\boldsymbol{\varrho}_i) \mathrm{d}^3\mathbf{r} + \sum_i \int_{\Omega'} \mathfrak{d}_i(\boldsymbol{\varrho}_i) : \mathfrak{d}_i(\boldsymbol{\varrho}_i) \mathrm{d}^3\mathbf{r} + \sum_{i \neq j} \sum \int_{\Omega'} \mathfrak{d}_i(\boldsymbol{\varrho}_i) : \mathfrak{d}_j(\boldsymbol{\varrho}_j) \mathrm{d}^3\mathbf{r} \right] \tag{9}$$

where V is the volume of solution being sheared, which, since we are ultimately calculating an intrinsic viscosity, we shall regard as containing just a single polymer molecule.

The integral in the last term of (9) is awkward, because of the complexity of the region Ω' and leads to terms involving three spheres simultaneously. To avoid this we resort to a device employed in our earlier paper.[4] The last two terms in (9) represent the integral of a perfect square over Ω'. Their contribution will thus be increased if we replace Ω' by the full volume V; since E^* is already an upper bound on E, it will retain this property after the replacement has been made. Indeed, we can obtain a somewhat improved result by applying Schwartz's inequality to the integral over the region $(V - \Omega')$ which has been added by this operation

(6) W. Prager in "Studies in Mathematics and Mechanics Presented to R. von Mises," Academic Press, New York, N. Y., 1954, p 208.

(7) E. Guth and R. Simha, *Kolloid Z.*, **74**, 266 (1936).

$$E < E^* < \frac{1}{2\eta_0}\left[\gamma_0^2\boldsymbol{\Gamma}:\boldsymbol{\Gamma}\left(V - \frac{4\pi a^3}{3}N\right) + 2\gamma_0\boldsymbol{\Gamma}:\sum_i\int_{\Omega'}\mathfrak{d}_i(\boldsymbol{\varrho}_i)\mathrm{d}^3\mathbf{r} + \sum_i\int_V \mathfrak{d}_i(\boldsymbol{\varrho}_i):\mathfrak{d}_i(\boldsymbol{\varrho}_i)\mathrm{d}^3\mathbf{r} + \sum_{i\neq j}\sum\int_V \mathfrak{d}_i(\boldsymbol{\varrho}_i):\mathfrak{d}_j(\boldsymbol{\varrho}_j)\mathrm{d}^3\mathbf{r} - + \frac{3}{-4\pi a^3 N}\sum_i\sum_j\left(\int_{V-\Omega'}\mathfrak{d}_i(\rho_i)\mathrm{d}^3\mathbf{r}:\int_{V-\Omega'}\mathfrak{d}_j(\boldsymbol{\varrho}_j)\mathrm{d}^3\mathbf{r}\right)\right] \quad (10)$$

In order to perform the integrals in (10), we must specify $\mathfrak{d}_i$ in the interior of sphere i as well. The most convenient choice is

$$\mathfrak{d}_i(\boldsymbol{\varrho}_i) = 0 \qquad (\rho_i < a) \quad (11)$$

which leads, in the limit of large V, to the relations

$$\boldsymbol{\Gamma}:\int_{\Omega'}\mathfrak{d}_i(\boldsymbol{\varrho}_i)\mathrm{d}^3\mathbf{r} = -2\pi a^3\gamma_0\beta\boldsymbol{\Gamma}:\boldsymbol{\Gamma} + 2z_i\boldsymbol{\Gamma}:\hat{\mathbf{z}}\mathbf{f}_i - \frac{4\pi a^3}{3}\sum_{j\neq i}(\beta\gamma_0 b_{ij} + \mathbf{f}_i\cdot\mathbf{c}_{ij})$$

$$\int_V \mathfrak{d}_i:\mathfrak{d}_i\mathrm{d}^3\mathbf{r} = \frac{\mathbf{f}_i^2}{3\pi a} + 2\pi\beta^2\gamma_0^2 a^3\boldsymbol{\Gamma}:\boldsymbol{\Gamma}$$

$$\int_V \mathfrak{d}_i:\mathfrak{d}_j\mathrm{d}^3\mathbf{r} = -\frac{2\pi a^3}{3}(\beta^2\gamma_0^2 b_{ij} - 3\gamma_0\beta(\mathbf{f}_j - \mathbf{f}_i)\cdot\mathbf{c}_{ij}) + \mathbf{d}_{ij}:\mathbf{f}_i\mathbf{f}_j$$

$$\boldsymbol{\Gamma}:\int_{V-\Omega'}\mathfrak{d}_i\mathrm{d}^3\mathbf{r} = \frac{4\pi a^3}{3}\sum_{j(\neq i)}(\beta\gamma_0 b_{ij} + \mathbf{f}_i\cdot\mathbf{c}_{ij}) \quad (12)$$

where the following definitions have been introduced

$$b_{ij} \equiv -\frac{5}{2}a^3\left[\frac{2}{r_{ij}^5}(\boldsymbol{\Gamma}\cdot\boldsymbol{\Gamma}):\mathbf{r}_{ij}\mathbf{r}_{ij} - \frac{5}{r_{ij}^7}(\boldsymbol{\Gamma}:\mathbf{r}_{ij}\mathbf{r}_{ij})^2\right] - 2a^5\left[\frac{1}{r_{ij}^5}(\boldsymbol{\Gamma}:\boldsymbol{\Gamma}) - \frac{10}{r_{ij}^7}(\boldsymbol{\Gamma}\cdot\boldsymbol{\Gamma}):\mathbf{r}_{ij}\mathbf{r}_{ij} + \frac{35}{2r_{ij}^9}(\boldsymbol{\Gamma}:\mathbf{r}_{ij}\mathbf{r}_{ij})^2\right]$$

$$\mathbf{c}_{ij} \equiv -\frac{1}{4\pi}\left[\frac{3}{r_{ij}^5}\boldsymbol{\Gamma}:\mathbf{r}_{ij}\mathbf{r}_{ij}\mathbf{r}_{ij} + \frac{8}{5}a^2\left(\frac{2}{r_{ij}^5}\boldsymbol{\Gamma}\cdot\mathbf{r}_{ij} - \frac{5}{r_{ij}^7}\boldsymbol{\Gamma}:\mathbf{r}_{ij}\mathbf{r}_{ij}\mathbf{r}_{ij}\right)\right]$$

$$\mathbf{d}_{ij} \equiv \frac{1}{4\pi}\left[\frac{1}{r_{ij}^3}\mathbf{r}_{ij}\mathbf{r}_{ij} + \frac{1}{r_{ij}}\mathbf{I} + \frac{2}{3}a^2\left(\frac{1}{r_{ij}^3}\mathbf{I} - \frac{3}{r_{ij}^5}\mathbf{r}_{ij}\mathbf{r}_{ij}\right)\right]$$

with $\mathbf{r}_{ij} \equiv \mathbf{r}_j - \mathbf{r}_i$ and z_i the distance of the point $\mathbf{r}_i$ from a plane midway between the two parallel plates.

Substitution of (12) into (10) will produce a quadratic expression in the $\mathbf{f}_i$ which is of the same form as (1), and which, for any configuration of the chain, constitutes an upper bound on the true rate of energy dissipation produced by the forces $\mathbf{f}_i$ in the presence of a shear stress

$$\gamma = \gamma_0 + \frac{1}{V}\boldsymbol{\Gamma}:\hat{\mathbf{z}}\sum_i \mathbf{f}_i z_i \xrightarrow[V\to\infty]{} \gamma_0 \quad (13)$$

acting on the solvent at large distances from the chain.

Before making this substitution, however, we should realize that we know neither the $\mathbf{f}_i$ nor the chain configuration, nor the relation between them. This is the problem we shall take up in the following section.

Configurational Averaging

Clearly it does not make sense to treat, as we have done so far, a particular configuration of the chain—some sort of average is called for. Since the shear stress γ is assumed to be small, it is appropriate to use the equilibrium, zero shear configurational distribution function $\Psi_e(\mathbf{r}_1, \ldots, \mathbf{r}_N)$ for this purpose. Accordingly we seek to calculate the mean rate of energy dissipation

$$\langle E\rangle \equiv \int_V\cdots\int_V E(\mathbf{r}_1, \ldots, \mathbf{r}_N;\ \mathbf{f}_1 \ldots \mathbf{f}_N)\times \Psi_e(\mathbf{r}_1, \ldots, \mathbf{r}_N)\mathrm{d}^3\mathbf{r}_1 \ldots \mathrm{d}^3\mathbf{r}_N \quad (14)$$

The forces $\mathbf{f}_i$ to be used in the expression 1 for E consist of the direct interaction between adjacent and nonadjacent beads in the chain, plus a thermodynamic contribution coming from gradients in the configurational distribution function. More usefully, we can say that the $\mathbf{f}_i$ are produced by the deviation of the actual distribution function $\Psi(r_1, \ldots, r_N)$ in a steady shear from the no-shear equilibrium form Ψ_e

$$\mathbf{f}_i = -kT\frac{\partial \ln(\Psi/\Psi_e)}{\partial\mathbf{r}_i} \xrightarrow[\gamma\to 0]{} -kT\frac{\partial\left(\frac{\Psi}{\Psi_e} - 1\right)}{\partial\mathbf{r}_i} \quad (15)$$

The distribution function Ψ satisfies a many-body diffusion equation of the type used by Kirkwood;[5] in the steady state, we have

$$0 = \sum_i\frac{\partial}{\partial\mathbf{r}_i}\cdot(\Psi\mathbf{v}_i) \xrightarrow[\gamma\to 0]{} \sum_i\frac{\partial}{\partial\mathbf{r}_i}\cdot(\Psi_e\mathbf{v}_i) \quad (16)$$

$$\mathbf{v}_i = \frac{1}{2}\frac{\partial E}{\partial\mathbf{f}_i} = \frac{1}{kT}\sum_j\mathbf{D}_{ij}\cdot\mathbf{f}_j + \mathbf{A}_i\cdot\boldsymbol{\gamma} \quad (17)$$

where $\mathbf{v}_i$ is the velocity of the ith bead.

Now let us consider the variational problem of minimizing $\langle E\rangle$ with respect to $\mathbf{f}_i$, subject to the condition

$$\mathbf{f}_i = \frac{\partial W}{\partial\mathbf{r}_i} \quad (18)$$

It is readily found that the Euler–Lagrange equation for the optimum choice of W is

$$\sum_i\sum_j\frac{\partial}{\partial\mathbf{r}_i}\cdot\left[\Psi_e\left(\frac{1}{kT}\mathbf{D}_{ij}\cdot\frac{\partial W}{\partial\mathbf{r}_j} + \mathbf{A}_i\cdot\boldsymbol{\gamma}\right)\right] = 0 \quad (19)$$

with boundary conditions

$$\frac{1}{kT}\sum_j\mathbf{D}_{ij}\cdot\frac{\partial W}{\partial\mathbf{r}_j} + \mathbf{A}_i\cdot\boldsymbol{\gamma} = 0 \ (\mathbf{r}_i \text{ on surface of } V) \quad (20)$$

Equation 19 is identical with what would have been

obtained by combining (15), (16), and (17), and making the identification

$$W = -kT\left(\frac{\Psi}{\Psi_e} - 1\right) \tag{21}$$

The boundary condition 20 merely confines each bead to the volume V.

What we have shown is that if, in place of the optimum set of $\mathbf{f}_i$, which are rather inaccessible, we choose a trial set $\mathbf{f}_i^*$ satisfying (18) for some function W^*, the resulting estimate of the mean energy dissipation rate will always be larger than the true value. This inequality will be further reinforced if, in place of using (1) to calculate E, we substitute E^* as given by (10)

$$\langle E(\mathbf{r}_1, \ldots, \mathbf{r}_N;\ \mathbf{f}_1, \ldots, \mathbf{f}_N)\rangle < \langle E^*(\mathbf{r}_1, \ldots, \mathbf{r}_N;\ \mathbf{f}_1^*, \ldots, \mathbf{f}_N^*)\rangle \tag{22}$$

Bounds on the Intrinsic Viscosity

The intrinsic viscosity is directly related to the decrease in the mean energy dissipation produced by a single polymer molecule when the applied shear stress γ is kept fixed

$$[\eta] \equiv \lim_{V\to\infty}\left(\frac{\eta - \eta_0}{\eta_0 M} V\right) = \frac{\eta_0}{\gamma^2 M}\left(\lim_{V\to\infty}\left[\frac{\gamma^2 V}{\eta_0} - \langle E\rangle\right]\right) \tag{23}$$

where $M \equiv NM_0$ is the molecular weight; eq 23 is simply a restatement of the more familiar relation $\langle E\rangle = \gamma^2 V/\eta$ between energy dissipation rate and solution viscosity. An upper bound on $\langle E\rangle$ is therefore equivalent to a lower bound on $[\eta]$, which leads to the inequality

$$[\eta] > \frac{\eta_0}{\gamma^2 M} \times \left(\lim_{V\to\infty}\left[\frac{\gamma^2 V}{\eta_0} - \langle E^*(\mathbf{r}_1, \ldots, \mathbf{r}_N;\ \mathbf{f}_1^*, \ldots, \mathbf{f}_N^*)\rangle\right]\right) \tag{24}$$

It remains to choose the trial functions $\mathbf{f}_i^*$, which means formulating an approximation W^* to the perturbation W of the configurational distribution. The simplest choice appropriate to a polymer molecule in the presence of a shear is

$$W^* = 2\pi\alpha a\gamma_0 \boldsymbol{\Gamma}:\sum_i \mathbf{s}_i\mathbf{s}_i \tag{25}$$

in which α is a variation parameter to be adjusted, like the parameter β introduced earlier, to maximize the right-hand side of (24), and

$$\mathbf{s}_i \equiv \mathbf{r}_i - \frac{1}{N}\sum_j \mathbf{r}_j$$

is the position of bead i measured from the center of mass of the chain. The resulting set of $\mathbf{f}_i^*$ is

$$\mathbf{f}_i^* = \frac{\partial W^*}{\partial \mathbf{r}_i} = 4\pi a\alpha\gamma_0 \boldsymbol{\Gamma}\cdot\mathbf{s}_i \tag{26}$$

Substituting this into (24), we find that the configurational averages of the terms appearing in E (eq 10 and 12) are considerably simplified by the isotropy of the polymer coil

$$\langle b_{ij}\rangle = 0$$

$$\boldsymbol{\Gamma}:\hat{\mathbf{z}}\sum_i\langle \mathbf{f}_i\mathbf{z}_i\rangle = \frac{2\pi a\alpha\gamma_0}{3}(\boldsymbol{\Gamma}:\boldsymbol{\Gamma})\sum_i s_i^2$$

$$\langle f_i^{*2}\rangle = \frac{16\pi^2}{3} a^2\alpha^2\gamma_0^2 \boldsymbol{\Gamma}:\boldsymbol{\Gamma}\langle \mathbf{s}_i^2\rangle$$

$$\langle(\mathbf{f}_i^* - \mathbf{f}_j^*)\cdot\mathbf{c}_{ij}\rangle = \frac{2a\alpha\gamma_0}{5}\boldsymbol{\Gamma}:\boldsymbol{\Gamma}\left\langle\frac{1}{r_{ij}}\right\rangle$$

$$\langle \mathbf{d}_{ij}:\mathbf{f}_i^*\mathbf{f}_j^*\rangle = 16\pi^2 a^2\gamma_0^2\alpha^2 \boldsymbol{\Gamma}:\langle \mathbf{s}_i\mathbf{d}_{ij}\mathbf{s}_j\rangle:\boldsymbol{\Gamma} = 16\pi^2 a^2\gamma_0^2\alpha^2 \boldsymbol{\Gamma}:\boldsymbol{\Gamma}\langle Q_{ij}\rangle \tag{27}$$

where

$$Q_{ij} \equiv \frac{1}{120\pi}\left[13\frac{\mathbf{s}_i\cdot\mathbf{s}_j}{r_{ij}} + \frac{2a^2}{3}\frac{\mathbf{s}_i\cdot\mathbf{s}_j}{r_{ij}^3} + \frac{\mathbf{s}_i\mathbf{s}_j:\mathbf{r}_{ij}\mathbf{r}_{ij}}{r_{ij}^3} - 2a^2\frac{\mathbf{s}_i\mathbf{s}_j:\mathbf{r}_{ij}\mathbf{r}_{ij}}{r_{ij}^5}\right]$$

The last term in (10) is somewhat more difficult to average, but, according to Schwartz's inequality, it may be replaced by

$$-\frac{3}{4\pi a^3 N}\sum_i\sum_j\left(\left\langle\int_{V-\Omega'}\mathfrak{d}_i d^3\mathbf{r}\right\rangle:\left\langle\int_{V-\Omega'}\mathfrak{d}_j d^3\mathbf{r}\right\rangle\right) = -\frac{4\pi\gamma_0^2\alpha^2 a^5}{75N}(\boldsymbol{\Gamma}:\boldsymbol{\Gamma})\left(\sum_{i\neq k}\sum\left\langle\frac{1}{r_{ik}}\right\rangle\right)^2 \geq -\frac{3}{4\pi a^3 N}\sum_i\sum_j\left\langle\int_{V-\Omega'}\mathfrak{d}_i d^3\mathbf{r}:\int_{V-\Omega'}\mathfrak{d}_j d^3\mathbf{r}\right\rangle \tag{28}$$

without affecting the validity of our bounds. Upon minimizing with respect to the parameters α and β, we arrive at our final result

$$[\eta] > \frac{4\pi a^3}{3M_0} \times \left[\frac{5}{2} + \frac{\left(\frac{7}{10}(N-1)\xi^{-1} - R^2\right)^2}{\frac{4}{3}R^2 + 12\pi(N-1)q - \frac{(N-1)^2}{10}\xi^{-2}}\right] \tag{29}$$

where the quantities

$$R \equiv \left[\frac{1}{Na^2}\sum_i\langle s_i^2\rangle\right]^{1/2}$$

$$\xi \equiv \left[\frac{a}{N(N-1)}\sum_{i\neq j}\sum\left\langle\frac{1}{r_{ij}}\right\rangle\right]^{-1}$$

$$q \equiv \frac{1}{N(N-1)a}\sum_{i\neq j}\sum\langle Q_{ij}\rangle$$

are reduced lengths representing various combinations of mean coil dimensions (for example Ra is the root-mean-square radius of gyration).

A simpler (though poorer) bound may be obtained from (9) by replacing Ω' with V, setting β equal to zero, and optimizing with respect to α alone

$$[\eta] > \frac{\pi a^3}{M_0}\left[\frac{R^4}{R^2 + 9\pi(N-1)q}\right] \tag{30}$$

Two Examples

Up to this point we have not introduced any assumptions beyond those listed in the introduction; the inequalities 29 and 30 are rigorous consequences of the hydrodynamic diffusion model which was used. To proceed further, we must calculate the averages R, ξ, and q. Essentially there are two choices: either we assume a rigid collection of beads so that each r_{ij} can be specified individually, or we make an approximation which will allow us to treat the system in which we are really interested, the random coil polymer. In what follows we shall give one example of each type.

A. Dumbbells. This is certainly the simplest model to which our inequalities can be applied, and may even be broadened somewhat by allowing the distance r between the two spheres to vary (though always subject to the restriction $r \equiv r_{12} \geq 2a$). For variable r we obtain

$$R^2 = \frac{1}{4a^2}\langle r^2\rangle \qquad \xi = \frac{1}{2a}\left(\left\langle\frac{1}{r}\right\rangle\right)^{-1}$$

$$q = \frac{1}{120\pi}\left(\frac{1}{3}a\left\langle\frac{1}{r}\right\rangle - \frac{7}{2a}\langle r\rangle\right) \tag{31}$$

The inequality 29 thus becomes

$$[\eta] > \frac{4\pi a^3}{3M_0} \times \left[\frac{5}{2} + \frac{\left(\frac{7a}{5}\left\langle\frac{1}{r}\right\rangle - \frac{1}{4a^2}\langle r^2\rangle\right)^2}{\frac{1}{3a^2}\langle r^2\rangle + \frac{a}{30}\left\langle\frac{1}{r}\right\rangle - \frac{7}{20a}\langle r\rangle - \frac{2a^2}{5}\left\langle\frac{1}{r}\right\rangle^2}\right] \tag{32}$$

while (30) gives the simpler bound

$$[\eta] > \frac{\pi a}{4M_0}\langle r^2\rangle\left[1 + \frac{a^2}{10\langle r^2\rangle}\left(a\left\langle\frac{1}{r}\right\rangle - \frac{21}{2a}\langle r\rangle\right)\right]^{-1} \tag{32a}$$

If the two spheres are in contact, so that $R = 1$, (32) and (32a) reduce to

$$\frac{3M_0}{4\pi a^3}[\eta] > 2.66 \quad \text{and} \quad \frac{3M_0}{4\pi a^3}[\eta] > 1.54$$

respectively. On the other hand, if R becomes large, (32) and (32a) converge to the same result

$$[\eta] > \frac{\pi a}{4M_0}\langle r^2\rangle$$

which is the correct intrinsic viscosity in the absence of hydrodynamic interaction.

B. Looped Polymer Chains. To avoid extraneous complications, we shall consider, in place of the usual linear polymer, a chain molecule whose two ends have been joined to one another; this has the advantage that all beads are now equivalent and do not have to be distinguished according to their position along the chain.

In order to estimate q, we now propose the approximation that the equilibrium joint distribution function for the positions of any two beads relative to the center of mass may be written in the form

$$P(\mathbf{s}_i,\mathbf{s}_j) \cong g\left(\frac{\mathbf{s}_i + \mathbf{s}_j}{2}\right)h(\mathbf{r}_{ij}) \tag{33}$$

In other words, we are taking $(\mathbf{s}_i + \mathbf{s}_j)/2$ and $\mathbf{r}_{ij} \equiv (\mathbf{s}_i - \mathbf{s}_j)$ to be independent random variables. In defense of this assumption, it may be pointed out that it is perfectly correct for a loop whose configurational distribution follows Gaussian statistics (the average $\langle(\mathbf{s}_i + \mathbf{s}_j)\mathbf{r}_{ij}\rangle$ vanishes for a looped chain); whether it continues to hold reasonably well even when excluded volume effects and other non-Gaussian interactions between the beads are present is, of course, another question.

If we allow (33), the average q is easily reduced to

$$q \cong \frac{1}{9\pi}\left(\frac{R^2}{\xi} - \frac{1}{4}\xi - \frac{21}{80}\mu + \frac{1}{40\xi}\right) \tag{34}$$

where

$$\zeta \equiv \frac{1}{N(N-1)a}\sum\sum_{i\neq j}\left(\left\langle\frac{1}{r_{ij}}\right\rangle\langle r_{ij}^2\rangle\right)$$

$$\mu \equiv \frac{1}{N(N-1)a}\sum\sum_{i\neq j}\langle r_{ij}\rangle$$

If we go beyond (33) and assume a completely Gaussian distribution function, the reduced lengths ζ, R, and ξ are

$$\zeta = 3\mu/2 = (3\pi N/32)^{1/2}l/a$$

$$R = (N/12)^{1/2}l/a \tag{35}$$

$$\xi = (N/6\pi)^{1/2}l/a$$

where l is the root-mean-square distance between adjacent beads. Actually, since no two beads may overlap, the Gaussian distribution, which imposes no such restriction, is acceptable only if configurations with overlapping beads are very improbable. A crude estimate of the number of overlapped beads to be expected in an N-bead Gaussian chain gives the order of magnitude $N^2a^3/2R^3$, or $12^{3/2}N^{1/2}a^3/2l^3$, and for this to be small compared to unity requires

$$\frac{l}{a} \gg 2.7N^{1/2} \tag{36}$$

If (36) is satisfied, there is no point, for large N, in going beyond inequality 30, since the improvement made by using (29) instead becomes negligible in this limit. For the Gaussian loop, (30) gives

$$[\eta] > \frac{\pi a l^2}{12M_0}\left[\frac{N}{1 + 1.55N^{1/2}a/l}\right] \tag{37}$$

Comparison with Other Theories

For a single bead ($N = 1$), the bound 29 becomes $(2.5)(4\pi a^3/3M_0)$, which is just the familiar Einstein result; the bound 30 simply goes to zero. The reason is not hard to see: the trial stress which leads to (30) contains only Stokes contributions of the form $\boldsymbol{\sigma}^{(S)}$; using (30) to estimate $[\eta]$ takes into account the forces $\mathbf{f}_i$ acting on the beads, but not the disturbance which a given bead can produce in the shear flow even in the absence of such forces. The right-hand side of (30) thus resembles the expressions for $[\eta]$ derived by many authors for high-molecular-weight polymers.

At lower molecular weights, the difference between (29) and (30) becomes sufficiently important to make the added complexity of the former worthwhile, as illustrated by example A of the preceding section. To get a rough idea of how good an estimate 29 might be expected to provide in such cases, we may compare the Einstein factor of 2.66 it predicts for two spheres in contact to the value 2.91 given by Kuhn and Kuhn[8] for an elongated ellipsoid of revolution with an axis ratio of 2.

As N becomes large, (29) may be replaced by (30) with negligible effect. The most natural comparison here is with the Kirkwood–Riseman (KR) theory, since it is based on the same general model. As we shall see below, the choice of the trial function 26 precludes a direct test of this kind. However, we can argue that the chief approximation of the KR treatment lies in the substitution of the "preaveraged" diffusion tensor

$$\langle \mathbf{d}_{ij} \rangle = \frac{1}{3\pi}\left\langle \frac{1}{r_{ij}} \right\rangle \mathbf{I} \tag{38}$$

for $\mathbf{d}_{ij}$ itself. In our calculation, we therefore replace $\langle \mathbf{s}_i \mathbf{d}_{ij} \mathbf{s}_j \rangle$ in (27) by $\langle \mathbf{s}_i \langle \mathbf{d}_{ij} \rangle \mathbf{s}_j \rangle$; inserted into (30), this gives the estimate

$$q_{\text{preav.}} = \frac{1}{9\pi}\left(\frac{R^2}{\xi} - \frac{1}{2}\zeta\right) \tag{39}$$

for the second term in the denominator, to be compared with the value given by eq 34, which was obtained from the more reasonable assumption 33. For the Gaussian loop, for which (33) is strictly valid, the resulting estimate for $[\eta]$ is

$$[\eta]_{\text{preav.}} = \frac{\pi a l^2}{12M_0}\left[\frac{N}{1 + 1.07N^{1/2}a/l}\right] \tag{40}$$

when N and l/a are large. This result lies above the lower bound 37 and cannot therefore be ruled out on the basis of that inequality; nevertheless comparison of (40) to (37) seems a reasonable, though far from conclusive, test of the effect of preaveraging.

The trial function 26 may be generalized by setting

$$\mathbf{f}_i^* = 4\pi a \alpha \gamma_0 \sum_m \lambda_{im} \boldsymbol{\Gamma} \cdot \mathbf{s}_m \tag{41}$$

where the coefficients λ_{im} are to be treated as variational parameters, subject to the restrictions

$$\sum_i \lambda_{im} = 1; \quad \lambda_{im} = \lambda_{mi} \tag{42}$$

which ensure that condition 18 is satisfied. Repeating the steps which led to (30) now gives the bound

$$[\eta] > \frac{\pi a^3}{M} \frac{\left(\sum_i \sum_m \lambda_{im} R_{im}\right)^2}{\sum_i \sum_m \sum_n \lambda_{im}\lambda_{in} R_{mn} + 9\pi \sum_{i \neq j} \sum_m \sum_n \lambda_{im}\lambda_{jn} q_{mijn}} \tag{43}$$

where

$$R_{mn} \equiv \langle \mathbf{s}_m \cdot \mathbf{s}_n \rangle / a^2$$

$$q_{mijn} \equiv \frac{1}{30a}\left(\langle \mathbf{s}_m \cdot \mathbf{d}_{ij} \cdot \mathbf{s}_n \rangle + 3\langle \mathbf{s}_m \cdot \mathbf{s}_n \operatorname{tr} \mathbf{d}_{ij} \rangle\right)$$

If we choose λ_{im} to be the Kronecker delta, (43) reduces to (30). The KR result is obtained by replacing d_{ij} by $\langle d_{ij} \rangle$ in the definition of q_{mijn}, and then maximizing the right-hand side of (43) with respect to the λ_{im} without regard to (42); taking (42) into account produces the intrinsic viscosity as given by Zimm.[9]

A perturbation approach which avoids preaveraging has been developed by Pyun and Fixman (PF).[10] Although their result is expressed in terms of the same averages as those which appear in (43), the relationship between the two treatments is not entirely clear at this time. Very roughly, PF theory corresponds to choosing the $\mathbf{f}_i^*$ to be the forces calculated in the free draining limit.

To understand the relation of our treatment to the Debye porous sphere (PS) model, we consider a W^* of the form

$$W^* = \boldsymbol{\Gamma} : \sum_i \omega(s_i) \mathbf{s}_i \mathbf{s}_i \tag{44}$$

to obtain

(8) W. Kuhn and H. Kuhn, *Helv. Chim. Acta*, **28**, 97 (1945).
(9) B. H. Zimm, *J. Chem. Phys.*, **24**, 269 (1956).
(10) C. W. Pyun and M. Fixman, *ibid.*, **42**, 3838 (1965).

$$\mathbf{f}_i^* = \frac{\partial W^*}{\partial \mathbf{r}_i} = \boldsymbol{\Gamma}\cdot\left(2\omega(s_i)\mathbf{s}_i + \frac{1}{s_i}\frac{\mathrm{d}\omega}{\mathrm{d}s_i}\mathbf{s}_i\mathbf{s}_i\mathbf{s}_i\right) - \frac{1}{N}\boldsymbol{\Gamma}\cdot\sum_j\left(2\omega(s_j)\mathbf{s}_j + \frac{1}{s_j}\frac{\mathrm{d}\omega}{\mathrm{d}s_j}\mathbf{s}_j\mathbf{s}_j\mathbf{s}_j\right) \quad (45)$$

The trial function 26 corresponds to setting the function ω equal to a constant; maximization of the lower bound 24 to obtain the optimum $\mathbf{s}$ dependence of ω may thus be expected to produce an improved value for the intrinsic viscosity.

The sum appearing in the second term of (45) causes $\mathbf{f}_i^*$ to depend on $\mathbf{s}_1, \ldots, \mathbf{s}_N$ rather than on $\mathbf{s}_i$ alone, which makes the use of such a trial function exceedingly awkward in practice. The difficulty disappears if we restrict ourselves to configurations of beads having a center of inversion, since the sum in (45) will then vanish identically (this is not, of course, a realistic assumption for a polymer chain, except perhaps in an average sense). The PS model corresponds to making this simplification and postulating a distribution function W_e such that (33) is replaced by

$$P(\mathbf{s}_i,\mathbf{s}_j) = \begin{cases}\left(\frac{3}{4\pi a^3R^3}\right)^2 & (s_i < R,\ s_j < R)\\ 0 & \text{otherwise}\end{cases}$$

If this is inserted into (24) and the Einstein stress contributions are eliminated by setting the parameter β equal to zero, optimization with respect to the function ω becomes equivalent to solving the creeping flow Navier–Stokes equations for a uniform porous sphere of radius aR in a shear flow; the result obtained will be the value of $[\eta]$ given by Debye.

Debye's theory is thus a rigorous development of the PS model, but the relation between the model and the actual system is unclear—setting the radius of the sphere equal to the radius of gyration of the polymer molecule is an entirely arbitrary decision. The KR treatment, in seeking to avoid this difficulty, makes a number of approximations, of which the most serious is the use of a preaveraged diffusion tensor. In the calculation of polymer friction coefficients, the preaveraging procedure could be somewhat justified by showing it to be equivalent to the choice of a trial set of forces $\mathbf{f}_i$ which were independent of position.[4] No such possibility seems to exist in the presence of a shear—even the simplest choice for the $\mathbf{f}_i$, the trial function 26, introduces position dependence.

At high molecular weights, the results 37 and 40 suggest that preaveraging raises the calculated intrinsic viscosity by about 50%; this conclusion has also been reached by Pyun and Fixman for straight chains although they estimated the effect at only 5%. Application of KR theory to looped chains has been carried out by Bloomfield and Zimm,[11] and the PF calculation for these systems has been performed by Fukatsu and Kurata.[12] For Gaussian loops, the KR result, in the limit of large N, is $[\eta] = 0.31N^{1/2}l^3/M$, while the PF result is again only slightly lower, the numerical coefficient being reduced to 0.29. The corresponding figures given by the large N limit of (30) are 0.25 with preaveraging (eq 40), and 0.17 if preaveraging is avoided (inequality 37). Thus preliminary indications are that preaveraging the diffusion tensor has a larger effect on $[\eta]$ than does using the simplified trial function 26 in place of (41); however, optimization of the inequality (43) would provide a more conclusive test of this statement.

Conclusion

Although some examples have been worked out for illustration purposes, the main result of this paper is the inequality 29, which is a rigorous consequence of the N-bead model of a polymer chain described in the Introduction. Regarded as an estimate of the intrinsic viscosity, (29) appears to give reasonable results for all N, from 1 to ∞. For a true test of the theory, one needs values for the parameters R, ξ, and q, obtained from an equilibrium distribution function which takes excluded volume effects and other forces acting between polymer segments into account. Although R and ξ should be accessible through light scattering measurements, since only pair distributions are involved, evaluation of q requires the probability $w(\mathbf{s},\mathbf{s}')\mathrm{d}\mathbf{s}\mathrm{d}\mathbf{s}'$ that, if the center of mass is taken as the origin, there are two chain segments located in volume elements $\mathrm{d}\mathbf{s}$ and $\mathrm{d}\mathbf{s}'$ at $\mathbf{s}$ and $\mathbf{s}'$; because $\mathbf{s}$ and $\mathbf{s}'$ are measured from the center of mass, w is essentially a three-segment distribution and so not obtainable by the usual optical methods. For polymers of modest size, say up to $N = 10$ or so, it should, however, be possible to obtain even q by computer simulation,[8] and it is probably in this direction that tests of the inequality 29 must be sought.

(11) V. Bloomfield and B. H. Zimm, *J. Chem. Phys.*, **44**, 315 (1966).
(12) M. Fukatsu and M. Kurata, *ibid.*, **44**, 4539 (1966).

Anion Exchange in Mixed Organic–Aqueous Solutions. I. Dioxane–Water[1]

by C. H. Jensen[2] and R. M. Diamond*

Lawrence Radiation Laboratory, University of California, Berkeley, California 94720 *(Received April 6, 1970)*

Publication costs assisted by the U. S. Atomic Energy Commission

The idea, developed earlier, that ion-exchange resin selectivity occurs as the result of a competition of the exchanging ions for that phase providing the best solvation, a competition won by the ion most in need of solvation (usually that ion with the highest charge density, the most acidic cation, or the most basic anion), has been applied to the water–dioxane system. Usually, the dilute external aqueous phase provides the better solvating medium, so the smaller ion, or for ions of different structure the more basic anion, goes there, relegating the losing ion to the resin phase. But as dioxane replaces water, the mixed external solution becomes a poorer solvating agent, and since the resin phase preferentially takes up water, the latter becomes relatively a better solvating phase. Thus the ion most in need of solvation decreasingly prefers the external solution; separation factors should get smaller, and this is what is observed experimentally. In fact, by properly choosing the nature of the macro-electrolyte and of the resin group, the normal aqueous-phase selectivity order of the halides can be reversed in dioxane–water mixtures.

Introduction

Earlier papers[3–5] have discussed the selectivity shown by (organic) ion-exchange resins with dilute aqueous solutions as a competition between the exchanging ions for solvation in the resin phase and in the external phase. Water molecules usually provide the main means of ionic solvation, and so for the usual conditions of a dilute external solution and a (concentrated) resin phase with strongly acidic or basic exchange groups, the external solution furnishes the most favorable medium. That ion whose need for solvation is the more urgent, that is, will yield the larger free energy of solvation, goes into that phase which provides the better solvation, and so forces the remaining ion into the other phase even though the latter ion also would obtain a larger free energy of solvation in the better-solvating phase. For example, with a family of similar ions such as the halides, the smallest ion goes into the aqueous phase and the largest ion is pushed into the resin phase, thus achieving a maximum hydration energy and a minimum free energy for the system as a whole, even though the larger ion is not achieving optimum solvation. For still larger monovalent anions such as ReO_4^- and $AuCl_4^-$, it has also been suggested[3–5] that this selectivity order is further enhanced by an entropy effect; the very large ions tend to tighten up the water structure surrounding them in the same way that (hydrophobic) molecules do. That is, the neighboring water molecules tend to hydrogen-bond out to each other rather than in to the large ion, and the zone of the "thawed" water existing around smaller ions, a disordered region in which water molecules can bond either in to the ion (or to the ions' hydration shell) or out to "ordinary" bulk water molecules,[6,7] disappears. Since this effect would be reduced in the less-structured water of the (concentrated) resin phase, large ions would tend to be still further squeezed out of the aqueous solution into the resin phase by such an entropy change, in addition to the effect of optimizing the heat of hydration. Evidence for such behavior is shown by the corresponding case of the large tetraalkylammonium cations in cation exchange where, in fact, it has been shown[8] that the replacement of Na^+ by NPr_4^+ or NBu_4^+ occurs because of a large positive ΔS and in spite of a positive ΔH.

Thus the dilute solution anion-exchange selectivity order expected for the halides and ReO_4^- would be $F^- < Cl^- < Br^- < I^- < ReO_4^-$, and this is indeed observed. Furthermore, it has been possible to affect this order in a predictable way by changing the nature of the exchange group and by substituting various concentrated solutions for the dilute external phase.[4] In this paper we want to consider the situation where the water in the system is partially replaced with an organic solvent which does not solvate anions very well but is miscible with water. Dioxane was chosen for this first study.

Experimental Section

Reagents. The anion-exchange resins used were Dowex 1-X4, 100–200 mesh, a strong-base resin with a

(1) Work supported under the auspices of the U. S. Atomic Energy Commission.

(2) Summer visitor, 1965, 1967, NSF College Teachers Research Participation Program, Cabrillo College, Aptos, California.

(3) B. Chu, D. C. Whitney, and R. M. Diamond, *J. Inorg. Nucl. Chem.*, **24**, 1405 (1962).

(4) C. H. Jensen and R. M. Diamond, *J. Phys. Chem.*, **69**, 3440 (1965).

(5) R. M. Diamond and D. C. Whitney in "Ion Exchange," Vol. 1, J. Marinsky, Ed., M. Dekker, New York, N. Y., 1966, pp 277–351.

(6) H. S. Frank and M. W. Evans, *J. Chem. Phys.*, **13**, 507 (1945).

(7) R. M. Diamond, *J. Phys. Chem.*, **67**, 2513 (1967).

(8) G. E. Boyd and Q. V. Larson, *J. Amer. Chem. Soc.*, **89**, 6038 (1967).

polystyrene matrix, and Dowex 3-X4, 100–200 mesh, a weak-base resin having as functional groups a mixture of primary, secondary, and tertiary amino groups. The capacity and water uptake of the Dowex 1 were 4.04 mequiv and 1.73 g, respectively/g of dry Cl^--form resin, and the corresponding figures for the Dowex 3 were 5.5 mequiv and 0.58 g/g of dry Cl^-- form resin. The solutions of LiCl, and $N(CH_3)_4Cl$ were prepared by volumetric dilution with conductivity water of analyzed stock solutions of reagent grade materials. The $^{18}F^-$ tracer was prepared at the Lawrence Radiation Laboratory 88-in. cyclotron from conductivity water by the nuclear reaction $^{16}O(\alpha,d)^{18}F$. The $^{82}Br^-$ was prepared by neutron irradiation of reagent grade LiBr at the Vallecitos Reactor. The $^{131}I^-$ tracer (carrier-free in Na_2SO_3) was purchased from New England Nuclear Corp. The carrier-free $^{183-184}ReO_4^-$ was chemically extracted from a tungsten deflector plate which had been subject to α and d bombardment over an extended period of time at the 88-in. cyclotron.

Procedure. Batch measurements were made with all tracer anions by placing weighed samples (0.1000–0.3500 g) of resin and 10.0 or 20.0 ml of solution of known tracer content into 30-ml polyethylene screw-cap bottles and shaking for at least 6 hr. Two 2.00-ml aliquots of solution were removed through filter paper and γ-counted using a well-type NaI(Tl) scintillation counter with single-channel analysis. Samples of the stock solution were also counted to give the initial tracer activity. After correction for background count, and for the moisture contained in the resins at 47% humidity (all resin used in the batch measurements was weighed at 47% humidity), the distribution coefficient was calculated in the usual way

$$D = \frac{\left\{[(\text{counts/min})_{\text{initial}} - (\text{counts/min})_{\text{equil}}]/\left(\text{g of dry } Cl^-\text{-form resin}\right)\right\}}{(\text{counts/min})_{\text{equil}}/\text{ml of solution}}$$

All experimental work was done at room temperature, 23 ± 2°.

The ion-invasion into the Dowex 1-X4 by the LiCl was determined at various concentrations of dioxane. Three small columns were each filled with 1 g of resin at 47% humidity (17.3% H_2O). The columns were washed with the dioxane–water–lithium chloride solution until equilibrium was established and were then placed in a centrifuge for 5 min to remove excess liquid. The columns were then washed with distilled water to remove all trace of LiCl and the Cl^- was titrated by the Fajans method. The quantity of LiCl adhering to the outside surface of the resin was estimated by repeating the above procedure using a volume of glass beads of 170–230 mesh equal to that of the resin.

The uptake of dioxane–water by the resin at various concentrations was determined in the following manner. A weighed amount of dry resin and a weighed amount of solution of known composition were placed in a 2-ml volumetric flask and shaken for about 8 hr to reach equilibrium. The solution was then filtered through a small polyethylene filter by centrifugation and weighed. (A correction was made for solution caught in the filter and adhering to the walls.) The concentration (mole fraction dioxane) of the solution before and after equilibrium was determined by measuring its index of refraction with a Bausch and Lomb Abbé refractometer. From these data, the weight and composition of the solution taken up by the resin were calculated.

Results

A plot of the resin-phase composition (dioxane mole fraction) for the Dowex 1-X4 resin *vs.* the equilibrium external-phase dioxane mole fraction is shown in Figure 1. A plot of the LiCl resin invasion in meq of Cl^-/g of dry Cl^--form resin *vs.* the equilibrium external-phase dioxane mole fraction for the Dowex 1-X4 resin with a constant concentration of 0.0104 *M* LiCl in the external solution is shown in Figure 2. Figures 3–5 show the distribution ratio

$$D = \frac{\text{mequiv/g of dry } Cl^-\text{-form resin}}{\text{mequiv/ml of solution}}$$

for tracer F^-, Br^-, I^-, and ReO_4^- as a function of the dioxane mole fraction with LiCl of 0.0104 *M* (Figure 3), 0.0311 *M* (Figure 4), and 0.104 *M* (Figure 5) as the macro-electrolyte in the external phase. Similarly, Figures 6–8 show *D* for the same tracers as a function of the dioxane mole fraction with $N(CH_3)_4Cl$ of 0.0101 *M* (Figure 6), 0.0303 *M* (Figure 7), and 0.101 *M* (Figure 8) as the macro-electrolyte in the external phase. Finally, Figures 9 and 10 give examples of the results obtained with the weak-base resin Dowex 3-X4. A plot of *D* for tracer Br^-, I^-, and ReO_4^- *vs.* dioxane mole fraction in the external phase is shown in Figure 9 for 0.0104 *M* LiCl and in Figure 10 for 0.0101 *M* $N(CH_3)_4Cl$.

Discussion

The partial replacement of water in an aqueous solution by dioxane will certainly have at least three effects. First of all, since the cyclic ether dioxane

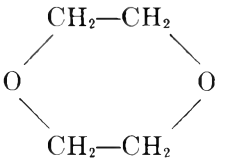

does not possess any (acidic) hydrogen capable of hydrogen-bonding to (basic) anions, as does the water molecule, the mixed solvent will become a poorer and poorer solvating agent for anions. That is, if we can think of single-ion activity coefficients, these will rise steeply for anions with an increase in dioxane content,[9]

(9) E. Grunwald, G. Baughman, and G. Kohnstam, *J. Amer. Chem. Soc.*, 82, 5801 (1960).

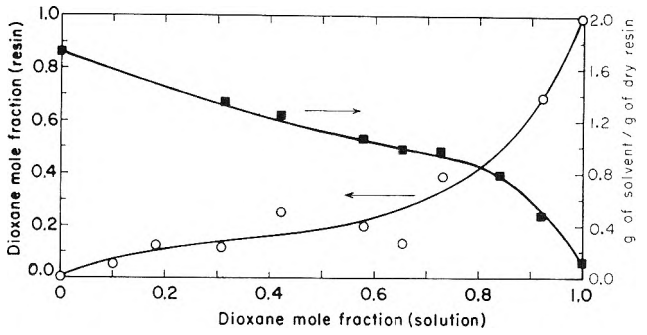

Figure 1. The mole fraction of dioxane in the resin phase and the total weight of solvent (dioxane + water) uptake per gram of dry resin for Dowex 1-X4 *vs.* the mole fraction of dioxane in the equilibrium solution.

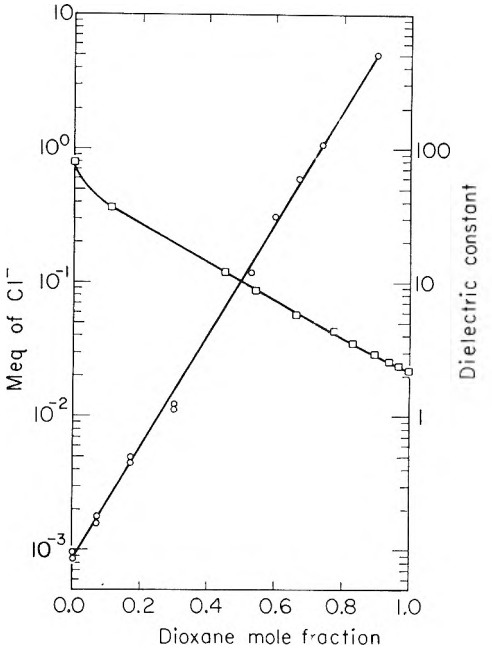

Figure 2. Nonexchange or resin-invasion electrolyte in Dowex 1-X4 resin from 0.0104 *M* LiCl solutions of dioxane–water *vs.* the mole fraction of dioxane (disregarding the LiCl) in the equilibrium solution. The left-hand ordinate scale is in mequiv of Cl^-/g of dry Cl^--form resin; the resin capacity is 4.04 mequiv/g of dry Cl^--form resin. Also shown is a plot of the dielectric constant of a dioxane–water solution *vs.* the dioxane mole fraction; the ordinate is to be read off the right-hand scale.

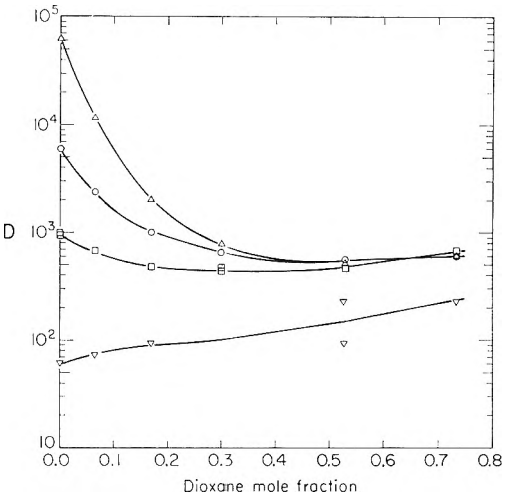

Figure 3. Plot of *D vs.* dioxane mole fraction in the solution for 0.0104 *M* LiCl and Dowex 1-X4 resin and the tracer anion: F^-, ▽; Br^-, □; I^-, ○; and ReO_4^-, △.

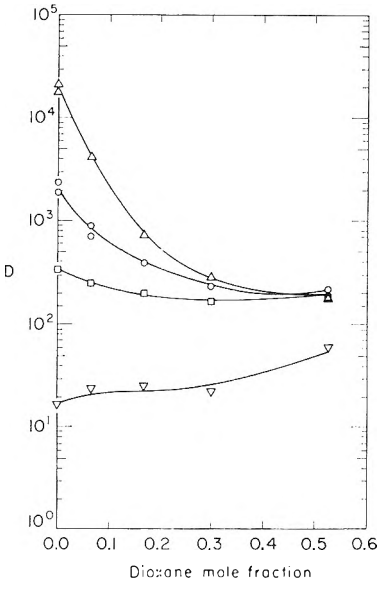

Figure 4. Plot of *D vs.* dioxane mole fraction in the solution for 0.0311 *M* LiCl and Dowex 1-X4 resin and the same tracer anions as in Figure 3.

and the more so, the smaller and/or more basic the anion. Secondly, the dioxane molecule will act as a base toward the water molecule, competing with the anions for hydrogen-bonding to the water, and breaking up the hydrogen-bonded water structure. Finally, the addition of dioxane, because of its low dielectric constant and because of the destruction of the water structure, will cause an increasingly marked drop in the dielectric constant of the mixed solvent.[10] (This is shown in Figure 2.) For all of these reasons, the dioxane solution provides a much poorer solvating medium for anions than the original water solution, both chemically (through bonding to the anions) and electrostatically (through the effect of the lower dielectric constant in raising the electrostatic free energy of the ions), and the effect is more marked the higher the basicity and charge density of the anion. The results of this poorer solvating ability have been remarked on by a number of workers.[9,11]

But obviously then, to be able to predict the effect of dioxane on the selectivity order of a family of anions, one must first determine the distribution of dioxane between the resin phase and the external solu-

(10) C. A. Kraus and R. M. Fuoss, *J. Amer. Chem. Soc.*, **55**, 21 (1933).
(11) D. Feakins and D. J. Turner, *J. Chem. Soc.*, 4986 (1965).

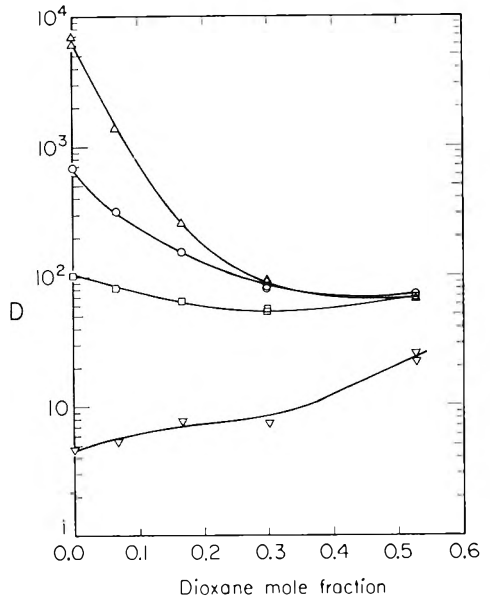

Figure 5. Plot of D *vs.* dioxane mole fraction in the solution for 0.104 M LiCl and Dowex 1-X4 resin and the same tracer anions as in Figure 3.

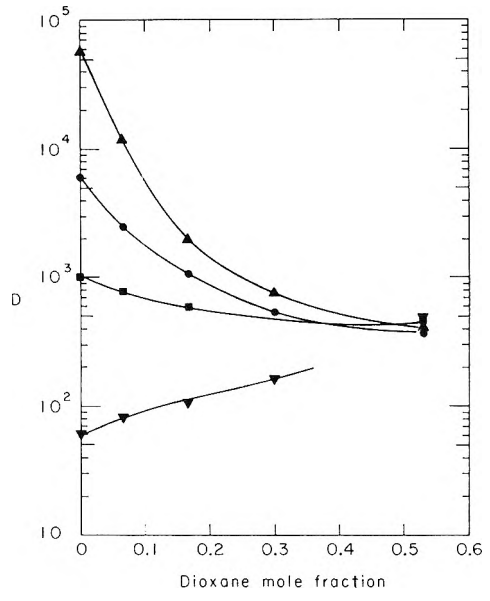

Figure 6. Plot of D *vs.* dioxane mole fraction in the solution for 0.0101 M $(CH_3)_4$ NCl and Dowex 1-X4 resin and the same tracer anions as in Figure 3.

tion. Figure 1 shows that with Dowex 1-X4, Cl^--form, the resin phase preferentially rejects dioxane and takes up water. Up to an external solution dioxane mole fraction of 0.8, the resin-phase dioxane mole fraction is only $^1/_2$ to $^1/_3$ that of the equilibrium solution. This behavior seems to be usual for most anion resins and for most of the mixed solutions studied, but not all.[12-16] Why should this be so? We do not know the answer in detail, but surely this is a combination of the hydration needs of the ions in the concentrated resin phase, and an electrostatic effect of the high-charge density there.

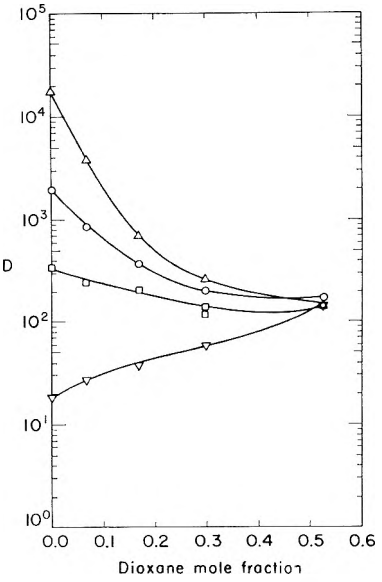

Figure 7. Plot of D *vs.* dioxane mole fraction in the solution for 0.0303 M $(CH_3)_4NCl$ and Dowex 1-X4 resin and the same tracer anions as in Figure 3.

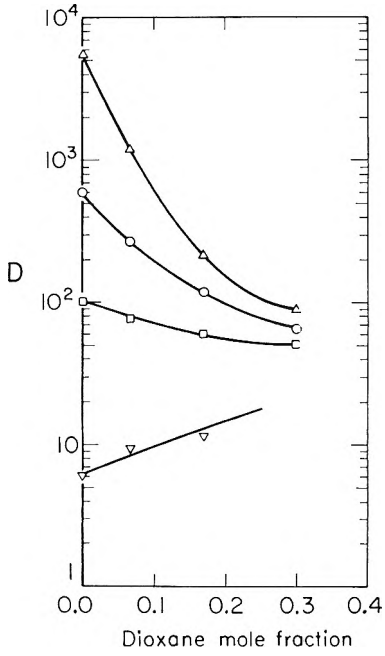

Figure 8. Plot of D *vs.* dioxane mole fraction in the solution for 0.101 M $(CH_3)_4$ NCl and Dowex 1-X4 resin and the same tracer anions as in Figure 3.

The first part of the previous sentence is obvious; the second part perhaps needs further explanation. The

(12) H. P. Gregor, D. Nobel, and M. H. Gottlieb, *J. Phys. Chem.*, **59**, 10 (1955).

(13) O. D. Bonner and J. C. Moorefield, *ibid.*, **58**, 555 (1954).

(14) C. W. Davies and B. D. R. Owen, *J. Chem. Soc.*, 1676 (1956).

(15) H. Rückert and O. Samuelson, *Acta Chem. Scand.*, **11**, 303 (1957).

(16) Y. Marcus and J. Naveh, *J. Phys. Chem.*, **73**, 591 (1969).

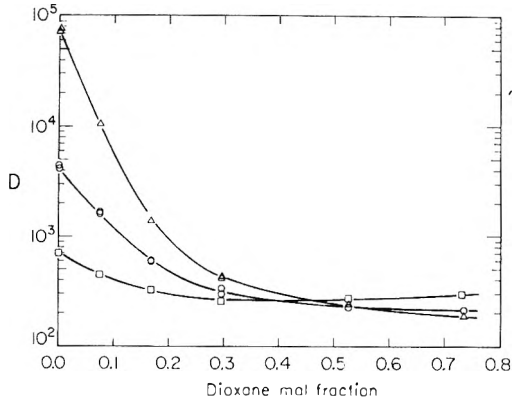

Figure 9. Plot of D *vs.* dioxane mole fraction in the solution for 0.0104 M LiCl and Dowex 3-X4 resin and the tracer anions: Br^-, □; I^-, ○; and ReO_4^-, △.

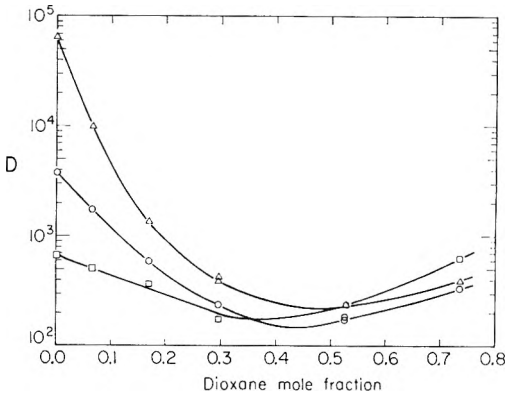

Figure 10. Plot of D *vs.* dioxane mole fraction in the solution for 0.0101 M $(CH_3)_4NCl$ and Dowex 3-X4 resin and the same tracer anions as in Figure 9.

addition of dioxane results in a lowering of the dielectric constant of the mixture. But the resin phase, with its high density of charge, both fixed resin sites and mobile counter ions, will have a much larger increase in electrostatic free energy with lowering of the dielectric constant than will the much more dilute external phase. To keep the total system free energy at a minimum value, water must preferentially go into that phase with the highest concentration of charge to provide electrostatic (but not necessarily chemical) solvation. However, all of this water is not likely chemically bound directly to the quaternary alkyl ammonium ions of the resin, but still has some freedom to solvate chemically the counterions. Thus, as the concentration of dioxane in the total system increases, the resin phase absorbs a higher proportion of water than exists in the external solution, and the superiority of the external phase over the resin phase for solvating anions decreases.

With water alone as the solvent medium, anions will obtain the best solvation in the dilute external phase and so will go into that phase in the order of their size or basicity, resulting in the resin selectivity order $F^- < Cl^- < Br^- < I^- < ReO_4^-$. But as dioxane is added to the system, the external solution becomes increasingly richer in dioxane compared to the resin phase, and so less desirable to the (smaller) anions with the greater need for solvation. They are held less tightly in the external phase, and so the degree of separation or selectivity among the anions should decrease.

This is precisely the behavior observed with Dowex 1 with 0.0104, 0.0311, and 0.104 M LiCl as the macroelectrolyte and with F^-, Br^-, I^-, and ReO_4^- tracers, Figures 3–5. The values of D for ReO_4^- and F^- from water solution differ by more than 1000, but with 20% mole fraction dioxane this ratio has decreased to about 15 and by 50% mole fraction to about 3.

Thus, it seems that the expectations based on the suggested model have been fulfilled. Actually, of course, other factors must also be taken into account with the addition of dioxane to the system. Two of the most important of these are (A) the increase of nonexchange or "resin-invasion" electrolyte, and (B) the occurrence of ion pairing in the system with the decrease in dielectric constant.

A. Because of the high concentration of charge sites on the resin matrix, most co-ions are excluded from the resin phase (the Donnan potential).[17,18] But as dioxane is added, the activity of the ions increases greatly. (The solubility of LiCl in dioxane is of the order of 100 times lower than in water.) Therefore, nonexchange electrolyte increasingly distributes into the resin phase of proportionately greater water content than the external solution. In addition, the occurrence of ion pairing (see *B*, below) also promotes resin invasion, as an ion pair, being electrically neutral, can distribute into the resin phase without much hindrance from the Donnan potential. The result is illustrated in Figure 2 where the nonexchange electrolyte in mequiv of Cl^-/g of dry Cl^--form resin is plotted *vs.* dioxane mole fraction in the external phase of 0.0104 M LiCl. It can be seen that with increasing dioxane content the amount of LiCl in the resin phase increases enormously, going from $\sim 10^{-3}$ mequiv/g for aq 0.0104 M LiCl to ~ 5 mequiv/g for 0.0104 M LiCl in 0.9 mole fraction dioxane. Below 0.5 mole fraction dioxane, the region covered in this paper, this effect is not too important, but it does contribute to a slight turning up of the plots in Figures 3–10 for the higher dioxane mole fractions. This is for two reasons. The more obvious, but less important, reason is that this Li^+ concentration acts roughly to a first approximation as additional "resin capacity" as additional cationic sites. The other reason is due to the experimental technique employed in determining D by the batch method. Since the amount of resin used, 0.100–0.350 g, is equilibrated with a finite volume of solution, 10.0–20.0 ml, the LiCl absorbed by the resin

(17) F. G. Donnan, *Z. Physik. Chem., Abt. A*, **168**, 369 (1934).

(18) F. Helfferich, "Ion Exchange," McGraw-Hill, San Francisco, Calif., p 139 ff.

must correspondingly decrease the actual concentration of LiCl in the external phase at equilibrium. For example, if 0.100 g of resin is mixed with 10.0 ml of 0.0100 *M* LiCl of 0.5 dioxane mole fraction, up to 0.100 × 0.100 = 0.0100 mequiv Cl^- would be absorbed, but the external solution only contains 10.0 × 0.0100 = 0.100 mequiv of LiCl to start with. Thus the equilibrium LiCl concentration in the external phase will be less than the initial value, and all *D*'s will be correspondingly higher. Both of these reasons can be summarized in the easily derived relation, $D \propto [\overline{Cl^-}]/[Cl^-]$.

B. The other factor to consider is the effect of the decrease in dielectric constant with increase in dioxane content (also plotted in Figure 2). This will increasingly favor electrostatic, or Bjerrum-type ion pairing in both phases.[19,20] Since such Coulombic ion pairing can be expected to occur more readily between the anions and the Li^+ than between the anions and the large alkyl ammonium cations of the resin sites, the result of the occurrence of such ion pairing is to offer the smaller ions, or those which most urgently need solvation, an additional type of electrostatic solvation in the external phase. This tends to help hold these ions in that phase, and so partially compensates for the main effect already described upon adding dioxane to the system, namely a lowering of the anion solvation capabilities in the external solution. If this suggestion is correct, then the use of $N(CH_3)_4Cl$ (providing a large cation similar to the resin group) rather than LiCl as the macro-electrolyte should reduce the amount of ion pairing, that is, should decrease this partial compensation. Under these conditions the halide tracer ions should show even less selectivity in dioxane solutions than with LiCl, and this should be most important for the smallest ions.

This is exactly what is observed if one compares the results with $N(CH_3)_4Cl$ solutions, Figures 6–8, and those with LiCl solutions, Figures 3–5. With $N(CH_3)_4Cl$, the halides may even invert their order above 0.5 dioxane mole fraction; certainly the selectivity coefficients between these ions are near unity at that composition, even those involving the fluoride ion.

As has been described,[4] still another way to make the resin phase more inviting to the (smaller) anions needing solvation the most urgently is to change the nature of the resin group from a strongly basic quaternary ammonium cation to a weakly basic primary, secondary, or tertiary ammonium ion. Then the protons on the resin group can hydrogen-bond, even though weakly, to the anion. The effect of this additional measure of (chemical) solvation in the resin phase for the smaller anions is shown in Figure 9 where the values of *D* for tracer Br^-, I^-, and ReO_4^- are plotted *vs.* the dioxane mole fraction for a 0.0104 *M* LiCl solution with Dowex 3-X4, a weak-base resin. It can be seen that Br^- and I^- appear to reverse their selectivity around 0.4 mole fraction dioxane, but do not do so until about 0.6 mole fraction dioxane with Dowex 1-X4. Presumably the effect would be more obvious with the fluoride ion, but it cannot be easily studied (though possible) as it requires a slightly basic solution to prevent hydrolysis, while the weak-base resin, to be effective, requires a slightly acidic system. Combining the use of this resin with $N(CH_3)_4Cl$ as the macro-electrolyte moves the point of Br^-–I^- reversal below 0.4 dioxane mole fraction, as can be seen in Figure 10 for 0.0101 *M* $N(CH_3)_4Cl$, and again fluoride might be expected to show a bigger effect.

Although the only anions treated in this paper are the monoatomic halide ions and one stable complex ion, ReO_4^-, the arguments presented are quite general and should hold for all other simple and stable anions. Since the agreement between expectation and experiment has been good in the systems studied, we believe, in fact, that this will prove to be true for other anions, with one important caution. Consideration of complex metal anions such as $GaCl_4^-$, $FeCl_4^-$, $InBr_4^-$, $ZnCl_4^{2-}$, etc., which must be produced in the solution by replacement of the first hydration shell of the metal cation with the ligand of the supporting electrolyte, has this additional feature of complex-formation to take into account, as the organic solvent replaces water in the system. This can be done, leading to somewhat different predictions, but that is another story. Finally, it should be pointed out that there is a practical result. Clearly, if the ideas presented are valid, one obtains the best possible separation of *stable anions* in water solution, not in mixed low-dielectric-constant organic solvent aqueous media. But conversely, the rapid elution of a stable anion which has an enormously large *D* in water should be possible by the use of water–dioxane (or other miscible organic solvent) to lower the value of *D*. Such a scheme has already been presented for the cyano complexes of silver and gold on anion resin using acetone–aqueous HCl mixtures.[21]

Acknowledgments. The authors wish to thank Mr. J. Bucher and Mr. L. Huber for help with some phases of the experiments.

(19) N. Bjerrum, *Kgl. Danske Selskab.*, **7**, [9] (1926).

(20) C. A. Kraus, *J. Phys. Chem.*, **60**, 129 (1956).

(21) F. H. Burstall, P. J. Forrest, N. F. Kember, and R. A. Wells, *Ind. Eng. Chem.*, **45**, 1648 (1953).

Ion-Exchange Selectivity of the Synthetic Zeolite Linde A in Anhydrous and Mixed Media[1a]

by R. B. Barrett*[1b] and J. A. Marinsky

Department of Chemistry, State University of New York at Buffalo, Buffalo, New York 14214 *(Received April 13, 1970)*

Publication costs borne completely by The Journal of Physical Chemistry

The selectivity coefficients for the ion exchange of cesium with sodium A zeolite and cesium and sodium with potassium A zeolite have been determined in nonaqueous and mixed media. The exchanging ions were at radioactive tracer level concentrations so that the fraction of the macroion of the zeolite was essentially unity in both the zeolite and external liquid phase. The dramatic increase in ion selectivity at very high alcoholic content of the liquid phase could only be qualitatively examined and was attributed to the significant solvation of the zeolite by the alcohol in the alcohol-rich media. Quantitative interpretation of the data obtained in the mixed media prior to this sharp increase in selectivity was attempted by assuming that the zeolite phase may be treated as a highly concentrated electrolyte solution having only one diffusible ion and as a cross-linked network which exerts a pressure on the internal solution phase. The special properties of the zeolite, rigidity, resistance to electrolyte incursion, and high selectivity for water, were believed to permit recourse to this model in mixed media over an alcohol–water weight per cent composition ranging from 0 to 70%. Correlation of experimental and calculated selectivity points was sufficiently good to support the validity of this approach.

Introduction

In recent years, several theoretical approaches to an understanding of ion-exchange phenomena in aqueous solution have met with considerable success. It seemed appropriate, then, to extend the limits of investigation to test the applicability of the models proposed for aqueous solutions in nonaqueous and mixed media.

Studies for this purpose were limited to uni-univalent exchange of the alkali cations in anhydrous methanol, ethanol, and ethylene glycol as well as water–alcohol solutions. The synthetic zeolite Linde A was selected as the ion exchanger because its structure and ion-exchange behavior in aqueous solutions have been well characterized.

Experimental Section

NaA zeolite was kindly supplied by the Linde Division of the Union Carbide Corp. Its preparation for use and the synthesis of the potassium form have been described elsewhere.[2] To prepare the sodium zeolite for use in nonaqueous media, it was heated to 500° under vacuum for 12 hr. No further weight loss was discernible upon ignition in Pyrex tubes. It was not feasible to dehydrate KA similarly. The KA zeolite has been found to undergo subtle irreversible structural modifications upon prolonged heating. Instead, this form of the zeolite was exhaustively rinsed with methanol and then placed under vacuum at room temperature overnight. The final product was 92 wt % matrix, 7 wt % methanol, and 1 wt % H_2O. For experiments in which water was added to alcohols fully hydrated zeolites were employed.

To facilitate the ion-exchange selectivity studies in nonaqueous media, Fisher Certified methanol and 200 proof ethanol from Publicker Industries were distilled over Linde 5-A molecular sieves and collected under nitrogen prior to their use. Water content of the product was below the limits of detection by Karl Fischer titration. The ethanol and methanol were usually used as received when employed in mixed media. They contained <0.06 wt % water as determined by Karl Fischer titration. Ethylene glycol from Fisher Scientific Co., contained 0.12% H_2O by weight and was used throughout without further purification.

Carrier-free γ-emitting radioactive nuclides, 30-year Cs^{137} and 2.6-year Na^{22}, were obtained from Nuclear Science and Engineering Corp. Analytical grade sodium and potassium iodide and potassium chloride were from the Fisher Scientific Co. Cesium nitrate from K & K Laboratories was converted into the iodide by passage through an anion-exchange column. The product was recrystallized twice from water–methanol solution.

Equilibrations were carried out with 0.01–0.5 g of zeolite in contact with 4–8 g of solution. In these experiments, a particular homoionic zeolite was placed in contact with iodide solution of the same ion and tracer level concentrations of the competing ion. The solu-

(1) (a) Abstracted in part from a dissertation submitted to the Faculty of the Graduate School of the State University of New York at Buffalo by R. B. Barrett in partial fulfillment of the requirements for the degree of Doctor of Philosophy, 1969. (b) To whom correspondence should be addressed at Department of Chemistry, Rosary Hill College, Buffalo, N. Y. 14226.

(2) S. Bukata and J. A. Marinsky, *J. Phys. Chem.*, **68**, 994 (1964).

tion varied in solvent composition while the molality was held constant. Throughout this technique, the internal environment is assumed to be ion invariant, the only perturbation being in solvation. This mixture, contained in polyethylene test tubes sealed with rubber stoppers, was enclosed in stoppered glass test tubes which were shaken on an automatic shaking machine. In the initial experiments within each system, aliquots were withdrawn by syringe, were filtered into counting tubes through a Millipore Solvinert filter of 0.50-μ size, and counted in a 1.25 × 2 in. well-type sodium iodide, thallium-activated γ-ray scintillation crystal detector, until no further change in solution radioactivity was noted. The time to attain equilibrium varied from 1 to 14 days, the longer times being required in the anhydrous systems.

In those experiments designed to investigate ion-exchange behavior in each nonaqueous medium selected for study, all transfers were made in a nitrogen atmosphere. Introduction of trace level concentrations of the exchanging cation to these systems was accomplished by dissolution in the salt-containing anhydrous solvent of an aliquot portion of the aqueous radioactive source previously evaporated to dryness. This solution was transferred to another polyethylene vessel to avoid the possibility of additional radioactivity being introduced into the anhydrous medium by a slow leaching step in the dissolution process during sampling of this solution for the equilibration studies. The quantity of zeolite and liquid in each experiment was determined by weight. All activity measurements were made at a fixed geometry by carefully controlling the volume of the liquid sample in the counting tube which was weighed before and after introduction of the sample.

Results

The measured trace selectivities, K_N^{M*}, where

$$K_N^{M*} = \frac{\text{cpm } \overline{M}^*}{\text{cpm } M^*} \times \frac{\text{mequiv of N/g of solution}}{\text{mequiv of exchangeable N/g of zeolite}} \quad (1)$$

are presented in Tables I through IV. A specific characteristic of the data is the sudden increase of the ion selectivity coefficient at very high external alcohol concentrations.

Discussion

A full discussion of theoretical approaches to ion exchange has been presented by Helfferich.[3] Of those discussed, the electrostatic approach advanced by Eisenman[4] and the osmotic pressure approach first advanced by Gregor[5] were deemed most applicable to studies in mixed and anhydrous media.

1. Electrostatic Approach. The various electrostatic approaches utilize Coulomb's law, or a variation of it, for calculating electrostatic interaction energies.

Table I: Trace Selectivity in Water–Methanol

Wt % external MeOH	K_N^{M*}
A. KI–Na*I; KI = 0.5 *m*	
0	3.52, 3.42[a]
17	3.72
50	4.47
80	5.25
85	5.40
90	5.60
98.8	10.3
99.2	27
99.5	21[a]
99.6	33
100	43, 46,[a] 40[b]
B. KCl–Na*Cl; KCl = 0.1 *m*	
0	2.41
10	2.69
20	2.74
30	2.85
40	2.80
50	2.74
60	2.53
70	2.47
C. KI–Cs*I; KI = 0.5 *m*	
0	28.9
26.3	23.5
62.9	23.1
89.4	57.5
95.8	93
99.0	450
99.7	1000
100 (extrapolated)	1650
D. NaI–Cs*I; NaI = 0.5 *m*	
0	5.80
28.1	6.29
61.5	8.56
82.3	24.4
85.0	28
90.14	58
95.5	160
99.0	810
100 (extrapolated)	1554 (extrapolated)

[a] 0.1 *m* KI. [b] 0.06 *m* KI.

Pauley[6] has derived the following equation for univalent exchange

$$\ln K_A^B = \frac{-\Delta G}{RT} = \frac{Ne^2}{RT\epsilon}\left(\frac{1}{a_B^\circ} - \frac{1}{a_A^\circ}\right) \quad (2)$$

(3) F. Helfferich, "Ion Exchange," McGraw-Hill, New York, N. Y., 1962.

(4) G. Eisenman, "Glass Electrodes for Hydrogen and Other Cations," Marcel Dekker, New York, N. Y., 1967.

(5) H. P. Gregor, *J. Amer. Chem. Soc.*, **70**, 1293 (1948); **73**, 642 (1951).

(6) J. L. Pauley, *ibid.*, **76**, 1422 (1954).

Table II: Trace Selectivity in Water–Ethanol

Wt % external EtOH	K_N^{M*}
A. KI–Na*I; KI = 0.1 *m*	
95.0	3.88
99.0	11.20
100 (extrapolated)	82 (extrapolated)
B. KI–Cs*I; KI = 0.5 *m*	
0	28.9
45.4	16.2
70.7	20.7
82.15	23.1
94.10	42.7
96.91	96
99.94	356, 310,[a] 358[b]
100 (extrapolated)	400
C. NaI–Cs*I; NaI = 0.1 *m*	
0	5.80
75.7	17.6
94.12	54
96.89	160
98.07	308
99.43	832, 830[c]
100	5350,[d] 6500[e]

[a] 0.10 *m* KI. [b] 0.01 *m* KI. [c] 0.5 *m* NaI. [d] Thermally dried NaA. [e] Methanol rinsed NaA.

Table III: Trace Selectivity in Water–Ethylene Glycol

Wt % external glycol	K_N^{M*}
A. KI–Na*I; KI = 0.5 *m*	
71.3	2.31[a]
85.3	2.73[a]
95.05	4.31[a]
96.60	9.61[b]
99.88	11.5
100 (extrapolated)	30.4
B. NaI–Cs*I; NaI = 0.1 *m*	
0	5.80
53.5	9.2
79.01	25
87.0	38
94.95	66
97.40	96
99.88	330[c]
100 (extrapolated)	400

[a] 0.1 *m* KI. [b] Thermally dried NaA. [c] 0.5 *m* NaI.

where a° is the distance of closest approach between mobile ions A and B and a fixed exchange site. This model has been extended by Eisenman in a consideration of ion selectivity and electrode potentials in aluminosilicate systems.[4,7] By assuming that cations and framework sites form ion pairs with no solvent interposed between them, the extent of exchange between exchanger and solution ions will be a measure of the differences in electrostatic and solvation free energies of the two ions. That is

$$\Delta F_{AB}^\circ = [F_A^{el} - F_B^{el}] - [F_A^{hyd} - F_B^{hyd}] \quad (3)$$

However, there are severe limitations in applying this approach to the present work. Since bare ionic radii and a dielectric of unity are employed in the calculations, the only parameter accountable for selectivity changes with this model is solvation energy. However, values for the free energy of solvation published by Ismailow[8] suggest that this value is relatively constant in water, methanol, and ethanol. Sherry[9] has recently reexamined Eisenman's approach to consider its relevancy to zeolite exchangers. He concludes that site heterogenity and entropy affects which arise from the coupling of internal solvation and ion composition are often the determining factors in ion selectivity. A model based on an essentially homogeneous, dense, and solvent-free internal environment (Eisenman's) cannot be expected to take these factors into account.

Huang, Mizany, and Pauley[10] have investigated cation exchange in Linde 13-X, a synthetic faujasite, in water and alcohols but not in the mixed solvent. They do not report large selectivity enhancement. However, their results, even in the aqueous system, are not in agreement with more recent values obtained by Sherry.[11] Part of their difficulty may have arisen from the fact that the potassium, lithium, and silver forms of the zeolite were dried at 600°, a procedure which brings about structural changes in Linde A. In contrast, Barrer has noted significant selectivity enhancement in methanolic Na–K exchange with Linde Y.[12] Fessler and Strobel[13] and Schwarz[14] reported that Na–Li ex-

Table IV: Summary of Trace Selectivities in One-Component Solvent[a]

	Water[b]	Methanol	Ethanol	Glycol
K_K^{Na*}	3.42	46	82[c]	73[d]
K_K^{Cs*}	28.9	1650	400[d,e]	...
K_{Na}^{Cs*}	5.8	1554	*ca.* 5750	400[d]

[a] 0.5 *m* I^- unless noted. [b] 0.1 *m* Cl^-, ref 14. [c] 0.1 *m* I^-. [d] Extrapolated value. [e] 0.05 *m* I^-.

(7) G. Eisenman, *Biophys. J.*, 2, 259 (1962).

(8) N. A. Ismailov, *Dokl. Akad. Nauk USSR*, **149**, 884 (1963).

(9) H. S. Sherry, "Ion Exchange," Vol. II, J. A. Marinsky, Ed., Marcel Dekker, New York, N. Y., 1968.

(10) P. C. Huang, A. Mizany, and J. L. Pauley, *J. Phys. Chem.*, **68**, 2575 (1964).

(11) H. S. Sherry, *ibid.*, **70**, 1158 (1966).

(12) R. M. Barrer, J. A. Davies, and L. C. V. Rees, *J. Inorg. Nucl. Chem.*, **30**, 3333 (1968).

(13) R. G. Fessler and H. A. Strobel, *J. Phys. Chem.*, **67**, 2562 (1963).

(14) A. Schwarz, *ibid.*, **72**, 789 (1968).

change in the organic exchanger Dowex-50-X-8 showed a selectivity enhancement as the exchange medium was made progressively alcoholic. Although log K did not vary in a linear fashion with $1/\epsilon$ the deviation was attributed to an internal activity coefficient ratio which deviated from unity. There is no information available for resin phase solvent composition to permit reconsideration of their data on this basis.

At the present time, no case of ion selectivity enhancement brought about by change of solvent has proved amenable to simple treatment. The results of this investigation are no exception. A straightforward electrostatic approach predicts that log K should be a linear function of the internal dielectric, but the observed selectivity enhancements would appear to extend beyond the range of dielectric perturbation.

In our opinion, classical electrostatics cannot provide a satisfactory explanation of trace ion selectivity enhancement in this system without appropriate consideration of the effect of site heterogenity and entropy changes introduced by the solvent state.[9] The unavailability of such information at this point precludes further resort to this approach here.

2. The Osmotic Pressure Approach. This approach was introduced previously as a route to the understanding of solvent selectivity in the Linde A zeolite.[15] That these concepts can be extended to include ion selectivity in aqueous media as well has been demonstrated by Marinsky and Bukata.[2] Their working equation

$$\ln K_M^N = \frac{\pi}{RT}[\bar{V}_M - \bar{V}_N] + \ln \frac{\bar{\gamma}_{M^+}}{\bar{\gamma}_{N^+}} - 2 \ln \frac{\gamma_{\pm MX}}{\gamma_{\pm NX}} \quad (4)$$

for the general reaction

$$\bar{M}Z + N^+ \rightleftharpoons \bar{N}Z + M^+$$

was employed in the study of ion exchange in concentrated electrolyte solutions. The exchange equilibrium is assumed to be between two univalent cations M^+ and N^+, associated with a common anion, X^-, with solvent and electrolyte being freely diffusible in and out of the exchanger. The left-hand term is the experimentally determined mass product, K_M^N, or selectivity coefficient, when the molal concentration of the species is employed. The symbols $\bar{\gamma}_+$ and $\gamma_\pm$ designate the activity coefficient of the ion in the zeolite phase and the mean molal activity coefficient of the electrolyte in the external solution phase, respectively.

Application of the osmotic pressure approach to the interpretation of the selectivity data in mixed media, however, has also been attempted.[15] It was argued that, of the three terms in eq 4, two ($\pi\Delta\bar{V}/RT$ and $\ln (\bar{\gamma}_{M^-}/\bar{\gamma}_{\bar{N}^+})$ should resemble aqueous values and $\ln (\bar{\gamma}_{M^+}/\bar{\gamma}_{N^+})$ should remain constant over a large range of external solution composition for the internal environment is expected to remain essentially aquatic until high external alcohol concentrations have been reached. [Representative figures are given in Table V for the system NaA–H_2O–MeOH. The potassium form of the exchanger shows roughly twice the selectivity as the sodium form.] It was suggested that on this basis selectivity should be primarily a function of activity coefficient ratios of the salts in the liquid phase until significant alcohol invasion occurs.

Table V: Internal Solvent Composition of NaA in Water–Methanol Mixtures

Mole fraction external alcohol	Mole fraction internal alcohol
0.866	0.123
0.910	0.250
0.930	0.330
0.948	0.365
0.974	0.480
0.980	0.640

To test this estimate of the situation, the $[\bar{V}_M - V_N]$ and $\ln (\bar{\gamma}_{M^+}/\gamma_{N^+})$ terms of eq 4 were assumed to be invariant until entry into the zeolite of alcohol in measurable quantity.[15] The value of the $(\pi/RT)\cdot(V_M - V_N) + \ln (\bar{\gamma}_{M^+}/\bar{\gamma}_{N^+})$ term of eq 4 in the aqueous system was first evaluated by subtracting the last term of eq 4 (evaluated from published data) from the experimental value of $\ln K_N^M$ determined in the aqueous system. The variation of $(\pi/RT)(V_M - V_N) + \ln (\bar{\gamma}_{M^+}/\bar{\gamma}_{N^+})$ in the different mixed media was then obtained by first estimating the variation of $\pi V_w/RT$ with eq 5.

$$\ln \frac{a}{\bar{a}_w} = \frac{\pi V_w}{RT} \quad (5)$$

This variable term was then multiplied by $(\bar{V}_M - \bar{V}_N)/\bar{V}_w$ to provide the net change in $\pi(\bar{V}_M - \bar{V}_N)/RT + \ln (\bar{\gamma}_{M^+}/\bar{\gamma}_{N^+})$ as a function of the solution composition. The difference between the interpolated value of $\ln K_N^M$ and the corrected value of $\pi(\bar{V}_M - \bar{V}_N)/RT + \ln (\bar{\gamma}_M/\bar{\gamma}_N)$ at each solvent composition yield values of $-2 \ln (\gamma_{\pm MX}/\gamma_{\pm MX})$ in the different mixed media. The results of this computation presented in an earlier publication[15] are relisted in Table VI for the convenience of the reader.

The increasing deviation between the mean molal activity coefficient of KI and NaI with methanol content that is observed is reasonable. As the dielectric of the solution medium decreases with larger methanol content, differences in the ion-pair formation capability of Na^+ and K^+ are expected to be enhanced with the

(15) R. B. Barrett, J. A. Marinsky, and P. Pavelich, "The Properties of Linde A in Aqueous, Non-Aqueous and Mixed Media," accepted for Symposium Volume "Second International Conference on Molecular Sieve Zeolites," September 1970 to be published in "Advances in Chemistry Series."

Table VI: Computation of the Mean Molal Activity Coefficient Ratio of Simple Electrolytes in Mixed Media

Wt % MeOH	$\pi\Delta V/RT$ + ln ($\bar{\gamma}_K/\bar{\gamma}_{Na}$)	ln K_{exptl}	-2 ln, ($\gamma_{\pm KI}/\gamma_{\pm NaI}$)
0	1.091	1.235	0.142
10	1.077	1.280	0.203
20	1.058	1.344	0.286
30	1.037	1.385	0.348
40	1.009	1.440	0.431
50	0.970	1.500	0.530
60	0.917	1.549	0.632
70	0.842	1.610	0.768

more highly polarizable iodide ion to yield the above result.

The mean molal activity coefficient data that are published for the alkali chlorides[16] facilitate a more meaningful prognosis of the osmotic pressure model. With the availability of these data it has been possible to evaluate the -2 ln ($\gamma_{\pm MX}/\gamma_{\pm NX}$) term of eq 4 by assuming that distortion of this ratio by cation–cation interaction is negligible at the low ionic strength of the experiments. A comparison of $K_N{}^{M^*}{}_{(calcd)}$ and $K_N{}^{M^*}{}_{(exptl)}$ for the KA–KCl–Na*Cl–MeOH–H_2O system as a function of solvent composition is presented in Table VII for this purpose. Good agreement between experiment and prediction is obtained until the weight per cent of alcohol exceeds 50%.

Table VII: Prediction of Ion-Exchange Selectivity in Mixed Media

System KA–KCl–Na*Cl–CH_3OH–H_2O; m_{KCl} = 0.1

Wt % methanol	$\pi/RT/(\bar{V}_K - \bar{V})_{Na}$ + ln ($\bar{\gamma}_{K^+}/\bar{\gamma}_{Na^+}$)	-2 ln ($\gamma_{\pm KCl}/\gamma_{\pm NaCl}$)	$K_K{}^{Na^*}{}_{(calcd)}$	$K_K{}^{Na^*}{}_{(exptl)}$
0	0.8579	0.0207	2.41	2.41 ± 0.1
10	0.8268	0.1058	2.54	2.69 ± 0.1
20	0.8022	0.1270	2.53	2.74 ± 0.1
30	0.7788	0.1904	2.64	2.85 ± 0.1
40	0.7509	0.3059	2.88	2.80 ± 0.1
50	0.7169	0.3114	2.80	2.74 ± 0.1
60	0.6776	0.6261	3.68	2.53 ± 0.1
70	0.6163	0.9168	4.63	2.47 ± 0.1

The apparent failure of the osmotic model in the higher alcohol-containing media may be a consequence (1) of more significant entry of the alcohol into the zeolite phase than is anticipated from extrapolation of the solvent selectivity data, (2) of the change of $\bar{V}_M$ and $\bar{V}_N$ in these alcohol-enriched media, or (3) of error in the values of $\gamma_{\pm MX}$ and/or $\gamma_{\pm NX}$ that are published for the 60 and 70% alcohol by weight media. The first possibility is considered unlikely since the selectivity behavior of K and Na* in ethanol (where the affinity of H_2O over alcohol for the zeolite is much greater) parallels almost exactly the behavior in methanol.[17] The second possibility is also unreasonable since the apparent molal volume of KCl has been shown to be constant over the solvent composition range investigated[18] in this study. The regular decrease in the activity coefficient of KCl with the alcoholic content of the mixed medium under investigation appears to be a linear function of the alcoholic content of the solvent until 50% by weight alcohol content is exceeded. Beyond this composition range the mean molal activity coefficient of KCl seems to drop much too rapidly with increasing alcoholic content. This irregular behavior of $\gamma_{\pm KCl}$ may indeed be indicative of error in the published values in the higher alcoholic media.

In any case the correlation of $K_M{}^{N^*}{}_{(calcd)}$ and $K_M{}^{N^*}{}_{(exptl)}$ over a large alcohol–water composition range is supportive of the osmotic model. It is suggested that the osmotic pressure approach may be as useful for the estimate of thermodynamic properties of simple electrolyte mixtures in mixed solvents as in aqueous media.

At present this model cannot be usefully employed to interpret ion selectivity in the essentially pure nonaqueous solvent. Various parameters essential to the model are not yet available in the literature. However, since ion selectivity is so sensitive to the solvent content of the exchanger it appears that the most important selectivity term in eq 4 must be ln ($\bar{\gamma}_{M^+}/\bar{\gamma}_{N^+}$). A number of speculative approaches are presently under consideration to facilitate a quantitative interpretation of the ion selectivity of the A zeolite in anhydrous media.

Acknowledgment. Financial support through Contract No. AT(30-1)-2269 with the U. S. Atomic Energy Commission is gratefully acknowledged. The selectivity data for the KCl–Na*Cl–MeOH–H_2O system were obtained by Mrs. P. Pavelich of this laboratory.

(16) R. Parsons, "Handbook of Electrochemical Constants," Academic Press, New York, N. Y., 1959.

(17) P. Pavelich and J. A. Marinsky, unpublished data, 1970.

(18) H. A. Neidig, *J. Chem. Educ.*, **42**, 309 (1965).

Ionic Equilibria in Mixed Solvents. VI. Dissociation Constants of Aliphatic Diamines in Water–Methanol Solutions

by Hitoshi Ohtaki* and Nobuo Tanaka

Laboratory of Analytical Chemistry, Faculty of Science, Nagoya University, Chikusa, Nagoya, Japan
(Received May 11, 1970)

Publication costs borne completely by The Journal of Physical Chemistry

Dissociation constants of protonated 1,2-diaminoethane, 1,3-diaminopropane, and 1,4-diaminobutane have been determined potentiometrically at 25° in various water–methanol mixtures containing 0.1 *M* sodium chloride as an ionic medium. Ion products, $K_w(s)$, in the mixtures have been calculated and used for calculations of pK's of the acids, equilibrium of hydronium ions with alkoxonium ions being taken into consideration. Since values of $pK_2 - pK_1$ of the diamines have been independent of solvent compositions, it may be seen that interactions between charged sites in a molecule may scarcely be affected with the variation of the solvent composition.

Introduction

In comparison with accumulation of data for dissociation constants of dicarboxylic acids, the number of pK values of diamines is limited. Moreover, theoretical considerations have been made only for dissociation of protons from dicarboxylic acids.[1-5] We have undertaken the present study to throw a little more light on dissociation equilibria of diprotic acids in mixed solvents.

In the present work we determined dissociation constants of protonated 1,2-diaminoethane, 1,3-diaminopropane, and 1,4-diaminobutane in various water–methanol mixtures containing 0.1 *M* sodium chloride as an ionic medium.

Experimental Section

A. Reagents. 1,2-Diaminoethane Dihydrochloride and 1,3-Diaminopropane Dihydrochloride. Each base (reagent grade; Wako Pure Chemicals Co., Osaka) was dissolved in water and then was treated with diluted hydrochloric acid at low temperature. The solution was concentrated under a reduced pressure at 30–40°. Diamine dihydrochlorides thus prepared were recrystallized three times from aqueous ethanol and crystals were dried *in vacuo*.

1,4-Diaminobutane Dihydrochloride. 1,4-Diaminobutane (Aldrich Chemical Co., Inc., Milwaukee, Wis.) was distilled twice under a reduced pressure and dissolved in water, and then was treated with dilute hydrochloric acid in a vessel cooled with ice. The solution was concentrated under a reduced pressure until crystals were formed. Temperature was kept lower than 40° in the course of evaporation. The crystals were dissolved in aqueous ethanol solution and recrystallized by addition of ethyl ether to the solution. They were dried *in vacuo* at room temperature.

Sodium chloride (ultra pure) from E. Merck Co. was used after drying at 500°.

Sodium Hydroxide. A saturated solution of reagent grade sodium hydroxide was allowed to stand for several days in a polyethylene bottle. The solution was filtered through a G4 glass filter under nitrogen atmosphere and diluted with distilled water free from carbon dioxide. The solution was kept in a polyethylene bottle filled with nitrogen gas.

Methanol. Reagent grade methanol was distilled once and was stored in a glass bottle. The concentration of water in the methanol was analyzed by means of Karl Fischer titrations.

B. Apparatus. Beckman glass electrodes (No. 40498) were used. Silver–silver chloride electrodes were prepared according to Brown.[6] The "Wilhelm" type of half-cell described by Forsling, Hietanen, and Sillén[7] was used for emf measurements. A Beckman Research pH meter Model 1019 or an Orion Digital pH meter Model 801 was used.

All titrations were performed in an ionic medium of 0.1 *M* sodium chloride at 25.00 ± 0.01° in a paraffin oil thermostat, which was placed in a room thermostated at 25 ± 1°. Potentials at each point of measurements were determined within an accuracy of 0.1 mV. The

* Correspondence should be addressed to Department of Electrochemistry, Tokyo Institute of Technology, O-okayama, Meguro, Tokyo, Japan.

(1) R. Gane and C. K. Ingold, *J. Chem. Soc.*, 2153 (1931).

(2) J. G. Kirkwood and F. J. Westheimer, *J. Chem. Phys.*, **6**, 506 (1938).

(3) H. M. Peek and T. L. Hill, *J. Amer. Chem. Soc.*, **73**, 5304 (1951).

(4) C. Tanford, *ibid.*, **79**, 5348 (1957).

(5) A. Ninomiya and K. Toei, *J. Chem. Soc. Jap.* (*Nippon Kagaku Zasshi*), **90**, 655 (1969).

(6) A. S. Brown, *J. Amer. Chem. Soc.*, **56**, 646 (1934).

(7) W. Forsling, S. Hietanen, and L. G. Sillén, *Acta Chem. Scand.*, **6**, 901 (1952).

pH never exceeded 10.1 in the course of measurements in all systems.

Liquid Junction Potentials

Activity coefficients of species being assumed to be kept constant in a constant ionic medium with a given solvent composition, an emf measured, E, is related with the concentration of hydrogen ion, $[H^+]_s$, through the equation

$$E = E_0 + \frac{RT \ln 10}{F} \log [H^+]_s + E_j \qquad (1)$$

where $[H^+]_s$ denotes the concentration of the relevant species in a solution; E_0 is a constant, which is determined experimentally by means of a Gran plot[8] in each titration procedure; E_j represents the liquid junction potential at the junction, 0.1 M NaCl in aqueous solution|0.1 M (Na, H)Cl in water–methanol mixture. The liquid junction potential, E_j, was determined in each solvent system. Values of E_j in various water–methanol solutions of 0.1 M sodium chloride are given in Table I. Uncertainties of the results were estimated to be ± 50 mV$\cdot[H^+]_s^{-1}$. The decrease of liquid junction potential with increasing methanol concentration may be due to the decrease of mobility of protons in mixed solvents.

Table I: Values of Liquid Junction Potential, E_j

Concn of methanol, % (w/w)	E_j, mV/M $[H^+]_s$
0	−600 (−440,[a] −550[b] in 0.1 M $NaClO_4$)
10	−550
20	−500
30	−450
40	−400
50	−400
60	−350
70	−350
80	−300

[a] D. Dyrssen, *Sv. Kem. Tidskr.*, **64**, 213 (1952). [b] M. Tanaka, N. Nakasuka, and H. Yamada, *J. Inorg. Nucl. Chem.*, in press.

Ionic Product, $K_w(s)$ of Solvents in Aqueous Methanol Solutions

In an aqueous methanol solution the following equilibria hold for both water and methanol

$$H_2O \rightleftharpoons H^+(H_2O) + OH^-, \qquad K_{H_2O} = (H^+(H_2O))_s(OH^-)_s/(H_2O)_s \qquad (2)$$

and

$$ROH \rightleftharpoons H^+(ROH) + OR^-, \qquad K_{ROH} = (H^+(ROH))_s(OR^-)_s/(ROH)_s \qquad (3)$$

Here H_2O and ROH in parentheses in eq 2 and 3 show molecules on which protons are distributed.

The equilibrium constant of the reaction 4

$$H^+(H_2O) + ROH \rightleftharpoons H^+(ROH) + H_2O \qquad (4)$$

is given as

$$\varkappa = \frac{(H^+(ROH))_s(H_2O)_s}{(H^+(H_2O))_s(ROH)_s} = \frac{x(1-y)}{y(1-x)} \qquad (5)$$

where x denotes a fraction of alkoxonium ion produced from 1 mol of proton and y the mole fraction of methanol in a solvent, activities of the species being assumed to be equal to their mole fractions.

Since both hydronium and alkoxonium ions are considered to be thermodynamic entities which determine the chemical potential of hydrogen ion, the activity of hydrogen ion, $(H^+)_s$, is given as[9]

$$(H^+)_s = (H^+(H_2O))_s^{1-n} \cdot (H^+(ROH))_s^x \qquad (6)$$

A similar relationship with eq 6 for hydrogen ion is obtained for $(OH^-)_s$; thus

$$(OH^-)_s = (OH^-)_s^{1-x} \cdot (OR^-)_s^x \qquad (7)$$

Since the ion product of a solvent, $K_w(s)$, is defined as

$$K_w(s) = (H^+)_s(OH^-)_s \qquad (8)$$

the ion product of a mixed solvent is given as

$$K_w(s) = K_{H_2O}^{1-x} \cdot K_{ROH}^x \cdot (H_2O)_s^{1-x} \cdot (ROH)_s^x \qquad (9)$$

Under assumptions of $K_{H_2O} = 10^{-14.0}$, $K_{ROH} = 10^{-16.7}$,[10] and $\varkappa = 0.23$[11] even in 0.1 M sodium chloride solutions, we calculated values of $K_w(s)$ in various water–meth-

Table II: Values of $-\log K_w(s)$ Evaluated from Eq 9

Concn of methanel, % (w/w)	$-\log K_w(s)$
0	14.0
10	14.1
20	14.2
30	14.3
40	14.4
50	14 5
60	14.7
70	15.0
80	15.3
90	15.8
100	16.7

(8) G. Gran, *Analyst*, **77**, 661 (1952).

(9) H. Ohtaki, *Bull. Chem. Soc. Jap.*, **42**, 1573 (1969).

(10) N. Bjerrum, A. Unmack, and L. Zechmeister, *Kgl. Dansk. Vidensk. Selsk., Mat. Fys. Medd.*, **5**, 11 (1952); A. Unmack, *Z. Phys. Chem. (Leipzig,)*, **133**, 45 (1928); G. Charlot and B. Trémillon, "Chemical Reactions in Solvents and Melts," Pergamon Press, Elmsford, N. Y., and Oxford, 1969, p 274.

(11) B. E. Conway, J. O'M. Bockris, and H. Linton, *J. Chem. Phys.*, **24**, 834 (1956).

Table III: Dissociation Constants of 1,2-Diaminoethane (1,2-En), 1,3-Diaminopropane (1,3-Pn), and 1,4-Diaminobutane (1,4-Bn) in Various Water–Methanol Mixtures Containing 0.1 *M* NaCl

Concn of methanol, % (w/w)	1,2-En			1,3-Pn			1,4-Bn		
	pK_1	pK_2	$pK_2 - pK_1$	pK_1	pK_2	$pK_2 - pK_1$	pK_1	pK_2	$pK_2 - pK_1$
0	7.12	9.87	2.75	8.70	10.26	1.56	9.42	10.38	0.96
10	7.04	9.76	2.72	8.68	10.24	1.56	9.30	10.26	0.96
20	6.92	9.65	2.73	8.34	9.95	1.61	9.19	10.15	0.96
30	6.82	9.50	2.68	8.33	9.88	1.55	9.02	10.08	1.06
40	6.69	9.31	2.62	8.24	9.78	1.54	8.96	9.96	1.00
50	6.60	9.18	2.58	8.12	9.64	1.52	8.77	9.79	1.02
60	6.50	9.02	2.52	8.00	9.53	1.53	8.64	9.60	0.96
70	6.53	9.09	2.56	8.07	9.47	1.40	8.63	9.61	0.98
80	6.50	8.98	2.48	8.02	9.43	1.41	8.59	9.49	0.90

anol mixtures, which are listed in Table II. The values of $K_w(s)$ thus obtained were used for calculation of dissociation constants of diamines.

Results and Discussion

Dissociation constants, K_1 and K_2, for each diamine were determined from the formation function, $\bar{n}$, by means of a generalized least-squares method with the help of an electronic computer FACOM 230-60 in order to make the error square sum ($U = \Sigma(\bar{n} - \bar{n}_{calcd})^2$) a minimum for the set of dissociation constants, K_1 and K_2. $\bar{n}_{calcd}$ denotes the value $\bar{n}_{calcd} = ([H^+]_s K_1^{-1} + 2[H^+]_s^2 K_1^{-1}K_2^{-1})/(1 + [H^+]_s K_1^{-1} + [H^+]_s^2 K_1^{-1}K_2^{-1})$ for a particular set of the constants, K_1 and K_2. Dissociation constants thus obtained are summarized in Table III. In all cases both pK_1 and pK_2 decreased with increasing methanol concentration up to 80% (w/w). Such variations of pK's of diamines are similar to those of monamines.[9]

Values of both ΔpK_1 (= pK_1(in aqueous solution) − pK_1(in aqueous methanol solution)) and ΔpK_2 (= pK_2(in aqueous solution) − pK_1(in aqueous methanol solution)) were strongly dependent on the concentration of methanol. Moreover, it was found that ΔpK_1 and ΔpK_2 were very similar for 1,3-diaminopropane and 1,4-diaminobutane. For 1,2-diaminoethane, however, the decrease of pK_1 was less pronounced than that of pK_2, although variation of ΔpK_2 for 1,3-diaminoethane with the methanol concentration was almost the same as those for other diamines.

A thermodynamic comparison of dissociation constants of an acid in different solvents can be made through a comparison of free-energy differences of the acid existing in the different media. The difference of the free energies may be regarded as the energy change of transfer of the acid from one solvent to the other. The solvent dependence of the free energy may include two terms; one of them is the solvent dependence of interaction of a proton with a relevant conjugate basic group, and the other is the solvent effect on interaction of the proton with the other acid group situated at the end of the molecule in cases of symmetrical diprotic acids such as aliphatic α,ω-dicarboxylic acids and -diamines.

The value of $pK_2 - pK_1$ can be regarded as a measure of interaction between charges at the both ends of a diprotic acid.[2] Table III includes values of $pK_2 - pK_1$ at various compositions of mixed solvents. The values of $pK_2 - pK_1$ remained fairly constant over a wide range of the methanol concentration in spite of relatively large variation of each pK_1 and pK_2. The fact that $pK_2 - pK_1$ remained constant with variation of the solvent composition shows that the interaction between charges in a diamine molecule is practically unchanged with variation of the concentration of methanol, provided that effects of the ionic medium do not appreciably contribute to the solvent effects on the interaction between charged sites. On the contrary, values of $pK_2 - pK_1$ of corresponding carboxylic acids with the same number of methylene groups increase with increasing methanol concentration in solutions.[12]

Acknowledgments. The authors wish to thank Professor Motoharu Tanaka for his continued interest. Financial support given by the Ministry of Education is acknowledged.

(12) M.-L. Dondon, *J. Chim. Phys.*, **54**, 290 (1957)

The Complex Solubility of Silver Chloride in Methanol–Water, Acetone–Water, and Dioxane–Water Mixtures

by K. P. Anderson,* E. A. Butler, and E. M. Woolley

Department of Chemistry, Brigham Young University, Provo, Utah 84601 *(Received August 31, 1970)*

Publication costs assisted by Brigham Young University

Results of a study of the solubility of silver chloride at 25° as a function of chloride ion concentration in 10, 20, 30, 40, and 50% by weight methanol–water, acetone–water, and dioxane–water mixtures and in a 60% by weight dioxane–water mixture are presented. These results were obtained with a previously established radiotracer technique that is modified to include specific ion electrode measurements. All observed solubilities are interpreted in terms of the presence of silver ions, undissociated silver chloride molecules, and dichloroargentate ions. Values of the thermodynamic equilibrium constants relating the activities of these species to the chloride ion activity are obtained by a least-squares treatment of the solubility data for each solvent mixture. The observed changes in these equilibrium constants are discussed in terms of electrostatics theory, hydration theory, and other specific solvent effects.

Introduction

The work reported in this paper is a continuation[1] of our study of the solubility of silver chloride as a function of chloride ion concentration in aqueous–nonaqueous solvent mixtures. The solubility of silver chloride and the various equilibria involved has been investigated in 10, 20, 30, 40, and 50% by weight methanol–water, acetone–water, and dioxane–water mixtures and in a 60% dioxane–water mixture at chloride ion concentrations between $10^{-5.5}$ and 10^{-1} M. A radiotracer technique described previously[1] was used to determine total silver concentrations. The measurement of silver ion concentration with an Orion Model 94-16 sulfide specific ion electrode supplemented the tracer technique. Our purpose was to determine quantitatively the effects of the composition of the solvent on the concentrations and equilibrium constants of the silver-containing species in solution for different solvent systems and to interpret these effects. The results of a previous investigation of the solubility of silver chloride in water and in ethanol–water mixtures are included in our discussion and are plotted in all figures.

Experimental Section

All chemicals used were reagent grade. Solutions were prepared from doubly distilled water which had a specific conductance $<1.3 \times 10^{-6}$ ohm^{-1} cm^{-1} at 25°. Gas chromatographic analysis of the acetone, methanol, and dioxane used in solution preparations indicated the absence of water (<0.1%) and volatile organic impurities.

The method of solution preparation, equilibration, and analysis has been described.[1] Solubility determinations (25–40), each at a different chloride ion concentration, were made in each methanol–water, acetone–water, and dioxane–water mixture. The solubility product constant, K_s, associated silver chloride formation constant, K_1, and the stepwise dichloroargentate ion formation constant, K_2, were calculated using the modified least-squares method of data treatment previously outlined.[1,2] The notation for the various equilibrium constants has been changed from that used previously to the more generally accepted notation for consecutive or stepwise constants.[3] The mass balance equation (eq 1a and 1b) for these systems includes previously[1] defined activity coefficients. Values for the densities of the solutions were obtained by interpolation

$$[Ag_{total}] = [Ag^+] + [AgCl] + [AgCl_2^-] \quad (1a)$$

$$[Ag_{total}] = \frac{K_s}{[Cl^-]\gamma_1^{*2}} + \frac{K_1K_s}{\gamma_0^*} + K_1K_2K_s[Cl^-] \quad (1b)$$

of data reported by Griffiths,[4] Othmer,[5] and Hovorka[6] for the methanol–water, acetone–water, and dioxane–water mixtures, respectively. Values for the dielectric constants for the solutions were obtained by interpolation of data reported by Akerlof[7] and Albright.[8] The potential difference between an Orion Model 94-16 silver–sulfide electrode (which senses free silver ion in solution and free sulfide ion when silver ion is absent)

(1) K. P. Anderson, E. A. Butler, D. R. Anderson, and E. M. Woolley, *J. Phys. Chem.*, **71**, 3566 (1967).

(2) K. P. Anderson and R. L. Snow, *J. Chem. Educ.*, **44**, 756 (1967).

(3) J. Bjerrum, "Stability Constants, Part II: Inorganic Ligands," The Chemical Society, London, 1958.

(4) V. S. Griffiths, *J. Chem. Soc*, 1954, 860.

(5) D. F. Othmer, D. Friedland, and E. G. Schiebel, *Ind. Eng. Chem.*, **44**, 1872 (1952).

(6) F. Hovorka, R. A. Schaefer, and D. Driesbach, *J. Amer. Chem. Soc.*, **58**, 2264 (1936).

(7) G. Akerlof, *ibid.*, **54**, 4125 (1932).

(8) P. S. Albright, *ibid.*, **59**, 2098 (1937).

Table I: Equilibrium Constants in the Solvent Mixtures[a]

Wt % nonaqueous component	Dielectric constant	$-\log a_{H_2O}$[b]	$-\log K_s$	$\log K_1$	$\log K_2$	$-\log B$	% SD[c]
			A. Methanol–Water Mixtures				
0.00	78.54	0.000	9.75	3.31	1.95	6.44	7.4
9.47	74.36	0.050	10.03	3.59	1.85	6.53	16.7
19.84	69.28	0.111	10.27	3.83	1.99	7.00	11.6
34.48	62.19	0.211	10.47	4.03	2.20	7.09	33.7
42.10	58.61	0.272	10.87	4.43	2.27	6.75	11.8
54.20	52.88	0.382	11.38	4.94	2.45	6.75	17.3
			B. Acetone–Water Mixtures				
9.64	73.28	0.050	10.10	3.66	2.02	6.52	27.9
19.80	67.73	0.108	10.29	3.85	2.27	6.39	9.2
34.43	59.17	0.206	10.92	4.48	2.56	6.56	25.9
42.08	54.41	0.266	10.99	4.55	2.99	6.44	8.4
54.15	46.87	0.386	12.13	5.69	3.44	6.61	12.9
			C. Dioxane–Water Mixtures				
8.20	71.28	0.035	10.11	3.67	2.02	6.44	12.9
20.47	60.37	0.093	10.30	3.80	2.25	6.40	16.7
28.49	53.24	0.137	10.61	4.17	2.54	6.27	13.4
40.75	42.33	0.215	11.02	4.58	2.94	6.50	14.5
48.75	35.25	0.276	11.77	5.33	3.17	6.31	16.1
60.73	25.24	0.390	12.36	5.92	3.63	6.61	13.7

[a] The assignment of meaningful values of uncertainties to be associated with our reported values of equilibrium constants is a difficult problem. The values we report here are given to what we consider to be a "reasonable" number of significant figures. [b] See eq 20. [c] Relative (percentage) standard deviation of the experimental solubility data from the least-squares calculated solubility curve of eq 1.

and a double-junction calomel reference electrode was measured in each equilibrated solution. A Beckman Research Model pH meter or an Orion Model 801 digital pH meter was used to measure the potential differences. The silver–sulfide electrode was calibrated to read silver ion concentrations by measurements in standard $AgNO_3$ solutions of the same organic solvent content as the equilibrated sample solutions. Corrections for ionic strength effects were made.

For solvent mixtures containing relatively high chloride ion concentrations ($>10^{-3}$ M) the free chloride ion concentration was calculated from total chloride mass-balance considerations alone, as in ethanol–water solutions.[1] At chloride concentrations lower than 10^{-3} M the mass balance value of chloride ion concentration and the specific ion electrode value of silver ion concentration were used to obtain a preliminary value of K_s. This preliminary value of K_s and the specific ion electrode value of silver ion concentration were used to calculate a better value of the chloride ion concentration. This process was repeated until successively calculated values of K_s and free chloride concentration were the same. These best values of the free chloride ion concentrations ($<10^{-3}$ M) were then used in the least-squares calculations.

Results and Discussion

The solubility data and least-squares calculated solubility curves for the solvent mixtures, when plotted in the same manner as for the ethanol–water solutions, namely, $-\log [Ag_{total}]$ *vs.* $-\log [Cl^-]$, produce families of hyperbolic curves. The minima for these curves move toward lower total silver and free chloride ion concentrations as the per cent nonaqueous component in the solvent mixture increases, in the same fashion depicted for ethanol–water.

Values for K_s, K_1, and K_2 listed in Table I were calculated from the least-squares solubility curves.[1,2] Since the experimental solubility data lie on the calculated least-squares curves within experimental precision at high chloride ion concentrations it was assumed that there were no appreciable concentrations of complexes of the form $AgCl_n^{1-n}$ where $n > 2$, even in 0.13 M chloride ion solutions.

The second term on the right-hand side of eq 1b, K_1K_s/γ_0^*, is the B term of Table I and is equal to the molar concentration of the undissociated AgCl species in each solution. If the activity coefficient, γ_0^*, is always unity, then this B term remains essentially constant in all the solvents studied and differences in the experimentally obtained values can be attributed to

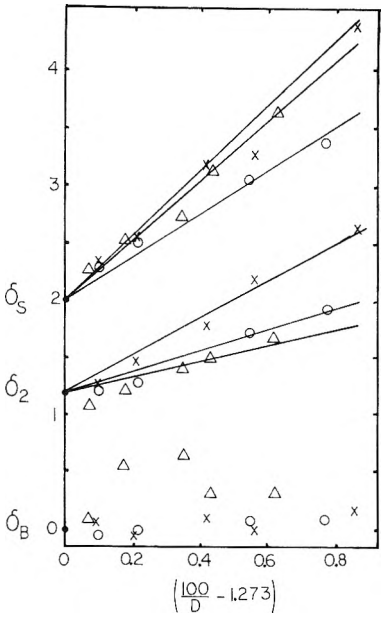

Figure 1. Plots of δ_B = log B (water) − log B (solvent), δ_2 = log K_2 (solvent) − log K_2 (water) +1.20, and δ_s = log K_s (water) − log K_s (solvent) + 2.00 according to Born electrostatic model (eq 2): ●, solvent = water;[1] ○, solvent = ethanol–water mixtures;[1] △, solvent = methanol–water mixtures; ×, solvent = acetone–water mixtures. The lines correspond to the least-squares slopes in Table II.

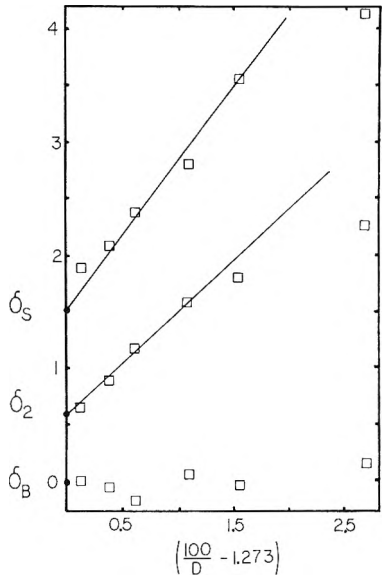

Figure 2. Plots of δ_B = log B (water) − log B (solvent), δ_2 = log K_2 (solvent) − log K_2 (water) +0.60, and δ_s = log K_s (water) − log K_s (solvent) + 1.50 according to Born electrostatic model (eq 2): ●, solvent = water; □, solvent = dioxane–water mixtures. The lines correspond to the least-squares slopes in Table II.

experimental uncertainty. The values of $-\log B$ are plotted *vs.* the reciprocal of the dielectric constant of the solvent mixture in Figures 1 and 2. Experimental uncertainty may well account for the deviation of B from its value in pure water in all except the methanol–water solutions. The deviations of B from the pure water value in methanol–water solutions appear to be greater than can be attributed to experimental error and may indicate deviations in γ_0* from unity, possibly reflecting solvent–solvent interactions or partial solvation of species by methanol.[9]

In the calculation of values of K_1 and K_2 we have assumed in all cases that variations in B were caused either by experimental error or by variations in γ_0* so that the product of K_1K_s is always equal to its value in pure water. The tabulated values of K_2 were also calculated using this assumption.

The values of $-\log K_s$ in Table I for aqueous methanol solutions and for the 20% dioxane–water solution are in good agreement with K_s values (obtained by emf measurements of cells with liquid junctions) recently reported by Feakins, *et al.*[10] Kratohvil and Tezak[11] report values of K_s and K_1 for a 50% ethanol–water mixture and for a 48.5% acetone–water mixture (obtained by solubility measurements) that are in reasonably good agreement with the values in Table I.

An equation derived by Born[12] which considers electrostatic interactions has the general form

$$\log K' = M(1/D' - 1/D'') + \log K'' \qquad (2)$$

where K' is the equilibrium constant measured in a solvent of dielectric constant D', K'' is the same constant in a solvent of dielectric constant D'', and M is a function of the charges and radii of the ions involved. Figures 1 and 2 are plots of log K and log B values *vs.* $1/D$ with all calculated curves constrained to pass through the water points. (The actual coordinates used are differences between values in the solvent mixtures and in pure water.) Table II gives values of M, the slope, corresponding to least-squares fitting of the best straight lines to these data. It is apparent that the linear relationship predicted by Born is a fair approximation of the general trends observed, but the different values of M indicate that other effects are also important.

The inconstancy of the slopes of log K *vs.* $1/D$ plots, though noted often in the literature, is still not adequately explained. It has been attributed to different ion-pair parameters[13] and it has been passed off as having no immediate theoretical significance.[14]

Theories of ion pair and triple ion formation as developed by Bjerrum[15] and by Fuoss and Krauss[16] pro-

(9) K. P. Anderson, E. A. Butler, and E. M. Woolley, *J. Phys. Chem.*, **71**, 4584 (1967).

(10) D. Feakins, K. G. Lawrence, P. J. Voice, and A. R. Willmott, *J. Chem. Soc. A*, 837 (1970).

(11) J. Kratohvil and B. Tezak, *Arh. Kem.*, **26**, 243 (1954).

(12) M. Born, *Z. Phys.*, **1**, 45 (1920).

(13) "Solute–Solvent Interactions," J. F. Coetzee and C. D. Ritchie, Ed., Marcel Dekker, New York, N. Y., 1969, Chapter 5: "The Selective Solvation of Ions in Mixed Solvents," by H. Schneider.

(14) J. E. Prue, "Ionic Equilibrium," Pergamon Press, Elmsford, N. Y., 1966, p 111.

Table II: Slopes of Plots of Log K *vs.* $1/D$ (Equation 2 and Figures 1, 2)

	MeOH	EtOH	Acetone	Dioxane
$-\log K_s$ and $\log K_1$	266[a]	184[b]	278[c]	128[d]
$\log K_2$	78[e]	98[f]	170	90[g]

[a] 30% point omitted from calculations. [b] 10% point omitted from calculations. [c] 40% point omitted from calculations. [d] 60% point omitted from calculations. [e] 10% and 20% point omitted from calculations; however, inclusion of the 20% changes the value to 76 and including all points changes it to 74. [f] 10% and 20% points omitted from calculations; the value changes to 94 if they are included. [g] 50% and 60% points omitted from calculations. The break in the line shown occurs at about 0.13 dioxane mole fraction; a 1:6 dioxane water complex has been reported. J. R. Goates and R. J. Sullivan, *J. Phys. Chem.*, **62**, 188 (1958).

vide tests to determine whether or not a particular species forms through purely electrostatic bonding. These tests indicate that bonding in the various silver chloride species is polar covalent rather than purely ionic in character.

The structure-breaking effects of small amounts of organic solvent added to water are a possible explanation of the noticeable deviations from the "straight" lines in Figures 1 and 2 at low organic component concentrations.[17]

The slopes for the log K_1 ($-\log K_s$) curves appear to be inversely proportional to the molar volume of the organic component and directly proportional to its dipole moment. In the solutions containing dioxane the ions apparently "see" only one of the dioxane oxygens at a time, *i.e.*, dioxane acts as if this "half-molecule" has a dipole moment of about 1.7. Equations 3, 4, and 5 illustrate this relationship when the slope of the log K_1 line in methanol (molar volume 40.5 and dipole moment 1.70) is taken as the reference slope. The appropriate values of molar volume and dipole moment for ethanol are 58.3 and 1.69, for acetone 73.5 and 2.89, and for dioxane 85.2 and "1.7."

$$266 \times \frac{40.5}{58.3} \times \frac{1.69}{1.70} = 184 \text{ (ethanol)} \quad (3)$$

$$266 \times \frac{40.5}{73.5} \times \frac{2.89}{1.70} = 249 \text{ (acetone)} \quad (4)$$

$$266 \times \frac{40.5}{85.2} \times \frac{1.70}{1.70} = 126 \text{ (dioxane)} \quad (5)$$

These results seem to indicate that the effective radii of solvated ions are a function of the opposing effects of organic molecule size and electrostatic effects as reported by Amis.[18] These simple relationships do not appear to hold for log K_2 (the formation of the $AgCl_2^-$ species).

Marshall[19] and Matheson[20] used the activity of water in equilibrium equations to explain the results of thermodynamic investigations of ionic reactions in mixed solvents. Using this approach the equations for our studies are

$$AgCl(H_2O)_m \rightleftharpoons AgCl(s) + mH_2O \quad (6)$$

$$K_d = \frac{a_{AgCl(s)} \times a_{H_2O}{}^m}{a_{AgCl(H_2O)m}} \quad (7)$$

$$Ag^+(H_2O)_n + Cl^-(H_2O)_p \rightleftharpoons AgCl(H_2O)_m + (n + p - m)H_2O \quad (8)$$

$$AgCl(H_2O)_m + (n + p - m)H_2O \rightleftharpoons AgCl(s) + (n + p)H_2O \quad (9)$$

$$K_s' = \frac{a_{Ag^+(H_2O)_n} \cdot a_{Cl^-(H_2O)_p}}{a_{H_2O}{}^{(n+p)}} \quad (10)$$

$$K_1' = \frac{a_{AgCl(H_2O)_m} \cdot a_{H_2O}{}^{(n+p-m)}}{a_{Ag^+(H_2O)_n} \cdot a_{Cl^-(H_2O)_p}} = \frac{a_{AgCl(H_2O)_m} \cdot a_{H_2O}{}^{(n+p-m)}}{K_s' a_{H_2O}{}^{(n+p)}} = \frac{a_{AgCl(H_2O)_m}}{K_s' a_{H_2O}{}^m} \quad (11)$$

$$AgCl(H_2O)_m + Cl^-(H_2O)_p = AgCl_2^-(H_2O)_q + (m + p - q)H_2O \quad (12)$$

$$K_2' = \frac{a_{AgCl_2^-(H_2O)_q} \cdot a_{(H_2O)}{}^{(m+p-q)}}{a_{AgCl(H_2O)_m} \cdot a_{Cl^-(H_2O)_p}} = \frac{a_{AgCl_2^-(H_2O)_q} \cdot a_{H_2O}{}^{(m+p-q)}}{K_1' K_s' a_{H_2O}{}^m a_{Cl^-(H_2O)_p}} = \frac{a_{AgCl_2^-(H_2O)_q} a_{(H_2O)}{}^{(p-q)}}{K_1' K_s' a_{Cl^-(H_2O)_p}} \quad (13)$$

$$[Ag_{total}] = [Ag^+(H_2O)_n] + [AgCl(H_2O)_m] + [AgCl_2^-(H_2O)_q] \quad (14)$$

$$[Ag_{total}] = \frac{K_s' a_{H_2O}{}^{(n+p)}}{\gamma_1{}^{*2}[Cl^-[H_2O)_p]} + \frac{K_1' K_s' a_{H_2O}{}^m}{\gamma_0{}^*} + \frac{K_1' K_2' K_s' [Cl^-(H_2O)_p]}{a_{H_2O}{}^{(p-q)}} \quad (15)$$

Using this interpretation the constant terms in eq 1 which were solved by least-squares calculations[1] are

$$A = K_s' a_{H_2O}{}^{(n+p)}; \quad B = \frac{K_1' K_s' a_{H_2O}{}^m}{\gamma_0{}^*}; \quad C = \frac{K_1' K_2' K_s'}{a_{H_2O}{}^{(p-q)}} \quad (16)$$

(15) J. Bjerrum, *Kgl. Danske Videnskab, Selskab. Mat. Fys. Medd.*, **7**, No. 9 (1926).

(16) R. M. Fuoss and C. A. Kraus, *J. Amer. Chem. Soc.*, **55**, 1019 (1933).

(17) F. Franks, "Physico-Chemical Processes in Mixed Solvents," F. Franks, Ed., American Elsevier, New York, N. Y., 1967, pp 50–75.

(18) E. S. Amis, *Inorg. Chim. Acta Rev.*, **3**, 7 (1969).

(19) W. L. Marshall, *J. Phys. Chem.*, **74**, 346 (1970).

(20) R. A. Matheson, *ibid.*, **73**, 3635 (1969).

$$\log A = (n + p) \log a_{H_2O} + \log K_s' \quad (17)$$

$$\log B = m \log a_{H_2O} + \log \frac{K_1'K_s'}{\gamma_0^*} \quad (18)$$

$$\log C = (q - p) \log a_{H_2O} + \log K_1'K_2'K_s' \quad (19)$$

It should be noted that A, B, and C are empirical constants whose values are not dependent upon theoretical assumptions regarding which species are present. The negative logs of A, B, and the log of C are plotted *vs.* the negative log of the activity of water for all four solvent mixtures in Figure 3. We have chosen to define the activity of water as[19]

$$a_{H_2O} = [H_2O]/55.36 \quad (20)$$

The structure-breaking effects of small amounts of organic compounds are notable as discussed earlier. When these effects are ignored, one obtains nearly straight lines as indicated in eq 17–19. The slopes of these lines are tabulated in Table III.

Table III: Slopes of Plots of log K *vs.* $-\log a_{H_2O}$ (Equations 17–19 and Figure 3)

	MeOH	EtOH	Acetone	Dioxane
$(n + p)$	4	4	6	6
$(p - q)$	1	2	4	4
m	1	0	0	0

A reasonable interpretation of these results in terms of hydrated species is given in Table IV.

These results indicate two water molecules strongly bonded to silver ion as with the diammine silver(I) ion. Chloride ion has been reported[21] to have a primary solvent shell of 4 in water. (However, many different values for coordination number of solvated cations and anions have been reported and the number appears to be a function of the method of measurement.[21–23]) Apparently the primary solvent layer of chloride ion is not breached by dioxane or acetone, at least up to the concentrations indicated. The fewer numbers of water for chloride ions in methanol and ethanol may be due to penetration of the primary hydration shell by these protic water-like molecules.

Table IV: Possible Hydration of Species Present in Solvent Mixtures

MeOH	EtOH	Acetone	Dioxane
$Ag(H_2O)_2^+$	$Ag(H_2O)_2^+$	$Ag(H_2O)_2^+$	$Ag(H_2O)_2^+$
$Cl(H_2O)_2^-$	$Cl(H_2O)_2^-$	$Cl(H_2O)_4^-$	$Cl(H_2O)_4^-$
$AgCl(H_2O)_1$	AgCl	AgCl	AgCl
$AgCl_2^-(H_2O)_1$	$AgCl_2^-$	$AgCl_2^-$	$AgCl_2^-$

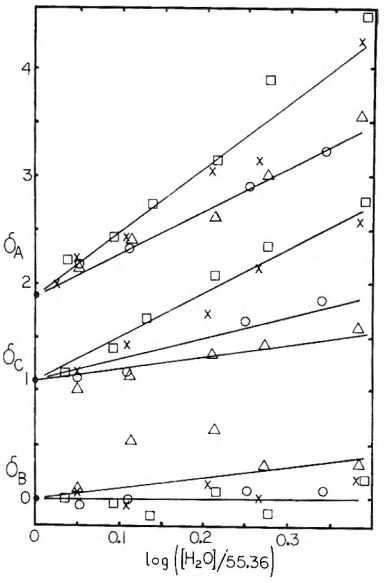

Figure 3. Plots of δ_B = log B (water) − log B (solvent), δ_C = log C (solvent) − log C (water) +1.10, and δ_A = log A (water) − log A (solvent) + 1.90 according to solvation model (eq 17, 18, and 19): ●, solvent = water; ○, solvent = ethanol–water mixtures;[1] △, solvent = methanol–water mixtures; ×, solvent = acetone–water mixtures; □, solvent = dioxane–water mixtures. The lines correspond to the least-squares slopes in Table III.

(21) K. D. Mischchenko, *Zh. Fiz. Khim.*, **26**, 1736 (1952).

(22) I. N. Maksimova and N. N. Zatsepina, *ibid.*, **43**(4), 1023 (1969).

(23) Yu. P. Aleshko-Ozhevskii, *Zh. Strukt. Khim.*, **10**(6), 1107 (1969).

Viscosity and Local Liquid Structure in Dimethyl Sulfoxide–Water Mixtures[1]

by Steven A. Schichman and Ralph L. Amey*

Department of Chemistry, Occidental College, Los Angeles, California 90041 *(Received September 16, 1969)*

Publication costs assisted by The Petroleum Research Fund of the American Chemical Society

The shear viscosity and density of ten dimethyl sulfoxide (DMSO)–water mixtures have been measured over the concentration range 0.1 to 0.8 mole fraction (mf) DMSO and over the temperature range $213 \leq T \leq 293°K$. Density data are reported and have been fitted to a quadratic equation of the form $\rho = a + bT + cT^2$. The maximum in the viscosity–concentration curve observed by others at elevated temperatures is found to sharpen considerably at low temperatures. The very large positive ΔS_η^* calculated for viscous flow in the region of 0.33 mole fraction DMSO at low temperatures is indicative of an extensive disordering process. Analysis in terms of WLF theory yields $T_o = 120°$ in the region of 0.3 mf DMSO.

Introduction

Recent interest in the DMSO–water system and of its role in biochemical processes has spurred the measurement of some of its excess properties. Analysis is hindered by the fact that it represents one of the more complicated binary systems, namely an associating component plus a second component which is capable of forming hydrogen bonds with the first. The likelihood of resolving this problem at present is small, since the complete answer must await an intimate knowledge of the intermolecular potential governing the system. As has been pointed out by Rice and his coworkers, however, much can be accomplished to describe liquid behavior if experimental data are available against which theoretical constructs may be tested.[2]

Viscosity studies at elevated temperatures on mixtures of dimethyl sulfoxide (DMSO) and water have led several investigators[3-5] to suggest strong association between DMSO and water. Cowie and Toporowski[3] and Lindberg and Lauren[5] have proposed the existence of a 2:1 water–DMSO association complex in liquid mixtures. The former's analysis was based upon the method of Geddes[6] in which he measured the greatest deviation from linearity for a viscosity *vs.* mole fraction plot at constant temperature. They concluded that the complex was thermally labile and could exist in an undissociated state only at low temperatures.[3]

It has been noted by others, however, that the freezing point–composition curve indicates a eutectic rather than compound formation[7] at an approximate DMSO mole fraction of 0.33. Furthermore, the lack of any observed splitting in the Raman sulfur–oxygen stretching band has been submitted as evidence by Lindberg and Majani that there is no H-bonded complex formed between the components.[8]

As part of our study of aprotic solvent systems we have extended the viscosity measurements on DMSO–water mixtures to much lower temperatures. In this paper we report viscosity and density data on ten mole fractions taken at several subambient temperatures. The results are discussed in terms of several model systems.

Experimental Section

Materials. Reagent grade dimethyl sulfoxide (J. T. Baker, and Matheson Coleman and Bell) was used directly without further purification. Maximum original water content as stated on the label was 0.03%. The mixtures were prepared with distilled water by an addition method using a top loading balance.

Density Measurements. Densities were obtained with a Sprengel–Ostwald-type pycnometer of approximately 11-ml capacity. The pycnometer was calibrated above 0° with distilled water[9] and below 0° with absolute methanol.[10] The temperature bath used was a Lauda Type NB circulator with an average temperature control accuracy of ±0.02°. The circulator liquid was methanol, and the circulator thermometer was cali-

(1) A portion of this work was presented at the 158th National Meeting of the American Chemical Society, New York, N. Y., Sept 11, 1969.

(2) S. A. Rice, J. P. Boon, and H. T. Davis in "Simple Dense Fluids," H. L. Frisch and Z. W. Salsburg, Ed., Academic Press, New York, N. Y., 1968, p 251.

(3) J. M. G. Cowie and P. M. Toporowski, *Can. J. Chem.*, **39**, 2240 (1961).

(4) R. J. Fort and W. R. Moore, *Trans. Faraday Soc.*, **62**, 1112 (1966).

(5) J. J. Lindberg and R. Lauren, *Finska Kemistsamfundets Medd.*, **71**, 37 (1962).

(6) J. A. Geddes, *J. Amer. Chem. Soc.*, **55**, 4532 (1933).

(7) R. K. Wolford, *J. Phys. Chem.*, **68**, 3392 (1964).

(8) J. J. Lindberg and C. Majani, *Acta Chem. Scand.*, **17**(5), 1477 (1963).

(9) G. S. Kell, *J. Chem. Eng. Data*, **12**, 66 (1967).

(10) S. Young and E. C. Fortey, *J. Chem. Soc.*, **81**, 717 (1902).

Table I: Densities of DMSO–H_2O Mixtures at Several Temperatures[a]

	Density, g/cm³, at t =										
X_{DMSO}[b]	−60°	−55°	−50°	−45°	−30°	−15°	−10°	0°	10°	15°	20°
0.10						1.062	1.060	1.055	1.050	1.048	1.045
0.20				1.121	1.112	1.101	1.098	1.090	1.082	1.079	1.076
0.25		1.143	1.140	1.136	1.125	1.113	1.110	1.101	1.093	1.090	1.086
0.30	1.159[c]	1.155	1.151	1.147	1.134	1.121	1.118	1.109	1.100	1.096	1.092
0.33		1.159	1.154	1.151	1.137	1.124	1.120	1.112	1.104	1.099	1.096
0.35		1.160	1.156	1.151	1.139	1.126	1.121	1.113	1.104	1.100	1.096
0.40		1.167	1.162	1.158	1.145	1.131	1.127	1.117	1.108	1.104	1.099
0.50					1.151	1.136	1.132	1.122	1.112	1.108	1.103
0.60							1.132	1.122	1.112	1.108	1.103
0.80									1.112	1.107	1.102

[a] Temperatures in degrees Celsius. [b] Mole fraction DMSO. [c] The relative error ($\Delta\rho/\rho$) of each density is ±0.12%.

brated at the *o*-xylene melting point (−25.19°), the ice point of distilled water, and 20.00°. A nonlinear calibration curve was obtained for the pycnometer. Densities of the ten DMSO–water mixtures were obtained in each case over their liquid range.

Viscosity Measurements. Viscosity data were obtained with a Haake Model B precision falling ball viscometer. Ball constants were supplied by the manufacturer and compared favorably with those obtained with standard calibration fluids. Falling times were measured to an accuracy of ±0.05 sec. Low-temperature operation was maintained with a Dry Ice heat exchanger in conjunction with the Lauda NB circulator.

Results

Table I lists the densities of ten DMSO–water mixtures in grams per cubic centimeter over the temperature range $213 \leq T \leq 293$°K. Table II presents the coefficients for a least-squares quadratic fit of the density data to an equation of the form

$$\rho = a + bT + cT^2 \quad (1)$$

The valid temperature range for the fit of each mole fraction is shown also in Table II. Table III lists the viscosities of the ten binary mixtures, and Figure 1 shows their behavior as a function of mole fraction for several isotherms.

Table II: Parameters for Eq 1 for the Density of Various DMSO–H_2O Mole Fractions

X_{DMSO}	a	$b \times 10^4$	$c \times 10^7$	Temperature range, °K
0.10	1.107	+1.003	−10.62	258–293
0.20	1.219	−2.075	−9.618	228–293
0.25	1.295	−6.310	−2.784	218–293
0.30	1.338	−8.290	−0.3393	213–293
0.33	1.425	−14.80	+12.14	218–293
0.35	1.338	−7.906	−1.222	218–293
0.40	1.346	−7.568	−2.940	218–293
0.50	1.414	−11.81	+4.132	243–293
0.60	1.575	−22.28	+24.51	263–293

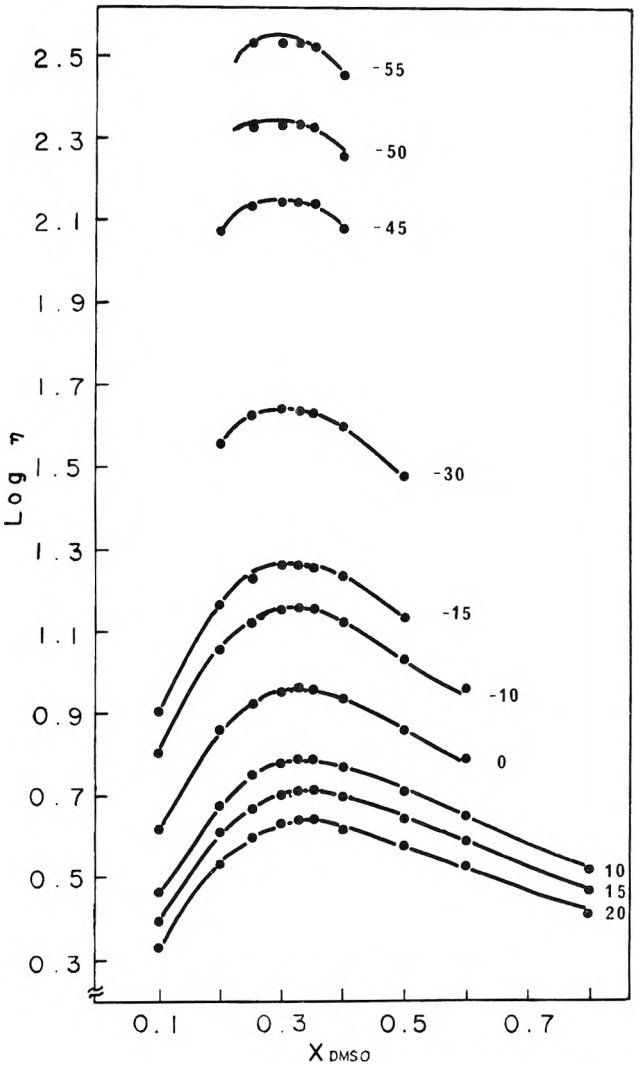

Figure 1. Log viscosity of DMSO–H_2O mixtures as a function of mole fraction at various temperatures. Temperatures noted on graph are in degrees Celsius. Extrema of each curve approximately correspond to the melting points of appropriate mole fraction.

Table III: Viscosities of DMSO–H_2O Mixtures at Several Temperatures[a]

Viscosity, cP, at t =											
−60	−55	−50	−45	−30	−15	−10[b]	0[b]	10[b]	15[b]	20[b]	X_{DMSO}
					8.12[b]	6.41	4.205	2.941	2.496	2.152	0.10
			118.9[d]	36.15[d]	14.79[b]	11.43	7.27	4.899	4.097	3.455	0.20
	341.3[c]	213.7[c]	138.0[c]	42.60[d]	17.13[d]	13.24	8.46	5.72	4.719	4.00[e]	0.25
570[b]	339.4[c]	214.7[c]	139.9[c]	43.81[d]	18.25[d]	14.20	9.07	6.09	5.10	4.310	0.30
	339.6[c]	214.7[c]	140.2[c]	43.47[d]	18.25[d]	14.27	9.16	6.17	5.18	4.383	0.33
	336.8[c]	212.6[c]	139.3[c]	43.00[d]	18.17[d]	14.23	9.17	6.16	5.19	4.398	0.35
	283.1[c]	181.1[c]	123.8[c]	40.00[d]	17.20[d]	13.43	8.71	5.94	5.02	4.267	0.40
				29.37[d]	13.58[b]	10.91	7.37	5.19	4.445	3.838	0.50
						9.15	6.25	5.30	3.904	3.398	0.60
								3.362	2.964	2.627	0.80

[a] Temperatures in degrees Celsius. [b] Average relative error = ±0.55%. [c] Average relative error = ±0.41%. [d] Average relative error = ±0.34%. [e] Extrapolated value.

Error Analysis

The viscosity of a liquid when measured by a falling ball viscometer may be calculated from $\eta = FDK$ where F is the falling time in seconds, D is the difference between ball and liquid densities at a specified temperature, and K is the ball constant supplied by the manufacturer (and rechecked against standard calibration liquids). The total uncertainty in the viscosity was taken to be due to the uncertainties in the falling time (estimated as ±0.05 sec), the liquid density, and the specified temperature (typically ±0.05 to ±0.2°). The relative errors in the viscosity, $\Delta\eta/\eta$, were calculated in the usual manner.[11] These are included in Table III.

Discussion

No other low-temperature values have been reported for DMSO–water mixtures. However, upon extrapolation of our highest temperature values (20°), good agreement is reached with published density data measured at 25°.[3-5,12] Our reported relative error of about 0.5% for the viscosity (see Table III) reflects what is thought to be a conservative estimate of the accuracy of our data. Comparison of our viscosity results with the literature is compatible with our error figure when it is recognized that there is little agreement among the present literature values for this system. As can be seen from Table IV, our value falls between the two reported literature values.

Due to the high melting points of DMSO (18.51°) and water, it is not possible to calculate partial molal excess functions for the binary mixtures at low temperatures. Thus we are deprived of one of the most important parameters for the comparison of nonelectrolyte mixtures.[13]

The measured isotherms of viscosity *vs.* mole fraction demonstrate a progressively sharper maximum at lower temperatures occurring in the region of 0.3 mole fraction DMSO. This is consistent with the observations of other workers at higher temperatures.[3-5]

Table IV: Comparison of Densities and Viscosities with Literature Values

Mole fraction DMSO	Density in g/cm³ at 25°		
	Fort–Moore[a]	Schichman–Amey[b]	Cowie–Toporowski[c]
0.20	1.0742	1.072	1.0717
0.25	1.0816	1.082	1.0809
0.30	1.0885[d]	1.088	1.0880
0.40	1.0959	1.095	1.0956
Mole fraction DMSO	**Viscosity in cP at 25°**		
	Fort–Moore[a]	Schichman–Amey[b]	Cowie–Toporowski[c]
0.20	3.156	3.045	2.97
0.40	3.799		3.69
0.60	3.008		2.98

[a] Reference 4. [b] Calculated according to quadratic coefficients. [c] Interpolated from published values, ref 3. [d] Interpolated value.

Figure 1 shows these isotherms in terms of log η to facilitate display of all the data on a single graph. Because of the nature of the logarithmic function, the peaking of the isotherms is not as apparent as it would be on a viscosity–mole fraction plot. At present, no successful quantitative analysis of such maxima in associated mixtures has been made.[13,14] Although vis-

(11) (a) E. B. Wilson, Jr., "An Introduction to Scientific Research," McGraw-Hill, New York, N. Y., 1952, p 272. (b) The viscosity of both distilled water and reagent grade glycerol was measured at 20° and was found to be accurate in each case to within at least 0.3%. This is less than any relative error which we have reported in Table III for our data. Due to the uncertainties in (and unavailability of) low-temperature density and viscosity data, comparable direct accuracy checks at low temperatures are less satisfactory. However, measurements made by us on glycerol–water mixtures at low temperatures indicate that we are justified in reporting our error in a comparable manner to that reported at higher temperatures.

(12) R. G. Lebel and D. A. I. Goring, *J. Chem. Eng. Data*, **7**, 100 (1962).

(13) R. L. Scott and D. V. Fenby, *Ann. Rev. Phys. Chem.*, **20**, 111 (1969).

(14) A. Bondi in "Rheology: Theory and Applications," Vol. 4, F. R. Eirich, Ed., Academic Press, New York, N. Y., 1967, p 75.

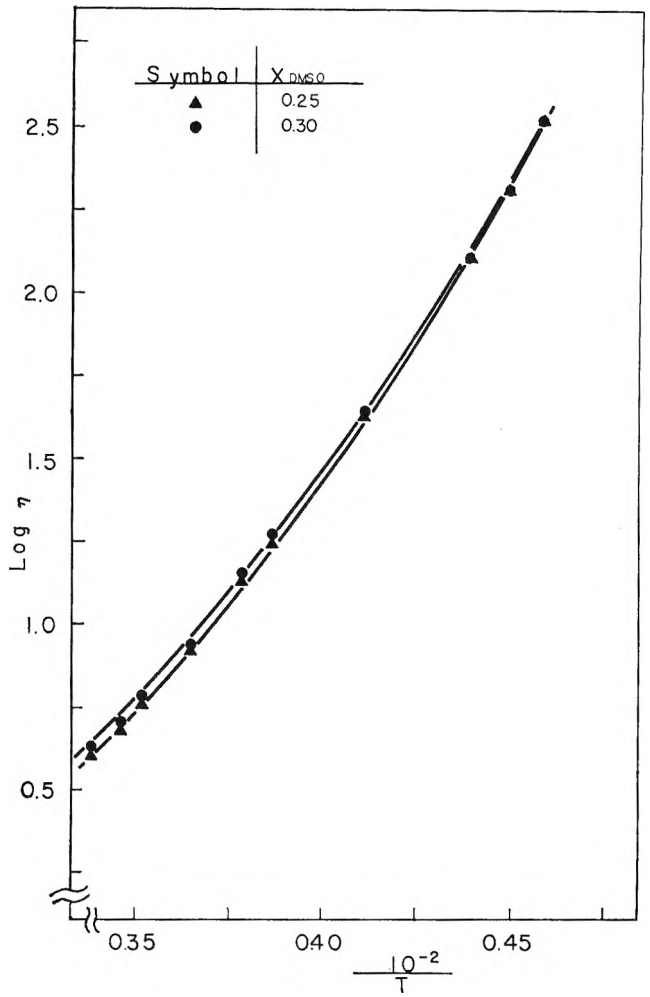

Figure 2. Log viscosity of several DMSO–H_2O mixtures as a function of reciprocal Kelvin temperature.

cosity maxima of this type are frequently identified with compound formation, there are several experimental observations which appear to be in conflict with such an interpretation. The lack of compound formation has been identified with the presence of a eutectic rather than a maximum at 0.33 mole fraction DMSO in the DMSO–H_2O phase diagram.[7] Lindberg and Majani have measured the Raman spectra of DMSO–H_2O mixtures.[8] They find no splitting in the sulfur–oxygen stretching band and conclude from this that no H-bonded complex can be present.

Nevertheless, significant evidence to support the presence of an equilibrium of the form

$$\text{DMSO} + 2H_2O \rightleftharpoons \text{complex}$$

appears to be available from calorimetric, nmr, and earlier viscosity results. These have been adequately summarized by both Wolford[7] and Jezorek and Mark[15] and will not be repeated here.

Typical of the nonlinear deviation from Arrhenius behavior observed at lower temperatures is the plot of log η *vs.* reciprocal Kelvin temperature shown in Figure 2 for several DMSO mole fractions. Such nonlinearity cannot be ascribed uniquely to a single phenomenon nor to a particular model system. McLaughlin and Ubbelohde have treated deviations from Arrhenius behavior in a number of liquids as a consequence of cluster formation near the melting point.[16] Such an interpretation of behavior in the DMSO–water system is tempting but not feasible by the McLaughlin–Ubbelohde method due to the greater complexity of the DMSO–water interaction. Jezorek and Mark,[15] in their discussion of this type of system, indicate that an extensive network of branched polymeric forms may be responsible for many of the properties of DMSO–water mixtures. An alternative view might assume an equilibrium between a DMSO–water complex similar to the one previously mentioned and an n-mer cluster of complex units. The question of whether one is dealing with branched polymeric chains or icebergs cannot be answered readily from present data.

From a fit of the linear high-temperature region of each curve in Figure 2 to the Arrhenius expression

$$\eta_{mix} = A \exp\left[\frac{E_\eta}{RT}\right] \tag{2}$$

values of the parameter E_η were obtained. By identification of E_η with the enthalpy of activation for viscous flow, ΔH_η^*, and use of the Eyring rate equation

$$\eta_{mix} = \frac{Nh}{V} \exp\left[\frac{-\Delta S_\eta^*}{R}\right] \exp\left[\frac{\Delta H_\eta^*}{RT}\right] \tag{3}$$

the entropy of activation, ΔS_η^*, for each mole fraction was obtained. At the lowest temperatures obtainable with each mole fraction—usually the melting points—tangents were drawn to the curves, and the appropriate parameters were obtained. These are listed in Table V.

Table V: Activation Parameters of Viscous Flow for DMSO–H_2O Mixtures

	$T \gg T_{mp}$		Near T_{mp}	
X_{DMSO}	E_η, kcal	ΔS_η^*, cal/mol-deg	E_η, kcal	ΔS_η^*, cal/mol-deg
0.10	2.02	+4.14	2.0	+4.1
0.20	2.24	+4.68	4.4	+13.3
0.30	2.50	+4.80	(7.7)	(+28)
0.40	2.17	+4.52	4.2	+12.6
0.50	2.04	+4.24	3.0	+7.9
0.60	1.92	+4.08	2.4	+5.8
0.80	1.65	+3.52	1.6	+3.5

Examination of the high temperature calculations indicate a sharp increase in ΔS_η^* in the region of 0.3 mole fraction DMSO. This suggests that viscous flow in

(15) J. R. Jezorek and H. B. Mark, Jr., *J. Phys. Chem.*, **74**, 1627 (1970).

(16) R. K. Hind, E. McLaughlin, and A. R. Ubbelohde, *Trans. Faraday Soc.*, **56**, 328, 331 (1960).

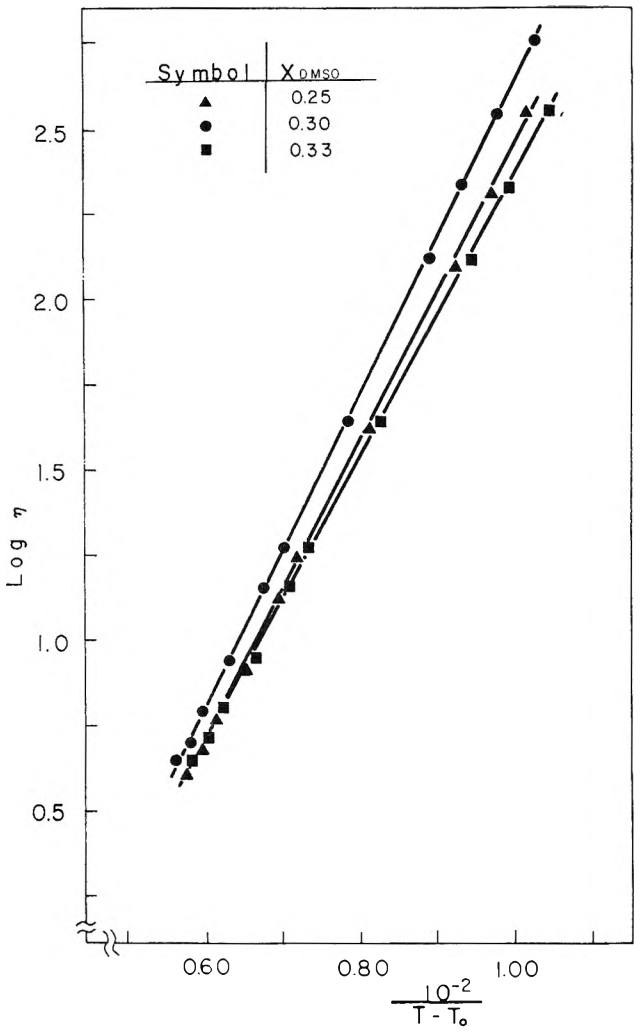

Figure 3. Log viscosity of several DMSO–H_2O mixtures plotted as a function of $(T - T_o)^{-1}$. Values for T_o, obtained by least-squares analysis, are listed in Table VI.

this mixture involves an extensive disordering process at low temperatures.

The dramatic increase in viscosity, particularly in the region of 0.3 mole fraction, may suggest the onset of a glassy state.[17] With this in mind we have analyzed our data in terms of the Williams–Landel–Ferry–Doolittle (WLFD) free volume model of viscous flow.[18] The results of fitting the data by least-squares computation to an expression of the form

$$\log \eta = A + \frac{B}{T - T_o} \qquad (4)$$

are presented in Figure 3 and Table VI. The fundamental parameter, T_o, is defined as the temperature below which the viscosity becomes essentially infinite, and within the framework of the WLFD theory, defines the temperature below which free volume is no longer available for viscous flow. Bondi has observed that since viscosity is a function of more than just the free volume, discussions utilizing free volume models are necessarily qualitative in nature.[14]

Table VI: WLFD Parameters for DMSO–H_2O Mixtures

X_{DMSO}	T_o	B
0.25	120 ± 1	438 ± 2
0.30	116 ± 1	458 ± 2
0.33	122 ± 1	397 ± 2

Tommila and Pajunen[19] have measured the dielectric constants and surface tensions of DMSO–water mixtures at 20–75°. As one would expect of high dielectric constant components, the ratio $(\epsilon - 1)/(\epsilon + 2)$ changes little with mole fraction. Hence the total molar polarization appears to vary linearly with concentration and is rather insensitive as a probe of local liquid structure in this case. The excess dielectric constant, $\epsilon^E = \epsilon_{obsd} - (X_1\epsilon_1 + X_2\epsilon_2)$, exhibits a maximum value at a DMSO mole fraction of 0.28, whereas the excess viscosity maximum at 25° occurs at about $X_{DMSO} = 0.33$. The difference probably is not significant, although since the mechanisms for dielectric polarization and viscous flow are not identical there is no need to expect agreement among their excess functions.

Conclusions

Despite the considerable efforts made by investigators to determine the origin of behavior in DMSO–H_2O mixtures, little of certainty yet can be said. Viscosity data seem to indicate an increase in local order—perhaps through the formation of polymeric structures—with a decrease in temperature. The very large positive ΔS_η^* calculated for viscous flow in the region of 0.33 mole fraction DMSO at low temperatures is indicative of an extensive disordering process and may be suggestive of the important role which the DMSO–H_2O ratio plays in local liquid structure at these temperatures. However, evidence for establishing the exact nature of its local liquid structure remains inconclusive. Analysis of such systems in terms of eq 4 and the free volume model, although necessarily qualitative at present, appears to hold more promise than one which employs any expression which assumes Arrhenius behavior.

Acknowledgment. Acknowledgment is made to the donors of the Petroleum Research Fund, administered by the American Chemical Society, and to the National Science Foundation for partial support of this work.

(17) A. Bondi, "Physical Properties of Molecular Crystals, Liquids and Glasses," Wiley, New York, N. Y., 1968, p 350.

(18) M. L. Williams, R. F. Landel, and J. D. Ferry, *J. Amer. Chem. Soc.*, **77**, 3701 (1955).

(19) E. Tommila and A. Pajunen, *Suom. Kemistilehti B*, **41**, 172 (1968).

Effects of Gas Pressure on the Viscosities of Molten Alkali Nitrates. II. Potassium Nitrate with Helium, Argon, and Nitrogen[1]

by James L. Copeland* and James R. Christie

Department of Chemistry, Kansas State University, Manhattan, Kansas 66502 *(Received August 17, 1970)*

Publication costs assisted by The National Science Foundation

Viscosities of fused KNO_3, pressurized with He, Ar, and N_2, have been measured by a capillary flow technique at temperatures from 335 to 467° and at pressures from 1 to 414 bars. The results are compared to earlier data for $NaNO_3$. A naive pressure-dependent free volume model, deduced from the work of Batchinski, provides a reasonable interpretation of the effect of pressure alone on the fluidities of KNO_3 and $NaNO_3$, and shows fair agreement with present results using He pressurization. According to the model, at a given pressure the fluidity should be depressed by that pressure to an ever-increasing extent with increasing temperature. Conversely, dilution of a melt by gas solubility should tend to *increase* the fluidity at a given pressure to an ever-increasing extent with increasing temperature, as a result of endothermic heats of solution. At a given gas pressure and temperature, then, the resultant effect on fluidity should reflect which of the two factors, dilution or pressure, is dominant. Apparently at higher temperatures the depressive effect of pressure on fluidity exceeds the augmentative effect of gas solubility, and *vice versa* at sufficiently low temperatures.

Introduction

Recently this laboratory has reported on the effects of inert gas solubility and pressure on the viscous properties of molten $NaNO_3$.[2] Also, this laboratory has reported studies of the electrical conductances of fused salts under like conditions.[3a,b,4] Investigations of this type are quite useful in gaining information pertaining to interactions among the various particles in the melt.

Of all the transport properties, the coefficient of viscosity lends itself most easily to measurement. By utilizing a capillary flow technique for $NaNO_3$ it was possible to obtain values for ΔV_η^* (the "activation volume" for viscous flow), E_V (the "activation energy" for viscous flow at constant volume), and E_P (the activation energy" for viscous flow at constant pressure). In the present work we report recently determined results for the viscosity of molten KNO_3 while pressurized with He, Ar, and N_2 over significant ranges of temperature and pressure. The aforementioned quantities are calculated and are compared to the results of the $NaNO_3$ studies and to investigations performed by Barton, Cleaver, and Hills[5] on the effects of pressure alone on the electrical conductances of fused salts. Furthermore, results obtained using He pressurization, for both KNO_3 and $NaNO_3$, lend themselves fairly well to an interpretation based on the naive free volume model of Batchinski[6] and Macleod.[7]

Experimental Section

The general apparatus and method are identical with those employed in the $NaNO_3$ work.[2]

Reagent grade KNO_3 was obtained from the Baker and Adamson Co., and Ar, He, and N_2 were from the National Cylinder Gas Co. The gases had stated purities of better than 99.8%.

The viscometer was calibrated at ten temperatures from 338 to 448° and at atmospheric pressure, using the KNO_3 viscosity data of Protsenko and Razumovskaya.[8] The effective viscometer constant,[2] K, obtained by least squares, resulted as

$$K = (6.220 \pm 0.021) \times 10^{-2} - (3.644 \pm 0.054) \times 10^{-5} t \text{ cP cm}^3 \text{ g}^{-1} \text{ sec}^{-1} \quad (1)$$

where t is temperature in °C and the errors are probable errors. The densities of molten KNO_3, ρ, were obtained from the empirical expression

$$\rho = 2.116 - (7.29 \times 10^{-4})t + 2.88 \times 10^{-5} P \text{ g cm}^{-3} \quad (2)$$

where P is applied pressure in atm. In eq 2 the temperature coefficient is that of Bloom, *et al.*,[9] while the

(1) (a) This paper was presented in part at the Sixth Midwest Regional Meeting of the American Chemical Society, Lincoln, Neb., Oct 1970.

(2) J. L. Copeland and J. R. Christie, *J. Phys. Chem.*, **73**, 1205 (1969).

(3) (a) J. L. Copeland and W. C. Zybko, *ibid.*, **70**, 181 (1966); (b) J. L. Copeland and S. Radak, *ibid.*, **70**, 3356 (1966).

(4) J. L. Copeland and S. Radak, *ibid.*, **71**, 4360 (1967).

(5) A. F. M. Barton, B. Cleaver, and G. J. Hills, *Trans. Faraday Soc.*, **64**, 208 (1968).

(6) A. J. Batchinski, *Z. Phys. Chem.*, **84**, 643 (1913).

(7) D. B. Macleod, *Trans. Faraday Soc.*, **19**, 6 (1923).

(8) P. I. Protsenko and O. N. Razumovskaya, *Zh. Prikl. Khim.*, **38**, 2355 (1965).

(9) H. Bloom, I. W. Knaggs, J. J. Molloy, and D. Welch, *Trans. Faraday Soc.*, **49**, 1458 (1953).

Table I: Summary of Least-Squares Intercepts and Slopes, with Probable Errors, of Ln ϕ *vs.* P Data for Fluidity of Molten KNO_3 at Various Temperatures under He, Ar, and N_2 Pressures, and Comparative Data for $NaNO_3$ and from Modified Batchinski Model

Temp, °C	Intercepts (±0.0001) He	Ar	N_2	Slopes, 10^{10}(d ln ϕ/dP)$_T$, cm^2 dyn^{-1} He	Ar	N_2	Av slopes derived from Batchinski eq	$\Delta V_\eta^* = -RT$(d ln ϕ/dP)$_T$, cm^3 mol^{-1} From He data	Batchinski
				For KNO_3					
355	3.625	3.624	3.627	−1.226 ± 0.003	−0.116 ± 0.008	0.369 ± 0.015	−2.644	6.40	13.8
380	3.767	3.766	3.769	−1.411 ± 0.001	−0.711 ± 0.011	0.063 ± 0.011	−2.644	7.66	14.4
401	3.873	3.873	3.875	−1.554 ± 0.002	−1.137 ± 0.024	−0.175 ± 0.009	−2.641	8.71	14.8
422	3.978	3.979	3.980	−1.703 ± 0.003	−1.544 ± 0.018	−0.419 ± 0.008	−2.639	9.84	15.2
448	4.088	4.092	4.090	−1.862 ± 0.003	−2.161 ± 0.085	−0.686 ± 0.006	−2.639	11.2	15.8
467	4.170	4.168	4.171	−1.988 ± 0.004	−2.376 ± 0.027	−0.893 ± 0.006	−2.639	12.2	16.2
				For $NaNO_3$[a]					
328	3.614	3.615	3.616	−1.146 ± 0.003	1.759 ± 0.007	0.105 ± 0.013	−3.138	5.73	15.7
350	3.741	3.741	3.743	−1.293 ± 0.003	1.422 ± 0.009	−0.194 ± 0.012	−2.878	6.70	14.9
379	3.877	3.878	3.879	−1.465 ± 0.004	1.063 ± 0.007	−0.542 ± 0.010	−2.612	7.94	14.1
401	3.962	3.964	3.964	−1.569 ± 0.004	0.736 ± 0.012	−0.751 ± 0.010	−2.452	8.79	13.7
420	4.056	4.057	4.056	−1.695 ± 0.003	0.531 ± 0.009	−0.991 ± 0.005	−2.334	9.77	13.4
444	4.150	4.151	4.151	−1.814 ± 0.005	0.241 ± 0.014	−1.241 ± 0.006	−2.210	10.8	13.2

[a] See ref 2.

pressure coefficient is deduced from the work of Owens.[10] Densities of the high-pressure gases were obtained from the Beattie–Bridgeman equation, as before.[2,11]

Flow times in this investigation varied from 19 sec (for high temperatures and at atmospheric pressure) to 33 sec (for low temperatures and high pressures) and were reproducible to within ±0.05 sec.

Results

The primary calculations are made as before.[2] The equations employed are

$$E_P = -R[\mathrm{d} \ln \phi/\mathrm{d}(1/T)]_P \quad (3)$$

$$\Delta V_\eta^* = -RT(\mathrm{d} \ln \phi/\mathrm{d}P)_T \quad (4)$$

and

$$E_V = E_P - (\alpha/\beta)T\Delta V_\eta^* \quad (5)$$

where E_P and E_V are the apparent viscous activation energies at constant pressure and volume, respectively, ΔV_η^* is the so-called activation volume for viscous flow, ϕ is fluidity (reciprocal viscosity), and α and β are the coefficient of thermal expansion and the isothermal compressibility of fused KNO_3, respectively.

It has been shown previously[2,8] that the viscosity of molten $NaNO_3$ follows isobaric Arrhenius behavior at atmospheric pressure[8] and at other gas pressures, but to different extents with different gases.[2] This is also the case with KNO_3. Again there is a distinct effect of gas solubility on the viscous property. The important points can be obtained from Figures 1 and 2 and from the summaries in Tables I and II. Figure 1 illustrates plots of ln ϕ for KNO_3 *vs.* pressure for the three gases at the different temperatures employed (similar to the plots in the $NaNO_3$ work[2]), while Figure 2 features plots of the *slopes* of the various isotherms of Figure 1 *vs.* temperature for KNO_3 (solid curves) and for the earlier $NaNO_3$ work (dashed curves) for comparison. The curves of Figure 1 appear similar to those for $NaNO_3$,[2] but Figure 2 serves better to articulate the differences between the KNO_3 and $NaNO_3$ systems. The major feature of Figure 2 is the striking similarity in the behaviors caused by He pressurization of the two salts. Other salient points in this graph are: (a) transposition of the curves for Ar and N_2 in going from $NaNO_3$ to KNO_3, (b) crossing of the Ar curve with that for He in the KNO_3 work, (c) negative slopes for all curves, with those for He being flattest, and (d) predominantly negative values for [d ln ϕ/dP]$_T$ at all temperatures studied with the exceptions of Ar with $NaNO_3$, two points for N_2 with KNO_3 at temperatures below *ca.* 390°, and one point for N_2 with $NaNO_3$ at temperatures below *ca.* 335°. Back extrapolation of the Ar with KNO_3 curve

Table II: Comparison of Transport Parameters for Viscosity (Using He-Saturated Melt) and Equivalent Conductance (Using Pressure Alone) for Molten KNO_3 and $NaNO_3$ at 400°

	Viscosity (this work) $NaNO_3$[a]	KNO_3	Equivalent conductance[5] $NaNO_3$	KNO_3
E_P, kcal	3.93	4.37	3.21	3.61
ΔV_η^*, cm^3 mol^{-1}	8.79	8.71	3.8	7.0
E_V, kcal	1.42	1.98	2.11	1.68

[a] See ref 2.

(10) B. B. Owens, *J. Chem. Phys.*, **44**, 3918 (1966).

(11) J. L. Copeland and L. Seibles, *J. Phys. Chem.*, **72**, 603 (1968).

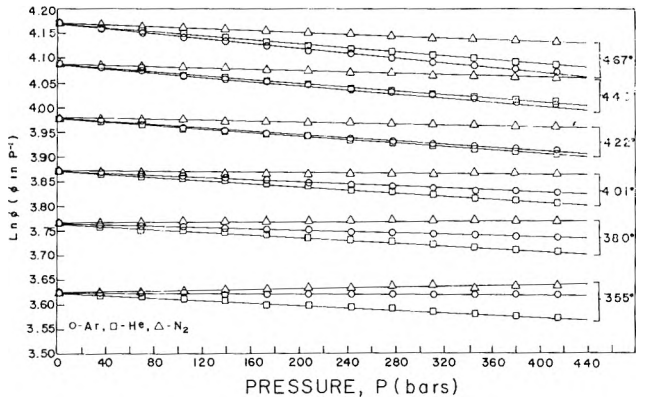

Figure 1. Plots of ln ϕ (ϕ is the fluidity in P^{-1}) *vs.* gas-saturating pressure, P (in bars), for molten KNO_3 under He, Ar, and N_2 gases, at various temperatures.

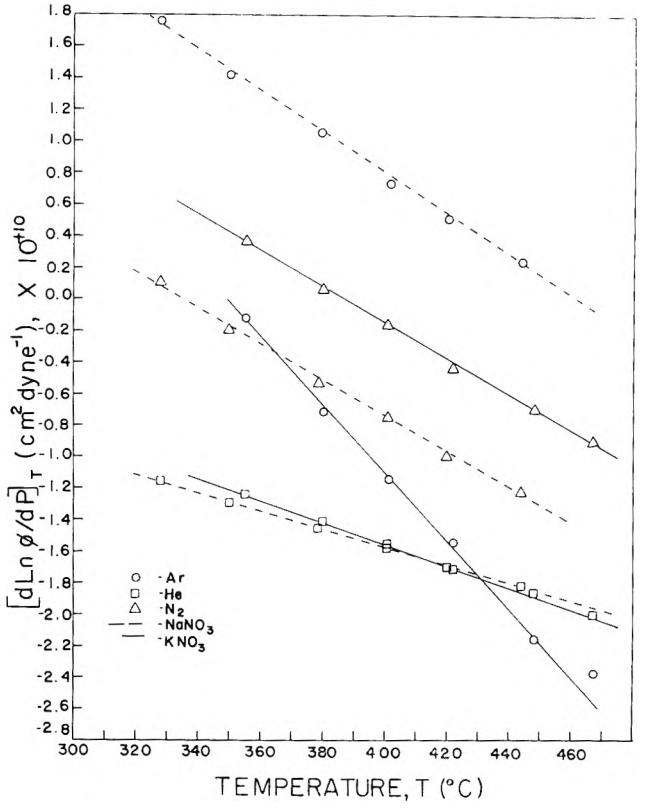

Figure 2. Plots of slopes, (d ln $\phi/dP)_T$, *vs.* temperature, T (°C), for molten KNO_3 and $NaNO_3$ pressurized with He, Ar, and N_2.

would doubtless also lead to positive values for [d ln $\phi/dP]_T$ at temperatures less than *ca.* 350°. Since the mp of KNO_3 is 337°, and that of $NaNO_3$ is 310°, back extrapolation of the He curves for these salts would not result in any such sign changes.

Discussion

As noted before,[2] two factors should affect viscosity at a given temperature: (a) pressure and (b) gas solubility. Intuitively one would expect the effect of pressure alone to decrease fluidity owing to the decreased free volume, which should restrict transport motions of the basic flow units. Many of the present theories of viscous flow indicate that any factor which diminishes free volume should increase viscosity at a given temperature.[12] Thus, in the present study, one would assume that pressure alone acts in the normal fashion to tend to produce negative slopes of ϕ *vs.* P and ln ϕ *vs.* P isotherms.

We shall consider the effect of He pressure first, since it appears to be the least complicated. It can be seen in Figure 2 that the effect of He on molten KNO_3 is very similar to the effect on fused $NaNO_3$.[2] This result may help further to substantiate the assumption made in the $NaNO_3$ study,[2] namely that the slight solubility of tiny, relatively nonpolarizable He atoms may have a nearly negligible effect on the viscous properties of such melts. With this assumption, "activation volumes" have been calculated from eq 4 and are tabulated in the next to last column of Table I. At 1 atm, E_P for viscosity of KNO_3 is calculated from eq 3 as 4.37 kcal, and at 400° and 1 atm, $\alpha = 3.99 \times 10^{-4}$ deg^{-1} and $\beta = 2.34 \times 10^{-11}$ cm^2 dyn^{-1} for this liquid.[13] Thus, use of our $\Delta V_\eta^* = 8.71$ cm^3 mol^{-1} at 401°, from Table I, with eq 5 yields an E_V of 1.98 kcal at *ca.* 400°, 1 atm. These values may be compared to corresponding ones for the equivalent conductance of KNO_3 found by Barton, *et al.*,[5] in Table II. It is seen (as for $NaNO_3$) that the ΔV_η^* calculated from viscosity measurements is somewhat larger than ΔV_Λ^* calculated from conductance measurements. This may not be surprising if one accepts Frenkel's[14] notion of the larger anion (NO_3^- here) controlling viscosity, and the smaller cation (K^+ or Na^+ here) dominating conductance. However, ΔV_η^* at 400° is essentially the same for KNO_3 as it is for $NaNO_3$, whereas ΔV_Λ^* is 50% greater for KNO_3 than for $NaNO_3$.

In attempting to relate the He results to a theoretical model of the pressure dependence of viscosity, one finds it difficult to employ recent, more sophisticated theories because of a lack of the necessary accurate experimental parameters for the *pure* alkali nitrates (*e.g.*, theoretical or experimental glass transition temperatures, T_0 or T_g). However, the naive, semiempirical model advanced by Batchinski,[6] and amplified by Macleod,[7] has proven to be of interesting value. This model is virtually a free volume model alone, and the basic equation for fluidity is

$$\phi = (V_{sp} - b)/B \qquad (6)$$

where V_{sp} is the actual specific volume at 1 atm and the temperature in question, b is in the nature of an ex-

(12) J. L. Copeland, "Transport Processes in Ionic Liquids," Gordon and Breach Science Publishers, New York, N. Y., 1971.

(13) G. J. Janz, "Molten Salts Handbook," Academic Press, New York, N. Y., 1967, pp 250, 252.

(14) J. Frenkel, "Kinetic Theory of Liquids," Dover Publications, New York, N. Y., 1955, pp 439–445.

cluded volume (often roughly equal to the solid volume), and B may be thought of as related to the average size of the flow unit. Plots of ϕ *vs.* V_{sp} for many ionic melts, including $NaNO_3$ and KNO_3, are quite linear.[15] From such plots for the present work at 1 atm, one calculates for $NaNO_3$: $b = 0.4946$ cm^3 g^{-1}, $B = 9.297 \times 10^{-4}$ cm^3 P g^{-1}; and for KNO_3: $b = 0.5041$ cm^3 g^{-1}, $B = 9.175 \times 10^{-4}$ cm^3 P g^{-1}. Equation 6 may be modified to reflect pressure dependence by incorporating such dependence of V_{sp}

$$\phi = [V_{sp,0}(1 - \beta P)/B] - b/B \quad (7)$$

where $V_{sp,0}$ is a reference value at 1 atm and the temperature in question, and b and B are assumed pressure independent. The isothermal compressibility, β, given by Owens[10] at temperatures of 400 and 500° and pressures of 1 and 5000 atm, may be written analytically as

$$\beta_{NaNO_3} = 22 \times 10^{-6} - [1.4 \times 10^{-9} + (4 \times 10^{-12})(t - 400)](P - 1) + 3 \times 10^{-8}(t - 400) \text{ atm}^{-1} \quad (8)$$

and

$$\beta_{KNO_3} = 21 \times 10^{-6} - [1.6 \times 10^{-9} + (1.8 \times 10^{-11})(t - 400)](P - 1) + 1 \times 10^{-7}(t - 400) \text{ atm}^{-1} \quad (9)$$

where t is again in °C and P is in atm. The reference $V_{sp,0}$ is taken as the reciprocal density value at each temperature and under 1 atm. Plots of ϕ *vs.* P for KNO_3 and $NaNO_3$, comparing experimental data for He pressurization of these melts with theoretical values computed from eq 7 at the various temperatures, are fairly linear. Table III summarizes and compares slope values for such plots. In this table one observes the tendency for both experimental and theoretical curves to *decrease* in *slope* with *increasing temperature* (just as occurs also for experimental ϕ *vs.* P data for *all* the gases studied with KNO_3 and $NaNO_3$), with experimental He slopes decreasing somewhat more rapidly. The latter phenomenon results in somewhat improved agreement between experiment and theory at higher temperatures for both salts, as can also be seen from the last column in Table III. In column 8 of Table I are found values of the slopes of ln ϕ *vs.* P obtained from the modified Batchinski model. These slopes may be compared to the experimental values using He in column 5. For the particular numerical values of ϕ encountered here, theoretical ln ϕ *vs.* P slopes actually *increase* slightly with temperature, as compared to *decreasing* values from experiment, even though both sets of data were seen to behave similarly when plotted in terms of ϕ *vs.* P. The last column of Table I lists ΔV_η^* values calculated from the model, and it can be seen that these are somewhat larger, but more nearly constant than those from the He experiment.

Table III: Comparison of Experimental ϕ *vs.* P Plots for Molten KNO_3 and $NaNO_3$ under He Pressure, with Theoretical Values Calculated from Modified Batchinski Equation (Errors Are Least-Squares Probable Errors)

Temp, °C	$10^9(d\phi/dP)_T$, P^{-1} cm^2 dyn^{-1} — Exptl (He pressure)	$10^9(d\phi/dP)_T$, P^{-1} cm^2 dyn^{-1} — Theoret (pressure alone)	Ratio of slopes, theoret/exptl
	For KNO_3		
335	−4.49 ± 0.01	−9.37 ± 0.01	2.09
380	−5.93 ± 0.01	−10.8 ± 0.02	1.82
401	−7.24 ± 0.03	−12.0 ± 0.02	1.67
422	−8.80 ± 0.03	−13.3 ± 0.03	1.51
448	−10.7 ± 0.05	−14.9 ± 0.03	1.39
467	−12.4 ± 0.05	−16.1 ± 0.04	1.30
	For $NaNO_3$		
328	−4.15 ± 0.01	−10.9 ± 0.01	2.63
350	−5.30 ± 0.01	−11.3 ± 0.01	2.13
379	−6.88 ± 0.03	−11.9 ± 0.02	1.73
401	−7.96 ± 0.03	−12.4 ± 0.02	1.56
420	−9.45 ± 0.04	−12.8 ± 0.02	1.35
444	−11.1 ± 0.05	−13.3 ± 0.02	1.20

Gas solubility effects on fluidity may also be at least qualitatively interpreted from the viewpoint of the naive pressure-dependent Batchinski model. Previously[2] this laboratory interpreted its $NaNO_3$ viscosity results on the basis of presumed *exothermicity* of Ar and N_2 solubilities in that melt.[11,16] It has since been learned[17] that a superior technique has been developed to determine heats of solution and solubilities of such high-pressure gases in fused $NaNO_3$. These heats are apparently *endothermic*, and the solubilities are about ten times as small as measured by the crude technique of this laboratory. Thus, the temperature effect on fluidity as a result of *gas solubility* alone will have to be interpreted in this new light. The dilution hypothesis is still tenable; *i.e.*, at a given temperature the solubility of inert gas molecules dilutes the melt without destroying any inherent free volume, thereby tending to *increase* fluidity in competition with the pressure-induced *decrease* in that property. Since, therefore, at any given T and P the solubility of "hard sphere" inert gas molecules should tend to increase ϕ *via* dilution, one would anticipate (a) that the full expected depression of ϕ due to pressure alone would never be realized in gas pressure studies and (b) that gases diluting the melt least would produce an overall effect on ϕ most nearly like that of pressure alone. Such is the case observed for KNO_3 and $NaNO_3$, at least in regard to point a. Although He is probably more soluble than Ar or N_2 in a given melt at given T and P, its *dilution*

(15) B. S. Harrap and E. Heymann, *Chem. Rev.*, **48**, 45 (1951).
(16) J. L. Copeland and L. Seibles, *J. Phys. Chem.*, **70**, 1811 (1966).
(17) B. Cleaver, private communication to J. L. C.

effect could be considerably smaller in view of its smaller molecular size (molecular radius of ~1.79 Å compared to Ar with ~1.92 Å and N_2 with ~2.0 Å) and its virtually zero polarizability. This could account for the He results being closest to those predicted for pressure alone. It is seen from Table III that at a given pressure our model predicts a greater depression of ϕ, due to that pressure, as the temperature is increased. The negative slopes of Figure 2 illustrate that with every gas studied the overall effect of gas pressure on ϕ is felt more strongly with increasing temperature. We may tentatively conclude, then, that although the gases at a given pressure are more soluble at higher temperatures, apparently a more pronounced effect of pressure alone on ϕ at such temperatures more than offsets the oppositely directed effects of augmented dilution. This occurs to an ever-increasing extent with increasing temperature; *i.e.*, the depressive effect of pressure on ϕ increases more rapidly with temperature than does the dilution effect of dissolved gas on ϕ as a result of the enhanced solubility. At sufficiently *low* temperatures, conversely, effects of dilution especially by the large Ar and N_2 molecules apparently are adequately great to overcompensate for the milder pressure alone effect, resulting in the observed net *increase* in ϕ with gas pressure at those temperatures.

Conclusions

The foregoing discussion no doubt stretches this oversimplified model to its extremes. It would be asking too much of the model to expect it further to interpret the detailed differences in effects of Ar and N_2, as described in the Results. Certainly the model suffers from complete neglect of any energetic properties of transport. Also, one cannot be certain as to what extent the ignoring of any pressure dependences of the b and B parameters is justified. The model, while tenuous, seems to provide some interesting food for thought as regards the role of free volume in the viscosity of molten alkali nitrates and appears to provide some reasonable interpretations of the results at hand. These experimental results, taken either alone or in the light of the model, would seem definitely to indicate the role of dissolved inert gases in these melts to be as a diluent and *not* to occupy any existing free volume. This laboratory is currently embarking on a project to attempt to measure viscosities of $NaNO_3$ and KNO_3 under pressure alone, by means of a rolling sphere device. If successful, forthcoming data should help to clarify the effects of gas solubility and the nature of the theoretical model.

Acknowledgment. The authors express their appreciation to the National Science Foundation for support of this work by Grant No. GP-12002.

Demonstration of the Existence of La_2F_6 Gas and Determination of Its Stability

by Harry B. Skinner and Alan W. Searcy*

Inorganic Materials Research Division, Lawrence Radiation Laboratory, and Department of Materials Science and Engineering, College of Engineering, University of California, Berkeley, California *(Received April 20, 1970)*

Publication costs assisted by the U. S. Atomic Energy Commission

Intensities of ion peaks attributable to $LaF_3(g)$ and $La_2F_6(g)$ have been measured as functions of temperature in a mass spectrometer study of the equilibrium vapor of lanthanum trifluoride. The vaporization data for the monomer are in very good agreement with torsion-effusion data of Mar and Searcy. The heat of the reaction $La_2F_6(g) = 2LaF_3(g)$ is 71.3 ± 1.9 kcal/mol at 1577°K. The apparent entropy of sublimation of the dimer is about 11 eu/mol lower than expected from studies of aluminum halides. It is argued that the principal ion fragment produced from $La_2F_6(g)$ in the mass spectrometer is masked by that from $LaF_3(g)$ and that the partial pressure of $La_2F_6(g)$ is about 1% that of the monomer at 1575°K, a value about 100 times that calculated by conventional interpretation of the mass spectrometer data. The vapor pressure of the dimer at 1220 to 1780°K is $\log P_{atm} = -(2.173 \pm 0.009 \times 10^4/T + 9.608 \pm 0.0065$.

I. Introduction

Dimers are present at high concentrations in the vapors of aluminum trihalides, but although scandium, yttrium, and lanthanum trifluorides[1] and many lanthanide trifluorides[2-4] have been studied with mass spectrometers, no dimers of these fluorides have been reported. By using effusion cells with multiple orifices of small diameter we have extended mass spectrometer measurements of lanthanum fluoride to higher temperatures and have measured as a function of temperature a low-intensity peak ($La_2F_5^+$) that arises from dissociative ionization of La_2F_6. This paper reports the measurements and compares the data obtained for $La_2F_6(g)$ with data for aluminum trihalide dimers,[5-7] $Fe_2Cl_6(g)$,[5] and $La_2Cl_6(g)$.[8] Analysis of the enthalpy and apparent entropy data for the dimer leads to the conclusion that the true pressure of the dimer is not four orders of magnitude lower than that of the monomer as suggested by conventional interpretation of intensity data, but only about two orders of magnitude lower.

II. Experimental Section

This study was carried out with a 60° sector, 1 ft radius, magnetic deflection mass spectrometer built by Nuclide Associates. The sample of lanthanum trifluoride obtained from Semi-Elements, Inc. was heated by electron bombardment in a molybdenum Knudsen cell with a graphite liner. The lanthanum fluoride of this study was a nominal 99.9% purity, and showed 0.015% iron as the principle impurity by spectrographic analysis. The same material was used for the torsion–effusion portion of the study of Mar and Searcy.[9]

Three small orifices were employed in each lid to increase the ion current signal without exceeding the mean free path to diameter ratio above which molecular flow equations become invalid. The limiting ratio for LaF_3 gas has been demonstrated to be about 0.4 as calculated from the hard sphere model.[9] Two orifice sizes were used, 0.01 cm diameter and 0.04 cm diameter drilled in graphite cell lids of thicknesses 0.025 cm and 0.1 cm, respectively. It should be noted that while some measurements were made close to the upper pressure limit for molecular flow, other measurements were made well below the limit. The molecules of the beam could not, therefore, have undergone the kind of adiabatic cooling with the resultant cluster formation that has recently been described.[10,11] No shutterable species were observed at the mass numbers of LaF_3^+ or $La_2F_6^+$, but peaks at masses corresponding to LaF_2^+ and $La_2F_5^+$ were concluded to be produced solely by dissociative ionization of the monomer $LaF_3(g)$ and the dimer $La_2F_6(g)$, respectively.

(1) R. A. Kent, K. F. Zmbov, A. S. Kana'an, G. Besenbruch, J. D. McDonald, and J. L. Margrave, *J. Inorg. Nucl. Chem.*, 28, 1419 (1966).

(2) K. F. Zmbov and J. L. Margrave, *J. Chem. Phys.*, 45, 3167 (1966).

(3) G. Besenbruch, T. V. Charlu, K. F. Zmbov, and J. L. Margrave, *J. Less-Common Metals*, 12, 375 (1967).

(4) K. F. Zmbov and J. L. Margrave, *ibid.*, 12, 494 (1967).

(5) "JANAF Thermochemical Data," Dow Chemical Co., Midland, Mich., 1965.

(6) R. F. Krause, Jr., and T. B. Douglas, *J. Phys. Chem.*, 72, 475 (1968).

(7) A. Büchler, E. P. Marram, and J. L. Stauffer, *ibid.*, 71, 4139 (1967).

(8) J. W. Hastie, P. Ficaloro, and J. L. Margrave, *J. Less-Common Metals*, 14, 83 (1968).

(9) R. W. Mar and A. W. Searcy, *J. Phys. Chem.*, 71, 888 (1967).

(10) T. A. Milne and F. T. Greene, *J. Chem. Phys.*, 47, 4095 (1967).

(11) T. A. Milne, A. E. Vandegrift, and F. T. Greene, *ibid.*, 52, 1552 (1970).

Identification of the species $La_2F_5^+$ was made by use of the calibrated gauss indicator to establish the mass as correct for $La_2F_5^+$. A cell exhaustion experiment proved that the $La_2F_5^+$ intensity dropped in conjunction with the LaF_2^+ intensity. Agreement of $La_2F_5^+$ intensity data from a graphite-lined tantalum cell with that from the graphite-lined molybdenum cell showed that a foreign metal did not contribute to the mass peak. Thermodynamic calculations indicate that contributions to LaF_2^+ and $La_2F_5^+$ ion intensities by dissociation reactions or reaction with graphite should be negligible.

The intensities of the LaF_2^+ and the $La_2F_5^+$ ions were followed as functions of temperature using 70-eV ionizing electrons. Many data points were taken during each run with temperatures varied up, then down. Temperatures were measured with a Pt—Pt–10% Rh thermocouple clamped securely to the molybdenum cell. About 15 min was allowed between measurements to ensure that equilibrium had been reached.

It was necessary at high temperatures to follow the LaF_2^+ that resulted from contributions from the low abundance isotope ^{138}La because intensities from LaF_2^+ that contained ^{139}La were so high that they flooded the detector. All data were divided by the appropriate isotopic fractional abundance.[12]

The pressure of $LaF_3(g)$ calculated from a least-squares fit of the I^+T *vs.* $1/T$ data of each run was made to coincide at the average temperature of the run with the lanthanum fluoride pressure of Mar and Searcy.[9] The same factor, corrected for estimated relative cross sections and electron multiplier gain, was applied to the dimer intensity. The electron multiplier gain for the dimer was estimated to equal that of the monomer and the cross section for electron impact ionization for La_2F_6 was estimated to be 1.5 times the cross section of LaF_3. This value is the approximate average found for dimers of alkali halides by Berkowitz, *et al.*[13]

III. Results and Discussion

Figure 1 shows the results of two mass spectrometer runs. Preliminary exploratory runs with the 0.01-cm diameter orifices gave data in reasonable agreement with the data of Figure 1 but the data were not included because instrumental variables were not as well controlled in the exploratory runs as in the subsequent runs.

Because the monomer data extend over a 500° range from 1221° to 1736°K, the enthalpy of sublimation changes significantly with temperature, and the change in heat capacity for vaporization, ΔC_p, should not be neglected in calculation of enthalpies and entropies of vaporization. Mar and Searcy[9] have estimated the heat capacity for the solid and monomer to be $C_p(s) = 19.796 + 8.42 \times 10^{-3}T - 5.90 \times 10^4T^{-2}$ and C_p (monomer) $= 21.323 - 4.065 \times 10^{-4}T - 3.375 \times 10^5T^{-2}$, respectively. The heat capacity difference for reactions, 2 monomer → dimer from JANAF[5] for aluminum halides and iron chloride are all about 4 cal/deg-mol of dimer. This constant 4 cal/deg-mol of dimer was applied to give for sublimation of 1 mol of La_2F_6 $\Delta C_p = -11$ cal/deg. Second-law enthalpies of sublimation were calculated for the monomer at 1487°K, the midpoint of the experimental range of Mar and Searcy,[9] and 1577°K, the midpoint of the range of measurements, to be 97.8 ± 0.8 kcal/mol and 96.7 ± 0.8 kcal/mol, respectively. The enthalpy of sublimation at 1487°K for the monomer is in satisfactory agreement with the value of 99.3 kcal/mol of Mar and Searcy but in only fair agreement with the value 92.0 kcal/mol reported by Kent, *et al.*,[1] at 1324°K. The calculated entropy of sublimation of the monomer at 1577°K is 42.03 ± 0.72 eu/mol.

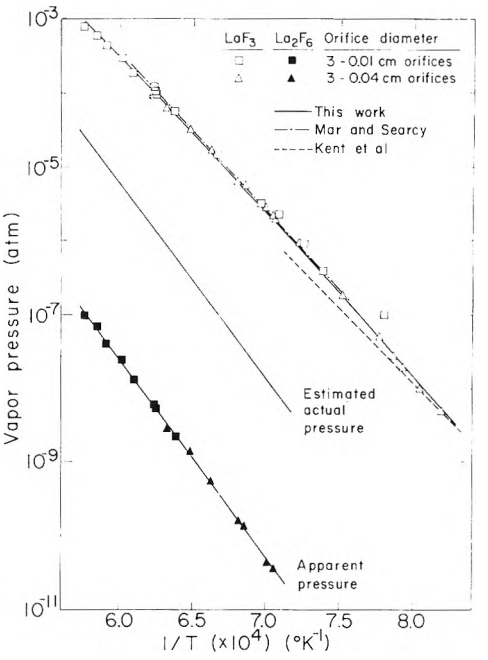

Figure 1. Vaporization data for lanthanum trifluoride.

From the least-squares fit of the heat capacity-corrected data for the La_2F_6 molecule, the entropy and enthalpy of sublimation at 1577°K were calculated to be 38.4 ± 1.0 eu/mol and 122.1 ± 1.1 kcal/mol, respectively. The enthalpy and entropy of sublimation of monomers and dimers measured in this study yield a dimerization enthalpy for $LaF_3(g)$ of −71.3 ± 1.9 kcal/mol and a dimerization entropy of −45.6 ± 1.8 eu/mol, where quoted error limits are standard deviations from the least-squares fit.

Since temperature-dependent errors are easier to control in our torsion–effusion apparatus than in our mass spectrometer and since Mar and Searcy[9] demon-

(12) W. H. Sullivan, Trilinear Chart of the Nuclides, U. S. Government Printing Office, Washington, D. C., 1957.

(13) J. Berkowitz, H. A. Tasman, and W. A. Chupka, *J. Chem. Phys.*, **36**, 2170 (1962).

strated careful temperature measurement by obtaining a heat of sublimation for tin, $\Delta H_{298} = 72.0$ kcal, in close agreement with the value recommended by Hultgren, *et al.*,[14] the Mar and Searcy value of 99.3 kcal/mol at 1487°K should be accepted as the most reliable. Correction of our measured temperature dependences for the difference between this value and the value 97.8 that we measured at 1487°K yields a corrected value of 123.7 ± 5.0 kcal/mol for sublimation of the dimer at 1577°K. This change in enthalpy plus the partial pressure of La_2F_6 at 1577 yields for the entropy of dimer sublimation 40.3 ± 3.0 eu/mol at 1577°K. The quoted error limits take into consideration uncertainties in measurement of relatively low pressures. These estimated limits yield probable error limits on the enthalpy and entropy of dimerization of ±5.5 kcal/mol and 3.2 eu/mol, respectively.

Appearance potentials of ions observed in this work were determined by the method of extrapolated differences using Hg and are shown in Table I. Our

Table I: Appearance Potentials of Ions in the Mass Spectra of $LaF_3(g)$

Ion	This work, eV	Kent, *et al.*, eV[1]
La^+	26.9	26.5
LaF^+	18.5	18.5
LaF_2^+	11.8	12.0
$La_2F_5^+$	12.4	

appearance potential data are in good agreement with those reported by Kent, *et al.*,[1] for fragments of the monomer.

The surprising result of this study is not that a dimer of a rare earth fluoride has been identified, but that its apparent concentration is so low; the intensity of $La_2F_5^+$ is only about 10^{-4} times that of LaF_2^+. In contrast, Al_2F_6 is reported to constitute about 1.7% of the vapor of the aluminum trifluoride when the total vapor pressure is 10^{-5} atm.[5] The aluminum chloride, bromide, and iodide dimers vaporize at still higher relative concentrations. The enthalpy of dissociation of $La_2F_6(g)$ to two $LaF_3(g)$ molecules when the monomer pressure is 10^{-5} atm is 72.6 kcal compared with 48.8 kcal for $Al_2F_6(g)$.[7] The ratio of the enthalpy of sublimation of the monomer to the enthalpy of dissociation of the dimer to two monomers, which is usually critical in determining whether a dimer will be a major species,[15-17] is 1.37 for the LaF_3 molecules compared with 1.38 for the AlF_3 molecules. The partial pressures calculated for La_2F_6 are anomalously low because of the exceptionally high entropy measured for dissociation of the La_2F_6 dimer to monomer. The exceptional entropy for La_2F_6 dissociation is apparent from Table II,

Table II: Entropy Changes for the Reaction $2MX_3(g) \rightarrow (MX_3)_2(g)$ in the Experimental Temperature Range

Associated compd	$-\Delta S$, eu	Ref
$(AlI_3)_2$	33.9	5
$(AlCl_3)_2$	34.3	5
$(AlBr_3)_2$	37.4	5
$(AlF_3)_2$	35.0	6, 7
$(FeCl_3)_2$	33.9	5
$(LaCl_3)_2$	30.0 ± 3	8
$(LaF_3)_2$	(45.6)[a]	This work

[a] But see text.

which reports entropies for dissociation of trihalide dimers to monomers.

In the absence of molecular structure and internal energy data which would permit calculation of entropies of the lanthanum fluoride vapor species by the methods of statisitical mechanics, one cannot say with absolute certainty that the apparent entropy determined in this study is erroneous, but the anomalous entropy argues strongly that some systematic error was made either in measurement of $La_2F_5^+/LaF_2^+$ ion intensity ratios or in calculation of La_2F_6/LaF_3 pressure ratios from the measured intensities. The most obvious possible source of such an error, failure to attain equilibrium for dimer vaporization, is ruled out by excellent agreement in intensity ratios measured with orifice areas that differed by a factor of 16.

The discrepancy could be explained by a breakdown in the proportionality rule

$$P \propto I^+T$$

This possibility was suggested by Berkowitz, *et al.*,[13] for lithium fluoride. The probable cause favored by those authors to explain the temperature trend in fragmentation of LiF(g) was the formation of Li^+ with excess kinetic energy. The agreement obtained in the present study for the temperature dependence of $LaF_3(g)$ pressures with that obtained by the torsion–effusion method implies that no such error exists for the monomer and, therefore, that such an effect would have to be an exclusive peculiarity of the dimer. To reconcile the measured intensity ratio with an expected entropy of ~35 for dimer dissociation to monomers would require that the efficiency of ionization at the highest temperature of measurement relative to that

(14) R. Hultgren, R. L. Orr, P. D. Anderson, and K. K. Kelly, "Selected Values of Thermochemical Properties of Metals and Alloys," Wiley, New York, N. Y., 1963.

(15) L. Pauling, *Phys. Rev.*, 54, 899 (1938).

(16) G. Verhaegen, F. E. Stafford, P. Goldfinger, and M. Ackerman, *Trans. Faraday Soc.*, 58, 1929 (1962).

(17) G. DeMaria, "Chemical and Mechanical Behavior of Inorganic Materials," A. W. Searcy, D. V. Ragone, and U. Colombo, Ed., Wiley-Interscience, New York, N. Y., 1970, Chapter 5.

at the lowest temperature of measurement vary by a factor of about 5. Since significant temperature dependences for fragmentation have not been clearly established for any high-temperature systems, such a large variation in ionization efficiency seems highly improbable. Furthermore, a less drastic explanation of the anomalous data is provided by comparison with fragmentation patterns for complex salt molecules.

Table III lists fragmentation patterns reported for several complex molecules for which the principal ion has been identified as a small fragment of the parent molecule. In each of these examples, the reaction that

Table III: Fragmentation Patterns for Some Complex Molecules

Parents	Observed ions	Intensity	Ref
$KCl–ErCl_3$	K^+	59	*a*
(30-V electrons)	KCl^+	0.76	
	Er^+	0.63	
	$ErCl^+$	0.56	
	$ErCl_2^+$	1.9	
	$KErCl_2^+$	0.16	
	$KErCl_3^+$	1.0	
$CsCl–ErCl_3$	Cs^+	67.6	*b*
(52-V electrons)	$CsCl^+$	0.88	
	Cs_2Cl^+	0.96	
	$ErCl_2^+$	0.79	
	$CsErCl_2^+$	0.04	
	$CsErCl_3^+$	1.0	
$CsCl–NdCl_3$	Cs^+	526	*b*
(51-V electrons)	$CsCl^+$	5.84	
	Cs_2^+	0.26	
	Cs_2Cl^+	4.58	
	Nd^+	1.05	
	$NdCl^+$	1.74	
	$NdCl_2^+$	6.05	
	$NdCl_3^+$	0.16	
	$CsNdCl_2^+$	0.05	
	$CsNdCl_3^+$	1	
$LiBeF_3$	Li^+	2.9	*c*
(60-V electrons)	$LiBeF_2^+$	1	
	LiF^+	0.06	
Li_2BeF_4	Li_2F^+	40	*c*
(60-V electrons)	$Li_2BeF_3^+$	1	

[a] G. A. Semenov and F. G. Gavryuchenkov, *Zh. Neorgan. Khim.*, **9**, 224 (1964). [b] F. G. Gavryuchenkov and G. I. Novikov, *Vestn. Leningrad Univ.*, **21**, No. 4., *Ser. Fiz. Khim.*, No. 1., 106 (1965). [c] A. Büchler and J. L. Stauffer in "Thermodynamics," Vol. 1, Int. At. Energy Agency, Vienna, 1966, p 271.

seems most reasonably to explain production of the observed ion from the singly ionized parent molecule is one that yields the observed ion, a halogen atom, and a neutral monomer of one of the constitutent salts. For example

$$[(Li_2F_2)BeF_2]^+(g) = Li_2F^+(g) + BeF_2(g) + F(g) \quad (1)$$

It is well established[18] that a sequence of monomolecular dissociation reactions can give rise to several fragments of the parent ion such as indicated in reaction 1. The analogous reaction for the lanthanum fluoride dimer would be

$$(LaF_3)_2^+(g) = LaF_2^+(g) + LaF_3(g) + F(g) \quad (2)$$

It is reaction 2, rather than $La_2F_6^+ = La_2F_5^+ + F$, which from behavior of related polymeric species under electron bombardment would be expected as the principal reaction of an excited $La_2F_6^+$ ion. But this reaction is masked by the higher LaF_2^+ intensity from LaF_3^+ fragmentation.

The appearance potential for LaF_2^+ from reaction 2 can be calculated from the enthalpy of dissociation of the dimer to monomer and from the appearance potentials of $La_2F_5^+$ and LaF_2^+ to be 14.9 eV compared with 11.8 eV for LaF_2^+ from the monomer. The occurrence of reaction 2, therefore, would not be revealed by measurement of LaF_2^+ intensities as a function of electron energies.

We conclude that reaction 2 is probably the principal reaction undergone by La_2F_6 when ionized by 70-eV electrons. The temperature dependence for vaporization of the dimer calculated from $La_2F_5^+$ intensity measurements and the enthalpy of dissociation of dimer to monomer and of sublimation of the dimer derived from that temperature dependence are correct. The partial vapor pressure of the dimer is best estimated by assuming the entropy of dissociation of dimer to monomer to be about the same as for Al_2F_6, 35 eu/mol of dimer, from which the partial pressure of La_2F_6 dimer is calculated to be 3.5×10^{-8} atm when the partial pressure of the monomer is 10^{-5} atm. Figure 1 shows the estimated true pressure of the dimer, which is given by the equation

$$\log P_{atm} = -\frac{(2.173 \pm 0.009) \times 10^4}{T} + 9.608 \pm 0.065$$

We plan next to study $Ce_2F_6(g)$. We anticipate that the extra electron of each cerium atom will give rise to a small increase in stability of the dimer relative to the monomer and will cause a change in fragmentation patterns[19] for both monomer and dimer. A higher intensity of dimer would, and a changed fragmentation pattern could, make easier the problem of analysis of the monomer–dimer stability relationships. The cerium fluoride study should, therefore, not only be interesting in itself but should strengthen or weaken the credibility of the analysis we have presented of our lanthanum fluoride data.

Acknowledgment. This research was sponsored by the Metallurgy and Materials Branch of the U. S. Atomic Energy Commission.

(18) F. P. Lossing in "Mass Spectrometry," Charles A. McDowell, Ed., McGraw-Hill, 1963, p 449.

(19) J. W. Hastie and J. L. Margrave, *High Temp. Science*, 1, 481 (1969).

A Thermodynamic Investigation of the Tungsten–Oxygen–Bromine System

by Suresh K. Gupta

Lamp Research Laboratory, General Electric Co., Nela Park, Cleveland, Ohio 44112 *(Received July 17, 1970)*

Publication costs assisted by the General Electric Co.

A Knudsen effusion mass spectrometric technique has been employed to study thermodynamic properties of the W–O–Br system. Vaporization of solid WO_2Br_2 in a Knudsen cell has been found to occur without dissociation in the temperature range 398–452°K, and 35.8 ± 1.0 kcal/mol has been obtained for its sublimation enthalpy at 298°K. Equilibrium studies of the WO_2–Br_2–I_2 reaction in the temperature range 740–980°K have yielded −131.4 ± 2.0 kcal/mol for the $\Delta H_f°$ of gaseous WO_2Br_2 at 298°K. Comparisons have been made with the published calorimetric thermochemical data. Vaporization of solid $WOBr_4$ examined in the range 360–403°K has yielded its enthalpy of sublimation 30.5 ± 1.0 kcal/mol at 298°K, which is combined with the published data on solid $WOBr_4$ to give −98.9 ± 2.0 kcal/mol for the $\Delta H_f°$ of gaseous $WOBr_4$ at 298°K.

Introduction

Tungsten oxybromides, WO_2Br_2 and $WOBr_4$, first reported nearly a century ago,[1-3] have been the subject of some recent thermodynamic[4-6,9,10,14] and structural investigations.[7,8,11-13] Thermodynamic data reported are the calorimetrically measured heats of formation which suffer from the use of yet unestablished thermochemical data on solid H_2WO_4.[5,14] The published tensimetric vaporization measurements lack definitive gas phase characterizations which are essential to the understanding of their complex decomposition behavior.[9,14]

In the present study using the Knudsen effusion mass spectrometric techniques, we have attempted to establish the nature of the vaporization behavior and other important thermodynamic properties of these oxybromides.

Experimental Section

The mass spectrometric method has been described in detail earlier.[15] Calculated isotopic distributions, background mass counting, and magnetic field calibration were used to unambiguously establish the ionic species. Only shuttered ion currents were used in the calculations. The appearance potentials (A.P.) were measured from automatically recorded ionization efficiency curves using a Hewlett-Packard 7035B X-Y recorder and a Beckmann DC motor potentiometer Model 939 coupled to the variable electron energy control. Krypton and background mercury were used as voltage calibrant. The A.P.'s were evaluated by the extrapolated voltage difference method[16] unless the ion currents were very small where the vanishing current method[16] was more suitable.

Tungsten and quartz Knudsen cells (0.75 in. i.d. × 1.0 in. long) provided with 3 in. long inlet gas extensions were used for the study of WO_2(s)–halogen reactions. WO_2(s), prepared by the H_2–H_2O reduction method,[17] was contained in a tungsten cup in the tungsten crucible or filled directly in the quartz cell. The $^1/_8$ in. o.d. extension of the tungsten cell was connected to $^1/_4$ in. o.d. Monel inlet gas line using Monel Gyrolok fittings. The quartz cell extension fitted snugly on the Monel gas line. Baker analytical grade bromine was further purified by repeated distillation and filled in an all stainless steel container equipped with a packless stainless steel Hoke valve. Fisher reagent grade iodine was resublimed over dehydrated magnesium perchlorate before use.

Solid WO_2Br_2, prepared by flowing bromine in a nitrogen stream over solid WO_2 at 500°, was collected downstream as shiny, orange, flaky crystals, which gave an X-ray diffraction pattern in good agreement with that reported.[6] Solid $WOBr_4$, prepared and purified by a reported procedure,[4] also produced an X-ray diffraction pattern that matched well with the reported

(1) A. Bonnet, *L'Instit.*, **5**, 46 (1837); *J. Prakt. Chem.*, **10**, 206 (1837).

(2) C. W. Blomstead, *ibid.*, **82**, 432 (1861).

(3) H. E. Roscoe, *Justus Liebigs Ann. Chem.*, **162**, 349 (1872).

(4) H. Hartung, *Z. Chem.*, **4**, 232 (1964).

(5) S. A. Shchukarev and G. A. Kokovin, *Russ. J. Inorg. Chem.*, **9**, 849 (1964).

(6) G. A. Kokovin and N. K. Toropova, *ibid.*, **10**, 304 (1965).

(7) H. Hess and H. Hartung, *Z. Anorg. Allg. Chem.*, **344**, 157 (1966).

(8) C. G. Barraclough and J. Stals, *Aust. J. Chem.*, **19**, 741 (1966).

(9) G. A. Kokovin, *Russ. J. Inorg. Chem.*, **12**, 7 (1967).

(10) R. Colton and I. B. Tomkins, *Aust. J. Chem.*, **21**, 1975 (1968).

(11) J. H. Canterford, R. Colton, and I. B. Tomkins, *Inorg. Nucl. Chem. Lett.*, **4**, 471 (1968).

(12) D. M. Adams and R. G. Churchill, *J. Chem. Soc. A*, 2310 (1968).

(13) B. G. Ward and F. E. Stafford, *Inorg. Chem.*, **7**, 2569 (1968).

(14) J. Tillack, R. Kaiser, and J. H. Dettingmeijer, Philips Zentrallaboratorium (Aachen), private communication.

(15) S. K. Gupta, *J. Phys. Chem.*, **73**, 4086 (1969).

(16) E. H. Field and J. L. Franklin in "Electron Impact Phenomena and the Properties of Gaseous Ions," Academic Press, New York, N. Y., 1957.

(17) J. A. M. van Liempt, *Z. Anorg. Allg. Chem.*, **126**, 183 (1923).

one.[6] All samples were handled in a drybox and transferred to the crucibles very carefully.

Results and Discussion

A. Vaporization of Solid WO_2Br_2. The mass spectrum of the vapor species over solid WO_2Br_2 in the tungsten Knudsen cell with 0.025-in. orifice is given in Table I. The relative ion intensities refer only to the largest isotopic m/e of the species. The mass spectrum is quite similar to that reported for WO_2I_2[15] and exhibited no change over the investigated temperature range 398–452°K. The A.P.'s are also given in Table I. Br_2^+ ion currents were too small for A.P. evaluation. Thus, WO_2Br_2 is considered as the only gaseous species below 450°K which agrees with Kokovin's tensimetric observation of the WO_2Br_2 decomposition only above 570°K.[9] The reported mass spectra by Barraclough and Stals, although in general agreement with ours, contain minor additional polymeric ionic species, *e.g.*, $W_2O_4Br_2^+$, etc.[8] They have not given the vaporization temperature of the WO_2Br_2 solid samples. Kokovin's data indicate the presence of bromine besides WO_2Br_2 and $WOBr_4$ in the gas phase above 600°K and minor amounts of polymeric WO_2Br_2 species above 720°K.[9] Thus, in addition to the decomposition reaction[3,9]

$$2WO_2Br_2 = WO_3(s) + WOBr_4(g) \qquad (1)$$

other possible reaction may involve the formation of lower valent oxybromides[18,19] and dissociation to $WO_2(s)$ and bromine at these temperatures.

Table I: Mass Spectrum and Appearance Potentials Data for Gaseous WO_2Br_2

m/e	Ionic[a] species	Relative[b] intensity	Appearance potential, eV
376	$WO_2Br_2^+$	100	11.4 ± 0.2
360	$WOBr_2^+$	3.2	
344	WBr_2^+	1.5	
297	WO_2Br^+	34.0	13.0 ± 0.4
281	$WOBr^+$	10.3	20.0 ± 0.8
265	WBr^+	3.9	
216	WO_2^+	6.6	
200	WO^+	9.3	
184	W^+	4.0	
160	Br_2^+	0.06	
81	Br^+	5.4	

[a] WO_2Br_2 is considered as the only molecular precursor to these ionic species. [b] Relative intensity values are the ion currents for the indicated m/e peak at 50 eV ionizing electron energy.

The enthalpy of sublimation of $WO_2Br_2(s)$ was determined by a least-squares treatment of the $\log T \times I_{WO_2Br_2^+}$ *vs.* $1/T$ plots. A typical set of data is depicted in Figure 1. Two different sets of data gave values 35.2 ± 0.2 and 34.9 ± 0.6 kcal/mol and the mean enthalpy

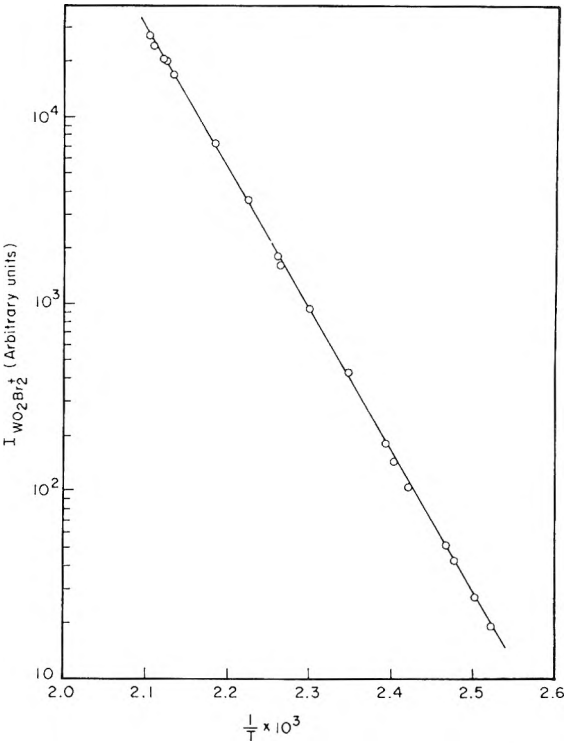

Figure 1. Mass spectrometric determination of the enthalpy of sublimation of solid WO_2Br_2.

35.0 ± 0.6 kcal/mol at 430°K with an overall estimated uncertainty of ±1.0 kcal/mol. A value of 34.7 kcal/mol at 640°K is derived from Kokovin's tensimetric data.[9] Agreement between the two results is very good although Kokovin has pointed out that his data are approximate due to the complexity of the WO_2Br_2 vaporization in the examined temperature range.[9] Assuming ΔC_p^0 for $WO_2Br_2(s)$ sublimation identical with that for $WO_2Cl_2(s)$,[20] the sublimation enthalpy of solid WO_2Br_2 is 35.8 ± 1.0 kcal/mol at 298°K.

B. $WO_2(s)$ + $Br_2(g)$ Reaction. WO_2Br_2 is the predominant gaseous species resulting from the reaction

$$WO_2(s) + Br_2(g) = WO_2Br_2(g) \qquad (2)$$

in the temperature range 500–1100°K. The mass spectra and the A.P.'s agreed with that from the vaporization study of solid WO_2Br_2 except for the Br_2^+ and Br^+ ion currents, which arise primarily from the molecular and/or atomic bromine in the cell. The bromine pressure in the cell is estimated to be less then 10^{-2} Torr. The measured A.P. for Br_2^+, 10.8 ± 0.3 eV, compares well with the reported electron impact[21] and photoionization values,[22] 10.69 and 10.55 eV, respectively. The

(18) G. W. A. Fowles and J. L. Frost, *Chem. Commun.*, 252 (1968).
(19) J. Tillack and R. Kaiser, *Angew. Chem., Int. Ed. Engl.*, **7**, 142, 294 (1968).
(20) "Janaf Thermochemical Tables," Dow Chemical Co., Midland, Mich., March, 1967.
(21) D. C. Frost and C. A. McDowell, *Can. J. Chem.*, **38**, 407 (1960).
(22) K. Watanabe, T. Nakayama, and J. R. Mottl, *J. Quant. Spectrosc. Radiat. Transfer*, 2, 339 (1962).

ionization efficiency curve for Br_2^+ failed to show any distinct break due to very low contributions from WO_2-Br_2 fragmentation. A.P. determinations for Br^+ were complicated by the presence of background HBr in the mass spectrometer. The presence of $WOBr_3^+$, WBr_3^+, and $WO_3Br_2^+$ ion currents of less than 1% of the WO_2-Br_2^+ ion intensities was also observed. $WOBr_3^+$ is the major fragment ion in the mass spectrum of $WOBr_4$ (see section F and Table IV), and is thus attributed to the presence of $WOBr_4$(g) in the cell. The observed ratio of $WOBr_3^+$ and WBr_3^+ ion currents was identical with that observed in the fragmentation pattern of $WOBr_4$. WO_3-Br_2^+, observed only at higher bromine pressures, is attributed to WO_3Br_2 species which may be formed by reactions with deposits (*e.g.*, WO_2Br_2) on the radiation shields. It is doubtful if ion-neutral reactions are responsible for $WO_3Br_2^+$ ions as the ion source region pressure is kept $\sim 10^{-7}$ Torr. $WOBr_4$ could not be detected at temperatures above 850°K.

In the experiments with WO_2(s) in the tungsten cell, it was concluded that nonequilibrium conditions existed for reaction 2 at 430–880°K because the slopes of the isothermal log $I_{WO_2Br_2^+}$ *vs.* log $I_{Br_2^+}$ plots in this temperature range varied from 0.5 to 0.95. It is believed that lack of sufficient WO_2 surface imposed kinetic limitations on reaction 2, and thus further experiments were conducted with the quartz cell nearly half filled with WO_2(s). With this new set up the measured $I_{WO_2Br_2^+}/I_{Br_2^+}$ ratios, which are proportional to the equilibrium constant for reaction 2, were higher than those observed earlier and also were invariant with bromine inlet pressure at cell temperatures above 900°K. A large number of measurements made in the temperature range 900–1200°K displayed unusual scatter in the log $I_{WO_2Br_2^+}/I_{Br_2^+}$ *vs.* $1/T$ plot. The $I_{WO_2Br_2^+}/I_{Br_2^+}$ ratios showed a distinct decreasing trend with time. A fresh sample of WO_2(s) always produced the highest value for the ion current ratio. Although these data are not useful for thermochemical calculations, it may be worthwhile to mention that the evaluated second-law $\Delta H_2°$ ranged from 0.8 to 4.4 kcal/mol. X-Ray diffraction analysis failed to reveal any changes in the WO_2 samples used in these experiments.

In a kinetic study of WO_2(s) + Br_2(g) reaction at 600–1000°K and 0.1 Torr bromine pressure, using the microbalance-flow method, the rate of the reaction has been observed to decrease in successive runs at a specified temperature.[23] Greenish yellow WO_3 deposit was observed on the reaction tube walls and the sample holder. The WO_2 sample surface appeared blue but failed to show any phase change on X-ray diffraction analysis.[23] Slow surface oxidation of WO_2 sample is belived to be responsible for the observed behavior of the system in the mass spectrometric and kinetic investigations. It is noteworthy that no such effect was observed in the earlier WO_2 + I_2 investigation[15] and the one discussed below.

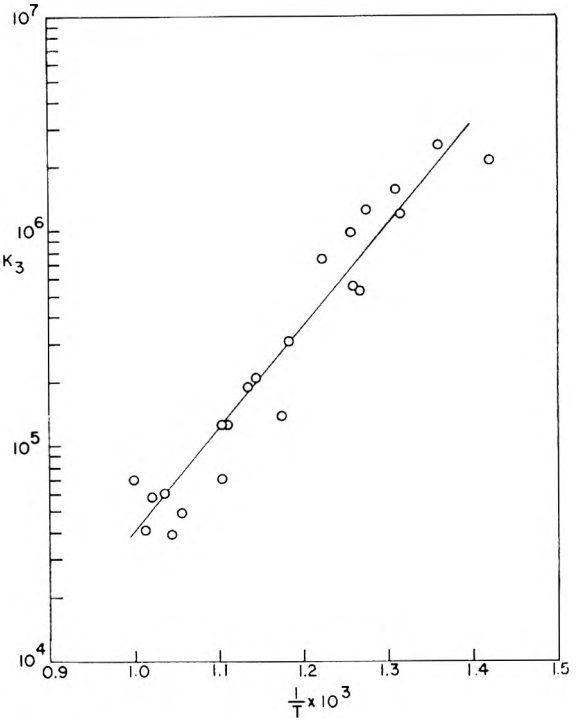

Figure 2. Equilibrium constant data for the reaction: WO_2I_2(g) + Br_2(g) = WO_2Br_2(g) + I_2(g).

C. WO_2(s) + I_2(g) + Br_2(g) Reaction. Investigation of this mixed halogen system was undertaken to obtain enthalpy of the following gas-phase reaction

$$WO_2I_2(g) + Br_2(g) = WO_2Br_2(g) + I_2(g) \quad (3)$$

which will be free from complexities of reactions involving solid phases. Mass spectra indicated the presence of WO_2Br_2, WO_2I_2, WO_2IBr, I_2, Br_2, and atomic halogens in the cell. Ion currents at *m/e* 470, 376, 254, and 160 corresponding to the $WO_2I_2^+$, $WO_2Br_2^+$, I_2^+, and Br_2^+ ionic species, respectively, were measured at 50-eV ionizing electron energies in the range 740–980°K. At temperatures beyond this range, the WO_2-I_2^+ ion currents became quite small. These ion currents were converted to their respective total currents using the known[15] and measured fragmentation patterns, and the following equilibrium constants were evaluated (Figure 2)

$$K_3 = \frac{I_{WO_2Br_2^-} \times I_{I_2^+}}{I_{WO_2I_2^+} \times I_{Br_2^+}} \times \sigma \times S_m$$

To a good approximation, the ratios of the total ionization cross section, σ, and multiplier efficiencies, S_m, would be unity because of the identical nature of the species in the reaction.

The data listed in Table II were treated both by the second- and third-law procedures. In the third-law treatment, $\Delta S_3°$ was taken as zero, which is a valid assumption for the simple exchange reaction 3, and

(23) E. G. Zubler, private communication.

Table II: Thermochemical Calculations for Reactions 2 and 3

Temp, °K	I_{470}	I_{376}	I_{254}	I_{160}	K_2	$\Delta H_2°$,[a] kcal/mol	K_3	$-\Delta H_3°$,[a] kcal/mol
844	9.6	81.4×10^2	27.8×10^3	36.5	374.8	2.31	30.7×10^4	21.1
794	4.2	27.5×10^3	41.0×10^3	230	200.9	3.16	55.4×10^4	20.9
958	4.2	68.5×10^3	16.8×10^2	335	343.5	2.57	38.8×10^3	20.1
785	4.2	32.0×10^2	56.0×10^3	16	336.0	2.34	12.7×10^5	21.9
763	5.0	69.0×10^2	10.5×10^3	43	269.6	2.62	15.5×10^5	21.6
795	3.6	80.0×10^2	43.0×10^3	46	292.2	2.58	98.8×10^4	21.8
901	4.5	23.7×10^3	48.5×10^2	96	414.8	2.17	12.6×10^4	21.0
986	5.7	58.8×10^3	29.2×10^2	240	411.3	2.22	59.5×10^3	21.5
788	6.3	36.0×10^3	50.0×10^3	260	232.6	2.92	52.2×10^4	20.6
946	4.2	78.0×10^3	21.3×10^2	385	340.4	2.57	48.9×10^3	20.3
880	4.6	44.0×10^3	81.0×10^2	200	369.6	2.34	18.5×10^4	21.2
802	4.2	18.5×10^3	37.5×10^3	107	292.0	2.60	75.5×10^4	21.6
850	5.6	75.1×10^3	10.5×10^3	490	257.5	2.91	13.8×10^4	20.0
759	1.4	10.4×10^3	30.5×10^3	93	188.6	3.15	12.0×10^5	21.1
703	1.5	27.4×10^3	86.2×10^3	35	131.5	3.47[b]	21.4×10^5	20.4
734	1.8	67.0×10^2	76.8×10^2	54	208.1	2.92	25.1×10^5	21.5
903	4.4	23.1×10^3	47.5×10^2	94.5	410.7	2.18	12.7×10^4	21.1
965	1.4	20.4×10^3	76.0×10^1	84	408.0	2.24	60.5×10^3	21.1
873	4.5	30.8×10^3	11.5×10^2	178	291.0	2.78	20.8×10^4	21.2
904	5.7	61.7×10^3	44.5×10^2	320	323.9	2.61	71.5×10^3	20.1
1003	1.3	15.6×10^3	54.0×10^1	45.6	574.7	1.53[b]	69.6×10^3	22.2
977	4.8	27.0×10^3	21.5×10^2	99	454.0	2.01	57.9×10^3	21.3

[a] The mean values are: $\Delta H_2° = 2.6 \pm 0.4$ and $\Delta H_3° = -21.1 \pm 0.6$ kcal/mol at 298.15°K. [b] These values are rejected in the average computation.

-21.1 ± 0.6 kcal/mol was derived as $\Delta H_3°$ at 298°K. Least-squares evaluation of the second-law plot of log K_3 *vs.* $1/T$ gave -21.3 ± 1.3 kcal/mol and -0.3 ± 1.5 gibbs/mol for $\Delta H_3°$ and $\Delta S_3°$, respectively, at 298°K. Agreement between the second- and third-law values is quite good and well within the experimental error. The indicated standard deviations for these quantities do not reflect the magnitude of the overall uncertainty, which is estimated to be ± 1.5 kcal/mol in consideration of a factor of 2 uncertainty in the measured equilibrium constants and other sources of errors.

Although attempts to obtain equilibrium data were unsuccessful in the $WO_2(s) + Br_2(g)$ investigation, the data from the $WO_2 + I_2 + Br_2$ study were found to be fairly consistent also for reaction 2. Equilibrium constants, K_2, were evaluated by using the total ion currents, I, estimated ionization cross section ratio, σ, and measured multiplier efficiency ratio, S_m.

$$K_2 = \frac{I_{WO_2Br_2^+}}{I_{Br_2^+}} \times \frac{\sigma \times S_m}{a_{WO_2}}$$

Mann's cross sections[24] were employed to evaluate σ using the additivity rule.[25] The multiplier gain ratio, S_m, was unity within 10% accuracy. The activity of solid WO_2 was assumed unity. The second-law plot, log K_2 *vs.* $1/T$ (see Figure 3), on least-squares treatment gave 3.9 ± 0.7 kcal/mol and 15.9 ± 0.8 gibbs/mol for the $\Delta H_2°$ and $\Delta S_2°$, respectively, at 860°K.

The entropy and free energy functions for the WO_2Br_2 molecule were estimated for the third-law treatment.

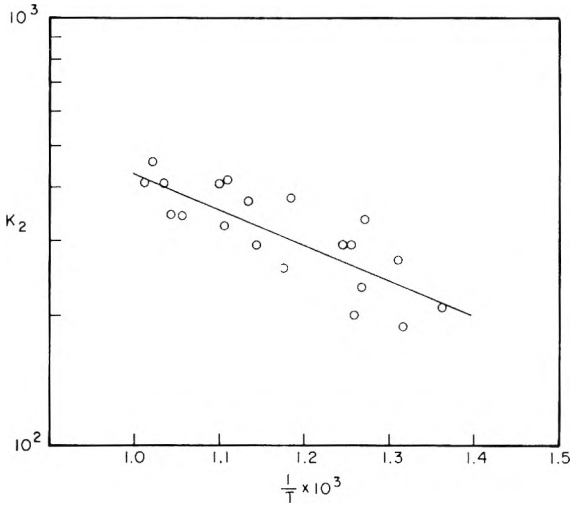

Figure 3. Second-law plot for the reaction: $WO_2(s) + Br_2(g) = WO_2Br_2(g)$.

The WO_2Br_2 molecular structure has not been determined, although some work on the infrared and Raman spectra has been reported.[8,11-13] Molecular structure was assumed to be distorted tetrahedron similar to the isostructural molecules, CrO_2Cl_2, SO_2Cl_2, and the fluorides that have been studied in great details.[26a] The

(24) J. B. Mann, *J. Chem. Phys.* **46**, 1646 (1967).

(25) J. W. Otvos and D. P. Stevenson, *J. Amer. Chem. Soc.*, **78**, 546 (1956).

(26) (a) F. A. Miller, G. L. Carlson, and W. B. White, *Spectrochem. Acta*, **9**, 709 (1959); (b) For experimental values see ref 13.

following vibrational frequencies and molecular parameters were estimated: $\nu_1 = 985$,[26b] $\nu_2 = \nu_3 = 350$, $\nu_4 = 100$, $\nu_5 = 150$, $\nu_6 = 973$,[26b] $\nu_7 = 220$, $\nu_8 = 350$, and $\nu_9 = 280$ cm^{-1}; bond distance[20] W–Br = 2.41 Å, W–O = 1.81 Å; bond angles[20] Br–W–Br = 113°, O–W–O = 109.47°, and O–W–O = 90. The computed thermodynamic functions are given in Table III. Free energy functions[20] for $WO_2(s)$ and $Br_2(g)$ were combined to derive $\Delta H_2° = 2.6 \pm 0.4$ kcal/mol at 298°K as compared to the second-law value of 4.9 ± 0.7 kcal/mol at 298°K converted from 860°K by using $C_p°$ data.[20] The second-law $\Delta S_2°$ derived at 298°K is 17.8 ± 0.8 gibbs/mol as compared to the estimated value, 15.1 gibbs/mol. The error limits given are the standard deviations, but in view of the uncertainties in equilibrium constants and estimated parameters, the overall assigned limits for the $\Delta H_2°$ and $\Delta S_2°$ are ± 2.0 kcal/mol and ± 2.0 gibbs/mol, respectively. The discrepancy between the second- and third-law $\Delta H_2°$ is of the order expected on the basis of the disagreement in the two $\Delta S_2°$ values. Small reductions in the estimated vibration frequencies, especially ν_4 and ν_5, would increase the WO_2Br_2 entropy and hence the estimated $\Delta S_2°$. Thus, until complete structural information on WO_2Br_2 molecule is available, the observed discrepancy cannot be explained. On the basis of the intercomparison of the thermochemical data for reactions 2 and 3 discussed in the next section, we tend to accept the third law $\Delta H_2°$ and our estimated $\Delta S_2°$ as better values for reaction 2. Also, it is always difficult to obtain good thermochemical data by second-law treatment when the enthalpy change is so small and the temperature range is limited.

Table III: Thermodynamic Functions for Gaseous WO_2Br_2

T, °K	$C_p°$, gibbs/mol	$-(G_T° - H_{298}°)/T$, gibbs/mol	$S°$, gibbs/mol
298	20.84	85.79	85.79
400	22.34	86.63	92.25
500	23.30	88.26	97.25
600	23.93	90.13	101.55
700	24.37	92.03	105.28
800	24.67	93.90	108.55
900	24.89	95.69	111.47
1000	25.06	97.40	114.11
1100	25.19	99.03	116.50
1200	25.28	100.58	118.70
1300	25.36	102.05	120.72

The consistent nature of the experimental data obtained in the WO_2–Br_2–I_2 study is in sharp contrast to the observation in the WO_2–Br_2 investigation discussed in the preceding section. It is not possible, at present, to offer any reasonable explanation of the differences in the two systems.

D. Heat of Formation of Gaseous WO_2Br_2. The third-law enthalpy for reaction 3 and thermochemical data on $Br_2(g)$,[20] $I_2(g)$,[20] and $WO_2I_2(g)$[15] give for the $\Delta H_f°$ of $WO_2Br_2(g)$ at 298°K a value -131.4 ± 2.0 kcal/mol which compares well with -130.9 ± 2.0 kcal/mol evaluated from the third-law $\Delta H_2°$ for reaction 2. This agreement supports the earlier argument against accepting the second-law $\Delta H_2°$. Shchukarev and Kokovin have reported -179.7 ± 0.5 kcal/mol for $\Delta H_f°$ of solid WO_2Br_2 at 298°K evaluated from calorimetric determination of the enthalpy of solution in sodium hydroxide.[5] However, they used for the $\Delta H_f°$ of $NaWO_4(s)$ a value -379.6 kcal/mol which has been revised to -369.2 ± 2.0 kcal/mol[20] on the basis of a recent calorimetric determination of the $\Delta H_f°$ of $H_2WO_4(s)$.[27] Using the recent data for $NaWO_4(s)$ and our enthalpy of sublimation of solid WO_2Br_2, their value for the $\Delta H_f°$ of $WO_2Br_2(g)$ at 298°K is -133.5 ± 2.0 kcal/mol as compared to our -131.4 ± 2.0 kcal/mol. The agreement is fair in view of the different nature of the two experimental approaches. Shchukarev and Kokovin have also reported the hygroscopic nature of the WO_2Br_2 samples and their extremely slow dissolution rate in the sodium hydroxide solutions.[5] Any sample deterioration or lack of complete dissolution would tend to make the calorimetric value less negative, and thus in better agreement with our results. Use of the calorimetric $\Delta H_f°$ would make reaction 2 exothermic by 0.8 kcal/mol at 850°K, which is in contrast to its experimentally observed endothermic nature.

It may be worthwhile delving into the controversy about the heat of formation of $H_2WO_4(s)$. The two values, -270.5 and -280.2 kcal/mol, are based, respectively, on the calorimetric determination of solution enthalpy of a specially prepared, easily soluble, $WO_3(s)$ in NaOH solution by Sptizyn and Patsukova,[27] and on the $H_2WO_4(s)$ dissociation pressure measurements by Huttig and Kurre.[28] Tillack and coworkers[14,29] have not been successful in preparation of the easily soluble variety of $WO_3(s)$ reported by Sptizyn and Patsukova. They have also found that the dissociation pressure of $H_2WO_4(s)$ cannot be measured by Knudsen effusion method because of an extremely slow rate of equilibriation.[14] After nearly 3 months of heating in a quartz spiral manometer at 107.5°, they have obtained for the solid $WO_3 \cdot xH_2O$ ($x = 0.7$) a saturated pressure which is identical with the water vapor pressure at the temperature.[14] This observation supports the calorimetric value of Sptizyn and Patsukova[27] and also the doubt expressed in the Janaf Table on $H_2WO_4(s)$[20] concerning the equilibrium nature of Huttig and Kurre's experimental data.[28] Our present results on the $\Delta H_f°$ of

(27) V. I. Spitzyn and N. N. Patsukova, *Russ. J. Inorg. Chem.*, **10**, 1304 (1965).

(28) G. F. Huttig and B. Kurre, *Z. Anorg. Allg. Chem.*, **122**, 44 (1922); **126**, 163 (1923).

(29) J. Tillack, *ibid.*, **357**, 11 (1968).

$WO_2Br_2(g)$ also favor the calorimetric value of Sptizyn and Patsukova.[27]

E. $WO_2(s)$ + $HBr(g)$ Reaction. Major products of this reaction in the quartz cell are identified by the mass spectra as WO_2Br_2 and H_2. The equilibrium constant, K_4, for the reaction

$$WO_2(s) + 2HBr(g) = WO_2Br_2(g) + H_2(g) \quad (4)$$

can be written as

$$K_4 \propto K_4' = \frac{I_{WO_2Br_2^+} \times I_{H_2^+}}{(I_{HBr^+})^2}$$

where K_4' is the constant using only the ion currents. Data obtained in the range 920–1120°K gave erratic and pressure-dependent K_4' values. A higher HBr inlet pressure tended to give larger K_4' values. The data could not be used as we believe equilibrium conditions were not maintained in the cell. Rather large differences in the effusion flow rates of H_2 *vs.* WO_2Br_2, *i.e.*, $\sqrt{376/2} = 13.7$ *vs.* 1, may make it difficult to maintain equilibrium pressure of H_2 in the reaction cell.

F. Vaporization of $WOBr_4(s)$. Vaporization of $WOBr_4(s)$ was studied in the tungsten crucible in the temperature range 360–403°K. The mass spectrum and the A.P.'s are given in Table IV. Lack of any temperature dependence in the mass spectrum and analysis of the A.P. values suggest that $WOBr_4$ is the only vaporizing species. Minor ion currents due to WO_2Br_2 and HBr species, also observed, are believed to have arisen from a slight dissociation of the $WOBr_4$ sample during transfer to the crucible. $WOBr_4$ samples, extremely hygroscopic, are known to decompose to HBr and WO_2Br_2.[5] $WOBr_4$ in the wax-sealed capillaries changed from dark purple-black to yellowish orange color in a day or two, and the X-ray diffraction pattern would then be typical of the WO_2Br_2 samples.

Table IV: Mass Spectrum and Appearance Potential Data for Gaseous $WOBr_4$

m/e	Ionic[a] species	Relative[b] intensity	Appearance potential, eV
520	$WOBr_4^+$	1.0	10.3 ± 0.3
504	WBr_4^+	0.28	
441	$WOBr_3^+$	100	10.3 ± 0.2
425	WBr_3^+	6.26	18.1 ± 0.5
360	$WOBr_2^+$	35.7	14.4 ± 0.5
344	WBr_2^+	15.3	21.4 ± 0.5
281	$WOBr^+$	13.5	18.1 ± 0.8
265	WBr^+	11.0	
200	WO^+	6.50	
184	W^+	6.71	
160	Br_2^+	13.0	
81	Br^+	29.3	

[a] $WOBr_4$ is considered as the only molecular precursor to these ionic species. [b] Relative intensities refer to the peak heights at the indicated m/e's at 50-eV ionizing electron energies.

The enthalpy of sublimation of $WOBr_4(s)$ was determined by the second-law log $T \times I_{WOBr_4^+}$ *vs.* $1/T$ plots (Figure 4). Least-squares treatment of two independent sets of data give 30.6 ± 0.5 and 28.8 ± 0.5 kcal/mol for enthalpy. The indicated error limits are the evaluated standard deviations. The mean value is 29.7 kcal/mol at 380°K with an overall estimated uncertainty of ± 1.0 kcal/mol. Reported enthalpy values are 27.9 ± 0.5 kcal/mol at T = 530°K from tensimetric measurements,[9] 29.5 kcal/mol from Knudsen effusion measurements[14] at 410°K, and 25.5 kcal/mol obtained from static pressure determinations using a quartz spiral manometer at 545°K.[14] Our results agree with the effusion value very well. Partial dissociation of the $WOBr_4$ samples to evolve gaseous HBr may be responsible for lower heats of sublimation derived from the static vapor pressure measurements.[9,14] $\Delta C_p°$ for the $WOBr_4$ sublimation is assumed identical with the $WOCl_4$ sublimation,[20] *i.e.*, −10 gibbs/mol, and the sublimation enthalpy of $WOBr_4(s)$, 30.5 ± 1.0 kcal/mol, at 298°K is obtained.

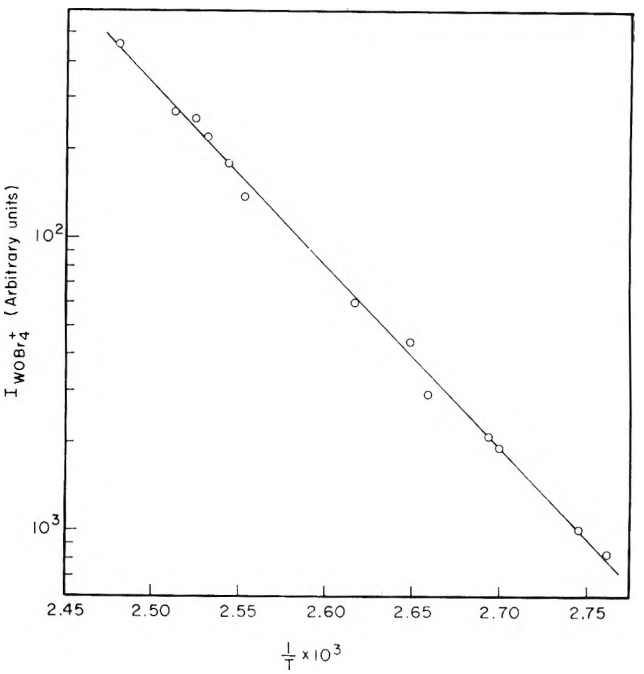

Figure 4. Mass spectrometric data for $WOBr_4$ sublimation.

G. Heat of Formation of $WOBr_4(g)$. The two reported calorimetric determinations of the $\Delta H_f°$ of solid $WOBr_4$, −139.2 ± 0.8[9] and −139.9 ± 0.8 kcal/mol[14] are changed to −128.8 and −129.9 kcal/mol, respectively, if the recent $\Delta H_f°$ $NaWO_4(s)$ = −369.2 kcal/mol[20] is used. The mean value, −129.4 kcal/mol, is combined with the present enthalpy of sublimation to derive −98.9 ± 2.0 kcal/mol as the $\Delta H_f°$ of $WOBr_4(g)$

at 298°K. The corresponding thermochemical data for $WOCl_4(g)$[20] and $WOF_4(g)$[30] are -137 ± 5 and -316 ± 10 kcal/mol, respectively. These data indicate the relatively high stability of the oxyfluoride species and a distinct trend toward reduced stabilities down the halogens subgroup.

Acknowledgments. The author wishes to express sincere thanks to Drs. E. G. Zubler and L. V. McCarty for many helpful discussions and critical review of the manuscript.

(30) K. F. Zmbov, O. M. Uy, and J. L. Margrave, *J. Phys. Chem.*, **73**, 3008 (1969).

Thermogravimetric Investigation of the Vaporization of Lead Telluride, Tin Telluride, and Germanium Telluride[1]

by David A. Northrop

Sandia Laboratories, Albuquerque, New Mexico 87115 *(Received December 31, 1969)*

Publication costs assisted by The U. S. Atomic Energy Commission

The vaporization of PbTe, SnTe, and GeTe has been studied with special emphasis placed upon such aspects as congruency, stoichiometry, vapor species, and the attainment of steady state and/or equilibrium within the effusion cell. Different vaporization behavior was noted for each compound with the overall complexity increasing from PbTe to SnTe to GeTe. A consistent set of free energy functions has been developed and the M–Te phase relations have been reviewed. The results are reported for effusion experiments with two different cell materials and utilizing a continuous weighing technique; pressures have been calculated on the basis of a MTe(g)-only vapor. These total pressures yield second- and third-law enthalpies of vaporization at 298°K of 54.12 ± 1.04 and 53.77 ± 1.36 kcal/mol for PbTe, 54.49 ± 1.06 and 53.13 ± 1.37 kcal/mol for SnTe, and 47.18 ± 0.82 and 48.55 ± 1.35 kcal/mol for GeTe, where the uncertainties are the result of careful examination of possible errors. In the case of SnTe and GeTe, where the assumption of a MTe(g)-only vapor is no longer valid, estimates have been calculated for the properties of the partial equilibrium MTe(s) $\rightleftarrows$ MTe(g). Cursory free surface vaporization experiments with single-crystal specimens gave vaporization coefficients between 0.25 and 0.5 which are independent of temperature.

I. Introduction

PbTe, SnTe, GeTe, and alloys between them are the primary constituents in several thermoelectric materials either in use or under development for isotope power generator systems. Their use in a vacuum environment at high temperature demands an accurate knowledge and understanding of their vapor pressures, heats of vaporization, and vaporization mechanisms. These properties have been the objects of previous investigations and appear to be well documented in the literature. Generally, however, closer inspection reveals inconsistencies in the results, poorly defined starting materials, or outmoded experimental methods. No systematic investigation has been made of these three materials with the exception of the excellent optical absorption work of Brebrick and Strauss[2-4] in the 0.1–100 Torr region. Mass spectrometric investigations have detailed the mechanism of vaporization, but this method alone cannot provide accurate pressure information.

This investigation of the vaporization of PbTe, SnTe, and GeTe has the following features. (1) Pressures are calculated from continuous weight–temperature data obtained with a recording microbalance. The rates of weight loss were determined from strictly linear portions of the weight record at different temperatures. Nonlinearity due to temperature fluctuations, lack of steady-state conditions in the effusion cell, or incongruent vaporization can be readily detected. Previously reported pressures depend on rates obtained from before and after weighings of the sample or effusion cell in air and at room temperature and yield only one datum point per run. (2) Each of the compounds exhibits a limited range of stoichiometry, and the total vapor pressure can vary with composition within this

(1) This work was supported by the U. S. Atomic Energy Commission.

(2) (a) R. F. Brebrick and A. J. Strauss, *J. Chem. Phys.*, **40**, 3230 (1964); (b) *ibid.*, **41**, 197 (1964).

(3) R. F. Brebrick, *ibid.*, **41**, 1140 (1964).

(4) R. F. Brebrick, *J. Phys. Chem. Solids*, **27**, 1495 (1966).

single-phase region. The T–X phase relations in the metal–tellurium systems are reviewed, and the influence of stoichiometry on the vaporization is discussed. (3) The congruency of vaporization has been examined carefully, and the results are presented in detail in each case. (4) A self-consistent set of free energy functions has been calculated from existing thermodynamic data and accepted estimation methods. (5) The same experimental apparatus and methods, calculations, and effusion cell calibrations have been applied to all three compounds, and thus their vaporization properties can be readily compared.

Features common to the individual investigations are discussed in section II. Discussion of the experimental data, results, and previous work pertinent to each compound are presented in the separate sections III, IV, and V. The results of cursory free surface vaporization experiments are given in section VI.

II. General Description

Experimental Details. The experimental apparatus is built around an Ainsworth semimicro recording balance with a sensitivity that was routinely checked and adjusted to give a recorder deflection of 1 in./1 mg of weight change. The effusion cell or single-crystal sample hangs from the balance into a measured zone of constant temperature (1 in. diameter by 1.5-in. length, constant to ±0.5°). A Pt—Pt–10% Rh thermocouple extends down inside the vacuum system and into this hot zone. The thermocouple is arranged so that the end 2 in. of the assembly is in the hot zone to reduce temperature error due to thermal conduction. A resistance furnace external to the vacuum system is controlled by an off–on controller actuated by a thermocouple located near the furnace windings for maximum sensitivity. The system is oil diffusion pumped, and pressures are measured with an ionization gauge located approximately 18 in. from the hot zone. Background pressures during vaporizations were always less than 2×10^{-5} Torr.

During an effusion run, a graphite or alumina cell contained 500–900 mg of −200 mesh powdered telluride material. Approximately 10–15 mg of sample was vaporized near the highest temperature of the run before the first datum point was taken. No definite temperature routine was followed, but each run included data taken during both steps of increasing and decreasing temperature. Fifteen to thirty data points were obtained during a run without breaking vacuum. The balance provided a continuous record of weight and temperature. The linearity of the weight–time record gave the best indication of steady-state conditions in the cell, and, unless noted, only strictly constant rates were accepted as valid data points in the effusion runs. Rates between 1×10^{-8} and 2×10^{-4} g/sec could be measured. However, the error in the rate measurement, which is a function of chart speed and balance sensitivity, is greater than 1% outside the 1×10^{-7} to 4×10^{-5} g/sec range, and deviate rates outside this range were discarded on this basis. Errors due to variations in chart shrinkage or speed and in balance sensitivity were found to be negligible.

While the temperature indicated by the sample thermocouple was continuously recorded, a more precise temperature for each datum point was measured manually with a potentiometer (±0.002 mV) and 0° reference junction. The excellent linearity of weight–time records up to 2-hr duration attests to the precision of the temperature control. However, the overall accuracy of the reported temperature must be conservatively estimated at ±5°.

Calculations. The pressures were calculated from the thermogravimetric data by the following form of the Knudsen equation

$$P = \left(\frac{1}{A}\right)\left(\frac{dw}{dt}\right)\sqrt{\frac{2\pi RT}{M}} \qquad (1)$$

where P is the pressure in atmospheres and R is the gas constant. Two experimental parameters for a given run are A, the effective orifice area in square centimeters, and M, the molecular weight of the vapor species. The experimental data to be obtained under steady-state conditions consist of dw/dt, the rate of weight loss in grams per second, and T, the temperature in degrees Kelvin.

Various factors prevented the usual calculation of an orifice area by application of a Clausing-type correction[5] to the projected area. For example, loss of material due to the porosity of the graphite cells[6] or cell-lid leakage in the alumina cells could not be distinguished from the loss due to molecular flow through the orifice since the total rate of weight loss is measured. Therefore, an effective orifice area was determined experimentally for the four graphite and three alumina cells by the effusion of a lead standard. Rate–temperature effusion data were combined with a published lead vapor pressure,[7] and eq 1 was solved for the area term. The reported cell area is the average of approximately 20 data points taken between 550 and 750°. The standard deviation of this average ranged between 3 and 8% for these cells. The "effective orifice area" is simply a proportionality factor that relates the observed rate–temperature effusion data to the vapor pressure of the standard, and thus it reflects all factors that contribute to the total weight loss. The basic assumption is that this A is independent of the material under study. A detailed description of the factors affecting total weight loss and the selection of this calibration method has been reported elsewhere.[8]

(5) P. Clausing, *Ann. Phys.*, 12, 961 (1932).

(6) D. A. Northrop, *J. Phys. Chem.*, 72, 4323 (1968).

(7) R. Hultgren, R. L. Orr, P. D. Anderson, and K. K. Kelley, "Selected Values of Thermodynamic Properties of Metals and Alloys," Wiley, New York, N. Y., 1963, March 1966 Supplement.

The vapor species in apparent equilibrium with these telluride materials were investigated in this laboratory by qualitative mass spectrometry and were found to be the same as those previously reported.[9-11] A rigorous calculation of the total pressure requires the division of the total weight loss between the different vapor species according to their relative concentrations and the calculation and summation of the partial pressures. Thus, at a given temperature

$$P_{\text{total}} = \sum P_i = \sum x_i \left(\frac{dw}{dt}\right)_{\text{total}} \left(\frac{1}{A}\right) \sqrt{\frac{2\pi RT}{M_i}} \quad (2)$$

$$= K \sum x_i \sqrt{\frac{1}{M_i}} \quad (3)$$

where x_i and M_i are the weight fraction and molecular weight of the ith vapor species, respectively, and K is a constant. As vapor concentrations and especially their temperature dependence are not accurately known, all pressure calculations have ascribed the total weight loss to an MTe(g) vapor and eq 1 has been solved accordingly. The error in this assumption can be readily estimated by the use of eq 3 as shown in eq 10, for example. As the molecular weights involved are large and of the same general magnitude and the weight fraction of the minor species is generally small, the error in the total pressure introduced by this assumption is small.

A systematic increase in pressure and subsequent decrease in third-law ΔH_{298} was noted for data taken near the highest temperatures (or pressures) of a run. Apparently, molecular flow conditions through the orifice were not maintained due to too low a ratio of mean free path (λ) to orifice diameter (d).[12] An arbitrary acceptance criterion of $\lambda/d \geq 0.5$ was adopted, based on an approximate value of λ calculated from the measured pressure by assuming the diameter for the MTe(g) molecule to be equal to the lattice parameter of the face-centered-cubic MTe(g) lattice.[13,14] Approximately 5% of the data points were rejected on this basis, including all anomalously low ΔH_{298} values.

The total pressures are presented on a log P *vs.* reciprocal temperature plot and linear least-squares analyses were performed for each experimental run resulting in expressions of the form

$$\log P = (A \pm \sigma_A) + (B \pm \sigma_B)(10^3/T_K) \quad (4)$$

where P is the pressure in atmospheres and σ_i are the standard deviations of the coefficients. The intercept and slope of this linear fit yield second-law values and standard deviations of ΔS_T and ΔH_T, respectively, where T is taken as the average temperature of the data set. Third-law values of ΔH_{298} were calculated by the equation

$$\Delta H_{298} = T_K[-R \ln P - \Delta\text{fef}] \quad (5)$$

Δfef is the change in the calculated free energy functions for the assumed vaporization reaction, a value of ΔH_{298} was obtained for each datum point, and an average and standard deviation was obtained for each experimental run.

The final values reported for each material were the weighted ($1/\sigma_i^2$) averages of the results for each individual experimental run. These values were selected in preference to values derived from a comprehensive least-squares fit of all data points for that material. The slope and intercept determined by the comprehensive fit differed from the averaged values by an amount greater than that which could be ascribed to a reasonable estimate of the random and systematic experimental errors. This error originates when a comprehensive least-squares fit is made of individual sets of data which have different ranges along the x axis and which are displaced slightly with respect to each other along the y axis. For these log P *vs.* reciprocal temperature plots, the displacements are due primarily to the uncertainty in the effective orifice areas and are quite small as a $\pm 10\%$ uncertainty is reflected by a ± 0.04 displacement of log P.

Each least-squares fit provided a standard deviation of the fit between log P_{calcd} and log P_{obsd}. This number can be expressed in a more recognizable form as the per cent deviation between P_{calcd} and P_{obsd} by the exponentiation

$$\sigma_{\%} \approx 100 \frac{10^{(\log P + \sigma)} - 10^{(\log P)}}{10^{(\log P)}} \quad (6)$$

$$\approx 100(10^{\sigma} - 1) \quad (7)$$

A slightly different value of $\sigma_{\%}$ will result if (log $P - \sigma$) is chosen as the exponent. $\sigma_{\%}$ gives a convenient measure of the precision of an experimental run.

The reported uncertainties reflect the precision of the experimental data and do *not* include the uncertainties introduced by possible systematic errors associated with temperature ($\pm 5°$), Δfef (± 1.5 cal/(deg mol)), and pressure ($\pm 10\%$). These affect the derived thermodynamic quantities as follows: ΔH_T, due to temperature, ± 0.6 kcal/mol; ΔH_{298}, due to temperature, ± 0.3 kcal/mol, due to pressure, ± 0.2 kcal/mol, due to Δfef, ± 1.3 kcal/mol; ΔS_T due to temperature, ± 0.3 cal/(deg mol), due to pressure, ± 0.2 cal/(deg mol).

The overall accuracy of these results is difficult to assess. As the pressure is proportional to $1/A$, the uncertainties and errors associated with a single effusion

(8) D. A. Northrop, Sandia Laboratories Report SC-RR-68-774, Feb 1969.

(9) R. F. Porter, *J. Chem. Phys.*, **34**, 583 (1961).

(10) R. Colin and J. Drowart, *Trans. Faraday Soc.*, **60**, 673 (1964).

(11) R. Colin and J. Drowart, *J. Phys. Chem.*, **68**, 428 (1964).

(12) K. C. Wang and P. G. Wahlbeck, *J. Chem. Phys.*, **47**, 4799 (1967).

(13) M. Hansen, "Constitution of Binary Alloys," McGraw-Hill, New York, N. Y., 1958.

(14) R. F. Bis and J. R. Dixon, *J. Appl. Phys.*, **40**, 1918 (1969).

run are effectively doubled by this method of orifice calibration. A pressure calculation utilizing maximum and minimum error limits on each parameter, including uncertainties in the lead vapor pressure, gives a pessimistic pressure uncertainty of at least ±80%. Vapor pressure determinations of cadmium and silver have been made to obtain a more realistic measure of the overall accuracy. Linear least-squares fits of log P *vs.* reciprocal temperature were made based on two effusion runs each for cadmium between 200 and 300° and for silver between 980 and 1250°. The per cent difference between P_{obsd} and P_{calcd}, $\sigma_{\%}$, was ±4 and ±3% for cadmium and silver, respectively. This random experimental scatter is then superimposed on the per cent difference between the experimental and an accepted vapor pressure for the element.[15,16] For cadmium the experimental pressures were 5 and 7% higher at the low and high ends of the temperature range, respectively. For silver, the difference ranged from 4% low to 5% high. These results give confidence but do not prove that the limits of accuracy for the total pressures reported in these telluride studies are close to ±10%.

Free Energy Function Calculations. Sets of free energy functions for the solid and gas phases have been calculated which are based on existing or estimated thermodynamic data. The free energy function was calculated by the equation

$$-\text{fef} = -\frac{H_T - H_{298}}{T} + (S_T - S_{298}) + S_{298} \quad (8)$$

S_{298} was taken from the literature in each case.[17,18] $H_T - H_{298}$ and $S_T - S_{298}$ can be calculated from the heat capacity which is generally expressed in the form

$$C_p = A + BT + CT^{-2} \quad (9)$$

This information is given for the gaseous species by Kelley.[19] The heat capacity of the solid had to be estimated.[20] A linear variation of C_p with temperature was assumed between 298°K and the melting point, where C_p was taken as 14.50 cal/(deg mol). (The cubic–rhombohedral displacive transition in GeTe at ~430–450° was ignored.) A value of 12.0 cal/(deg mol) at 298°K was adopted for GeTe and SnTe based on a published value of 12.08 cal/(deg mol) for PbTe.[17] The constants for the C_p expression and S_{298} are given in Table I, and the calculated free energy functions for the phases are given in Table II for selected temperatures. A graphical method was used to interpolate the free energy function between these temperatures for subsequent calculations.

Phase Relations. The phase relations are reviewed here as they bear upon the exact composition of the starting materials and upon the interpretation of some aspects of the vaporization behavior. A schematic of the T–X relations is shown in Figure 1.[21-27] The solid lines represent the case where the metal is Pb or Sn and the eutectic temperatures are within a few degrees of the

Table I: Quantities Used in the Calculation of the Free Energy Functions

	$C_p = A + BT + CT^{-2}$			S_{298},
	A	B	C	cal/(mol deg)
PbTe(g)	8.94	0	-0.14×10^5	64.9 ± 0.5
SnTe(g)	8.94	0	-0.22×10^5	62.7 ± 0.5
GeTe(g)	8.93	0	-0.30×10^5	61.1 ± 0.6
PbTe(s)	11.28	2.69×10^{-3}	0	26.3 ± 0.5
SnTe(s)	11.05	3.20×10^{-3}	0	24.2 ± 1.0
GeTe(s)	10.93	3.58×10^{-3}	0	19.9 ± 1.0

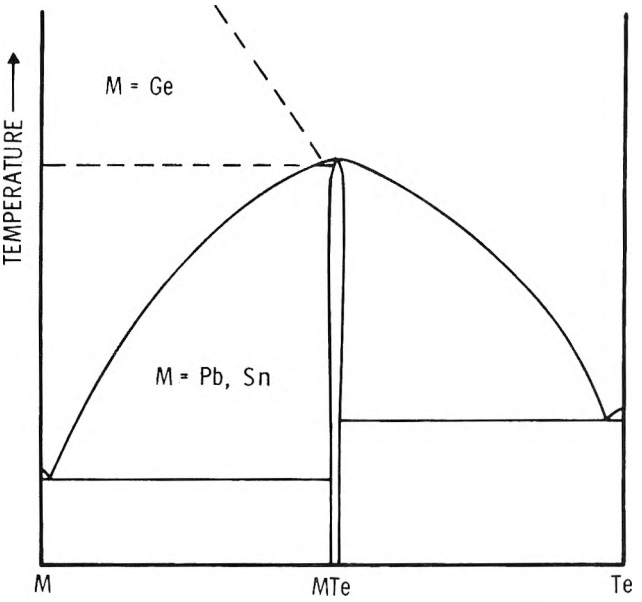

Figure 1. Schematic diagram of the T–X phase elations, where the MTe(s) single-phase region has these parameters: congruent melting composition, maximum melting point, and maximum width of the single phase, respectively. PbTe: 50.08 atom % Te at 924°, 49.997–50.013 atom % Te at 775;[22-25] SnTe: 50.4 atom % Te at 806°, 50.1–51.1 atom % Te at 600°;[25,26] GeTe: 50.61 atom % Te at 724°, 50.4–51.2 atom % Te at 500°.[21,24,27]

(15) R. Hultgren, R. L. Orr, P. D. Anderson, and K. K. Kelley, "Selected Values of Thermodynamic Properties of Metals and Alloys," Wiley, New York, N. Y., 1963, Feb 1967 Supplement.

(16) R. Hultgren, R. L. Orr, P. D. Anderson, and K. K. Kelley, "Selected Values of Thermodynamic Properties of Metals and Alloys," Wiley, New York, N. Y., 1963.

(17) K. K. Kelley and E. G. King, *U. S. Bur. Mines Bull.*, **No. 592** (1961).

(18) C. Hirayama, *J. Chem. Eng. Data*, **9**, 65 (1964).

(19) K. K. Kelley, *U. S. Bur. Mines Bull.*, **No. 584** (1960).

(20) O. Kubaschewski, E. L. Evans, and C. B. Alcock, "Metallurgical Thermochemistry," 4th ed, Pergamon Press, Oxford, 1967.

(21) L. E. Shelimova, N. K. Abrikosov, and V. V. Zhdanova, *Russ. J. Inorg. Chem.*, **10**, 650 (1965).

(22) R. F. Brebrick and R. S. Allgaier, *J. Chem. Phys.*, **32**, 1826 (1960).

(23) R. F. Brebrick and E. Gubner, *ibid.*, **36**, 1283 (1962).

(24) R. P. Elliott, "Constitution of Binary Alloys, First Supplement," McGraw-Hill, New York, N. Y., 1964.

(25) F. A. Shunk, "Constitution of Binary Alloys, Second Supplement," McGraw-Hill, New York, N. Y., 1969.

(26) R. F. Brebrick, *J. Phys. Chem. Solids*, **24**, 27 (1963).

(27) J. P. McHugh and W. A. Tiller, *Trans. AIME*, **218**, 187 (1960).

Table II: Calculated Free Energy Functions: $-\left(\frac{F_T - H_{298}}{T}\right)$ in cal/(mol deg)

	PbTe		SnTe		GeTe	
T, °K	Solid	Ideal gas	Solid	Ideal gas	Solid	Ideal gas
298.15	26.30	64.90	24.20	62.70	19.90	61.10
300	26.31	64.90	24.21	62.70	19.91	61.10
400	26.78	65.24	24.67	63.04	20.38	61.44
500	27.69	65.90	25.58	63.69	21.28	62.09
600	28.72	66.63	26.62	64.42	22.34	62.81
700	29.76	67.38	27.66	65.16	23.37	63.55
800	30.79	68.09	28.69	65.87	24.40	64.25
900	31.76	68.77	29.67	66.55	25.39	64.92
997					26.31	65.54
1000	32.70	69.41	30.61	67.19		65.56
1079			31.33	67.67		
1100	33.60	70.01		67.79		66.17
1197	34.42	70.58				
1200		70.59		68.37		66.73
1300		71.13		68.90		67.28
1400		71.65		69.41		67.79
1500		72.13		69.91		68.27

melting point of the pure end member as shown. The metal-rich portion of the GeTe system is given by the dashed line. For clarity, the cubic-to-rhombohedral transition in GeTe is not shown, but it has been delineated by Shelimova, *et al.*[21]

The exact relations near the melting point of GeTe are still uncertain. McHugh and Tiller[27] have determined that GeTe melts congruently at 50.61 atom % Te and 724° with a Ge-rich eutectic at 49.85 atom % Te at 723°. Brebrick,[4] by a different method, inferred a congruent melting composition of 49.84 atom % Te at 724 ± 1°. A single crystal which was made for the present study and which was pulled from an original 50–50 atom % melt covered with a B_2O_3 flux[28] gave a two-phase, Ge–GeTe material as the last to freeze portion. This is indirect evidence in support of the McHugh and Tiller description.

III. PbTe

Material. A granular PbTe from Electronic Space Products, Inc., was used in the effusion experiments. This material was probably made by allowing equal atomic amounts of the elements to react in a sealed, evacuated quartz tube. The material used in the free surface vaporizations was made by this method in this laboratory. The resulting boule contained several large grains, and these were cleaved parallel to the cubic directions. The large grains probably solidified first on cooling through the liquidus and thus have the maximum melting composition. After completion of this work, a newly developed method allowed a single crystal to be pulled from the melt through a borate flux layer.[28] Cursory free surface and effusion vaporizations with this material gave results that were indistinguishable from those presented here.

Vaporization Characteristics. PbTe appears to vaporize congruently. An X-ray diffraction pattern of the residue of an isothermal effusion run in which 95 wt % of the sample was vaporized indicated that only a PbTe phase remained. Two special lead-rich samples of 51 and 52 atom % lead were made by reaction of the elements in an evacuated quartz tube, and in both cases the lead metal phase could be detected by X-ray diffraction. After a 95 wt % vaporization during an isothermal effusion run, the residue from the 51 atom % lead sample was only PbTe; the lead phase could not be detected. The composition had shifted toward PbTe indicating that PbTe was the congruently subliming composition in this region of the phase diagram. The 52 atom % lead sample lost PbTe preferentially and gave a lead metal residue. The single-phase field of PbTe is so narrow that the congruently subliming composition must be inferred from calculations based on the carrier concentrations.[22,23]

Brebrick and Strauss[1] have shown that the equilibrium partial pressure of $Te_2(g)$ varies greatly with the exact stoichiometry of PbTe(s) within its very narrow homogeniety range. However, dissociation of PbTe(g) due to electron bombardment in the ion source of a mass spectrometer hinders the unambiguous identification of the equilibrium vapor above congruently subliming PbTe. Lyubimov and Bespal'tseva[29] showed parallel log I^+T plots for $PbTe^+$, Pb^+, and Te^+ as a function of the reciprocal temperature between 710 and 860°, and

(28) R. J. Baughman and R. A. Lefever, *Mater. Res. Bull.*, **4**, 721 (1969).

(29) A. P. Lyubimov and I. I. Bespal'tseva, *Russ. J. Phys. Chem.*, **41**, 798 (1967).

Table III: Summary of Results for PbTe

		No. 160	No. 161	No. 249	No. 250	Average[a]
Cell material		Graphite	Graphite	Alumina	Alumina	
Effective orifice area, cm²		0.005639	0.001258	0.002652	0.000449	
Number of data points		25	16	28	26	95
Temperature range, °C		529–732	588–774	542–729	599–763	529–774
Average temperature, °C		601	676	610	667	634
Second law						
ΔH_T		51.71 ± 0.14	50.49 ± 0.27	51.91 ± 0.18	52.39 ± 0.31	51.68 ± 0.81
ΔS_T		34.77 ± 0.16	33.53 ± 0.29	34.86 ± 0.20	35.14 ± 0.33	34.66 ± 0.72
Third law						
ΔH_{298}		53.71 ± 0.05	53.63 ± 0.06	53.84 ± 0.06	54.02 ± 0.08	53.77 ± 0.13
Summary						
Log P(atm) = A + $B(10^3/T_K)$	A	7.60 ± 0.04	7.33 ± 0.06	7.62 ± 0.04	7.68 ± 0.07	7.575 ± 0.157
	B	−11.30 ± 0.03	−11.03 ± 0.06	−11.34 ± 0.04	−11.45 ± 0.07	−11.294 ± 0.177
Fit: σ%		2.5	3.7	2.8	3.6	

[a] Uncertainties shown do not reflect possible systematic errors; see text for discussion.

Table IV: Previously Reported Data for the Vaporization of PbTe

Reference	Curve (Figure 3)	Temp range, °C	A[a]	B[a]	ΔH_T (second law)	ΔH_{298} (third law)	Comments[b]
Brebrick and Strauss[2a]	A	725–924	7.731	−11.430	52.3 ± 1.0	...	Optical absorption PbTe(g) pressure based on ref 31 Te_2(g) partial pressure measured directly
Lyubimov and Bespal'tseva[29]	B	606–700	8.310	−11.445	53.28	...	Effusion; quartz cells Mass spectrometry yields ΔH Pressure based on single two-point weighing
Pashinkin and Novoselova[31]	C	511–688	7.946	−11.636	53.3	...	Effusion and pseudo-Langmuir[32] Two-point gravimetric method Concluded α_v was nearly unity
Bates and Weinstein[33]	D	400–600	7.79	−11.78	53.9	...	Free surface; rates only reported Pb-saturated PbTe thermoelement[34] Two-point gravimetric method
Hansen and Munir[35]	E	646–769	7.119 ± 0.261	−11.09 ± 0.26	50.7 ± 1.2	53.34 ± 0.13	Torsion–effusion; graphite cells Powdered single crystals
Hansen and Munir[35]	F	598–720	6.716 ± 0.536	−10.85 ± 0.49	49.6 ± 2.3	54.95 ± 0.37	Torsion–Langmuir Single crystal, [100] face
Sokolov, *et al.*[36]	G	609–699	7.435 ± 0.072	−11.140 ± 0.067	51.0 ± 0.3	53.43 ± 0.03	Effusion; quartz cells Two-point gravimetric method
This work		529–744	7.575 ± 0.157	−11.294 ± 0.177	51.68 ± 0.81	53.77 ± 0.13	

[a] A and B are the constants in the equation: log P(atm) = A + $B(1000/T)$. [b] Two-point gravimetric method: rate of weight loss is calculated from two weighings of the cell or condensate in air and at room temperature before and after each experimental run.

they concluded that Pb^+ and Te^+ are the result of fragmentation. Porter,[9] by a double-effusion oven technique, obtained a dissociation constant of $\sim 1.7 \times 10^{-7}$ based on partial pressures calculated from the respective ion currents at 650° for the reaction PbTe(g) $\rightleftharpoons$ Pb(g) + Te(g). This corresponds to a degree of dissociation of approximately 0.045. Therefore, dissociation has been neglected and PbTe(g) has been taken to be the only vapor species.

PbTe has a congruently subliming composition, and thus the total pressure above the solid during vaporization is independent of the amount vaporized once this exact composition is attained. Thus the observed rate of weight loss must be constant if steady-state conditions are realized within the effusion cell. The vaporization coefficient of PbTe determined in this work is greater than 0.1, and the attainment of steady-state conditions is not hindered by a low α_v as discussed by Motzfeldt.[30] In isothermal effusion runs where entire 50-mg samples were vaporized, constant rates of weight loss were observed up to a 96 wt % loss. The rate then decreased slightly and continuously to zero (a constant, empty cell weight). These results indicate that as little as 2 mg of sample was required to maintain steady-state conditions in the cell. There was at least 300 mg in the cell during all of the pressure determinations.

In addition, there was no systematic change of observed pressures with effective orifice areas ranging from 0.000449 to 0.005639 cm^2. Thus the rate of material loss through the orifice has no apparent effect upon the steady-state pressure within the cell, and a case can be made that the measured pressures represent the equilibrium pressure of PbTe.

Results. Ninety-five data points from four separate experiments and different effusion cells were obtained between 529 and 775°. The pressures and resulting thermodynamic quantities were calculated as described in section II, and the complete results are presented in Table III and Figure 2. Table IV and Figure 3 compare these results to previously published investigations. ΔH_T can be corrected to 298°K by the heat capacity data given in Table I. Combining the possible errors discussed previously, the precision of the experimental results, and allowing a ±1 cal/(deg mol) uncertainty in the heat capacity estimate, the two enthalpies of vaporization agree well within the probable experimental error. These values are 54.12 ± 1.02 and 53.77 ± 1.35 kcal/mol at 298°K for the second- and third-law methods, respectively.

IV. SnTe

Material. The SnTe used in the effusion experiments was made by the reaction of equal atomic amounts of the elements at 850° in a sealed, evacuated quartz tube. The resulting boule was reground, and the powder was vacuum annealed at 600° in a sealed quartz tube. An

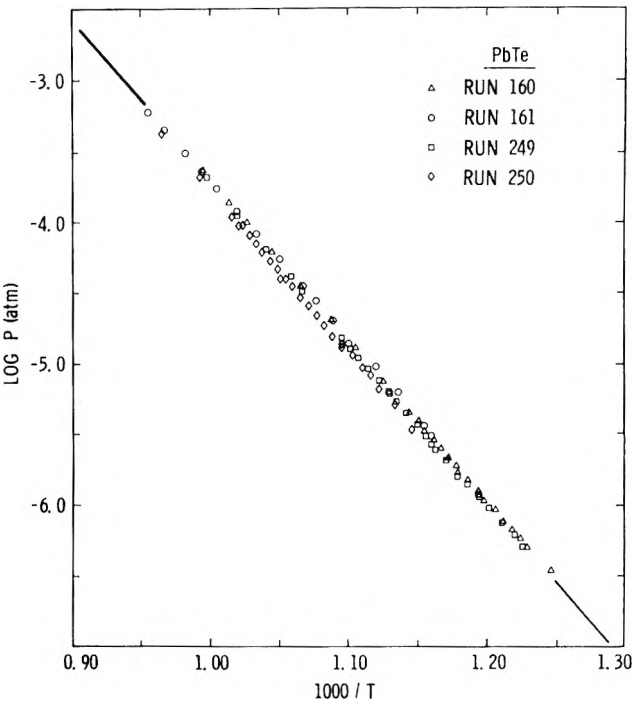

Figure 2. Total vapor pressure of congruently subliming PbTe determined by effusion experiments.

X-ray diffraction pattern indicated only SnTe present with a measured lattice constant of $a_0 = 6.327$ Å. SnTe exhibits a variation of lattice constant with composition (and thus carrier concentration also) within the single-phase region.[14] This value is consistent with a carrier concentration of 1×10^{26} cm^{-3}, which corresponds to 50.02 atom % Te according to the calculations of Brebrick,[26] and thus the initial overall stoichiometry was maintained in the reaction.

A single crystal was pulled from the melt through a borate flux,[28] and specimens cut from this boule were used in the Langmuir experiments. A Hall measurement at 298°K gave a p-carrier concentration of 6×10^{20} corresponding to the maximum melting composition of 50.4 atom % Te.[26] Cursory effusion experiments with this material gave results which were indistinguishable from those reported here.

Vaporization Characteristics. Colin and Drowart[10] reported an Sn metal residue after a complete effusion of SnTe, and Brebrick and Strauss[2] concluded that SnTe-

(30) K. Motzfeldt, *J. Phys. Chem.*, 59, 139 (1955).

(31) A. S. Pashinkin and A. V. Novoselova, *Russ. J. Inorg. Chem.*, 4, 1229 (1959).

(32) I. V. Korneeva, A. S. Pashinkin, A. V. Novoselova, and Y. A. Priselkov, *ibid.*, 2, 14 (1957).

(33) H. E. Bates and M. Weinstein, *Advan. Energy Convers.*, 6, 177 (1966).

(34) Type 3N, 3M Co., St. Paul, Minn.

(35) E. E. Hansen and Z. A. Munir, *J. Electrochem. Soc.*, 117, 121 (1970).

(36) V. V. Sokolov, A. S. Pashchinkin, A. V. Novoselova, A. A. Ryazantsev, V. A. Dolgikh, and S. A. Klinchikova, *Izv. Akad. Nauk SSSR, Neorgan. Mater.*, 5, 15 (1969).

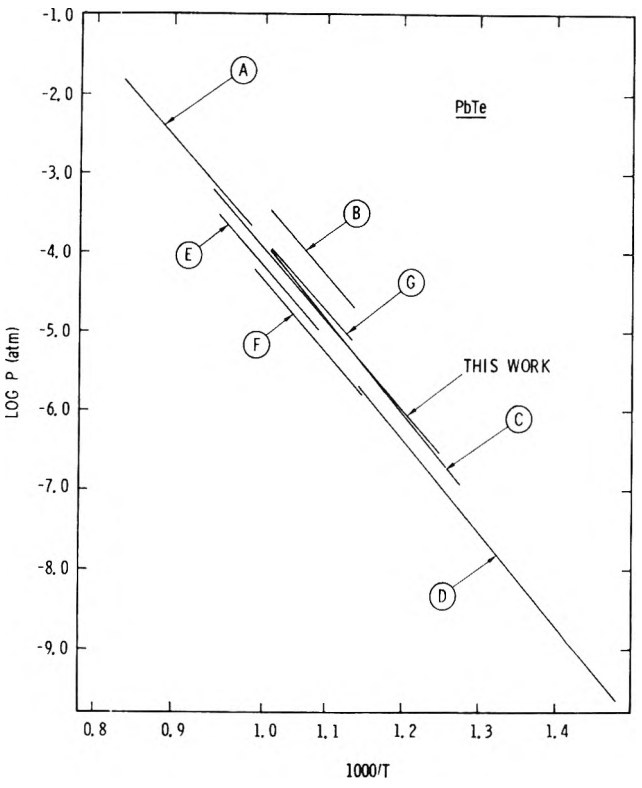

Figure 3. Previously reported vapor pressures for PbTe: A, Brebrick and Strauss;[2a] B, Lyubimov and Bespal'tseva;[29] C, Pashinkin and Novoselova;[31] D, Bates and Weinstein;[33] E, F, Hansen and Munir;[35] G, Sokolov, *et al.*[36]

(g) has no congruently subliming composition above 550°. Noncongruency can also be inferred from the chemical analysis of original material and its sublimate, given by Nesterova, *et al.*[37] Congruency was examined for both of the telluride materials described above and a noncongruent vaporization for SnTe has been confirmed. Isothermal effusion runs at 730° with an alumina cell with an effective orifice area of 0.000449 cm^2 produced a two-phase Sn–SnTe assemblage, as identified by X-ray diffraction, at a 95 wt % loss and a pure Sn metal residue at constant observed weight. The rate of effusion of pure Sn(l) at this temperature is below the level of detection. The amount of residue in each case was less than 0.3 wt % of the original sample. The effect of changes in temperature and orifice area on the amount of residue was not examined.

Colin and Drowart[10] have reported that the saturated vapor above SnTe is composed mainly of SnTe(g) with small concentrations of Sn_2Te_2, Te_2, $SnTe_2$, and Te atoms. Quantitative determination of vapor concentrations is complicated by electron impact dissociation in the mass spectrometer ion source. However, some estimates of the relative concentrations of the vapor species can be made. Brebrick and Strauss[2b] have calculated a minimum Te_2 partial pressure in equilibrium with SnTe which has become saturated with Sn due to the noncongruent nature of the vaporization. This calculation is based on a published vapor pressure for SnTe[37] and a free energy of formation determined from their own work. The calculated ratio, P_{Te_2}/P_{SnTe}, has the minimum values of 0.004 and 0.045 at 530 and 750°, respectively. From their measured partial pressure of Te_2, this ratio increases from 0.1 at 730° to approximately unity at the melting point. The ratio will also be increased slightly since the P_{SnTe} used by Brebrick and Strauss is the pressure given by Nesterova, *et al.*,[37] from total weight loss experiments and calculated with the assumption that SnTe is the only vapor species; the known presence of Te_2 will lower the reported SnTe partial pressure. The concentrations of Sn(g) and Te(g) are negligible at these temperatures.[38]

For the purposes of this investigation, the vapor consists mainly of SnTe(g) with a Te_2(g) concentration varying from 0.4% to at least 10% over the experimental temperature range.

As SnTe vaporizes noncongruently, the initial total pressure above single-phase SnTe will continuously change until the composition shifts into the two-phase Sn–SnTe region. As required by the phase rule, the equilibrium total pressure over such a two-phase region must be constant even though the composition is continuously changing, and thus the observed rate of weight loss must also be constant if steady-state conditions are realized in the effusion cell. The vaporization coefficient of SnTe determined in this work is greater than 0.1 and the attainment of steady-state conditions is not hindered by a low α_v as discussed by Motzfeldt.[30]

Isothermal effusion runs at 730° were not able to detect a changing effusion rate for the single-phase $Sn_{0.496}Te_{0.501}$ starting material as the composition shifted toward the phase boundary. Apparently the boundary had been reached by the time constant temperature was attained. The other material, $Sn_{0.4998}Te_{0.5002}$, is already at the phase boundary.

In isothermal effusion runs where 50 mg of each material was vaporized to a constant weight, constant rates of weight loss were observed up to a 90 wt % loss. The rate then decreased slightly and continuously until the rate broke essentially discontinuously to zero at an observed constant cell weight. It was not determined if this rate decrease was due to the loss of steady-state conditions or due to a continuously decreasing total pressure over the liquid single phase as its composition shifted toward pure Sn. These results indicate that as little as 5 mg was required to maintain steady-state conditions in the cell. There was at least 300 mg in the cell during all of the pressure determinations.

In addition, there was no systematic change of pressures with effective orifice areas ranging from 0.000449

(37) Y. M. Nesterova, A. S. Pashinkin, and A. V. Novoselova, *Russ. J. Inorg. Chem.*, 6, 1031 (1961).

(38) D. R. Stull and G. C. Sinke, *Advan. Chem. Ser.*, No. 18 (1956).

Table V: Summary of Results for SnTe

		No. 177	No. 178	No. 254	No. 255	Average[a]
Cell material		Graphite	Graphite	Alumina	Alumina	
Effective orifice area, cm^2		0.002820	0.000894	0.000449	0.004575	
Number of data points		25	26	13	22	86
Temperature range, °C		553–713	589–753	625 742	527–689	527–753
Average temperature °C		620	654	680	603	635
Second law						
ΔH_T		51.44 ± 0.27	52.07 ± 0.32	53.26 ± 0.34	51.60 ± 0.29	51.98 ± 0.83
ΔS_T		35.07 ± 0.30	35.43 ± 0.34	36.67 ± 0.36	35.41 ± 0.33	35.58 ± 0.70
Third law						
ΔH_{298}		53.06 ± 0.07	53.32 ± 0.10	53.30 ± 0.11	52.94 ± 0.10	53.13 ± 0.19
Summary						
Log P(atm) = A + $B(10^3/T_K)$	A	7.66 ± 0.07	7.74 ± 0.08	8.01 ± 0.08	7.74 ± 0.07	7.776 ± 0.154
	B	−11.24 ± 0.06	−11.38 ± 0.07	−11.64 ± 0.07	−11.28 ± 0.06	−11.360 ± 0.182
Fit: σ%		3.6	4.3	2.4	4.8	

[a] Uncertanties shown do not reflect possible systematic errors; see text for discussion.

Table VI: Previously Reported Data for the Vaporization of SnTe

Reference	Curve (Figure 5)	Temp range, °C	A[a]	B[a]	ΔH_T (second law)	ΔH_{298} (third law)	Comments[b]
Brebrick and Strauss[2b]	A	727–806	6.50 ± 0.26	−10.19 ± 0.26	46.6 ± 1.2	...	Optical absorption SnTe(g) pressure based on ref 37 Te_2(g) partial pressure measured directly
Hirayama, *et al.*[39]	B	519–660	7.672	−11.211 ± 0.258	51.3 ± 1.2	53.1 ± 1.0	Effusion; porous graphite cells Two-point gravimetric method Assumed SnTe(g) only vapor species
Nesterova, *et al.*[37]	C	575–731	6.128	−9.8173	44.9 ± 4.3	...	Effusion; quartz cells Two-point gravimetric method Assumed SnTe(g) only vapor species
Colin and Dowart[30]	D	559–717	6.40	−9.92	45.8 ± 2.5	52.1 ± 0.4	Effusion; quartz cells Mass spectrometry Pressures by time-integration of intensities Equation calculated from their data
Lyubimov and Bespal'tseva[40]	E	670–790	6.457	11.273	51.57 ± 3.61	...	Effusion; quartz cells Mass spectrometry yields ΔH Pressure by several two-point weighings
Sokolov, *et al.*[36]	F	606–695	5.942 ± 0.218	−9.478 ± 0.200	43.4 ± 0.9	52.1 ± 0.2	Effusion; quartz cells Two-point gravimetric method
This work		527–753	7.776 ± 0.154	−11.360 ± 0.182	51.98 ± 0.83	53.13 ± 0.19	Assumed SnTe(g) only vapor species

[a] A and B are the constants in the equation log P(atm) = A + $B(1000/T)$. [b] Two-point gravimetric method: rate at weight loss is calculated from two weighings of the cell or condensate in air and at room temperature before and after each experimental run.

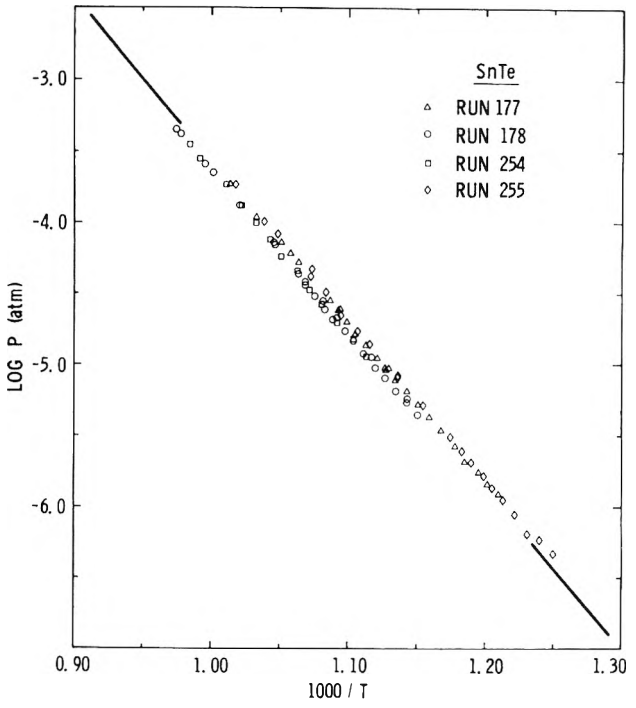

Figure 4. Total pressure of Sn-saturated SnTe determined by effusion experiments.

to 0.004575 cm². Thus the rate of material loss through the orifice has no apparent effect upon the steady-state pressure within the cell, and a case can be made that the measured pressures represent the equilibrium total pressure over a two-phase Sn–SnTe assemblage.

Results and Discussion. Eighty-six data points from four separate experiments and different effusion cells were obtained between 527 and 753°; SnTe(g) was assumed to be the only vapor species. The pressures and resulting thermodynamic quantities were calculated as described in section II, and the complete results are presented in Table V and Figure 4. According to eq 3, the ratio of these total pressures to a rigorous calculation of the total pressure is given by

$$\frac{P_{\text{reported}}}{P_{\text{rigorous}}} = \frac{(1)M_{\text{SnTe}}{}^{-1/2}}{(1-x)M_{\text{SnTe}}{}^{-1/2} + xM_{\text{Te}_2}{}^{-1/2}} \quad (10)$$

where x is the weight fraction of Te_2 in the vapor. This ratio has a value of 1.000 and 1.002 at Te_2 concentrations of 0.4 and 10%, respectively. The very small difference is due to the similarity of the molecular weights (246 and 255 for SnTe and Te_2, respectively), and thus the increasing fraction of Te_2 at higher temperatures has no effect upon the reported total pressure.

ΔH_T can be corrected to 298°K by the heat capacity data in Table I. Combining the possible errors discussed in section II, the precision of the experimental results, and allowing a ±1 cal/(deg mol) uncertainty in the heat capacity estimate, the second- and third-law enthalpies of vaporization at 298°K are 54.49 ± 1.06 and 53.13 ± 1.37 kcal/mol, respectively. Table VI and Figure 5 compare these results to previously published investigations.

This paper reports (Table V) the *total* equilibrium pressure and its temperature dependence over Sn-saturated SnTe(s), and no major error results from ignoring the known presence of Te_2(g). However, with increasing temperature, the partial pressure of SnTe(g) does become significantly less than the total pressure, and its slope on a log P *vs.* $1/T$ plot will be less than the total pressure. Further, Δfef has been calculated for the equilibrium SnTe(s) ⇌ SnTe(g) and should be applied only to the the SnTe(g) partial pressure in the third-law calculation. Such a rigorous analysis could not be applied to the experimental data as vapor concentrations and their temperature dependences were not accurately known. Rough estimates of the pressures and enthalpies for the SnTe(s) ⇌ SnTe(g) equilibrium alone can be made based on Te_2(g) concentrations discussed earlier. The calculated end points of an assumed linear log P *vs.* $1/T$ curve for SnTe(g) are given by $0.90P_{\text{total}}$ and $0.996P_{\text{total}}$ at the high and low ends, respectively, of the experimental temperature range. These estimates are

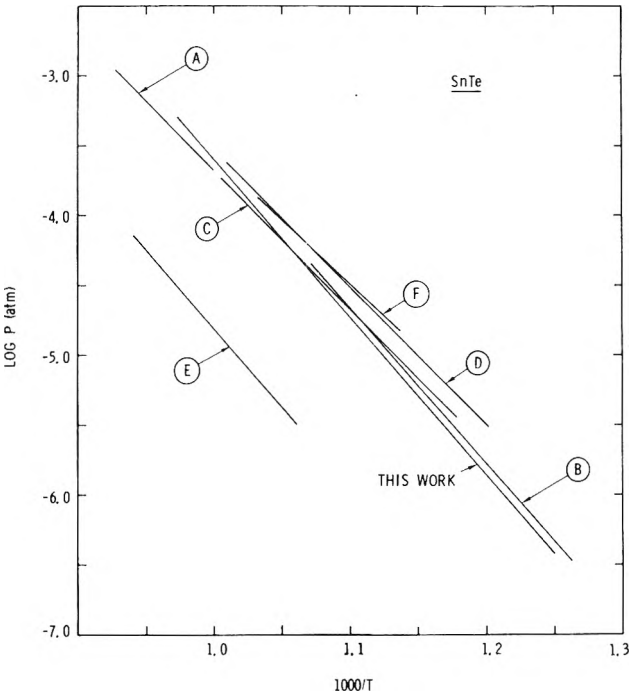

Figure 5. Previously reported vapor pressures for SnTe: A, Brebrick and Strauss;[2b] B, Hirayama, *et al*;[39] C, Nesterova, *et al.*;[37] D, Colin and Drowart;[10] E, Lyubimov and Bespal'tseva;[40] F, Sokolov, *et al.*[36]

(39) C. Hirayama, Y. Ichikawa, and A. M. DeRoo, *J. Phys. Chem.*, 67, 1039 (1963).

(40) A. P. Lyubimov and I. I. Bespal'tseva, *Izv. Akad. Nauk SSSR, Neorgan. Mater.*, 5, 1289 (1969).

$$\log P_{SnTe}(\text{atm}) = 7.58 - 11.20(1000/T)$$

$$\Delta H_{298}(\text{second law}) = 53.8 \text{ kcal/mol}$$

$$\Delta H_{298}(\text{third law}) = 53.2 \text{ kcal/mol}$$

Note that there is now better agreement between the two enthalpies, but all these new values lie well within the experimental uncertainties assigned to the results for the total pressure.

V. GeTe

Material. A single boule of GeTe grown from a melt covered with a borate flux[28] was used for all experiments. From the phase relations given by McHugh and Tiller,[27] the stoichiometry of the first-grown material was $Ge_{0.494}Te_{0.506}$, the maximum melting composition. Most of the boule was a single crystal which had a micalike cleavage parallel to the (0001) plane of the rhombohedral structure stable at room temperature. The last-to-freeze portion was polycrystalline and a Ge second phase could be identified by X-ray diffraction.

Vaporization Characteristics. Hirayama[41] and Ch'ün-hua, *et al.*,[42] analyzed the condensate from a vaporization of GeTe and found that it had not changed from the original material. They made no statement concerning the congruency of the vaporization and assumed that GeTe(g) was the only vapor species. Colin and Drowart[11] found that approximately 10 atom % of the initial Ge content (~3 wt % of the original sample) remained in the cell after a complete vaporization of GeTe. They identified $GeTe^+$, Te_2^+, and $GeTe_2^+$ as parent ions with observed relative intensities of 1.0, 8.9×10^{-2}, and 1.3×10^{-2}, respectively, "which did not vary much with temperature." They concluded that GeTe vaporizes mainly by the expected reaction

$$GeTe(s) \rightleftharpoons GeTe(g) \qquad (11)$$

but that the Ge residue and other vapor species resulted from the minor reactions

$$GeTe(s) \rightleftharpoons Ge(s) + {}^1/_2Te_2(g) \qquad (12)$$

$$GeTe(s) \rightleftharpoons {}^1/_2Ge(s) + {}^1/_2GeTe_2(g) \qquad (13)$$

In this investigation, isothermal effusion runs to constant weight always produced a Ge(s) residue, and qualitative mass spectrometry also confirmed the presence of the ions observed by Colin and Drowart. In lieu of further mass spectrometric studies, the above reactions have been accepted as the vaporization scheme for GeTe, and the following detailed study of congruency and equilibrium is based on them.

A series of isothermal effusion runs with ~50 mg of freshly ground −200 mesh material was performed to investigate the relation of temperature and orifice size to the amount of Ge(s) residue to get a semiquantitative measure of the magnitude of the minor reactions and thus the relative concentrations of the vapor species. Each of the runs produced the same qualitative rate–time behavior shown schematically in Figure 6. The continuous decrease in rate from the point where constant temperature was attained to point A is interpreted as the vaporization of single-phase GeTe(s) as the initial $Ge_{0.494}Te_{0.506}$ composition shifted toward the two-phase boundary as a result of the noncongruent vaporization. An X-ray diffraction pattern of a sample quenched just after A indicated that a Ge second phase was present. The equilibrium total pressure over this two-phase region must be constant, and thus the observed rate from A to B must also be constant if steady-state conditions are realized in the effusion cell. Actually, the observed rate decreased 5–10% in this region except during one run to be described later. The rate decreased continuously from B to C as the small amount of remaining material in the cell was definitely not sufficient to maintain steady-state conditions. The solid solubility of GeTe in Ge is negligible, and this decrease is not due to vaporization in such a single-phase region. At C, the rate broke essentially discontinuously to zero.

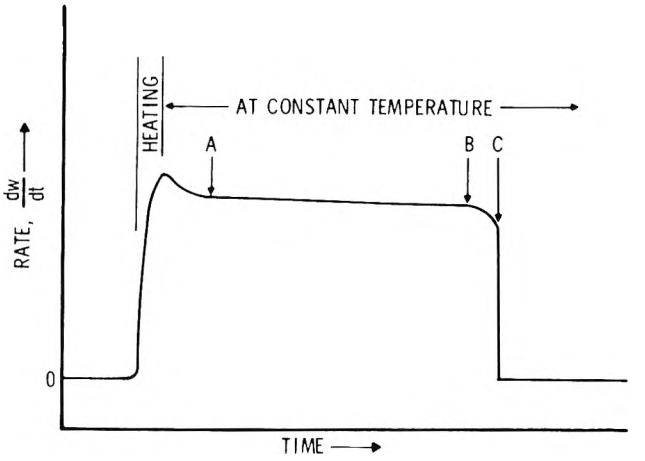

Figure 6. Rate–time behavior for an isothermal GeTe effusion run to constant weight.

The weight per cent of residue (with respect to the original sample weight) is plotted in Figure 7 as a function of the logarithm of the observed rate of loss. The amount of residue does not appear to be a function of temperature alone, but there does appear to be a relationship with the rate, which is dependent on both the orifice area and temperature. The line shown has been eye-fitted to the data and has been drawn deliberately through the highest residue point. In this one run, a zirconia bead was placed over the orifice of the cell with the smallest effective orifice area in order further to reduce the rate of loss. For this run only, the observed rate of loss in the A to B region in Figure 6 was con-

(41) C. Hirayama, *J. Phys. Chem.*, 66, 1563 (1962).

(42) L. Ch'ün-hua, A. S. Pashinkin, and A. V. Novoselova, *Russ. J. Inorg. Chem.*, 7, 496 (1962).

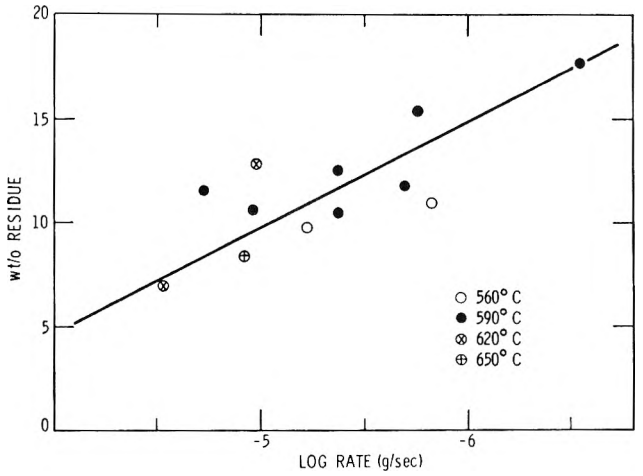

Figure 7. Germanium residue as a function of rate of loss for isothermal GeTe effusion runs to constant weight.

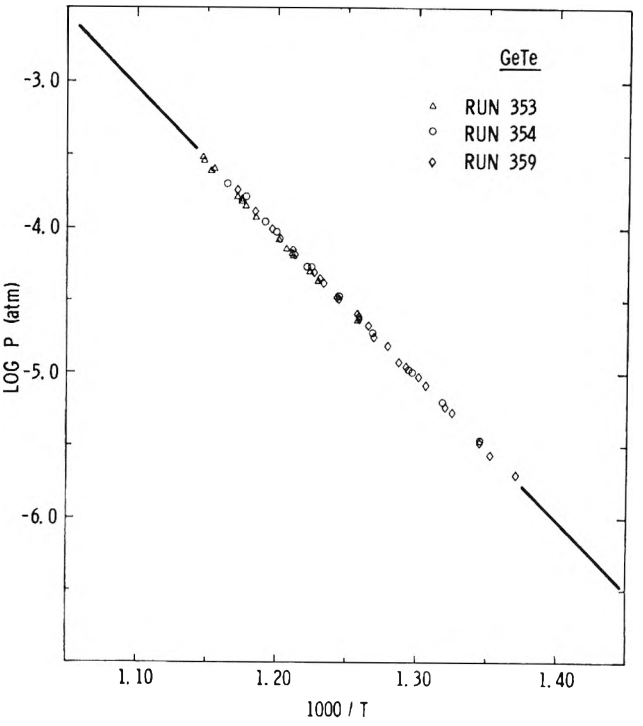

Figure 8. Total vapor pressure of Ge-saturated GeTe determined by effusion experiments.

stant, and steady-state conditions appear to have been attained. As measured by a ratio of observed rates, the effective orifice area had become $\sim 6 \times 10^{-5}$ cm^2.

Designating x, y, and z as the fraction of GeTe which vaporizes according to reactions 11, 12, and 13, respectively, the overall stoichiometry of the vaporization is given by

$$(x + y + z)\mathrm{GeTe(s)} \rightleftharpoons x\mathrm{GeTe(g)} + \frac{y}{2}\mathrm{Te_2(g)} + \frac{z}{2}\mathrm{GeTe_2(g)} + \left(y + \frac{z}{2}\right)\mathrm{Ge(s)} \quad (14)$$

The vapor composition can be determined for each of the runs in Figure 7 from the initial weight of GeTe(s), the final weight of Ge(s), and assuming $y/z = 6$ and is independent of temperature as suggested by the data of Colin and Drowart.[11] The calculated mole fractions of gas range from 0.64 (GeTe), 0.31 (Te_2), 0.05 ($GeTe_2$) to 0.88, 0.10, 0.02 for the isothermal effusion runs believed closest and furthest, respectively, from equilibrium.

To summarize, GeTe(s) vaporizes noncongruently with the formation of a Ge(s) second phase. This solid, nonvolatile phase presumably prevents the attainment of steady-state conditions in effusion cells, except, apparently, where the rate of effusion is extremely slow. Equilibrium cannot be proved in any case. It appears doubtful that true equilibrium information can be obtained for this vaporization by effusion experiments.

Results and Discussion. In light of these difficulties, the pressures have been calculated and reported in the following manner. Data points were limited to a small total weight loss just within the two-phase region (just past A in Figure 6) where the rate had become essentially constant. The material in run no. 354 (Figure 8) was ground from the two-phase portion of the boule, and the rate was essentially constant from the time that constant temperature was attained. From the previous discussions, it is clear that true steady-state conditions were not obtained in these effusion runs. However, there were at least 300 mg of sample in the cell, and the slight decrease in rate in the two-phase region was not evident for these runs of small overall weight loss and corresponding small composition change. In addition, a variation of observed pressure with orifice size was not noticeable as the ranges of observed rate (grams per second) were similar for each run.

Fifty-four data points from three separate experiments and effusion cells were obtained between 456 and 599°; the entire weight loss has been ascribed to GeTe(g). The pressures and resulting thermodynamic quantities were calculated as described above and in section II, and the overall results are given in Table VII and Figure 8. ΔH_T can be corrected to 298°K by the heat capacity data in Table I. Combining the possible errors discussed in section II, the precision of the experimental results, and allowing a ±1 cal/(deg mol) uncertainty in the heat capacity estimate, the second- and third-law enthalpies of vaporization at 298°K are 47.18 ± 0.82 and 48.55 ± 1.35 kcal/mol, respectively. Table VIII and Figure 9 compare these results to previously published investigations.

The vapor concentrations calculated for the isothermal effusion run believed closest to equilibrium indicates that the equilibrium vapor above Ge-saturated GeTe is composed of less than 65% GeTe(g) molecules and has a higher concentration of other species than has generally been recognized. The equilib-

Table VII: Summary of Results for GeTe

	No. 353	No. 354	No. 359	Average[a]
Cell material	Alumina	Alumina	Alumina	
Effective orifice area, cm^2	0.000449	0.002652	0.004575	
Number of data points	16	12	26	54
Temperature range, °C	522–599	470–585	456–580	456–599
Average temperature, °C	569	531	519	537
Second law				
ΔH_T	45.68 ± 0.37	45.19 ± 0.30	44.79 ± 0.23	45.08 ± 0.49
ΔS_T	36.20 ± 0.44	35.78 ± 0.37	35.26 ± 0.29	35.61 ± 0.50
Third law				
ΔH_{298}	48.63 ± 0.05	48.44 ± 0.07	48.43 ± 0.08	48.55 ± 0.12
Summary				
Log P(atm) = A +	A 7.91 ± 0.10	7.82 ± 0.08	7.71 ± 0.06	7.782 ± 0.109
$B(10^3/T_K)$	B −9.98 ± 0.08	−9.87 ± 0.06	−9.79 ± 0.05	−9.851 ± 0.106
Fit: σ%	2.4	2.9	3.1	

[a] Uncertainties do not reflect possible systematic errors; see text for discussion.

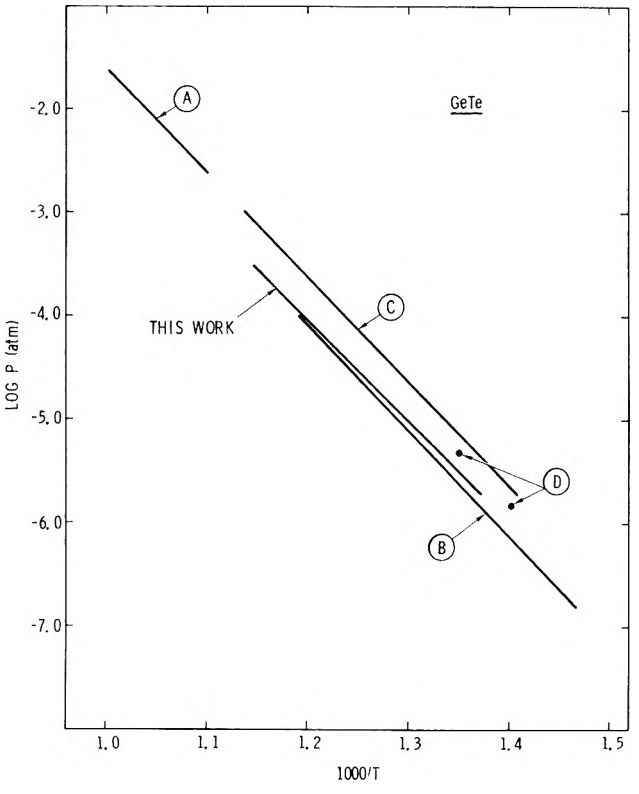

Figure 9. Previously reported vapor pressures for GeTe: A, Brebrick;[3,4] B, Hirayama;[41] C, Ch'ün-hua, *et al.*;[42] D, Colin and Drowart.[11]

rium experiments of Brebrick[3,4] performed in a closed system give different results. A GeTe(g) fraction of ~0.90 can be calculated from his measured Te_2(g) partial pressure over Ge-saturated GeTe and the total pressures determined in this work. The discrepancy is not readily explained but could easily be due to an unknown systematic error in the comparison of results from widely different experimental methods. The isothermal effusion run with the greatest rate of loss (least Ge(s) residue) yields a GeTe(g) fraction of 0.88, and this value agrees well with the compositions reported by Colin and Drowart[11] for similar effusion rates.

According to eq 3, the ratio of these reported total pressures to a rigorous calculation of the total pressure, which recognizes the presence of other vapor species, is given by

$$\frac{P_{\text{reported}}}{P_{\text{rigorous}}} = \frac{M_{\text{GeTe}}{}^{-1/2}}{aM_{\text{GeTe}}{}^{-1/2} + bM_{\text{Te}_2}{}^{-1/2} + cM_{\text{GeTe}_2}{}^{-1/2}} \quad (15)$$

where a, b, and c are the weight fractions of the vapor species and can be calculated from the stoichiometry of eq 14. This ratio is 1.061 based on concentrations calculated for the isothermal effusion run believed closest to equilibrium. For the average rates of weight loss encountered in these effusion runs, there is a higher GeTe(g) fraction (~0.80) and the ratio becomes ~1.03.

This paper reports (Table VII) the *total* equilibrium pressure and its temperature dependence of Ge-saturated GeTe(c) and no serious error results from ignoring the known presence of Te_2(g) and $GeTe_2$(g). However, the partial pressure of GeTe(g) is significantly less than the total pressure and, according to the data of Brebrick[3,4] and Colin and Drowart,[11] its vapor fraction changes only slightly over the temperature range of these experiments. Further, $\Delta f e f$ has been calculated for the equilibrium GeTe(s) $\rightleftharpoons$ GeTe(g) and should be applied only to the GeTe(g) partial pressure in the third-law calculation. Such a rigorous analysis could not be applied to the experimental data as vapor concentrations and their temperature dependences were not accurately known. However, rough estimates for the GeTe(s) $\rightleftharpoons$ GeTe(g) equilibrium alone can be made

Table VIII: Previously Reported Data for the Vaporization of GeTe

Reference	Curve (Figure 9)	Temp range, °C	A^a	B^a	ΔH_T (second law)	ΔH_{298} (third law)	Comments[b]
Brebrick[3,4]	A	635–724	8.50	−10.1 ± 0.2	46.2	...	Optical absorption GeTe(g) pressure based on ref 42
Hirayama[41]	B	407–564	8.255 ± 0.598	−10.255 ± 0.451	46.86 ± 2.06	...	Te_2(g) partial pressure measured directly Effusion; porous graphite cells Two-point gravimetric method Assumed GeTe(g) only vapor species
Ch'un-hua, *et al.*[42]	C	437–606	8.433	−10.058	45.8 ± 3.0	...	Concluded P(measured) = P(equilibrium) Effusion; quartz cells Two-point gravimetric method Assumed GeTe(g) only vapor species
Colin and Drowart[31]	D	351–691	...	...	(46)	...	Reported congruent vaporization Effusion; quartz cells Mass spectrometry Pressures by time-integration and intensities
This work		456–599	7.782 ± 0.109	−9.851 ± 0.106	45.08 ± 0.49	48.55 ± 0.12	Two points yield approximate ΔH

[a] A and B are the constants in the equation log P(atm) = $A + B(1000/T)$. [b] Two-point gravimetric method: rate of weight loss is calculated from two weighings of the cell or condensate in air and at room temperature before and after each experimental run.

based on the GeTe(g) partial pressure calculated for the vapor compositions for the isothermal effusion run believed closest to equilibrium. The calculated end points of an assumed linear log P *vs.* $1/T$ curve for GeTe(g) lie at $0.57P_{total}$ and $0.58P_{total}$ at the high and low ends, respectively, of the experimental temperature range. These estimates are

$$\log P_{GeTe}(atm) = 7.50 - 9.82(1000/T)$$

$$\Delta H_{298}(\text{second law}) = 47.0 \text{ kcal/mol}$$

$$\Delta H_{298}(\text{third law}) = 49.4 \text{ kcal/mol}$$

Note that these new values lie within the experimental uncertainties assigned to the results for the total pressure.

VI. Free Surface Vaporization

Cursory free surface vaporization experiments have been performed with the single crystals described previously. These results must be considered approximate as complicated rate–time behavior was observed in each case and steady-state rates were not obtained in any run. These problems were due to some or all of the following factors: poor orientation, constantly changing effective surface area due to loss of material, formation of a nonvolatile phase produced by noncongruency, and a complicated vaporization mechanism for SnTe and GeTe. The problems are evident in the data, and further work is definitely required to describe accurately the free surface vaporization of these materials.

Specimens were cut or cleaved from single crystals and were placed flat on a quartz plate suspended from the balance. An apparent vapor pressure, P_L, was calculated from the rate–temperature data, the geometrical surface area, and the assumption of an MTe(g)-only vapor. The experiments are shown in Figure 10 and summarized in Table IX by linear least-squares fit of log P_L *vs.* reciprocal temperature. A vaporization coefficient, α_v, defined by P_L/P_K where P_K is the effusion pressure, has been calculated in the region of overlapping temperatures.

The most consistent results and nearly steady-state rates were obtained for PbTe specimens cleaved parallel to the [100] face. Hansen and Munir[35] reported an α_v of ~0.7 at 725° as a result of torsion–effusion and torsion–Langmuir experiments on [100] oriented single crystals.

The SnTe specimens were cut perpendicular to the axis of the single-crystal boule without regard to crystallographic orientation. Unlike the other materials, α_v for SnTe appears to have a strong temperature dependence. However, examination of the surface after vaporization revealed formation of spongelike holes each terminated by a crystallographic face with the same orientation. These holes can act like Knudsen cells and cause an enhanced rate of vaporization for a

Table IX: Results of the Cursory Free Surface Vaporization Experiments

	Surface primarily exposed	Temperature range, °C	Log P(atm) = $A + B(1000/T)$ A	B	α_v	$\sigma_{\%}$
PbTe	[100]	478–541	8.0 ± 0.4	−11.8 ± 0.3	0.5 at 525°	±10
SnTe	Unknown	492–598	11.5 ± 1.4	−14.7 ± 1.2	0.25 at 525°	±42
GeTe	(0001)	376–485	7.0 ± 0.6	−9.7 ± 0.4	0.25 at 475°	±22

given geometrical surface area. Increased pit formation with an approach to effusion conditions at higher temperatures could explain the anomalous slope and apparent temperature dependence. Actually, α_v is probably independent of temperature based on the results for PbTe and GeTe.

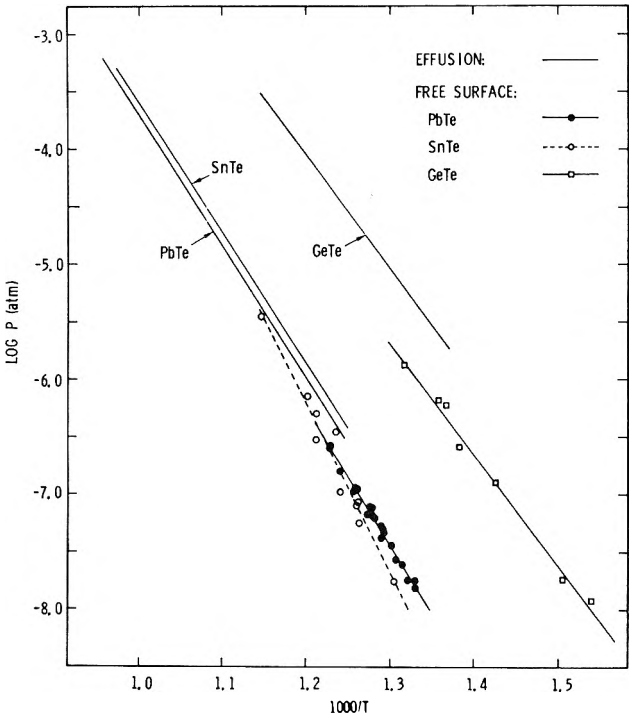

Figure 10. Comparison of the total vapor pressures determined by effusion experiments and apparent vapor pressures calculated from the rate–temperature data for the cursory free surface vaporization experiments.

GeTe has an easy micalike cleavage parallel to the (0001) rhombehedral plane. The observed rate–time behavior in each run was similar to and could be interpreted in the same way as that shown in Figure 6. The major difference was that the A to B portion decreased faster. A surface powder of Ge(s) accumulated during every run. The pressures have been calculated from a rate obtained by extrapolation of the initial A-to-B portion back to zero weight loss.

VII. Summary

The vaporization of PbTe, SnTe, and GeTe has been studied with special emphasis placed upon such aspects as congruency, stoichiometry, vapor species, and the attainment of steady-state and/or equilibrium conditions within the effusion cell. The overall complexity of the vaporization increases from PbTe to SnTe to GeTe. PbTe vaporizes congruently by the loss of PbTe(g). SnTe vaporizes noncongruently; the vapor is predominantly SnTe(g) but with an increasing fraction of Te_2 at higher temperatures. GeTe vaporizes noncongruently; the vapor exhibits a decreasing fraction of GeTe(g) and increasing fraction of Te_2 and $GeTe_2$ as steady-state conditions are approached. Ge(s) is formed as a result of the noncongruency and prevents the attainment of steady-state or equilibrium conditions within the cell except, perhaps, at very low effusion rates.

All results are based on total equilibrium pressures of congruently subliming PbTe and the two-phase Sn–SnTe and Ge–GeTe assemblages, and they have been calculated by ascribing the entire weight loss to an MTe vapor. The total pressures are affected very little by this assumption, but estimates have been made for the partial pressures and enthalpies of vaporization for the SnTe(s) $\rightleftharpoons$ SnTe(g) and GeTe(s) $\rightleftharpoons$ GeTe(g) equilibria based on approximate vapor compositions. In general, these latter results lie within the range of experimental error assigned to the total pressure calculations. The total effusion pressures for the three materials are given in Figure 10, and the numerical results are best summarized by the "average" column in Tables III, V, and VII. A striking feature is the similarity of the pressures and enthalpies of vaporization between PbTe and SnTe which results in an apparent congruent vaporization for all PbTe–SnTe alloy compositions in gravimetric experiments.[43]

Acknowledgments. The author expresses his appreciation to W. Meador and F. T. Gurule for their technical assistance, to R. J. Baughman for the single-crystal samples, and to Dr. A. R. Miller for numerous discussions on various aspects of this investigation.

(43) D. A. Northrop, submitted for publication.

Surface Diffusion of Single Sorbates at Low and Intermediate Surface Coverage

by E. M. Reed, Jr., and J. B. Butt*

Department of Engineering and Applied Science, Yale University, New Haven, Connecticut 06520 *(Received June 3, 1970)*

Publication costs borne completely by The Journal of Physical Chemistry

The rates of surface diffusion of propane and 2,2-dimethylpropane through a well-characterized porous matrix of molybdenum sulfide have been determined under conditions of known and controlled surface coverage. Temperature ranges from 20 to 90° and surface coverage from 0.3 to 15% of monolayer have been investigated. Under such conditions surface transport accounts for a substantial portion of the total mass diffusion flux. For propane at 20°, 32% of the total flux through the matrix is due to surface transport, while at 70° this decreases to 11%. For 2,2-dimethylpropane the contribution of surface diffusion varies from 42% at 20° to 11% at 90°. Surface diffusion coefficients evaluated according to a Fick's law expression were on the order of 10^{-5} cm²/sec. Below a surface coverage of about 1% for propane and 2% for 2,2-dimethylpropane this coefficient was independent of surface coverage; variations in surface diffusivity at higher coverages can be correlated with variation in heat of adsorption. Activation energies for surface diffusion were 3.5 kcal/mol for propane and 3.9 kcal/mol for 2,2-dimethylpropane, while limiting heats of adsorption were 8.8 and 9.7 kcal/mol, respectively.

Introduction

Diffusional mass transport in porous structures has important effects in many catalytic systems and has been the object of considerable interest in recent years.[1] In such structures the transport of gaseous materials is governed by molecule–wall and/or molecule–molecule collisions, or a combination,[2] and in the event of adsorbed gases a parallel transport along the surface is possible. Under suitable conditions such surface diffusion can become the predominating mechanism of transport through a porous structure.[3,4] A complete theory for surface diffusion over the entire range of surface coverage has not been set forth, primarily because no single transport mechanism is operative over this range. Nonlocalized sorbates have been treated as two-dimensional gases,[5,6] either ideal or van der Waals, while motion in localized sorbate layers has been considered an activated process consisting of discrete steps between adsorption sites.[7,8] For localized adsorption, which is of primary interest in this investigation, the surface diffusivity can be shown to obey the equation[8]

$$D_s = D_0 \exp(-E_s/RT) \tag{1}$$

where the preexponential factor is a function of distance between adsorption sites and the lattice vibrational frequency. The activation energy E_s is of course an average value of the distribution of localization energies on the heterogeneous surface.

The theory derived for the transport of nonadsorbed gases in fine capillaries, where both intermolecular and Knudsen mechanisms can be involved, is applicable with modification to porous structures. For a binary mixture the resulting transport coefficient is

$$D_g = \left[\frac{1 - \alpha y_1}{D_{12}\left(\frac{\epsilon}{\tau}\right)} + \frac{1}{D_{K1}(\bar{r})}\right] \tag{2}$$

in which y_1 is the mole fraction of transferred component, D_{12} the normal intermolecular diffusion coefficient, ϵ the porosity of the matrix, τ a tortuosity factor related to the internal geometry, $D_{K1}(\bar{r})$ the Knudsen diffusion coefficient evaluated for an average capillary radius characteristic of the matrix ($D_{K1}(\bar{r}) = {}^2/_3\bar{r} \times \sqrt{8RT/\pi M_1}$), and α a flux ratio related quantity ($1 + N_2/N_1$). It has been shown both theoretically and experimentally that the flux ratio for isothermal, isobaric diffusion is equal to the inverse square root of the molecular weight ratio of the diffusing pair.[2,9]

Similar transformation to porous media is possible for the surface diffusivity equation, so that net trans-

* Department of Chemical Engineering, Northwestern University, Evanston, Ill. 60201 (to whom correspondence should be addressed).

(1) C. N. Satterfield, "Mass Transfer in Heterogeneous Catalysis," MIT Press, Cambridge, Mass., 1970.

(2) R. B. Evans, B. M. Watson, and E. A. Mason, *J. Chem. Phys.*, **35**, 2076 (1961).

(3) E. R. Gilliland, R. F. Baddour, and J. L. Russell, *AIChE J.*, **4**, 90 (1958).

(4) P. Schnieder and J. M. Smith, *ibid.*, **14**, 886 (1968).

(5) C. Kemball, *Proc. Roy. Soc., Ser. A*, **187**, 73 (1946).

(6) S. Ross and J. Oliver, "On Physical Adsorption," Wiley, New York, N. Y., 1964.

(7) J. R. Dacey, *Ind. Eng. Chem.*, **57**, 27 (1965).

(8) J. H. deBoer, "The Dynamical Character of Adsorption," Oxford University Press, London, 1953.

(9) For experimental examples: J. Hoogschagen, *Ind. Eng. Chem.*, **47**, 906 (1955); R. H. Villet and R. H. Wilhelm, *ibid.*, **53**, 837 (1961); M. R. Rao and J. M. Smith, *AIChE J.*, **10**, 293 (1964).

port through the porous structure is essentially defined in terms of diffusion through a set of parallel capillaries[2] for which an effective transport coefficient may be written. Assuming the additivity of fluxes

$$N_0 = N_g + N_s = -D'\nabla C - D'_{s,p}\nabla C_{s,p} \qquad (3)$$

where N_g is the gas-phase flux per unit area in mol/(cm² sec), N_s the corresponding surface flux, D' an effective gas-phase diffusion coefficient, eq 2, $D'_{s,p}$ an effective surface diffusion coefficient based on surface flux per unit total area, C the gas-phase concentration of adsorbate in moles per cubic centimeter, and $C_{s,p}$ the surface concentration of adsorbate in moles per cubic centimeter of pore space.

In the following we shall be concerned with data on diffusion fluxes through a porous plug of dimension L in the direction of transport, subject to a total concentration difference ΔC in L. The corresponding form of eq 3 integrated for transport through the distance L is

$$N_0 = -\left(D' + \frac{\rho}{\epsilon}D'_{s,p}K\right)\frac{\Delta C}{L} = -D\frac{\Delta C}{L} \qquad (4)$$

where adsorption equilibrium is assumed and is given as $K = X/C$, with X in moles adsorbed per gram of adsorbent, and the surface concentration is $C_{s,p} = (\rho/\epsilon)\cdot KC$, with ρ the bulk density of the structure in grams per cubic centimeter. The temperature dependence of total flux follows from eq 4 as

$$N_0(T) = -\left[\frac{(1/B)T^{1/2}}{(A/B) + T} + M\exp\left(\frac{-E_s(\theta) + Q(\theta)}{RT}\right)\right]\frac{\Delta C}{L} \qquad (5)$$

in which A and B are the temperature-independent factors of eq 3, the activation energy for surface diffusion $E_s(\theta)$ and the heat of adsorption $Q(\theta)$ are both functions of surface coverage θ, and M is defined as $(\rho/\epsilon)D^\circ_{s,p}K^\circ$, with $D^\circ_{s,p}$ and K° defined by

$$D_{s,p} = D^\circ_{s,p}\exp[-E_s(\theta)/RT]$$

and

$$K = K^\circ\exp[Q(\theta)/RT] \qquad (6)$$

From eq 4 it is possible to determine values of D and then the surface diffusion coefficient from flux measurements at various levels of ΔC, provided K and D' are determined separately. The apparent temperature dependence is a function of temperature level at constant total pressure: at lower temperatures it is possible for K (and hence $C_{s,p}$) to be large and surface transport to predominate with its associated exponential temperature dependence, while with increasing temperature surface flux decreases and the temperature dependence approaches T^n with $1/2 \leq n \leq 3/2$ depending on the relative importance of Knudsen and bulk diffusion in the pore volume.

It is clear from eq 4 that a simple Fickian form of the flux equation for both overall and surface transport applies, yet it has been the experimental observation that surface diffusivities evaluated from experiment *via* a Fick's law analysis are almost invariably concentration dependent.[3,10] In spite of the limitations of the elementary theory of eq 4, there should be at least a limiting region of low surface coverage where the Fickian description is adequate. One of the major reasons for this observed variation is that many prior studies of surface transport through microporous media have not retained surface coverages as a controlled experimental variable,[11] at least in the range where constancy might be expected, and in many cases a wide range of surface coverage is involved in an experiment whose results are given in terms of a single "surface diffusivity" value.

A major objective of the present work is the experimental study of surface transport rates under conditions of known and controlled surface coverage, determination of the corresponding transport coefficients, and evaluation of the relative magnitudes of surface and gas-phase transport.

Experimental Section

Materials. The porous matrix employed in this study was composed of a molybdenum sulfide powder, Harshaw Chemical Co. Mo-0401-P, made up into a

Table I: Properties of the Porous Structure

Powder, Mo-0401-P	
Average particle size, μ	250
Pore volume, Vg, cm³/g	0.023
Average pore radius, Å[a]	17.2
Surface area, S, m²/g	26.8
Pellet	
Diameter, cm	2.542
Thickness, cm	0.953
Bulk density, g/cm³	1.57
Total porosity	0.24
Macropore porosity[b]	0.22
Most probable macropore radius, Å[c]	360
Average macropore radius, Å	650

[a] $\bar{r} = 2Vg/S$. [b] Macropore range: pore radius from 75 to 5000 Å. [c] Peak of macropore distribution.

(10) R. M. Barrer and J. A. Barrie, *Proc. Roy. Soc., Ser. A*, **213**, 250 (1952).

(11) For typical examples, see J. B. Rivarola and J. M. Smith, *Ind. Eng. Chem., Fundam.*, **3**, 308 (1965); J. R. Dacey, Advances in Chemistry Series, No. 33, American Chemical Society, Washington, D. C., 1961, p 172; R. M. Barrer and J. A. Barrie, ref 10; J. A. Weaver and A. B. Metzner, *AIChE J.*, **12**, 655 (1966); R. M. Barrer, *J. Phys. Chem.*, **57**, 35 (1953); R. M. Barrer and R. Gabor, *Proc. Roy. Soc., Ser. A*, **256**, 267 (1960); R. M. Barrer and E. E. Strachan, *ibid.*, **231**, 52 (1955); R. M. Barrer and D. M. Grove, *Trans. Faraday Soc.*, **47**, 826, 837 (1951); P. C. Carman, *Proc. Roy. Soc., Ser. A*, **211**, 526 (1952); S.-T. Huang and K. Kammermeyer, *Can. J. Chem. Eng.*, **44**, 82 (1966); J. Popielawski, *J. Catal.*, **7**, 263 (1967); R. N. Foster, H. Bliss, and J. B. Butt, *Ind. Eng. Chem., Fundam.*, **5**, 579 (1966).

disk by compression in a laboratory press. Some physical properties of both powder and pellet are given in Table I. The internal volume–area distribution of the pellet was determined by mercury penetration and nitrogen desorption; this distribution was almost identical with one reported for similar material previously,[12] characterized by a near-symmetric macropore distribution between 100- and 5000-Å pore radius and very little micropore structure ($r < 75$ Å); some geometric properties determined from the distribution are also given in Table I.

Pure gases were supplied by Air Products Co.; the argon and helium used each had quoted minimum purities of 99.99%. Several gas mixtures composed of helium and varying amounts of argon, propane, and 2,-2-dimethylpropane (1.00% Ar; 4.97, 0.95, 0.29% C_3; 4.75, 0.87, 0.29% C_5) were supplied, with analysis, by Air Products. All gases were dried to a dew point of −78° before use.

Diffusion Studies. Rates of diffusion of nonadsorbed and adsorbed gases through the porous matrix were measured using a modified Wicke–Kallenbach[13] counterdiffusion apparatus which is similar in design and operation to one described previously.[12] The system allows flux measurements to be made at constant temperature and total pressure and, in the case of adsorbed species, near-constant surface coverage when small composition differences are maintained across the pellet. The pellet is formed directly in a cylindrical containing ring which fits into the counterdiffusion cell, and approximately 2 mm is machined from each face of the disk to eliminate surface inhomogeneities (film effects). The result, for a compressive force of 5000 psig maintained for 1 min, is a porous structure of bulk density about 1.6 g/cm³ (Table I). Previous data[12] indicate that density inhomogeneity in the formed disk is less than 10% of the measured bulk density.

Prior to a diffusion run, the disk was permeated with helium at 95° for a minimum of 4 hr to remove any adsorbed material. The diffusion experiment itself consisted of passing at set temperature and total pressure a stream of helium over one face of the porous disk while a mixture (helium plus minor component) of known composition at identical conditions of temperature and total pressure passed by the other face. Measurements of the flow rate (by soap film meter) and the composition of each stream (by thermal conductivity) are the data required to determine counterdiffusion fluxes. In experiments with adsorbed gases, the surface coverage is changed by changing the composition of the mixture feed stream or by changing the temperature at a set composition. A complete description of detailed experimental procedure is given elsewhere.[14]

Sorption Studies. Separate data on adsorption are required for determination of surface concentrations and heats of adsorption. Adsorption measurements were made on a separate sample of the molybdenum sulfide at five temperatures over the range 5–90° for both propane and 2,2-dimethylpropane. A commercial sorptometer was employed for these measurements and for determination of the nitrogen desorption isotherm at liquid nitrogen temperature employed in determination of the pore size distribution. The sorptometer was of the flow type, in which a gas mixture containing a known concentration of adsorbate in helium is passed through a fixed bed of the adsorbent and permitted to equilibrate with the solid. The composition of the exit stream from the fixed bed is continuously monitored by a thermal conductivity detector, with the depletion of the adsorbate and the amount adsorbed determined by simple material balance.

Results

For nonadsorbed gases both theory and experiment[2] agree that flux ratios in isothermal, isobaric counterdiffusion are given by the inverse square root of the molecular weight ratio. This is a convenient means for establishing the consistency of the counterdiffusion experiment. In the present work flux determinations were made for the pure argon–pure helium system at 1 atm and 25°, both before and after experimentation with adsorbed gases. The results of ten experiments give an average flux ratio (He/Ar) of 3.25 ± 0.12, which, within the range of experimental error, is equivalent to the theoretical value of 3.16. No significant differences were noted between measurements made before and after the surface diffusion experiments.

Because it was desired to work at low surface coverages, experiments for the propane–helium system and the 2,2-dimethylpropane–helium system were conducted only for the case of dilute adsorbate–helium mixtures counterdiffusing against pure helium. The thermal conductivity detector could not detect the concentration change of helium across the pellet under these circumstances so helium flux could not be measured directly; only the total flux of the absorbing gas was measured. The method of determining surface fluxes requires data on diffusion of nonadsorbed gases under identical conditions; hence experiments on dilute argon–helium mixtures counterdiffusing against helium were also carried out. Some typical measurements of total diffusion flux as a function of gas-phase concentration drop across the pellet for each of the three systems studied is presented in Figure 1. All of these results pertain to a total pressure of 760 ± 10 mm in the diffusion cell. A notable feature of these measurements is the linear relationship between the total flux and the

(12) Pellet 3 of R. N. Foster, J. B. Butt, and H. Bliss, *J. Catal.*, **7**, 179 (1967).

(13) E. Wicke and R. Kallenbach, *Kolloid-Z.*, **97**, 135 (1941).

(14) E. M. Reed, Jr., Ph.D. Thesis, Yale University, New Haven, Conn., 1969.

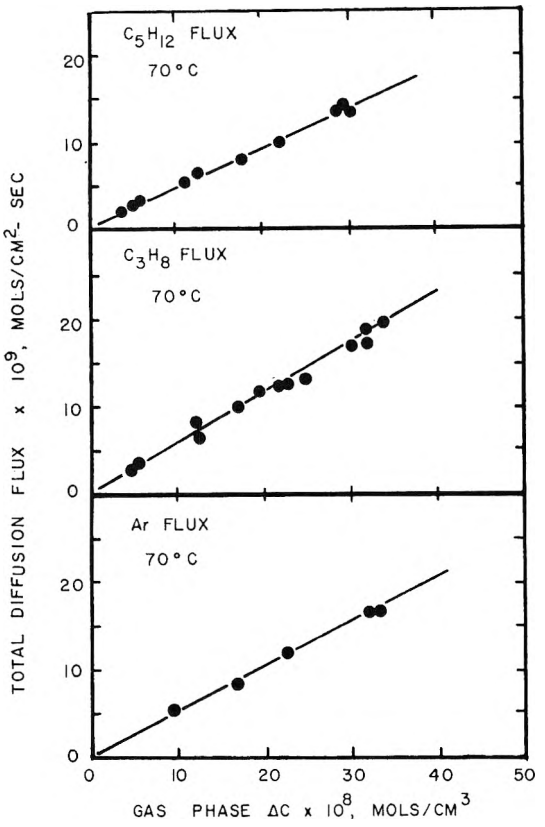

Figure 1. Typical data on diffusion flux as a function of gas phase concentration drop across pellet, counterdiffusion with respect to helium.

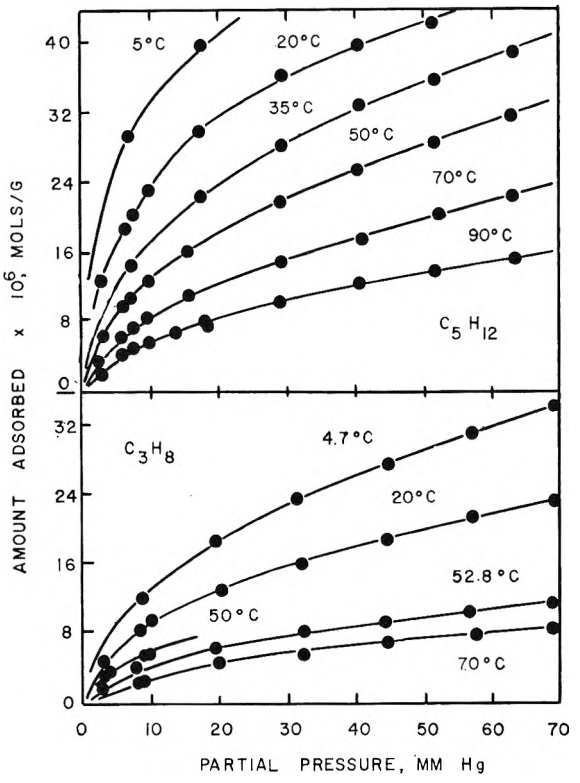

Figure 2. Adsorption isotherms: propane and 2,2-dimethylpropane on molybdenum sulfide.

gas-phase concentration drop across the pellet in the concentration range investigated.

Adsorption isotherms for propane and 2,2-dimethylpropane on molybdena were determined at the same temperatures as used in the diffusion runs. These results are given on Figure 2.

The identification of the surface transport contribution to the total diffusion flux requires a knowledge of the gas-phase flux separately. Since flux ratios in the gas phase obey the inverse square root ratio of molecular weight relationship, it follows that for a given concentration drop across the pellet, the gas-phase portion of the total flux of adsorbing gas can be calculated from the measured argon flux under identical conditions of concentration drop by

$$N_i = N_{Ar}\sqrt{M_{Ar}/M_i} \tag{7}$$

where i refers to either C_3 or C_5. The ratio in eq 7 is 0.9518 for C_3 and 0.7440 for C_5. The argon flux is determined from counterdiffusion experiments with helium (Figure 1), and the computed gas-phase contribution is subtracted from the measured total flux to yield the surface diffusion flux per unit area normal to the direction of transport. This procedure presumes that partial pore blocking due to the presence of an adsorbed layer is not important; in view of the relatively large pore sizes and the low surface coverages involved in this work, this should be a good assumption.

The major results regarding diffusion fluxes are summarized in Table II. Since the observed fluxes were linear with concentration drop across the pellet, they may be reported independently of surface coverage, as in the table. Surface coverages are computed from equilibrium surface concentrations and the concentration for monolayer coverage, determined from

$$X_m = S/N_0\sigma_i \tag{8}$$

in which X_m is the concentration of sorbate at monolayer coverage in moles per gram, S is the specific surface area of the solid in square centimeters per gram, N_0 is Avogadro's number, and σ_i is determined from the Emmett and Brunauer expression[15]

$$\sigma_i = 1.091\left[\frac{M_i}{\rho_l N_0}\right]^{2/3} \tag{9}$$

where ρ_l is the density of the liquid sorbate at the temperature in question. Equation 9 assumes that the adsorbed molecules behave as a liquid and arrange themselves on the surface in a two-dimensional close-packed hexagonal configuration, hence the packing factor of 1.091. Both of these assumptions are subject to question, particularly at very low surface coverages, so the values of surface coverage reported may be subject to

(15) P. H. Emmett and S. Brunauer, *J. Amer. Chem. Soc.*, 59, 1553 (1937).

Table II: Summary of Diffusion Flux Results[a]

	Temp, °C			
	20	50	70	90
Total flux × 10^8, mol/(cm² sec)				
Propane	0.692	0.603	0.570	...
2,2-Dimethylpropane	0.642	0.499	0.470	0.460
Gas-phase flux × 10^8, mol/(cm² sec)				
Helium	1.58	1.63	1.68	1.74
Argon	0.500	0.517	0.531	0.551
Propane	0.476	0.492	0.505	...
2,2-Dimethylpropane	0.372	0.384	0.395	0.410
Surface flux × 10^8, mol/(cm² sec)				
Propane	0.216	0.111	0.065	...
2,2-Dimethylpropane	0.270	0.115	0.075	0.050
Ratio of surface flux to total flux				
Propane	0.312	0.184	0.114	...
2,2-Dimethylpropane	0.420	0.231	0.160	0.109
Ratio of helium flux to total flux				
Propane	2.28	2.70	2.95	...
2,2-Dimethylpropane	2.46	3.27	3.58	3.78
Effective overall diffusion coefficient[b] × 10^2, cm²/sec				
Argon	4.76	4.92	5.06	5.25
Propane	6.59	5.74	5.43	...
2,2-Dimethylpropane	6.11	4.75	4.48	4.38

[a] All fluxes are referred to a gas-phase concentration drop of 0.10 μmol/cm³. [b] Defined by eq 4.

Table III: Properties of the Adsorbed Layer

	Temp, °C			
Property	20	50	70	90
Liquid density, g/cm³				
Propane	0.4998	0.4505	0.4067	...
2,2-Dimethylpropane	0.5949	0.5591	0.5317	0.5043
Area of adsorbed molecule, Å²				
Propane	30.3	32.4	34.7	...
2,2-Dimethylpropane	37.6	39.2	40.4	41.7
Monolayer coverage, μmol/g, based on surface area of 26.8 m²/g				
Propane	147.0	137.4	128.2	...
2,2-Dimethylpropane	118.3	113.6	110.2	106.7

some magnitude of absolute error. None of the adsorption data of Figure 2, however, are very well represented by a BET correlation, particularly at low relative pressures, so we have not presented surface areas or monolayer volumes determined from that theory, although they are in general agreement with those given here. In Table III is given a summary of the properties of the adsorbate layer according to eq 8 and 9; all fractional surface coverage values reported refer to the monolayer coverages reported in this table.

The value of K was determined from the coefficients of a least-squares polynomial fit to the isotherm data. The limiting value of K at low coverage, the Henry's law constant, so obtained is given for each gas at several temperatures in Table IV and heats of adsorption determined from the temperature variation of this constant are reported in the table. Isosteric heats of adsorption have also been evaluated as a function of surface coverage from the adsorption isotherms by means of the Clausius–Clapeyron equation. These results are shown in Figure 3; in both cases the heats fall rapidly at first, then more slowly with increasing surface coverage. As usual, this variation cannot be uniquely assigned as due to any particular factor but is probably the result of a combination of surface heterogeneity and interactions among adsorbed molecules. The very strong decrease in heat of adsorption at low surface coverage, however, does suggest considerable energetic inhomogeneity of the surface. Limiting values of the heat of adsorption at zero surface coverage, also tabulated in Table IV, are about 7% smaller in both cases than those computed from the polynomial fit of iso-

Table IV: Adsorption Parameters in the Henry's Law Region

Temp, °C	K, adsorption coefficient, cm³/g: Propane	2,2-Dimethylpropane
20	182.8	426
50	48.3	101
70	23.0	44.8
90	...	21.8
Heat of adsorption from K values, cal/mol	8300	9050
Heat of adsorption from Clausius–Clapeyron interpretation (Figure 3), cal/mol	9050	9750

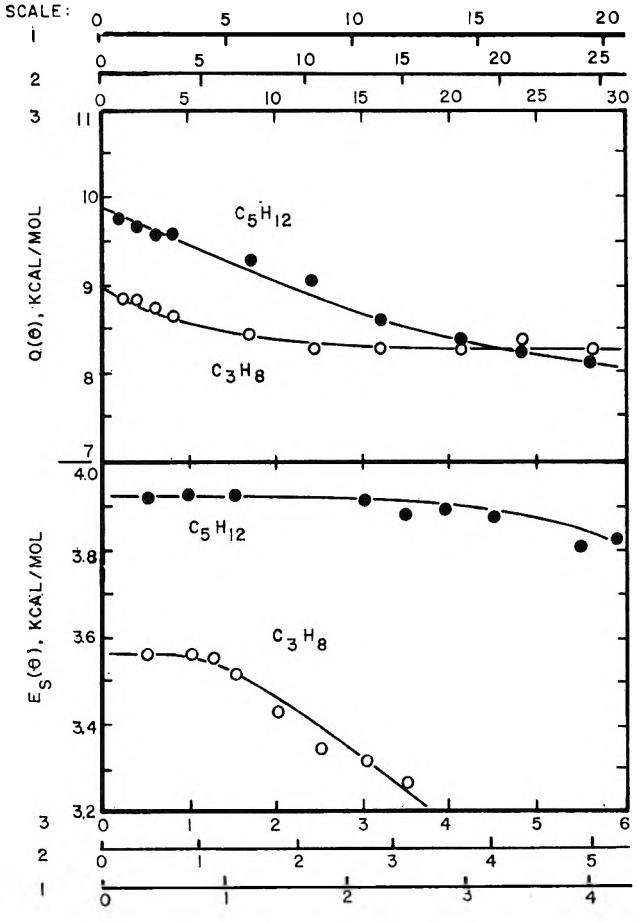

Figure 3. Heat of adsorption, $Q(\theta)$, and activation energy for surface diffusion, $E_s(\theta)$, as functions of surface coverage: scale 1, surface coverage of C_3H_8, per cent of monolayer; scale 2, surface coverage of C_5H_{12}, per cent of monolayer; scale 3, surface concentration of C_3 or C_5, mol/g × 10^6.

therm data. This is excellent agreement in view of the well-known hazards of the latter procedure.

From the overall flux determined by direct measurement, the gas-phase contribution determined by measurement and calculation according to eq 7, and the properties of the sorbate layer determined as a function

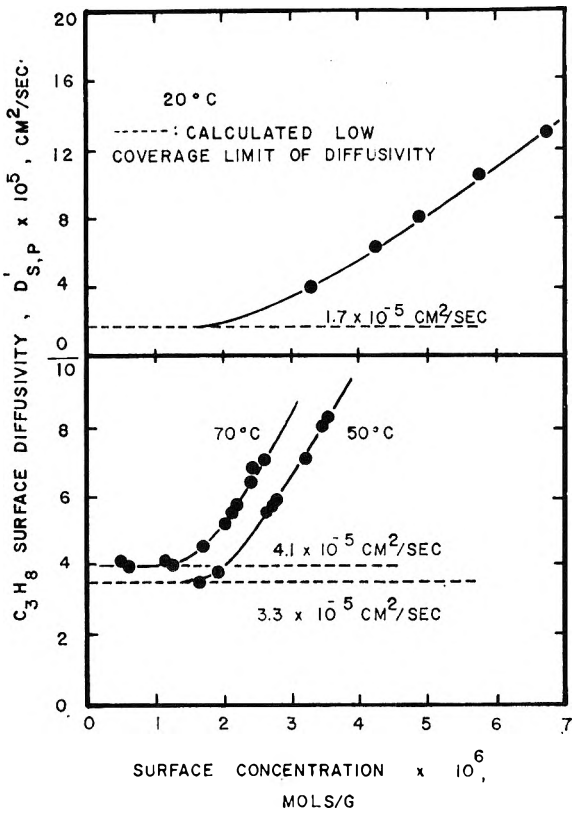

Figure 4. Surface diffusivity of propane as a function of surface concentration.

of temperature and surface coverage, it is possible to obtain values of the surface diffusion coefficient in eq 4. For the Henry's law region the adsorption coefficient used in this interpretation is the constant value as reported in Table IV. Outside the linear region of the adsorption isotherm the equilibrium adsorption coefficient is evaluated at the mean gas-phase concentration in the pellet. Surface diffusion coefficients so determined are shown on Figures 4 and 5 as a function of surface concentration. The limiting values at low surface concentration correspond generally to the Henry's law region of adsorption equilibrium. The fortunate linear relationship between total diffusion flux and gas-phase concentration drop, observed over the entire range of conditions studied, allows reliable estimation of these limiting values even at lower temperatures where they were not directly measured. Such limiting diffusivities are determined from the value of the effective gas-phase diffusion coefficient (constant in the range investigated because of the linear flux—ΔC relationship), the Henry's law equilibrium adsorption coefficient, and the relative contribution of gas-phase flux to total flux (also linear with ΔC).

The precision of total flux measurements at a level of 10^{-8} mol/(cm² sec), as reported in Table II, is determined primarily by errors in concentration measurement, about ±10% of the absolute value of concentration, and in flow rate, about ±1% of the absolute value

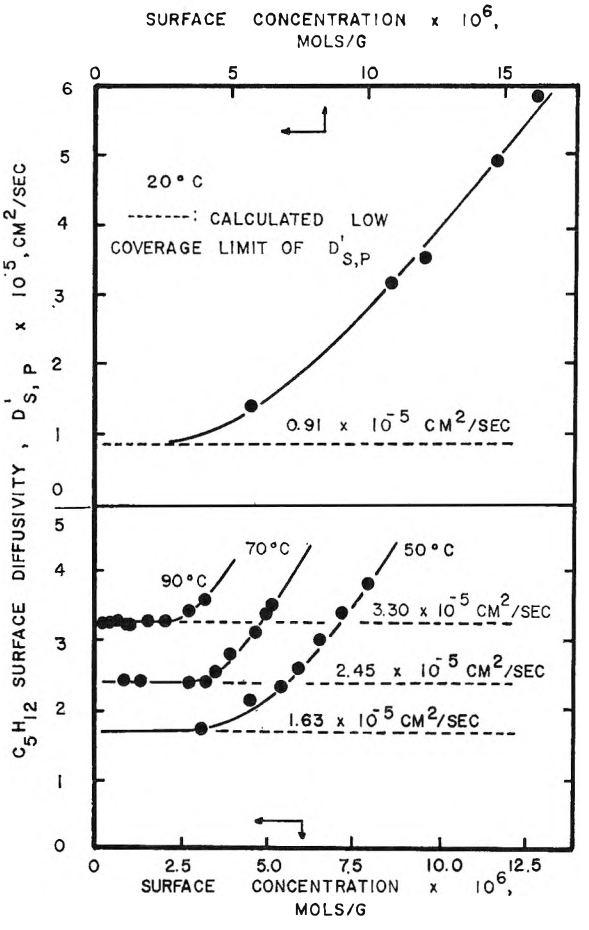

Figure 5. Surface diffusivity of 2,2-dimethylpropane as a function of surface concentration.

of flow, a net of ±5% in total flux. Similar estimates hold for the gas-phase (Ar–He) flux measurements, so the expected error in surface diffusion flux, the difference between these two, as well as the corresponding surface diffusivity value, approximates ±10%.

The surface diffusivity values obtained give linear Arrhenius-type plots, verifying the assumption of activated transport employed in derivation of eq 4. Activation energies $E_s(\theta)$, for surface diffusion as a function of surface coverage determined from the surface diffusivity result, are given on Figure 3. The limiting low coverage values are 3.55 and 3.93 kcal/mol for propane and 2,2-dimethylpropane, respectively, and are constant in the range of surface coverage for which $D'_{s,p}$ itself is constant. The decrease in $E_s(\theta)$ with increasing coverage is also indicative of surface heterogeniety where the more active sites, *i.e.*, those with the highest energy barriers to diffusion, are occupied first.

Discussion

Flux Ratios. The agreement of the helium–argon flux ratio with the square root law indicates that diffusion in the pore structure was occurring by a Knudsen or transition mechanism. Simple calculation indicates the latter to be the case; for example, the Knudsen number (λ/r) for the 2,2-dimethylpropane–helium system at 20° in pores of 360-Å radius is 5.2, well within the transition range of Knudsen numbers. The experimental He–Ar ratio also suggests that surface transport is insignificant, and such experiments may indeed be used to determine the gas-phase transport. The flux ratios for adsorbed systems given in Table II show the degree to which surface diffusion alters the value from that predicted by the square root law. For the same example as before, the flux ratio for 2,2-dimethylpropane–helium at 20° is 2.46, almost a factor of 2 less than the theoretical value of 4.25. At higher temperatures surface flux decreases relative to the gas-phase flux, and the flux ratio approaches the theoretical value.

Total Diffusion Flux and Surface Diffusivities. The linearity observed between total diffusion flux and gas-phase concentration drop indicates that D in eq 4 is independent of concentration. This agrees with transition region diffusion theory when the concentration of the diffusing species is small ($y_1 \approx 0$ in eq 2), and no difficulties are involved in such an interpretation for the argon–helium experiments.

For the two adsorbed systems, however, the linear relationship has important implications. When the adsorbate concentration in the gas phase is low, the gas-phase flux of the adsorbate is linear with concentration drop for the same reasons that the argon flux at low concentration is linear; namely, the limiting value of eq 2 is attained. It follows, then, that the adsorbed flux, which is the difference between total flux and gas-phase flux, is also linear in gas-phase concentration drop. Consequently, the product of the surface diffusion coefficient and the adsorption coefficient, $D'_{s,p}K$, must be independent of gas-phase concentration. Certainly for the Henry's law region the equilibrium adsorption coefficient does not depend on gas-phase concentration so the surface diffusion coefficient, evaluated from Fick's law for this region, is independent of the amount adsorbed. Surface transport, then is satisfactorily described by a Fickian mechanism in this region of very low surface coverage, as indicated in Figures 4 and 5, and the point value of the surface diffusion coefficient is equivalent to the experimentally determined average surface diffusion coefficient. This is true even though the surface coverage changes somewhat throughout the pellet due to the variation of adsorbate partial pressure with distance through the pellet.

For propane adsorbed on molybdenum sulfide, the extent of this region of ideal behavior is for coverages below about 1% and is nearly independent of temperature, the maximum surface coverage varying from 0.85% at 20° to 0.9% at 70°. A similar region exists for 2,2-dimethylpropane below about 2% coverage, the maximum surface coverage varying slightly with temperature from 1.85% at 20° to 1.90% at 90°.

At higher concentration the equilibrium adsorption coefficient ceases to be constant, becoming a function of

gas-phase concentration. In view of the observed linearity of surface flux with gas-phase concentration drop, the surface diffusion coefficient must then also become a function of gas-phase concentration or, more appropriately, surface concentration. This dependency accounts for the nonlinear portions of Figures 4 and 5.

Concentration-dependent surface diffusion coefficients, evaluated at a mean value of the surface concentration in the pellet, are average values. Consider a typical experiment at higher adsorbate concentrations. Near the pellet face exposed to essentially pure helium Henry's law is applicable. Near the other pellet face, however, the concentration of adsorbate is high enough to be in the nonlinear region of the adsorption isotherm. As a consequence, there is a region some distance into the pellet from the pure helium side where Henry's law holds, while equilibrium in the remainder of the pellet is nonlinear. By choosing an average value of the surface concentration the effect of the nonlinear isotherm is partially reduced; however, the surface diffusion coefficient is still concentration dependent. The apparent concentration dependency of surface diffusion coefficients is due to two effects: (1) the nonlinear nature of the equilibrium adsorption coefficient, as discussed, and (2) interaction between adsorbate molecules on the surface. It is not possible to separate these two effects in the present experiment. Nonlinear sorption equilibria may be responsible for apparent concentration dependence of surface diffusivity in regions of surface coverage where Fick's law is still adequate for correlation.

Variations of surface diffusivity with surface coverage have been reported by a number of investigators. For example Carman and Raal[16] found such behavior at near-monolayer coverage, and Haul and Boddenberg[17] presented results for benzene diffusion on aerosil showing the surface diffusion coefficient increasing to a maximum at about 50% monolayer coverage and then falling off rapidly. Their data also indicated that the dependence of surface coverage commences at coverages on the order of several per cent of monolayer, in agreement with the present experiment, although their work did not include specific results at very low coverages.

The limiting values of surface diffusivity evaluated in this study, on the order of 10^{-5} cm^2/sec, are in general agreement with most reports for other surface diffusing systems. Direct comparison is possible for propane: Schneider and Smith[4] reported a value of 1.5×10^{-5} on silica gel ($\bar{r}$ = 11 Å) at 50° and Smith and Metzner[18] 1.1×10^{-5} on alumina (r = 45 Å), both at low surface coverage; the limiting value in the present work is 3.3×10^{-5} cm^2/sec at 50°. These values are of the magnitude of diffusivities in condensed places; indeed, the relative sizes of the surface diffusivities for the two sorbates at equivalent temperature and surface coverage, differing by a factor of about 2 ($C_3 > C_5$),

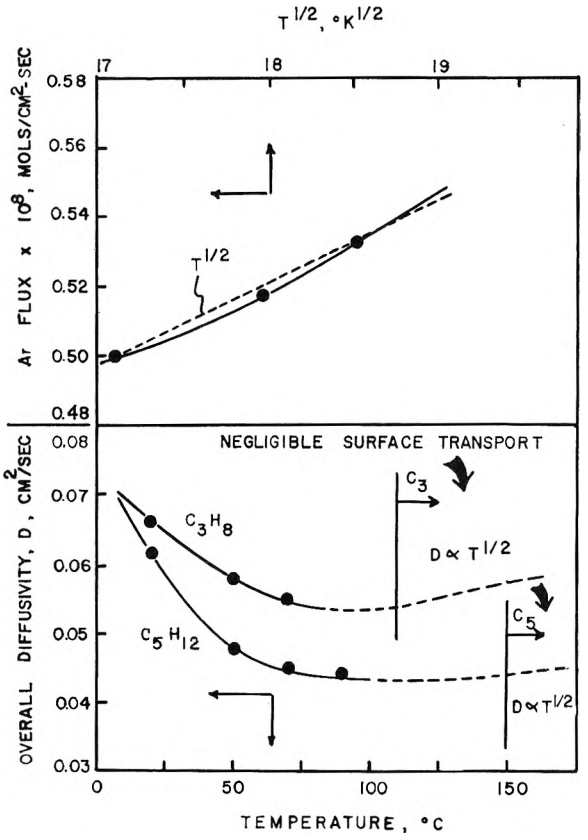

Figure 6. Temperature dependence of flux and diffusivity values.

are not greatly removed from what one might expect from various liquid-phase diffusion correlations, if one visualizes the effect of the surface on the adsorbate layer as that of a solvent. This is not, however, to suggest ascribing liquidlike properties to the adsorbate layer at small fractions of monolayer coverage.

Temperature Dependence. For argon–helium diffusion, in the pore volume alone, the temperature dependence of flux is given by the first term of eq 5. The ratio of A/B appearing in that term has a numerical value for these experiments of approximately 40, about 15% of T, so that the gas-phase flux is approximately proportional to $\sqrt{T}$. Accordingly, the experimentally measured argon flux relative to a gas-phase concentration of 0.1 μmol/cm^3 is plotted *vs.* $\sqrt{T}$ on Figure 6. One can, in general, expect for transition region transport a relatively weak dependence on temperature, flux increasing with temperature.

The temperature dependence of surface diffusion is an exponential function of the difference between the heat of adsorption and the activation energy for diffusion. The heat of adsorption is generally greater than

(16) P. C. Carman and F. A. Raal, *Proc. Roy. Soc., Ser. A*, 209, 38 (1951).

(17) R. Haul and B. Boddenberg, Fourth International Congress on Catalysis, Symposium III, Novosibursk, U.S.S.R., 1968.

(18) R. K. Smith and A. B. Metzner, *J. Phys. Chem.*, 68, 2741 (1964).

the activation energy for surface transport (the ratio is about 2.5 in the present study), so that the surface flux decreases as temperature increases and consequently the relative importance of surface transport declines. Extrapolation of the measurements in Table II of surface flux indicates that near 150° surface transport of 2,2-dimethylpropane would be negligibly small, while near 110° that of propane would be negligibly small.

The net effect of such opposing trends of transport mechanisms with temperature must be that the overall effective diffusivity displays a minimum with temperature. In Figure 6 are plotted the overall diffusion coefficients, D, as a function of temperature. The temperature coefficient of D is negative in the range of experimentation, although the locus of minimum value for D can be determined approximately by defining the temperature at which surface transport becomes negligible and noting that $D\alpha\sqrt{T}$ beyond this point, as shown on the figure. The intermediate region is estimated using both gas-phase and surface contributions to D.

Conclusions

The results are in general agreement with the theory of activated surface transport, and it is interesting that the magnitudes of surface fluxes are so large, even at very low coverage. The Fick's law correlation of surface flux in the Henry's law region of the adsorption isotherm gives constant values of the surface diffusivity, on the order of 10^{-5} cm^2/sec. For the two systems studied surface diffusion proceeds by an activated process with an apparent activation energy in both cases of approximately 0.4 of the heat of adsorption.

The linear relationship observed between total flux and gas-phase concentration drop is in accord with limiting transition diffusion theory for low concentrations of the diffusing species in the nonadsorbed system. For the two adsorbed systems, however, the observed linearity suggests that the surface transport process is also linear in gas-phase concentration drop, which requires that the product of the equilibrium adsorption constant and the surface diffusion coefficient be constant over the range of gas-phase concentrations investigated. For adsorption in the Henry's law region, below about 2% of monolayer coverage in this study, both of these coefficients are constant and independent of concentration. At higher gas-phase concentrations the adsorption equilibrium is concentration dependent, and surface diffusivity also becomes concentration dependent in a manner to preserve the linearity of the flux–concentration relationship. While such behavior would not be expected to persist to very high surface coverages (20% of monolayer is about the maximum studied here) nor to be a general property of physical sorbates in macroporous structures, its existence in the present case indicates that linear extrapolation may be a reasonable means for estimation of surface diffusivity in the Henry's law and "near Henry's law" region for such systems from a minimum of experimentation. The physical reason for this behavior appears to be a type of compensation resulting from the coupled decreases in heat of adsorption and activation energy for surface transport with increasing surface coverage.

Acknowledgment. This research was supported by NSF Grant GK-1703. We wish to thank Dr. V. W. Weekman, Jr., of Mobil Research and Development Corporation, for providing the macropore size distribution of the molybdenum sulfide pellet.

Thermodynamics of Elasticity in Open Systems. Elastin[1]

by F. Mistrali, D. Volpin, G. B. Garibaldo, and A. Ciferri

Chemistry Department, University of Genoa, Genoa, Italy, Institute of Histology, University of Padua, Padua, Italy, and Research Laboratory for Polymer Technology and Rheology, C.N.R., Arco Felice (Naples), Italy
(Received July 10, 1970)

Publication costs assisted by the National Research Council

The elastic and thermoelastic behavior of collagen-free elastin samples obtained from ox *ligamentum nuchae* is investigated. The measurements are performed for samples maintained in equilibrium swelling with an excess of one of the following diluents: H_2O, dimethyl sulfoxide (DMSO), or glycol. Thermoelastic data at constant volume are obtained either by the application of theoretical correction to data obtained when the volume–temperature coefficient was not zero (DMSO, glycol, H_2O, $T < 50°$) or by working under conditions where the latter coefficient was equal to zero (H_2O, $T > 50°$). Isothermal elasticity data indicate that elastin can be very satisfactorily described by the rubber elasticity theory with an elasticity modulus corresponding to network chains of ~70 amino acid residues and nongaussing behavior manifesting at elongations greater than 20% extension. Stress–temperature plots generally exhibit large curvatures which, when properly analyzed, yield consistent results for the f_e/f ratio of the energy component to the total retractive force under constant-volume conditions. Average f_e/f values are 0.15 in H_2O, −0.02 in glycol, and −0.04 in DMSO. The latter results are discussed in light of former results in the literature and of the conformational properties of elastin.

I. Introduction

Long-range elastic behavior is typical of amorphous, rubbery polymers. In so-called ideal rubbers[2a] the fundamental elastic mechanism is a purely entropic one and it is due to the reduced conformational probability of stretched random-coiled chains.[2b] However, systems exhibiting long-range elasticity where the entropic mechanism plays a secondary role are also known. Keratin fibers are a typical example in which elasticity primarily arises from a transition involving two ordered conformational states of the macromolecules.[3] Intermediate between the cases of an ideal rubber and of an ideal fiber[4] undergoing a crystal–crystal transformation there are a variety of systems exhibiting entropic as well as energetic components in their elastic mechanisms. Examples are amorphous networks where the constituent chains exhibit hindred internal rotation,[2a] anisotropic rubber networks,[5] polymers crystallizing under stress,[6] and some semicrystalline polymers.[7]

A central problem in elasticity and thermoelasticity studies has been that of using experimental conditions allowing a relatively unambiguous molecular interpretation of the measured thermodynamic components of the stress. This problem has been particularly serious in the case of so-called open systems such as those where the polymeric material is deformed while in equilibrium swelling with an excess of diluent. The use of open systems is particularly recommendable for investigating the elastic behavior of biological polymers, of polyelectrolytes, and of those synthetic polymers for which it is convenient to depress greatly the melting or the glass transition temperature.

Elastin is a typical biopolymer which may be conveniently investigated as an open system and for which controversial results have been reported. Earlier investigators of the thermoelastic behavior of the elastin–water system,[8,9] noted the occurrence of a large negative component of the stress measured at constant length, pressure, and equilibrium swelling and interpreted this effect in terms of stress-induced crystallization. More recently, Hoeve and Flory[10,11] have recognized that the latter conclusion was unwarranted without taking proper account of the large decrease of swelling with decreasing temperature which occurs for elastin in water. The latter effect was circumvented by analyzing the thermoelastic behavior in a water–glycol mixture where the volume of the swollen sample was independent of temperature. Hoeve and Flory's approach was, in turn, criticized[12] on account of the

(1) Thesis submitted by F. Mistrali as a partial requirement for the doctoral degree in chemistry.

(2) (a) A. Ciferri, C. A. J. Hoeve, and P. J. Flory, *J. Amer. Chem. Soc.*, **83**, 1015 (1961); (b) L. R. G. Treloar, "The Physics of Rubber Elasticity," Oxford University Press, London, 1958.

(3) A. Ciferri, *Trans. Faraday Soc.*, **58**, 562 (1963).

(4) A. Ciferri and K. J. Smith, Jr., *J. Polym. Sci., Part A-2*, 731 (1964).

(5) A. Greene and A. Ciferri, *Kolloid-Z. Z. Polym.*, **186**, 1 (1962).

(6) K. J. Smith, Jr., A. Greene, and A. Ciferri, *ibid.*, **194**, 49 (1964).

(7) D. Puett, K. J. Smith, Jr., and A. Ciferri, *J. Phys. Chem.*, **69**, 141 (1965).

(8) K. H. Meyer and C. Ferri, *Pfluegers Arch. Gesamte Physiol. Menschen*, **238**, 78 (1936).

(9) E. Wölisch, H. Weitnauer, W. Gruning, and R. Rohrbach, *Kolloid-Z. Z. Polym.*, **104**, 14 (1943).

(10) C. A. J. Hoeve and P. J. Flory, *J. Amer. Chem. Soc.*, **80**, 6523 (1958).

(11) C. A. J. Hoeve and P. J. Flory, *J. Polym. Sci.*, **60**, 155 (1962).

(12) A. Oplatka, I. Michaeli, and A. Katchalsky, *ibid.*, **46**, 365 (1960).

neglect of possible effects due to a probable water–glycol disproportion during the measurements.

More recently there has been some controversial electron microscopy and X-ray[13,14] evidence as to the fine structure of elastin, as revealed by these techniques, and the possibility that some degree of order is possessed by unstretched elastin was suggested. Evidence for the occurrence of some degree of α-helix conformation in the soluble[15] and in the native[16] protein was also reported.

We have therefore found it desirable to reinvestigate the elastic and thermoelastic behavior of elastin using recent theoretical approaches[17] to the analysis of open systems. In the present article we report an investigation of the elastic and thermoelastic behavior of collagen-free elastin in swelling equilibrium with several diluents (a preliminary report of the thermoelastic behavior of the elastin–water system has already been published[18]).

II. Theoretical Considerations

In order to characterize the deformation of molecular chains, without the complications associated with dilational and compositional changes of a network in swelling equilibrium with a diluent, it is necessary to use energy and entropy components of the stress corresponding to constant volume and fixed composition. The latter components are defined by the relationship

$$f = f_e + f_s = \left(\frac{\partial E}{\partial L}\right)_{VTN} - T\left(\frac{\partial S}{\partial L}\right)_{VTN} = \left(\frac{\partial E}{\partial L}\right)_{VTN} + T\left(\frac{\partial f}{\partial T}\right)_{VLN} \quad (1)$$

where f is the tensile force; E, L, V, T are, respectively, the internal energy, the length, the volume, and the temperature of the network, and N indicates constancy of the mole number of the individual components.

In practice, it is convenient to measure stress–temperature coefficients under equilibrium swelling at constant pressure and length, *i.e.*, $(\partial f/\partial T)_{pLeq}$. The conversion of the latter to $(\partial f/\partial T)_{VLN}$ can, in principle, be achieved using the relationship[10,11]

$$\left(\frac{\partial f}{\partial T}\right)_{pLeq} = \left(\frac{\partial f}{\partial T}\right)_{VLN} + \left(\frac{\partial f}{\partial V}\right)_{TLN}\left(\frac{\partial V}{\partial T}\right)_{pLeq} + \sum_i \left(\frac{\partial f}{\partial n_i}\right)_{TLVn'}\left(\frac{\partial n_i}{\partial T}\right)_{pLeq} \quad (2)$$

where the summation is over all components of the diluent and n' indicates constancy of the mole number of all components except component i. Hoeve and Flory[10,11] suggested that if both $(\partial V/\partial T)_{pLeq}$ (assumed to be essentially equal to $(\partial V/\partial T)_{peq}$, *i.e.*, the temperature coefficient measured when the length is unrestricted) and the last term on the right-hand side is negligible, then

$$\left(\frac{\partial f}{\partial T}\right)_{pLeq} = \left(\frac{\partial f}{\partial T}\right)_{VLN} \quad (3)$$

Accordingly, they proceeded to the evaluation of f_e/f for elastin using the experimentally measured values of f and $(\partial f/\partial T)_{pLeq}$ in a 70:30 water–glycol mixture where $(\partial V/\partial T)_{peq}$ was effectively equal to zero.

When, in an open system, $(\partial V/\partial T)_{peq} = 0$, a decrease of the total amount of liquid absorbed by the network must occur on increasing temperature to compensate for the thermal expansion of the various components. Thus, $\Sigma_i(\partial n_i/\partial T)_{pLeq} < 0$. Hoeve and Flory argued that the magnitudes of the $(\partial n_i/\partial T)_{pLeq}$ terms for the various components of a mixed diluent are small and, moreover, that the terms $(\partial f/\partial n_i)_{TVLn'}$ (equal to $-f(\partial \ln \langle r^2\rangle_0/\partial n_i)_{Tn'}$ according to the molecular theory of rubber elasticity, *cf. seq.*) are likewise small and negligible thus making acceptable eq 3 when $(\partial V/\partial T)_{peq} = 0$.

This approach is certainly a reasonable one in the case of a one-component diluent. However, its application to multicomponent diluents must be considered with caution. The results to be presented later indicate that while in the case of elastin in a 70:30 water–glycol mixture the unrestricted length (or volume) is independent of temperature, in reality the temperature coefficients in pure water and in pure glycol (*cf.* Figure

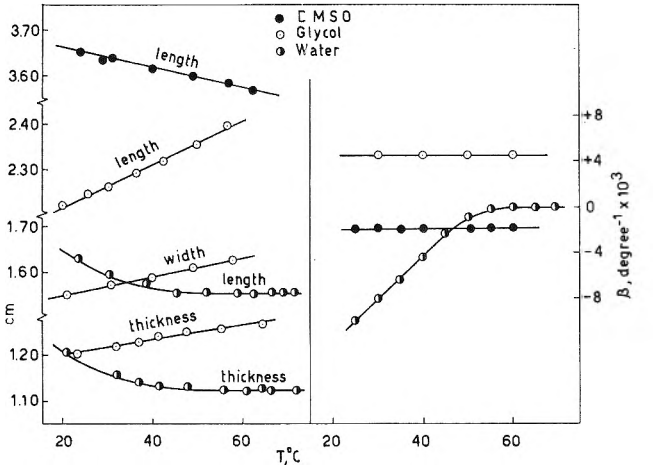

Figure 1. Temperature variation of length, width, thickness, and volume expansion coefficient β for elastin samples in swelling equilibrium with three different diluents.

(13) L. Gotte, M. Mammi, and G. Pezzin in "Symposium on Fibrous Proteins," W. G. Crewter, Ed., Butterworths, Australia, 1968, p 236.

(14) R. C. Cox and K. Little, *Proc. Roy. Soc., Ser. B*, **155**, 232 (1961).

(15) M. Mammi, L. Gotte, and G. Pezzin, *Nature (London)*, **220**, 371 (1968).

(16) M. Mammi, L. Gotte, and G. Pezzin, *ibid.*, **225**, 380 (1970).

(17) J. Bashaw and K. J. Smith, Jr., *J. Polym. Sci., Part A*, **61**, 041 (1968).

(18) (a) D. Volpin and A. Ciferri, *Nature (London)*, **225**, 382 (1970); (b) "Chemistry and Molecular Biology of the Intercellular Matrix," E. A. Balasz, Ed., Academic Press, New York, N. Y., 1970.

1) are largely different and have opposite signs. Thus, it may be inferred that in the case of a 70:30 water–glycol mixture, a decrease of the overall amount of diluent swelling the network on increasing temperature is simultaneous with a decrease of the amount of absorbed water. The actual compositional change (*cf. seq.*) is such that the composition of the diluent inside the network is 76:24 at 5° and 65:35 at 48°. Since it is known that strong specific interactions with the diluent may alter the conformation of proteins, it is not generally justifiable to neglect the possible effect of compositional changes. In particular, the results of Mammi, *et al.*,[15,16] indicate that both native and soluble elastin contain an appreciable amount of α helix. Moreover, the temperature coefficient of the α helix for soluble elastin is not the same in water as in glycol.[19]

In view of the above complicating possibilities, it becomes of interest to consider the determination of $(\partial f/\partial T)_{VLN}$ in single-component diluents. However, it is not generally easy to find a single-component diluent which satisfies the condition $(\partial V/\partial T)_{peq} = 0$. The use of single-component dilutents generally entails the determination of $(\partial f/\partial T)_{pLeq}$ when $(\partial V/\partial T)_{peq} \neq 0$. Using the molecular theory of rubber elasticity it is possible, however, following Bashaw and Smith,[17] to derive the appropriate correction to the measured $(\partial f/\partial T)_{pLeq}$ and calculate constant-volume coefficients. The retractive force of a network in swelling equilibrium is given by[2a,17]

$$f = \left(\frac{\nu kT}{L_s}\right)\frac{\langle r^2\rangle_i}{\langle r^2\rangle_0} v^{-2/3}\left(\alpha - \frac{V}{V_s\alpha^2}\right) \tag{4}$$

where ν is the number of network chains having a mean-square end-to-end distance $\langle r^2\rangle_i$ with $\langle r^2\rangle_0$ being the corresponding quantity for a chain unrestricted by the cross-linkages; k is the Boltzmann constant, v ($= V_i/V_s$), L_s, V_s are, respectively, the volume fraction of polymer, the length, and the volume of the unstrained, swollen network; V and L ($\alpha = L/L_s$) are the corresponding quantities for the stretched, swollen network, and V_i is the dry volume. Differentiation of eq 4 according to eq 2 neglecting[11] the term containing $(\partial f/\partial N)_{TLV}$, taking $\langle r^2\rangle_i \propto V_i^{2/3}$, $\langle r^2\rangle_0$ independent of volume, and solving for f_e/f gives[2a,17]

$$\frac{f_e}{f} = 1 - \frac{T}{f}\left(\frac{\partial f}{\partial T}\right)_{pLeq} - \frac{\beta T}{\alpha^3(V_s/V) - 1} \tag{5}$$

where $\beta = (1/V)(\partial V/\partial T)_{pLeq}$.

On the basis of the Flory–Huggins theory of polymer solutions, Bashaw and Smith[17] obtained for $v \ll 1$

$$\frac{V_s}{V} \simeq \alpha^{-1/2} \tag{6}$$

and

$$\beta = \frac{5}{6}\left(\frac{\partial \ln V_s}{\partial T}\right)_{peq} = \frac{5}{6}\beta_s \tag{7}$$

Using the latter equations, eq 4 and 5 are rewritten as

$$f = \left(\frac{\nu kT}{L_s}\right)\frac{\langle r^2\rangle_i}{\langle r^2\rangle_0} v^{-2/3}\left(\alpha - \frac{1}{\alpha^{3/2}}\right) \tag{8}$$

and

$$\frac{f_e}{f} = 1 - \frac{T}{f}\left(\frac{\partial f}{\partial T}\right)_{pLeq} - \frac{5}{6}\frac{\beta_s T}{(\alpha^{5/2} - 1)} \tag{9}$$

which will be used for the analysis of our thermoelasticity data.

For the analysis of our isothermal elasticity data, eq 8 is written in terms of the stress τ (the force referred to the unstretched, unswollen cross-sectional area $= V_i/L_i$) as

$$\tau = \frac{\nu kT}{V_i v^{1/3}}\frac{\langle r^2\rangle_i}{\langle r^2\rangle_0}\left(\alpha - \frac{1}{\alpha^{3/2}}\right) \tag{10}$$

where the modulus $\nu kT/V_i$ is equal[2b] to $\rho RT/M_c$, M_c being the molecular weight of a network chain and ρ the polymer density.

III. Experimental Section

Elastin samples of ~0.02 cm² cross-sectional area and 2 cm long were obtained from frozen ox *ligamentum nuchae* using a slicing machine and cutting the samples in the direction parallel to the fiber axis of the *ligamentum*. The material was purified from collagen by autoclaving at 120° for 6 hr. This differs with the material used by Hoeve and Flory[10] which contained collagen. Samples were allowed to dry in a vacuum desiccator over P_2O_5 at 20° for 48 hr. After this period, moisture of the specimen ranged from 2 to 3% in reference to the dry weight of elastin heated at 100°. Samples were stored under vacuum (sealed glass tubes) in a refrigerator. Storage times never exceeded 2 months. As noted by Gotte, Mammi, and Pezzin,[13] the collagen-free sample had the appearance of a fiber bundle and X-ray diffraction patterns exhibited four diffuse rings at 8.9, 4.4, 2.2, and 1.12 Å.

Measurement of length, width, thickness, and weight was made on each dry sample. Before use, samples were placed in a large excess of the swelling agent of distilled water, glycol, DMSO (dimethyl sulfoxide), or a 70:30 water–glycol mixture, at 22° until equilibrium was reached. The temperature variation of the unstretched, swollen length, width, and thickness was determined using a cathetometer (for these particular measurements precision was improved by using elastin cubes of about 1.5-cm sides).

No soluble material was detected in the swelling liquids after equilibration with the samples. In no case were samples kept in the swollen state for periods longer than 1 week. Within this time all measurements were completely reproducible.

(19) L. Gotte, M. Mammi, and G. Pezzin, "Chemistry and Molecular Biology of the Intercellular Matrix," E. A. Balasz, Ed., Academic Press, New York, N. Y., 1970.

In the case of samples equilibrated with the 70:30 water–glycol mixture, the composition of the mixture outside the network, after equilibrium swelling was reached, was analyzed by gas chromatography. At 5° the composition of such a mixture was found to be 69.33% water and 30.67% glycol. At 48° the corresponding figures were 70.49% and 29.51%. Knowing the total amounts of liquid absorbed and surrounding the network it was possible to calculate the composition of the mixture inside the gel.

Stress–strain temperature measurements were performed as described elsewhere[6,20] (the use of invar rods supporting the sample[21] was found to be absolutely essential). The sample was maintained in swelling equilibrium with a large excess of solvent contained in a water-jacketed glass cell. A nitrogen stream was used in the case of DMSO to prevent moisture absorption. Temperature regulation was provided by circulating water from a constant-temperature bath through the water jacket surrounding the cell.

The sample was extended at the highest temperature and length and allowed to relax at constant length during a night. Then the temperature was lowered (usually by 5–8° decrements) and the tension was recorded as soon as it appeared constant (within 30–45 min). The tension was measured at some 5–10 different temperatures in order to determine with accuracy the shape of the force–temperature curve. This is considerably more precise than the procedure used by Hoeve and Flory,[10] who measured the stress only at 50 and 0°. The force observed on increasing temperature always reproduced that observed on lowering temperature.

Stress–strain isotherms were obtained before and a night after each force–temperature cycle.

For these measurements the sample was stepwise extended recording the tension after a 15-min interval at each elongation.[21] Negligible set on the rest length L_s (determined by extrapolation at $f = 0$) was observed. The values of L_s determined at 50° for water and 40° for glycol and DMSO were used to calculate the reported values of α. The latter were used to calculate α values at other temperatures using the corresponding linear expansion coefficients.

IV. Results

Typical variations of length, thickness, and width with temperature for elastin samples in equilibrium with water, glycol, and DMSO are reported in Figure 1. In water and in DMSO the dimensions of the sample decrease on increasing temperature. However, in the case of water from ~50 to 70°, the dimensions remain constant.[18] In glycol length, width, and thickness increase with increasing temperature. In the 70:30 water–glycol mixture the sample dimensions were found to be independent of temperature in the temperature interval 0–70° in line with the results of Hoeve and Flory.[10]

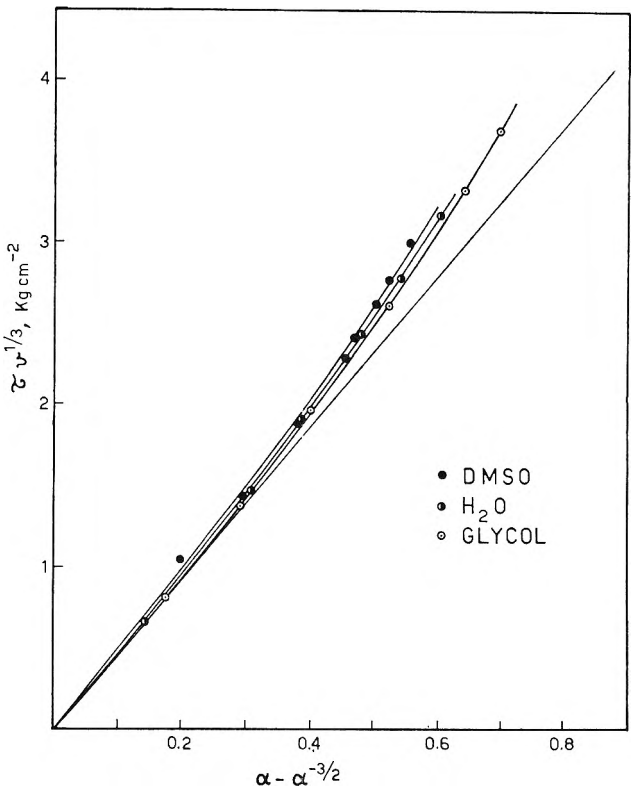

Figure 2. Typical stress–strain isotherms for elastin samples 7, 5, and 1 in swelling equilibrium with three different diluents. Data, obtained from stepwise stretching at $T = 40°$, plotted according to eq 10.

Also included in Figure 1 is the change of the cubical expansion coefficient $\beta_s = (1/V_s)(dV_s/dT)$ with temperature in water, DMSO, and glycol. β_s was taken equal to the sum of the three linear expansion coefficients $\lambda = (1/L_s)(dL_s/dT)$. β_s values obtained as 3λ using λ values corresponding to the temperature variation of length, thickness, or width did not result in differences in β_s values large enough to alter the final value of the f_e/f ratio (*cf.* eq 9) by more than 0.10. A certain degree of anisotropy was also evidenced by the isothermal equilibrium degree of swelling data of Table I where the

Table I: Isothermal Equilibrium Swelling Behavior of Elastin

	$T = 22°$				$T = 40°$
Diluent	L_i/L_s	W_i/W_s	T_i/T_s	ν	ν
Water	0.943	0.877	0.877	0.726	0.853
Glycol	0.820	0.775	0.787	0.497	0.468
DMSO	0.667	0.637	0.629	0.266	0.279

(20) D. Puett, A. Ciferri, and L. V. Rajagh, *Biopolymers*, **3**, 461 (1965).

(21) A. Ciferri and P. J. Flory, *J. Appl. Phys.*, **30**, 1498 (1959).

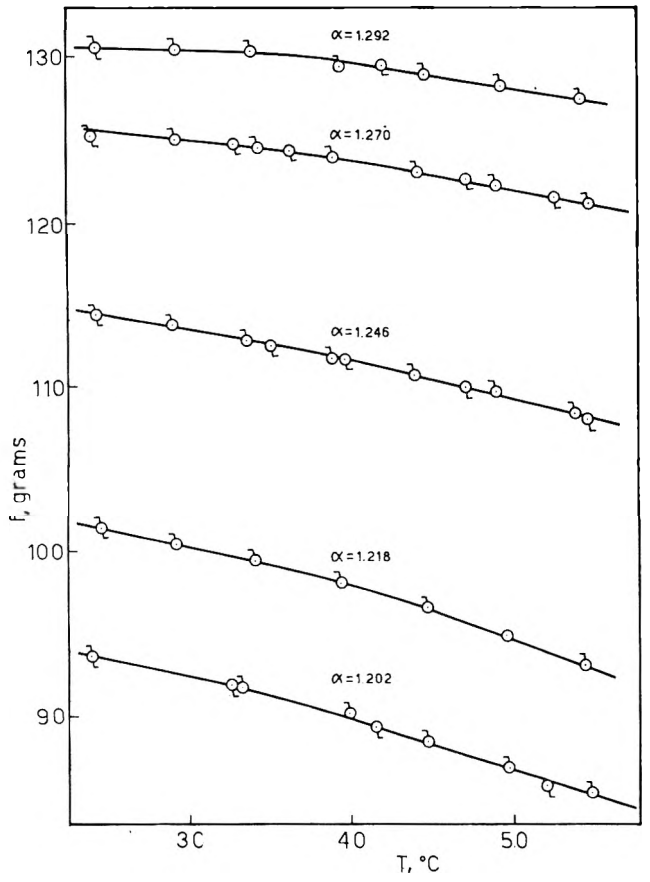

Figure 3. Variation of the tensile force with temperature for an elastin sample in glycol at constant length (dry cross-sectional area = 0.0250 cm²). The elongation ratios α were measured at 40°: ○, decreasing temperature; ●, increasing temperature.

ratios of dry length, width, thickness, and volume to the corresponding swollen quantities are collected.

Typical stress–strain isotherms for swollen elastin samples are illustrated in Figure 2. At high α the experimental curves deviate from the theoretical prediction based on eq 10. However, we note that correction by the $v^{1/3}$ factor has the effect of bringing the stresses very close together, in spite of the large differences in the v values themselves. This satisfactory feature leads to the result that the M_c values obtained from the initial slopes in Figure 2 exhibit only a minor scatter from sample to sample. M_c values for all samples investigated are collected in Table II.

Typical force–temperature data using glycol as the swelling agent are reported in Figure 3. Since the coefficient of thermal expansion β_s is positive (*cf.* Figure 1), on increasing temperature at constant length, a decrease of force is observed. The situation is similar to the well-known case of the thermal inversion phenomenon occurring in rubbers[2b] at low α with the difference that here the phenomenon is much more evident because of the relatively large value of β_s for elastin in glycol. We note the occurrence of a small curvature which is not unexpected in a region of thermoelastic inversion. Because of this we have calculated f_e/f according to eq 9 at three temperatures using α values determined in the corresponding temperature ranges. Results are collected in Table III. It is seen that the average f_e/f values are not essentially different at T = 30, 40, and 50°. The results suggest that the energy component f_e is essentially zero and that in glycol elastin behaves as in ideal rubber.

Table II: Characteristics of Samples Investigated

Sample no.	Dry cross-sectional area, cm²	Diluent used	M_c[a]
1	0.0218	Glycol	6880
2	0.0250	Glycol	5660
3	0.0258	Glycol	6390
4	0.0327	Water	6530
5	0.0264	Water	6800
6	0.0400	Water	
7	0.0237	DMSO	6570
8	0.0148	DMSO	6390
9	0.0137	DMSO	6400
		Av	6450

[a] From stress–strain data at 40°.

Typical force–temperature data in water are reported

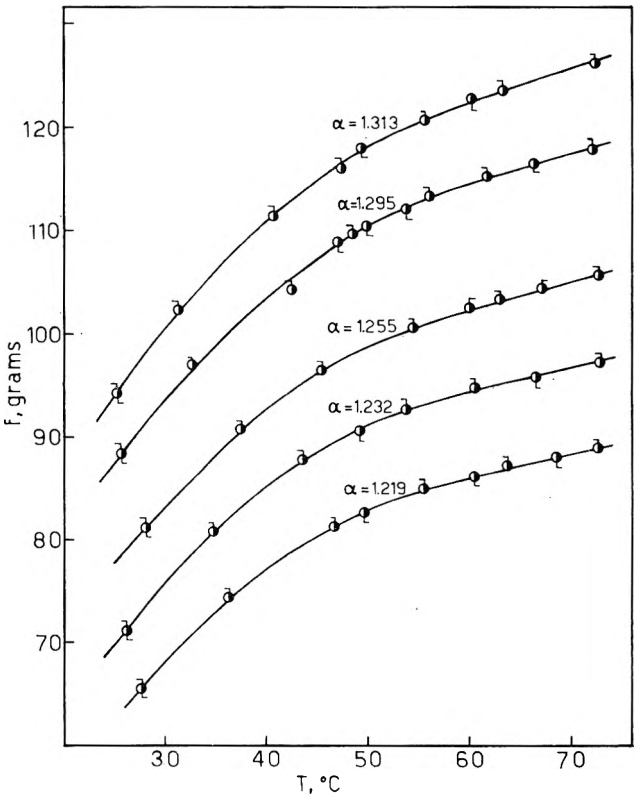

Figure 4. Variation of the tensile force with temperature for an elastin sample in water at constant length (dry cross-sectional area = 0.0327 cm²). The elongation ratios α were measured at 50°: ○, decreasing temperature; ●, increasing temperature.

Table III: Thermoelastic Data for Elastin in Swelling Equilibrium with Glycol in the Temperature Range 25–55°

	$\bar{T}$ = 30°, β = 4.50 × 10^{-3}			$\bar{T}$ = 40°, β = 4.50 × 10^{-3}			$\bar{T}$ = 50°, β = 4.50 × 10^{-3}		
$\alpha_{40°}$	f, g	$\left(\frac{\partial f}{\partial T}\right)_{pLeq}$	$\frac{f_e}{f}$	f, g	$\left(\frac{\partial f}{\partial T}\right)_{pLeq}$	$\frac{f_e}{f}$	f g	$\left(\frac{\partial f}{\partial T}\right)_{pLeq}$	$\frac{f_e}{f}$
				Sample No. 1					
1.245	74.60	−0.13	+0.11	73.2	−0.17	0.12	71.05	−0.20	+0.03
1.310	93.55	−0.03	+0.03	93.2	−0.06	0.00	92.20	−0.11	+0.02
1.341	103.50	0.00	+0.04	103.4	−0.03	0.01	102.95	−0.06	−0.05
				Sample No. 2					
1.202	92.40	−0.21	−0.03	89.9	−0.28	−0.03	86.80	−0.30	−0.25
1.218	100.25	−0.20	+0.01	98.0	−0.26	0.00	94.70	−0.35	0.00
1.246	113.45	−0.17	+0.06	111.5	−0.20	−0.04	109.20	−0.24	−0.17
1.270	125.00	−0.10	−0.01	123.8	−0.14	−0.06	121.95	−0.18	−0.19
1.292	130.40	−0.04	−0.06	129.7	−0.11	−0.04	128.05	−0.16	−0.11
				Sample No. 3					
1.238	96.10	−0.18	+0.13	94.2	−0.21	+0.03	91.70	−0.24	−0.11
1.265	107.00	−0.11	+0.02	105.8	−0.14	−0.05	104.07	−0.22	−0.03
1.285	113.50	−0.10	+0.07	112.5	−0.11	−0.04	111.10	−0.21	−0.04
1.291	119.00	−0.08	+0.06	118.0	−0.11	−0.02	116.45	−0.16	−0.08
		Av	0.03		Av	−0.01		Av	−0.08
			Av − 0.02						

Table IV: Thermoelastic Data for Elastin in Swelling Equilibrium with Water in the Temperature Range 20–74°

	$\bar{T}$ = 30°, β = −8.1 × 10^{-3}			$\bar{T}$ = 40°, β = −4.4 × 10^{-3}			$\bar{T}$ = 62°, β = 0		
$\alpha_{60°}$	f, g	$\left(\frac{\partial f}{\partial T}\right)_{pLeq}$	$\frac{f_e}{f}$	f, g	$\left(\frac{\partial f}{\partial T}\right)_{pLeq}$	$\frac{f_e}{f}$	f, g	$\left(\frac{\partial f}{\partial T}\right)_{pLeq}$	$\frac{f_e}{f}$
				Sample No. 4					
1.219	68.1	1.02	0.29	77.1	0.67	0.16	86.8	0.23	0.10
1.232	75.6	1.06	0.33	85.2	0.71	0.14	95.0	0.24	0.15
1.254	83.3	1.07	0.28	92.7	0.73	0.11	103.0	0.25	0.17
1.295	93.9	1.08	0.13	103.2	0.75	0.04	115.2	0.28	0.18
1.313	100.5	1.10	0.11	110.9	0.78	0.02	123.0	0.32	0.13
				Sample No. 5					
1.222	59.6	0.88	0.30	67.6	0.59	0.12	75.1	0.20	0.11
1.255	69.7	0.91	0.20	77.3	0.61	0.09	86.4	0.23	0.12
1.288	80.0	0.93	0.17	89.0	0.65	0.06	97.4	0.25	0.13
				Sample No. 6					
1.266	105.2	1.32	0.20	116.3	0.89	0.09	129.4	0.35	0.11
		Av	0.23		Av	0.09		Av	0.14
			Av 0.15						

in Figure 4.[18] The situation appears drastically different from that observed in the case of glycol. The force–temperature coefficients in water are strongly positive and a large curvature is exhibited, particularly at low temperatures. Part of this effect can be attributed to the fact that β_s is strongly negative (*cf.* Figure 1) and this accentuates the decrease of f with decreasing of T, owing to the rubber-like behavior. The results presented in Figure 1 indicate that for $T > 50°$ β_s in water is zero. Thus, the entire correction to $(\partial f/\partial T)_{pLeq}$ can be neglected and f_e/f can be calculated from eq 3. Results in the temperature range 50–70° are given in Table IV. Using the data in Figure 4 we can also calculate f_e/f when $T < 50°$ and $\beta \neq 0$. Since β_s is not constant with temperature, f_e/f was calculated at different temperatures using β_s and α values determined at the corresponding temperatures. Results are included in Table IV. We note that practically the same f_e/f values are obtained at 30, 40, and 62°, the large difference in the corresponding β_s values notwithstanding. The results indicate about a 15% positive contribution of energy to the total force. There is no evidence of stress-induced crystallization[8,9] occurring at low temperatures.

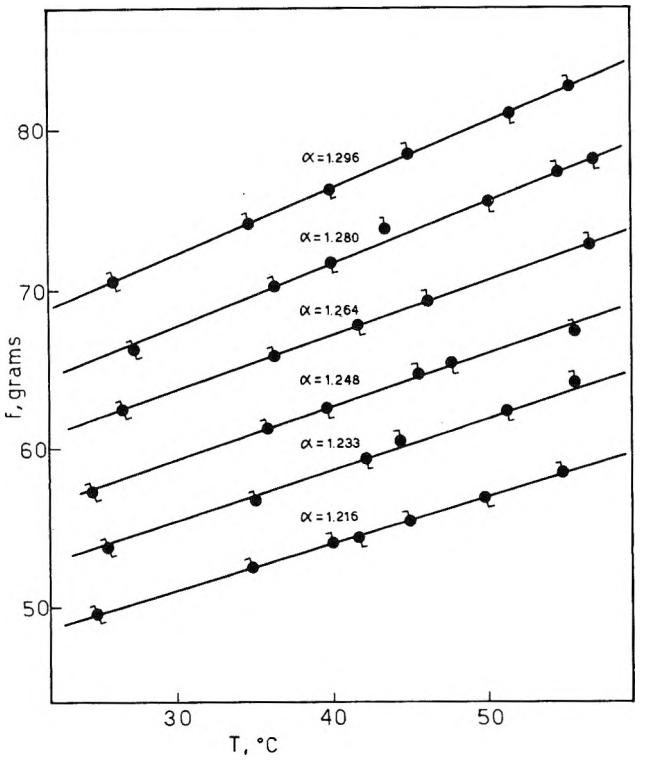

Figure 5. Variation of the tensile force with temperature for an elastin sample in dimethyl sulfoxide at constant length (dry cross-sectional area = 0.0137 cm²). The elongation ratios α were measured at 40°: ○, decreasing temperature; ●, increasing temperature.

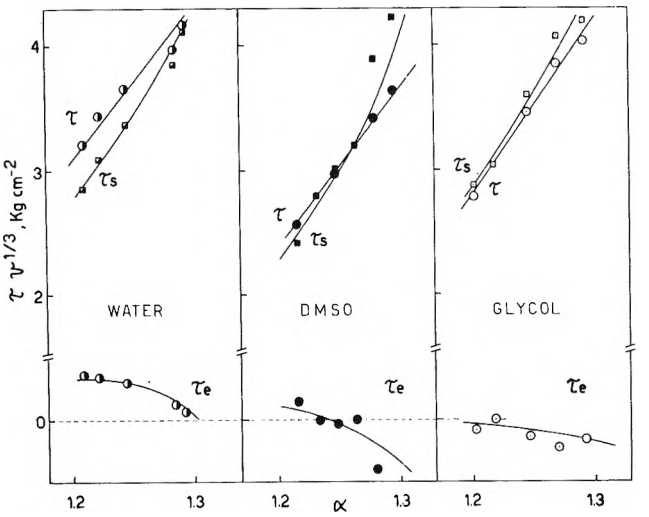

Figure 6. Strain dependence of the entropy (τ_s) and energy (τ_e) components of the stress (τ) for elastin samples in swelling equilibrium with three different diluents. $T = 40°$. τ values correspond to those reported in Figures 3, 4, and 5. τ_e and τ_s values are constant-volume data obtained from data in Tables III, IV, and V (samples number 2, 4, and 9, respectively). All data corrected by the $v^{1/3}$ factor measured at 40°.

Typical force–temperature data in DMSO are reported in Figure 5. The situation is again different from that observed in the cases of glycol and water since in DMSO the force–temperature coefficients are positive and no curvature is exhibited. This effect is attributed to the fact that β_s is negative (*cf.* Figure 1) and independent of temperature. f_e/f values calculated using eq 9 are reported in Table V. The results indicate about a 4% negative contribution of the energy to the total tensile force.

The separation of the energy and the entropy components of the stress is schematized in Figure 6 where, in line with eq 10, stress values τ corrected by the factor $v^{1/3}$ have been used. When plotted on a τ *vs.* $\alpha - \alpha^{-2}$ plot, the stress data in Figure 6 exhibits a deviation from eq 10 qualitatively similar to that exhibited by the data reported in Figure 2. The latter data are, however, more accurate than those in Figure 6 for a quantitative description of the stress–strain isotherm. In all cases the entropy component is the largest component of the stress. There is, generally, a tendency for the ratio f_e/f to decrease slightly with increasing α.

Table V: Thermoelastic Data for Elastin in Swelling Equilibrium with Dimethyl Sulfoxide in the Temperature Range 25–55°

	$\bar{T} = 40°, \beta = -1.89 \times 10^{-4}$		
$\alpha_{40°}$	f, g	$\left(\frac{\partial f}{\partial T}\right)_{pLeq}$	f_e/f
	Sample No. 7		
1.207	82.90	0.49	−0.04
1.217	87.60	0.49	0.00
1.235	95.00	0.54	−0.07
1.248	100.30	0.57	−0.13
1.263	108.55	0.60	−0.11
	Sample No. 8		
1.196	52.78	0.30	+0.09
1.212	57.10	0.33	−0.02
1.230	62.35	0.35	−0.05
1.246	67.12	0.37	−0.05
	Sample No. 9		
1.216	54.00	0.30	+0.06
1.233	58.70	0.32	0.00
1.248	62.60	0.33	−0.01
1.264	67.10	0.35	0.00
1.280	71.65	0.39	−0.14
1.296	76.35	0.41	−0.16
			Av −0.04

V. Discussion

Interesting features of this work are the use of the Bashaw and Smith[17] method for calculating constant-volume coefficients and the large curvature exhibited by the force–temperature data. The latter has been handled by applying eq 9 to several small temperature intervals along with the corresponding values of elongation ratio and volume expansion coefficient. This approach has yielded consistent results for f_e/f in a wide temperature range indicating that the nonlinearity

in the force–temperature plots is primarily due to the peculiar variations of β_s with temperature and solvent type. The latter, in turn, reflects rather large (and opposite in sign) heats of dilution for the elastin–water and elastin–glycol systems.

Another unusual feature (with respect to the ordinary elastic system) exhibited by elastin, is the occurrence of a certain degree of anisotropy exhibited by a larger swelling of the width than the length. Part of this effect can, no doubt, be attributed to the fiber–bundle character of the elastin samples from which collagen had been removed. Our results are inadequate for assessing if anisotropic behavior exists even at the molecular level, *i.e.*, within the individual fibril units composing the bundle or in homogeneous elastin.

Although the body of results obtained indicate that the behavior of elastin can be very satisfactorily described in terms of the rubber elasticity theory, the lack of isotropy in our samples entails a criticism of the use of a theory valid for homogeneous systems. Moreover, some of the approximations used in the derivation of eq 6–9 may be open to criticism. It is, therefore, a fortunate circumstance that we could report f_e/f values in pure water at 62° when β_s is equal to zero and the correction term in eq 9 vanishes. Thus, no direct recourse to the molecular theory was made in this case, yet, the results obtained are similar to those obtained (at 30 and 40°) when recourse to the theory was necessary. Thus we may conclude that in water $f_e/f > 0$ and that the limitations connected with the Bashaw and Smith theory, as well as those connected to the lack of isotropy, are negligible. To support the latter conclusion we also note that occurrence of a small degree of anistropy (in the rest state) did not affect the f_e/f ratio in the case of slightly anisotropic[5,22] and isotropic[6] rubbers. It is also reassuring to observe that in water at 62° f_e/f remains independent of α, as theoretically predicted. Small decreases of f_e/f with α, such as those observed here, have sometimes been reported in other polymer systems.[23]

The variations of f_e/f for the three solvents investigated suggest that, whereas in water the energetic component makes a nonnegligible contribution ($\sim$15%) to the total stress, in DMSO and in glycol elastin behaves very nearly as an ideal rubber. The result obtained in glycol is similar to that reported by Hoeve and Flory in the case of 70:30 water–glycol mixture. It is unfortunate that, with the exception of the data obtained in water at 62°, the experimental indetermination on f_e/f is of the order of 10% [the occurrence of large β_s values and the necessity of working at $\alpha < \sim 1.3$, due to the breaking of the material, has entailed the use of correction terms $(5/6)\beta_s T/(\alpha^{5/2} - 1)$ considerably larger than the corresponding ones generally used for closed systems].[23] Thus, the difference between the f_e/f values obtained in DMSO, in H_2O, and in glycol is just outside the experimental indetermination.

The values of the elastic modulus, obtained from the initial slope of the stress–strain plot in Figure 6, must also be regarded with the provision that our samples were not homogeneous. The measured value of M_c suggests that a network chain contains an average of about 70 amino acid residues. One of the most interesting results of this investigation is the observed constancy of M_c in several diluent systems. This fact supports the description of elastin as a typical rubber-like network. The occurrence of an upward curvature in the plot in Figure 6, at elongation greater than $\alpha \sim 1.2$, indicates the occurrence of deviations from eq 10. In terms of the Mooney–Rivlin equation[2b] these deviations could be described by a negative C_2 term. Since our material is collagen-free, we cannot associate the upturn to the deformation of the high-modulus fibrous protein, as done by Hoeve and Flory.[10] The effect may be attributed to nongaussian behavior (this may not entail a too-serious correction[6] to eq 9).

Concerning the interpretation of the f_e/f values obtained in water, glycol, and DMSO, in terms of the current rubber elasticity theory we obtain[2a]

$$f_e/f = T\left(\frac{\partial \ln \langle r^2\rangle_0}{\partial T}\right) \qquad (11)$$

and thus the results obtained indicate a temperature coefficient of the unperturbed mean-square end-to-end distance of $\sim 5 \times 10^{-4}$ in water, $\sim -0.5 \times 10^{-4}$ in glycol, and $\sim -1 \times 10^{-4}$ in DMSO. This could be associated with the occurrence of minima favoring the coiled conformation in the potentials of internal rotation of the polypeptide chain. It is difficult to describe why these potentials should be different in H_2O, in glycol, and in DMSO. Likewise, f_e/f values reported cannot be easily related to the occurrence of a small amount of helical structure[6,19] and to the effect, on the latter, of variables such as temperature, diluent type, or content. Nevertheless, it is interesting to note that in a solvent such as DMSO, where the degree of swelling reaches a maximum and any kind of structure is very likely absent, elastin behaves as an ideal rubber.

In any case the energy component makes only a small to negligible contribution to the total stress, and any significant effect associated to stress-induced crystallization[8,9] or to conformational rearrangement of "globular" units[24] must be ruled out. The fundamental elastic mechanism in elastin is essentially an entropic one and, as in conventional rubbers, may be interpreted in terms of the unwinding of randomly coiled molecules.

(22) A. Greene, K. J. Smith, Jr., and A. Ciferri, *Trans. Faraday Soc.*, **61**, 2772 (1965).

(23) A. Ciferri, *J. Polym. Sci., Part A-2*, 3089 (1964).

(24) S. M. Partridge, *Gerontologic*, **15**, 85 (1969).

Acknowledgments. We express our gratitude to Professors U. Bianchi, L. Gotte, G. Pezzin, and M. Mammi for their interest in this work and their very useful advice.

The Iodination of Alkyl Pyruvates. I. The Spontaneous and General-Base-Catalyzed Iodination of Methyl and Ethyl Pyruvates

by J. E. Meany

Department of Chemistry, Central Washington State College, Ellensburg, Washington 98926 *(Received June 30, 1970)*

Publication costs assisted by Central Washington State Research Fund

The rates of iodination of the methyl and ethyl esters of pyruvic acid in formate buffers were studied at 25° and an ionic strength of 0.1 *M* using a spectrophotometric method at 353 nm. Although the rates of these reactions were found to be insensitive toward acids, kinetic analysis indicates strong catalysis by water and formate ions. The pseudo-zero-order rate constants, $k_{obsd} = k_0 + k_{HCO_2^-}[HCO_2^-]$, were obtained over a wide range of buffer concentrations and buffer ratios from which the kinetic rate coefficients associated with methyl pyruvate ($k_0 = 1.9 \times 10^{-6}$ sec^{-1}, $k_{HCO_2^-} = 19.4 \times 10^{-5}$ l. mol^{-1} sec^{-1}) and ethyl pyruvate ($k_0 = 1.7 \times 10^{-6}$ sec^{-1}, $k_{HCO_2^-} = 16.8 \times 10^{-5}$ l. mol^{-1} sec^{-1}) were deduced. In calculating these kinetic values, account was taken of the fact that the alkyl pyruvates are partially hydrated in aqueous solutions. Absence of the concerted action of formic acid and the formate ion was demonstrated by lack of a termolecular term in the rate expression. A comparison made between the spontaneous rates of iodination of the alkyl pyruvates and pyruvic acid shows that they behave similarly.

Introduction

For reactions subject to both general-acid and general-base catalysis, it has often been suggested that an important (and sometimes dominant) path may arise through the simultaneous action of the acidic and basic catalyst.[1-3] In support of this view is the existence of extremely powerful catalysis observed for substances which can act both as acids and bases. The classical example of a process believed to represent such simultaneous "polyfunctional" catalysis is the 2-hydroxypyridine catalyzed mutarotation of tetramethyl glucose.[4] Indeed, the catalytic nature of enzyme systems is presumably derived from their polyfunctionality. An even more efficient mode of catalysis often arises for reactants which contain acidic or basic groups, or both, properly oriented with respect to the site of reaction where intramolecular catalysis is operative. Various workers have investigated tautomerization reactions involving systems specifically designed such that conformations allowing the active participation by intramolecular catalytic groups in the transition state are favorable.[5-7] For these processes in which such intramolecular catalytic paths are important, it is usually observed that the "uncatalyzed" or "spontaneous" rates of reaction are unusually high as compared to the catalytic components arising from intermolecular catalysis. However, such systems must be chosen carefully since it is sometimes difficult to distinguish rate acceleration due to "genuine" intramolecular general-acid and/or general-base catalysis from that due to inductive or steric effects resulting from the nearby acidic or basic groups.

Bell and Fluendy have concluded from investigations of the rates of iodination of a series of keto acids, $CH_3CO(CH_2)_nCO_2H$, that an intramolecular acid-catalyzed path arising through cyclic transition state is dominant for the rate-determining enolization step.[5] In apparent accord with this interpretation are the results obtained

(1) T. M. Lowry and I. J. Faulkner, *J. Chem. Soc.*, 2883 (1925); C. G. Swain, *J. Amer. Chem. Soc.*, **72**, 4578 (1950); Y. Pocker, *Chem. Ind. (London)*, 968 (1960); B. E. Banks, *J. Chem. Soc.*, 63 (1962); P. R. Rony, W. E. McCormack, and S. W. Wunderly, *J. Amer. Chem. Soc.*, **91**, 4244 (1969).

(2) For reactions in aqueous solutions, termolecular terms in the rate expression involving reactant, acid and base may often be masked by catalytic effects arising from the solvent.[3]

(3) R. P. Bell and J. C. Clunie, *Proc. Roy. Soc. Ser. A*, **212**, 33 (1952); Y. Pocker and J. E. Meany, *J. Phys. Chem.*, 71, 3113 (1967).

(4) C. G. Swain and J. F. Brown, *J. Amer. Chem. Soc.*, **74**, 2534, 2538 (1952).

(5) R. P. Bell and M. A. D. Fluendy, *Trans. Faraday Soc.*, 59, 1623 (1963).

(6) E. T. Harper and M. L. Bender, *J. Amer. Chem. Soc.*, **87**, 5625 (1965).

(7) J. K. Coward and T. C. Bruice, *ibid.*, **91**, 5339 (1969).

by Fluendy[8] from Monte Carlo calculations pertaining to the probability of forming cyclic transition states. Albery, Bell, and Powell[9] extended this work to include the iodination of pyruvic acid where the intramolecular-catalyzed enolization promoted by the carboxyl (for pyruvic acid) or carboxylate (for pyruvate ion) group may presumably be envisaged as proceeding *via* transition states such as I and II, respectively. Similarily, for the *hydration* of pyruvic acid, Eigen *et al.*,[10] and Strehlow[11] have suggested that the relatively high spontaneous rate is indicative of the participation of an intramolecular acid-catalyzed mechanism.

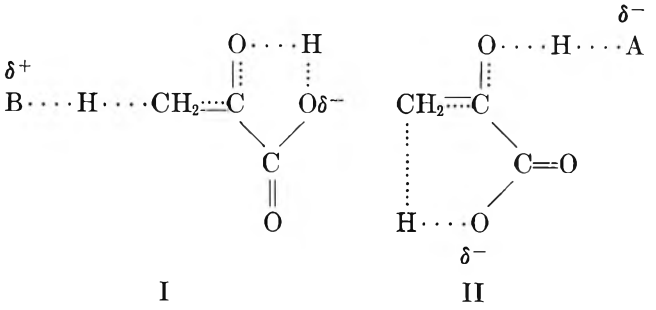

I II

Comparative studies have been carried out in this laboratory on the spontaneous rates of iodination of methyl and ethyl pyruvate and pyruvic acid. It will be noted that whereas similar inductive effects would be expected to be operative both for the alkyl pyruvates and for pyruvic acid, only in the enolization of the latter could a dominant intramolecular-catalyzed path be possible. Results from studies involving formate buffer and hydronium ion catalysis are also reported.

Experimental Section

Pyruvic acid (Baker Analyzed Products) and methyl and ethyl pyruvate (Aldrich Chemical Co.) were obtained in reagent grade and twice distilled under reduced pressure in an atmosphere of nitrogen directly prior to use: bp(pyruvic acid) 61–62° (12 mm); bp(methyl pyruvate) 50–51° (15 mm); bp(ethyl pyruvate) 53–54° (15 mm). All other chemicals were obtained from commercial sources in analytical or reagent grade and used without further purification. The aqueous solutions used for kinetic studies were prepared from deionized water.

Reaction rates were monitored on a Beckman Kintrac high speed recording spectrophotometer thermostated to 25 ± 0.02° by means of a Beckman Thermocirculator accessory. The rates of enolization of the systems under consideration were determined by following the uptake of iodine which was calculated from the diminution of the triiodide absorption band at 353 nm (ϵ 24,500 l. mol^{-1} cm^{-1}).[9] The kinetic runs were initiated by injection 0.050 ml of a solution formally 2.05×10^{-3} *M* in iodine and 1.00 *M* in potassium iodide[12,13] into 3.00 ml of the reaction solution using a calibrated Hamilton μl syringe. Since the pyruvic acid or pyruvate ester concentration always greatly exceeded that of the triiodide ion, pseudo-zero-order kinetics were observed. The reaction velocities were calculated from the slopes of the linear traces obtained, v = slope ÷ 24,500 l. mol^{-1}. The velocities thus obtained were reproducible to within 1%.

The values of pH reported in the present paper were determined before and after each run by means of a Beckman Century SS expanded scale pH meter.

The pyruvic acid–pyruvate solutions were prepared by titration with previously standardized sodium hydroxide or hydrochloric acid followed by dilution to obtain the desired concentration. The ionic strength for the runs was maintained at 0.06 *M* by adding appropriate quantities of sodium chloride. The hydration of pyruvic acid and of its conjugate base was allowed to reach equilibrium[14,15] before the iodination process was initiated. Like Albery, *et al.*,[9] we observed an initial rapid diminution of absorbancy following the injection of the triiodide solution which ultimately conformed to the expected linear zero-order change. This initial deviation was more prominent at low ratios of [pyruvic acid]/[pyruvate] and became negligible when pyruvic acid concentrations exceeded that of its conjugate base. It was also noted that just prior to the end of the runs (after 2–3 half-lives) the rate tapered off slightly.

The iodinations of pyruvate esters were carried out in a similar fashion except that they were usually run in formate buffers and at an ionic strength of 0.10 *M* which, as before, was regulated by the incorporation of the appropriate quantities of sodium chloride. Methyl pyruvate, $CH_3COCO_2CH_3$, and ethyl pyruvate, $CH_3COCO_2C_2H_5$ solutions were allowed to equilibrate with water at least 1 min before the iodination was initiated. It was observed that the half-lives for the hydrations were in the order of 3–6 sec at this temperature. It has previously been shown[15,16] that under conditions employed in the work reported herein the hydrolysis of these esters is exceedingly slow and consequently the iodination was essentially complete before any significant quantity of pyruvic acid was generated. It was also observed for all reactants discussed in this paper

(8) M. A. D. Fluendy, *Trans. Faraday Soc.*, **59**, 1681 (1963).

(9) W. J. Albery, R. P. Bell, and A. L. Powell, *ibid.*, **61**, 1194 (1965).

(10) M. Eigen, K. Kustin, and H. Strehlow, *Z. Physik. Chem.*, **31**, 140 (1962).

(11) H. Strehlow, *Z. Elektrochem.*, **66**, 3921 (1962).

(12) The equilibrium constant[13] for $I^- + I_2 \rightleftarrows I_3^-$ has the value 714 M^{-1}.

(13) G. Jones and B. B. Kaplan, *J. Amer. Chem. Soc.*, **50**, 1845 (1928).

(14) Y. Pocker, J. E. Meany, B. J. Nist, and C. Zadorojny, *J. Phys. Chem.*, **73**, 2879 (1969).

(15) Y. Pocker and J. E. Meany, *ibid.*, **74**, 1486 (1970).

(16) A. Kirrmann, *Memoires Presentes A La Societe Chimique*, 247 (1934).

that the rate of iodination was independent of the concentration of iodine.

The presence of the formate buffer causes a slow decrease in the absorbancy of the triiodide ion, the magnitude of which does not exceed 5–7% that caused by the iodination of the alkyl pyruvates in the range of formate buffer concentrations reported herein. The observed rate constants were corrected accordingly. Unlike the traces obtained for the iodination of pyruvic acid, an initial burst in the apparent uptake of triiodide was not observed and consequently immediate pseudo-zero-order kinetics were obtained. There was again, however, a slight falling off in the rate after 2–3 half-lives. The velocities for the processes were again calculated from the slopes of the linear portion of the straight lines. An example of a family of such runs for the iodination of methyl pyruvate is given in Figure 1.

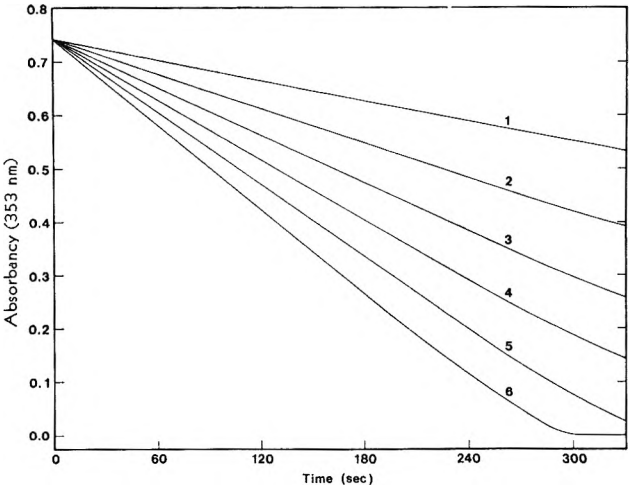

Figure 1. A series iodination runs at 25.0° involving a total concentration of 0.0185 *M* methyl pyruvate at ionic strength 0.1 *M* in formate buffers r = 1.07: (1), $[HCO_2H]$ = 0.0178 *M*; (2), $[HCO_2H]$ = 0.0357 *M*; (3), $[HCO_2H]$ = 0.0535 *M*; (4), $[HCO_2H]$ = 0.0714 *M*; (5), $[HCO_2H]$ = 0.0890 *M*; and (6), $[HCO_2H]$ = 0.107 *M*.

Results and Discussion

A detailed kinetic analysis of the iodination of pyruvic acid around its pK_a (pK_a = 2.49)[17] appears more complex than the other related halogenation processes. Since, under these conditions, pyruvic acid is in equilibrium with the pyruvate ion, two parallel iodination paths must be taken into account. Assuming these processes are subject to catalysis by general acids, HA, and to general bases, B, the rate of uptake of the triiodide ion may be represented by the following expression

$$v = [HP]\{\Sigma k_i[HA]_i + \Sigma k_j[B_j]\} + [P^-]\{\Sigma k_i^-[HA]_i + \Sigma k_j^-[B]_j\} \quad (1)$$

where HP and P^- refer to pyruvic acid and its conjugate base and k and k^- are the rate constants associated with their respective iodinations.

An additional complicating factor results from the partial hydration of pyruvic acid and its anion (Table I) from which arises the existence of four potential acid–base catalysts derived from pyruvic acid itself[18]

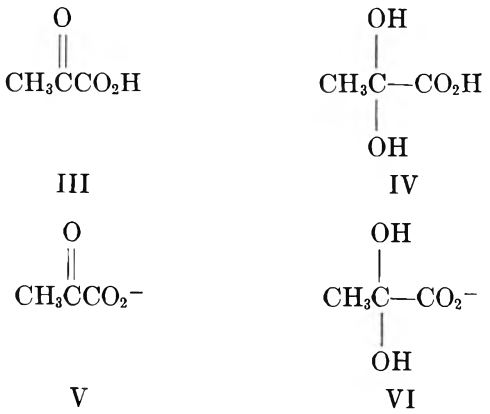

In aqueous solution, other catalytic components due to water, hydronium, and hydroxide ion smight also contribute to the overall rate.

Although a complete kinetic analysis of the iodination of pyruvic acid is presently in progress in this laboratory, the purpose of the present work is to determine the value of the spontaneous rate constant, k_0, for the iodination of pyruvic acid. Consequently, conditions were chosen such that the uptake of the triiodide ion was predominantly a result of the spontaneous enolization of pyruvic acid where all other pathways were negligibly small. Thus, the runs were carried out in a pH range where catalysis by the hydronium ion and hydroxide ion was not detectable.[19] Since in general, the iodination is rather insensitive to acid catalysis[19] any catalytic contribution by either pyruvic acid or by its hydrate would be imperceptible at the low concentrations of pyruvic acid employed. The concentration of pyruvate ion was comparatively small in order to avoid its action as a catalyst or as a competitive reactant. One also would assume, in analogy to the *hydration* of pyruvic acid as

Table I: Hydration Equilibria for Pyruvic Acid, Pyruvate Ion, and the Alkyl Pyruvates at 25.0°

	$K_{eq} = \frac{[\text{hydrated}]}{[\text{unhydrated}]}$	x	1 − x
Pyruvic acid[a]	1.63	0.62	0.38
Pyruvate ion[a]	0.064	0.06	0.94
Methyl pyruvate[b]	2.85	0.74	0.26
Ethyl pyruvate[b]	3.74	0.70	0.30

[a] Reference 14. [b] Reference 20.

(17) Refers to a thermodynamic constant; G. Kortum, W. Vogel, and K. Andresson, "Dissociation Constants of Acids in Aqueous Solution," Butterworths, London, 1961, p 335.

(18) For a discussion pertaining to the relative concentrations of these species as a function of pH and temperature see ref 14.

(19) E. D. Hughes and H. B. Watson, *J. Chem. Soc.*, 1929 (1945).

compared to that of its conjugate base[15] that the rate of iodination of pyruvic acid would likewise be much more rapid than that of the pyruvate ion.

Table II summarizes the results obtained from several runs of the iodination of pyruvic acid. The spontaneous rate coefficient, k_0, was obtained by dividing the observed velocities by the concentration of unhydrated pyruvic acid

Table II: The Spontaneous Rate of Iodination of Pyruvic Acid at 25° at 0.06 *M* Ionic Strength

pH	10^4 $[HP]_{total}$, *M*	10^4 $[P^-]_{total}$, *M*	$10^6 v_{obsd}$, M^{-1} sec^{-1}	$10^6 \left\{k_0 = \frac{v_{obsd}}{(1-\chi)[HP]_{total}}\right\}$, sec^{-1}
1.85	71	20	3.07	1.14
1.54	73	10	3.08	1.11
1.54	73	10	3.19	1.14
1.38	70	6.5	3.04	1.14
1.20	64	4.0	2.79	1.15

$$k_0 = \frac{v_{obsd}}{(1-\chi)[HP]_{total}} \qquad (2)$$

where χ is the fraction of hydration, at this temperature (Table I).[14]

From the consistency of the values of k_0 throughout the range of pH's and pyruvate concentrations indicated, the absence of any significant catalytic contribution by hydroxide, hydronium or pyruvate ion is clearly demonstrated.

Calculation from data of earlier workers[9,19] produced the value $k_0 = 1.16 \times 10^{-6}$ sec^{-1} at 25.0° and ionic strength 0.05 *M* which is in excellent agreement to our average value of 1.14×10^{-6} sec^{-1} at the same temperature and at an ionic strength of 0.06 *M*.

The iodination of methyl and ethyl pyruvates was run in formic acid buffers ($pK_a = 3.66$). The rate constants, k_{obsd}, again were calculated from the observed velocities divided by the concentration of unhydrated ester (see Table I). The formal concentrations employed for methyl and ethyl pyruvate were 0.0185 and 0.0150 *M*, respectively.

The family of runs shown for methyl pyruvate in Figure 1 shows that a slight curvature always arises at the end of each run. It has been suggested by Albery, *et al.*,[9] that for pyruvic acid, this deviation may be due to the reduction of pyruvic acid by the iodide ion. Although such a reduction may indeed occur, it probably would do so at a rate considerably slower than the rate at which these iodinations occur. We have observed that regardless of the rate of iodination of the alkyl pyruvates (as varied by changes in buffer strength) the tailing off always occurs just prior to the end of the run. Since there is no reason to suspect catalysis of the "reduction" by formate buffers, it would appear that a better explanation is needed.

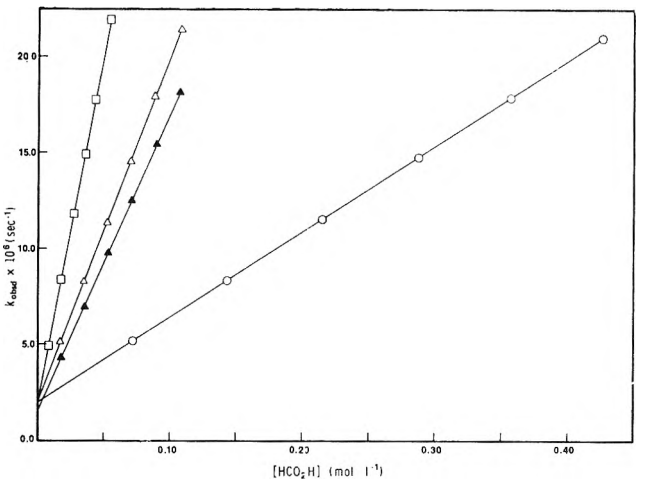

Figure 2. Formate-catalyzed iodination of methyl and ethyl pyruvate at 25.0°, $\mu = 0.1$ *M*: □, methyl pyruvate, $r = 0.54$; △, methyl pyruvate, $r = 1.07$; ○, methyl pyruvate, $r = 4.28$; ▲, ethyl pyruvate, $r = 1.07$.

Assuming a catalytic contribution for the iodination for each acid–base component in solution, the overall observed rate constant in formic acid buffers may be written as a sum of catalytic terms

$$\begin{aligned} k_{obsd} &= k_0 + k_{H_3O^+}[H_3O^+] + k_{OH^-}[OH^-] + \\ &\quad k_{HCO_2H}[HCO_2H] + k_{HCO_2^-}[HCO_2^-] \\ &= k_0 + k_{H_3O^+}[H_3O^+] + k_{OH^-}[OH^-] + \\ &\quad [HCO_2H][k_{HCO_2H} + k_{HCO_2^-}/r) \qquad (3) \end{aligned}$$

Thus if a series of runs are carried out at a given buffer ratio, $r = [HCO_2H]/[HCO_2^-]$, (Figure 1) a plot of k_{obsd} *vs.* $[HCO_2H]$ would be expected to result in a straight line, the slope of which could be expressed as

$$S = k_{HCO_2H} + k_{HCO_2^-}/r \qquad (4)$$

and the intercept as

$$I = k_0 + k_{H_3O^+}[H_3O^+] + k_{OH^-}[OH^-] \qquad (5)$$

If this procedure is carried out at several buffer ratios (and consequently at correspondingly different values of pH) the individual catalytic components may be evaluated. Figure 2 illustrates such a graphical treatment in which the open points refer to methyl pyruvate runs and the solid points to ethyl pyruvate runs. It will be noted from the figure that the various plots of k_{obsd} against formic acid concentration indeed are linear for both methyl and ethyl pyruvate iodinations precluding any significant catalysis arising from the concerted action of both formic acid and its conjugate base. Table III summarizes the results obtained from the data which indicate the following.

(1) For methyl pyruvate, the values of the intercepts do not vary in the pH range in which the runs were

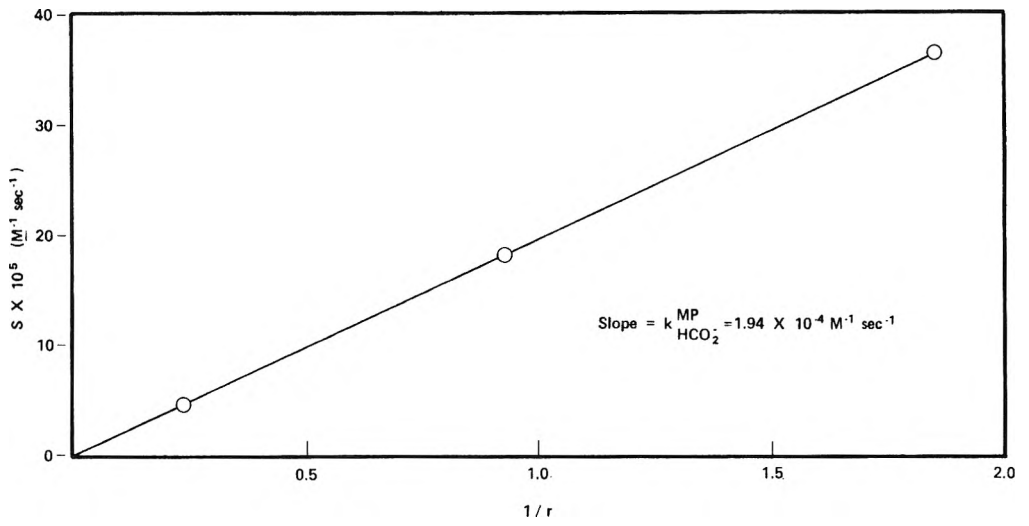

Figure 3. Determination of the specific rate coefficient for the formate ion catalyzed iodination of methyl pyruvate at 25.0° and μ = 0.1 M.

Table III: The Spontaneous and Formate-Catalyzed Rate of Iodination of Methyl and Ethyl Pyruvate at 25.0° and Ionic Strength 0.1 M

	r	$S \times 10^5$, M^{-1} sec^{-1}	$I \times 10^6$, sec^{-1}	pH	$S \cdot r \times 10^5$, M^{-1} sec^{-1}
MeP	0.54	36.4	2.0	4.03	19.6
	1.07	18.1	1.9	3.70	19.4
	4.28	4.5	1.9	3.07	19.3
EtP	1.07	15.7	1.7	3.70	16.8

carried out. Consequently from eq 5, $I = k_0^{MP} = 1.9 \times 10^{-6}$ sec^{-1}. The constancy of this value of k_0 was further tested in solutions of pure water to which various quantities of hydrochloric acid were added. No detectable increase in rate was observed up to and including 0.1 N HCl.

(2) If S is plotted against $1/r$ for the methyl pyruvate data (eq 4), the slope of the resultant straight line allows the evaluation of $k_{HCO_2^-}{}^{MP} = 19.4 \times 10^{-5}$ l. mol^{-1} sec^{-1} (Figure 3).

(3) It will also be noted from Figure 3 that the intercept is indistinguishable from the value zero and consequently catalysis by formic acid itself is experimentally undetectible under these conditions. This is also indicated from the constancy of the product $S \times r$ (Table III) which therefore represents the catalytic component, $k_{HCO_2^-}{}^{MP}$ alone.

(4) Assuming similar acid–base characteristics for methyl and ethyl pyruvate, it may be assumed that the iodination of ethyl pyruvate is also insensitive toward general and specific-acid catalysis in the buffers under consideration. Therefore, $k_0^{EP} = 1.7 \times 10^{-6}$ sec^{-1} and $k^{EP}{}_{HCO_2^-} = 16.8 \times 10^{-5}$ l. mol^{-1} sec^{-1} were evaluated from the intercept, I, and the product $S \times r$, respectively.

The data reported in the present paper shows that the iodination (and hence the rate-determining enolization) of methyl and ethyl pyruvates are rather sensitive toward general-base catalysis but insensitive toward even specific-acid catalysis. More important perhaps is the finding that the rate of spontaneous iodination of these compounds is of comparable magnitude (actually somewhat larger) than that corresponding to the iodination of pyruvic acid. This finding renders the assumption of an intramolecular acid-catalyzed enolization of the latter difficult to justify since in the corresponding process involving the alkyl pyruvates no such intramolecular acid-catalyzed path is possible. A similar comparison has recently been reported regarding the *hydrations* of pyruvic acid and the same alkyl pyruvates in which a similar conclusion has been reached.[20]

Interestingly, both the enolization and hydration of pyruvic acid (Table IV) are more sensitive toward specific-acid catalysis (intermolecular) than the corresponding processes involving the alkyl pyruvates. Furthermore, the *enolizations* of the alkyl pyruvates in comparison to the corresponding hydrations are apparently more sensitive to the basicity of general bases. It would seem that for the enolizations, the direct removal of carbon bound hydrogen is more dependent on base strength than is the indirect action of the base in facilitating the addition of a molecule of water.

The relative insensitivity of the enolizations of pyruvic acid, and the alkyl pyruvates toward acid catalysis suggests that in the transition states for these processes, bond breaking associated with the carbon bound hydrogen is more important than oxygen to hydrogen bond making. Thus the rupture of the

(20) Y. Pocker, J. E. Meany, and C. Zadorojny, *J. Phys. Chem.*, submitted for publication.

Table IV: Catalysis of the Hydration and Iodination of Pyruvic Acid and the Alkyl Pyruvates

	Hydration[a,b]			Enolization		
	Pyruvic acid	methyl pyruvate	Ethyl pyruvate	Pyruvic acid	methyl pyruvate	Ethyl pyruvate
k_{H_2O} (M^{-1} sec^{-1})[c]	6.0×10^{-4}	5.95×10^{-4}	4.66×10^{-3}	2.05×10^{-3}	3.4×10^{-3}	3.1×10^{-3}
$k_{HCO_2^-}$ (M^{-1} sec^{-1})	[d]	8.8×10^{-2}	7.2×10^{-2}	[d]	1.94×10^{-4}	1.68×10^{-4}
$k_{HCO_2^-}/k_{H_2O}$ (M^{-1} sec^{-1})	[d]	150	150	[d]	5700	5500
$k_{H_3O^+}$ (M^{-1} sec^{-1})	1.73	0.78	0.68	1.8×10^{-5}	[f]	[f]

[a] Reference 15. [b] Reference 20. [c] $k_{H_2O} = k_0/55.5$ mol l.$^{-1}$. It should, however, be pointed out that the respective transition states may contain more than one molecule of water. [d] Analysis of the general catalysis of both the hydration and enolization of pyruvic acid by formate buffers is difficult since the inherent acidity of pyruvic acid causes pH changes as the concentrations of HCO_2H and HCO_2^- are simultaneously varied. [e] Reference 19. [f] Too small to be detected.

carbon–hydrogen bond is already aided to such an extent by the strongly electron withdrawing effect of the adjacent carboalkoxy group that neither inter- nor intramolecular acid catalysis is required.

Structural Studies of Magnesium Halide–Potassium Halide Melts by Raman Spectroscopy

by V. A. Maroni,* E. J. Hathaway, and E. J. Cairns

Chemical Engineering Division, Argonne National Laboratory, Argonne, Illinois 60439
(Received August 5, 1970)

Publication costs assisted by the U. S. Atomic Energy Commission

Raman spectra of MgX_2–KX melts (X = Cl, Br, and I) have been obtained over a range of X^-/Mg^{2+} mole ratios. Results for the $MgCl_2$–KCl and $MgBr_2$–KBr systems are interpreted in terms of a complex equilibrium between a residual ionic lattice, $[MgX_2]_p$, similar in structure to solid $MgCl_2$ and solid $MgBr_2$, and a complex anion of the form $MgX_n^{(2-n)}$. The concentration of $MgX_n^{(2-n)}$ units increases as the X^-/Mg^{2+} ratio is increased from 2.5 to 4.0. Raman spectra of MgI_2–KI melts with $I^-/Mg^{2+} = 3.0$ and 3.5 indicate the presence of a single, highly symmetric species. The observation of two depolarized, primarily bond-bending modes for this species is most consistent with the existence of tetrahedral MgI_4^{2-}. This indicates that three large I^- ions do not effectively shield the field of the Mg^{2+} ions. Extrapolation strongly suggests that with Cl^- and Br^-, the lower coordination, MgX_3^-, is even less likely.

Introduction

Raman studies of divalent metal halides in the molten state have been directed primarily toward (1) investigating the existence of complex ions in these melts and (2) determining the structures of the complex ions. The chlorides of Mg(II), Zn(II), Cd(II), Hg(II), Sn(II), and Pb(II), the bromides of Mg(II), Zn(II), and Hg(II), and the iodide of Hg(II) have been subjected to Raman investigation. Comprehensive discussions of these investigations with references to many of the original papers have appeared in several review articles;[1-3] consequently only a brief summary will be presented here.

In studies of the chloride melts of Mg(II),[1b,4] Zn(II),[5-7] Cd(II),[7,8] and Sn(II),[9] evidence was found for

(1) (a) V. A. Maroni and E. J. Cairns, "Molten Salts: Characterization and Analysis," G. Mamantov, Ed., Marcel Dekker, New York, N. Y., 1969, pp 231–251; (b) pp 263–280; (c) pp 256–260.

(2) D. W. James in "Fused Salt Chemistry," M. Blander, Ed., Interscience, New York, N. Y., 1964.

(3) G. J. Janz and S. C. Wait, *Quart. Rev., Chem. Soc.*, **17**, 225 (1963).

(4) K. Balasubrahmanyam, *J. Chem. Phys.*, **44**, 3270 (1966).

(5) D. E. Irish and T. F. Young, Jr., *ibid.*, **43**, 1765 (1965).

(6) R. B. Ellis, *J. Electrochem. Soc.*, **113**, 485 (1966).

(7) W. Bues, *Z. Anorg. Allg. Chem.*, **279**, 104 (1955).

(8) M. Tanaka, K. Balasubrahmanyam and J. O'M. Bockris, *Electrochim. Acta*, **8**, 621 (1963)

the existence of a polymeric species $[MCl_2]_p$ with a structure resembling that of the solid in each case. On increasing the amount of excess halide in these melts, usually by addition of an alkali metal halide, smaller discrete units of the type $MCl_n^{(2-n)}$ were found to separate from the polymeric structure. The species MCl_2, MCl_3^-, and MCl_4^{2-} have all been reported to exist in the chloride melts of Zn(II)[5-7] and Hg(II).[10] MCl_3^- has been reported in Cd(II)[7,8] and Sn(II)[9] chloride melts, and MCl_4^{2-} has been reported in Pb(II) chloride melts.[11]

There is some controversy concerning the existence of MX_3^- in molten binary salt systems.[12] In this regard, Moyer, Evans, and Lo[13] reinvestigated the Raman spectra of $ZnCl_2$–KCl melts and found it possible to explain the data without invoking $ZnCl_3^-$. In other cases, notably for Cd(II) and Sn(II), the available data[7-9] are incomplete in terms of evidence for either MCl_3^- or MCl_4^{2-} and do not allow a conclusive assignment to be made.

From a Raman study of the $MgCl_2$–KCl system, Balasubrahmanyam[4] concluded that the layer structure of solid $MgCl_2$ was at least partly broken up in pure liquid $MgCl_2$ to form octahedral $MgCl_6^{4-}$ units. When the relative amount of chloride ion was increased by addition of KCl, $MgCl_3^-$ and possibly $MgCl_4^{2-}$ were said to replace $MgCl_6^{4-}$ as the principal species.

A subsequent Raman study of the $MgCl_2$–KCl system, carried out in our laboratory,[1b] gave somewhat different results for the number of bands, the peak frequencies, and the states of polarization than were obtained by Balasubrahmanyam; results analogous to those for the $MgCl_2$–KCl system were also reported for the $MgBr_2$–KBr system. Since the publication of these results, we have performed additional studies of the $MgCl_2$–KCl and $MgBr_2$–KBr systems and have also recorded Raman spectra of MgI_2–KI melts. In light of these new data, we now wish to revise several of our earlier conclusions regarding the $MgCl_2$–KCl and $MgBr_2$–KBr systems. A discussion of the most plausible species involved in each magnesium(II)–halide complex equilibrium is also presented.

Experimental Section

The Raman spectrophotometer used in this investigation consisted of a Spectra-Physics Model 125 Helium–Neon Laser (nominal power 50 mW at 6328 Å) in tandem with a Spex Industries Model 1400 double spectrometer. The exciting radiation was chopped at 400 cps and the scattered light was detected with a Hamamatsu TV Co., Ltd., R-136 photomultiplier tube (cryostated at −50°) coupled to an ac lock-in amplifier. The amplified signal was measured with a phase-angle voltmeter and plotted by a strip-chart recorder. A typical Raman cell consisted of a quartz tube with an optically flat window at each end. Each cell was provided with a side arm through which the sample could

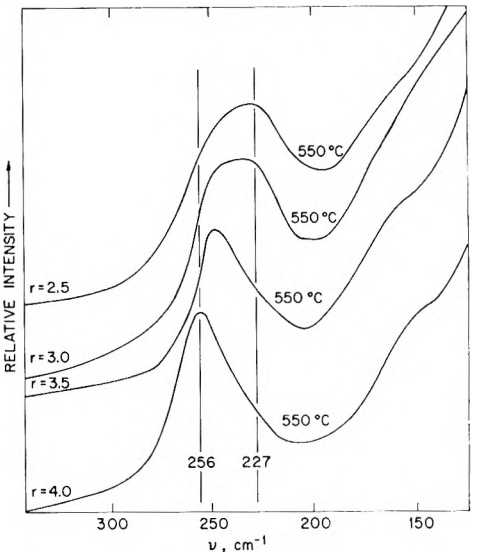

Figure 1. Raman spectra of $MgCl_2$–KCl melts: r = mol of Cl^-/mol of Mg^{2+}; time constant = 50 sec; scan speed = 2 cm^{-1}/min; spectral band pass = 10 cm^{-1}.

be loaded. After loading, the side arm was sealed, and the cell was placed in a split-tube furnace with its axis vertical. The laser beam was passed through the upper optical flat collinear with the axis of the quartz tube. Scattered radiation emerging perpendicular to the tube axis through a slot in the side of the furnace was collected with a biconvex lens and focused into the spectrometer slit. The apparatus and general technique for these experiments have been described and diagramed in greater detail elsewhere.[1c]

Samples were prepared using commercially available analytical grades of KCl, KBr, and KI which were heated at 200° under vacuum for several days prior to use. Anhydrous $MgCl_2$ (Anderson Physics Laboratory), 98+% $MgBr_2$, and 98+% MgI_2 (Research Organic/Inorganic Chemicals) were sublimed under vacuum prior to use. All subsequent handling of the anhydrous salts was carried out in a helium atmosphere having a moisture content of less than 1 ppm. Salt mixtures of the required composition were equilibrated and then filtered through fine quartz frits under helium pressure. Care was taken to ensure that all of the liquid material passed the frit. Chemical analyses of the filtered samples were in excellent agreement with the compositions determined from the weights of material used to form the prefiltered mixtures. The filtered samples were ground to a fine powder, and por-

(9) J. H. R. Clarke and C. Solomons, *J. Chem. Phys.*, **47**, 1823 (1967).

(10) G. J. Janz and D. W. James, *ibid.*, **38**, 905 (1963).

(11) K. Balasubrahmanyam and L. Nanis, *ibid.*, **40**, 2657 (1964).

(12) (a) See reference 1b, pp 55–80; (b) M. A. Bredig, *Electrochim. Acta*, **5**, 299 (1961).

(13) J. R. Moyer, J. C. Evans, and G. Y-S. Lo, *J. Electrochem. Soc.*, **113**, 158 (1966).

tions were loaded into the Raman cells for the spectral measurements.

Results and Discussion

A. The $MgCl_2$–KCl System. Raman spectra of $MgCl_2$–KCl melts are characterized by an intense band at 256 cm^{-1} for Cl^-/Mg^{2+} mole ratios ≥ 4.0. As the Cl^-/Mg^{2+} ratio is decreased below 4.0, this band loses intensity and a broader, somewhat weaker band grows in steadily on the low-frequency side (at ≈ 227 cm^{-1}), as shown in Figure 1. The entire band envelope in the 200–300-cm^{-1} region is polarized for all Cl^-/Mg^{2+} ratios. A broad depolarized shoulder (on the Rayleigh line) at 160 cm^{-1} is also found to decrease steadily in intensity as the Cl^-/Mg^{2+} ratio is reduced from 4.0. This behavior suggests a magnesium(II)–chloride complex equilibrium involving at least two structurally different species. The polarized bands in the 200–300-cm^{-1} region no doubt arise from symmetric Mg–Cl bond stretching vibrations; however, the number of bands in this envelope is uncertain. Previously we reported having resolved this envelope into four bands using computerized curve resolution techniques.[1c] Since that time, we have found that two, three, five, or more bands could be computer-fitted under the envelope, and therefore we prefer to regard the value for the number of bands in this region as ≥ 2.

Our previous interpretation of these results in terms of a complex equilibrium involving a residual ionic lattice, $[MgCl_2]_p$, in equilibrium with several complexes of the type $MgCl_n^{(2-n)}$ is still generally applicable.[1b] However, it appears from the results presented here that only one such complex is involved in the equilibrium with $[MgCl_2]_p$. The most plausible explanation for these results parallels one presented by Ellis[6] for the $ZnCl_2$–KCl system; *i.e.*, the existence in the melt of polynuclear aggregates (similar in structure to the solid divalent metal halide lattice) at halide/metal(II) ratios near 2.0 from which smaller units split off as the halide/metal(II) ratio is raised by the addition of KCl. The equilibrium expression describing this situation for $MgCl_2$–KCl melts might take the form

$$[MgCl_2]_p + (n-2)Cl^- \rightleftharpoons MgCl_n^{(2-n)} + [MgCl_2]_{p-1} \quad (1)$$

The $[MgCl_2]_p$ aggregates are perhaps structurally somewhat similar to solid $MgCl_2$, which has the $CdCl_2$-type lattice[14] ($CdCl_6$ octahedra linked together by shared edges).

The results in Figure 1 are difficult to explain for a complex equilibrium which involves several species of the type $MgCl_n^{(2-n)}$. If, for example, $MgCl_4^{2-}$ were in equilibrium with $MgCl_3^-$ or $MgCl_2$, the species having the higher coordination number, in this case $MgCl_4^{2-}$, would be expected to predominate at the higher Cl^-/Mg^{2+} ratios and, therefore, would be characterized by the symmetric stretching vibration at 256 cm^{-1}.

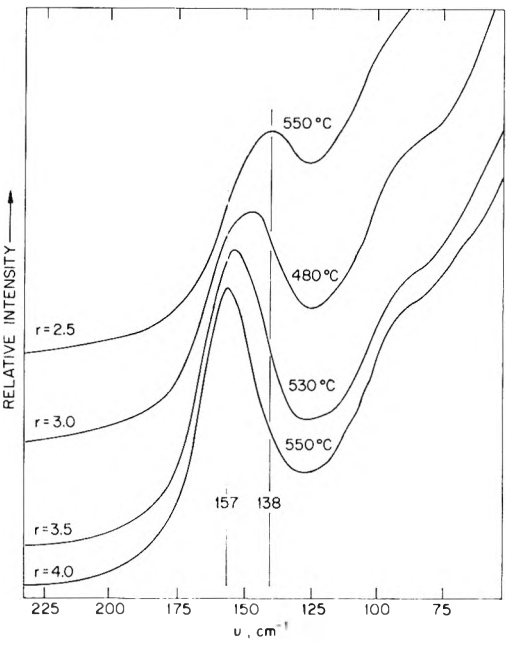

Figure 2. Raman spectra of $MgBr_2$–KBr melts: r = mol of Br^-/mol of Mg^{2+}; time constant = 50 sec; scan speed = 2 cm^{-1}/min; spectral band pass = 7 cm^{-1}.

Decreasing the Cl^-/Mg^{2+} ratio should then lead to formation of a complex with a lower coordination number; but the complex with the lower coordination number, hence higher metal–halogen bond order, and, therefore, a greater metal–halogen force constant, should have a higher symmetric stretching frequency than $MgCl_4^{2-}$. An example of this type of behavior is found for the $HgCl_2$–KCl system where the complexes $HgCl_4^{2-}$ (ν_1 = 267 cm^{-1}), $HgCl_3^-$ (ν_1 = 282 cm^{-1}), and $HgCl_2$ (ν_1 = 314 cm^{-1}) were reported.[10] In Raman spectra of $HgCl_2$–KCl melts, the peak frequency of the band envelope containing the Hg–Cl symmetric stretching vibrations shifts steadily to higher frequency as the Cl^-/Hg^{2+} ratio is decreased. This is opposite to the observations for the $MgCl_2$–KCl system as shown in Figure 1. The steady downward displacement of the peak frequency (from 256 cm^{-1}) for the band envelope containing Mg–Cl symmetric stretching vibrations as the Cl^-/Mg^{2+} ratio is decreased suggests that only one species of the type $MgCl_n^{(2-n)}$ is involved in the equilibrium given by equation 1 above. Further consideration of the spectra in Figure 1 in terms of determining the value of n are presented in section *D* of the Results and Discussion.

B. The $MgBr_2$–KBr System. Raman spectra for $MgBr_2$–KBr melts are presented in Figure 2. The experimental observations for this system are analogous to those obtained for the $MgCl_2$–KCl system. An intense, polarized band at 157 cm^{-1} for Br^-/Mg^{2+} mole ratios ≥ 4.0 yields to a weaker, polarized band centered

(14) A. F. Wells, "Structural Inorganic Chemistry," Oxford University Press, New York, N. Y., 1962, p 345.

near 138 cm^{-1} as the Br^-/Mg^{2+} ratio is reduced from 4.0. The broad, depolarized shoulder centered near 90 cm^{-1} also descreases in intensity with decreasing Br^-/Mg^{2+} ratio. The interpretation presented in the previous section for the $MgCl_2$–KCl results can be applied to the $MgBr_2$–KBr system as well. Solid $MgBr_2$ has the $Cd(OH)_2$ type lattice which is a layered structure similar to that of $MgCl_2$.[14] This layered structure, $[MgBr_2]_p$, persists to some extent into the melt phase for Br^-/Mg^{2+} ratios near 2.0 and probably accounts for the band near 138 cm^{-1}. As the amount of excess bromide is increased, a second species, $MgBr_n^{(2-n)}$, becomes predominant in the equilibrium. Further interpretation of these data in terms of a value for n is left to section *D* of the Results and Discussion.

C. The MgI_2–KI System. The vapor pressures of MgI_2 at most of the liquidus temperatures for the MgI_2–KI system were too high to permit the recording of reliable Raman spectra for a wide range of I^-/Mg^{2+} mole ratios. The high melting compositions tended to reflux in the Raman sample tubes causing some turbulence at the surface of the liquid. Reproducible spectra were obtained for two compositions near the eutectic,[15] I^-/Mg^{2+} = 3.0 and 3.5.

For the $MgCl_2$–KCl and $MgBr_2$–KBr systems significant changes in the envelope shape and peak position of the magnesium–halogen stretching band were observed when the Cl^-/Mg^{2+} and Br^-/Mg^{2+} mole ratios were raised from 3.0 to 3.5 (see Figures 1 and 2). For the MgI_2–KI system, this was not the case. Raman spectra for the two compositions studied were identical. The Raman spectrum for I^-/Mg^{2+} = 3.5 is shown in Figure 3. Curves a and b show the dependence of the band intensities on the direction of polarization of the exciting radiation. The polarized band of 109 cm^{-1} is attributed to symmetric stretching of the Mg–I bonds. In contrast with the results obtained with the $MgCl_2$–KCl and $MgBr_2$–KBr systems, the lower frequency band in Figure 3 is resolved into two components, 58 and 39 cm^{-1}, both depolarized.

Based on the limited amount of data presented here, little can be concluded regarding the nature or even the existence of a complex ion equilibrium in MgI_2–KI melts. The intensity, narrow band width, and extensive polarization of the 109-cm^{-1} band favor the predominance of a discrete, highly symmetric species of the type $MgI_n^{(2-n)}$ rather than a polymeric structure (for the compositions studied here). A discussion of plausible structures for this species is presented in the following section.

D. Conclusions Regarding the Assignment of Structures for $MgX_n^{(2-n)}$. For the $MgCl_2$–KCl and $MgBr_2$–KBr systems, the complex equilibrium appears to terminate at the higher X^-/Mg^{2+} mole ratios with the formation of a species with a coordination number of 4 or less. At X^-/Mg^{2+} ratios $\geq$4.0, the principal features (peak frequency and shape) of the band envelope for the Mg–X stretching vibrations are invariant; but in the absence of an internal intensity standard, it is not possible to make a more conclusive determination of the upper limit for the value of n from this work.

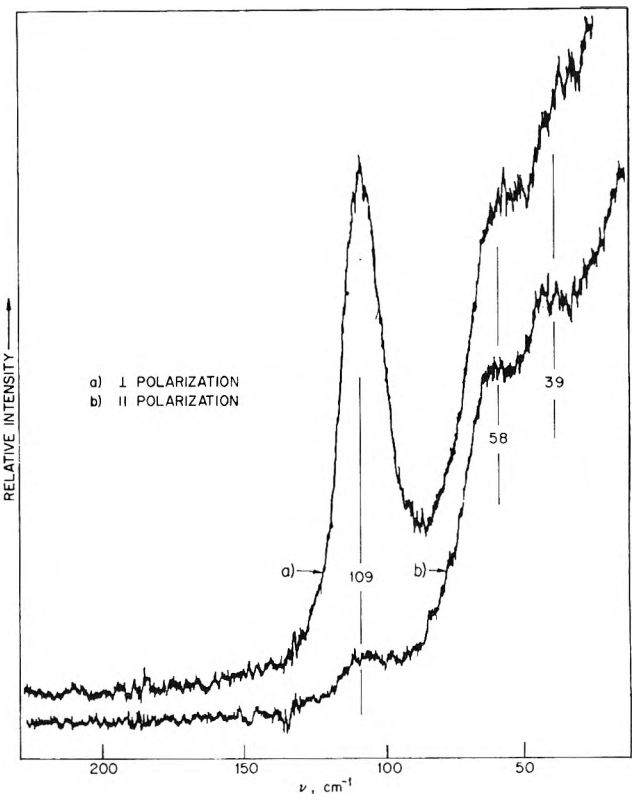

Figure 3. Raman spectrum of an MgI_2–KI melt with mol of I^-/mol of Mg^{2+} = 3.5: temperature = 360°, time constant = 10 sec, scan speed = 5 cm^{-1}/min; spectral band pass = 5 cm^{-1}.

Studies of vapor pressure,[16] viscosity,[17] surface tension,[18] and activity[19] in $MgCl_2$–KCl melts have been interpreted in terms of the existence of monomeric complexes. The results of two of these studies[16,18] favor $MgCl_3^-$ as the principal species; two of the studies,[17,19] implied the existence of $MgCl_4^{2-}$. Kleppa and McCarty[20] concluded that $MgCl_4^{2-}$ is the predominant species in $MgCl_2$–KCl melts based on a calorimetric determination of integral enthalpies of mixing. Bredig's considerations of the interaction parameter in charge-unsymmetric systems also support this view.[12a] Electrical conductance measurements[21] and previous Raman

(15) The eutectic is at 39 mole % MgI_2 and 255°. W. Klemm, K. Beyersdorfer, and J. Oryschkewitsch, *Z. Anorg. Allg. Chem.*, 256, 25 (1948).

(16) E. G. Schrier and H. M. Clark, *J. Phys. Chem.*, 67, 1259 (1963).

(17) S. Karpachev and A. Stromberg, *Z. Anorg. Allg. Chem.*, 222, 78 (1935).

(18) O. G. Desyatnikov, *J. Appl. Chem., USSR*, 29, 945 (1956).

(19) H. Flood and S. Urnes, *Z. Elektrochem.*, 59, 834 (1955).

(20) O. J. Kleppa and F. G. McCarty, *J. Phys. Chem.*, 70, 1249 (1966).

(21) E. A. Ukshe and E. B. Kachina-Pullo, *Russ. J. Inorg. Chem.*, 11, 638 (1966).

spectral data[4] for the $MgCl_2$–KCl system favor $MgCl_3^{-1}$ as the predominant species.

Table I lists the expected Raman spectral characteristics for MgX_3^- and MgX_4^{2-} species having a number of different structures. The primarily bond-stretching vibrations of metal–halogen complexes are generally at least a factor of 2 higher in frequency than the primarily bond-bending modes, which in most cases leads to a separation of the stretching and bending modes into two distinct spectral regions.[22] For each structure listed in Table I, two Raman-active, primarily bond-stretching vibrations are predicted, one polarized and one depolarized. Only the polarized primarily stretching vibration was recorded in the Raman spectra presented in the previous sections. Additional spectra of all the samples were recorded between 50 and 500 cm^{-1} with the exciting radiation polarized parallel to the direction of observation so as to minimize the intensity of the polarized stretching vibration. Careful examination of these spectra in the vicinity of the polarized band and in the higher frequency region failed to reveal a depolarized band attributable to antisymmetric stretching motions. The absence of this band is puzzling, and the only plausible explanation in terms of the structures listed in Table I is that it is both much weaker than and much broader than the polarized Mg–X stretching vibration and, therefore, has escaped detection.[23] If this is the case, and if one of the structures in Table I indeed prevails, it should be recognized that the observation of the depolarized stretching vibration would still not allow a conclusive structural assignment to be made.

Table I: Characteristics of Raman Active Vibrations for MgX_4^{2-} and MgX_3^- Species of Different Geometries[a]

Species	Geometry	Point symmetry	Vibration[b]	State of polarization[c]	Primary Mg–X coordinate involved
MgX_4^{2-}	Tetrahedral	T_d	ν_3	dp	Mg–X bond stretch
			ν_1	p	Mg–X bond stretch
			ν_4	dp	X–Mg–X bend
			ν_2	dp	X–Mg–X bend
MgX_4^{2-}	Planar	D_{4h}	ν_1	p	Mg–X bond stretch
			ν_2	dp	Mg–X bond stretch
			ν_4	dp	X–Mg–X bend
MgX_3^-	Pyramidal	C_{3v}	ν_1	p	Mg–X bond stretch
			ν_3	dp	Mg–X bond stretch
			ν_2	p	X–Mg–X bend
			ν_4	dp	X–Mg–X bend
MgX_3^-	Planar	D_{3h}	ν_3	dp	Mg–X bond stretch
			ν_1	p	Mg–X bond stretch
			ν_4	dp	X–Mg–X bend

[a] Raman inactive vibrations are not listed. [b] Vibrations are listed in their usual order of occurrence by frequency, highest first. It is recognized that exceptions to these orderings exist. [c] p = polarized; dp = depolarized.

A clue to the existing structure may be found among the primarily bond-bending frequencies. The band envelope in the low-frequency region of the spectra for $MgCl_2$–KCl and $MgBr_2$–KBr melts with $X^-/Mg^{2+} \geq 4.0$ is depolarized but poorly resolved. It is possible that in both systems this envelope is composed of more than one vibrational mode; however, this cannot be demonstrated with certainty. The observation of one polarized primarily Mg–X stretching mode and at least one depolarized primarily bond-bending mode for Cl^-/Mg^{2+} and $Br^-/Mg^{2+} \geq 4.0$ make the Raman spectra of $MgCl_n^{(2-n)}$ and $MgBr_n^{(2-n)}$ consistent with all the structures in Table I and incomplete in terms of any one of these structures.

For the MgI_2–KI melts investigated here, the situation is somewhat different in the bending region. Two well-resolved, depolarized bands are observed. Although the depolarized primarily stretching mode is not observed, the spectra are nonetheless consistent only with tetrahedral MgI_4^{2-}, the only structure in Table I characterized by two depolarized bending modes. The extension of the conclusions for the MgI_2–KI system to the chloride and bromide systems appears to be reasonable. If indeed four iodide ions are required to effectively shield an Mg^{2+} ion, Mg(II) must be expected to coordinate at least four chloride ions or four bromide ions. Therefore, the results presented here are considered to be in closest agreement with the conclusions of Kleppa and McCarty[16] and of Bredig[12] that $MgCl_4^{2-}$ is the predominant complex in $MgCl_2$–KCl melts. The predominance of $MgBr_4^{2-}$ in $MgBr_2$–KBr melts is also implied.

Acknowledgments. The authors are indebted to M. A. Bredig for helpful discussions pertaining to the conclusions of this investigation. The support and encouragement of Drs. R. C. Vogel and A. D. Tevebaugh are gratefully acknowledged. This work was performed under the auspices of the U. S. Atomic Energy Commission.

(22) This generalization is based on a review of extended compilations of vibrational data for metal–halogen complexes. See, for example, K. Nakamoto, "Spectra of Inorganic and Coordination Compounds," Wiley, New York, N. Y., 1963, pp 86, 106, and 114.

(23) We have recently obtained spectra of $MgCl_2$–KCl melts with $Cl^{-1}/Mg^{2+} = 4.0$ using the 5145-Å line of an argon ion laser. These spectra show a broad depolarized band centered near 331 cm^{-1} which is probably due to the antisymmetric stretching vibration. Also, because of the greater exciting power of the argon ion laser, we have been able to significantly reduce our slit widths and our noise level so that we can now resolve the band in the 75–175-cm^{-1} region into two depolarized components. Our studies using the the argon ion laser will be extended to the $MgBr_2$–KBr system and, if possible, to the MgI_2–KI system. We plan to publish these results as soon as possible.

NOTES

Concentration Dependence of Vapor Pressure Isotope Effect of Methylamine and *N*-Deuteriomethylamine in Hexane

by H. Wolff

Physikalisch-Chemisches Institut, Universität Heidelberg, 69 Heidelberg, Germany *(Received July 13, 1970)*

Publication costs borne completely by The Journal of Physical Chemistry

The concentration dependence of the vapor pressure isotope effect of dimethylamine and *N*-deuteriodimethylamine in hexane was described[1] by the two-state function

$$\frac{p}{p'} = \left(\frac{p}{p'}\right)_{\text{bonded}}^{1-x} \left(\frac{p}{p'}\right)_{\text{free}}^{x} \quad (1)$$

where p/p' is the ratio of partial pressures of the heavy (p) and of the light (p') isotopic compound at the fraction x of molecules with free amino groups. $(p/p')_{\text{free}}$ and $(p/p')_{\text{bonded}}$ are the ratios at the limit of dilution and at the hypothetical state of complete association which can be calculated from the intramolecular vibrations of gaseous compounds and from the inter- and intramolecular vibrations of monomers or associated compounds in the liquid state. In order to check eq 1 in more detail the ratios of methylamine and *N*-deuteriomethylamine in solution with hexane were investigated. Equation 1 takes into account only two forms of the associating component and can be used for the methylamine solutions since according to infrared and Raman measurements[2-4] molecules with free groups and molecules forming a bond to only one H or D atom of the amino group are present. However, molecules forming bonds to both atoms are absent.[4c,5,6]

ln p/p' was plotted *vs.* the fraction x of molecules with free groups. If eq 1 is valid, a straight line must result since eq 1 can be formulated as

$$\ln p/p' = x \ln \frac{(p/p')_{\text{free}}}{(p/p')_{\text{bonded}}} + \ln (p/p')_{\text{bonded}} \quad (2)$$

The ratios of partial pressures determined at +20 and −10° in the investigations of ref 6 were used. The ratios at −10° are not given explicitly in this reference; therefore the values are reproduced with those at +20° in Figure 1. The fractions x of free groups at the temperatures of +20° and −10° resulted from

$$x = \beta_1 + {}^1/_2\beta_2 + {}^1/_3\beta_3 + {}^1/_4\beta_4 + {}^1/_5\beta_{\text{residual}} \quad (3)$$

an expression which was extended with respect to our former treatment.[1] It implies that each of the associated forms contains one amino group not engaged in association. β_1, β_2, β_3, and β_4 are the fractions of monomers, dimers, trimers, and tetramers, respectively. β_{residual} is defined as $1 - (\beta_1 + \beta_2 + \beta_3 + \beta_4)$. The values of β_1 to β_4 for the mole fractions of methylamine from $x_1 = 0.1$ to $x_1 = 0.3$ were taken from ref 7 where

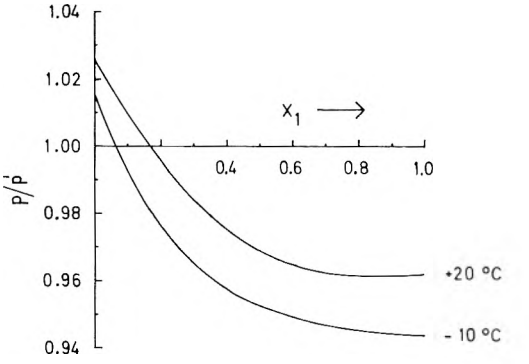

Figure 1. p/p' of CH_3ND_2 and CH_3NH_2 in hexane *vs.* mole fraction x_1 of methylamine according to ref 6.

they are calculated from the activity coefficients and from the association constants $K_{\nu-1,\nu}{}^{x} = x_\nu/x_{\nu-1}\cdot x_1$ (x_ν is the mole fraction of the ν-mer) assuming CH_3NH_2/C_6H_{14} as an ideal associated solution. (The β_i's do not change noticeably, whereas the association constants may do so if in the calculation of the activity coefficients according to Barker,[8] a representation of the coefficients by the equations of Redlich and Kister,[9] is chosen with five instead of three constants as in our

(1) H. Wolff and R. Würtz, *J. Phys. Chem.*, **74**, 1600 (1970).

(2) H. Wolff and U. Schmidt, *Ber. Bunsenges. Phys. Chem.*, **68**, 579 (1964).

(3) (a) H. Wolff and D. Horn, *ibid.*, **71**, 467 (1967); (b) **72**, 419 (1968).

(4) (a) H. Wolff and D. Staschewski, *ibid.*, **65**, 840 (1961); (b) *ibid.*, **66**, 140 (1962). (c) This result has been derived from the observation that the shift to lower wave number with association is greater for the symmetric NH_2 vibration than for the antisymmetric NH_2 vibration.[2-4b,5] The observation has been made for solutions of methylamine with hexane[4a,4b] as well as for solutions with other solvents.[2,3,6] In solutions, *e.g.*, in carbon tetrachloride where the amine is thought to associate with the solvent, the degree of self-association is lowered only.

(5) H. Wolff and J. Eints, *Ber. Bunsenges. Phys. Chem.*, **70**, 728 (1966).

(6) H. Wolff and A. Höpfner, *ibid.*, **69**, 710 (1965).

(7) H. Wolff and A. Höpfner, *ibid.*, **66**, 149 (1962).

(8) J. A. Barker, *Aust. J. Chem.*, **6**, 207 (1953).

(9) O. Redlich and A. T. Kister, *Ind. Eng. Chem.*, **40**, 345 (1948).

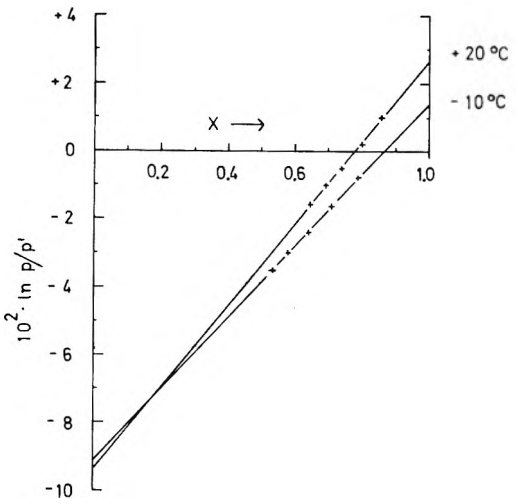

Figure 2. ln p/p' of CH_3ND_2 and CH_3NH_2 in hexane *vs.* fraction x of molecules with free amino groups; + = points calculated at x_1 = 0.10, 0.15, 0.20, 0.25, and 0.30.

treatment, *cf.* ref 10.) Table I gives the x values which we have obtained. Figure 2 shows ln p/p' *vs.* x.

Table I: Fractions x of Free Groups of CH_3NH_2 in Hexane According to Eq 3

Mole fraction x_1 of CH_3NH_2 in C_6H_{14} soln	β_1	β_2	β_3	β_4	β_{resid}	Fraction x of free groups ($\beta_1 + {}^1/_2\beta_2 + {}^1/_3\beta_3 + {}^1/_4\beta_4 + {}^1/_5\beta_{resid}$)
			+20°C			
0.10	0.746	0.177	0.053	0.021	0.002	0.858
0.15	0.653	0.207	0.083	0.044	0.013	0.799
0.20	0.575	0.219	0.105	0.067	0.034	0.744
0.25	0.509	0.220	0.120	0.088	0.064	0.694
0.30	0.451	0.213	0.127	0.101	0.108	0.647
			−10°C			
0.10	0.653	0.202	0.082	0.044	0.020	0.796
0.15	0.539	0.211	0.109	0.075	0.066	0.713
0.20	0.451	0.204	0.121	0.095	0.129	0.643
0.25	0.381	0.189	0.123	0.106	0.201	0.584
0.30	0.324	0.171	0.119	0.110	0.275	0.533

A linear dependence of ln p/p' on x is indeed observed. The values of 1.02_6 (ln $p/p' = 0.02_6$) at +20° and of 1.01_4 (ln $p/p' = 0.01_4$) at −10° are obtained by extrapolation from Figure 2 for p/p' at $x = 1$. They agree fairly well with the approximate value of 1.02 which was calculated from the solvent shift of the intramolecular vibrations.[11] The value of approximately 0.91 (ln $p/p' \approx -0.09$) is obtained by extrapolation from Figure 2 for p/p' at $x = 0$ for both temperatures. This ratio is smaller than the ratios of 0.96_2 and 0.94_4 measured for the undiluted compounds since it corresponds to complete association. Conversely, using the curves of Figure 2, the fractions of free groups of 0.46 and 0.33 at +20 and −10° are obtained from the measured values of 0.96_2 and 0.94_4 (ln $p/p' = -0.03_9$ and -0.05_8). These fractions are somewhat higher than expected, but they are smaller than the fractions of free groups of undiluted dimethylamines which have been found to be 0.64 and 0.44 between +20 and −20°.[1] The smaller values may be explained by the stronger association of methylamine which has been pointed out previously.[12] Insofar as these results permit a judgment, the dependence of the vapor pressure isotope effect of methylamine and *N*-deuteriomethylamine in hexane on concentration is also shown in eq 1. The model of association used in the calculation is thus supported.

(10) H. Wolff and A. Höpfner, *Ber. Bunsenges. Physik. Chem.*, **71**, 461 (1967).
(11) H. Wolff, *ibid.*, **73**, 399 (1969).
(12) H. Wolff and H.-E. Höppel, *ibid.*, **70**, 874 (1966).

Kinetics of the Proton-Transfer Reactions of Serine and Threonine

by R. D. White, L. J. Slutsky,* and S. Pattison

Department of Chemistry, University of Washington, Seattle, Washington 98105 *(Received August 31, 1970)*

Publication costs borne completely by The Journal of Physical Chemistry

Recently there has been a certain amount of discussion of the role of perturbation of the proton-transfer equilibria of basic residues in determining the overall relaxation spectrum of proteins in aqueous solution.[1,2] The rates of the diffusion-controlled proton-transfer reactions of amino acids

$$-R-NH_3^+ + OH^- \underset{k_b}{\overset{k_f}{\rightleftarrows}} -R-NH_2 + H_2O \quad (1)$$

are also of some interest in their own right. We wish to present values of k_f, k_b, and the standard volume change ΔV for the proton-transfer reactions of serine and threonine and briefly discuss the possible utility of these results and similar results for amino acids and simple peptides in the interpretation of the relaxation spectra of more complex systems.

In the absence of significant dispersion the ultrasonic absorption, α, due to a single process with relaxa-

(1) R. Zana and J. Lang, *J. Phys. Chem.*, **74**, 2735 (1970).
(2) (a) F. Dunn and L. W. Kessler, *ibid.*, **74**, 2736 (1970); (b) L. W. Kessler and F. Dunn, *ibid.*, **73**, 4256 (1969).

tion time, τ, may be expressed as a function of the frequency (f) by[3]

$$\frac{\alpha}{f^2} = A + \frac{C\tau}{1 + (2\pi\tau f)^2} \qquad (2)$$

where A represents the attenuation due to the viscosity and the thermal conductivity of the medium. For the process represented by eq 1

$$C = 2\pi^2\rho c_0\bar{V}^2RT\Gamma_M[(\beta\Delta H/C_pRT) - (\Delta V/\bar{V}RT)]^2$$

$$\Gamma_M = (M_{OH^-}{}^{-1} + M_{R-NH_3^+}{}^{-1} + M_{R-NH_2}{}^{-1})^{-1} \qquad (3)$$

where ρ is the density, c_0 the velocity of sound, $\bar{V}$ the volume per mole of solution, β the coefficient of thermal expansion, C_p the molar heat capacity at constant pressure, the M's molar concentrations of reactants, and ΔH and ΔV the enthalpy and volume changes for the process in question. The enthalpy change for the process represented by eq 1 is 1.3 kcal/mol; the volume change is 20–30 cc/mol. In aqueous solution near room temperature, where β is relatively small, neglect of the first term in the square brackets in eq 3 alters the calculated value of ΔV by less than 2%. The relaxation time in terms of the constants which appear in eq 1 is

$$\tau = [k_f(M_{OH^-} + M_{R-NH_3^+}) + k_b]^{-1} \qquad (4)$$

Ultrasonic absorption in solutions of serine and threonine at 25° as a function of frequency and pH is presented in Figure 1. Equation 2 is linear in A and C and least-squares values of these constants corresponding to any assumed value of τ are easily calculated. It is a simple matter to vary τ until an optimal set of parameters is arrived at. The solid curves in Figure 1 represent the result of least-squares adjustment of the constants of eq 2; the values of the parameters being $A = 21.6 \times 10^{-17}$ neper sec^2/cm, $C\tau = 90.4 \times 10^{-17}$ neper sec^2/cm, and $\tau = 8.5 \times 10^{-9}$ sec for serine. The corresponding values for threonine are $A = 26.8 \times 10^{-17}$, $C\tau = 82.0 \times 10^{-17}$, and $\tau = 9.7 \times 10^{-9}$. Equation 2 gives quite a good description of the data in the frequency range considered and there is no reason to believe that more than one process contributes significantly to α.

The frequency dependence of α has been determined at pH sufficiently high (11.45) so that the equilibrium concentration M_{R-NH_2} can be taken to be the analytic concentration (0.5 M). The concentrations of hydroxide ion and R–NH_3^+ are calculated from the pH determined by a Beckman SS-2 meter and 39003 electrode assuming the activity coefficients to be one. Values of the rate constants calculated from the parameters of eq 2 are listed in Table I. If these values are used in conjunction with eq 3 and 4 to compute absorption as a function of pH, the broken curve in Figure 1 results. The agreement with the experimental pH dependence is good enough to nominate perturbation of

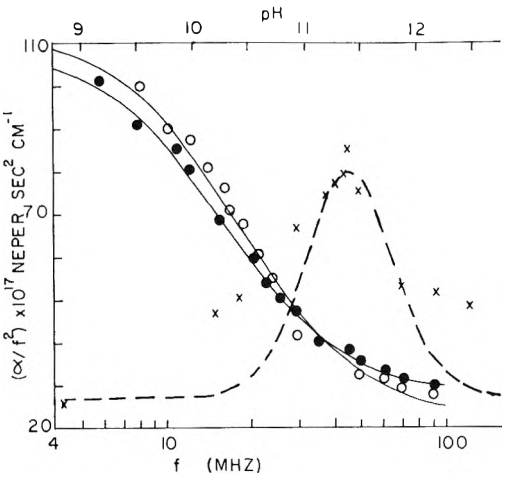

Figure 1. Ultrasonic attenuation at 25° and pH 11.45 in 0.5 M serine (open circles) and threonine (closed circles) as a function of frequency. The crosses represent the pH dependence of the attenuation in 0.5 M threonine at 12.25 MHz. The broken curve represents the pH dependence deduced from eq 2–4.

Table I: Experimental and Calculated Rate Constants for Proton-Transfer Reactions of R–NH_3^+

	k_{12}, M^{-1} sec^{-1} × 10^{-10}	k_f, M^{-1} sec^{-1} × 10^{-10}	k_b (calcd), sec^{-1} × 10^{-6}	k_b, sec^{-1} × 10^{-6}	pK_a[a]
Triglycine[b]	2.0	2.1	0.14	0.18	7.91
Threonine	2.1	2.0	2.5	2.6	9.10
Serine	2.1	2.2	2.8	3.1	9.15
Glycine[b]	2.2	1.9	14	8.0	9.60
Piperidine[c]	2.1	2.2	298	300	11.21

[a] M. Katake, Ed., "Constants of Organic Compounds," Asakura Publishing Co., Tokyo, 1953. [b] Reference 7. [c] Reference 6.

the proton-transfer equilibrium as the significant source of excess acoustic absorption.

Debye[4] has derived an expression for the diffusion-controlled rate of reaction of ions in solution, and Eigen[5] has considered the reverse process of dissociation to form ions. Their results are, respectively

$$k_{12} = \frac{\sigma 4\pi N z_A z_B e_0{}^2(D_A + D_B)}{\epsilon kT[\exp(z_A z_B e_0{}^2/\epsilon r_d kT) - 1]}$$

$$k_{21} = \frac{\sigma 3 z_A z_B e_0{}^2(D_A + D_B)}{\epsilon kT r_d{}^3[1 - \exp(-z_A z_B e_0{}^2/\epsilon r_d kT)]} \qquad (5)$$

where N is Avogadro's number, σ a steric factor, e_0 is the electronic charge, z_A and z_B are the algebraic charges of

(3) K. F. Herzfeld and T. A. Litovitz, "Absorption and Dispersion of Ultrasonic Waves," Academic Press, New York, N. Y., 1959.
(4) P. Debye, *Trans. Electrochem. Soc.*, **82**, 265 (1942).
(5) M. Eigen and G. G. Hammes, *Advan. Enzymol.*, **25**, 1 (1963).

the ions, ϵ is the dielectric constant of the solvent, D_A and D_B are the diffusion coefficients of the reacting ions, and r_d is an effective radius for reaction.

The kinetics of a number of proton-transfer reactions of the -NH_3 group[6,7] have been rationalized in terms of a "mechanism"

$$-R-NH_3^+ + OH^- \underset{k_{21}}{\overset{k_{12}}{\rightleftharpoons}} -R-NH_3^+-OH^- \underset{k_{32}}{\overset{k_{23}}{\rightleftharpoons}} -R-NH_2 + H_2O \quad (6)$$

the rate constants of the first step being adequately described by Debye's theory of diffusion-controlled association reactions.[6] If the proton-transfer in the ion pair is very fast, then the rate constants for the overall reaction may be expressed in terms of the constants which appear in eq 6 as $k_f = k_{12}$, $k_b = k_{21}/(1 + K_{23})$ where $K_{23} = k_{23}/k_{32}$. The forward rate is just the diffusional rate, the reverse rate is the diffusional rate diminished by an equilibrium constant, hopefully simply related to the pK_a of the amino group, which expresses the predominance of free amine and water over ion pair.

Equation 5, with the reaction radius taken to be a hydrogen bond distance (2.7 Å) and a steric factor of 0.4–0.6, has been found to give good values of k_f for a number of amines, amino acids, and simple peptides,[6,7] some representative results being given (for $r_d = 2.7$, $\sigma = 0.6$) in Table I. The values of k_{12} for serine and threonine calculated from eq 5 on this basis also are seen to be in quite good agreement with the experimental values of k_f.

The expression $\log K_{23} = 14.2 - pK_a$, used in conjunction with the Debye–Eigen theory, has been found to give a good account of k_b for amines, amino acids, and peptides with pK_a's ranging from 7.9 (triglycine), to 11.2 (piperidine). The values of k_b for serine and threonine calculated in this way [k_b (cal) in Table I] are also seen to be in fairly good agreement with experiment. Thus, it would appear that it is possible to make a reasonable estimate of k_f, k_b, and, by means of eq 4, τ as a function of pH, if the pK_a of a given amine group is known. The volume change for the reaction represented by eq 1 is 22.3 cc/mol for threonine, 24.2 cc/mol for serine as compared with 28 cc/mol for ammonia, 27 cc/mol for methylamine, 21 cc/mol for β-alanine, γ-aminobutyric acid, and for $H^+ + OH^- \rightarrow H_2O$.[7] It would seem that with eq 1–6, using a reaction radius of 2.7 Å, a steric factor of 0.6, and a volume change of 25 cc/mol, and taking $D_A + D_B$ equal to the diffusion coefficient of the hydroxide ion, one can expect to compute the magnitude and frequency and pH dependence of ultrasonic absorption due to proton-transfer reactions of basic groups within an accuracy of about 30%. For data such as those presented by Zana and Lang[1] and Dunn and Kessler[2] it should be possible to approximately deduct the effect of proton transfer, insofar as it is independent of conformational change, and to deal with the remaining excess absorption.

(6) (a) M. Eigen and L. de Maeyer, "Technique of Organic Chemistry," Vol. VIII, Part 2, A. Weissberger, Jr., Ed., Wiley, New York, N. Y., 1961, p 1032; (b) M. Eigen, *Angew. Chem.*, **75**, 489 (1963).

(7) K. Applegate, L. J. Slutsky, and R. C. Parker, *J. Amer. Chem. Soc.*, **90**, 6909 (1968).

COMMUNICATIONS TO THE EDITOR

Electron Spin Resonance Study of the Photolysis of Formaldazine

Publication costs assisted by The University of Iowa

Sir: Formaldazine appears to be particularly interesting as an analog of butadiene, but investigations concerning this molecule are reported only in two short communications.[1,2] One of them reported the photolysis of formaldazine, resulting in the speculation of the production of the methylene imino radical as an intermediate in the photolysis.

In the present study, the photolysis of formaldazine was followed by electron spin resonance, and the identification of the methylene imino radical was made. The dependence of the production of the methylene imino radical on irradiated wavelength in the rigid matrix at −196° was observed.

The electron spin resonance spectra were measured using an X-band homemade spectrometer of 455-kHz field modulation and with a 30-cm electromagnet of Japan Electron Optics Laboratory Co. The maximum value of radiofrequency field in this spectrometer was 25 mW. The electron spin resonance spectra were measured in such modulation amplitudes as resonance lines were not broadened and distored. The sample was held in a quartz dewar with an unsilvered lower section and kept at a suitable low temperature. The irradiation of the samples was carried out using a 1-kW high-pressure mercury lamp. Wavelengths were selected by Toshiba glass filters.

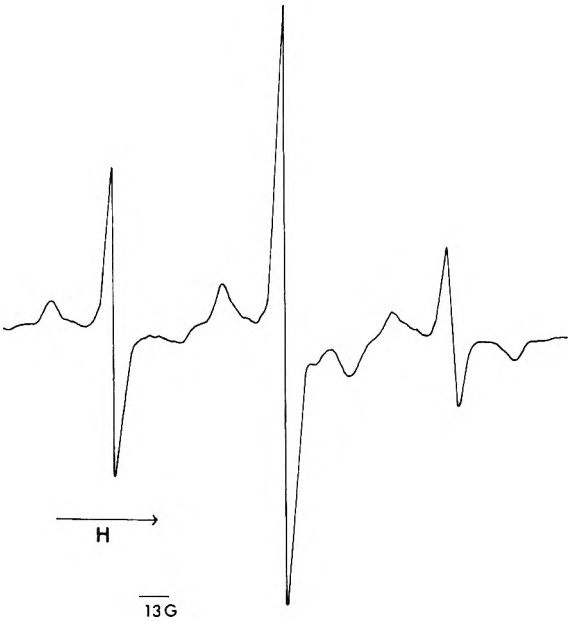

Figure 1. Esr spectrum (−196°).

The electron spin resonance spectrum of formaldazine irradiated for 2 hr is shown in Figure 1.

The spectrum is a triplet of triplets and is shown to be due to the $CH_2{=}N\cdot$ radical. This result is consistent with that of Cochran, *et al.*, who prepared methylene imino radical by photolyzing at 4.2°K a solid deposit containing 1% HI, 9% HCN, and 90% argon.[3]

No change of this spectrum was noticed on photobleaching with visible light and ultraviolet light above 3200 Å. This suggests that no radical except the methylene imino radical may be present in the primary reaction, and no secondary reaction may occur in these regions. The radical disappeared within a few seconds on warming at −78°. This shows that the methylene imino radical can defuse and react at −78° and a secondary reaction occurs. Formaldazine was not photolyzed on irradiation with a light above 3200 Å, indicating that 2537 Å is an effective wavelength for photolyzing formaldazine.

The uv spectrum of formaldazine is shown in Figure 2.

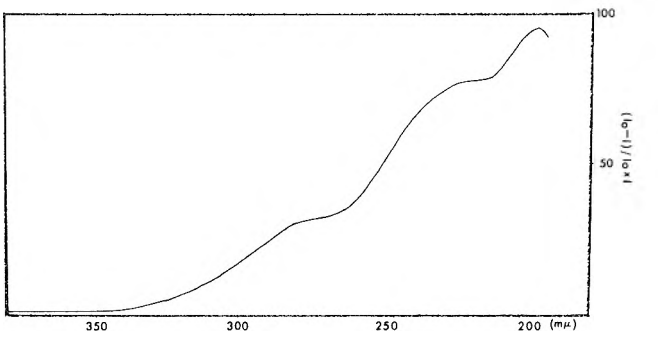

Figure 2. Uv spectrum of formaldazine (gas).

The comparison of this spectrum with that of butadiene or unsaturated ketone shows that the absorption band at about 2700 Å is reasonably assigned to be an $n \rightarrow \pi^*$ transition.[4] Therefore, the effective wavelength corresponds to the $n \rightarrow \pi^*$ transition.

Inferences of the mechanism were made from the consideration of these facts and the products obtained from the photolysis.

(1) N. P. Neureiter, *J. Amer. Chem. Soc.*, **81**, 2910 (1959).

(2) J. F. Ogilve, *Chem. Commun.*, 359 (1965).

(3) E. L. Cochran, F. J. Adrian, and V. A. Bowers, *J. Chem. Phys.*, **36**, 1938 (1962).

(4) H. H. Jaffe and M. Orchin, "Theory and Application of Ultraviolet Spectroscopy," Wiley, New York, N. Y., 1962, pp 196–207.

In the photolysis of formaldazine, methyleneimine and hydrogen cyanide were obtained. Therefore, the excitation of formaldazine by the light of 2537 Å is followed by rapid intramolecular transfer and then bond scission before the molecule returns to the ground state.

$$CH_2{=}N{-}N{=}CH_2 \xrightarrow[2537\ \text{Å}]{h\nu} (CH_2{=}N{-}N{=}CH_2)^*$$

$$(CH_2{=}N{-}N{=}CH_2)^* \longrightarrow 2CH_2{=}N\cdot$$

$$2CH_2{=}N\cdot \longrightarrow CH_2{=}NH + HC{\equiv}N$$

The details of the nature and the reactivity of methylene imino radical will be reported at a later date.

Acknowledgment. The authors are greatly indebted to Professor Kozo Hirota for his encouragement.

(5) Author to whom correspondence should be addressed at the Department of Chemistry, The University of Iowa, Iowa City, Iowa 52240.

FACULTY OF SCIENCE
OSAKA UNIVERSITY
TOYONAKA, OSAKA, JAPAN

MIKIHARU KAMACHI*[5]
KEIJI KUWATA
SHUNSUKE MURAHASHI

RECEIVED JUNE 10, 1970

Electron Paramagnetic Resonance Probes for Hydrophobic Interaction in Aqueous Solutions

Publication costs borne completely by the Journal of Physical Chemistry

Sir: Aqueous solutions of hydrophobic solutes or solutes with substantial hydrophobic groups exhibit a number of remarkable properties[1] among which is a relatively large $d\eta/dm$, increase in viscosity η with molality m, even at low m. While one expects to be able to trace this back to the local influence of the hydrophobic solute particle upon neighboring water molecules (its "cosphere"), nothing is known in detail either of the nature of the influence nor of the size of the cosphere. Such solutions also show a large sound absorption, in one case arising from a process as slow as 10^9 Hz at 0°,[2] which might be due to a slow relaxation process in the cospheres or to a slowly relaxing interaction of two or more hydrophobic particles. This suggests that an epr probe might be useful for the study of the dynamics of these solutions since it might just enable one to get away from the extreme narrowing limit characteristic of the widely investigated nmr probes in this problem, in which one sees only a global response not so different from the viscosity.[3]

We have studied the epr spectra of relevant solutions of several hydrophobic epr probes, typically 2,2,6,6-tetramethyl-4-piperidine-1-oxyl, a stable nitroxide radical, and bispicolinato vanadyl. Only small changes in epr spectra are found, with no new lines, even at 0°. Careful measurements on these spectra do show changes which may be helpful in elucidating the interactions of hydrophobic groups with water and with each other. For example, the procedure of Stone, *et al.*,[4] for getting the tumbling correlation time τ from the nitroxide spectra leads to the results in Figure 1.

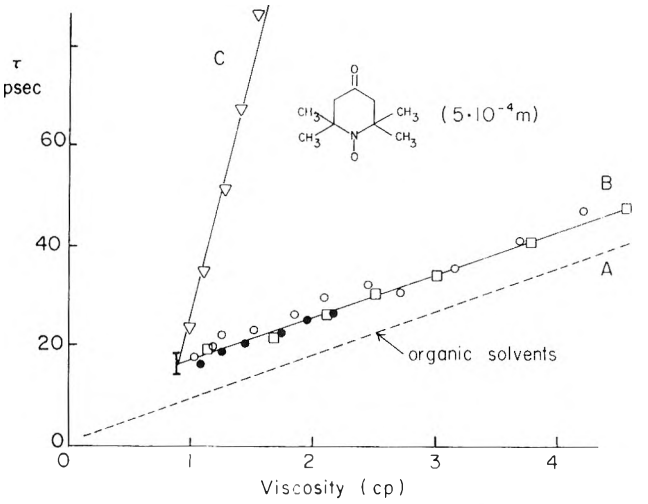

Figure 1. Rotational correlation time of the nitroxide probe in various media at 25°: □, aqueous glycerine (0–50 wt %); ●, aqueous *tert*-butanol (0–3 *m*); ○, aqueous Bu_4NBr (0–1.4 *m*); ▽, aqueous $NaBPh_4$ (0–0.5 *m*). Aqueous solutions of Ph_4AsCl and Ph_4PCl, although not shown, also lie on line B. Line A is the best line drawn through points representing the following solvents, having viscosities from 0.5 to 3.5 cP: MeOH, CCl_4, EtOH, dodecane, $PhNO_2$, DMSO, propylene carbonate, *n*-BuOH, formamide, and $PhNH_2$.

Comparison of lines A and B in Figure 1 shows that τ is larger for the probe in aqueous solutions than in nonaqueous solvents when compared at the same viscosity. Since the probe molecule itself has hydrophobic regions, this may be a manifestation of the local influence of hydrophobic groups on water. In the aqueous solutions containing a second hydrophobic species (line B) the composition dependence of τ is very nearly given by Walden's rule τ/η = constant as verified by including the data for glycerol solutions. These are so concentrated, unlike solutions of hydrophobic species of the same viscosity, that they are likely to be dynamically homogeneous because most water molecules are next to a glycerine molecule and *vice versa*. Relaxation measurements on aqueous glycerol[5] are

(1) For a recent contribution see S. Lindenbaum, *J. Phys. Chem.*, **74**, 3027 (1970).

(2) J. Stone and R. E. Pontinen, *J. Chem. Phys.*, **47**, 2407 (1967).

(3) H. G. Hertz, "Progress in N. M. R. Spectroscopy," Vol. 3, J. W. Emsley, J. Feeney, and L. H. Sutcliffe, Ed., Pergamon Press, London, 1967, p 159.

(4) T. J. Stone, T. Buckman, P. L. Nordio, and H. M. McConnell, *Proc. Nat. Acad. Sci., U. S.*, **54**, 1010 (1965).

(5) T. A. Litovitz and C. M. Davis in "Physical Acoustics," Vol. IIA, W. P. Mason, Ed., Academic Press, New York, N. Y., 1965, p 281; G. E. McDuffie, R. G. Quinn, and T. A. Litovitz, *J. Chem. Phys.*, **37**, 239 (1962).

consistent with this view. These results are all negative in the sense that getting microscopic information about hydrophobic interactions from them depends more on the power of the theory which may be applied than anything else.

A more promising result is shown by line C in Figure 1, which gives evidence of a probe, BPh_4^- interaction markedly at variance with Walden's rule behavior. This can be discussed in terms of the expression

$$d\tau/dm \sim \int g_{PH}(r)e_{PH}(r)d^3r$$

where g_{PH} is the equilibrium pair correlation function for the probe P and the other hydrophobic species H and e_{PH} is a measure of the effect of H upon τ of P at the separation r. It remains to learn in this case whether the extra interaction compared to line B is more due to hydrophobic binding ($g_{PH} \gg 1$ at some r) or to a slowly relaxing cosphere of the hydrophobic species [large $e_{PH}(r)$ at some r]. It is hoped that this can be elucidated by more detailed epr studies.

A most surprising feature of the present results is the marked difference in behavior of BPh_4^- and such similar species as $AsPh_4^+$ which are found near line B.

Using $VOPi_2$ as the probe, aqueous glycerine and *tert*-butyl alcohol are again indistinguishable at the same viscosity while Bu_4NBr solutions deviate markedly from the Walden's rule behavior.

(6) Fellow of the National Research Council of Canada, 1969–1970.

(7) The support of this research by the National Institutes of Health is gratefully acknowledged.

DEPARTMENT OF CHEMISTRY
STATE UNIVERSITY OF NEW YORK
AT STONY BROOK
STONY BROOK, NEW YORK 11790

CARMEL JOLICOEUR[6]
HAROLD L. FRIEDMAN*[7]

RECEIVED AUGUST 10, 1970

The Relationship between the Acentric Factor and the Entropy of Vaporization

Publication costs borne completely by The Journal of Physical Chemistry

Sir: The acentric factor, ω, was introduced by Pitzer[1,2] as an imperical factor to characterize the deviation of molecules from spherical symmetry. The factor is defined as

$$\omega = \log p_r^\circ(0.7) - 1.00 \qquad (1)$$

where $p_r^\circ(T_r)$ is the reduced vapor pressure at the reduced temperature, T_r. The particular method of defining ω, results from the experimentally observed fact that for spherically symmetrical molecules such as Xe, Ar, and Kr, ω is essentially zero. For nonspherically symmetrical molecules, $\omega > 0$.[2] Any thermodynamic property of a large number of fluids (with the exception of associated fluids, or fluids containing molecules of high dipole moment) can be characterized as a function of the three parameters T_r, p_r, and ω.

Pitzer[3,4] has shown that a group of molecules will obey the principle of corresponding states if they obey Boltzmann statistics, are approximately spherically symmetrical (*i.e.*, the rotational, vibrational, and translational partition functions are separable), and have intermolecular potential of the same general form, *i.e.*

$$\frac{U}{kT} = \sum_{ij} \frac{U_{ij}}{kT} = \sum_{ij} \frac{\epsilon}{kT} f\left(\frac{r_{ij}}{\sigma}\right)$$

where ϵ and σ are energy and distance parameters, and f is any general function.

For a molecular species obeying the above assumptions, the entropy of vaporization, Δs, at a constant ratio of saturated gas to liquid molar volume should be constant. This has indeed been verified by examining the inert gases Ar, Kr, and Xe, where Δs at a gas to liquid molar volume ratio of 335.0 has been found to be 18.67, 18.60, and 18.66, respectively.[5]

Therefore, a measure of the nonideality of a given molecular species may be obtained if Δs is examined at a constant gas to liquid molar volume ratio. Choosing a ratio of 335.0, the inherent problem which remains is finding that point in p–V–T space where this ratio is satisfied. This can be accomplished by solving the following set of equations.

$$\frac{V_g}{V_l} = \frac{ZRT}{p^\circ V_l} \qquad (2)$$

$$V_l^{-1} = \frac{1}{M}(\alpha + \beta(T - T_0) + \delta(T - T_0)^2) \qquad (3)$$

$$\ln p^\circ = A + \frac{B}{C + T} \qquad (4)$$

$$\Delta s = 0.024218 V_l \frac{dp^\circ}{dT}\left(\frac{V_g}{V_l} - 1\right) \qquad (5)$$

In the above, p° is the vapor pressure of the pure component, Z is the compressibility factor, M is the molecular weight, and T is the temperature. For a given ratio of V_g/V_l, there exists only one unique solution for T, which can be found by solving eq 2, 3, and 4. This was done using the Newton–Raphson

(1) K. S. Pitzer, *J. Amer. Chem. Soc.*, **77**, 3427 (1955).

(2) K. S. Pitzer, D. Z. Lippmann, R. F. Curl, C. M. Huggins, and D. E. Peterson, *ibid.*, **77**, 3433 (1955).

(3) K. S. Pitzer, *J. Chem. Phys.*, **7**, 583 (1939).

(4) G. N. Lewis and M. Randall, "Thermodynamics," 2nd ed, revised by K. S. Pitzer and L. Brewer, McGraw-Hill Book Co., New York, N. Y., 1961, p 605.

(5) J. H. Hildebrand and R. L. Scott, "Regular Solutions," Prentice-Hall, Englewood Cliffs, N. J., 1962, p 75.

iterative procedure, on the SDS 940 computer. The density constants α, β, and δ were taken from ref 6. The vapor pressure constants for the Antoine equation, A, B, and C, were taken from NBS Bulletin 510.[7] The results of this procedure, for a gas to liquid molar volume ratio of 335.0, are shown in Table I. As can be seen, a linear relationship does exist between the empirically derived acentric factor, ω, and the entropy ($\Delta s^{VAP} - 18.00$) required to vaporize a nonspherically symmetrical molecule. For spherically symmetrical atoms or molecules both ($\Delta s^{VAP} - 18.00$) and ω approach zero. From these results, it appears that

Table I

Compound	T, °K	Δs, eu	ω(calcd)	ω
n-C_2	180.7	19.05	0.0815	0.105
n-C_3	224.4	19.85	0.147	0.152
n-C_4	261.4	20.32	0.189	0.201
n-C_5	294.8	21.14	0.255	0.298
n-C_6	325.6	21.52	0.285	0.290
n-C_7	352.3	22.40	0.358	0.352
n-C_8	376.5	22.72	0.383	0.398
n-C_9	398.3	23.48	0.445	0.441
n-C_{10}	418.8	23.88	0.478	0.586
n-C_{11}	437.8	24.46	0.525	0.530
n-C_{12}	456.0	24.76	0.550	0.553
n-C_{13}	472.0	25.37	0.598	0.593
n-C_{14}	488.1	25.75	0.630	0.626
n-C_{15}	502.1	26.21	0.667	0.650
n-C_{16}	515.9	26.52	0.693	0.704
n-C_{17}	529.9	26.95	0.728	0.763
n-C_{20}	562.8	27.96	0.81	0.710
Neopentane	266.9	20.61	0.212	0.195
3-Methylhexane	346.1	21.83	0.311	0.327
3-Ethylpentane	348.1	21.82	0.310	0.314
2,2-Dimethylpentane	332.5	21.33	0.271	0.300
2,4-Dimethylpentane	333.9	21.60	0.293	0.307
3,3-Dimethylpentane	340.1	21.53	0.271	0.284
2,2,3-Trimethylbutane	334.6	21.11	0.253	0.260
Ethylcyclopentane	362.1	21.58	0.275	0.275
Methylcyclohexane	359.4	20.99	0.243	0.244

$$\Delta s_{335} - \Delta s^{\circ}_{335} = (12.7)\omega \qquad (6)$$

where Δs°_{335} denotes the entropy of vaporization of spherically symmetrical atoms (or molecules) as measured at a gas to liquid molar volume ratio of 335.0.

It was previously noted that at a gas to liquid molar volume ratio of 335.0, the entropy of vaporization of the inert gases Ar, Kr, and Xe are approximately 18.65, and have acentric factors of 0. Equation 6 would project for these elements acentric factors of 0.053. This discrepancy can be resolved by examining the neon atom. The acentric factor, ω, for neon has previously been estimated to be 0.[8] Ne can, however, be determined using eq 1. Over the range $1 < p^{\circ} < 10$ atm, neon vapor pressure data[9] can be accurately fitted to the Clausius–Clapeyron equation, resulting in a value for of -0.057. From eq 6, a value of 0.057 is equivalent to 0.7 eu. This is in excellent agreement with the value (18.65–18.00) eu found experimentally. Thus Δs°_{335}, for these measurements, represents the entropy of vaporization of the carbon atom core, for which $\omega = 0$.

For those data points which vary considerably from the linear relationship, it appears that the ω values are inconsistent rather than Δs. For example, n-$C_{10}H_{22}$ has an acentric factor that is significantly greater than either n-C_9H_{20} or n-$C_{11}H_{24}$, whereas Δs values increase in a continuous fashion.

For polar and associated molecules, there is essentially no correlation between the acentric factor and Δs_{335}. The reason for this is inherent in the initial assumptions. The intermolecular potential for polar molecules cannot be approximated by a simple two-parameter equation, since two parameter potential functions ignore dipole–dipole interactions. Thus any suitable intermolecular potential (such as the Stockmeyer potential function) involves an additional term and is no longer of the same general form as eq 1.

In conclusion, it does appear that the acentric factor, for normal fluids, is a direct measure of the deviation of the entropy of vaporization from the spherically symmetrical molecule.

Acknowledgment. I would like to acknowledge the help of R. Moore in conceiving this study and D. Lebow for his assistance in programming.

(6) E. W. Washburn, Ed., "International Critical Tables," McGraw-Hill Book Co., New York, N. Y., 1926.

(7) Rossini, *et al.*, "Selected Values of Properties of Hydrocarbons and Related Compounds," American Petroleum Institute Research Project 44, Thermodynamic Research Center, Texas A & M University, College Station, Texas.

(8) R. C. Reid and T. K. Sherwood, "The Properties of Gases and Liquids," McGraw-Hill Book Co., New York, N. Y., 1966, p 571.

(9) R. C. Weast, Ed., "Handbook of Chemistry and Physics," Chemical Rubber Publishing Co., Cleveland, Ohio, 1969, p D-145.

SHELL CHEMICAL CO. MORTON SCHRAGER
PLASTICS AND RESINS TECHNICAL CENTER
WOODBURY, NEW JERSEY 08096

RECEIVED AUGUST 19, 1970

Concerning "Kinetics of Isopropyl Alcohol Radicals by Electron Spin Resonance–Flow Techniques"

Publication costs assisted by the National Research Council of Canada

Sir: In their recent paper, James and Sicilio[1] purport to have measured the rates of reaction of the radicals $(CH_3)_2\dot{C}OH$ (R_1) and $CH_3CHOH\dot{C}H_2$ (R_2) with H_2O_2

(1) R. E. James and F. Sicilio, *J. Phys. Chem.*, **74**, 1166 (1970).

in the system aqueous Ti(III)–H_2O_2–2-propanol. It is the purpose of this communication to demonstrate that the kinetic analysis and the conclusions drawn by the authors are inconsistent with their own data and with previous work in the field and to present an alternative interpretation of their observations.

The kinetic analysis by the authors is based upon the following assumed mechanism

$$\text{Ti(III)} + H_2O_2 \longrightarrow \text{Ti(IV)} + OH^- + OH \quad (1)$$

$$OH + \text{2-propanol} \longrightarrow H_2O + R_1 \quad (5)$$

$$OH + \text{2-propanol} \longrightarrow H_2O + R_2 \quad (6)$$

$$R_1 + H_2O_2 \longrightarrow \text{termination} \quad (7)$$

$$R_2 + H_2O_2 \longrightarrow \text{termination} \quad (8)$$

and is dependent on the assumption (not explicitly stated) that reaction 1 is entirely complete in a time shorter than that required for the first observation of the radicals. Values of k_1 ranging from 200 to 1800 l. mol^{-1} sec^{-1} have been determined.[2,3] Using a reasonable[4] value of 1000 l. mol^{-1} sec^{-1} for k_1 would give a half-life of 14 msec for reaction 1 in the systems depicted in Figures 2–6 of ref 1 where the initial $[H_2O_2]$ (after mixing) is 0.05 *M*. Thus the initiating reaction is only slightly more than half complete at the time of the first observation (~20 msec) and is continuing at a significant rate during almost the whole of the period of observation (~70 msec, or five half-lives). Thus the primary assumption, on which the remaining analysis rests, has manifestly not been met. This invalidates the kinetic treatment used and the conclusions drawn from it. (The same invalid assumption is found in an earlier publication.[4])

To demonstrate that the kinetic analysis and the conclusions drawn from it are inconsistent with the data, a concentration–time profile has been calculated for a system initially (after mixing) 0.005 *M* in Ti(III), 0.05 *M* in H_2O_2, and 0.25 *M* in 2-propanol. The mechanism outlined above and the values of k_1 and k_7 advanced by the authors (1000 and 400 l. mol^{-1} sec^{-1}, respectively) and $k_5 = 1.2 \times 10^9$ l. mol^{-1} sec^{-1} [5] have been used to evaluate $[R_1]$ as a function of time after mixing. The resulting curve, shown in Figure 1, may be compared directly with Figure 3 of ref 1. It is immediately apparent that the rate constants and mechanism claimed by James and Sicilio would require radical concentrations almost four orders of magnitude greater than those actually observed, and radical concentrations *increasing* in magnitude over the first 35 msec of reaction time, whereas this is the period of most rapid concentration decrease in the experimental system.

On the other hand if, as has been previously suggested,[3] the rate of reaction 1 is clearly rate-determining, the absolute magnitudes of the radical concentrations are a function of their subsequent fast reactions but the kinetics of their decrease are simply those of the initiation. Whatever the mechanism(s) of the radical termination, the pseudo-steady-state condition may be represented as

$$\frac{-d[\text{Ti(III)}]}{dt} = k_1[\text{Ti(III)}][H_2O_2] = \frac{-d[R]}{dt}$$

where [R] represents the total concentration of radicals. This would give an apparent first-order decay when $[H_2O_2] \gg [\text{Ti(III)}]$, reducing to a second-order decay when $[H_2O_2] = [\text{Ti(III)}]$, as is observed in the experimental system.[1] The values attributed to k_7 and k_8

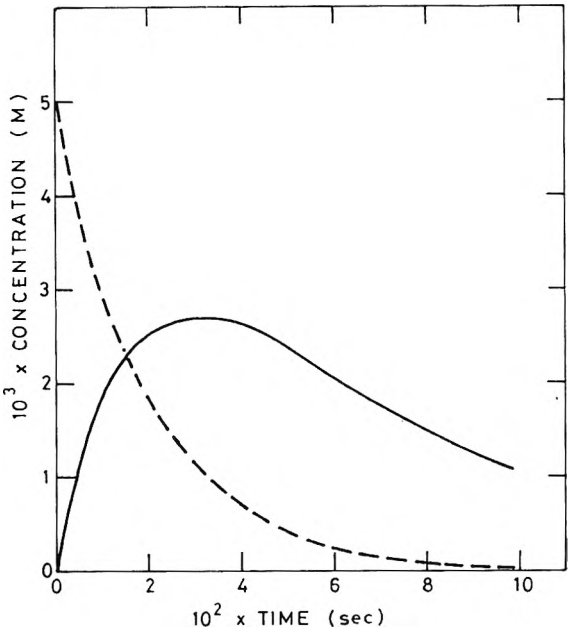

Figure 1. Concentration–time profile for solution 0.005 *M* in Ti(III), 0.05 *M* in H_2O_2, and 0.25 *M* in 2-propanol, calculated from mechanism of ref 1: – – –, [Ti(III)]; —, $[R_1]$.

thus bear no necessary relationship to these reactions but are, in fact, a measure of k_1. More particularly, if it is assumed that the radical termination is by bimolecular reaction, it has been shown[3] that the second-order rate constant calculated from the peroxide-dependent first-order decay constants is simply $k_1/2$. The average of the sum of the second-order rate constants so calculated in Table I of ref 1 is ~650 l. mol^{-1} sec^{-1}, which is in good agreement with the value of 1000 l. mol^{-1} sec^{-1} advanced for k_1. Moreover, substitution of a reasonable value of 4×10^9 l. mol^{-1} sec^{-1} for $2k_{\text{bimolecular}}$ [6] predicts total radical concentrations

(2) B. Chance, *J. Franklin Inst.*, 229, 737 (1940).

(3) R. E. Florin, F. Sicilio, and L. A. Wall, *J. Phys. Chem.*, 72, 3154 (1968).

(4) E. L. Lewis and F. Sicilio, *ibid.*, 73, 2590 (1969).

(5) C. E. Burchill and I. S. Ginns, *Can. J. Chem.*, 48, 1232 (1970).

within an order of magnitude of those displayed in Figures 2 and 3 of ref 1. Thus the assumption of a rate-controlling initiating step and bimolecular radical termination is more consistent with the experimental observations than the mechanism proposed by James and Sicilio.

One difficulty with this alternative mechanism would appear to be the observed relative concentrations of R_1 and R_2. The fraction of R_2 formed initially by OH attack on 2-propanol has been reported to be 0.10 or less.[7] More recent determinations of this fraction from the radiation-induced[5] and photo-induced[8] oxidation of 2-propanol by H_2O_2 give values of 0.14 or somewhat greater. Whatever the precise value, the initial reaction of OH with 2-propanol gives R_1 as the major species, whereas the concentrations of R_1 and R_2 observed by esr as intermediates are nearly equal and, in some instances, $[R_2] > [R_1]$ (see Figures 2 and 3 of ref 1). While a quantitative treatment would be difficult these observations may be qualitatively reconciled by recognizing that the concentrations observed in the esr experiment are steady-state values maintained in a dynamic system. If termination is by *nonselective* bimolecular reactions this would tend to equalize the concentrations of the radicals to some extent although it would be unlikely to reduce $[R_1]$ to less than $[R_2]$. This concentration inversion can, however, be explained by the different reactivities of R_1 and R_2 toward H_2O_2. It has been demonstrated[7] that R_2 is much less effective than R_1 as a reducing agent and it has been proposed[9] that R_2 reacts much more slowly with H_2O_2 than R_1. The kinetics of the radiation-induced oxidation of 2-propanol by H_2O_2 in aqueous solution have been explained[5] on the basis that *only* R_1 reacts with H_2O_2 in the chain propagating step (7a) while R_2 does not react in this manner. The OH pro-

$$R_1 + H_2O_2 \longrightarrow \text{acetone} + H_2O + OH \qquad (7a)$$

duced in reaction 7a may then react with 2-propanol to give either R_1 *or* R_2. If there is a significant chain reaction this sequence can readily give rise to concentrations of R_2 greater than R_1. (It is a corollary of the mechanism proposed for the radiation-induced oxidation of 2-propanol by H_2O_2 that, at the dose rates employed, the steady-state concentration of R_2 is much greater than that of R_1.) It should be noted particularly that this effect would depend upon the chain length. At high rates of initiation the kinetic chain length would be short and this effect would be small but would increase in significance with reduced rate of initiation. Comparing Figures 2 and 3 of ref 1 it may be seen that in Figure 2, which represents the smaller initial concentration of Ti(III) (and hence a lower rate of initiation at any particular time), $[R_2]$ is greater than $[R_1]$ at all observable times. In Figure 3, where the rate of initiation is greater, the concentration of R_2 becomes greater than that of R_1 only after the reaction is partly complete and the rate of initiation has thus decreased.

The occurrence of the chain reaction involving reaction 7a has been discounted by James and Sicilio, in part on the basis of the titration experiments described in Table III of ref 1. However, the conditions used in these experiments were such that, in the majority of cases, Ti(III) and H_2O_2 were present in the ratio required by the stoichiometry of reaction 1 thus leaving little or no H_2O_2 as oxidant for the chain reaction. Under these conditions it is not surprising that only a small yield of acetone was obtained.

Finally, the authors have attempted to account for their anomalous values of k_7, k_8, and k_9, and for the claimed lack of reactivity of the OH from reaction 7a by suggesting that the radicals are complexed to Ti(IV) and hence unreactive. They present no experimental evidence to support such a suggestion and, in fact, the esr spectra of the organic radicals are identical with those observed in a system with no metal ions,[10] whereas the formation of such a complex might reasonably be expected to modify the spectrum of the radical. To determine the effect of Ti(IV) on the free-radical chain reaction of H_2O_2 and 2-propanol a series of deaerated aqueous solutions 0.5 *M* in 2-propanol and 0.05 *M* in H_2O_2 was γ-irradiated to initiate reaction. As demonstrated in Table I, the addition of 0.005 *M* Ti(IV) introduced only a small, and possibly no significant, inhibition of the chain reaction—certainly far less than that implied by James and Sicilio.

Table I: *G* values for the Radiation-Induced Oxidation of 2-Propanol by H_2O_2 in Deaerated Aqueous Solution[a]

Conditions	*G*(acetone)
Neutral solution	54.8 ± 2.0
0.02 *M* H_2SO_4	55.6 ± 2.0
0.02 *M* H_2SO_4, 0.005 *M* Ti(IV)	48.7 ± 2.0

[a] [2-propanol] = 0.5 *M*, $[H_2O_2]$ = 0.05 *M*, dose rate = 1.35×10^{19} eV $l.^{-1}$ sec^{-1}.

It is suggested, therefore, that there are no anomalous rate constants or novel radical complexes in the system aqueous Ti(III)–H_2O_2–2-propanol, providing [2-pro-

(6) M. Simic, P. Neta, and E. Hayon, *J. Phys. Chem.*, **73**, 3794 (1969).

(7) G. E. Adams and R. L. Willson, *Trans. Faraday Soc.*, **65**, 2981 (1969).

(8) C. E. Burchill and P. G. Huminicki, unpublished results.

(9) R. O. C. Norman and P. R. West, *J. Chem. Soc. B*, 389 (1969).

(10) R. Livingston and H. Zeldes, *J. Amer. Chem. Soc.*, **88**, 4333 (1966).

panol] is sufficiently large to preclude attack on H_2O_2 by OH. The time dependence of the total radical concentration is consistent with reaction 1 being clearly rate determining, with $k_1 \sim 1000$ l. mol^{-1} sec^{-1}, and with radical termination occurring by bimolecular processes with normal velocity constants. The time dependence (or concentration dependence) of the relative concentrations of R_1 and R_2 may be explained on the basis of their differing reactivities toward H_2O_2, with only R_1 undergoing the chain propagating reaction.

Acknowledgment. Research support during the period of preparation of this communication was provided by the National Research Council of Canada. The useful comments by the referees are gratefully acknowledged.

DEPARTMENT OF CHEMISTRY
UNIVERSITY OF MANITOBA
WINNIPEG 19, CANADA

C. E. BURCHILL

RECEIVED AUGUST 26, 1970

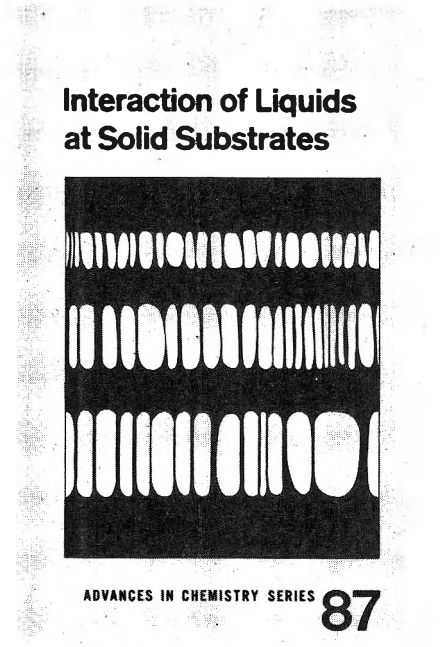

INTERACTION OF LIQUIDS AT SOLID SUBSTRATES

ADVANCES IN CHEMISTRY SERIES NO. 87

Papers from two symposia by the Division of Organic Coatings and Plastics Chemistry of the American Chemical Society.

This volume includes twelve papers comprising the symposium on "The Interaction of Liquids at Solid Substrates," chaired by Allen L. Alexander. These papers include work on "coupling agents," adhesion of polymers, organic/inorganic interfaces, and ultrasonic impedometry. Also included are four papers concerned with heparinized surfaces at the blood/material interface which were part of the symposium on "The Medical Applications of Plastics," chaired by R. I. Leininger.

212 pages with index Cloth (1968) $9.50

Free set of L. C. cards with library orders upon request.

Other books in the **ADVANCES IN CHEMISTRY SERIES** in colloid chemistry include:

No. 86 Pesticidal Formulations Research: Physical and Colloidal Chemicals Aspects. Fifteen papers survey contact angle of surface active agents, transport through a membrane, vapor pressure of pesticides, role of surfactants in sprays, biological activity, evaporation, spray formation and drift, and several studies on specific pests and pesticides.
212 pages Cloth (1969) $9.50

No. 84 Molecular Association in Biological and Related Systems. Nineteen articles survey and report new work on molecular association in fat digestion, in soap systems, in membrane constituents, and in mixed monolayers and membranes, include bile salt micelles, lipid monolayers and membranes, and a definitive review of biological membrane structure.
308 pages Cloth (1963) $10.50

No. 79 Adsorption from Aqueous Solution. Fifteen papers discuss thermodynamic and kinetic aspects of adsorption phenomena and the results of studies on a variety of adsorbate-adsorbent systems.
212 pages Cloth (1968) $10.00

No. 63 Ordered Fluids and Liquid Crystals. Twenty-two studies on characterization, properties, and occurrence of these phenomena in many substances such as tristearin, *p*-azoxyanisole, mono- and di-hydric alcohols, phospholipids, and polypeptides.
332 pages Cloth (1967) $11.50

No. 43 Contact Angle, Wettability, and Adhesion. Surface chemistry studies. Relation of equilibrium contact angle to liquid and solid construction, contact angle as a thermodynamic property, surface energy estimation from contact angle. Contact angle hysteresis, relationship between wetting and adhesion.
389 pages Cloth (1964) $10.50

No. 33 Solid Surfaces and the Gas-Solid Interface. Thirty-seven papers from the Kendall Award Symposium honoring Stephen Brunauer. Theory and techniques for studying surface phenomena.
381 pages Cloth (1961) $12.00

No. 25 Physical Functions of Hydrocolloids. Treats six broad physical functions-production of viscosity or body, gelatin, stabilization of emulsions, stabilization of suspensions, stabilization of foams, control of crystal growth—with emphasis on food applications.
103 pages Paper (1960) $5.00

No. 11 Natural Plant Hydrocolloids. The protective colloids or stabilizers, including calcium pectinate, agar, gum arabic, gum karaya, tragacanth, locust bean gum, alginates, Irish moss, and red seaweed.
103 pages Paper (1954) $5.00

All books postpaid in U.S. and Canada; plus 30 cents in PUAS and elsewhere.

Order from:

SPECIAL ISSUES SALES
AMERICAN CHEMICAL SOCIETY
1155 SIXTEENTH ST., N.W.
WASHINGTON, D.C. 20036

FUEL CELL SYSTEMS—II

ADVANCES IN CHEMISTRY SERIES NO. 90

Thirty-one papers from the fifth of the biennial Fuel Cell Symposia sponsored by the Division of Fuel Chemistry, chaired by Bernard S. Baker. Topics include:

- **fuel cell power systems**
- **electrode structure**
- **use of hydrocarbons**
- **electrode catalysis and mechanisms**
- **high temperature fuel cells**
- **fuel cell systems**

Fuel cells are still doing their job well in the space program. Total energy, stationary fuel cell power plants seem worth a commercial push, and some hybrid devices look promising.

456 pages with index Cloth bound (1969) $17.50

Free set of L. C. cards with library orders upon request

Other books in the ADVANCES IN CHEMISTRY SERIES in fuel chemistry include:

No. 80 Chemical Reactions in Electrical Discharges. A wide range of topics is covered in 37 papers by chemists, physicists, and engineers—treatments of decomposition and dissociation reactions, ion-molecule reactions, chemical syntheses, and chemical engineering aspects and physics of reactions in electrical discharges. 514 pages
Cloth (1969) $15.00

No. 78 Literature of Chemical Technology. Forty articles discuss the literature of many aspects of chemical technology; seven of these are related to fuel cells, including electrochemistry of non-metals, noble metals, ceramics, enamels and glass, refractories, resources for petroleum chemicals, rocket propulsion, and rocket construction materials. 732 pages
Cloth (1968) $17.50

No. 69 Fuel Gasification. Waning natural gas supplies and the threat of nuclear fuels are renewing interest in converting solid fuels to high B.t.u. gas. Sixteen studies survey current research in the U.S. and elsewhere from which commercial processes seem imminent. 276 pages
Cloth (1967) $10.50

No. 64 Regenerative EMF Cells. Seventeen papers survey current progress and research on regenerative systems for converting and storing electrical energy. Principal emphasis is on thermally regenerative systems, but chemical and photochemical systems are considered. 309 pages
Cloth (1967) $11.00

No. 55 Coal Science. Forty-seven papers include coal origins, coal metamorphosis, coal as an organic rock, physical and chemical structure of coals, reactivity and reactions of coal in relation to structure and rank. 743 pages
Cloth (1966) $17.50

No. 54 Advanced Propellant Chemistry. Primarily directed toward the search for new oxidizers. Topics include theoretical approaches to advanced oxidizers, surveys of oxygen- and fluorine-containing oxidizers, fuels and binders, liquid systems. 290 pages
Cloth (1966) $10.50

No. 47 Fuel Cell Systems. New systems for the energy converter proving itself in military and space uses. Topics include fuel cells for submarines and satellites, hydrogen-bromine fuel cells, molten carbonate fuel cells, and a coal burning fuel-cell power plant. 360 pages
Cloth (1965) $10.50

No. 20 Literature of the Combustion of Petroleum. Twenty-one papers about the chemistry and kinetics of combustion, petroleum products as the fuel for engines, and combustion studies in engines. 295 pages
Paper (1958) $8.00

No. 5 Progress in Petroleum Technology. Survey of 25 years of progress at the ACS Diamond Jubilee. Thirty-two papers on all aspects of petroleum processing and products. 392 pages
Paper (1951) $8.00

Postpaid in U.S. and Canada; plus 30 cents elsewhere.

Order from:

SPECIAL ISSUES SALES
AMERICAN CHEMICAL SOCIETY
1155 SIXTEENTH ST., N.W.
WASHINGTON, D.C. 20036